School Engineering and Material Sciences
Queen Mary University of London

Numerical investigation of the effects of free-surface flow past submerged bluff and streamlined bodies

Zaheer Ikram

A thesis submitted for the of Degree of Doctor of Philosophy
at the University of London

2012

I certify that this thesis, and the research to which it refers, are the product of my own work, and that any ideas or quotations from the work of other people, published or otherwise, are fully acknowledged in accordance with the standard referencing practices of the discipline.

Signed: _____

Zaheer Ikram

To my parents,

To whom I dedicate this work

Abstract

The last decade has been marked by a continuous growth in computational power, which has allowed for elaborate modelling techniques like LES and DES applied at engineering scales which generally imply a Reynolds number in excess of 1×10^6. One field that has seen a rapid growth in use of numerical methods in design and performance analysis is the navel sector, especially in the design of submarines where the free-surface boundary plays an important role.

This thesis is devoted to the study of free-surface flow past submerged bodies, with the objective of numerically studying free-surface flow past a submarine fairwater at periscope depth near actual operating conditions. This work is motivated by DSTL, who have reported that near periscope depth submarines exhibit an increased drag (private communication). In this work both LES and DES modelling approaches are also utilized, while the submerged body is accounted through the use of an immersed boundary method and the free-surface is through the use of a part moving mesh.

The thesis is split in two main parts. The first part of the thesis focuses on low and moderate Reynolds number flow about a submerged cube (bluff body) for various submergence depths. Two configurations are examined one being that of a single cube in a uniform flow, while the other is that of a matrix of equally spaced cubes. Results show that for both cases a reduction in submergence depth causes the forces, the fluctuation in the forces and shedding frequencies to alter, while the level of interaction between vortices and free-surface to increase.

The second part of this thesis focuses on the main study of free-surface flow past a submerged fairwater at a high and near operating Reynolds number. It is found that for both Reynolds numbers the flow behaviour shows little change, while the effects of

reducing submergence depth results in the forces, the force variation and shedding frequency to increase. Surface waves are found to disperse by an angle of up to 40° for all submergence depth and are of the Kelvin wave kind. No direct interaction between vortical structures shed from the fairwater and free-surface are found, whilst the increases in forces acting on the fairwater are directly attributed due to wave motion.

.

Acknowledgements

I would like to express my sincere appreciation to my supervisors Prof. John Williams and Dr. Eldad Avital, for their continuous guidance, advice, support and last but not the least, their transfer of knowledge.

I would I thank too the other members of staff who have contributed with their help and support, in particular Dr. Guangxu Yu, Dr. Tseng Yu, Dr. Christopher Walker, Mr Raymond Lam and Mr Alem Million.

I also thank all my colleagues in 374, in particular Dr. Oluwamayokun Adetoro, Dr. Chetan Jagadeesh, Dr Reza Hosseini, Mr. Jerome Irianto, Mr Hasan Ali, Ms Pilar Garcia and Ms Vasana Don for their assistance and for providing a pleasant working environment.

Finally, I am most thankful to my entire family, for their sacrifice, continuous support and understanding during the course of this study.

This research has been jointly funded by DSTL and the Engineering and Physical Sciences Research Council (EPSRC).

Table of Contents

Table of Figures

Table of Tables

List of Acronyms

Roman Symbols

$\boldsymbol{a}$	–	amplitude of wave	f_{v1}	–	viscous damping function
$\boldsymbol{a^{cf}}$	–	area of cell face	$\boldsymbol{g}$	–	gravity
$\boldsymbol{c}$	–	wave speed/celerity	G_{ν}	–	production of turbulent viscosity
$\boldsymbol{C_{des}}$		Spalart-Allmaras model coefficient	h	–	cube height
$\boldsymbol{C_{ij}}$	–	cross-stress tensor	$\boldsymbol{h_0}$	–	zero wave height of fluid
$\boldsymbol{C_s}$	–	Smagorinsky model constant	ij	–	directional and component subscripts
c_{α}	–	cosine of angle from y-plane	l	–	length
c_{β}	–	cosine of angle from z-plane	$\boldsymbol{L}$	–	wave length
c_{θ}	–	cosine of angle from x-plane	l_c	–	chord length
d	–	total submergence depth	L_c	–	characteristic length
d/h		submergence depth normalised to cube height	$\boldsymbol{L_T}$	–	large-eddy turnover time (letot)
d/ l_c	–	submergence depth normalised to chord length	l^*	–	non-dimensional length
$\boldsymbol{d_{lc}}$	–	local distance	$\dot{m}^{cf}$	–	flux through cell face
f_i	–	forcing value	$\boldsymbol{n}$		normal vector
f_x	–	linear interpolation to face	Q	–	iso-surface identification of Vortex structure

$\boldsymbol{R}$	–	wave run-up height	u_{ij}^{+}	–	non-dimensional velocity
$\mathrm{Re_{lc}}$	–	Reynolds number based on chord length	u^{*}	–	non-dimensional velocity
$\mathrm{Re_{mc}}$	–	Reynolds number for multiple cube	$\boldsymbol{U^{*}}$	–	shear velocity
$\mathrm{Re_{sc}}$	–	Reynolds number for single cube	U_i^r		resolved/filtered part of the velocity
S, $\mathrm{S_{ij}}$	–	symmetrical part of the velocity gradient / Strain tensor	v_b	–	grid velocity
$\boldsymbol{t}$	–	time	w_{stp}	–	wave steepness
$\boldsymbol{T}$	–	non-dimensional wave time	$\boldsymbol{y}$	–	vertical displacement
$\overline{T}$	–	normalised time by wave speed	Y_v	–	destruction of turbulent viscosity
t^{*}	–	non dimensional time	$\mathrm{z_n}$	–	free-surface nodal height
U_0	–	reference velocity	$\boldsymbol{z_n^{ref}}$	–	free-surface nodal height for reference wave
u_{ij}	–	velocity	z^{+}	–	non dimensional wall normal distance
u_{in}^{cf}	–	velocity at cell face on in flow boundary	$\overline{}$	–	filtered
$\overline{u_i}$	–	filtered velocity component	<.....>	–	time averaged
u’	–	velocity fluctuation	$'$	–	fluctuation
$\mathrm{u_i'u_j'}$	–	Reynolds stresses normal components for i=j	$\int_s$	–	surface/double integral
$\mathrm{u_i'u_j'}$	–	Reynolds stresses cross components for i≠j	$\int_v$	–	volume/triple integral

Greek Symbols

β_m	–	normalised variable limiter	Γ_{eff}	–	effective damping
γ	–	gamma blending factor	Δ_x	–	cell distance in x-direction
Γ_{d}	–	wall damping	Δ_y	–	cell distance in y-direction

Δ_z	–	cell distance in z-direction	τ_{ij}^{sg}	–	sub-gird shear stress
Δy	–	grid spacing in spanwise direction	$\tau_p(x,y)$	–	wall shear stress
Δz	–	grid spacing in vertical direction	$\boldsymbol{\nu_t}$	–	eddy viscosity
Δ	–	effective length/filter width	$\tilde{\nu}$	–	transport variable
Δx	–	grid spacing in streamwise direction	ϕ_f	–	face variable
ε	–	dissipation	ϕ_d	–	downstream variable
ε_{rr}	–	average error	ϕ_u	–	upstream variable
η	–	wave height	$\tilde{\phi}_d$	–	normalised downstream variable
μ	–	fluid viscosity	$\tilde{\phi}_u$	–	normalised upstream variable
Ω, Ω_{ij}	–	vorticity tensor	$\tilde{\phi}_c$	–	normalised centre variable
$\tilde{\nu}$	–	transport variable	ϕ	–	variable
$\boldsymbol{\nu_t}$	–	eddy viscosity	χ	–	approximate non-dimensional wall distance
ρ	–	density			

Abbreviations

AFF-1	–	SUBOFF bare hull	DKT	–	variation in time of turbulent kinetic energy
AFF-3	–	SUBOFF hull with stern appendages	DNS	–	direct numerical Simulation
AFF-8	–	SUBOFF hull with stern and fairwater appendages	DS	–	direct simulation
CD –	–	central differencing	FL	–	flux limiting
CFL	–	Courant Finchley Lewis number	Fr	–	Froude number
CV	–	convection of turbulent kinetic energy	Fst	–	fontal stagnation height
DES	–	detached eddy simulation	GPR	–	production of turbulent kinetic energy

Hscx	–	position of horse-shoe vortex centre in streamwise direction
Hscy	–	position of horse-shoe vortex centre in vertical direction
Hsh	–	horse-shoe vortex height
HSV	–	horse-shoe vortex
IB	–	immersed boundary
IBM	–	immersed boundary method
IOR	–	inter-obstacle region
KE	–	kinetic energy
LES	–	large eddy simulation
LUD	–	linear upwinding difference
NFL	–	without flux limiting
NS	–	Navier-Stokes
NSE	–	Navier-Stokes equation
NVD	–	normalised variable diagram
ONR Body-1	–	submarine configuration
PDF	–	pressure diffusion of turbulent kinetic energy
PE	–	potential energy
PST	–	pressure straining of turbulent kinetic energy
PVC	–	parallel code version
RANS	–	Reynolds averaged Navier-Stokes
Rcl	–	rear circulation length
Rcx	–	position of rear circulation vortex in the streamwise direction
Rcy	–	position of rear circulation vortex in vertical direction
Re	–	Reynolds number
RHS_i	–	remaining terms of the momentum equation
RK3	–	third order Runge-Kutta
Rsh	–	rear separation height
SA	–	Spalart-Allmaras
SAM	–	Spalart-Allmaras model
SBD	–	submergence depth
SG	–	sub-grid
SGM	–	sub-grid model
St	–	Strouhal number
TDF	–	turbulent diffusion of turbulent kinetic energy
TE	–	total energy
TKE	–	turbulent kinetic energy
TKEB	–	turbulent kinetic energy budget
Tsh	–	upper separation height
Tsl	–	upper separation length
TVD	–	total variation diminishing
UD	–	upwind differencing
VDF	–	viscous diffusion of turbulent kinetic energy

VS	–	vortical Structure
XY	–	plane view in the streamwise and spanwise directions
XZ	–	plane view in the streamwise and vertical directions

Chapter 1 Introduction

The study of free-surface flows has interested scientist and engineers for quite some time. Some of the earliest work in attempting to understand free-surface flows with and without body interaction dates back as far as Leonardo da vinci (1452 -1519). A dimensionless relationship that exists for free-surface boundaries that relates the fluids inertia to restorative force of gravity is the Froude number $f_r = \frac{u}{\sqrt{gh}}$. It is important in the classification of the state and behaviour of water i.e. if the fluid would undergo a hydraulic jump. Much of the early work had concentrated on producing inviscid and laminar solutions as well as trying to obtain valid measurements. It was not until the late 1970's (more specifically the last two and a half decades), that the exact behaviour and dynamics of viscous free-surface flows has received considerable interest. A common field of investigation for both engineers and scientists has been the understanding of gas transfer between the ocean and atmosphere - highly important for understanding the process of global warming. Moreover, in terms of an engineering context; civil, coastal and naval disciplines have also extensively studied free-surface flows.

Also, from the mid 1970's onwards computer capabilities have seen a constant improvement in performance and capacity. This increase in computing capabilities and extensive work into turbulence theories, had seen the use of computer based simulation become a more utilized tool in research. Prior to this, experimental means had been the most prominent method of research. Today, both experimental and computational methods are being used to extensively study many practical problems, including free-surface flows and related processes.

Vaguely put, most of the research conducted in the context of viscous free-surface flows can be organized into the following categories;

i) The effect of a free-surface on grid generated isotropic turbulence.
ii) Turbulence near the free-surface.
iii) The interaction between coherent structures and the free-surface.
iv) Interaction between submerged obstruction and/or shear flow with a free-surface.
v) Flow structure and wave profiles around surface piercing bodies.

Due to these varied aspects, a large amount of literature has been compiled. Various fields of work are reviewed to provide the reader with some detailed insight into the effects of free-surface flows and why they are of great interest. The literature reviewed is sub-divided into the following sections; i) Statistical aspects; ii) Coherent structures; iii) Effects of submergence; iv) Complex geometries and simplified cases. Figure 1.1 provides a road map for the current chapter. This chapter is then concluded by providing the motivations that have prompted this research and the achievements made.

1.1 Statistical Description

For a long time, turbulent flow had presented researchers with a difficulty in obtaining a viable description for any given study. A result owed due to the formation and stretching of eddies, producing an apparent unsteadiness and random behaviour within the flow. This consequently resulted in the development of statistical techniques for use with turbulent flows to provide consistent and repeatable numerical descriptions. For example, typical approaches used to describe turbulent flow include time averaged velocity (through dimensional scaling) and intensity distributions, as well as energy spectra and two-point correlation analysis.

1.1.1 Experimental measurements

Early work on turbulent flows includes that by Nikuradse (1929) and Reichardt (1938), who were amongst the first to experimentally study fully developed turbulent channel flow. Nikuradse's measurements focused on average-velocity distributions, while Reichardt focused on measuring the fluctuations in both the streamwise and wall normal

directions. However it was not until the work of Laufer (1951) that detailed turbulence statistics for fully developed channel flow were documented. Moreover, it was in the latter half of the 1950s that researchers succeeded in making measurements in open-channel flows. Ippen & Raichlen (1957) were the first to perform measurements in open channel flow measuring only the stream wise velocity distribution using a total pressure tube. Later, McQuivey & Richardson (1969) provided more accurate measurements for both the streamwise and vertical velocity distributions using a hot-film.

Much of the early measurements made using pitot tubes indicated a difference between open channel flow in comparison to boundary layer flow. The log-law was thought to apply from the bed to the free-surface, often a proper fit could be achieved by variation of the von karman constant κ and integral constant A [Nezu & Nakagawa (1993)]. Later disproved through the use of more advanced, highly sensitive and accurate measurement devices; it was shown that very close to the wall the velocity variation is linear with the log-law applicable across the remaining depth. Experimental studies of Nezu & Rodi (1986) on the log-law distribution in open channel flow showed that the velocity does in fact systematically deviate from the log-law in the outer near-surface region with increasing Reynolds number. Nezu and Rodi found that like boundary layers the Coles wake parameter could be used to correct for this deviation (Figure 1.2). Some of the initial works and measurements reported for turbulent free-surface flows are listed in Table 1.1, a more thorough review of early measurements can be found in Nezu & Nakagawa (1993).

Authors (year)	Measured	Re	Fr	Examined
Ippen & Raichlen (1957)	u	5.0 x10^4	3-4	Auto-correlation for flow over smooth beds using a total tube
Mc Quivey & Richardson (1969)	u v	0.7 x10^4, 1.2 x10^4	0.4, 0.6	Energy Spectrum and velocity distribution using a single channel yawed hot-film
Eckelmann (1974)	u v	0.56 x10^4, 0.82 x10^4	Oil flow	u',v', sublayer for a smooth bed with a 2 channel Hot-film
Nakagawa & Nezu (1979)	u v w	1.2 x10^4	0.17-0.6	Suction & injection over a smooth bed with a 2 channel Hot-film
Nakagawa & Nezu (1981)	u v	1.1 x10^4	0.16	Bursting, space-time correlations for a smooth bed with a 2x2 channel Hot-film
Nezu & Rodi (1986)	u v w	0.6 x10^4 – 11.0 x10^4	0.7-1.2	High accuracy measurements of u',v',U for smooth beds with a 2 channel LDV

Table 1.1: Early experimental work in open channel turbulence

Similarly, the analysis of turbulent concentration, through examining turbulent intensities has shown that the free-surface boundary does exhibit in a change in the turbulence distribution close to the free-surface. Smutek (1969) was among the first to obtain intensity measurements over rough and smooth beds. Though only measuring the horizontal and vertical components, Smutek was able to conclude that the free-surface has a damping effect on the vertical turbulence preventing the flow from reaching a homogeneous state in comparison to channel flow at about half width. It was not until the experiments by Komori et al. (1982) who, using laser doppler anemometry (LDA), showed that the vertical intensities are damped, the streamwise and spanwise intensities are enhanced (relative to a closed channel). Typical distribution of turbulent intensity in open channel flow compared to that of closed channel flow is shown in Figure 1.3.

It should be noted that Komori et al. (1982) were not the first to make turbulent intensities using LDA. In fact, it was Nakagawa *et al* (1975) who examined free-surface flow over both rough and smooth beds with LDA. Furthermore, Nakagawa et al's study also examined the energy transfer occurring in turbulent open channel flow. Their

experiments showed that irrespective of roughness, free-surface flow was similar to wall turbulence showing three distinct regions. The regions were characterised based upon different levels of turbulent energy production (P) and dissipation (ε). An initial region was identified near the wall, this corresponds to the 'inner layer' of a boundary layer and was classed on the bases of the production (P) exceeding the dissipation rate (ε) – a result contributable to the bursting phenomenon. In contrast, near the free-surface region it was found that the dissipation rate (ε) exceeded the rate of the production (P) of turbulent energy. However, between these two extremes existed a region where there was a dynamically equilibrium state for the turbulent energy budget (i.e. balance between production (P) and dissipation (ε)). This behaviour is comparable to Tennekes & Lumley (1972) analogy between spatial and spectral structures of wall turbulence at high Reynolds numbers where again three distinct regions exist (Figure 1.4).

1.1.2 Computers and Turbulence

Prior to the development of LDA and particle image velocimetry (PIV) much of the early measured data obtained near boundaries were in poor agreement [Nezu & Nakagawa (1993)]. Therefore, an alternative method was sought after for verifying and providing more detailed data near boundaries and led to the use of numerical simulations in studying turbulent flows. In fact, all of the early numerical studies for turbulent channel and open-channel flows (from literature reviewed) were performed using direct numerical simulations (DNS), in which the Navier-Stokes equations are solved for all scales down to the Kolmogorov length scale. Such work includes that by Kim *et al* (1987), whom carried out a DNS of fully developed turbulent channel flow at a low Reynolds number of 3300, with the aim of providing a better understanding of the near wall behaviour. In addition, their data formed a database allowing for development and improvement in already existing turbulence models. Statistical data from their study compared well with those obtained via experimental means, with the largest discrepancies concentrating in the near wall region. Kim et al attributed the discrepancies to uncertainties in the measuring of data in the near wall region. For example, renormalisation of experimentally obtained mean velocity and turbulent intensity data with a corrected shear velocity (u_τ) yielded better agreement between the computed and reported experimental data, especially in the mean velocity profiles. However, the near wall region, Reynolds stresses and intensity measurements were

consistently lower than experimental values. Possible reasons for this were given as cross-contamination and heat conduction problems of hot-films in near wall measurements.

In terms of fully developed turbulent free-surface flows Komori *et al* (1993) showed using DNS that near the interface/free-surface turbulence in the vertical direction is indeed redistributed in to the streamwise and spanwise directions, aiding in the validity of Komori et al. (1982) experimental findings. This is important, as it is very difficult to experimentally obtain measurements near the free-surface due to the boundary being free to deform without the risk of obtaining contaminated results. Other works that have statistically studied free-surface flows includes that by Lombardi *et al* (1996) who performed a DNS study of flow about an undisturbed air/water interface. They concluded that statistically the flow is significantly altered in the near interface region in comparison to the near wall region due the presence and interaction of vortex structures. Furthermore, vortical structures were noted to drastically change the Reynolds stress distribution close to the interface, with stress being higher on the fluid side compared to the air side, even though structures existed across the interface.

Handler *et al* (1993) also used DNS to study the structure of turbulence near the free-surface and its relation to energy redistribution. Analysis of dissipation rates in the streamwise, spanwise and vertical directions showed that near the free-surface dissipation rates in both streamwise and spanwise directions exhibited a sharp drop in magnitude, whilst in the vertical direction the dissipation rate showed a slight increase. Furthermore, length scale analysis revealed that close to the free-surface a significant flatting of eddies occurs, with the greatest stretching of eddies being in the spanwise direction. From an energy balance point of view, Handler et al. concluded that the key contributor for the stretching of eddies and consequently redistribution of energy occurred through pressure-straining. It was therefore concluded that the presence of a free-surface produces a damping effect on the vertical scales resulting in the redistribution of energy.

On the whole, experimental, theoretical and numerical studies have all contributed to a better understanding into some of the mechanisms controlling turbulence, energy transfer and its distribution in a variety of different flow situations, in addition to the effects of various boundary types. This has consequently allowed for the development

of more effective turbulence models and subgrid scale models allowing for less computer intensive approaches to be applied to flows with much higher Reynolds numbers. Such work includes that by Piomelli & Zang (1991) who showed that when modelling transitional flows, existing models at the time (which were of the eddy viscosity type – only dissipate energy) performed poorly. They contributed the poor performance due to the fact that in transitional flows back-scattering (energy transfer to large scales from small scales) plays a prominent role, even though models of the eddy viscosity type had been successfully applied to fully developed turbulent flows where the backscattering of energy also occurs.

Therefore, works such as that by Piomelli & Zang have led to the development of models which better allow for energy transfer. Similarly, work by Shen et al. (2000) and Shen and Yue (2001) have shown that in order for models to exhibit appropriate free-surface signatures and dissipation rates, factors such as; the variation of the eddy viscosity in the surface layer, the anisotropic nature of free-surface turbulence, and energy backscatter on coherent vortex structures needs to be considered.

Consequently, this has allowed for less computer intensive methods such as large-eddy simulation (LES) and Reynolds Averaged Navier-Stokes (RANS) to be used in various applications, producing results comparable to both experimental and direct numerical simulations (DNS). Such work includes that of Thomas *et al* (1994), Li & Wang (2000) and Wang *et al* (2005) who have used LES to simulate free-surface flows, while Venayagamoorthy *et al* (2003), Leupi & Altinakar (2005) and Meselhe *et al* (1995) have used the RANS approach to study free-surface flows.

1.2 Coherent Structures

Another prominent feature of turbulent flow is the presence and persistence of regularly repeating distinguishable structures, amongst a seemingly chaotic fluid motion. It is worth noting that the idea of coherent structures is not relatively new, for example, puffs in transitional pipe flow were observed and emphasized by Reynolds in 1883. Though, smoke screening and dye injection techniques have been used extensively in the past to study near field coherent structures such as jets and wakes. It was not until the pioneering work of Hama [Hama & Nutant (1963)], who devised the hydrogen bubble technique for the visualisation of the sub-layer, that the existence of coherent structures

existing in the boundary layer was recognised (low-speed streaks). Later Kline *et al* (1967) using the same approach recognized the significance of quasi-deterministic and quasi-periodic coherent structures in fully developed turbulent shear flow. Hussain (1983) in his review paper entitled 'coherent structures – myth or reality' provides a well-documented review of the earlier work.

1.2.1 Coherent Structures within a Boundary Layer

Much of the early work in identifying coherent structures after Hama devised the hydrogen bubble technique concentrated on examining structures that existed within turbulent boundary layer flow. The understanding of coherent structures within turbulent boundary layers (TBL) was viewed important because they provided the mechanism for the sustenance of unsteadiness and mixing with the surrounding flow, typically resulting in an increased skin friction drag. Researchers such as Hinze (1975) noted the existence of somewhat cyclic occurrences of bursting events occurring within a TBL, and proposed a conceptual model for the observed cycles and their effect on the local velocity profile (Figure 1.5). Another review of coherent motions and structures existing within the context of TBL flow was carried out by Robinson (1991) and provided an in-depth review of proposed concepts and findings today - 1991. Robinson stated:

'In general what is observed in a turbulent boundary layer is strongly dependent upon the tools used to make the observation.'

As a result a wide variety of structures had been reported, i.e. hockey stick and hairpin type vortices. Although, the type of structures did differ between the many studies conducted, Robinson was able to note the better known features consistent in all works these included:

1. The formation of low-speed streaks in the viscous sublayer.
2. Ejection of low-speed fluid outward from the wall, including the lifting of low-speed streaks.
3. Sweeps of high-speed fluid inward towards the wall, including inrushes from the outer region.
4. Vortical structures of various forms.

In terms of the different forms of coherent structures existing within different portions of a boundary layer, Robinson (1990) proposed an idealised schematic based on

population analysis (Figure 1.6). In this model, the viscous sub-layer is dominated by quasi-streamwise vortical structures and the outer wake region by arch like vortices. Whilst in the logarithmic region, both arches and quasi-streamwise vortices exist, often as elements of the same vortical structure. Though the model appears simple, it provides a rough idea of what structures exist and dominate in different portions of a boundary layer. In addition it also highlights possible interactions and influences that may exist.

1.2.2 Interaction between Coherent Structures & the Free-surface

Coherent structures existing in free-surface flows and their interaction with the surface boundary have been greatly studied over the last two and a half decades for reasons previously stated. Komori (1989) experimentally studied the relationship between bursts emanating from the wall region to the appearance of surface renewal patches. Their work was motivated by the observations of Jackson (1976), which stated that the frequency of surface renewal eddies maybe almost proportional to the frequency of bursting motions. Komori et al used a procedure of injecting methylene-blue in to the buffer layer to trace bursting events and used an optical probe positioned above the free-surface to detect and measure surface renewal eddies and the concentration of methylene-blue convected by a bursting event. The experimental were conducted for Reynolds numbers (based on hydraulic radius) and Froude numbers ranging from 9800 to 33700 and 0.1 to 0.71, respectively. Komori (1989) concluded that the correlation between the frequency of bursting events and the appearance of surface renewal events was high - up to 90 per cent of all ejected eddies generated during bursts become surface renewal eddies over the investigated range. In addition, Komori et al. concluded the rate of appearance of new structures at the free-surface were responsible for effecting mass transfer across the surface boundary.

Although, Kline et al. (1971) did observe and recognise the importance of low-speed streaks in wall boundary layers, it was not until the work by Rashidi & Banerjee (1990) that the existence of low-speed streaks near an sheared interface was discovered. Prior to this, low-speed streaks were considered a feature of flow past solid boundaries. However, Rashidi and Banerjee experimentally observed that low speed streaks were in fact not confined to the wall region as previously assumed, but also occur near a sheared gas liquid interface. Although the two boundaries act very differently on the flow, they both allow the formation of low-speed streaks. Therefore, Rashidi and Banerjee

concluded that the shear rate was the main condition that governed streak formation. Later, Lam & Banerjee (1992) extended the findings of Rashidi & Banerjee (1990) to provide the condition at which streak formation would appear based upon a non-dimensional shear parameter:

$$\frac{S\left|\langle u'w'\rangle\right|}{\varepsilon} = \widetilde{S} \tag{1.1}$$

where S, $u'w'$ and ε, are the mean shear rate, kinematic turbulent shear stress and dissipation rate of the kinematic energy, respectively. According to Lam and Banerjee, the condition at which low speed streaks will begin to occur is; when the turbulent production equals turbulent dissipation, i.e. when the non-dimensional shear parameter was approximately equal to one.

Later, Pan & Banerjee (1995) using DNS studied the evolution of free-surface turbulent structures occurring in open channel flows. In particular, their study was focused on providing a clear account on the formation of impinging vortices with the free-surface (under zero shear) for statistically steady state and freely decaying turbulent flows. It was found that at an unsheared free-surface the orientation of a vortex structure was normal to the free-surface where as in the near wall region they are aligned in the streamwise direction. The change in orientation was explained simply due to the fact that at the free-surface the following conditions must be true:

$$\omega_x = \omega_y = \frac{\partial \omega_z}{\partial z} = 0 \tag{1.2}$$

For statistically steady state turbulence, the most persistent structures identified at the free-surface were coined to be upwellings, downdrafts and spiral eddies. Such structures would exist for long periods of time, unless destroyed by new upwellings appearing on the free-surface. Upwellings are the result of the impingement of ejected eddies emanating from the wall, whilst Pan and Banerjee observed downdrafts to form in regions close to where upwellings interact, causing the flow between them to move outward. If the interaction between upwellings was strong, spiral eddies were commonly observed to form. According to Pan & Banerjee this occurred when stagnation lines were highly bent which indicated regions of high shear. Furthermore, it

was noted that the existence of these structures at or near the free-surface result in an increase in the anisotropy of turbulence at the free-surface. In contrast, when the mechanisms for sustaining the turbulent flow were retracted, giving rise to freely decaying turbulence (i.e. wall is turned from non-slip, to free-slip), upwellings and downdrafts that caused anisotropy near the free-surface began to disappear. Pan & Banerjee attributed this result directly to the turbulent production in the wall layer being halted. The predominate pattern was then found to be long-lived vortices that were attached to the free-surface. The behaviour of these vortices was to either merge or pair dependent upon the sign of their vorticity. Vortices of the same sign merge while those with opposite signs form a pair that is stable, either way both configurations were noted to decay slowly.

Experimentally this was confirmed by Kumar *et al* (1998), who extended this work to study the effect that depth variation had on the characteristics of free-surface turbulence in open channel flow. The experiments were conducted over a Reynolds number (based on flow depth) and Froude number ranging between 2722 to 8874 and 0.17 to 0.53, respectively. Unlike in previously mentioned experiments, Kumar et al. used silver coated "microballoons" sprinkled on the free-surface to visualize the structure interaction with the free-surface boundary. The velocity field at the free-surface was obtained using particle imaging velocimetry (PIV). Fluorescent dye was injected in to the boundary layer to visualise large scale coherent motion and structures emanating from near the channel bottom. Interestingly, Kumar et al. concluded that for fully developed turbulence at large depths the annihilation of existing surface structures occurred due to the appearance of new upwellings. However, as the depth was reduced the vortex merging process became the more dominate mechanism for the annihilation of existing surface structures.

Rashidi (1997) examined the influence of the bursting cycle on the free-surface for shallow flows, using a combination of LDV and hydrogen bubbles. From the conditional averaging of results and the analysis of video sequences, Rashidi found that after the occurrence of a bursting cycle structures shed in the form of horse-shoe vortices. These vortices would rise towards the surface causing the fluid between the interface and the structure to be accelerated, in turn causing the surface to rise and the formation of interfacial patches to occur. When in close proximity to the free-surface the head of the horseshoe structure was noted to cause a fall in free-surface height ahead

of itself. This is followed by the appearance of quasi two-dimensional vertically aligned vortices on the surface boundary, at the boundaries of the surface rise and fall events. Furthermore, the overall change in surface height resulting from inflow events was found to be smaller then that corresponding to the ejection event. Rashidi also examined the effect that the Reynolds number had on this behaviour, increasing Reynolds number yielded the increase in persistence of surface rise and falls, with the size of patches being reduced. Behaviour expected due to wall ejection frequency increasing with increasing Reynolds number.

Later, Tsai (1998) using DNS provided a clearer account between the interaction of a vortical structure classified as hairpin vortices and the free-surface. Analysis of the results indicated that as the vortex approached the free-surface, the interaction caused the free-surface to rise, whilst the head portion of the vortex begins to deform and flatten; indicating vortex stretching in the spanwise direction. The vortex head eventually dissipates resulting in two counter rotating vortices remaining which in turn connect with the free-surface. Tsai concluded that the effects of vortex stretching and dissipation controlled the connection process. In order for the head to dissipate and the shoulders of the hairpin vortex to join with the free-surface, viscous effects are required to cancel the effects of vorticity until the effects of vortex stretching is surpassed. Only then are the dynamics dominated by the effects of viscous dissipation, causing the head of the vortex to decay. Shen *et al* (1999) observed a similar behaviour in their simulations, they noticed that during the connection process of the hairpin vortex to the free-surface, high localized enstrophy (energy defined in terms of vorticity) dissipation occurred and after the connection was complete the enstrophy dissipation is locally reduced, resulting in significantly slower decay of the attached vortex. Since these events occur on a continuous basis, Shen et al. classified them as permanent and prominent features of the surface layer. Figure 1.7, shows visualizations by Tsai, and Shen et al. of the interaction between a hairpin vortex with the free-surface.

This section has briefly reviewed the study of the interaction of turbulent structures with the free-surface over the last two and half decades. It has shown that depending upon the state of the interface i.e. whether it is a free surface or a sheared interface, the type of structures and their interaction can be quite different. Furthermore, parameters such as depth can also influence the prevailing structures and demise mechanisms. However, for vortices that do impinge on the free-surface, in most cases are found to have their

life spans increased (dissipate slower). Table 1.2, is used to conclude the current section, taken from the Nezu & Nakagawa (1993) '*turbulence in open channel flows monograph*', it lists other larger flow structures that occur in deeper free-surface flows such as rivers and oceans that have not been covered within this section.

Type of motion	Characteristics	Location of occurrence
Periodic pulsation	Variation of the mean-flow field itself	Unsteady flows such as flood flows. Non-uniform flows. Abrupt changes of cross section.
Quasi-steady roller. (Less intermittent vortex)	2-D roller with vertical or horizontal axes. Large bank vortex	Upstream and downstream of bank, bed protection works in river and estuaries.
Strong, intermittent upward-tilting vortex called 'kolk'	Fluid and sediments are lifted vigorously up to the water surface. Separated vortex and boils	Downstream of crests of sand waves. Vicinity of hydraulic structures.
Downward vortex	Local scour on sand bed.	Front and side submerged obstacles.
Secondary currents of the first kind	Super-elevation of water surface at concave bank. Vortex stretching.	Bends, curved channels and meandering rivers.
Secondary currents of the second kind	Turbulence-driven corner and cellular currents.	Straight open channels. Formation of boils of the second kind.

Table 1.2: Additional structures occurring in open-channel flows [Nakagawa et al (1975)].

1.3 Submerged bodies and free-surface influence

The behaviour of free-surface flows in general has been extensively studied over the last century. The works have focused on understanding free-surface flows with and without the presence of submerged obstructions. Therefore, a large amount of literature has been compiled on this topic which can be divided into two distinct classes. The first class of research has focused on providing solutions to inviscid and laminar problems with and without the presence of a submerged obstruct. Lamb (1975) *'hydrodynamics'* provides a good summary covering much of the early work on free-surface flows, in determining

pressure, velocity and surface elevation. Whilst the second class has focused on the more practical problems, where the effects of viscosity cannot be neglected and are essential in understanding the physics and dynamics of the flow as well as the subsequent effect of the free-surface. It is the latter class of work on submerged cases that is reviewed in this section.

1.3.1 Submerged bodies beneath a free-surface

Outside of civil and coastal considerations, commonly investigated geometries have been cylinders and hydrofoils. Much of this work has largely focused on the study of surface piercing type problems. However, studies have been conducted into fully submerged bodies close to a free-surface boundary which have yielded interesting results. For instance, Sheridan *et al* (1995) studied the dynamics of vortex shedding from a submerged horizontal cylinder laying parallel to the free-surface. They concluded that the free-surface forms a boundary similar to a solid wall resulting in the reduction and even cessation of the von karman instability. Sheridan et al instead observed a metastable wake that was dependant upon the so-called jet behaviour. The jet was identified as the fluid travelling between the upper surface of the cylinder and the free-surface, shown in Figure 1.8. If the jet remained attached to the free-surface large-scale structures would develop in the wake region with large amplitude, quasi-stationary waves being produced. Consequently, detachment of the jet from the surface yielded a smaller wake due to the jet following closely the cylinder profile resulting in mild surface distortions. In a later publication, Sheridan *et al* (1997) extended upon this by examining the effects of submergence depth and Froude number on the wake behaviour. They showed that for varied combinations of Froude number and depths similar wake states could be achieved and that the surface deformation was controlled by a vorticity layer, which in turn was controlled by the jet (Figure 1.8).

Similarly, the effect of the free-surface on submerged streamlined bodies such as hydrofoils has also been conducted. Early experimental work includes that by Duncan (1983) who examined the effects of breaking and non-breaking waves on a submerged hydrofoil for various speeds and incidence angles. Duncan showed that the type of drag affecting the travelling body was dependant upon the type of wave generated. Non-breaking waves were observed to increase the drag through wave resistance that increased with the continued reduction in submergence depth, while breaking waves

resulted in a far smaller wave resistance effect but caused the total drag to increase drastically.

Likewise, numerical approaches have also been used to study free-surface effects on streamlined bodies. For example, Zhu *et al* (2006) numerically studied the effect the free-surface exhibits on the efficiency of oscillating foils. Two cases were considered where the NACA foil was either mounted horizontally or vertically beneath the free-surface. The foil either underwent a heaving oscillation in vertical direction or swaying in the horizontal direction. Zhu et al concluded that in terms of efficiency, thrust and drag the horizontal foil undergoing a constant heaving cycle showed the most sensitivity to the rate of foil oscillation as well as to submergence depth. While such parameters (depth and oscillating rate) had little affect on the vertical foil.

From the literature surveyed no experimental work has been found that had examined the effect of a free-surface on the shedding pattern for two- or three-dimensional hydrofoils. However, Chen & Chwang (2002) did numerically study such a case for an inclined foil for a similar configuration to that of Duncan (1983), see Figure 1.9. They noted that for Reynolds numbers ranging from 5,000 to 30,000, the trailing vortex sheet displayed a change in shedding pattern. The trailing vortex sheet went from a periodically altering Kármán vortex sheet in the lower regime to a configuration in which the vortices generated from the lower surface become stretched. Whilst those generated from the upper surface remain circular in form for increasing Reynolds number (Figure 1.10). A similar behaviour also observed in the numerical simulation conducted by Pascarelli *et al* (2002) for a lower Reynolds number range, whereby the wake vortices converge to an oscillatory motion before a transition in the shedding pattern. Furthermore, Chen & Chwang (2002) found from comparing shedding frequencies for various Reynolds and Froude number combinations, the free-surface is able to delay the onset of vortex shedding via the Froude number and in turn delay the vortex transitional process. From an energy point of view, the delay in shedding was assumed to arise from the amplification of energy variation from kinetic to potential forms through wave motions.

Another area that has been of considerable interest is the interactions between vortical structures and the free-surface, some of which have already been discussed in section 1.2.2 . The remainder of this section focuses on research conducted in terms of vortex

tube(s). Typically, vortex tube(s) arise from flow over three dimensional bodies like hydrofoils/airfoils or via impellers. Vortex tube(s) are generated as a result of a pressure difference existing in the limiting plane (free-end) causing the flow to rollup, or in the case of an impeller, the motion is naturally introduced. The major interest into such structures arises due to their long-lived persistence and strength after the creating bodies have gone. Consequently, many researchers have studied such vortices and/or vortex tubes. Most namely among these is Professor Sarpkaya, who has consistently studied such structures in homogeneous and stratified flows over the last two and a half decades. Early work of Sarpkaya (1983) includes having experimentally studied the behaviour of trailing vortices generated by sharp and rounded edged wings in both homogenous and stratified flows. In the stratified case the distance between the surface and trailing vortices was such that the effects of the free-surface was negligible. Hence, only the affect of linear stratification were considered. Sarpkaya noted that the shape of the foil affected the size and rise time of trailing vortices. For example, vortices generated by the sharp-edged wings were noted to have a larger diameter and relatively rougher surface compared with vortices generated from rounded edges, whilst vortices with smaller cores exhibited larger rise heights. Sarpkaya concluded that one of the effects of stable stratification was to inhibit the rise of trailing vortices in comparison to vortices in homogenous flows. A behaviour attributed due to factors including the change of turbulence structure and eddy diffusion by stratification.

Sarpkaya (1983) also investigated the method in which the demise of trailing vortices occurred. Typically, vortex break-down was observed to occur through vortex linking or core bulging/bursting. The vortex linking demise process of trailing vortices (also known as Crows instability) results in trailing vortices initially linking to form horseshoes, shortly after their formation the horseshoes change into rings inclining themselves at an angles of approximately 45˚. In general these rings undergo complex transformations [Widnall (1975)] before dispersing. Whereas for core bursting to occur, the axial velocity was required to be nearly equal to the maximum tangential velocity at the edge of the core. Sarpkaya did note that the vortex breakdown in the form of the 'core bulging and bursting' was different for trailing vortices in contrast to that observed for a single vortex tube. For a single vortex tube [Sarpkaya (1971)], the vortex breakdown was seen as the initial stage of a vortex tube undergoing an abrupt change from supercritical to subcritical flow either in a axisymmetrical, spiral or double-helix manor. However, Sarpkaya (1983) observed that for trailing vortices, the vortex

breakdown did not signal a transition from supercritical to subcritical flow. Instead core bulging and bursting occurred at various locations along the trailing vortices with little influence occurring on the vortex state upstream and downstream during such a process. From comparing the dominate demise mechanisms for various depths, Sarpkaya concluded that the stratification effect on the demise mechanisms of trailing vortices was a transition from Crows instability to core bulging/bursting.

In later publications, Sarpkaya and others extended this work to identify the affect and interaction that such structures (vortex tubes and couples) have close to a free-surface boundary where effects of stratification are high. In both cases the demise of vortex structures occurred through eventual vortex dissipation, rather than the previously mentioned mechanisms. Instead, the effect of the free-surface boundary and stratification results in the altering of the vortex structure.

Sarpkaya *et al* (1994) examined the interaction between a vortex tube and free-surface. The study was conducted for various vortex core depth ratios (8.3-1.0) relative to the free-surface using laser-induced fluorescence to visualise coherent structures and the interaction process. In general, a single vortex tube spinning about an axis produces numerous tentacle-like vortex sheets of finite length (a result of helical instabilities) that either stretch out or are thrown away from the outer edge of the vortex core randomly. Sarpkaya et al showed that as the proximity between the free-surface and vortex reduces, these shed sheets begin to connect with the free-surface giving rise to whirls. Whilst the remaining unconnected vortices roll up into vortex tubes with their axis being parallel to the free-surface. As the vortex proximity to the free-surface further reduces, the arrangement of vortex tubes with their axis parallel to the surface begins to dominate, with the flow near the free-surface becoming highly anisotropic. Coherence of the vortex core was observed to be nearly fully lost when the distance between the surface and vortex core is almost equal to the core radius. A property Sarpkaya et al attributed to the interaction of the vortex with its image across a shear-free boundary resulting in increased annihilation of vorticity. Sarpkaya & Neubert (1994) examined the same problem statistically, concluding that the free-surface acts as a highly stratified deformable layer that strongly affects the low-frequency end of the energy spectra (large scales) and is very efficient in damping large eddies as well as changing strongly the structure of nearby flows. Analysis of the turbulent energy showed that two distinct regions exist between the vortex and free-surface: the first was near the vortex where

the turbulent kinetic energy decayed rapidly and the second region existed close to the free-surface (on the order of millimetres) where the turbulent kinetic energy no longer decays but essentially remains constant, explained through the increase in anisotropy and two-dimensionalisation of the flow.

Similarly, Sarpkaya & Suthon (1991) examined the interaction of a vortex couple in the form of a Kelvin oval with the free-surface. The problem was studied using both experimental and computational approaches. For the experimental approach, the interaction and behaviour was observed using SAR (synthetic aperture radar) imagining. The interaction of the vortex couple was seen to be far from simple, due to surface deformation, the presence of 'striations which appear as ridges along the vortex oval (shape assumed by a vortex couple) and creation of bands of scars that are dominated by small vortical structures and whirls (Figure 1.11). Sarpkaya & Suthon attributed the creation of striations to the disturbances in the free-surface, while the creation of whirls and other vortical structures in the scar regions occurred only after striations had reached their maximum height. It should be noted that most of the aforementioned studies reported in this section examining the interactions of vortex tubes or couples with the free-surface have been at relatively high Froude numbers (Froude number > 0.8, where the Froude number was defined in terms of the vortex velocity and its distance from the free-surface). For lower Froude numbers Sarpkaya *et al* (1988) concluded that if the Froude number was greater than 0.15 the deformation and non-linear interaction between the free-surface and vortex couple became significant. However, for Froude numbers lower than 0.15 the free-surface was noted to remain relatively flat and the behaviour is well described by Lambs potential flow solution. Sarpkaya (1996) provides a good review of much of the work performed on the interaction of vortex couples and tubes in addition to other structures with a free-surface.

1.3.2 Wall mounted submerged obstructions

Work reviewed in the previous section has focused on the influence and interaction of objects located beneath the free-surface. This section focuses on the effect and interaction of free-surface flow resulting from bed/boundary topology, for which a vast amount of literature has also been compiled. Much of the work performed in this context has come from the coastal, civil and marine fields. Well documented cases

which have been studied both experimentally and computationally include, flow over backward facing steps, submerged cubes (dikes) and dunes. The reason such structures have been extensively studied is due to the fact that they are designed deliberately to give rise to separation through adverse pressure gradients or sudden separation in order to dampen and weaken waves to reduce wave damage/erosion. From a civil and coastal point of view, better understanding into such flows can help in the preservation of coastal lines and prolong the life of such defences. Such separated flows tend to give rise to high shear stresses, which influence the mechanisms of erosion and transportation of material. For dunes Muller & Gyr (1986) conducted flow visualizations of coherent vortices generated downstream of the crests of dunes. They suggested that two-dimensional vortex tubes that separate from the crest would change into hairpin-like vortices due to high shear stresses giving rise to lateral instability. If the flow was shallow enough such vortices could translate and appear on the free-surface as boils, a behaviour also concluded from simulations by Yue *et al* (2005). Figure 1.12 shows schematically open channel flow over dunes, produced by Nezu & Nakagawa (1989) from a laser-doppler anemometer study. The curved arrows indicate kolk-boils generated from flow reattachment which was also observed by Iseya & Ikeda (1986). Furthermore, deformation of the free-surface has been shown to influence parameters like separation, vortex size and strength. Work by Huang & Dong (1998) and Sue *et al* (2005) for flow around two-dimensional dikes has shown that travelling surface waves do influence the position and size of vortical structures, as well as, influencing the shedding behaviour. While wave steepness were found to be responsible for affecting both the size and strength of these vortices.

In summary, this section has shown that the free-surface influences the behaviour of flow signatures created by the presence of submerged bodies/structures. These signatures can be enhanced, changed or even completely damped due to the effects of wave/surface deformations or stratification effects. Whilst, the presences of structures near the free-surface results in the flow becoming highly anisotropic. Furthermore, through the surface boundary condition and deformable behaviour of the surface boundary, a slowed decay rate of energy is found near the free-surface. This is owed due to factors including realignment of vorticity occurring from an increased anisotropy and two-dimensionality near the surface, as well as, the continuous change between potential and kinetic energy through the presence of waves.

1.4 Complex Geometries and Simplification

All engineering bodies in full form, whether they are aircraft, bridges, ships, or windmills can in general be considered as complex geometries. This is because they are formed from various individual parts, each of which has a specific function. It is therefore of utmost importance that we know how such complex bodies behave within their working envelope and the magnitude of forces they experience. Not just from a safety aspect, but also from an efficiency point of view. However, it is often difficult to study and analyse the flow behaviour around such geometries due to their three-dimensionality, complexity or operating environment. This does not mean that such studies have not been performed, Hedges *et al* (2002) numerically studied the flow effect on aircraft landing gear and Tseng *et al* (2006) numerically studied the dispersion of pollutant over an urban town.

Much of our knowledge of the dynamics of flow around complex bodies has come from extensive experimental testing (i.e. wind tunnel testing), which have either been performed on a full scale body or a model representation. Such examples include the SUBOFF experiments by Huang *et al* (1992), who made wind-tunnel measurements around a generalised submarine body and Johnson *et al* (2002) whom experimentally studied the wake characteristics of a C-130 aircraft. Typically experimental data has comprised of surface-oil and smoke screen for the visualisation of the flow behaviour on or in the wake of the body. While measurements are usually made using combinations of techniques, such as, force plates, pressure tapings/transducers, particle velocity imagining (PIV) and hotwire techniques to name a few. The use of such approaches have all led to rapid improvements in aerodynamic efficiency, aerodynamics and body loading, to the point where further improvements have been slow. This slow down can be partly attributed to the need for a better understanding to the flow interaction and wake dynamics. However, such behaviours cannot be easily examined by experimental means alone. This is mainly due to the huge volume of data that would need to be collected, in addition to the level of expense required to perform such tests.

It is for this reason the that use of numerical simulations have grown and become a more utilised tool in both research and in industrial applications, helping further understand the flow behaviour around or through complex bodies. Though much of the early work was performed using Reynolds average Navier-Stokes (RANS) based

solvers, it is only recently that computer capability has reached a state where the more powerful techniques like Large-eddy simulation (LES) and detached-eddy simulation (DES) can be applied to many actual engineering problems. Examples of such works that have seen numerical modelling applied to study complex bodies include that of Johnson *et al* (2002) and Serrano *et al* (2003), whom computationally studied the flow behaviour around a C-130 Hercules for tailgate down and paratroops doors open, respectively. Although we have seen the use of numerical simulations applied to study complicated bodies they are still far from providing accurate data for any type of problem considered. This is due to turbulence models used to account for the effect of unsolved length scales requiring further improvement. For example, Bensow *et al* (2004) assessed the accuracy of two different sub-grid scale models for predicting the flow behaviour around a fully appended and bare hull body of a model submarine configuration known as the DARPA SUBOFF. Both models considered allowed for forward and back scatter of energy, an essential criteria of energy transfer when modelling complex flow configurations. The results were compared against available experimental measures made on the two different configuration types [Huang et al. (1992)]. It was found that the results produced by both models agreed well with the experimental measurements for the fully appended case, whilst agreement between the results for the bare hull case were not so good. The difference between the two cases was attributed due to the fact that the appendages had a more profound effect on the flow rather than the hull boundary layer. However in the case of the bare hull, the curvature effects on the boundary layer resulted in inaccurate predictions of the boundary layer indicating that current wall models and subgrid models are ineffective for such cases. Therefore, experimental work is still needed to aid the improvement and development of models until they are capable of correctly predicting complex flow behaviour.

Another difficulty in modelling complex bodies computationally lies in obtaining a good quality of mesh that avoids issues such as excessive skewness of elements. Such problems exist for both structured and unstructured mesh types and one approach that has been adopted to overcome such problems is to utilise hybrid or chimera meshing techniques. Such approaches combine the strengths of both mesh types at the expense of increased computational cost and memory. Examples of works that have utilized this type of meshing approach includes that of Senocak & Iaccarino (2005) and Murayama

et al (2006) who examined free-surface interactions with a ship hull and the aircraft response to control surface deflection, respectively.

Another modelling approach that has seen rapid growth over the past 10 years in the modelling of complex geometries which has the capability of handling fluid-body interaction in terms of movement or deformation is the immersed boundary method (IBM). This approach differs from conventional modelling approaches such that the required geometry is enforced as part of the solution rather than as part of the grid. Works based on this type of modelling approach have been applied in many various aspects of research. The immersed boundary (IB) approach was first introduced in the medical field for the modelling of heart flows [Peskin (1972)]. Since its introduction it has grown rapidly and recent medical applications include the modelling of blood cells under shear [Zhang & Zheng (2007)] and the transportation of blood vessels past blockages [Liu *et al* (2006)]. As well as to study the evolution of wake patterns for humans walking [Choi *et al* (2007)]. However the adoption of this modelling approach to other fields of research was initially slow due to the fact that the IB formulation was mainly developed to deal with deformable bodies using stiffened panels and resulted in numerical instability when modelling rigid bodies. However Goldstein *et al* (1993) and Modh-Yosuf (1997) have presented stable modified versions of the IB in dealing with rigid bodies. Since then, other fields have rapidly begun to adopt the use of the IB. Examples of such work includes that of Gilmanov & Sotiropoulos (2005) who examined flow patterns around anatomically correct insects, while Glowinski *et al* (1999) and Wan & Turek (2007) have used such approaches to model flow-body interaction problems (i.e. falling spheres). IB approaches have also been applied to the modelling of a pickup truck by Kalitzin *et al* (2003), the modelling of varied bed topology [Tseng & Ferziger (2004)], the modelling of flow around rotor blades [Ghias *et al* (2005)] and to even study the flow through a combustor by Iaccarino & Ham (2005). One of the main reasons why the IBM has seen a widened base of application, is that they allow for far simpler grids to be used, hence simplifying the equation needed to be solved i.e. avoid transformations associated with body fitted grids.

Unfortunately, performing detailed analysis of flow around complex geometries can still prove to be difficult. This is due to the fact that different parts of the body can influence the flow behaviour around other sections of the complete geometry. Although, we are able to experimentally study and computationally model highly complex geometries and

motions, in order to completely understand the emerging flow dynamics, simplified cases or parts of the geometry need to be studied in isolation. In most cases, complex bodies of engineering interest are often formed from combining together multiple sub-bodies to form the main structure. The result is that the final geometry consists of some what sharp changes in its resulting outline. For example, an aircraft fuselage with wings, tail-plane and rudder appendages or a fully appended submarine hull are prime examples of this. These structures all interact with each other as well as with the three-dimensional boundary layer, producing a very complex unsteady flow. One of the most notable features encountered around any bounded body is the presence of a junction vortex/vortices, such structures arise to aid in the redistribution of fluid in the near wall bounded regions. Junction vortices tend to form in the shape of a horse shoe vortex that is wrapped around the body with the legs extending into the wake region. Hence such structures can influence and change the local flow behaviour and have also been noted to result in increased surface pressure fluctuations, heat transfer and noise [Simpson (1996)]. Additionally in many civil applications, junction vortices are also responsible for increasing the rate of erosion ahead of the obstacle [Simpson (2001)].

Practically, before combined complex flows can be fully understood, simplified cases like the effect of each individual sub-structure that form the complete body need to be addressed separately. Only after this can the combined effects be truly comprehended. Such work includes that by Shekarriz *et al* (1992) who experimentally studied junction and tip vortices generated around a submarine like body (hull and fairwater) using particle displacement velocimetry (PDV). Conditional averaging and the super-imposition of velocity maps, revealed the existence of multiple co-rotating vortices in the vicinity of the wake that possess a similar strength and rotate in the same direction as the junction vortex. It was concluded, though not confirmed that wake structures may have a significant impact on the dynamics of a junction vortex, not only due to their strength but their region of influence frequently included parts of the boundary layer near the junction vortex. Furthermore, the behaviour of the tip vortex was noted to be consistent with the roll-up of a vortex sheet into a spiralled tip vortex. Visualizations also revealed a number of small vortices being entrained into the core of the tip vortex. In addition, circulation plots revealed the tip vortex was far stronger than the junction vortex by up to 12 times greater, with the junction vortex strength being comparable to that of the wake.

Similarly, Svennberg & Fureby (2003) computationally studied flow separating over a smoothly contoured ramp, as a simplified case of flow separating over the stern of a submarine. Their results revealed a chaotic behaviour within the flow field about the separation and reattachment positions, while time averaging of flow fields showed that separation and reattachment does not occur at fixed points but within a bandwidth. A behaviour they attributed due to the unsteady vortex shedding occurring about the separated region. Similar observations have also been made by Wasistho & Squires (2001). Later, Song & Eaton (2004) extended further to examine the effect that the Reynolds number has on a turbulent boundary going through separation, reattachment and its recovery behaviour. In terms of flow recovery back to a normal profile after separation; Song and Eaton's study showed that the turbulence in the outer layer after reattachment is dominated by vortices generated from the separation region. This hinders the recovery rate of the outer layer, in contrast to the near wall turbulence that recovers relatively quickly. As a result, a stress equilibrium layer forms near the wall, although the outer region is out of equilibrium with the mean flow (a characteristic of a non-equilibrium layer is the different Reynolds stress components evolve at different rates). The effect of Reynolds number on the mean flow was concluded to be small, as the mean separation and reattachments points hardly changed over the studied Reynolds number range.

In summary, this section has highlighted the need to study complex geometries in full to better understand their performance parameters. However, the rate of improvement in terms of aerodynamics and aerodynamic efficiency has slowed over the years, a factor contributable to a need to better understanding the flow interactions and wake influences being required. This can not be obtained by experimental means alone. Hence the use of computational simulations to examine complex problems has seen a rapid growth. Increase in computer power has allowed for more advanced methods to be utilized for practical engineering applications. However, simplified cases still need to be examined, whether it is numerically and experimentally before combined effects can be truly understood for complete bodies.

1.5 Motivations

A great deal of computational and experimental effort has been made into further understand how turbulence, whether it is natural or body induced, behaves and interacts

in the presence of a free-surface. Earlier work has concentrated on obtaining statistical descriptions of free-surface problems, while later work has been more confined to the behaviour of turbulence structures in the presence of a free-surface. Sections 1.2 and 1.3 showed that the free-surface is capable of changing and influencing the behaviour of turbulent structures within close proximity to itself, mainly through the effects of stratification, surface deformation and its zero shear constraint requiring vortices to realign. It has also been shown that the effects of various levels of stratification resulting from the free-surface (section 1.3) not only cause a change in vortical structure but also influenced the demise mechanisms. Whilst wave motion results in strong variation of forces acting on the generating or standing body, as well as affecting the local flow structure and behaviour.

Although the experimental approach has been the main utilised tool in industrial and research applications, the incorporation of numerical simulations as an alternative approach in both fields has been constantly increasing. While the increase in computer capabilities has allowed for more practical applications (high Reynolds number) to be considered. In addition, during this time less expensive computational approaches such as RANS and LES have seen rapid improvements in their predictions through improvements in their closure and subgrid models. This has resulted in both approaches becoming quite robust; such that in general good agreement is obtained in many practical applications in terms of flow features and measurements. Furthermore, the development of new approaches like detached-eddy simulation [Spalart *et al* (1997), Menter & Kuntz (2002)] and similar hybrid methods have allowed for better predictions in results with reduced solve time by combining the strengths of both Reynolds averaged and large-eddy simulation. Computationally this has resulted in a large amount of literature in varied applications to have been compiled.

One of the main reasons that numerical simulations have seen a rapid growth aside from the fact that results obtained using such techniques in general are comparable to those obtained experimentally, is the fact that, on the whole, numerical simulations can provide far more detailed information than would be obtained by any experimental method. In addition to being far less costly than experimental means, computational approaches are simpler in modelling the required conditions without the need for scaling. It is for these reasons that many industries and well as researchers have started to use such tools to understand complex flow configurations of engineering interest.

Such examples include the modelling and understanding flow behaviour around aircraft [Morton *et al* (2003)], submarines [Watt *et al* (2006)], vehicles [Mendonca *et al* (2002)], and also flows through internal bodies such as combustors [Iaccarino & Ham (2005)]. However, as mentioned before in section 1.4 much of the engineering applications outside of the research field lie in the study of full body configurations that are in general very complex, as the body is built of many different parts. Although full-body simulations are useful in showing how the flow tends to behave around a complete body and the interaction and forces that arising from the different appendages that form the body in question. If such solutions are to be truly understood the effects of each major structure that form the body in question need to be studied separately as covered in section 1.4 .

One of the most notable examples is that of submarines, it is only within the last 10 years that computational simulations at operating conditions on simplified or non-classified submarine configurations have been reported using RANS and more recently LES approaches. Although much of the work remains classified, two types of usage for numerical simulations are seen to be emerging:

1) the use of numerical simulations in studying full submarine configurations to examine wake and flow interactions.
2) the use of numerical simulations to predict the stability parameters during submarine manoeuvres.

Published work in terms of studying submarine configurations with all appendages includes that of Bensow *et al* (2004) who computationally studied the generalised configuration using LES (SUBOFF). The SUBOFF model is the first generalised configuration [Groves *et al* (1989)] specifically designed to allow for the testing and improvement in computational predictions, with the specific aim to allow utilisation of computational methods to assist in the development of advanced submarines. Comparison data for the SUBOFF was produced by Huang *et al* (1992) and Liu & Huang (1998) who performed extensive wind-tunnel testing on the different SUBOFF configurations, i.e. bare hull (AFF-1) and full appended (AFF-8).

In the work of Bensow *et al* (2004) both aforementioned configurations were considered. The complexity of the model especially in the fully appended case combined with a very high Reynolds number ($12x10^6$) makes such a problem quite challenging, especially when using the LES approach with its high near wall resolution

requirements. Bensow et al overcame this issue by employing a cylindrical body fitted grid, therefore providing sufficient resolution to effectively resolve the boundary layer with results comparing well with measured experimental data. In terms of the flow behaviour, Bensow et al noted that the flow over the mid-section of the AFF-8 configuration is dominated by a horseshoe-shaped vortex that is generated around the fairwater with the legs extending to the stern of the hull. Furthermore, as the vortex legs extend further towards the stern of the submarine, the interaction between the vortex legs and the hull boundary layer was noted to continually increase resulting in embedded vortices within the thickening hull boundary layer. Further effects of the unsteady wake and junction vortex generated by the fairwater were to significantly alter the velocity and turbulent stress distributions within the hull boundary layer. Similarly, the redistribution of Reynolds stresses in the stern region were also noted to be partly contributable to the flow structure arising from the fairwater. Figure 1.13 shows the LES visualisations of Bensow et al around the fully appended AFF-8 configuration.

Similarly, Yang & Lohner (2003) used the RANS approach to study both the AFF-1 and AFF-8 configurations using unstructured meshes, the results achieved were in good agreement with the measurements of Huang *et al* (1992). Whilst the work by Chang *et al* (2006) has seen the numerical simulation of internal and surface wave profiles performed for the SUBOFF AFF-8 configuration in a two-layer stratified fluid modelled using the unsteady RANS approach. The AFF-8 configuration was meshed using a hybrid mesh to allow for a body fitted mesh around the AFF-8 body and a structured mesh to be employed near interfacial regions. The intermediate region between the two meshes was accounted for using an unstructured mesh. Chang et al concluded from their study that the effect of increasing the Froude number of surface waves (from 0.068 to 0.312) resulted in the establishment of typical Kelvin waves with a fixed dispersive angle. Whilst for internal waves, the effect of increasing the Froude number was found to result in an increase in the wave length of the internal waves while the internal wave angle reduced. It was also found that for increasing Froude number the surface waves had an increased influence on the internal waves. Similarly, work by Yeung & Nguyen (1999) has shown that the influence of both surface and internal waves is dependant upon local Froude numbers and the density variation between the two layers.

The second application for which numerical simulations have seen an increased interest, is in the prediction of forcing and moments generated about a submarine during

manoeuvring. Typically, such information is obtained through experimental means or through coefficient-based simulations by solving the equations of motion for a submarine. However, it should be noted that much of the coefficients for the coefficient-based simulations are evaluated based on experimental data [Bettle *et al* (2009)] using scaled models that are either radio controlled or captive models. The costs associated with performing such tests is prohibitively high, furthermore, it is often difficult to obtain full similarity between what is required and what is possible within an experimental facility. It is for this reason that researchers have begun to assess and use RANS based simulations for this purpose. For example, Kim *et al* (2005) numerically modelled the force and moments acting on SUBOFF AFF-1 (bare hull) and AFF-3 (hull with four identical stern appendages) configurations for various drift angles. The results obtained showed good agreement with experimental data, with predicted hydrodynamic coefficients acting on a submarine agreeing with those obtained experimentally for the various drift angles considered.

More recently, Bettle *et al* (2009) have performed a RANS simulation to study to the effects of roll stability on a submarine during emergency surfacing conditions. Their work is unique in the way that the six degree of freedom, solid body equations of motion for a submarine were coupled together with the RANS solver, while the simulation of the emergency surfacing manoeuvre was performed within the context of a fixed grid. Overall, the simulation did predict the roll instability for the buoyantly rising submarine. Bettle et al concluded from their analysis of the flow as well as from the predicted forces and moments that the fairwater was the main contributor to the roll instability. The condition for the roll instability to occur was given as:

"when the rate of change of the sail moment with roll angle, overtakes the rate of change of the static restoring moment with roll angle."

This according to Bettle et al typically arises only during the last 10 seconds of the manoeuvre, when the ballast tanks are emptying and buoyancy is high.

Up until now very little work has been published on complete submarine configurations in the presence of a free-surface for both computational and experimental investigations. As emphasized in section 1.4, in order to be able to highlight free-surface effects on a complex structure such as a submarine with all it appendages, it is necessary to initially undertake studies of individual components such that the effects of the free-surface on each part can be understood and highlighted. Extensive work on hydrofoils moving

parallel to a free-surface has been conducted for various incidence angles, submergence depths, as well as for various Reynolds and Froude numbers. However, limited work has been published on vertical hydrofoils or submerged elliptical bodies that represent submarine hulls in the presence of a free-surface boundary. Therefore, before the effects of the free-surface can be fully comprehended on a fully appended submarine, more insight into the free-surface effects on individual appendages is required.

Typically, submarines tend to operate at three very different situations:

1. ***Surfaced:*** the hull of the submarine pierces the free-surface.
2. ***Periscope depth:*** the submarine is sufficiently close to the free-surface without piercing it.
3. ***Deep submergence:*** the submarine is free from any free-surface effects.

The surfaced case typically corresponds to that of normal ships operating condition for which there is already a wide range of experimental and computational work published. Typical work includes wave-hull interaction [Senocak and Iaccarino (2005), Huang *et al* (2008)] and wake profiles [Çelebi (2000)]. In terms of submarines, numerical simulations have been performed for surface waves over the submarine hull with stern appendages (SUBOFF AFF-3 configuration) by Zhang *et al* (2005) using a volume of fluid (VOF) method to account for the behaviour of surface waves. The simulations were conducted at a Reynolds number of 1.2×10^7 for Froude numbers of 0.17 and 0.26. Comparison of wave features for various Froude numbers yielded good agreement between the computed data and those observed experimentally. Similarly, Metcalf *et al* (2006) experimentally studied the unsteady, wave induced separation around a surface piercing foil for various Froude numbers. Metcalf et al observed that as the Froude number was increased the wave profile went from the expected Kelvin waves to a state where the free-surface turbulence was such that the Kelvin waves were no longer distinguishable. In addition the presence of surface-turbulence resulted in separation of the flow locally around the foil, while for the free-surface it was concluded to reduce both the strength and frequency of large-scale vortex shedding.

Similarly, for the deep submergence case where free-surface effects are negligible, both computational and experimental (wind-tunnel) results have been published in terms of the SUBOFF configuration. Much of the earlier work reviewed for submarines falls within this category. Researchers have also examined the effect of bed proximity on the

flow behaviour as well as the forces and moments that arise on a submarine [Wu *et al* (2005)].

At periscope depth where free-surface and wave effects are less negligible, limited geometries and orientations have been studied. This has motivated the study of a submarine fairwater near periscope depth. The incentive of studying solely the fairwater is that it is the largest and the closest to the free-surface out of all the appendages and parts that form a submarine. Therefore, if the free-surface is to influence the flow dynamics around a submarine its greatest influence should be on, or result from the fairwater. This in turn also lowers the computational resource requirements. Furthermore, the works by Bensow *et al* (2004), Alin *et al* (2005), Sung *et al* (2002) and Bettle *et al* (2009) have shown that the fairwater has the greatest influence upon the flow patterns over the submarine, in addition to having a influence on submarine manoeuvres and stability.

In terms of flow structure, the closest vortex structure to the free-surface would be the tip vortex generated by the fairwater. Observations and measurements by Shekarriz *et al* (1992), Sarpkaya (1971) and Sarpkaya (1983) have shown that the tip vortex is the strongest and most persistent vortex that occurs which is susceptible to different forms of instabilities and behaviour for different levels of stratification i.e. in the presence of a free-surface. If the free-surface is to influence any vortex structures its greatest effect should occur on those generated by the fin, which in turn would at the very least influence the flow over the upper stern region as well as other parts of the submarine.

These findings and arguments provide justification for solely studying the fairwater in the presence of the free-surface boundary. Furthermore, DSTL (Defence Science & Technology Laboratories) has shown interest at this operating condition reporting that near periscope depth submarines exhibit an increased drag. This has motivated a study of a simplified fairwater in the presence of a free-surface by means of large-eddy and detached-eddy simulation techniques. These modelling approaches are chosen as the large scale structures within the flow are well resolved, hence essentially capturing the evolution of major turbulent structures far better than using the RANS modelling approach.

The aim of this thesis is to computationally study the effect that the free-surface flow has on the flow structure around a fully submerged submarine fairwater for various submergence depths. The fairwater is considered in the absence of hull curvature and associated appendages. The flow conditions aimed to be achieved in this study are for a sub-critical Froude number regime ranging from 0.4-0.44 and for an operational Reynolds number of 11 $x10^6$ based on the fairwater chord length and cruise velocity at periscope depth (note that the operating Reynolds number for a full scale submarine away from periscope depth is of the order 10^9).

1.6 Achievements

The achievements of this work and authors contribution can be summarized as follows:

- ✓ An existing code (EXVOLES - Shi *et al* (2000)) has been successfully modified to handle the presence of an internal geometry in the presence of a free-surface, where the free-surface is modeled using a part moving mesh. Two approaches have been incorporated into the code for modeling the internal body:
  - ➢ Blocking of cells – in this approach the cells are blocked and appropriate corrections are made in the regions defined as the near wall. In addition, a power-law wall model is added to better estimate the wall stress close to the internal surfaces. The geometries modeled using this approach can be either a staircase approximation or form a smoothed body by using the curvilinear capability of the code.
  - ➢ IBM – This approach is used to force the body solution onto the flow field, rather than modifying the mesh to account for the body. In this thesis this approach is used to model most of the submerged and all two-dimensional bodies considered. The IB for all cases is applied on a stretched, Cartesian grid. However, it should be noted that the approach can be used along side or even on the curvilinear mesh, or with the blocking of cells approach. In addition, an instantaneous log-law is applied to help better estimate the near wall stresses.

- ✓ The IBEXVOLES code has been successfully parallelized using OpenMP to achieve a better runtime for the numerical simulations of the fairwater. Parallelization and optimization was performed independently with only textual

aid [Chandra *et al* (2001)]. The results of the OpenMP code were validated against serial computed results to ensure correct parallelization. Simulations were run on high performance computing facilities, initially at Edinburgh universities computing facility (HPCX). The simulations were later completed on Queen Mary's HTC computing facilities. The typical time per computational cell was $7.82e^{-6}$ seconds, while parallelization using OpenMP resulted in a speedup of approximately 12.5 times on 8 Xeon processors.

- ✓ A secondary code for constructing and extracting necessary information for use with an IBM has been developed. Such information includes the identifications of cells that lay within the body, flow and along the interface. Two-dimensional and three-dimensional symmetric bodies have been successfully constructed using this code. In addition, the code is capable of generating complex bed topology as well as combining the both aforementioned modeling approaches.

- ✓ Spalart *et al* (1997) detached-eddy simulation model is successfully incorporated within the IBEXVOLES code for use with the blocked cell and IBM. The model is discretized using the finite volume approach to keep consistency with the overall scheme used. The log-law is also applied close to the IB to provide a better prediction for the wall shear stress, while the blocking of cells approach uses a power-law in predicting wall stresses. The wall normal distances required by both the LES and DES models are computed during the generation of the grid files.

- ✓ Processing routines have been incorporated in the code that provide instantaneous, mean, statistical and time history data for the flow behavior. Separate standalone programs are written to be used in conjunction with the IBEXVOLES code in presenting the data in various formats. The various data formats are available as follows to aid in the analysis of the produced results:
  - ➢ Instantaneous data – is generated at fixed time intervals for the entire modeled domain. Data provided includes pressure and velocity distributions and vortical structures identified using the Q-criterion.
  - ➢ Mean data – time averaged data is generated in the form of pre-specified slices and for various positions around the modeled body as well as in

the wake region. Surface averaged data along the modeled body data is also provided.

- Statistical – statistical data is extracted in either planes or as rakes. The statistical data available for analysis are the turbulent intensities, Reynolds stresses, turbulent kinetic energy distributions, energy spectrums, probability density distributions, quadrant analysis as well as auto and spatial correlations.
- Time history – Time history of pressure loading, variation in lift and drag is also produced. Point based history of the flow around the body and in the wake region is also available.

✓ IBM in conjunction with LES and DES methods is validated around bluff and streamlined bodies, with results being compared with published experimental data and observations. The validation is perform of a large range of Reynolds numbers, ranging from $Re_{mc}=3854$ to $Re_{lc}=9\times10^{6}$.

✓ Flow around a single cube placed in a uniform flow and a matrix of equidistant cubes has been simulated using LES approach to study the effect that flow submergence has on the flow structure and behavior. Both cases are studied for $Re_h=3854$ and $Re_h=4\times10^{4}$, for submergence depths of $d/h=2.533$, $d/h=2.0$ and $d/h=1.733$. The Froude numbers for the three submergence depth considered is 0.3, 0.34 and 0.37, for both Reynolds numbers considered.

✓ Flow around a three-dimensional fairwater is simulated at moderate Reynolds number of $Re_{lc}=8\times10^{4}$, both LES and DES methods are utilized and compared to examine the difference in the predicated flow behavior. The study is performed over the submergence depths of $d/h=1.02133$, $d/h=0.96237$ and $d/h=0.90474$. The Froude numbers for the three submergence depth is 0.4, 0.42 and 0.44, respectively.

✓ Coarse DES simulation is around the three-dimensional fairwater is performed at operational conditions at periscope depth, for $Re_{lc}=11\times10^{6}$. The study like the moderate Reynolds number flow about the fairwater is performed over the same submergence depths of $d/h=1.02133$, $d/h=0.96237$ and $d/h=0.90474$. The

Froude numbers for the three submergence depth considered is 0.4, 0.42 and 0.44, respectively.

1.7 Figures

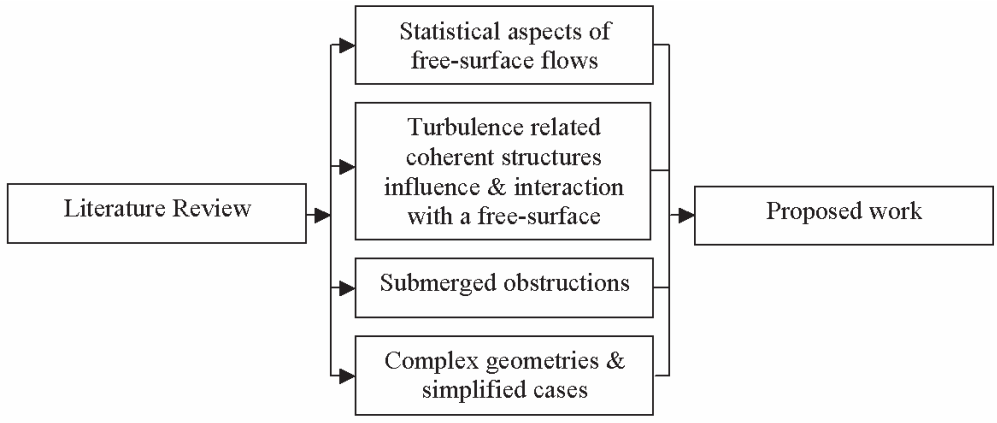

Figure 1.1: Road map to literature review

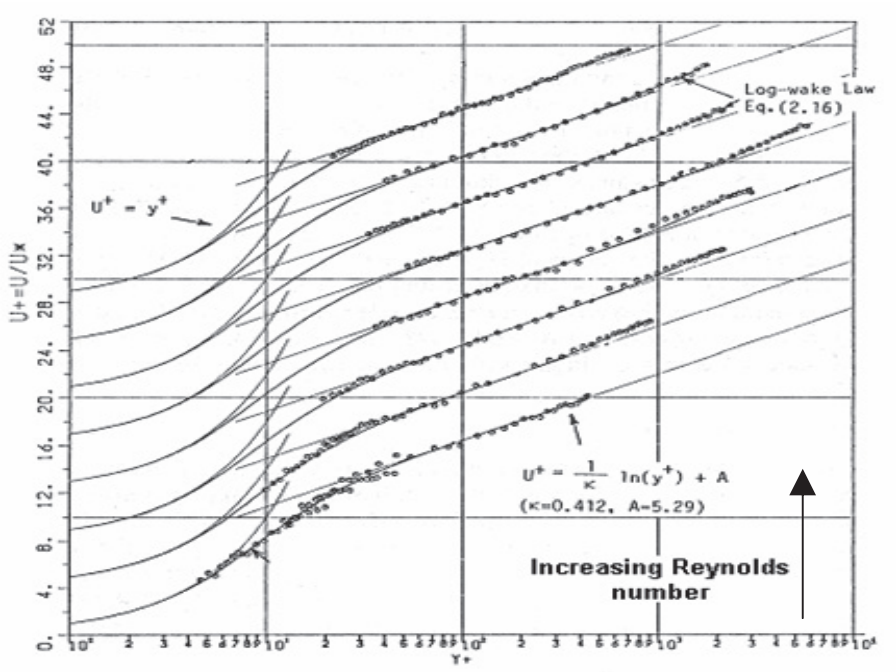

Figure 1.2: Non-dimensional velocity profiles for increasing Reynolds number

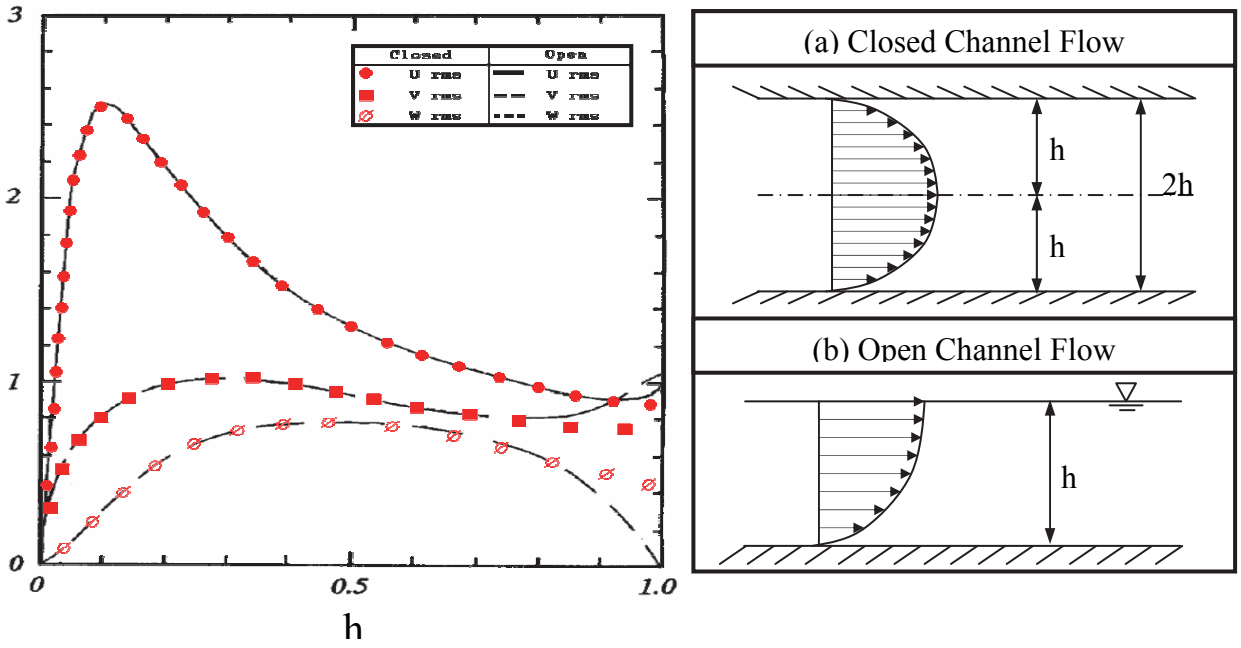

Figure 1.3: Comparison of turbulent intensities in open and closed channel flows.

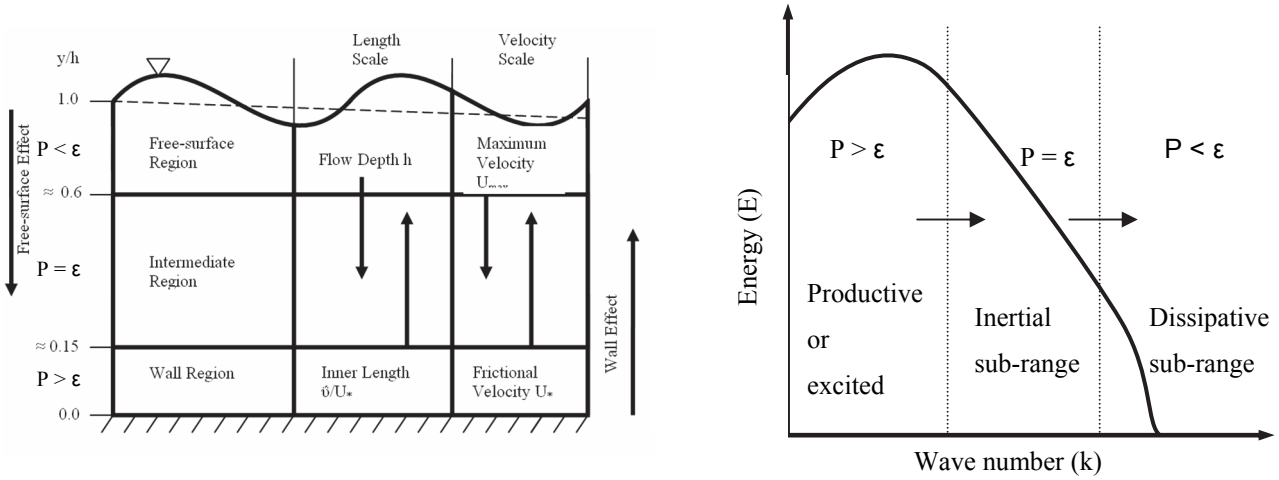

Figure 1.4: Distinct regions in physical and spectral space classified by production and dissipation of energy.

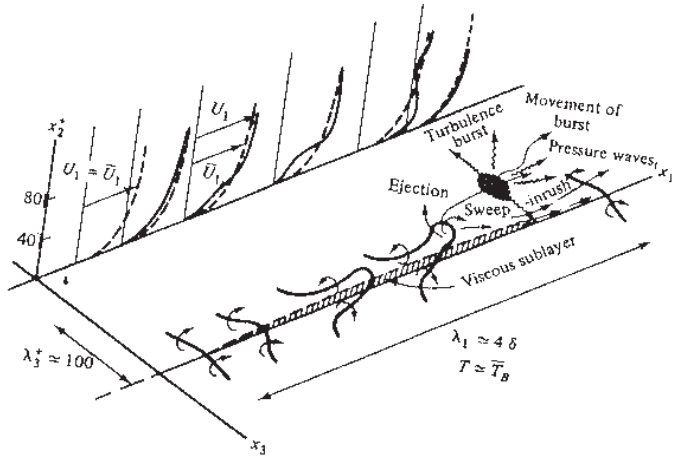

Figure 1.5: Conceptual effect of bursting motion on boundary layer [Hinze (1975)]

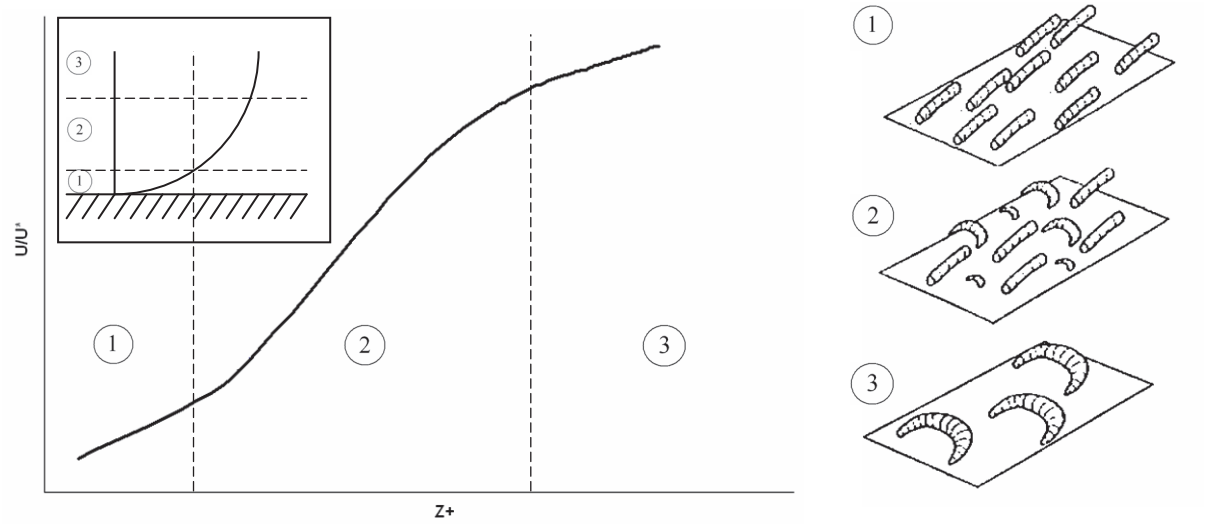

Figure 1.6: Structure population in different regions of a boundary layer [Robinson (1990)]

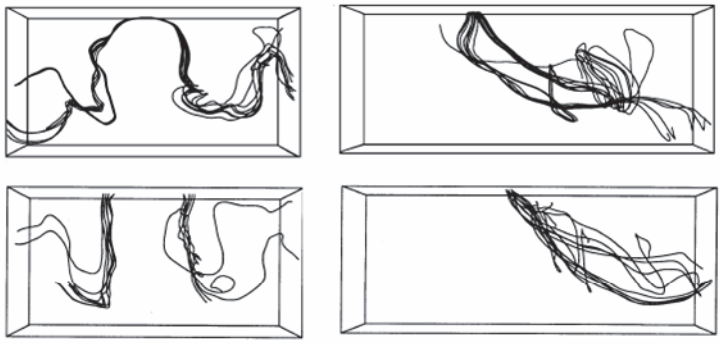

(a) Tsai (1998)

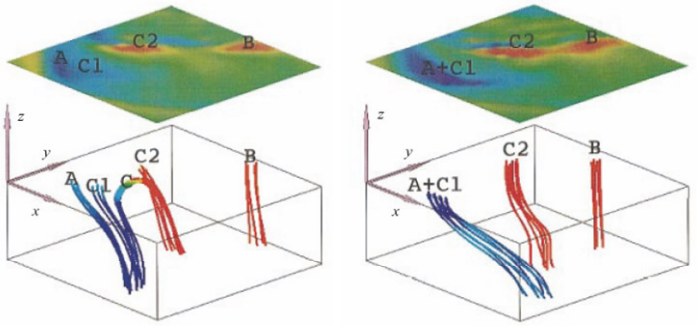

(b) Shen et al. (1999)

Figure 1.7: DNS results for interaction of horse-shoe with a free-surface

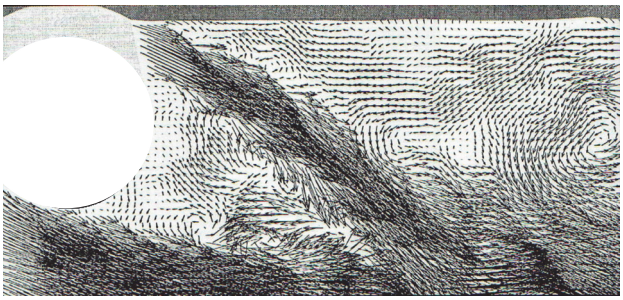

(a) Detached jet from surface

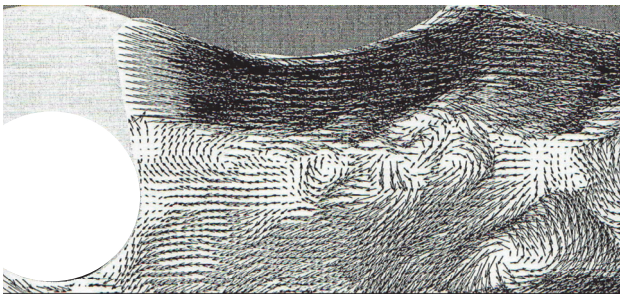

(b) Attached jet from surface

Figure 1.8: LDA of jet attachment and detachment from a cylinder near a free-surface [Sheridan et al (1995)]

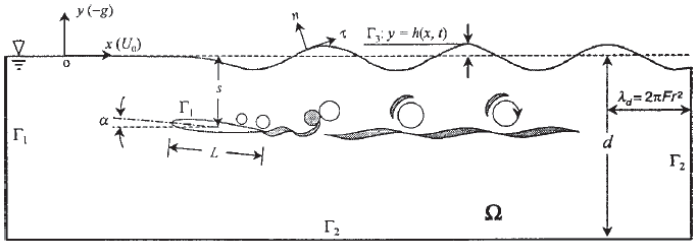

Figure 1.9: Numerically studied case for an inclined foil near a free-surface boundary [Chen & Chwang (2002)]

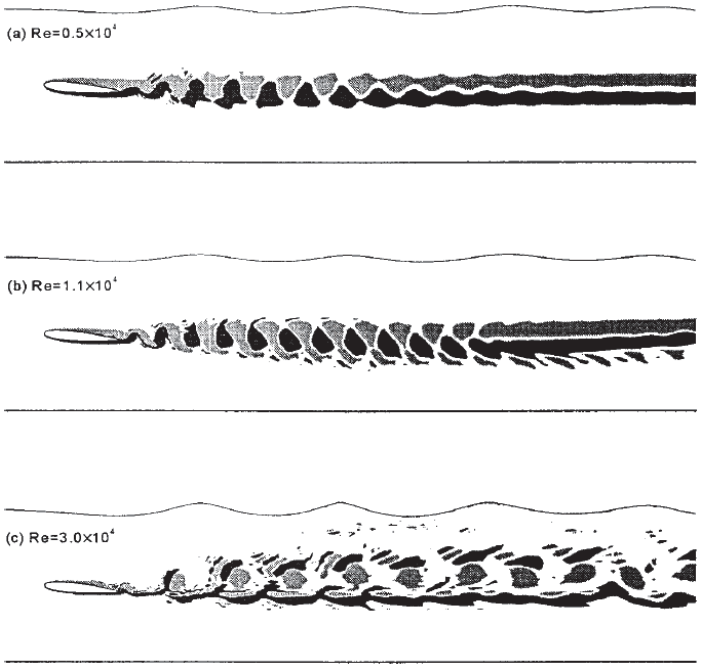

Figure 1.10: Numerically obtained vortex shedding from an inclined airfoil for various Reynolds numbers [Chen & Chwang (2002)]

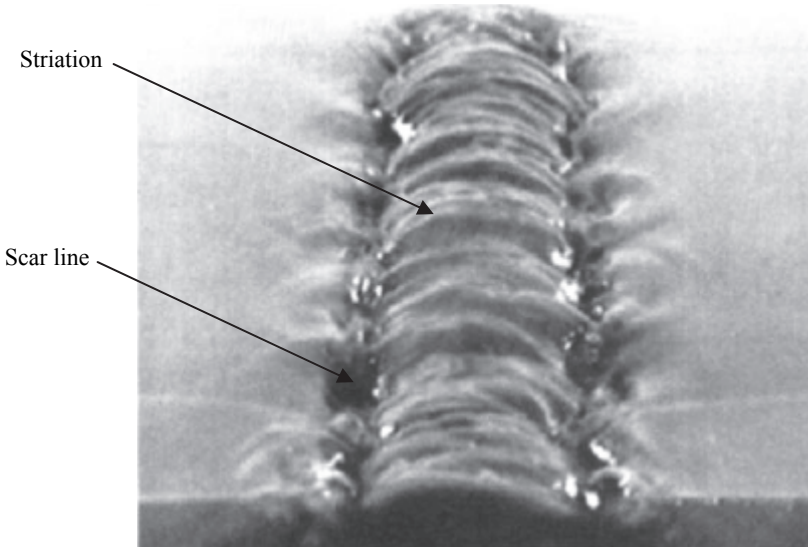

Figure 1.11: Presence of scars and striations on the free-surface boundary due the interaction of a vortex couple [Sarpkaya & Suthon (1991)]

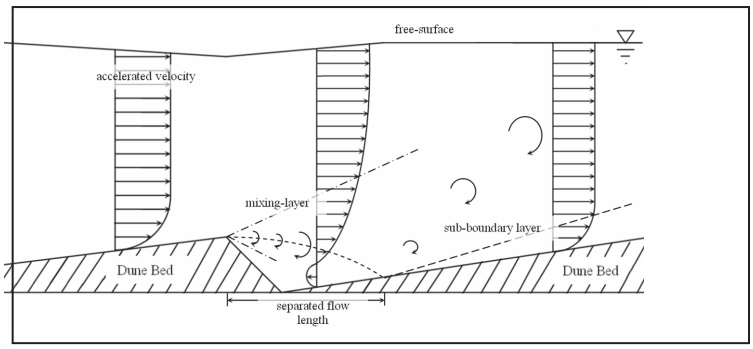

Figure 1.12: Behaviour of flow over dunes [Nezu & Nakagawa (1989)]

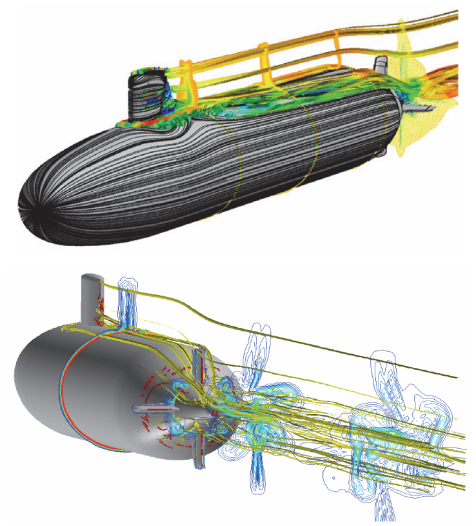

Figure 1.13: LES results around SUBHOFF configuration [Bensow et al (2004)]

Chapter 2 Computational Hydrodynamics

This chapter provides insight into the numerical aspects of the code used. Aspects addressed are; the governing and solved equations, time advancement, pressure velocity coupling, surface modelling and boundary conditions. To aid in the better understanding of the IBEXVOLES, Figure 2.1 shows the schematic outline for the code procedure.

2.1 The Governing Equations and Solved Equations

The equations that govern the motion of fluid substances such as liquids and gases are known as the Navier-Stokes equations, named after Claude-Louis Navier and George Gabriel Stokes, who independently derived the equations. Solution of these equations[1] through computational methods like DNS can yield accurate behaviour of a flow field that would otherwise have to be obtained experimentally. The advantage that simulations hold over experimental means is that parameters such as Reynolds number and Froude number are easily changed, which otherwise proves difficult to do experimentally (discussed further in section 2.1.4). Moreover, simulations can in general be more informative. They are capable of providing detailed instantaneous data for vortex structures and their influence on local Reynolds stresses and pressure

[1] In practice, these equations are too difficult to solve analytically. Therefore, bounded approximations to these equations are solved instead. The approximations include truncation errors introduced through discretisation and the use of turbulence models.

straining compared against using an experimental approach. In addition, numerical simulations are also easily repeatable.

In full form the Navier-Stokes equations along with the continuity constraint are given by equations 2.1 and 2.2. The expressions are simplified using Einstein's notation, where *i* and *j* range from 1 to 3 and represent the different directions and velocity components, respectively:

Continuity

$$\frac{\partial \rho}{\partial t} + \frac{\partial \rho u_i}{\partial x_i} = 0 \tag{2.1}$$

Momentum

$$\frac{\partial \rho u_i}{\partial t} + \frac{\partial \rho u_i u_j}{\partial x_j} = -\frac{\partial p_i}{\partial x_i} + \frac{\partial}{\partial x_j}\left(\mu \tau_{ij}^s - \frac{2}{3}\mu \delta_{ij}\frac{\partial u_j}{\partial x_j}\right) + \rho g_i \tag{2.2}$$

$$\tau_{ij}^s = \left(\frac{\partial u_j}{\partial x_i} + \frac{\partial u_i}{\partial x_j}\right)$$

For incompressible liquids $\left(\frac{\partial \rho}{\partial t} = 0\right)$, as is the case with the problem being studied the Navier-Stokes equations simplify to the following form:

$$\frac{\partial u_i}{dx_i} = 0 \tag{2.3}$$

$$\frac{\partial u_i}{\partial t} + \frac{\partial u_i u_j}{\partial x_j} = -\frac{1}{\rho}\frac{\partial p_i}{\partial x_i} + \upsilon \frac{\partial^2 u_i}{\partial x_j{}^2} + g_i \tag{2.4}$$

2.1.1 Filtering the Navier-Stokes Equation

In order to solve the above equations with the large-eddy methodology[2], the governing equations are required to be filtered such that scales smaller than the grid cell size are

[2] The large-eddy methodology involves solving for the largest scales of motion that are equal and larger than that of the filter width. Scales smaller than the grid cells are accounted for through the use of a model.

dropped, consequently equations 2.3 and 2.4 become 2.5 and 2.6 when used with the large-eddy simulation technique:

$$\frac{\partial \overline{u_i}}{\partial x_i} = 0 \tag{2.5}$$

$$\frac{\partial \overline{u}_i}{\partial t} + \frac{\partial \overline{\overline{u}_i \overline{u}_j}}{\partial x_j} = -\frac{1}{\rho}\frac{\partial \overline{p}_i}{\partial x_i} + \nu \frac{\partial^2 \overline{u}_i}{\partial x_j^{\,2}} + g_i + \frac{\partial \tau_{ij}^{sg}}{\partial x_j} \tag{2.6}$$

In the above equations the over bar denotes the filtered equations, the addition of the extra term τ_{ij}^{sg} is a direct result of the non-linear convective term. τ_{ij}^{sg} is the sub-grid tensor used to correct the flow by taking into account (via a model) the effects of the unresolved length scales, therefore accounting for the remainder of the energy spectrum and length scale interaction. Figure 2.2, illustrates the sub-grid scales in both physical space and Fourier space, in both cases the model is used to establish the behaviour in which the energy is transferred to the smallest scales. The use of sub-grid models is further addressed in section 2.3 .

2.1.2 Discretization Method

Discretization of equations 2.5 and 2.6 is performed via a conservative manor, namely, through the use of the finite volume methodology. This method entails the creation of small control volumes around each nodal point. In effect the Navier-Stokes equations are filtered locally over a control volume. Moreover, the use of the divergence theorem allows for the divergence terms inside the Navier-Stokes equations to be recasted into surface integrals. Hence any changes within a constructed volume are passed to surrounding volumes that share a face. Summing across all control volume faces results in the total divergence of the domain occurring due to the flux change across the domain boundaries (divergence theorem across the domain). It is for this reason that the finite volume method is considered conservative. Therefore, equations 2.5 and 2.6 are redefined below in integral form.

$$\int_v \frac{\partial \overline{u_i}}{dx_i} dv = 0 \Rightarrow \int_s \overline{u_i} \cdot n ds = 0 \tag{2.7}$$

$$\int_v \frac{\partial \bar{u}_i}{\partial t} dv + \int_v \frac{\partial \overline{\bar{u}_i \bar{u}_j}}{\partial x_j} dv = -\int_v \frac{1}{\rho} \frac{\partial \bar{p}_i}{\partial x_i} dv + \int_v \upsilon \frac{\partial^2 \bar{u}_i}{\partial x_j^{\,2}} dv + \int_v g_i dv - \int_v \frac{\partial \tau_{ij}^{sg}}{\partial x_j} dv \Rightarrow$$
$$\int_v \frac{\partial \bar{u}_i}{\partial t} dv + \int_s \overline{\bar{u}_i \bar{u}_j} \cdot nds = \int_s \left(\upsilon \frac{\partial \bar{u}_i}{\partial x_j} - \frac{\bar{p}_i}{\rho} \right) \cdot nds + \int_v g_i dv - \int_v \frac{\partial \tau_{ij}^{sg}}{\partial x_j} dv \quad (2.8)$$

2.1.3 Moving Grid and Space Conversation Law

Much of the work in this thesis concentrates on problems that involve a free-surface. This requires additional attention due to the ability of a free-surface to deform. In the current work the free-surface is accounted for via the use of a moving grid (further covered in section 2.7). The use of a moving grid implies that the volumes are changed every time the surface moves. When a control volume moves or is altered, it is required to satisfy the space conservation law, which relates the rate of change of a control volume to its surface velocity (v_b) as follows:

$$\frac{d}{dt}\int_v dv - \int_s v_b \cdot nds = 0 \qquad \Rightarrow \qquad \frac{d}{dt}\int_v dv = \int_s v_b \cdot nds \quad (2.9)$$

Substituting equation 2.9 into equation 2.8 gives the following equation to be solved that now enforces conversation on a moving grid. Note, grid movement is restricted to the vertical direction only, hence v_b=0 for $j \neq 3$:

$$\int_v \frac{\partial \bar{u}_i}{\partial t} dv + \int_s \bar{u}_i \left(\bar{u}_j - v_b \right) \cdot nds = \int_s \left(\upsilon \frac{\partial \bar{u}_i}{\partial x_j} - \frac{\bar{p}_i}{\rho} \right) \cdot nds + \int_v g_i dv - \int_v \frac{\partial \tau_{ij}^{sg}}{\partial x_j} dv \quad (2.10)$$

2.1.4 Dimensionless form of Navier-Stokes

In experiments, the requirement for scaling of real flow parameters to a scaled model is possible through dimensional relationships. The same procedure can be performed upon the Navier-stokes equations. Using the normalised dimensions shown below (equations 2.11-2.13) the momentum equation can be expressed as equation 2.14, where reference values typically used for normalisation purposes are the either free-stream velocity U_0 and characteristic length L_c or shear velocity U^* and viscous length l_τ.

$$u^* = \frac{u}{U_0} \tag{2.11}$$

$$l^* = \frac{l}{L_c} \tag{2.12}$$

$$t^* = \frac{t}{L_c / U_0} \tag{2.13}$$

$$St\int_v \frac{\partial \overline{u^*}_i}{\partial t^*} dv + \int_s \overline{u^*}_i \left(\overline{u^*}_j - v_b\right) \cdot nds = \frac{1}{\mathrm{Re}} \int_s \frac{\partial \overline{u^*}_i}{\partial x^*_j} \cdot nds - \int_s \frac{\overline{p}_i}{\rho} \cdot nds + \frac{1}{Fr^2} \int_v g^*_i dv - \int_v \frac{\partial \tau^*_{ij}}{\partial x^*_j} dv \tag{2.14}$$

Dimensionless relationships that appear in the momentum equations are the Strouhal, Reynolds and Froude numbers, respectively. In the dimensionless form, the momentum equations are useful for showing the relative importance of the above relationships on the flow.

2.2 Normalised Variable Diagram Criterion

The convective term of the fluid transport equation non-linear. Therefore it would be appealing to use higher order schemes during discretization to better represent its behaviour. In this work the convective term is discretized using a second-order central differencing (CD) scheme. The use of central differencing is known to produce unphysical oscillations in regions of the flow that exhibit sharp velocity gradients [Versteeg & Malalasekera (2007)] which can propagate throughout the domain corrupting the solution, especially in cases where the peclet number (ratio of advection to diffusion) is high. Furthermore, the use of a collocated grid can give rise to the well known problem of velocity-pressure decoupling (dependent upon discretization of pressure) which in turn can also induce velocity oscillations. Therefore some method is needed to ensure that the velocity remains bounded upwind.

Leonard (1991) performed an analysis of basic differencing schemes for the convective term in terms of a Taylor series expansion. He concluded that if the leading term of the truncation error included odd-order spatial derivatives, the solution is affected by a certain amount of numerical diffusion. Conversely, if the leading truncation term

includes even-order derivatives, numerical dispersion occurs, causing physical and unbounded oscillations.

For this reason – the occurrence of unphysical oscillations, researchers have examined and proposed various methods to ensure boundedness of a solution. Some of the early work in producing higher order schemes includes that of Leonard (1990) who proposed a partially unstable third order discretization scheme. Other approaches that have been pursued since then include the development of schemes that locally adjust the convective term based on the current solution. Commonly used approaches for determining the local behaviour of the convective term are based upon one-dimensional analysis, these schemes are typically based upon either the TVD (total variation diminishing) or NVD (normalised variable diagrams) criterion. Examples of schemes developed based upon the TVD procedure include the work by Roe (1983) whom devised the SUPERBEE scheme that flows the limiter regime exactly and the commonly used van Alabada scheme [van Albada *et al* (1982)]. While examples of schemes developed based upon the NVD procedure include works by Choi *et al* (1995), whom devised a more stable version of Leonards QUICK scheme namely SMARTER and the HLPA proposed by Zhu (1992).

The scheme implemented to ensure that the central differencing used to discretize the convective term remains bounded during the solution is based upon the NVD criteria. The scheme used is the gamma scheme as proposed by Jasak *et al* (1999) and is applied at all interior cell faces excluding forcing points via means of 1D analysis. Depending upon the direction of the flow through the face upstream, central and downstream nodes are identified as shown in Figure 2.3. All terms are normalised via equation 2.15, for use with the NVD based scheme. As illustrated in Figure 2.3, ϕ_d and ϕ_u become 0 and 1 respectively due to normalisation (2.15). If the determined value of $\widetilde{\phi}_c$ exceeds these normalised limits the scheme defaults to upwind differencing (UD) for prescribing the flux through the cell face to ensure boundedness.

$$\widetilde{\phi} = \frac{\phi - \phi_d}{\phi_u - \phi_d} \tag{2.15}$$

Figure 2.4 shows how upwind differencing (UD), central differencing (CD) and linearized upwind differencing (LUD) are represented in an NVD representation. In

accordance to the NVD criterion a scheme is well bounded if it passes though points (0,0) and (1,1) while remaining within the marked/bounded region. It can be observed that the UD is well bounded unlike the LUD which fails to pass through (1,1) and CD which fails to pass through (0,0). Therefore some form of intervention is needed to ensure that such schemes do pass through the required points. The majority of NVD schemes consequently use partial blending between LUD over a pre-specified range (β_m) to attain boundedness. The approach proposed by Jasak et al. establishes a smooth transition between UD and CD using a linear blending factor (γ) that is determined based upon the value of $\tilde{\phi}_c$ (equation 2.15), such that:

- If $\tilde{\phi}_c \leq 0 \Rightarrow \gamma = 0 \Rightarrow \phi_f$ is prescribed using UD
- If $\tilde{\phi}_c \geq \beta_m \Rightarrow \gamma = 1 \Rightarrow \phi_f$ is prescribed using CD

The use of a smooth transition function between UD and CD reduces the amount of switching in the differencing scheme needed to ensure boundedness, hence improving convergence. Figure 2.5 shows the transition from UD to CD using the gamma function in the form of an NVD, where the value of β_m can vary from 0.1 to 0.5. The limiting values on the range for β_m are imposed to ensure order of accuracy [Leonard (1991)] and stability of the scheme [Jasak *et al* (1999)].

The gamma scheme therefore works as follows once the flow directions are determined and local nodes identified, $\tilde{\phi}_c$ and γ are determined (equations 2.16 and 2.17).

$$\tilde{\phi}_c = \frac{\phi_c - \phi_{f-}}{\phi_{f+} - \phi_{f-}} = 1 - \frac{\phi_c - \phi_{f+}}{\phi_{f+} - \phi_{f-}} \tag{2.16}$$

$$\gamma = \frac{\tilde{\phi}_c}{\beta_m} \tag{2.17}$$

The convective term is then determined as follows, where the term f_x is the interpolation to the cell face:

- if $\tilde{\phi}_c \leq 0$ or $\tilde{\phi}_c \geq 1$ upwind differencing (UD) is used:

$$\phi_c = \phi_f \tag{2.18}$$

- if $\tilde{\phi}_c \geq \beta_m$ and $\tilde{\phi}_c < 1$ central differencing (CD) is used:

$$\phi_f = f_x \phi_c + (1 - f_x)\phi_d \tag{2.19}$$

- if $\tilde{\phi}_c > 0$ and $\tilde{\phi}_c < \beta_m$ blending between CD and UD is used:

$$\phi_f = (1 - \gamma(1 - f_x))\phi_c + \gamma(1 - f_x)\phi_d \tag{2.20}$$

2.3 Sub-grid and Closure Models

The need for sub-grid and closure models arise from the need to account for the energy transfer between the resolved and unresolved part of the energy spectrum (sub-grid models) or in case of the later (closure models), to account for the energy transfer across the entire spectrum [Sagaut (2002)]. This is a direct result of simplification the Navier-Stokes equations. This section provides an overview for the implemented Smagorinsky LES model and the Spalart-Almaras DES (detached eddy simulation) model.

2.3.1 LES Sub-grid Model

As previously mentioned, the need for sub-grid models arises from the need to account for the unresolved scales, which are a direct result of the expansion of the non-linear convective term. An expression for unresolved stresses (τ_{ij}^{sg}) can be obtained by expanding the filtered non-linear convective term as shown in equation 2.21, where the overbar again represent the filtered value (note the resolved part of the velocity $U^r = \bar{u} = u - u'$) [Sagaut (2002)]. It is apparent that the effects of the unresolved scales are relevant and cannot be easily ignored.

$$\overline{u_i u_j} = \overline{(U_i^r + u_i')(U_j^r + u_j')} = \underbrace{\overline{U_i^r U_j^r}}_{resolved} + \underbrace{\overline{U_i^r u_j'} + \overline{U_j^r u_i'}}_{C_{ij}} + \underbrace{\overline{u_i' u_j'}}_{R_{ij}} \tag{2.21}$$

The second and third terms in equation 2.21 represent the interaction between resolved and unresolved scales and are referred to as the cross-stress tensor (C_{ij}). The final term on the right-hand side refers to the interaction amongst the unresolved scales and is know as the Reynolds sub-grid tensor (R_{ij}). The sub-grid tensor (τ_{ij}) is used to group terms that are not exclusively dependent upon the large scales, hence the sub-grid tensor can be defined as:

$$\overline{u_i u_j} - \overline{U_i^r U_j^r} = R_{ij} + C_{ij} = \tau_{ij}^{sg} \tag{2.22}$$

Equation 2.22 is still difficult to solve as the term $\overline{U_i^r U_j^r}$ requires a second addition of the filter. A more commonly used definition is that proposed by Leonard (1974), where the sub-grid tensor can be expressed in the form of equation 2.23.

$$\overline{u_i u_j} - \overline{U_i^r}\ \overline{U_j^r} = L_{ij} + C_{ij} + R_{ij} = \tau_{ij}^{sg} \tag{2.23}$$

L_{ij} is the Leonard tensor, which represents interaction amongst large scales.

The most commonly used and stable sub-grid scale model is the Smagorinsky model. The Smagorinsky model falls within the category of eddy viscosity models; these types of models are absolutely dissipative and only account for the forward scattering of energy. This implies that locally, in many situations, the behaviour can be incorrect if backscattering of energy is possible. However, globally the solutions produced using this model have been successful. Equation 2.24 below defines the eddy viscosity in terms of the Smagorinsky model:

$$\nu_t = L_{eff}^{\ 2} \left(2 S_{ij} S_{ij}\right)^{\frac{1}{2}} \tag{2.24}$$

Where terms S_{ij}, Δ and C_s denote the symmetrical part of the mean velocity gradient, the effective length defined as the cubic root of the cell volume and the model constant that typically lies between 0.1-0.2, respectively.

Towards the wall boundary the eddy viscosity is damped using the damping function [Piomelli *et al* (1990)] given below. However, close to the immersed boundary and bed

exists a region in which both distances have influence, for example, near corner/junction type flows. In this region an effective damping and effective length scale is used [Shi *et al* (2000)].

$$\Gamma_d = l_{wall}\kappa\left(1-\exp\left(\frac{l_{wall}u^*}{25\nu}\right)^3\right)^{0.5} \tag{2.25}$$

$$\Gamma_{effl} = \left(\frac{1}{\Gamma_{d1}{}^2}+\frac{1}{\Gamma_{d2}{}^2}\right)^{-1/2} \tag{2.26}$$

$$L_{eff} = \left(\frac{1}{L_1{}^2}+\frac{1}{L_2{}^2}\right)^{-1/2} = \left(\frac{1}{\Gamma_{effl}{}^2}+\frac{1}{(\Delta C_s)^2}\right)^{-1/2} \tag{2.27}$$

2.3.2 DES Closure/Hybrid Model

The difficulty with LES, like with all methodologies is the need for higher resolution with increasing Reynolds number, especially close to near wall regions. This requirement of high wall resolution has been a major draw-back and hindrance in the application of LES to very high Reynolds number flows. Typically, wall resolution requirements by LES can require as many points needed by direct numerical simulation (DNS) to accurately capture the boundary. A commonly adopted approach to reduce the near wall resolution requirement of LES is to invoke the use of wall shear stress models to provide a general prediction of the near wall stresses. Such works include that of Tseng *et al* (2006), who used the log-law to account for the near wall stresses for urban buildings and by Bensow *et al* (2004) in their LES of the SUBOFF, a well documented submarine configuration.

Although wall models lack the ability to provide the full scale of motion within its applied area or provide accurate instantaneous information to a high degree, they do allow for a larger mesh to be used near the boundary. With the use of wall models intuitively larger wall normal spacing is attainable, however, an increase in cell size results in the increase of the filter width towards the wall. This can result in the effective eddy viscosity close to the wall being incorrect.

Spalart *et al* (1997) suggested another approach to the modelling of turbulence, namely Detached Eddy Simulation (DES). Originally, LES was used to bridge the gap that existed between DNS and RANS methods, however DES is used to bridge between LES and RANS. The basic aim of DES or hybrid models is to combine the effectiveness of a RANS model in the near wall region with the superior power of LES in separated/free-evolving flows. Spalart proposed using a modified version of the one-equation Spalart-Allmaras turbulence model [(Spalart, 1992)] instead of the Smagorinsky sub-grid model. Originally the one-equation Spalart-Allmaras was developed for use in turbulent boundary layers, shear layers, and separated flows. The modified Spalart-Allmaras model essentially acts like the Smagorinsky model away from the boundary, whilst near the wall defaults back its original model, where it has been calibrated to account for both attached and detached flows.

Piomelli & Balaras (2002) categorise such a model as a zonal approach. Conventional zonal approaches split the grid into two parts close to the wall. However with the DES approach only a single grid is used; instead the splitting occurs in the modelling of the eddy viscosity. Researchers have discovered since the original development of the model that the switching between models can result in early separation and reduced model stresses depending upon the grid resolution. Approaches such as delayed-DES [Spalart *et al* (2006)] and shielding for the SST version of a DES model [Menter & Kuntz (2002)], have been introduced to deal with the aforementioned issue. Despite this drawback, DES has been used to successfully model flow around a full body fighter jet [Forsythe *et al* (2004)] as well as the flow around a complete vehicle [Mendonca *et al* (2002)]. In depth reviews on the research and achievements of DES have been performed by Squires (2003) and Spalart (2009).

2.3.2.1 Spalart-Allmaras Model

The turbulent viscosity (ν_t) is computed from equation 2.28, where f_{v1} represents a viscous damping function similar to that used within the Smagorinsky model (van Driest damping). The term χ is used to approximate the non-dimensional wall distance.

$$\nu_t = \rho\tilde{\nu}f_{v1} \tag{2.28}$$

$$f_{v1} = \frac{\chi^3}{\chi^3 + c_{v1}{}^3} \tag{2.29}$$

$$\chi \equiv \frac{\tilde{\nu}}{\nu} \tag{2.30}$$

The switching between LES and RANS models is controlled by the local distance d. Where d is determined to be the lower of either the local distance to a boundary, or the maximum of the local cell size (equations 2.31 and 2.32). Depending upon the value of d, the model behaves either as the standard RANS model or similar to the Smagorinsky model.

$$d = \min(c_{des}\Delta, w_d) \tag{2.31}$$

$$\Delta = \max\left(\Delta_x, \Delta_y, \Delta_z\right) \tag{2.32}$$

The transport variable ($\tilde{\nu}$) in the model is identical to the turbulent kinematic viscosity except in the near-wall (viscous-affected) region. The transport equation is given by equation 2.33 and is discretized in a procedure consistent with the overall scheme used. Terms G_v and Y_v represent production and destruction of turbulent viscosity in the near-wall region, respectively.

$$\int_v \frac{\partial \rho \tilde{\nu}}{\partial t} + \int_v \frac{\partial \rho \tilde{\nu} u_i}{\partial x_i} = \int_v G_v + \frac{1}{\sigma_{\tilde{\nu}}}\left[\int_v \frac{\partial}{\partial x_j}\left\{\left(\mu + \rho\tilde{\nu}\right)\frac{\partial \tilde{\nu}}{\partial x_j}\right\} + c_{b2}\rho\int_v\left(\frac{\partial \tilde{\nu}}{\partial x_j}\right)^2\right] - \int_v Y_v \tag{2.33}$$

The production term is defined below, where $\tilde{S}$ is defined by equations 2.35 through to 2.39. Note, that the modified expression for S (scalar measure of deformation tensor) is used rather than the original expression. The original expression was formulated to account for turbulence through vortices near the wall. However, since then it has be acknowledged that the effect of the strain should also be considered in the turbulent production [Dacles-Mariani *et al* (1995)].

$$G_v = c_{b1}\rho\tilde{S}\tilde{\nu} \tag{2.34}$$

$$\tilde{S} \equiv S + \frac{\tilde{\nu}}{\kappa^2 d^2} f_{v2} \tag{2.35}$$

$$f_{v2} = 1 - \frac{\chi}{1 + \chi f_{v1}} \tag{2.36}$$

$$S = \left|\Omega_{ij}\right| + c_{prod} \min\left(0, \left|S_{ij}\right| - \left|\Omega_{ij}\right|\right) \tag{2.37}$$

$$\left|\Omega_{ij}\right| = \sqrt{2\Omega_{ij}\Omega_{ij}} \quad \left|S_{ij}\right| = \sqrt{2S_{ij}S_{ij}} \tag{2.38}$$

$$\Omega_{ij} = \frac{1}{2}\left(\frac{\partial u_i}{\partial x_j} - \frac{\partial u_j}{\partial x_i}\right) \quad S_{ij} = \frac{1}{2}\left(\frac{\partial u_i}{\partial x_j} + \frac{\partial u_j}{\partial x_i}\right) \tag{2.39}$$

The Destruction term Y_v is expressed in terms of equations 2.40 though to 2.43.

$$Y_v = c_{w1}\rho f_w \left(\frac{\tilde{\nu}}{d}\right)^2 \tag{2.40}$$

$$f_w = g\left[\frac{1 + c_{w3}{}^6}{g^6 + c_{w3}{}^6}\right] \tag{2.41}$$

$$g = r + c_{w2}\left(r^6 - r\right) \tag{2.42}$$

$$r \equiv \frac{\tilde{\nu}}{\tilde{S}\kappa^2 d^2} \tag{2.43}$$

Coefficients required to close the model are provided below:

$$c_{w1} = \frac{c_{b1}}{\kappa^2} + \frac{\left(1 + c_{b2}\right)}{\sigma_{\tilde{\nu}}}$$

$$c_{des} = 0.65$$

$$c_{v1} = 7.1$$

$$c_{b1} = 0.1355$$

$$c_{w2} = 0.3$$

$$c_{b2} = 0.622$$

$$c_{w3} = 2.0$$

$$c_{prod} = 2.0$$

$$\sigma_{\tilde{\nu}} = 0.6667$$

$$\kappa = 0.4187$$

2.4 Immersed Boundary Forcing

The concept of modelling the required structure as part of the solution itself is not a new concept; such approaches have often been used in much of classical aerodynamics i.e. lifting line theory. However, the use of such an approach in terms of the solution of the Navier-Stokes equations was first pioneered by Peskin (1972) in simulating cardiac mechanics and related blood flow [Peskin (1977), Peskin & McQueen (1989)]. Since then, numerous modifications and variants have been proposed, all following the fundamental idea of imposing a given structure as part of the steady or unsteady solution. Approaches that follow this concept are termed immersed boundary methods (IBM). The uniqueness of this type of approach lay in the fact that grid generation is greatly simplified, as non-conforming structured grids like Cartesian and curvilinear can be used. Examples include the earlier mentioned works of Peskin for the application of an IB to Cartesian grids. While the works of Ghias *et al* (2005) and Huang *et al* (2008) have employed the IB approach on curvilinear grids. Ghias et al. modelled a rectangular NACA 2415 using a combination of both curvilinear and IB, the IB was applied in regions where the curvilinear approach resulted in a poor mesh quality. Conversely, Huang *et al* (2008) used the IBM to model a sharp interface for a semi-coupled air-water interface. Furthermore, recent works of Pan (2006) and Lohner *et al* (2008) have seen the IBM applied on unstructured grids. In general, the use of an immersed boundary tends to alleviate much of the effort required in the generation of a mesh, in comparison to meshes that conform to the body of interest. However, it should be noted that the use of such simple grids results in a faster increase in the number of grid points in comparison to conforming grids [Mittal & Iaccarino (2005)]. Although the IB approaches do require a larger number of grid points, it does not necessarily entail a larger computational time. This is as a large portion of the grids points exist inside the virtually mapped body and are not taken into consideration.

In practice the use of simple grids results in many grid points not conforming to the boundary of the required body. Therefore, some form of fictitious forcing is required near the body interface to reproduce the desired near body flow behaviour. It is here in the determination of the fictitious force that many of the immersed boundary methods differ. Typically, immersed boundary forcing can be classed as either continuous or as discrete forcing. The continuous forcing approach was proposed and used by Peskin, who accounted for the immersed body by using a system of elastic fibres. The points

upon which the fibres are formed are tracked using a Lagrangian descriptor, the resulting stress associated with the contracting and stretching of the fibres is used to provide the forcing to the momentum equations. Though the approach is good for modelling deforming bodies, many engineering considerations are concerned with the modelling of rigid bodies. Lai & Peskin (2000) did modify the above procedure to allow for the modelling of rigid bodies[3]. This was achieved by increasing the stiffness of the elastic fibres and treating the points upon which the fibres are constructed as equilibrium positions. The drawback of modelling a rigid body in this manor is the need for using a distributed forcing function for stability. The smoothing of the forcing function inherent in this type of approach results in the inability to provide a sharp representation of the IB. In addition, for modelling high Reynolds number flows this can be undesirable, because the force distribution stencil can cause adverse effects on the solution. Furthermore, the uses of a continuous forcing approach in modelling a rigid entail sever stability constraints that are unavoidable during the start-up phase of the solution [Goldstein *et al* (1993), Mittal & Iaccarino (2005)].

The second class of IB methods are often referred to as discrete forcing approaches. Schemes that are formed based on this type of approach eliminate the aforementioned issue regarding stability for modelling rigid bodies [Mittal & Iaccarino (2005)]. Originally proposed by Modh-Yosuf (1997) and later extended to produce a sharper interface by Verzicco *et al* (1998) and Fadlun *et al* (2000). The discrete forcing approach extracts the forcing needed to impose a rigid body on the flow solution directly from the momentum equations. Furthermore, the discrete forcing (also termed direct forcing) versions of the immersed boundary method allow for better local accuracy of the solution near the boundary, by retaining a sharp interface as no forcing distribution function is required. It is for this reason that discrete methods are generally used for higher Reynolds number flows, where the local accuracy of the solution assumes greater importance and the spreading of a force distributor is less desirable.

The implemented immersed boundary approach namely, the ghost-cell immersed boundary (GCIBM) technique proposed by Tseng & Ferziger (2003) falls within the former category of direct/ discrete forcing. The use of the GCIBM over other immersed

[3] Modelling of rigid bodies through a continuous forcing technique was first introduced by Goldstein *et al* (1993), whom used a force feed-back model to control the velocity near the boundary of the geometry. According to Iaccarino & Verzicco (2003) the model can be envisioned as a damped oscillator.

boundary techniques is a result of its consistent treatment for both the pressure and velocity. In addition, with this approach cells that fall within the body are neglected. The later point implies that, in general, fewer calculations are required compared to the number of grid points. As a large number of points can tend to concentrate within the body itself solve time increase is marginal compared to alternative methods.

2.4.1 Application of GCIBM

To use a IB method, grid information such as the location of forcing points and local flow points are required to be determined. This can be done prior or during the initial stages of a simulation. In this work the information is extracted in advance – during the mesh generation stage. For simplicity the procedure for generating the immersed boundary in a grid (following a GCIBM approach) is omitted from this section but is provided in Appendix A for completeness. Figure 2.6 shows the fin geometry generated based on facial points determined for the immersed boundary representation, while Figure 2.7 shows the staircase approximation to the same geometry. Note, the mesh on which the fin is mapped is rectangular therefore the geometry is in fact that of the staircase outline. It is through the discrete forcing that the mapped fin is forced to assume the fin outlined in Figure 2.6.

As mentioned earlier a discrete IB method, namely, the ghost-cell immersed boundary method (GCIBM), is used to account for the presence of a body. The fictitious forcing is expressed as an additional term in the momentum equation (2.44), where the delta function (δ_k) is only active at cells closest to the modelled boundary.

$$\frac{\partial u_i}{\partial t} + \frac{\partial u_i u_j}{\partial x_j} = -\frac{1}{\rho}\frac{\partial p_i}{\partial x_i} + \upsilon\frac{\partial^2 u_i}{\partial x_j{}^2} + g_i + \frac{\partial \tau_{ij}^{sg}}{\partial x_j} + \delta_k f_i \tag{2.44}$$

The forcing term (f_i) is set, such that, at a specific location whether it is at a grid point or the location is arbitrary, the desired value is achieved. For example, if f_i should yield a solution V^{n+1} at a given point then the forcing function can be expressed as the following correction:

$$\delta_k f_i = \frac{V_i^{n+1} - u_i^{n}}{\Delta t} - \frac{\partial u_i u_j}{\partial x_j} + \frac{1}{\rho}\frac{\partial p_i}{\partial x_i} - \upsilon \frac{\partial^2 u_i}{\partial x_j^{2}} - g_i - \frac{\partial \tau_{ij}^{sg}}{\partial x_j} \tag{2.45}$$

For the GCIBM both pressure and velocity are extrapolated to cells that fall just within the prescribed boundary. Nodes at which the opposing force is applied are selected to be those whose cell-centers lie on or just within the prescribed boundary. Figure 2.8 illustrates some of the possible intersections between a cell and boundary that can occur, both figure 2.8a and figure 2.8b fail to satisfy the aforementioned criterion whilst in figure 2.8c and figure 2.8d the criterion is satisfied. Although immersed boundary techniques allow simple grid to be used when modeling irregular nonconforming shapes, additional time and effort is required during grid generation to identify ghost-cell points and when extracting necessary information i.e. positions of surrounding fluid cells.

Ghost-cell values are imposed in two steps: firstly, the values are interpolated at an mirror points located within the fluid domain, secondly the interpolated values are reflected to the ghost-cells [Majumdar *et al* (2001)]. As proposed by Tseng & Ferziger (2003) a second order interpolation is used to maintain a near second-order accuracy. As the model is three-dimensional, in order to evaluate the quadratic (equation 2.46) a 10 point stencil is required, this is depicted in Figure 2.9. Furthermore, as a general rule the grid resolution around the immersed boundary is required to be higher in regions that contain high curvature. In many IB cases this is accounted for through the use of multi-layer meshing. In this work a single stretched grid is used that is refined in close proximity to the body and in regions where there is a sharp curvature. The use of a stretched grid can result in the mirror points falling outside of the defined stencil in certain regions. To alleviate this problem the stencil is expanded; such that values are evaluated at intermediate locations rather than at cell centers (see Appendix A).

$$\phi_{x,y,z} = c_0 + c_1 x^2 + c_2 y^2 + c_3 z^2 + c_4 xy + c_5 xz + c_6 yz + c_7 x + c_8 y + c_9 z \tag{2.46}$$

To evaluate equation 2.46, the coefficients are determined in terms of nodal values using equation 2.47, where matrix $M_{n,n}$ is evaluated and stored during the grid generation stage rather than being computed or recomputed as part of the simulation. It should be noted that ϕ_0 is the desired boundary condition on the immersed boundary,

i.e. where the ghost-cell cuts the approximate plane to its normal mirror point. As the simulations considered are of the viscous type, the no-slip condition is imposed along the immersed boundary interface (ϕ_0=0). The coefficients for the matrix can be evaluated as flows:

$$\begin{bmatrix} c_0 \\ c_1 \\ \vdots \\ \vdots \\ c_n \end{bmatrix} = M_{n,n}^{-1} \begin{bmatrix} \phi_0 \\ \phi_1 \\ \vdots \\ \vdots \\ \phi_n \end{bmatrix}$$

$$M^{-1} = \begin{bmatrix} 1 & x_0^2 & y_0^2 & z_0^2 & x_0y_0 & x_0z_0 & y_0z_0 & x_0 & y_0 & z_0 \\ 1 & x_1^2 & y_1^2 & z_1^2 & x_1y_1 & x_1z_1 & y_1z_1 & x_1 & y_1 & z_1 \\ \vdots & \vdots & \vdots & \vdots & \vdots & \vdots & \vdots & \vdots & \vdots & \vdots \\ \vdots & \vdots & \vdots & \vdots & \vdots & \vdots & \vdots & \vdots & \vdots & \vdots \\ 1 & x_{10}^2 & y_{10}^2 & z_{10}^2 & x_{10}y_{10} & x_{10}z_{10} & y_{10}z_{10} & x_{10} & y_{10} & z_{10} \end{bmatrix}^{-1} \tag{2.47}$$

Similarly, the pressure is evaluated in the same way using equation 2.46. However the construction of the coefficient matrix does differ for the pressure when compared to the velocity. This is because the Neumann condition is used to enforce the pressure boundary condition on ϕ_0 (2.48).

$$\frac{\partial p}{\partial n} = \frac{\partial p}{\partial x}\hat{n}_x + \frac{\partial p}{\partial y}\hat{n}_y + \frac{\partial p}{\partial z}\hat{n}_z = 0 \tag{2.48}$$

Coefficients for the pressure matrix are evaluated via equation 2.49, where c_θ, c_α and c_β are the projections of the normal surface vector onto the *x*, *y*, *z* axis and terms ct_1, ct_2 and ct_3 are given by equations 2.50 through to 2.52.

$$\begin{bmatrix} c_0 \\ c_1 \\ \vdots \\ \vdots \\ c_n \end{bmatrix} = M_{n,n}^{-1} \begin{bmatrix} \partial p / \partial n \\ \phi_1 \\ \vdots \\ \vdots \\ \phi_n \end{bmatrix}$$

$$M^{-1} = \begin{bmatrix} 0 & 2x_0c_\theta & 2y_0c_\alpha & 2z_0c_\beta & ct_1 & ct_2 & ct_3 & c_\theta & c_\alpha & c_\beta \\ 1 & x_1^2 & y_1^2 & z_1^2 & x_1y_1 & x_1z_1 & y_1z_1 & x_1 & y_1 & z_1 \\ \vdots & \vdots & \vdots & \vdots & \vdots & \vdots & \vdots & \vdots & \vdots & \vdots \\ \vdots & \vdots & \vdots & \vdots & \vdots & \vdots & \vdots & \vdots & \vdots & \vdots \\ 1 & x_{10}^2 & y_{10}^2 & z_{10}^2 & x_{10}y_{10} & x_{10}z_{10} & y_{10}z_{10} & x_{10} & y_{10} & z_{10} \end{bmatrix}^{-1} \tag{2.49}$$

$$ct_1 = c_\alpha x_0 + c_\theta y_0 \tag{2.50}$$

$$ct_2 = c_\beta x_0 + c_\theta z_0 \tag{2.51}$$

$$ct_3 = c_\beta y_0 + c_\alpha z_0 \tag{2.52}$$

2.5 Time advancement

Unsteady problems require the solution to be marched forward in time, in order for the solution to progress and compile statistical data. To accurately advance in time, a third-order explicit Runge-Kutta (RK3) scheme based on Heun's method [Heun (1889)] is used. The advantages of Runge-Kutta schemes are their tendency to be more accurate and require less storage than their counter parts based on multi-step methods [Ferziger & Peric (2002)]. Higher accuracy is obtained due to Runge-Kutta schemes dividing a time step into sub-time steps rather than using data across past time steps. In addition, they also prove to be more stable for higher order schemes when compared to their counter parts based on multipoint methods. Equation 2.53 shows how the velocities are advanced to the new time step. As time is advanced explicitly, velocities at each sub-time step are computed based on already known values:

$$u_i^{n+1} = u_i^n + \frac{\Delta t}{4}\left(a_1 u_i^n + a_2 u_i^{n+\frac{1}{3}} + a_3 u_i^{n+\frac{2}{3}} \right) \tag{2.53}$$

where the coefficients a_1, a_2 and a_3 in the above equation are 1, 0 and 3, respectively, in accordance to Heun's method. Intermediate velocities are evaluated as follows:

$$u_i^{n+\frac{1}{3}} = u_i^n + \frac{\Delta t}{3}\left(u_i^n\right) \tag{2.54}$$

$$u_i^{n+\frac{2}{3}} = u_i^n + \frac{2\Delta t}{3}\left(u_i^{n+\frac{1}{3}}\right) \tag{2.55}$$

The drawback of using higher order schemes is the need to advance the pressure at every sub-time step to maintain the overall accuracy. This impacts on the overall computational cost in terms of CPU time. Le & Moin (1991) were able to reduce the computational cost per time-step for a third order Runge-Kutta scheme by only solving for the pressure at the final step. As the pressure is not solved, but approximated at sub-steps the former third order accuracy reduces to second order. The modified third-order scheme still maintains the advantage of being less computationally expensive for obtaining second order accuracy, in comparison to using an actual second order scheme where the pressure is solved twice per time step.

2.6 Pressure solution

The pressure term within the Navier-Stokes equations tends to complicate matters by lacking an independent equation. For compressible flows, the problem is simpler to address as the continuity equation plays a dynamic role and can be used to find the density. The pressure can then be determined from the equation of state. This is not the case for incompressible flows where the continuity equation is more a kinematic constraint than a dynamic equation.

2.6.1 Poisson Equation

Instead, the Poisson pressure equation is used to correct for pressure in incompressible flows. The equation is derived by taking the divergence of the momentum equation and using the continuity equation to simplify, yielding:

$$\frac{\partial}{\partial x_i}\left(\frac{\partial p}{\partial x_i}\right) = -\frac{\partial}{\partial x_i}\left[\frac{\partial}{\partial x_j}\left(\rho u_i u_j - \nu \tau_{ij}^s\right)\right] \tag{2.56}$$

For the case of constant density and viscosity (2.56) becomes:

$$\frac{\partial}{\partial x_i}\left(\frac{\partial p}{\partial x_i}\right) = -\frac{\partial}{\partial x_i}\left[\frac{\partial\left(\rho u_i u_j\right)}{\partial x_j}\right] \tag{2.57}$$

2.6.2 Projection Method

To solve for pressure, the two most commonly used approaches are those based on the SIMPLE method and the projection method. In this study, the pressure is solved using the projection method. In the projection method the solution of the discretized Navier-Stokes equations is split into two parts: in the initial step the pressure is omitted and the momentum equations are solved, meaning an approximate velocity is obtained.

$$u_i^{\,*} = u_i^{\,n} + \Delta t\left(\upsilon \frac{\partial^2 u_i^{\,n}}{\partial x_j^{\,2}} - \frac{\partial u_i^{\,n} u_j^{\,n}}{\partial x_j} + g_i\right) \tag{2.58}$$

In the second step the difference between the velocity solutions across the time step are related back to the pressure gradients.

$$\left(\frac{u_i^{\,n+1} - u_i^{\,*}}{\Delta t}\right) = -\frac{\partial p^{n+1}}{\partial x_i} \tag{2.59}$$

Alternatively,

$$u_i^{\,n+1} - u_i^{\,*} + \Delta t\left(\frac{\partial p^{n+1}}{\partial x_i}\right) = 0 \tag{2.60}$$

The problem with either (2.59) or (2.60) is that neither the pressure nor velocity are known at time n+1. Instead, by taking the divergence of either equation and noting that at time step n+1 the velocity field is required to satisfy continuity, giving:

$$\nabla\left(\frac{\partial p}{\partial x_i}\right) = \nabla \rho u_i^* \tag{2.61}$$

This result means that the divergence in the pressure gradients is solely related to the divergence of the intermediate velocity field, which is a known. Therefore the velocity at time n+1 becomes.

$$u^{n+1} = u_i^* - \frac{\Delta t}{\rho}\left(\frac{\partial p}{\partial x_i}\right) \tag{2.62}$$

2.6.3 Pressure Solver

In many cases the solution of the pressure takes a large portion of the overall computational cost. To minimise the pressure solve time, approximate iterative solvers are generally used. The implemented solvers in IBEXVOLES are the successive over relaxation (SOR) [Young (1971)] and the bi-conjugate gradient stabilized (BCGSTAB) [van den Vorst (1992)] solvers. Both solvers are parallelised for use with the block-cell approach while only the SOR is used parallelised for the use with the GCIBM approach.

2.7 Surface modelling

In order to model the free-surface aspects of flow past a submerged body or topography, the deformation of the free-surface boundary needs accounting for. Typically, two classes exist for modelling the free-surface phenomenon. The first class of methods referred to as surface tracking methods require the grid to be reconstructed every time the surface is advanced. Such grids are generally restricted to non-wave breaking situations. The second class is commonly referred to as interface-capturing methods, where computations are performed on a fixed grid and the shape of the free-surface is determined by computing the fraction of each near-interface cell that are partially filled. Such approaches have the advantage of being able to model breaking waves at the added expense of additional solving time. Examples of surface tracking and interface-capturing methods are moving grids and the volume of fluid (VOF) approach, respectively.

The surface tracking methodology is utilized in this work for the modelling of the free-surface. The use of a moving grid implies that the free-surface forms part of the bounding domain and cell movements occurs through the kinematic condition at the free-surface, implying that no mass can cross this boundary. Therefore, cells defining the free-surface are required to displace in order to avoid fluid crossing the interface. Since the cells are only required to move in the direction of the free-surface, cell movement takes place along vertical grid points such that grid cells stretch and contract with turbulence and wave motion. Equation 2.63 provides the kinematic condition for the free-surface in Eulerian form, but is non-conservative. Instead, the change in surface height is determined directly from the continuity equation as show by equation 2.64. The movement of vertices are determined by summing the flow over a pre-specified depth around the control volumes and interpolated to the local vertices using bilinear interpolation. Alternative interpolation procedures can be used, such as the inverse weighting method, however, the use of more points can be more dissipative for surface waves.

$$\frac{\partial \eta}{\partial t} + u\frac{\partial \eta}{\partial x_1} + v\frac{\partial \eta}{\partial x_2} - w = 0 \tag{2.63}$$

$$\Delta h = -\frac{\Delta t}{A_z}\int_{hbot}^{htop}\left(\Delta flux_i - \Delta flux_j\right) \tag{2.64}$$

Vertices are redistributed in the vertical direction using a linearized function, such that the change in cell size is gradual from its reference position i.e. above the modelled body.

2.7.1 Surface resorting Forces

If a liquid interface is disturbed from its equilibrium position, such as is with the case of waves the forces acting around the interface will try to obtain the original or a new equilibrium state. Depending upon the wavelength, two types of waves exist for which the restoring force differs:

1. ***Capillary waves*** – wave of this nature tend to have a relatively small wavelength such that the dominant resorting force is surface tension.

2. ***Gravity waves*** – for wave lengths far larger than those for capillary waves the dominant restoring force becomes gravity, which tends to return the disturbed surface of the water to its flat equilibrium condition.

Potential analysis performed on free-surface flows has provided a good approximation in accessing the importance and relevance between the two different types of restoring forces (in terms of wave speed) with respect to wavelength. This is illustrated in Figure 2.10 [Crapper (1984)], where a, b and c refer to the phase speed as a function of wave length, wave speed of gravity waves and the wave speed for capillary waves, respectively. As the wavelength increases the effects of surface tension reduce rapidly, while gravity wave effects become more pronounced. However there exists a narrow region of wavelengths for which both capillary and gravity waves effects are important, physically for wavelengths larger then 5cm capillary waves can be ignored. For the present study this is the case and hence surface tension forces are not taken into consideration.

2.8 Boundary Conditions

In order to solve the governing equations on a discretized domain the equations need to be bounded and this section describes the implemented boundary conditions. However, periodic boundaries are not discussed.

2.8.1 Wall model

The need for wall models in conjunction with large eddy simulations is inevitable with increasing Reynolds number. This is attributable to the fact that in order for LES to capture the near wall dynamics the resolution requirement tends closely to that required by DNS. Therefore, increasing Reynolds numbers requires for higher resolution near to the wall boundary, in order to capture the small but dynamically important eddies in this region to accurately represent the boundary layer influence. However, in many applications only a better prediction of wall stresses is truly required. This has resulted in the utilization of wall models to an provide improved estimation of wall stresses for a reduced level of near wall resolution. However, using such models constitutes

additional sources of error, a trade-off in contrast to the increased requirements and solving time if such models were not used.

Wall models in general have been formulated based on two universally considered boundary layer descriptors, namely, the log-law and power law descriptors. Both types of models are used in conjunction with the IBM modeling approach. The Werner & Wengle (1991) is used to account for the bed stress, whilst the log-law is used around the immersed boundary. Though the validity of using scaled power laws (i.e. over a large range of Reynolds numbers) remained questionable by many researchers for a period of time. Extensive research and comparative scaling against the log-law have shown both approaches are quite similar with no real significant preference found toward either law.

2.8.2 Power Law

The bed shear stress is determined through the use of a wall model based upon the power law [Werner & Wengle (1991)]. The key advantages of using the Werner & Wengle over other wall models are that firstly no time averaging of values is required; secondly no iteration method is required for determining the wall shear stress. Furthermore, numerical problems in reattachment regions are avoided.

In short, the assumptions are that the instantaneous tangential velocity components at the wall are in phase with the associated instantaneous wall shear stress, and that the instantaneous velocity profile is defined by equation 2.65.

$$u_{ij}^{+}(z) = \begin{cases} z^{+} & \text{for } z^{+} \le 11.81 \quad \text{(inner layer)} \\ A\left(z^{+}\right)^{B} & \text{for } z^{+} \ge 11.81 \quad \text{(outer layer)} \end{cases} \tag{2.65}$$

where factors A and B are 8.3 and 1/7, respectively.

The wall shear stresses are obtained through the integration of either equations 2.66 and 2.67 over the height of the first grid cell.

$$\tau_p(x,y) = \frac{2\mu|u_{ij}|}{\Delta z} \qquad \text{for} \quad |u_{ij}| \le \frac{\mu}{2\rho\Delta z} A^{\frac{2}{1-B}} \tag{2.66}$$

$$\tau_p(x,y) = \rho\left[\frac{1-B}{2} A^{\frac{1+B}{1-B}} \left(\frac{\mu}{\rho\Delta z}\right)^{1+B} + \frac{1-B}{A} A^{\frac{1+B}{1-B}} \left(\frac{\mu}{\rho\Delta z}\right)^{B} |u_{ij}|\right] \qquad \text{for} \quad |u_{ij}| \ge \frac{\mu}{2\rho\Delta z} A^{\frac{2}{1-B}} \tag{2.67}$$

The resulting equations can be solved analytically for the wall shear stress components.

2.8.3 Log-Law

The application of a wall model with the immersed boundary approach is not trivial. In most cases the surface facial point of the imposed body and its normal do not coincide with the cell centre and cell normal. Hence a direct integration over the cell distance is not possible. Two approaches can be used to approximately determine the shear stress for cells touching on to the immersed boundary. The first approach would require the normal distance and shear velocity to be determined at the point where the cell centre crosses the imposed immersed boundary face. This can be performed using an interpolation procedure, the simplest of which would be using an inverse distance weighting as proposed by Franke (1982). The shear stress can then be computed based upon the normal and projected distance in the direction in which the shear stress is being determined. The second approach entails resolving the wall normal distance (y^+) and shear velocity at the points closest to the immersed boundary, as illustrated in Figure 2.11. The velocity based upon the Log-Law can then be obtained by the direct interpolation between neighboring cells. The shear stress is then computed from the new velocity gradient across the cell[4]. The latter approach is used in conjunction with the immersed boundary due to its simplicity. Furthermore, no time averaging of tangential velocity and/or wall shear stress is performed as the local profile is taken to be logarithmic with the normal velocity component being zero, Kanda *et al* (2004) and Xie & Castro (2006) applied the log-law in a similar manor with no significant difference in results.

[4] Often immersed boundary faces exist inside the neighbouring cell; velocity for the immersed cell face should be set such that the shear force at the point of intersection is zero.

An iterative procedure (Newton-Raphson) is used to solve for the shear velocity as given by equations 2.68 and 2.69, the use of both the inner and Log-Law is to provide a better estimate for the shear velocity based upon the determined wall distance y^+. The shear velocity is computed for all time advancements via the Log-Law itself.

$$u^* \Rightarrow 0 = y^+ - u^+ \Rightarrow u^*_{c+1} = u^*_c - \left[\frac{\frac{yu^*_c}{\upsilon} - \frac{u_{wall}}{u^*_c}}{\frac{y}{\upsilon} + \frac{u_{wall}}{u^{*2}_c}} \right] \tag{2.68}$$

$$u^* \Rightarrow 0 = \frac{1}{\kappa}\ln y^+ + a - u^+ \Rightarrow u^*_{c+1} = u^*_c - \left[\frac{\frac{1}{\kappa}\ln\frac{yu^*_c}{\upsilon} + a - \frac{u_{wall}}{u^*_c}}{\frac{1}{\kappa u^*_c} + \frac{u_{wall}}{u^{*2}_c}} \right] \tag{2.69}$$

The velocity is determined from equations 2.70 to 2.72, based upon the determined non-dimensional wall distance y^+.

$$u^+ = y^+ \tag{2.70}$$

$$u^+ = \frac{5.0\ln\left(y^+\right)}{\kappa} - 3.05 \tag{2.71}$$

$$u^+ = \frac{\ln\left(y^+\right)}{\kappa} + a \tag{2.72}$$

2.8.4 Inflow

The use of an inflow boundary condition requires for either the velocity or pressure quantities to be prescribed, through Dirichlet or Neumann conditions respectively. In many cases, the prescribed inflow conditions can be far from the actual required conditions, i.e. developed turbulence. It is therefore preferable to keep such a boundary sufficiently far from the specific region of the domain that is being examined. Such a choice is to ensure that the inflow and geometric based disturbances do not influencing one and another, in addition to, allowing for any prescribed fluctuations to

stabiles/develop. Commonly, the velocity is prescribed at the inflow boundary; however, the use of a moving grid introduces the possibility of wave reflection back onto the inflow boundary when submerged or surface piercing bodies are present. This can be troublesome as the use of a fixed velocity can result in an increased flux into the domain. The velocity is therefore prescribed through a constant flux constraint. This has the advantage of allowing for large wave reflection without influencing the overall mass flowing into the domain. Furthermore, wave motion and perturbations to the inflow can be directly applied to the velocity determined to maintain constant flux. The inflow is initially prescribed by using equation (2.73), thereafter the velocity is determined using (2.74).

$$\dot{m}^{cf} = \rho \times a^{cf} \times u_{in}^{cf} \tag{2.73}$$

$$u_{in}^{cf} = \frac{\dot{m}^{cf}}{\rho \times a^{cf}} \tag{2.74}$$

2.8.5 Outflow

The outflow boundary gives rise to the following question:

'what constitutes a good boundary condition?'

For compressible flows, the choice of how such a boundary is implemented makes little difference, since flow disturbances cannot propagate upstream. Contrastingly, in low speed incompressible flows, disturbances introduced from reflections at an outflow boundary can impact on the entire computational domain. The following subsections describe to the two most commonly used outflow boundary conditions for preventing reflection.

2.8.5.1 Continuative Boundary Condition

The simplest and most commonly used outflow condition is that of a "continuatives" boundary. Continuatives boundary conditions consist of zero normal derivatives at the boundary for all quantities. The zero-derivative condition is intended to represent a smooth continuation of the flow through the boundary.

$$\frac{\partial u_i}{\partial x_i} = 0 \tag{2.75}$$

2.8.5.2 Convective boundary condition

Though the continuatives boundary condition ensures no reflection it is a mathematical statement that has no physical basis. Generally the outflow boundary can encompass more than just the normal flow parameters; in this case the outflow boundary must effectively transmit waves out of the domain. The use of a zero gradient boundary can therefore result in unreliable wave behavior at the boundary. To further improve the outlet boundary a convective outlet boundary is also implemented.

$$\frac{\partial u_i}{\partial t} = c\frac{\partial u_i}{\partial x_i} = \frac{u_i \Delta t}{\Delta x_i}\frac{\partial u_i}{\partial x_i} \tag{2.76}$$

This type of outflow boundary is suitable for moving vortical structures out of the computational domain.

Both boundary conditions are implemented within the code, however to ensure no reflection from the outflow boundary the continuative boundary condition is used to prescribe the velocity at the outflow boundary.

2.9 Figures

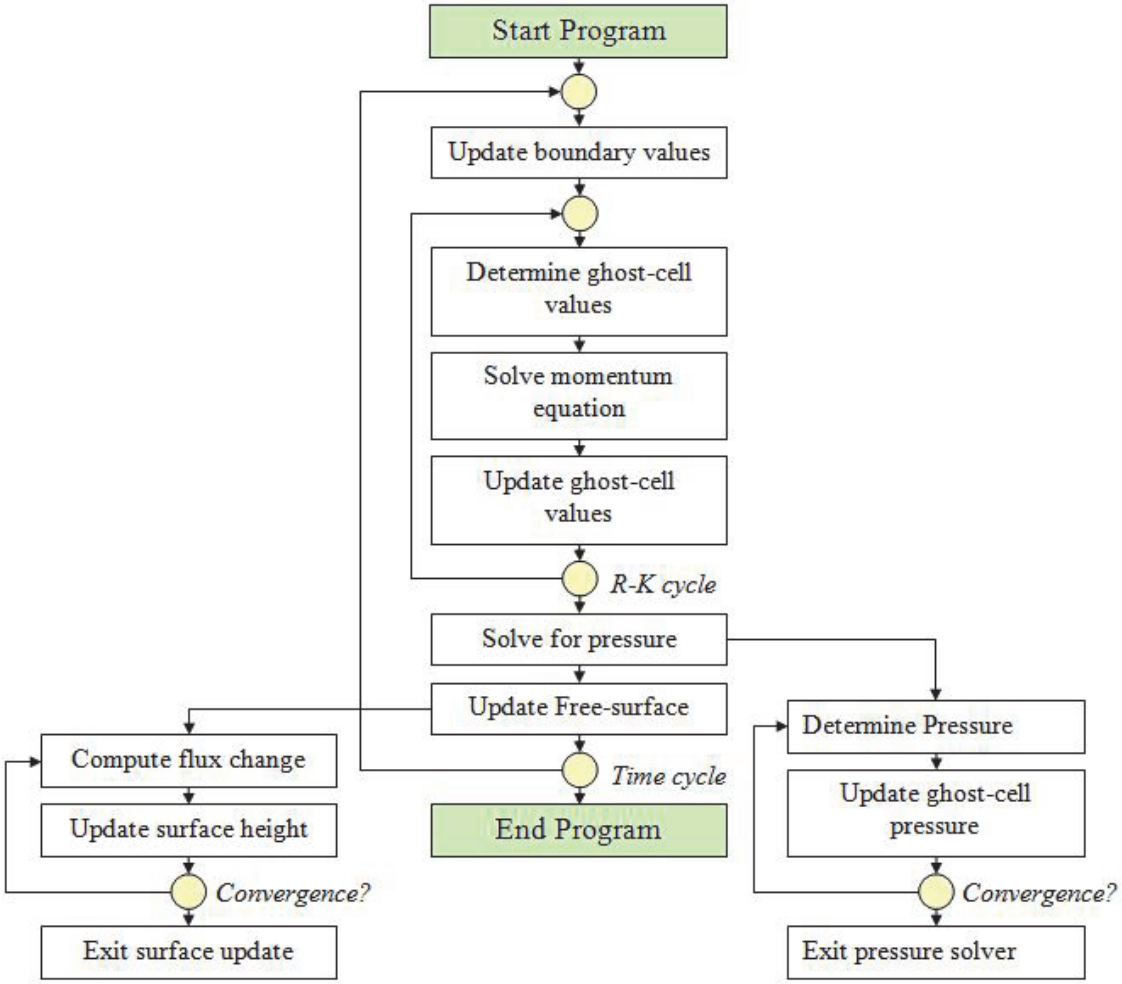

Figure 2.1: Flow diagram highlighting the procedure of the code.

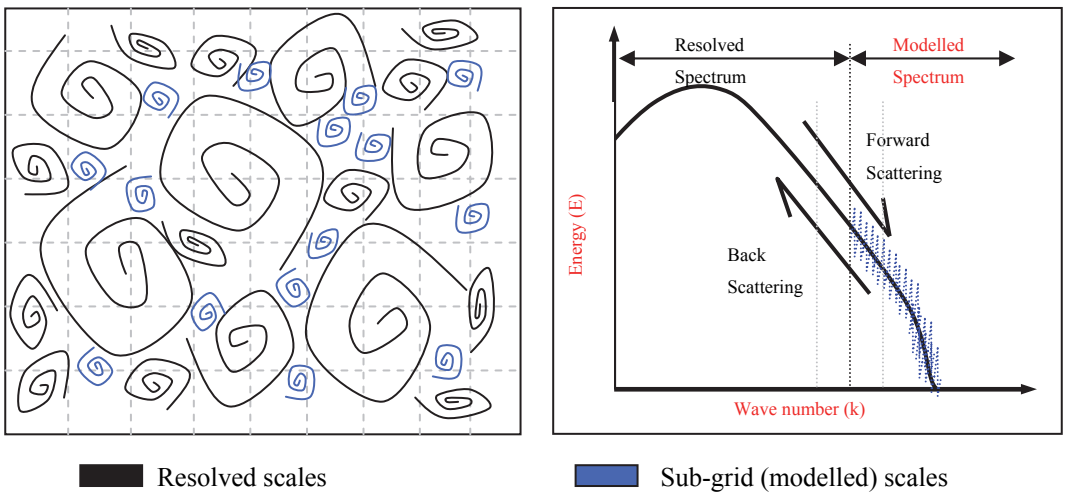

Figure 2.2: Sub-grid scales in physical and Fourier space.

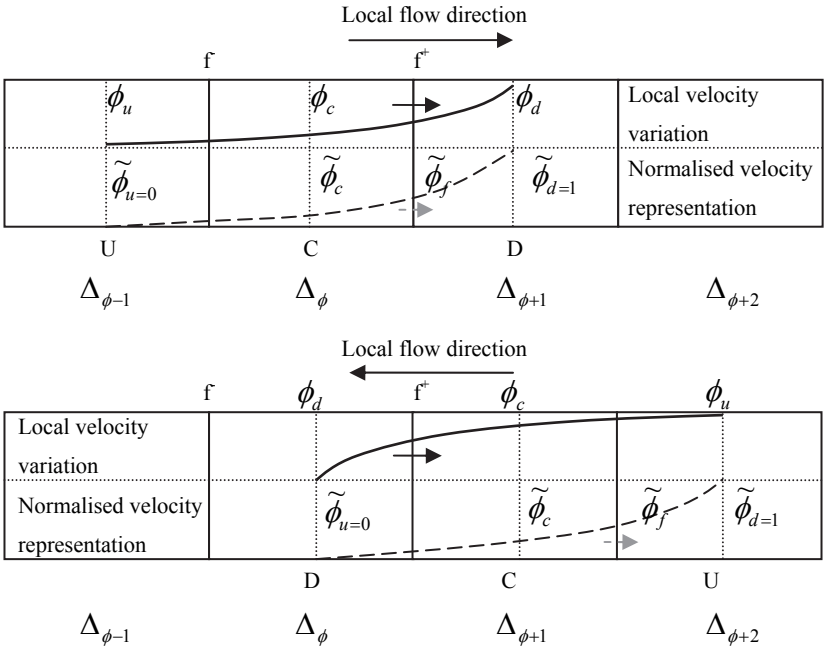

Figure 2.3: 1D stencil for determining flux across a face for a given flow direction.

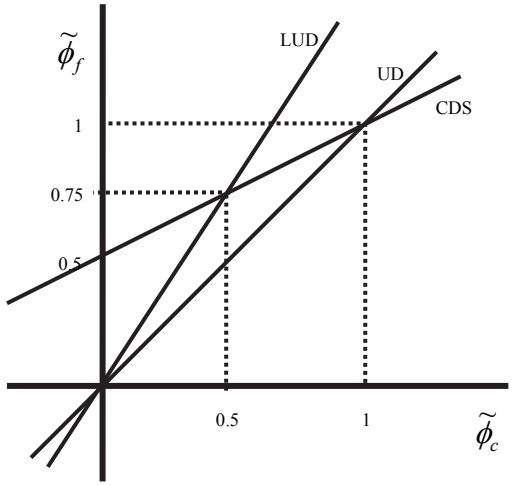

Figure 2.4: Normalised variable diagram for first and second order convective schemes.

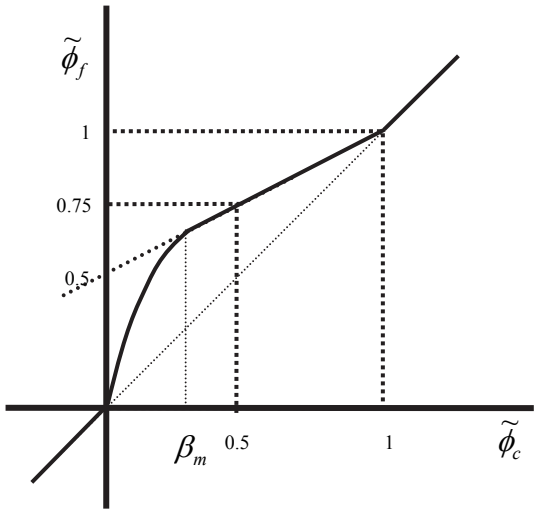

Figure 2.5: Normalised variable diagram for gamma scheme.

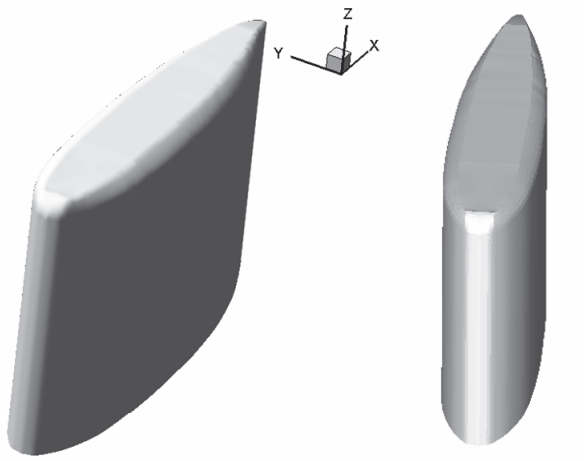

Figure 2.6: Three-dimensional fairwater geometry constructed based upon immersed boundary points.

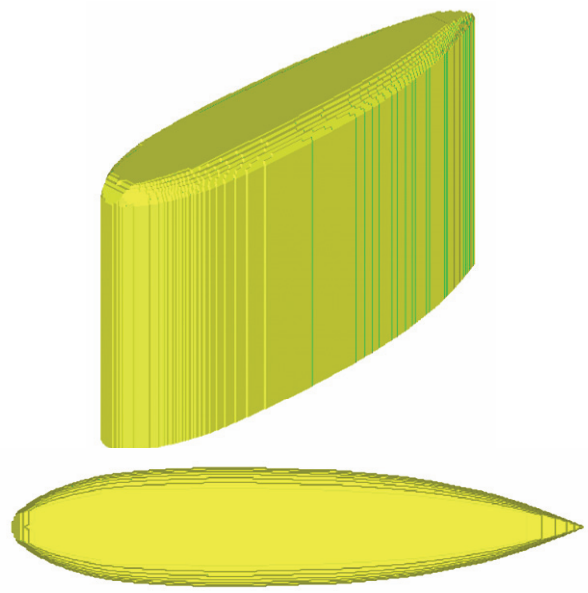

Figure 2.7: Fairwater generated via step approach

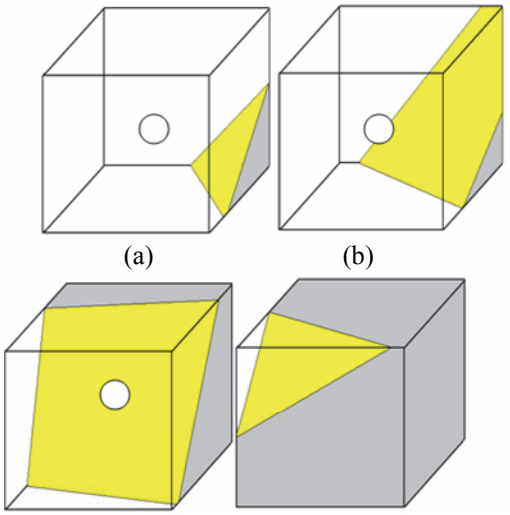

Figure 2.8: Possible types of intersections of an immersed boundary face within a cell; cases (a)-(c) are cells within the fluid while (d) is a ghost-cell node.

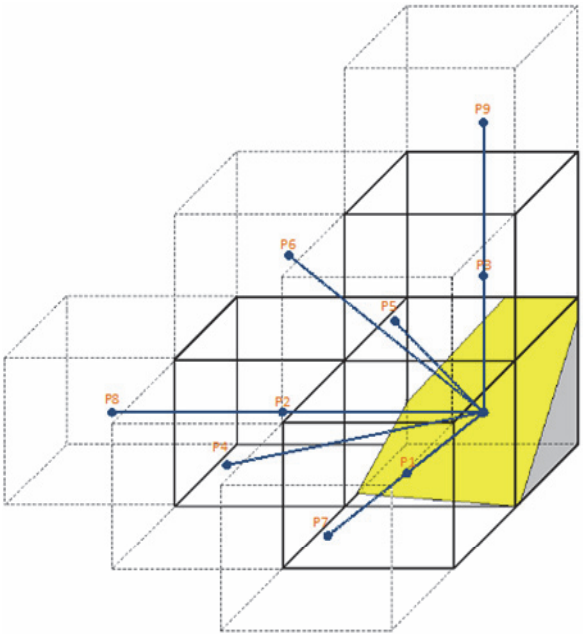

Figure 2.9: Quadratic stencil applied to an identified ghost-cell

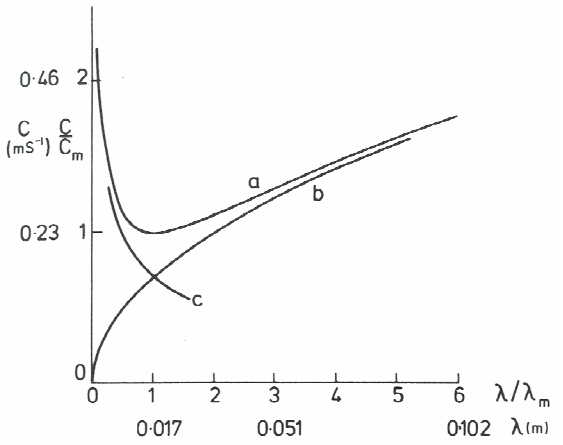

Figure 2.10: Effects of surface tension and gravity as a function of wave length on phase speed; (a) combined phase speed, phase speed based on (b) capillary (c) gravity [Crapper (1984)].

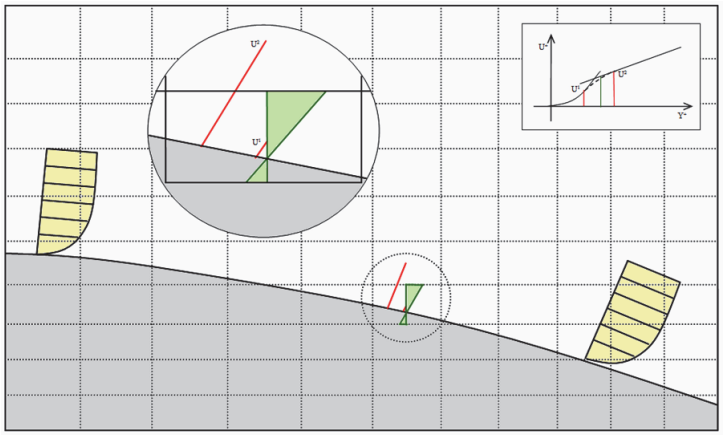

Figure 2.11: Determination of shear stress close to the modelled immersed boundary face.

Chapter 3 Analysis of wave behaviour

This thesis focuses on the study of free-surface flows about bluff and streamlined bodies and it is therefore necessary to assess the accuracy and behaviour of the free-surface boundary. The factors examined in the current chapter include the conservation of wave energy for small amplitude waves and the effectiveness of modelling non-linear waves. Where possible, data is compared with available experimental or computational results.

3.1 Conservation of wave energy

Conservation of energy is highly important not only from the perspective of accurately modelling wave motion but also from an LES aspect. Excessive energy loss results in the solution being smeared through increased numerical damping, while factors such as wave loading and large structure interaction (also energy transfer) are incorrectly accounted for. Factors that influence the rate at which the energy is numerically dissipated include; the method of discretising the Navier-Stokes equations in both time and space, the time interval, spatial resolution and possible residual errors. This section addresses the effects of spatial and temporal resolutions as well as effects of residual errors on wave motions through the examination of a standing (non-driven) wave.

The conservation properties of the IBEXVOLES code are examined by studying the amount of loss in wave energy over a single cycle of an airy/standing wave of steepness $w_{stp} = 0.05$. Both inviscid and viscid cases are considered. For the latter case a viscosity of 10^{-3} *kg/ms* is used for which the theoretical energy loss was determined to be *11.9%* by Thomas & Williams (1995) – originally obtained from Lamb (1975). Figure 3.1 shows the results for the free-surface over a single wave cycle for the viscid case. The

surface profiles plotted are for the most refined case considered, it can be seen that viscous dissipation is present in the second half of the wave cycle (symbols).

Table 3.1 lists the percentage change in potential energy (PE), kinetic energy (KE) and total energy (TE) for the viscous case after one complete wave period, for different temporal and spatial resolutions. Similarly, the change in TE for both inviscid and viscid cases is shown in Figure 3.2. From the results it is evident that as the time interval is reduced wave energy is better conserved. A behaviour expected as the NS equations are solved explicitly in time, moreover, for the explicit assumption to hold true the time step is required to be small. In addition, increasing the grid resolution does indeed aid in reducing the overall loss of wave energy. However, it is clear that the reduction in wave energy loss through grid refinement is marginal if the temporal error is large.

	Viscid case - viscosity = 0.001					
	16^3 Resolution			32^3 Resolution		
NT	% Δ PE	% Δ KE	% Δ TE	% Δ PE	% Δ KE	% Δ TE
125	35.08	-0.16	34.92	38.15	-0.08	38.07
250	28.10	-0.09	28.02	26.30	-0.07	26.23
500	17.04	-0.06	16.97	19.42	-0.06	19.36
1000	13.16	-0.06	13.10	15.65	-0.06	15.60
2000	2.86	-0.09	2.76	13.65	-0.06	13.59
4000	11.84	-0.06	11.78	12.61	-0.06	12.55
8000	11.22	-0.06	11.16	12.07	-0.06	12.01
16000	10.91	-0.06	10.86	11.80	-0.06	11.74

Table 3.1: Comparison of spatial and temporal resolution effects on energy conservation of wave energy for vicious case.

The aforementioned results are produced using a serial version of the IBEXVOLES code, without flux limiting (NFL). In this thesis a parallelised code version with flux limiting (FL) is used in latter simulations (section 2.2), therefore the effect of introducing a flux limiter and parallelisation are also examined. Table 3.2 lists the changes in the PE, KE and TE for the serial code with and without flux limiting, and

also results obtained from the parallel code. The changes in TE are plotted in Figure 3.3 and Figure 3.4 for both the viscid and inviscid cases. As seen in Figure 3.3, by introducing FL in both the parallelised code version (PVC) and serial version the energy is found to dissipate marginally slower in comparison with the previous data set (serial code - NFL) as the time step is reduced. For the viscid case this results in the energy being conserved better as Δt is reduced. Furthermore, the prediction in the total energy loss is in better agreement with that determined by Thomas *et al* (1994). The notable differences between the PVC and serial code with FL arise as a result of the pressure solution being slightly different. This is owed due to the FL altering the velocity in regions where the velocity gradients are large across the examined wave period.

Furthermore, the neutrally stable combination of using forward Euler (first-order Runge-kutta scheme - RK1) for time advancement and backward Euler for surface updating is compared with the current third-order Runge-kutta scheme and backward Euler combination. The variations in TE for both aforementioned combinations are also plotted in Figure 3.3 and Figure 3.4. Results for the inviscid and viscid cases indicate a similar trend between both combinations considered; with the RK1 combination showing the smallest change in TE. In all cases the use of large time steps produces unacceptable levels of energy loss. For the inviscid case, reducing time step size results in the change in TE predicted by the third-order Runge-kutta (RK3) combination becoming comparable with that of the RK1 combination. For the viscid case, the RK3 scheme dissipates energy slower, in comparison with using the RK1 scheme, which under predicts the loss in TE for finer time-steps.

	Viscid case - viscosity = 0.001								
	Serial (no limiter)			Serial (limiter)			Parallel (limiter)		
NT	% Δ PE	% Δ KE	% Δ TE	% Δ PE	% Δ KE	% Δ TE	% Δ PE	% Δ KE	% Δ TE
125	38.15	-0.08	38.07	38.24	-0.08	38.15	38.24	-0.08	38.15
250	26.30	-0.07	26.23	26.41	-0.07	26.33	26.41	-0.07	26.33
500	19.42	-0.06	19.36	19.54	-0.06	19.47	19.54	-0.06	19.47
1000	15.65	-0.06	15.60	15.78	-0.06	15.72	15.78	-0.06	15.72
2000	13.65	-0.06	13.59	13.78	-0.06	13.72	13.78	-0.06	13.72
4000	12.61	-0.06	12.55	12.74	-0.06	12.68	12.74	-0.06	12.68
8000	12.07	-0.06	12.01	12.20	-0.06	12.14	12.20	-0.06	12.14
16000	11.80	-0.06	11.74	11.93	-0.06	11.87	11.93	-0.06	11.87

Table 3.2: Comparison of viscid wave energy loss for serial and fully parallelised (open_MP) code versions with and without flux limiting for various temporal resolutions.

Another factor that influences the numerical dissipation and the solution as a whole is the level of residual errors (enforcement of continuity throughout the domain via the solution of the pressure field). Table 3.3 and depicted in Figure 3.5 is the effect of residual errors on the energy rate at which energy is lost over a cycle. The tabulated results are shown for a wave cycle of 1000 NT (time-steps for a total wave period), where the change in total energy was determine to be approximately 4.67% and 4.90% for the serial NFL, FL and PV codes. From the tabulated data, it is evident that if the solver tolerance is too relaxed the error in the solution is quite large. Interestingly, in this case it can be seen that the wave profile is unaffected through the percentage change in PE, but the kinetic energy is greatly affected by residual errors. As the residual tolerance is made stricter, the differences in energy loss stabilises to the previously defined values. Similarly, the effect that the solver tolerance has for finer time-steps is also computed (NT = 8000) and shown in Figure 3.5. Again a similar behaviour is found with the notable difference being that the finer time-step requires a higher tolerance to produce consistent results. For the viscous case (results not shown) the tolerance level is found to be unaffected by finer-time stepping. Therefore the minimum tolerance needed to be enforced to ensure consistent results is E-6.

	Inviscid case - viscosity = 0.001								
	Serial (no limiter)			Serial (limiter)			Parallel (limiter)		
Tol	% Δ PE	% Δ KE	% Δ TE	% Δ PE	% Δ KE	% Δ TE	% Δ PE	% Δ KE	% Δ TE
e^{-4}	4.28	-55.1	-50.8	6.11	-46.1	-40.0	3.59	-49.3	-45.7
e^{-5}	4.76	-0.65	4.11	5.08	-0.64	4.44	5.08	-0.65	4.44
e^{-6}	4.75	-0.10	4.65	4.97	-0.08	4.89	4.97	-0.09	4.88
e^{-7}	4.76	-0.09	4.67	4.98	-0.08	4.90	4.98	-0.08	4.90
e^{-8}	4.76	-0.09	4.68	4.99	-0.08	4.91	4.99	-0.08	4.91
e^{-9}	4.76	-0.09	4.67	4.98	-0.08	4.90	4.98	-0.08	4.90
e^{-10}	4.76	-0.09	4.67	4.98	-0.08	4.90	4.98	-0.08	4.90

Table 3.3: Comparison of inviscid wave energy loss for serial and fully parallelised (open_MP) code versions with and without flux limiting for different pressure solver tolerances.

3.2 Non-linear wave

The preceding section examined the typical behaviour of small non-driven wave motions. This section addresses the behaviour of larger, driven, non-linear wave motions. To assess the capability of the IBEXVOLES code in modelling non-linear wave motion, the classic problem of a solitary wave run-up and run-down from a vertical wall is initially considered. A wave height to depth ratio (*a/d*) of 0.1 was considered sufficient for testing the non-linear behaviour, as the expected wave height to depth ratios are not expected to exceed such a limit in any of the cases studied. The second problem considered is that of the interaction of a propagating solitary wave of height to depth ratio of $a/d = 0.15$ with a submerged obstruction in its path. Both serial and parallel code versions are considered.

3.2.1 Reflection of a solitary wave from a solid boundary

3.2.1.1 Problem definition

To test the effectiveness of the code in modelling non-linear waves, a test case of a solitary wave propagating within a closed domain is considered. Wave run-up heights

(R) and wave reflection behaviour are examined, with time refinement and error analysis. Figure 3.6, illustrates the problem being studied.

The initial conditions defining the surface elevation, velocity distribution and pressure field are computed from the work by Laitone (1960). Laitone's approximations for surface elevation, velocity distribution and pressure field are defined respectively as:

$$\eta_i = d + \left\{ a \times \operatorname{sech}^2 \left[\sqrt{\frac{3 \times a}{4 \times d^3}} \times \left(x_i - c \times t \right) \right] \right\} \tag{3.1}$$

$$u_i = \sqrt{g \times d} \times \frac{a}{d} \times \operatorname{sech}^2 \left[\sqrt{\frac{3 \times a}{4 \times d^3}} \times \left(x_i - c \times t \right) \right] \tag{3.2}$$

$$v_i = \sqrt{3 \times g \times d} \times \left(\frac{a}{d} \right) \times \left(\frac{y_i}{d} \right) \times \operatorname{sech}^2 \left[\sqrt{\frac{3 \times a}{4 \times d^3}} \times \left(x_i - c \times t \right) \right] \times \tanh \left[\sqrt{\frac{3 \times a}{4 \times d^3}} \times \left(x_i - c \times t \right) \right]$$

(3.3)

$$p_i = \rho \times g \times \left(\eta_i - y_i \right) \tag{3.4}$$

In the equations 3.1 to 3.3 the wave speed (c) is defined by equation 3.5, where 'O' represents truncation of higher order terms.

$$\frac{c}{\sqrt{g \times d}} = 1 + \left(\frac{1}{2} \times \frac{a}{d} \right) - \left[\frac{3}{20} \times \left(\frac{a}{d} \right)^2 \right] + O\left(\frac{a}{h} \right)^3 \tag{3.5}$$

The initial conditions are generated by setting $t = 0$ in the equations 3.1 to 3.3. It must be noted that the above equations describe the propagation for a two-dimensional infinitely long wave, with no boundaries present. In order to model the problem correctly within a finite domain a suitable domain length is required. Therefore the domain size is selected to correspond to that used by Chan and Street (1970), to validate their improved marked and cell method (MAC). Chan and Street obtained an effective wavelength by taking $L_{weff}/2$ (half of the actual effective wave length) equal to the distance from the wave crest to the section where the free-surface $\eta = 0.01a$, using the equation 3.6:

$$\frac{L_{weff}}{d} = 6.90 \times \left(\frac{d}{a}\right)^{1/2} \tag{3.6}$$

Equation 3.6 shows that as the wave amplitude increases, the effective wavelength (L/2) reduces. For a wave amplitude to depth ratio of 0.1 the effective wavelength is approximately 11, nonetheless Chan and Street were able to use an effective wavelength of 10 without problems. The same configuration has also been used by other researchers i.e. Hsu *et al* (2001) whom used this problem to validate their arbitrary Lagranian-Eulerian (ALE) free-surface code. To keep consistency the same effective wavelength of 10 is used in this study of wave run-up heights.

3.2.1.2 Non-linear results

According to the study performed by Hsu et al. for a wave amplitude to depth ratio (*a/d*) > 0.1 solitary waves that are reflected off a solid surface tend to exhibit trailing wiggles. A behaviour also observed in the experiments of Naheer (1978). Hsu et al. reported that for small wave amplitudes the trailing wiggles are sufficiently small such that the measured data is in good agreement with that of Laitone's solution. However as the wave amplitude is increased, the difference resulting from trailing wiggles becomes significantly large to the extent that Laitone's solution no longer agrees with measured data. Hsu et al. attribute such behaviour to the fact that the Laitone solution is used as an approximation for weak interaction of the reflected wave from a wall and cannot represent the trailing wiggle.

During this study a wave height to depth ratio of 0.1 has been considered sufficient for the testing of the non-linear wave behaviour of the code, as the expected wave height to depth ratio is not expected to exceed this limit in any of the problems studied.

Figure 3.7 shows obtained free-surface wave profiles at various times for incidence waves and their corresponding reflected waves. The resolution used is the same as that of Hsu et al. with the spacing in the streamwise direction (Δx) set to 0.04, and the spacing in the vertical direction (Δz) set to 0.035. Unlike Hsu *et al* (2001) and Chan *et al* (1970) whom modelled the problem on a two-dimensional grid, the same problem considered in this section is solved on a three-dimensional grid. As the problem is

typically two-dimensional the spanwise spacing (Δy) is set to a coarser spacing of 0.1. Note the spanwise length is taken as 1, while periodic boundary conditions are imposed in this direction. The total simulation time was taken to be $\overline{T} = 20$, where $\overline{T}$ is the non-dimensional time taken as:

$$\overline{T} = \left[t \Big/ \sqrt{h \Big/ g} \right]$$

According to Chan and Street this is a key test for the nonlinear behaviour of the free-surface, as the reflected wave should retrace the path of the original incident wave. Figure 3.7 shows that the reflected wave does coincide with the initial propagating wave. Differences between the propagating and reflected wave can be attributed due to the effects of numerical dispersion. Furthermore, wave run-up heights for larger wave amplitudes foe up to a maximum *a/d* of 0.3 are also compared with published data in Figure 3.8. Wave run-up heights for both the NFL and PVC code versions are computed and plotted alongside the experimental results by Camfield & Street (1969) and the numerical results of Chan and Street. In both cases (serial and parallel), the predicted wave run-up heights (*R*) compare well with the comparison data for all *a/d* considered. The maximum variation in run-up height (percentage), are listed in Table 3.4 for all computed heights. The readings show that the largest variation in run-up heights occurs for *a/d* of 0.1 when compared against the experimental data; this is attributed to experimental measuring uncertainties [*Chan and Street (1970)*] and the normalisation against the initial wave height. However, the agreement between the predicted run-up heights for both NFL and PVC code versions follow the same trend as with the results of Chan and Street (1970).

	% Variation in run-up wave heights		
a/d	Chan & Street	NFL	PVC
0.1	23.571	14.285	20.714
0.2	3.030	3.606	4.242
0.3	1.923	0.983	1.538

Table 3.4: Variation in wave run-up heights for computed results, with respect to experimental measurements.

The effect of streamwise, vertical and temporal resolution on the behaviour of nonlinear wave distribution has also been examined for *a/d* = 0.1. Figure 3.9 shows the average error determined for each surface nodal point based on wave height. The reference wave is taken to be that of the reflected wave at time $\overline{T}$=18.0 (as shown in Figure 3.7). Spanwise, streamwise and temporal resolutions are individually varied, whilst the remaining two are held constant. This is done in such a way that the effect of the aforementioned parameters can be individually studied in regard to a fixed reference. Reference conditions are taken as follows:

- 250 cells in the streamwise direction (Δx = 0.08)
- 22 cells in the vertical direction (Δz = 0.05)
- 2500 time steps (Δt = 2.53×10^{-4})

With any two references held constant the remaining parameter is varied as follows; the streamwise resolution is varied from Δx = 0.08 to 0.4, whilst the vertical resolution is varied from Δz = 0.05 to 0.14, finally the temporal resolution is varied from Δt = 6.4×10^{-4} to 0.0128.

The average nodal error (ε_{rr}) is determined using equation 3.7, where z_n^{ref} is the reference nodal height for the wave taken from Figure 3.7, and z_n is the nodal height for the comparing wave.

$$\varepsilon_{rr} = \frac{\sum_{n=1}^{m} \left| \left(z_n^{ref} - z_n \right) \right|}{m} \tag{3.7}$$

All data is normalised, by the maximum resolutions used i.e. streamwise resolutions are normalised by 250 corresponding to a Δx of 0.08. For example, the normalised horizontal resolution of 0.2 corresponds to $(0.2 \times 250) = 50$ cells set in the streamwise direction. Figure 3.9 shows that variation in the streamwise spatial resolution produces the largest discrepancies. This can be attributed to insufficient resolution in capturing the wave behaviour and increased numerical diffusion resulting from grid coarsening. A similar behaviour can be noted for the change in temporal resolution. Unexpectedly, changing the vertical resolution appears to have no real effect on the error.

3.2.2 Solitary wave interaction with a submerged obstacle

In the prior section the results produced for a solitary wave running up a wall were computed and the wave behaviour was assessed against published experimental and computational data. This section addresses the important feature of non-linear wave behaviour over a submerged obstruction. The wave behaviour for a solitary wave of finite amplitude passing over a submerged two-dimensional rectangular dike is considered.

The problem set-up is similar to that in the study of Apsley & Hu (2003) and Huang & Dong (2001), in the sense that *a/d*, the ratio of obstruction height to depth ratio (*o/d*) and the aspect ratio of the dike are kept consistent with the aforementioned works. However in both aforementioned works the initial values are prescribed differently. Apsley & Hu used a simpler relation based upon wave speed to describe the wave propagation velocity, while Huang & Dong used more elaborate expressions accounting for the non-slip condition at the bed. In both cases, both results exhibit the same behaviour regardless of initial conditions. The initial conditions used in this section are computed from the solitary wave expressions of Liatione used in the preceding section. The domain extents are set as follows; $5L_d$ in the streamwise, $0.1L_d$ in the spanwise, and $0.05L_d$ in the vertical direction, where L_d is the length of the dike. The wave to depth ratio is set as 0.15 in accordance with the previously mentioned works. As in the prior section both NFL and PVC code versions are computed and compared.

Unfortunately, no published experimental data for such a case exist; instead, the computed results are compared against published computational results. Figure 3.10a shows the time evolution for the computed propagating solitary wave over a submerged dike for a submergence ratio of 0.5 (based on the non-displaced free-surface height), whilst Figure 3.10b compares the computed wave progression (for the NFL code version) against the published computational results of Apsley & Hu (2003). The distinguishable features that have been observed and reported in the above mentioned computational works for a solitary wave passing over a submerged obstruction are as follows:

1. Small wave reflection as the solitary wave encounters the obstruction.
2. Steeping of the wave as it passes over the obstruction.
3. Breaking of the solitary wave into two waves travelling with phase speeds.

As seen in Figure 3.10a and Figure 3.10b, the aforementioned features are reproduced by the current code. In addition the results produced by the NFL code agree well with published data in terms of wave heights and behaviour. Results obtained from the PVC are also compared against the NFL and the results by Apsley & Hu (2003) in Figure 3.11. As can be noted, the results still agree with the previous observations and compared data. One should note at this stage that the two approaches do differ in the way that the body is accounted for. The dike in the NFL version was modelling using an initial approach of blanking cells to forming the desired body, while the PVC uses the GCIMB approach to account for the body. The difference between the two approaches for this case is that the blanking for cells produces the exact body while the GCIMB is approximately the same (edges of the body are approximated). This approximation in modelling does not influence the sharpness of the flow at edges and corners. Comparing the PVC results to those obtained by the NFL version (Figure 3.11), it can be seen the PVC produces a better agreement with the comparative data. This can be attributed to the introduction of a flux limiter. Early wave reflection (for both code versions) can be attributed to either modelling the problem in 3D or the initial conditions imposed.

3.3 Conclusions

This chapter has examined the effectiveness of the code in modelling and replicating expected wave behaviour for small amplitude standing waves to non-linear driven waves. Conservation of wave energy was examined through a standing small amplitude wave, revealing that from all the parameters examined (spatial, temporal and residual errors) the wave energy was greatly affected by the temporal resolution. Furthermore from comparing the combination of using RK1 for time advancement and backward Euler for surface update (a stable combination) to that of RK3 with backward Euler, showed that the later combination preserved wave energy better. Interestingly, it was found that introducing a flux limiter helped to better conserve wave energy for the viscid case considered. For driven non-linear waves it was found that the solution is most sensitive to grid resolution in the direction in which the wave is travelling.

Good agreement was achieved between both parallel and serial versions of the code for all cases considered. Comparing simulated wave behaviour and data with published findings showed that expected wave behaviour is achieved, while both observations and quantified data were accurately reproduced. Furthermore, comparing the GCIMB

modelling approach to that of the blocked cell approach showed that the wave behaviour is not influenced by either method.

3.4 Figures

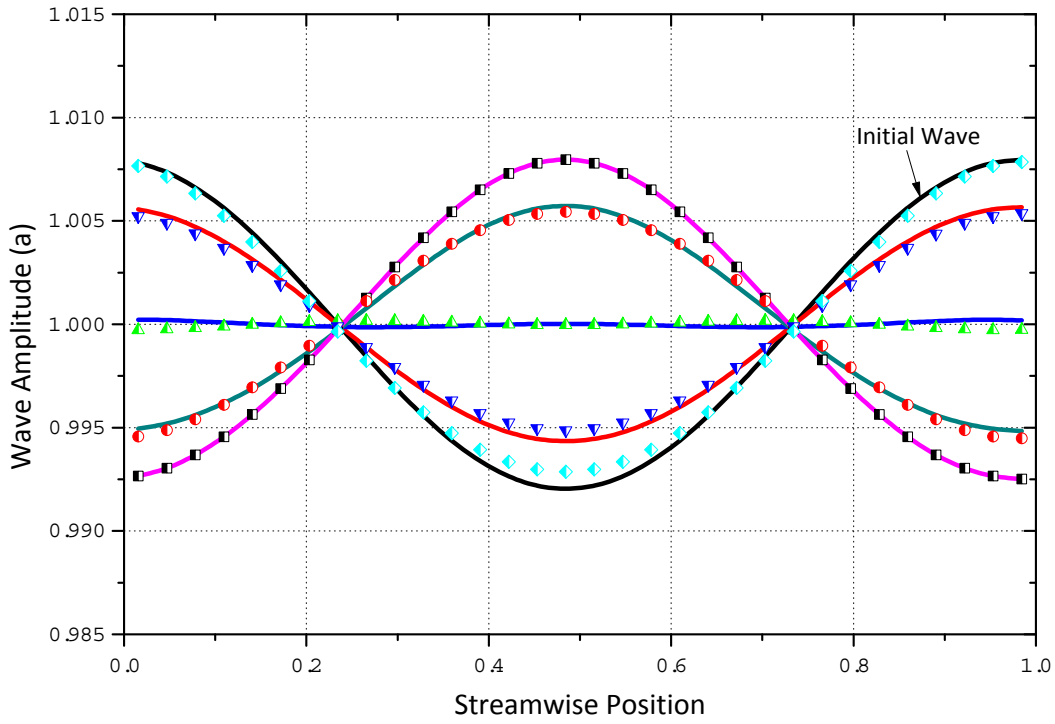

Figure 3.1: Free-surface evolution over a single wave cycle for the computed standing/airy wave - viscid case, initial waves (solid), returning wave (symbols).

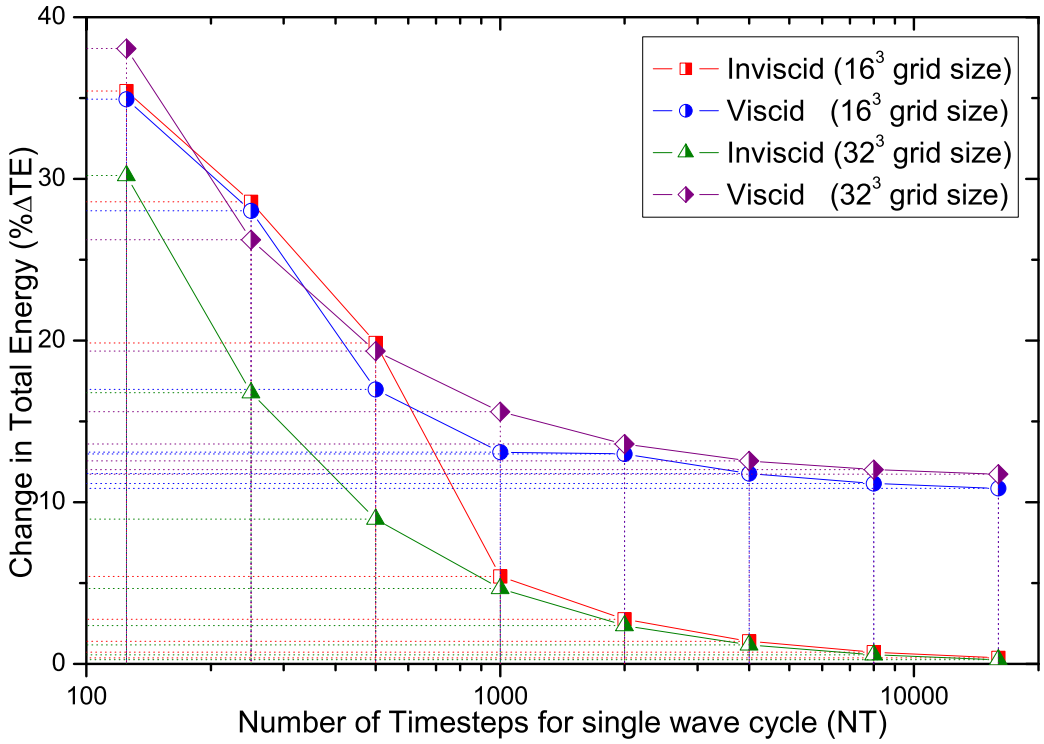

Figure 3.2: Effects of resolution change on loss of TE over a wave cycle for various temporal resolutions

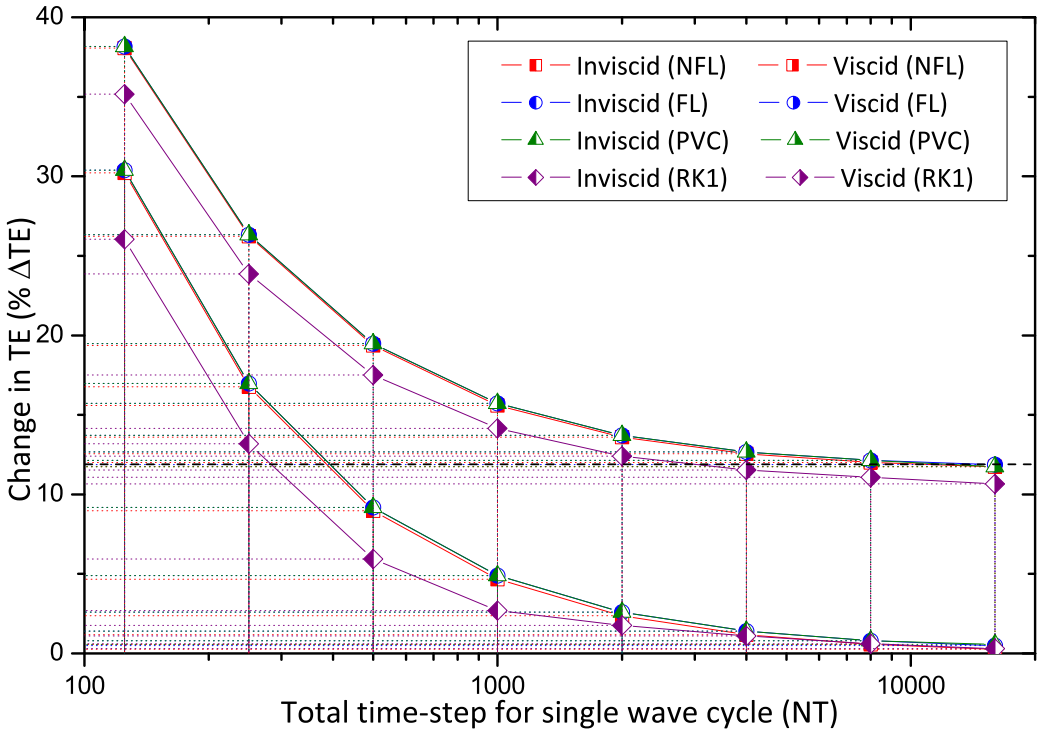

Figure 3.3: Effects of introducing a flux limiter and parallelisation of the code on loss of TE over a wave cycle for various temporal resolutions

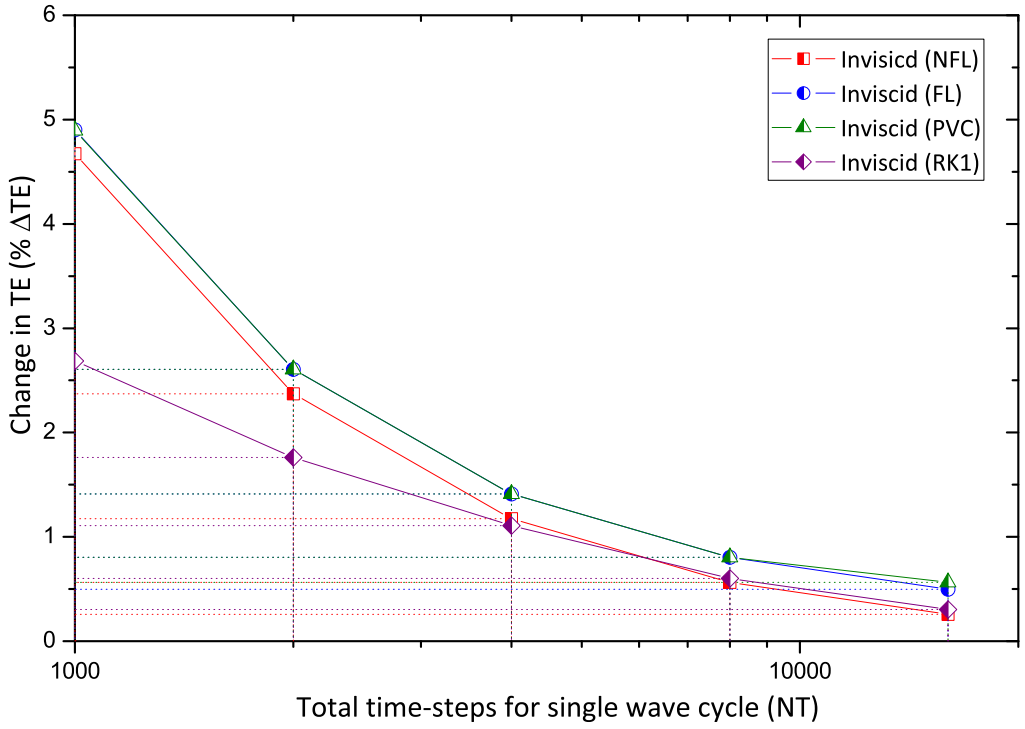

(a)

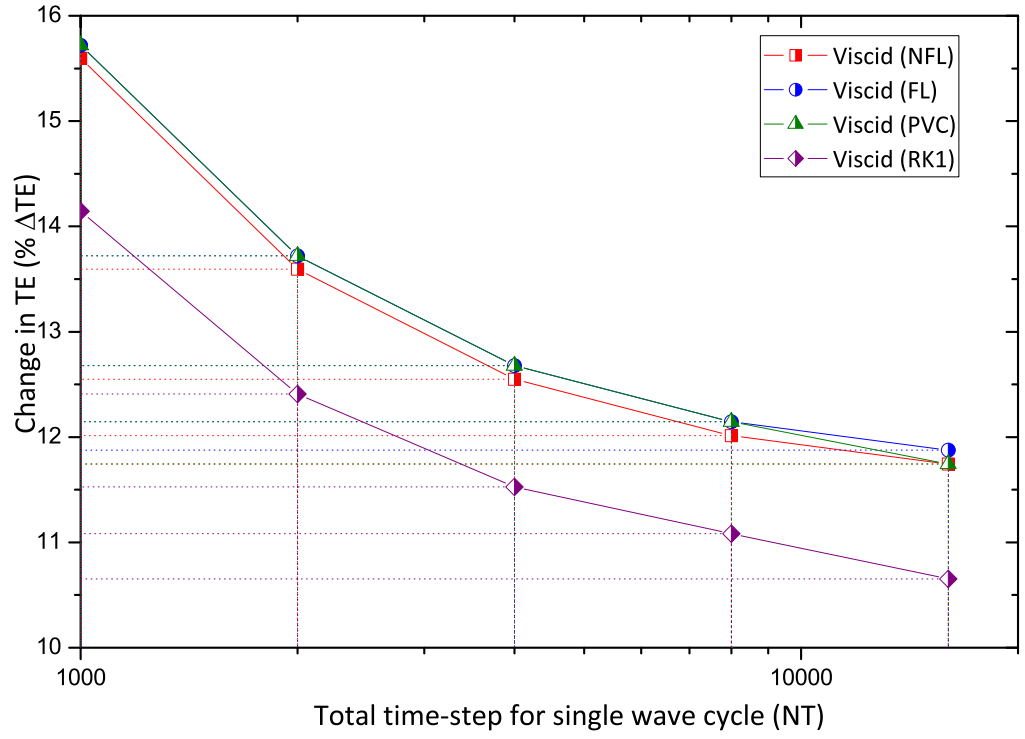

(b)

Figure 3.4: Enlargement of TE change for (a) inviscid and (b) viscid cases

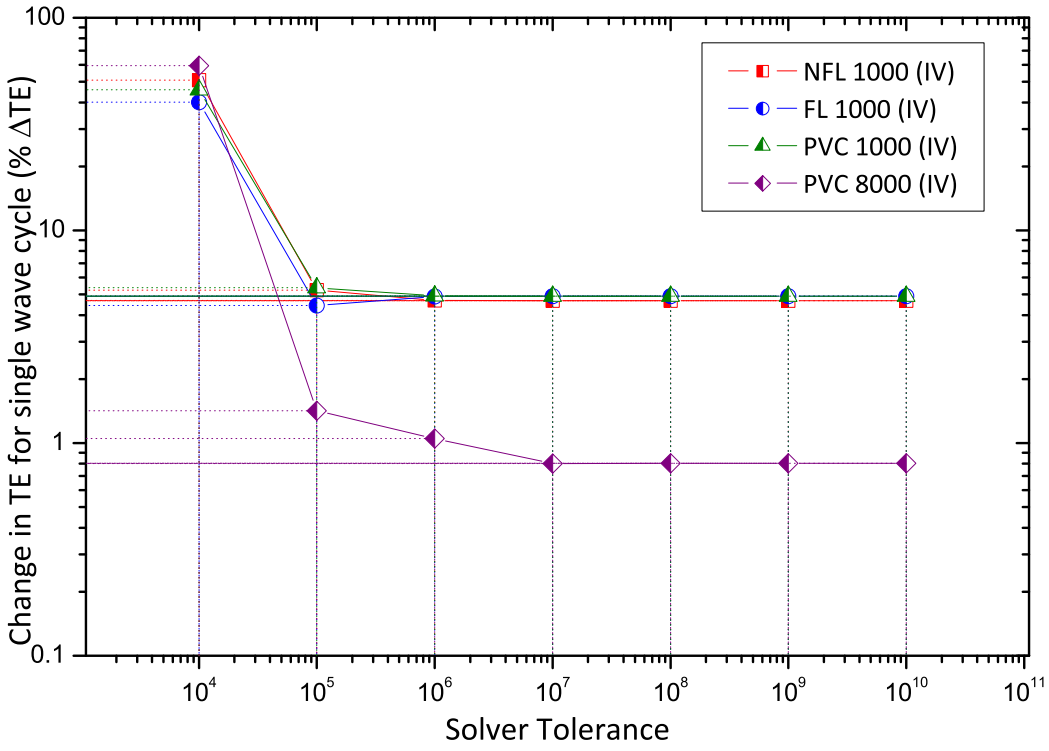

Figure 3.5: Tolerance effect on TE change for inviscid cycle of NT=1000, results from finer time-stepping are also included.

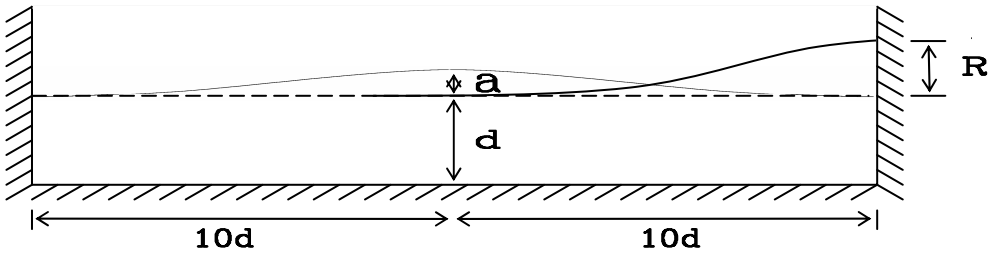

Figure 3.6: Sketch of non-linear wave reflection case.

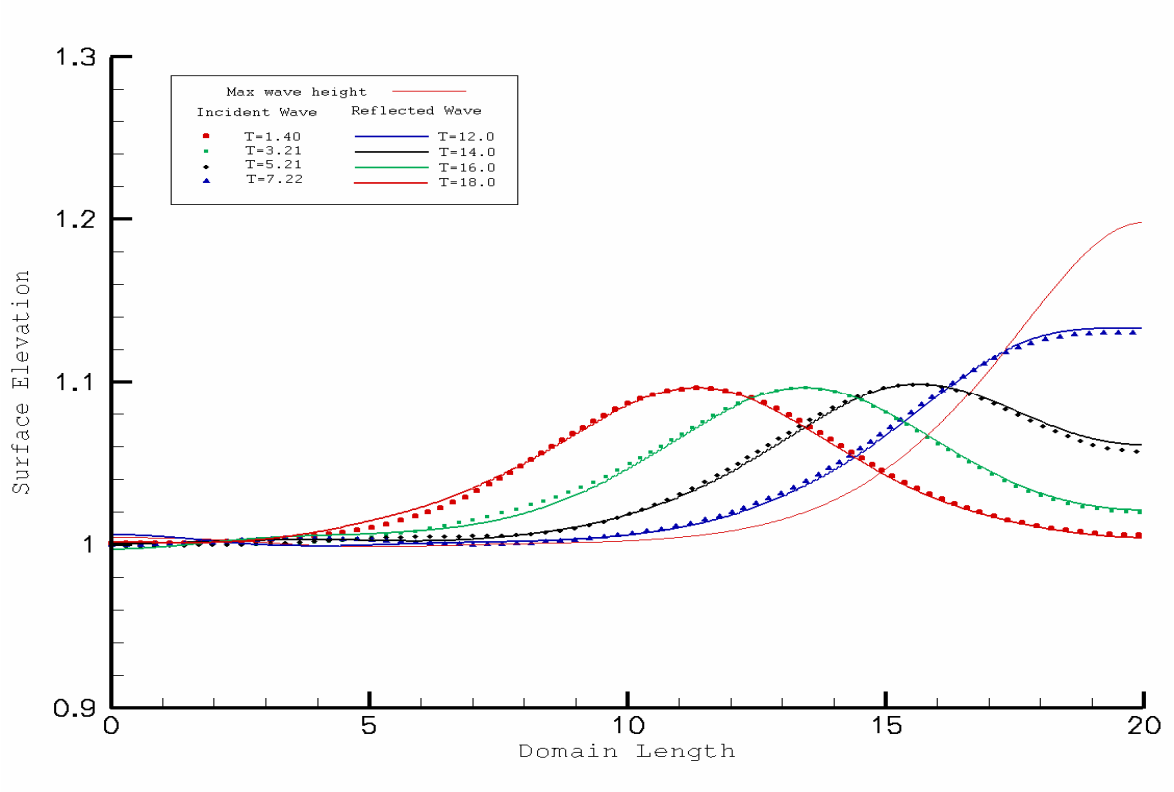

Figure 3.7: Comparison of surface profiles for incidence and reflected wave

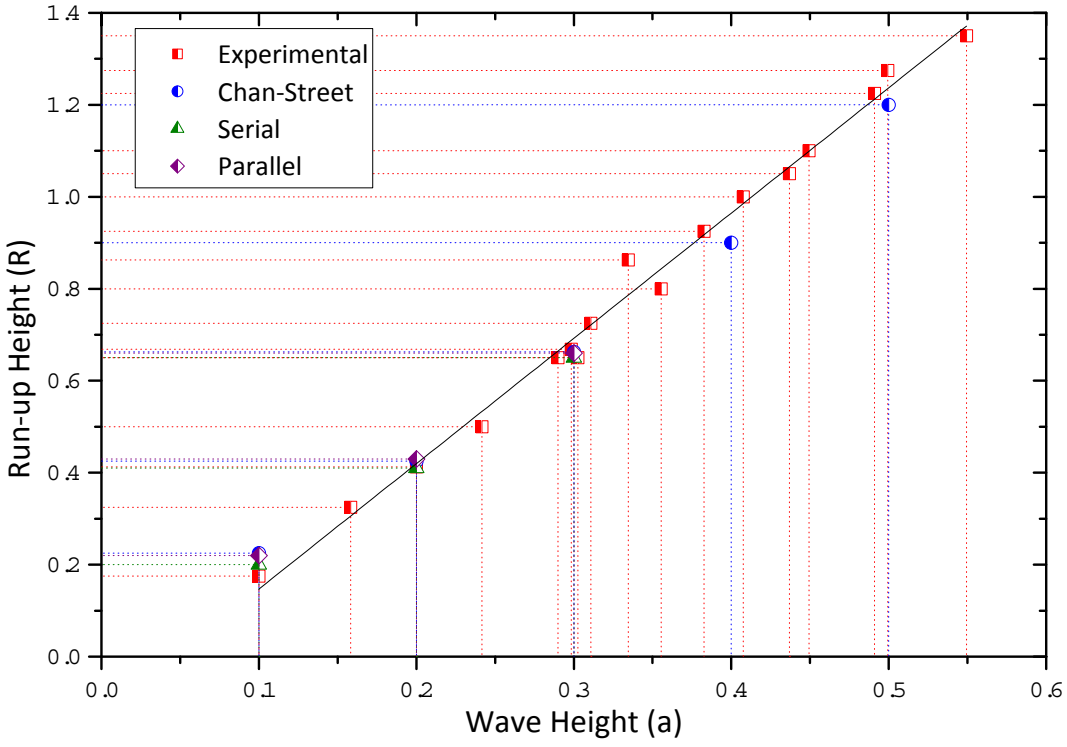

Figure 3.8: Wave run-up heights

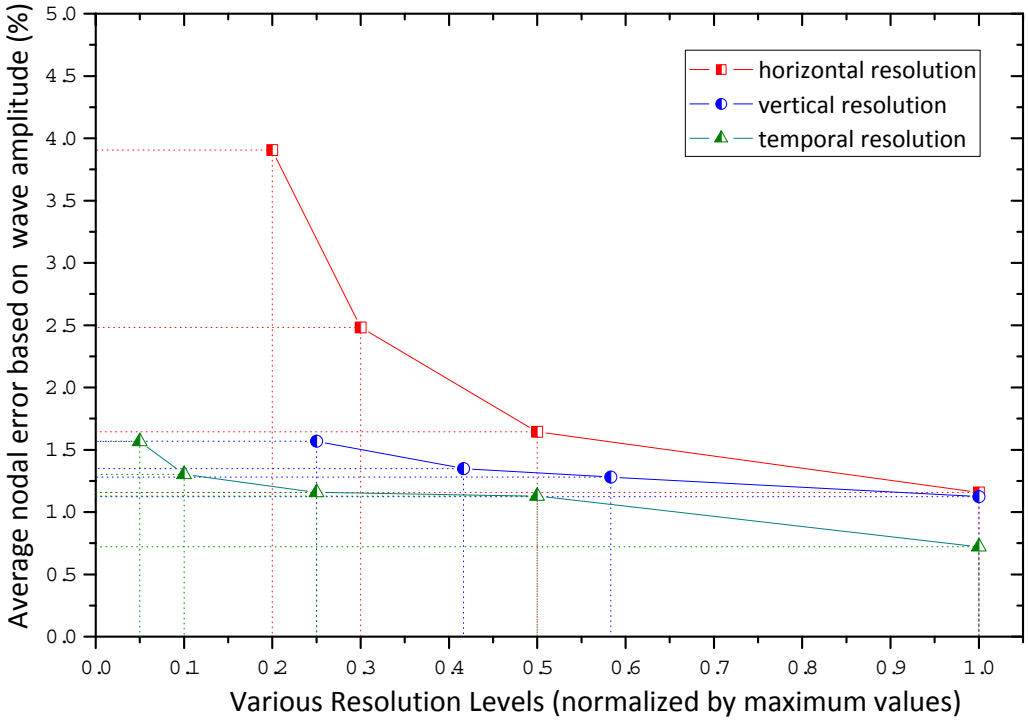

Figure 3.9: Mean error associated with streamwise, vertical and temporal resolutions

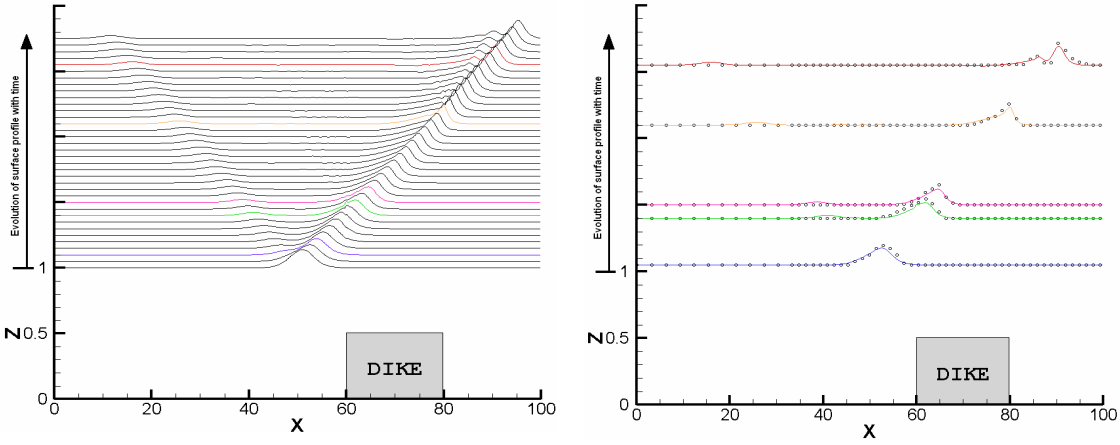

(a) wave evolution with time

(b) wave profile comparison against computed data

Figure 3.10: Solitary wave of 0.15 amplitude propagating past a submerged dike

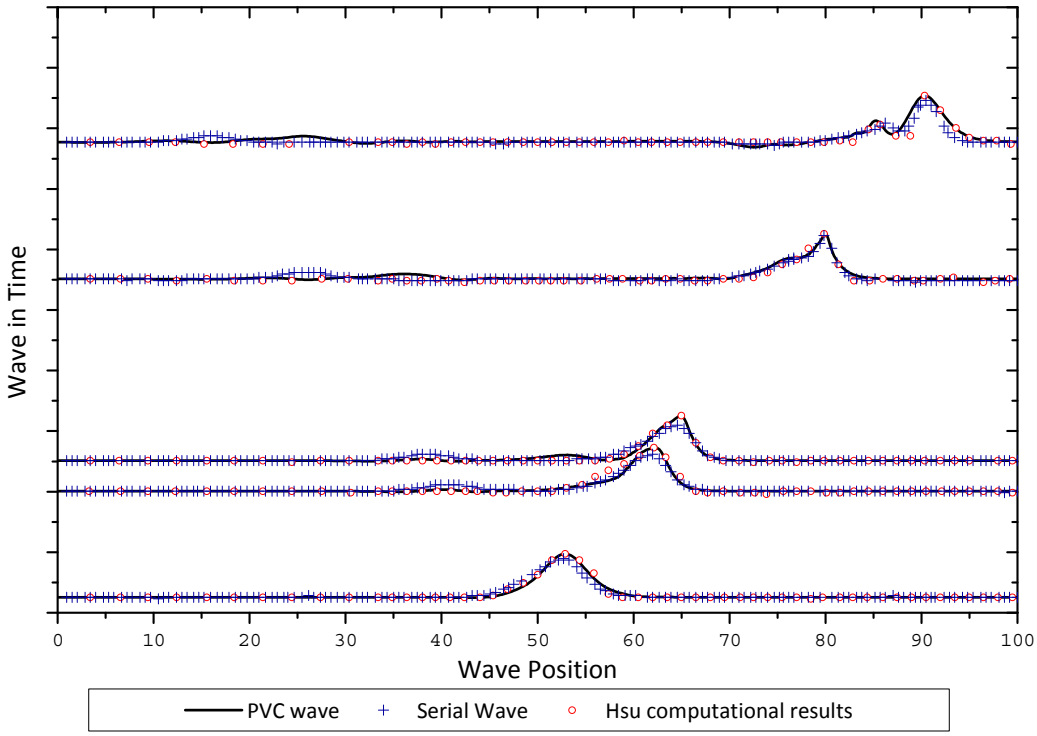

Figure 3.11: Comparison of Solitary wave over a submerged dike for PVC and NFL codes

Chapter 4 Free-surface flow past bluff bodies

This chapter examines the effect of depth variation on the flow behaviour around bluff bodies for two different Reynolds numbers - Re_h=3584 and Re_h=40,000. The considered geometries are of a single cube and an array of evenly spaced cubes. Initially, both configurations are computed using both LES and DES techniques, the results are validated against published experimental and computational data. The effect of submergence is then performed using only the LES approach.

4.1 Introduction

One of the simplest forms of a bluff body that has been extensively studied in various configurations is that of a cube. Although the geometry is relatively simple, it has been used to idealise many other types of structures. Some of the well known cases of where a cube and cube-like bodies have been used to simplify modelling include; the representation of a building or buildings [Tseng *et al* (2006)], as roughness elements [Stoesser *et al* (2003)] as well as components on circuit boards [Meinders & Hanjalic (1999)]. Such simple representation of the body or bodies have allowed for the detailed examination of turbulent and non-turbulent flows for convective transportation of mass, heat and pollutants in various practical situations that are encountered within the engineering field.

Although, such a geometry can provide a general engineering configuration that is relevant to many applications, the flow itself can be quite complex owing to the

formation of large separation regions and the interaction between various vortical structures generated about the body. It is for this reason that a simple geometry such as a cube has been used and is still used as a benchmark to aid in the development and improvement in numerical models.

Typical configurations in which research has been conducted on cubic bodies experimentally and computationally include; in the presence of fully developed flow [Hussein & Martinuzzi (1996), Shah & Ferziger (1997)], in a tandem configuration [Martinuzzi & Havel (2004), Farhadi & Sedighi (2008)] and within a matrix/array configuration [Meinders & Hanjalic (1999), Niceno *et al* (2002)]. Other works involving cubes include studying the geometry at a orientation to the flow i.e. as a prism [Thomas & Williams (1999)] or in a staggered arrangement of various size cubes [Xie & Castro (2006)]. However, from the vast amount of literature that has been compiled, most of the effort by researchers has focused on studying a single cube or matrix/array of cubes. The published works have either focused on providing a statistical description of the flow or focused on the structural features. In addition the effects of heat transfer around such bodies have also been well documented [Saha (2006) and Niceno *et al* (2002)].

Much of the early experimental work focused on providing a qualitative description for the flow around single cubes. Such work includes that of Castro & Robins (1977) and Hunt et al. (1978). Castro and Robins (1977) examined the flow velocity around a single cube mounted on a flat plate with various oncoming boundary layer heights. They found that the size of the separated flow region above the cube and the size of the wake region were strongly dependent on the boundary layer thickness of the oncoming flow. While Hunt *et al* (1978) experimentally studied the flow behaviour around a single cube observing the exchange of fluid between the separation regions. From this, they concluded that the separated regions around a three-dimensional bluff body (cube) cannot be closed.

Later, works by Martinuzzi & Tropea (1993) and Hussein & Martinuzzi (1996) provided the first complete databank of statistical measurements and estimates for the turbulent energy budget. The estimates arise from the technical limitations that exist within experimental methods such that certain quantities or terms are unattainable and appropriate approximations are required [Hussein & Martinuzzi (1996)]. In addition to

the statistical descriptions Hussein & Martinuzzi also provided the first complete model for the flow patterns around a singe cube in a fully developed flow.

To further understand such flows various numerical simulations have been conducted ranging from DNS to RANS. Rodi (1997), compared results obtained by various RANS and LES simulations with and without the use of wall models. Results showed that the LES results agreed better against the experimental data, compared to the solutions produced using various RANS models. In general for the wall mounted-cube all tested RANS models over predicted the extent of the separation region behind the cube, whilst under predicting the Reynolds stresses around the body. The inaccuracies in these calculations were attributed to the statistical turbulence models having difficulty in representing the complex flow phenomena occurring around a bluff body. Especially, when large-scale structures dominate the flow and when unsteady processes like vortex shedding and dynamic loading is of importance. However, due to computational limitations in terms of Reynolds numbers, many practical engineering applications of numerical simulations are still only attainable by using RANS modelling, as the computational requirements for approaches like full LES and DNS are still beyond today computing capacity. Hence RANS methods with statistical turbulence modelling are still needed today and will still be needed for years to come in many engineering calculations. This has led to the development and improvement of existing turbulence models that have yielded better agreement with experimental findings. Such work includes that of Iaccarino & Durbin (2000) and Isaev & Lysenko (2009) who used URANS to study the flow around a cubic body with results showing good agreement with the benchmarked data.

The use of LES in modelling bluff bodies began during the early 1990s. Sakamoto *et al* (1993) used this approach to model flow around a square cylinder, while Shah and Ferziger (1997) were amongst the first to use LES to study the of flow over a surface mounted cube at a Reynolds number of 40000 consistent with the flow conditions of that used by Hussein & Martinuzzi (1996) and Martinuzzi & Tropea (1993). The LES simulation was found to achieve a good correspondence with both experimental measurements and observations. Since the original application of LES to the modelling of flow around a wall-mounted cube, many researchers have examined this problem or similar cases with the use of various subgrid scale and wall models. Such works include that of Sedighi & Farhadi (2006), Alfonsi *et al* (2003) and Krajnovic & Davidson

(2002). More recently, researchers have begun to consider DES models around such bodies, examples include that of Paik *et al* (2009) and Schmidt & Thiele (2002).

Another well documented configuration that has been examined is that of a matrix of cubes. Both cases of a wall-mounted cube and a matrix of cubes have been the subject of numerous workshops including ERCOFTAC 1997; with the matrix configuration being considered at the 1998 and 1999 ERCOFTAC meetings. Okamoto *et al* (1996) were amongst the first to experimentally study the flow field around a matrix of surface-mounted square blocks for various separation distances at a relatively low Reynolds number. The cubes forming the matrix were equally spaced with separation distances ranging between 2 to 13. The study by Okamoto et al. showed that for a separation distance of less than 5, flow reattachment did not occur and that the region between cubes were covered by large flow recirculation zones. Reattachment of the flow with the wall after encountering a cube was detected at a cube separation spacing of 7. Their work was later followed by Meinders & Hanjalic (1999) who performed an experimental investigation of heat transfer and vortical structures around a matrix of equidistantly spaced wall mounted cubes at a Reynolds number of $Re_h=3854$. The heat transfer was examined by heating and monitoring a single cube of interest within the matrix of cubes. Meinders and Hanjalić concluded that a two-cell structure forms in the immediate proximity of the cube caused by the shear layer reattachment occurring in the inter-obstacle region. In terms of heat transfer Meinders and Hanjalić concluded that regions with intense flow recirculation and separation exhibited a low local heat transfer coefficient, while high heat transfer coefficients were found in areas with flow reattachment. Although the motivation to the work of Meinders and Hanjalić (1999) was to provide reference data on flow and heat transfer around surface-mounted protrusions relevant to electronic circuitry, their results served as reference data for validating the computational modelling at the 8th and 9th ERCOFTAC/IAHR/COST Workshops. As in the case of a single wall mounted cube placed in a channel, it was found that the presented LES results agreed well with the experimental data and findings of Meinders and Hanjalić (1999) and Meinders (1998). Examples of LES simulations performed considering this configuration include works by Mathey *et al* (1999) and Niceno *et al* (2002).

As both cases of flow around a wall-mounted cube and flow around a matrix of wall-mounted cubes have been well documented, in addition to being the focus of

international workshops; both configurations represent a good method for the validation of a code from a statistical and structural perspective. Furthermore, much of the published works mentioned earlier have been performed within the context of fully-developed flow conditions inside of a channel domain. No work has been presented has examined the affects that a deformable boundary such as a free-surface has on the solution around either a singe wall-mounted cube or around a matrix of cubes.

This chapter examines the affect that the free-surface boundary condition at a moderately low Froude number exhibits on the flow structure and statistical behaviour around a singe and a matrix of wall-mounted cube(s) for various submergence depths. However, for the single mounted cube, the problem examined in this chapter differs from that of the experiments of Hussein & Martinuzzi (1996) in the sense that a uniform inflow condition is applied rather than that of a fully developed profile. Hence the single wall-mounted cube is performed mainly to assess the uniform inflow boundary condition. The need to assess such a boundary condition is required so that the latter simulations of flow around a submarine fairwater can be conducted (studied in the proceeding chapter). Both LES and DES simulations are initially conducted for both mentioned cases in order to assess the accuracy of results predicted by both models; while the later study of the affect of submergence depth is examined using only the LES model.

4.2 Numerical outline

This section outlines the basic computational set-up for the numerical simulations performed for a single and multiple wall-mounted cube(s). Initially, a low Reynolds number flow simulation is performed around a matrix of cubes placed within a fully developed flow field that is similar to the experimental set-up of Meinders and Hanjalić (1999). While a moderate Reynolds number flow is simulated around a single cube, the flow and model conditions are set similar to that of Hussein & Martinuzzi (1996). Both cases differ from the mentioned works in the sense that the upper boundary is not treated as a non-slip wall. Instead, a free-slip, near rigid boundary is used by imposing a low Froude number of ~0.1. Furthermore, as mentioned earlier the flow around a single cube also differs from that of Hussein & Martinuzzi (1996) in the sense that a uniform inflow condition is used rather than that of a fully developed condition. Two reasons for the use of a different inflow condition rather then a fully developed inflow condition are

that, firstly, the code is designed for modelling open channel flow where the full developed profile differs from that of a closed channel. This means that the flow produced by the altered inflow profile would yield a different solution, as shown by Castro and Robins (1977). The second reason which has already been stated earlier is that the uniform inflow is required to be assessed, given it is to be used in the latter chapter for modelling flow around the fairwater of a submarine.

For both cases the effect of depth variation is examined at a low Reynolds number of 3854 and a moderate Reynolds number of 40,000 based upon the cube height and initial velocity. The depths considered are listed in Table 4.1, both the total and relative submergence depths are listed. The depth variation is maintained consistent between both the single and multiple wall-mounted cube(s) cases; such that the effect on the free-surface as well as surface signatures can be clearly identified.

d/h	***(d-h)/h***	***Fr***
2.533	1.533	0.30
2.0	1.0	0.34
1.73	0.73	0.37

Table 4.1: Depth and Froude numbers considered for numerical simulations about a Matrix of cubes.

4.2.1 Modelling of flow around a matrix of cubes

In order to obtain a developed flow around a cube, Meinders and Hanjalić (1999) used a matrix of equally spaced cubes in both the streamwise and spanwise directions. The matrix consisted of a total of 25 x 10 cubes in the streamwise and spanwise direction respectively; with the flow and heat transfer measurements being recorded from the 18th row at the mid-position of the channel, Figure 4.1 shows a basic schematic layout of the matrix considered by Meinders and Hanjalić for $l/h = 4$. Numerically such a flow is relatively easy to model, this is as each cube and the surrounding area is well repeated in the entire domain considered. Hence a periodic boundary around a single cube effectively reproduces the desired effect of Meinders and Hanjalić set-up as indicated by the dashed box region marked in Figure 4.1.

Figure 4.2 shows the modelled domain, a single cube of length *h* is considered. The total size of the domain is 4h in both the streamwise and spanwise directions, with periodic boundary conditions imposed on these boundaries. Niceno *et al* (2002), Schmidt & Thiele (2002) and Tseng *et al* (2006) have also used this approach in simulating this problem with their results producing good agreement with those obtained experimentally.

To ensure sufficient resolution around the cube, a stretched grid is utilised that reduces the element size around the cubes edges at the expense of increasing the local element size at the domain boundary. Stretching is performed via the use of a hyperbolic and/or a parabolic function given by equations 4.1 and 4.2, until the desired mesh is obtained. The level of increase in the mesh size is controlled by the parameters θ_{tanh} and θ_{power} in equations 4.1 and 4.2, respectively.

$$Pt_{pos} = length \times \left(1 - \frac{\tanh\left(\theta_{\tanh} \times P_{n-1} / P_{tot} \right)}{\tanh \theta_{\tanh}} \right) \tag{4.1}$$

$$Pt_{pos} = length \times \left(\frac{P_n^{\theta_{power}}}{P_{tot}^{\theta_{power}}} \right) \tag{4.2}$$

Figure 4.4 shows the spacing variation that can be achieved using equations 4.1 and 4.2. The use of a stretched grid results in the filter width $\left(\Delta = \sqrt[3]{\Delta x \Delta y \Delta z} \right)$ to change locally across the domain, hence the filter width for all cases is defined locally. Special care is taken to ensure that the cells in the streamwise direction at the domain boundaries are of comparable values so that they do not influence the periodic boundary condition. This is because a periodic boundary treats the two sides of a given direction as being linked, hence, ideally one would prefer both cells to be of equal or near equal size. Table 4.2 and Table 4.3 list the total number of grid points used in all directions with the minimum and maximum cell size for the coarse and fine grids. The three values listed for the Z direction in Table 4.3 correspond to the three depths considered, in all cases the minimum cell sizes are concentrated around the cube and kept consistent for all depths considered.

Direction	Cell No	Min Length	Max Length	Min^+ Length	Max^+ Length
X	80	0.018	0.178	~3	~30
Y	80	0.018	0.185	~3	~31
Z	40	0.018	0.124	~3	~21

Table 4.2: Resolution information for the coarse periodic cube grid

Direction	Reynolds No	Cell No	Min Length	Max Length	Min^+ Length	Max^+ Length
X	3584	200	0.014	0.063	~2.33	~11.0
	40000	200	0.014	0.063	~25.0	~144.1
Y	3584	100	0.014	0.057	~2.33	~9.5
	40000	100	0.014	0.057	~25.0	~144.1
Z	3584	80	0.014	0.080	~2.33	~13.3
				0.053		~9.0
				0.029		~5.0
	40000	80	0.014	0.080	~25.0	~14.5
				0.053		~9.60
				0.029		~5.25

Table 4.3: Resolution information for the fine periodic cube grid

The initial estimate for the shear velocity was obtained from Niceno *et al* (2002) giving Re_h*~167* based upon the cube height (*h*). This gives *v= 0.00361212* and u_∞*=13.9112* for a Re_h*=3854,* both *v and* u_∞ are dimensionless values that are normalised against shear velocity and cube height (y^+). Similarly, for the moderate Reynolds number cases the Reynolds number based on shear velocity is found to be Re_h*~1811* based upon the cube height. This gives *v= 0.00005522* and u_∞*=22.088* again , both *v and* u_∞ are normalised against shear velocity and cube height (y^+). For both considered Reynolds numbers the Froude number ranges between *0.3-0.37* for the various depths examined, Table 4.4 summaries the flow characteristics based upon the total depths considered. All simulations are started from an initially prescribed velocity distribution, and given sufficient time to stabilise. The stabilisation cycles are to allow for the flow to become fully developed, 105 wash through cycles (based on initial velocity) are used to ensure fully developed flow. In shedding frequency the stabilisation period is taken over ~30

shedding cycles. Statistics are then performed over approximately 20 shedding cycles of the flow.

		Submergence depth (Submergence ratio)		
	Re_h	2.533 (1.533)	2 (1)	1.7 (0.7)
Fr	3584	0.30	0.34	0.37
	40000	0.30	0.34	0.37
Re_d	3584	9068	7160	6193
	40000	101320	80000	69200
Re_d*	3584	~423	~334	~284
	40000	~4587	~3621	~3132

Table 4.4: Reynolds and Froude numbers for various depths considered

4.2.2 Modelling of flow around a single cube

The single cube is modelled in a domain of size $15h \times 10h \times dh$, with the cube of size h^3 being situated at a location of 4h from the streamwise boundary and centrally in the spanwise direction, as illustrated in Figure 4.3. Inflow and outflow (zero-gradient) boundary conditions are imposed in the streamwise domain extents while a periodic boundary condition is applied in the spanwise direction. The use of a periodic boundary condition in the spanwise direction can somewhat be questionable as noted by Yakhot *et al* (2006) due to possible contamination of the flow near the boundary. However, Shah & Ferziger (1997) performed LES on a cube in fully developed flow on a computational domain of $10h \times 7h \times 2h$ using periodic boundary conditions in the spanwise direction with little to no effect noted. In the present case the domain extents in both the streamwise and spanwise directions are larger than that considered by Shah and Ferziger. The main reason for this is to prevent possible wave reflections or re-entrance influencing the solution. For the chosen domain size neither velocity disturbances nor wave propagation are present the spanwise boundary. As noted earlier the inflow is prescribed as a constant flux boundary condition set initially based on a uniform flow of unity in the streamwise direction. The use of the uniform inflow rather than the developed profile is to assess this boundary condition for the latter fairwater simulations.

To ensure sufficient resolution around the cube is achieved, a stretched grid is again utilised. The mesh size is reduced as the cube body is approached, with the smallest cells concentrating around the cube faces. A similar stretching of cells is performed between the bed and upper cube wall. This results in the cells near the domain boundary having the largest cell sizes. Again, stretching is performed via the use of a hyperbolic and/or a parabolic function given by equations 4.1 and 4.2, until the desired mesh is obtained. Table 4.5 and Table 4.6 outline the typical domain information for both the coarse and refined grids considered.

Direction	Cell No.	Min Length	Max Length	Min^+ Length	Max^+ Length
X	80	0.010	0.364	~18.1	~659.2
Y	80	0.010	0.355	~18.1	~642.9
Z	40	0.010	0.098	~18.1	~177.5

Table 4.5: Resolution information for the coarse periodic cube grid

Direction	Reynolds No.	Cell No.	Min Length	Max Length	Min^+ Length	Max^+ Length
X	3584	200	0.010	0.152	~1.7	~25.4
	40000	200	0.010	0.152	~18.1	~374.9
Y	3584	100	0.010	0.207	~1.7	~34.6
	40000	100	0.010	0.207	~18.1	~275.3
Z	3584	80	0.010	0.067	~1.7	~11.2
				0.038	~1.7	~6.4
				0.038	~1.7	~64
				0.067	~18.1	~121.3
	40000	80	0.010	0.038	~18.1	~68.8
				0.038	~18.1	~68.8

Table 4.6: Resolution information for the finer single cube grid

The Froude number range was set to correspond with the multiple cube case. The Froude number ranges between *0.3-0.37* for the various depths examined. For the validation case the Froude number was set at ~0.1. All the simulations are started from a uniform inflow velocity distribution, sufficient time is provided for the turbulence in the wake and shedding patterns to stabilise. The time given for the flow to stabilise is four

domain wash through lengths ($4l_x$), that corresponds to a non-dimensional time of 90 and in terms of shedding frequency to ~9 cycles. The stabilisation cycles are to ensure that the wake is fully developed, the stabilisation period is considered sufficient based upon the experiences of the authors supervisors. Statistics are then taken over ~20 shedding cycles.

4.3 Validating Results

To ensure that the correct results are obtained numerically the streamwise statistics for the flow around a matrix of evenly spaced cubes are compared against the experimental data of Meinders & Hanjalic (1999). The LES results are produced using a constant coefficient Smagorinsky sub-grid model, while the DES results are computed from the Spalart-Allmaras model. Figure 4.5 shows the mean streamwise velocity components ($<u>$) at various locations along the XZ direction about the central plane. The plotted data include results of both coarse and fine LES and DES runs, along with the coarse LES and DES data obtained using the alternative modelling approach of blocking cells. It can be noted from the mean velocity profiles that a good agreement is found between the experimentally measured and numerically obtained results regardless of resolution and modelling approach. The finer mesh better predicts the average streamwise velocity in the near cube regions. In the IOR the DES model shows a slightly better agreement with the experimental data, while near the surface boundary the DES results show a slight reduction in the velocity. Near the surface the LES results are in better agreement with the experimental data of Meinders & Hanjalic (1999). Similarly, a good agreement is achieved when comparing the streamwise stresses with those produced numerically (Figure 4.6). The coarse mesh results in minor discrepancies with the predicted results which diminish as the grid is refined. On the finer mesh the LES results are found to show represent the streamwise Reynolds stresses along the IOR shear layer, while in this region the DES results slightly over predict.

The mean streamwise velocity distribution around a single cube is also compared to the experimental measurements of Hussein & Martinuzzi (1996), however as stated earlier, due to the varied inflow condition and the manner in which the problem is modelled, the agreement between the two is expected to be poor. This is found to be the case as illustrated in Figure 4.7 which compares the predicated streamwise velocity distribution with that of the experimental results of Hussein & Martinuzzi (1996). The upper

separation region and rear reattachment points are found to be larger than that obtained for the developed inflow condition. Although the results are different, they remain consistent for both the fine and coarse simulations, regardless of the modelling approach. Furthermore, confidence is provided by this as they confirm the documented behaviour reported by Castro and Robins (1977), namely that the flow behaviour around a cube in terms of the extent of the wake recirculation and the size of the vortex on top of the obstacle are strongly dependent on the conditions of the oncoming flow. In addition, the notable features of flow over a cube are well captured, firstly the horseshoe vortex is seen to form and become wrapped around the body, whilst in the wake reattachment region the convergent-divergent behaviour of the horseshoe vortex legs is observed. In addition momentum transfer between the separated regions is also noted, both are covered in more detail in the latter section (4.5).

Table 4.7 lists the measured time averaged separation regions about the central XZ plane for both validation cases. The listed data and their abbreviations are as follows; horse-shoe vortex height (*Hsh*), position of the horse-shoe vortex centre (*Hscx*, *Hscy*), frontal stagnation height (*Fst*), upper separation height (*Tsh*), upper separation length (*Tsl*), rear separation height (*Rsh*), rear circulation centre position (*Rcx*, *Rcy*), rear circulation length (*Rcl*), rear separation length (*Rsl*) and rear stagnation height (*Rst*). The above terms are also illustrated in Figure 4.8. It can be seen that for both cases, most of the measured data predict the same state of structures within measuring uncertainty. For the multiple cube case the greatest sensitivity occurs for the positions of the vortical structures ahead and behind the cube as well as for *Rsl* and *Rcl*. While for the single cube placed in a uniform flow, unsteadiness in the position of vortical structures is less evident. Instead the greatest unsteadiness is noted in the rear wake of the cube in terms of the length of the separation region. In both cases, the effect of numerical diffusion is notable on the flow structures with the coarse grid showing smaller structures. Similarly, both the LES and DES models are noted to show some difference in terms of the measured lengths; however both models capture the expected flow behaviour.

	Measured lengths ± 0.03							
	Single cube				*Matrix of cubes*			
	LES		*DES*		*LES*		*DES*	
	Coarse	*Fine*	*Coarse*	*Fine*	*Coarse*	*Fine*	*Coarse*	*Fine*
Hsh	0.059	0.118	0.059	0.118	0.246	0.215	0.246	0.215
Hscy	0.029	0.059	0.029	0.059	0.123	0.138	0.123	0.128
Hscx	0.706	0.529	0.706	0.529	0.385	0.600	0.369	0.600
Fst	0.294	0.412	0.294	0.411	0.769	0.800	0.785	0.800
Tsh	0.353	0.294	0.324	0.294	0.077	0.062	0.062	0.062
Tsl	0.765	0.824	0.765	0.824	0.523	0.577	0.523	0.585
Rsh	1.471	1.353	1.412	1.353	0.969	0.985	0.954	0.985
Rcy	1.088	1.059	1.000	1.059	0.831	0.846	0.862	0.869
Rcx	0.676	0.853	0.706	0.871	0.523	0.769	0.538	0.746
Rcl	1.529	1.765	1.500	1.782	1.077	1.020	1.015	1.031
Rsl	1.765	2.176	1.765	2.135	1.169	1.338	1.231	1.354
Rst	0.118	0.059	0.118	0.059	0.154	0.200	0.138	0.154

Table 4.7: Position and size measurements of time averaged vortical structures as well as separation and reattachment regions, for both LES and DES simulations of single and matrix cube data. The abbreviations are as follows: Hsh - *horse-shoe vortex height,* Hscx *and* Hscy - *position of the horse-shoe vortex centre,* Fst - *frontal stagnation height,* Tsh - *upper separation height,* Tsl - *upper separation length,* Rsh - *rear separation height,* Rcx *and* Rcy *rear circulation centre position,* Rcl - *rear circulation length,* Rsl - *rear separation length,* Rst - *rear stagnation height.*

4.4 Effects of submergence on flow statistics

4.4.1 Time averaged data

Time averaged velocity and pressure distributions of the flow around a cube in an equidistant matrix configuration are provided in Figure 4.9. The results are plotted along the XZ central plane. The plotted results are extracted at positions *x/h =-0.3*, *0.3*, *1.3*, *1.7* and *2.3* from the leading edge of the cube, which are consistent with those used for the purpose of validation in the previous section. The positions equate to *0.7x/h*, *1.3x/h*, *2.7x/h* and *3.3x/h* from the leading boundary of the domain, respectively, it is this numbering convention that is used to identify the positions for this case. Note that the

scaling of components does vary for purposes of clarity and that the appropriate scaling is shown for all figures. From Figure 4.9 it is clear that on average the velocity and pressure variation is the greatest over the cubic body, with an increase in Reynolds number having little effect on the time averaged distributions. For all cases in the inter-obstacle region the streamwise velocity distribution and the increase in pressure near the frontal region of the cube indicates flow reattachment, though no direct indication of reattachment of the separated flow is noticeable on the w component (insufficient downwash). To clarify this behaviour, Figure 4.10 shows the time averaged streamline plots for $d/h=2$ for both Reynolds number cases, the streamline plots show that the flow, in an averaged sense is divided in to three regions; the first being the core flow in the region above the cube which remains nearly undistorted, while the remaining regions are confined in the inter-obstacle region. The inter-obstacle space is divided by a two-cell structure, arising from the recirculation region at the rear of the cubic body and reattachment of the separated shear layer on to the frontal cube face. Although the time averaged images show a relatively simple cellular structure in the inter-obstacle space, in reality the interaction between the two cells is quite complex. Again the effect of increasing the Reynolds number shows little change in the time averaged structures, indicating that the flow for this configuration is independent of Reynolds number. Although the variation in the Reynolds number yields little change, reduction of the submergence depth results in the reduction of the overall free-stream velocity. While the velocities in the lower part of the inter-obstacle region ($z/h<0.6$) show little variation except close to the leading face of the cube, however, the pressure distribution shows to reduce across the whole depth for reducing submergence depth.

Table 4.8 compares the time averaged structures in terms of size and position. The notations of variables are the same as those used in the preceding section; the reader can also refer to Figure 4.8 for illustration. From examining the listed data on the time averaged structures the effect of reduced submergence (increased Fr) is shown to have little influence on the horseshoe vortex, upper separation region and leading stagnation position, the greatest influence on these measurements arises from the increase in Re. The effect of reducing submergence depth does show an influence on the size of the rear separation lengths *Rcl* and *Rsl*, both lengths show an increase for reducing depths.

	Measured lengths ±0.03					
	Re_h=3584			*Re_h=40,000*		
d/h	*2.53*	*2.0*	*1.73*	*2.53*	*2.0*	*1.73*
Hsc	0.231	0.246	0.215	0.169	0.154	0.148
Hscy	0.123	0.138	0.123	0.092	0.092	0.066
Hscx	0.354	0.431	0.292	0.677	0.492	0.508
Fst	0.769	0.800	0.646	0.800	0.800	0.492
Tsh	0.062	0.077	0.077	0.092	0.092	0.082
Tsl	0.615	0.615	0.615	0.523	0.523	0.525
Rsh	0.954	0.985	0.985	0.969	0.985	0.967
Rcy	0.831	0.846	0.846	0.846	0.846	0.836
Rcx	0.554	0.554	0.538	0.523	0.523	0.459
Rcl	1.015	1.046	1.169	1.015	1.017	1.213
Rsl	1.169	1.185	1.323	1.108	1.138	1.197
Rst	0.138	0.154	0.138	0.108	0.092	0.098

Table 4.8: Position and size measurements of time averaged vortical structures as well as separation and reattachment regions for a cube in a matrix configuration for all considered cases. The abbreviations are as follows: Hsh - *horse-shoe vortex height,* Hscx *and* Hscy - *position of the horse-shoe vortex centre,* Fst - *frontal stagnation height,* Tsh - *upper separation height,* Tsl - *upper separation length,* Rsh - *rear separation height,* Rcx *and* Rcy *rear circulation centre position,* Rcl - *rear circulation length,* Rsl - *rear separation length,* Rst - *rear stagnation height.*

Figure 4.11 shows the time averaged velocity and pressure distributions in the XY plane for *z/h=0.4*, it can be noted that in the inter-obstacle region it exhibits a momentum deficit, while flow in the spanwise direction is driven in and around the body. Both the momentum deficit and spanwise velocity gradients reduce with increasing *z/h*, indicating the momentum in the low region of the inter-obstacle region is supplied more from the spanwise flow, while with increasing height the separated regions draw momentum from the separated shear layer and the surrounding flow. The conclusions of a reduced momentum deficit and spanwise velocity gradients are obtained from comparing velocity and pressure distributions at various heights[5] along the cube, namely, at positions *z/h = 0.1*, *0.4*, *0.7* and *0.95*. The effects that variation along the

[5] Results for the additional planes are discussed but not presented in this section to avoid unnecessary repetitiveness, they included in appendix A2 for purposes of completeness.

cube height has on the time averaged pressure and vertical velocity distributions are that:

1) The cubic body experiences the greatest pressure variation head and around the sides of the body (0.7*x/h* and 1.3*x/h*), with the pressure reducing with increasing height ahead of the body.

2) While the pressure around the sides of the cube peaks near the mid-region of the cube.

3) The vertical velocity component indicates downwash of the flow in the near wall region ahead of the cube and around the sides, while in the near wake region the vertical velocity component induces an upwash behaviour.

Increasing *z/h* results in the vertical component exhibiting a change of direction at nearly all of the plotted positions. Furthermore, the vertical velocity component shows an increase near the spanwise extents, although no direct conclusion can be drawn for why this occurs, the presence (in a time averaged sense) of a weak cellular structure offers the best explanation for the increase. The effects of varying Re and submergence depth on the distributions remain the same. Little effect is observed from increasing Re, while reduction in the submergence depth results in a reduction in the pressure across the whole plane and clearly visible around the cube vicinity (for *x/h=1.0-7.0*), whilst the changes in the velocity distributions are more distinct above the cube.

Figure 4.12 shows the time averaged flow about the central XZ plane for the single cube placed in a uniform flow field. As with the multiple cube case results are extracted at various positions above and in the wake of the cube, the positions are defined about the leading edge rather than from the inflow boundary extent. The positions at which data are recorded are at 0.25*x/h*, 0.5*x/h*, 0.75*x/h*, 1.0*x/h*, 1.5*x/h*, 2.0*x/h*, 3.0*x/h*, 4.0*x/h*, 6.0*x/h* and 8.0*x/h*, respectively. From Figure 4.12 it is clear that the separated flow over the upper portion of the cube remains completely detached, while showing a slow recovery in the wake. Even after flow reattachment has occurred, variations in the spanwise and vertical velocity and incomplete recovery of the pressure show that strong unsteadiness is still present at 8.*0x/h* lengths downstream from the cube. The effect of variation in Re on the time averaged profiles is evident from position *0.5x/h* onwards; the higher Re flow exhibits a stronger shearing of flow along the separated shear lines created over the

upper surface of the cube and in the wake. This results in the separation height over the cube being reduced while causing the flow to reattach sooner, in comparison with the lower Re case. Similarly, the effect of reduced submergence depth causes a further reduction in the separated flow height over the upper surface of the cube, while causing for the flow to reattach earlier through increased pressure in the near wake region. While stronger variations in the vertical velocity component are noticeable near the free-surface boundary.

Time averaged streamlines for both Re_h=3584 and Re_h=40000 are shown in Figure 4.13 for *d/h=1.7*. The variation of the flow structure in terms of the horseshoe vortex ahead of the cube body and the variation in length of the wake separation region can be clearly seen to have altered in both Re cases. With increased Re the presence of multiple vortical structures ahead of the cube can be seen to have reduced, while the rear separation length reduces, these trends has also been reported in the numerical simulations of Farhadi & Rahnama (2006) who examined the effect of the Reynolds number on flow structure around a wall mounted cube in a fully developed flow. Similarly, from examining the free-surface in the wake of the cube, dependence between the wake region and surface wave lengths can be observed.

Table 4.9 lists the sizes and positions of the time averaged structures that exist around a single cube placed within a uniform flow field. The notations of measured variable are the same as those used earlier. From examining the listed data the effect of reduced submergence (increased Fr) shows little influence on the time averaged flow structure near the frontal regions of the cube, while increased Re results in the size of *Hsc* to decrease and the distance *Hscx* to increase. The effects of varying submergence depth (SBD) are more notable over and in the wake of the cube, with the separation flow region generated over the upper surface of the cube decreasing with reduced SBD. Similarly the length of the forward travelling flow over the upper surface near the rear edge is found to have decreased with a reduction in depth. The forward flow over the upper surface is associated with the presence of a vortex drawing in momentum from the wake region, rather then with the reattachment of the separated flow. Though the effect of SBD are notable on the height and length of the upper separation region the effects of varying Re is less notable. While in the wake, from the measured lengths, it can be seen that the flow shows a stark contrast that is dependent on both Re and SDB. The typical behaviour expected from flows where a body experiences an increased

restriction, which in this case is the reduction in the submergence ratio, would be an increase in the length of flow separation at the rear of the body. This is the case for the Re_h=3584 case, however in the case of Re_h=40000 the effect of the submergence is noted to show an opposite trend. Although the average separation is reduced with increased Re, the expected trend would be for the wake to extend with reducing *d/h*. The fact that this does not happen is due to the free-surfaces ability to deform; the reduction in the average wake separation region can occur through an increased pressure which is directly linked with the surface distribution. It can be concluded that with an increased Re and reduced depth the influence of surface deformation shows stronger influence on the wake flow around a single cube.

	Measured lengths ± 0.03					
	Re_h=3584			*Re_h=40,000*		
d/h	*2.53*	*2.0*	*1.73*	*2.53*	*2.0*	*1.73*
Hsc	0.265	0.265	0.265	0.147	0.147	0.147
Hscy	0.118	0.098	0.098	0.059	0.059	0.059
Hscx	0.647	0.618	0.588	0.824	0.853	0.882
Fst	0.353	0.353	0.353	0.353	0.353	0.353
Tsh	0.382	0.353	0.294	0.324	0.294	0.235
Tsl	0.647	0.765	0.882	0.647	0.794	0.912
Rsh	1.529	1.471	1.412	1.412	1.353	1.324
Rcy	1.118	1.059	1.059	1.118	1.059	1.059
Rcx	1.500	1.412	1.588	1.118	1.118	1.088
Rcl	3.353	3.235	3.059	2.118	2.000	1.882
Rsl	3.529	3.412	3.324	2.235	2.147	2.076
Rst	0.294	0.324	0.412	0.176	0.176	0.147

Table 4.9: Position and size measurements of time averaged vortical structures as well as separation and reattachment regions for a single cube for all considered cases.

Figure 4.14 shows the time averaged velocity components and pressure distributions about the XY plane for *z/h=0.4*. The results show that the flow remains separated along the lateral faces of the cube, while in the wake region the flow shows a slow recovery with a momentum deficit still present downstream of the reattachment points. This is found to be the case across all planes examined. The spanwise velocity indicates the presence of a secondary vortical structure situated near the rear face of the cube, this is indicated by the inflection points at *1.0x/h*. On average the spanwise velocity exhibits a

divergent-convergent-divergent trend, with the final divergence (directing flow outwards) noted to occur aft of the reattachment point; hence the spanwise velocity component on average aids in the redistribution mass in the near wake region. This effect (observed divergence aft of flow reattachment) is limited to the lower region of the cube and diminishes along the cubes height. The vertical component is noted to show a stark change in its influence on the flow along the cube height. On average it is noted that the vertical velocity component induces a downwash on the flow near the edges of the separated flow region along the lateral faces for $z/h<0.5$. The effect of downwash on the velocity is increased with reducing the depth and becomes notable on both the time averaged pressure and streamwise velocity component. The reason for the downwash is attributed due to the renewal of momentum within the region that is influenced by both the separated flow around the lateral faces and the presence of the horseshoe vortex. While for $z/h>0.5$ the vertical component induces an upward motion on the separated flow along the lateral faces, an influence that increases with increasing height. In the wake region the vertical component is seen to induce a downward motion on the flow, an effect that increases towards outer wake regions (spanwise direction). The average pressure is found increase along the cube and in the wake region for increasing z/h. The influence of Re on the time averaged results show that for $Re_h=3584$ on average a larger momentum deficit exists in the wake compared against the moderate Re case. Similarly, the effect of reducing the SBD shows little influence on the time averaged velocity components; while for the pressure an altering field is observed, with the smallest SBD showing the greatest and least pressure variation indicative of wave motion or wake-surface influence.

Comparison of the time averaged data for both a single and multiple cube(s) shows that; although the cases are different, increasing the Re results in an overall drop in the free-surface height when compared to the lower Re cases. This is evident in both Figure 4.9 and Figure 4.12. Similarly, the time averaged solutions for both cases show the presence of a vortex ahead of the cubic body, an upper separation and a wake region, which are the well-defining features of flow around a bluff body.

4.4.2 Turbulent intensity and Reynolds stresses

Figure 4.15 and Figure 4.16 show the turbulent intensity and Reynolds stress distributions about the XZ plane for the matrix of cube configuration. The turbulent

intensities show that the flow perturbation exists across the entire depth for all the components, with maximum flow variation occurring above and along the separated shear layer. Furthermore, damping of vertical turbulence near the free-surface boundary can be observed from the plots of w_{rms}, while the remaining components show an increased turbulence level with the greatest change occurring in the spanwise direction. This behaviour is indicative of free-surface flows and indicates flattening of vortical structures near the surface [Handler *et al* (1993)]. Variation in submergence depth results in the suppression of the vertical fluctuations and redistribution in the near surface region to increase, while causing an overall reduction in the level of turbulence. The effects of an increased Re results in an increase in the total level of turbulence (higher variation) around the cubic body, while the increase is less noticeable in the wake-cell of the inter-obstacle region (IOR).

The normal Reynolds stresses in Figure 4.16 also show this behaviour. From the Reynolds cross component stresses only the $<u'w'>$ is plotted along the XZ plane, for reasons of symmetry ($v' \rightarrow 0$) $<u'v'>$ and $<v'w'>$ yield no useful information. The Reynolds shear stress $<u'w'>$ on average reads negative across the entire upper region ($z/h>1.0$), reducing gradually towards the surface. The highest levels of shear stress are recorded over the cube and along the separated shear plane, with an increased region of influence (unsteadiness) occurring over the IOR; while towards the leading face of the cubic body the concentration in the Reynolds shear stress $<u'w'>$ reduces along the shear line and unsteadiness is the greatest. The fact that $<u'w'>$ remains negative along the upper portion of the domain shows that on average $<u'>$ and $<w'>$ have a opposite relationship. Similarly, the effects of variation in submergence depth (SBD) and Re remain the same as discussed earlier.

The variation in turbulent intensities and Reynolds stress distributions about the XY plane ($z/h=0.4$) are shown in Figure 4.17 and Figure 4.18. The maximum variations in all the components concentrate around the body and along the interfacial shear layer of the two-cells within the IOR. A reduction in the peak variation and an increase in the region of unsteadiness occur across the IOR for all components towards the leading face of the cubic body. This is owed due to the insweeping and redirecting of flow ahead of the cube. Variation in the turbulent intensities along the height of the cube show an increase ahead of the cubic body, while around the cubic body little influence is observed. An increase in the vertical variation is noted close to the body for $z/h=0.95$.

For the Reynolds stress the strongest contributions arise from the normal stresses, while the effects of cross stress components are found to show a varied level of influence along the height of the cube. The variation in SBD and Re show similar behaviours as mentioned before with increasing influence along the height of the cube.

The turbulent intensity and Reynolds stress distributions for a single cube are plotted in Figure 4.19 and Figure 4.20 about the central XZ plane. Results show that the major part of the turbulence is confined to the wake region. Whilst in the separation region above the cube results show/suggest that the streamwise and spanwise velocity fluctuations are dominate nearer to the leading edge, with the unsteadiness of all velocity components increasing towards the trailing edge of the cube. This indicates that the separated shear layer generated over the cube is initially of a constant height though this can only hold true for flow closest to the central plane due to the three-dimensionality of the flow towards the lateral edges; while increased fluctuations indicate a stronger intermittency between the separated region and the wake near the rear of the cube. Damping and redistribution of the vertical fluctuations is also visible near the surface, which is more pronounced at the lower SBDs. Based on the variation in positions of redistributions it can be concluded that such a process occurs only when turbulence or turbulent structures are near the free-surface boundary. Other notable effects of depth variation on the turbulent intensities are an initially lower separation region (based on peaks in data) and a higher level of turbulence in the streamwise and spanwise directions further downstream of the wake. The effect of an increased Re on the flow is to increase the level of velocity fluctuations and influence in the near wake region.

The same behaviour can be noted in the normal Reynolds stresses in Figure 4.20. Similarly, the Reynolds shear stress $<u'w'>$ peak along the separated shear layer above the cube (closer to the rear region) and in the wake region. The influence of the shear stress $<u'w'>$ is also noted to increase further downstream in the wake until *3-4x/h* after which $<u'w'>$ decreases due to flow reattachment. Increasing Re causes an overall increase in $<u'w'>$ and causes the peaking of turbulence in the lower wake region to occur faster. This is as flow reattachment is found to occur sooner for an increased Re. The effects of depth reduction on $<u'w'>$ result in a stronger shear stress to existing over the cube.

The distributions of turbulent intensities and Reynolds stresses about the XY plane for a single cube are plotted in Figure 4.21 and Figure 4.22 for *z/h=0.4*. The results show that the major portion of the turbulence is contained in the wake, with both turbulent intensities and normal Reynolds stresses increasing downstream until just after flow reattachment occurs. After which the turbulence is diffused showing a drop in the maximum level and an increase in the total spanwise direction influenced. The total span influenced is noted to reduce along the height of the cube. The streamwise intensity and Reynolds stress are maximum along the separated shear layer, while aft of reattachment the streamwise intensity and Reynolds stress shows an increase across the wake length. Similarly, the spanwise and vertical intensities and Reynolds stresses also show the greatest influence in the separated wake region, while the level of influence reduces aft of reattachment. The normal stresses and intensities all exhibit a drop in the strength along the height of the cube. $<u'v'>$ shows the greatest influence across the cube height from the cross Reynolds components with $<u'w'>$ and $<v'w'>$ showing increased influence over the upper portion of the cube. The effects of increased Re is an increase in the total variation, while the effects of varying the submergence depth are less noticeable.

Comparison between the two cases shows that the damping of vertical flow variation and redistribution only occurs if turbulence or turbulent structures are present near the free-surface boundary. While in both cases Reynolds stresses and turbulent intensities show the strongest variation within regions of high shear.

4.4.3 Turbulent kinetic energy distribution and spectra

Figure 4.23 shows the turbulent kinetic energy distribution about the XZ and XY planes, respectively. In both planes the turbulent energy is seen to be the highest around the cubic body and along the separated shear layer over the IOR, while in the IOR the turbulent kinetic energy (TKE) increases around the cellular interface region. Variation in TKE along the height of the cube shows an increase ahead of the cubic body, while little variation is observed around the cubic body and along the edges of the wake cell. Increasing Re shows an increase in TKE across all the extracted data sets (positions and heights), while reduction in SBD results in an overall reduction in TKE.

The TKE variation about the XZ and XY planes for a single cube placed in a uniform flow are plotted in Figure 4.24. As mentioned with the Reynolds stresses and turbulent intensities, the variation in TKE is confined to the wake region and in the separation region above the cube. This is expected as TKE acts as the resultant of the normal stresses; hence it shows a combined effect of the normal components. TKE exhibits a strong increase within the wake region near reattachment, before dispersing after reattachment occurs. The same trend is observed in both the XZ and XY planes plotted. Variation in height along the cube results in the total level of TKE to change, which reduces with increasing height. Variation in Re and SBD show the same behaviour as found for the turbulent intensities and Reynolds stresses.

TKE spectrums for both variations in Re and SBD are plotted in Figure 4.25 for the near wake region at PT_{mc1} (*2.54x/h*) along the XZ centre plane. Results are extracted at fixed heights of *0.3z/h*, *0.6z/h*, *0.95z/h* and *1.3z/h* behind the cube body in order to examine how energy transfer and energy redistribution is affected across the wake/shear layer region. Results show that for all depths and Re the plotted energy spectra's exhibit the *-5/3* energy cascade (inertial range), showing that the inertial range was captured in the wake; with the general trend in the energy cascade following a *-5/3* and *-3* behaviour. The effects of reducing SBD on the energy spectra is a net reduction in energy across all monitored points with the greatest reduction occurring across the upper portion of the monitored wake. An increase in Re results in the total level of energy across the spectra to increase, while exhibiting an increased rate of energy transfer across the smaller length scales.

Figure 4.26 compares the energy transfer for various positions in the wake along the XZ centre plane, for *d/h=1.7*. The points of interest are taken at PT_{mc1}=*2.54x/h* and PT_{mc2}= *3.44x/h* in the streamwise direction; point PT_{mc1} is located within the wake cell (approximately halfway based on time averaged streamlines), while point PT_{mc2} is located within the horseshoe cell (quarter way). The turbulent energy spectra shows that the distribution of turbulent energy becomes more isotropic (in the vertical direction) at PT_{mc2} in comparison with PT_{mc1}, with the level of turbulent energy increasing in the lower positions and reducing for *z/h=1.3*. While the energy spectra at *z/h=0.95* shows little change. The effects of variation in SBD and Re show little effect on this trend. From this behaviour it can be said that in the near cell interface region of the IOR, the lower region experiences an increase in the generation of turbulence while outside of

the separation region (vertically - *z/h=1.3*) turbulent energy experiences an increased dissipation or transferred of turbulent energy. Whilst an equilibrium range between the two exists where the turbulent energy remains unaffected.

Similarly for a single cube, TKE spectrums comparing the effects of variations in Re and SBD on the levels of energy and the rate of energy transfer in the near wake region at PT_{sc1} (*5.56x/h*), along the XZ centre plane are plotted in Figure 4.27. As with the cube in a matrix configuration the plotted energy spectra's exhibit the *-5/3* energy cascade (inertial range), with the general trend in the energy cascade following a *-5/3* and *-3* behaviour. The plotted energy spectra show that in the near wake region the effect of reducing the SBD is a net increase in the turbulent energy in the smaller length scales; while the variation in Re causes a shift in the wave lengths responsible for transferring energy, which is most noticeable at the larger length scales. The turbulent energy spectra's all exhibit a reduction in turbulent energy for reducing *z/h*.

Variations in turbulent energy spectra along the wake are plotted in Figure 4.28. Energy spectra's at three different positions along the XZ centre plane for a submergence ratio of *d/h=1.7* are compared. The points are located at *5.56x/h*, *7.54x/h* and *9.41x/h* which correspond to PT_{sc1}, PT_{sc2} and PT_{sc3}, respectively. The general trend for all the turbulent energy spectra's is to exhibit a continual reduction in net energy downstream of the cube, owed due to effects of energy diffusion and dissipation occurring through vortex interaction, stretching and viscous effects.

In summary, this section has examined the effects of depth variation and variation in Re have on the turbulent kinetic energy distributions as well as on the energy spectra's for a single cube placed in a uniform flow and for a cube in a matrix configuration. TKE distributions have shown that, TKE increases along the shear layer and near surface region for reducing depth. The effect of depth variation is clearly noticeable in the matrix configuration while being less noticeable for a single cube. In both cases increase in Re resulted in a higher level of TKE. In addition, both cases are found to have fully developed wakes, where the turbulent energy cascade follows a *-5/3* and *-3* behaviour.

4.5 Effect of submergence of flow structure

Unsteadiness is the result of disturbances or an imbalance existing within a flow. Although time averaged data provides basic information, it does not show the mechanics and the types on interactions present within the flow. This section utilises instantaneous data of the flow in terms of streamlines and identified vortical structures to examine how the flow structures vary around a single cube and a cube in a matrix configuration.

4.5.1 Three-dimensional streamline traces

Figure 4.29 shows the instantaneous streamline plots around the multiple cube case for both the moderate and low Re cases. Streamlines are traced trough points *y/h = 1.7*, *1.85*, *2.0*, *2.15* and *2.3* along the leading face of the cube to ensure that the flow variation across the face is well captured. The images are plotted at fixed intervals in time of $\Delta t=0.3$ for $Re_h=3584$ and $\Delta t=0.15$ for $Re_h=40000$ for $d/h=2.0$. The sequence of images helps piece together how the flow behaves around the cube in a matrix configuration. The flow pattern is seen to be strongly influenced by the shedding behaviour of the leading cube. The lower region of the cubes face is mostly influenced by the shedding pattern, whilst the upper portion of the face shows a reduced influence due to the presence of vortical structures passing over the cube. At times the spanwise velocity can cause a complete lob-siding of the flow hitting the face of the cube causing not just a strong variation in the force distribution around the cube body, but strongly influencing the separation regions (around the sides and top) around the cube, leading to a constant variation in the Reynolds stresses over the cube frontal regions. Furthermore, based on the streamline variation the presence of a horseshoe vortex would have to occur in a broken (hockey stick) and varying state. This is due to the highly unsteady flow variations and complete loss of symmetry of the flow hitting the cube. The effect of varying Re does not result in much change in this flow behaviour, only the rate of the unsteady cycle is seen to be influenced.

Figure 4.30 shows the same instantaneous streamlines around a single cube for Re_h=3584 and Re_h=40,000. The images show that the horseshoe vortex in both cases forms and is wrapped around the cube with the legs extending downstream, with a contraction and expansion between the vortex legs occurring around the point of flow

reattachment. This behaviour has been observed experimentally by Hussein & Martinuzzi (1996). Furthermore, for both cases the separated regions are found to be non-closed, this is shown by the deviation of streamlines in separated regions feeding to other separated regions around the cube body (enlargements of the flow around the cubic body are shown for both cases). Figure 4.31 shows the instantaneous images about the XY plane plotted at fixed time intervals for both cases. The images show the horseshoe vortex remains steady around the cube, while the wake has a direct influence on the horseshoe vortex legs downstream of the cube. For both cases the major variation in the horseshoe vortex occurs one shedding length downstream of the cube.

4.5.2 Two-dimensional streamlines

Vortex structures can be viewed and have been viewed using varied approaches. For a vortex core to exists, the structure is required to have a net circulation i.e. a net cross flow. This has resulted in the use of streamlines [Lugt (1979)], streamline and pressure field mapping as well as the vorticity magnitude to identify vortical structures [Metcalfe *et al* (1985)]. In this section streamlines across the XZ centre plane are used to examine the flow in the IOR, this is due to the high level of vorticity in the region making analysis of the general structures present difficult. Figure 4.32 and Figure 4.33 show the streamline plots for both Re_h=*3584* and Re_h=*40000* for all the studied submergence depths. Images are plotted at time intervals of Δt=0.3 and Δt=0.15 for both the low and moderate Re cases. Results show that in both cases the two cells are constantly being altered in terms of their shape, position and structure. The horseshoe vortex is seen to be completely unsteady undergoing a cycle of being created, undergoing a varied and complex processes of stretching and merging before being destroyed or ejected. Similarly, in the near wake region the structure of the flow is constantly altering, it is often formed from multiple groups of vortical structures that merge or pull apart to form a larger structure or smaller structures. Furthermore, vortices of varied alignments are also detected within the IOR, indicating that twisting and realignment of the flow does occur due to the presence of strong vortical structures or shearing existing. The separation region above the cube is seen to vary, however no discernable pattern is observed from the plotted and examined data. Similarly, no distinct effects of increased Re and reduction in the SBD are noticeable at such large time steps. This is due to the three-dimensionality and highly intermittent flow within the IOR.

Figure 4.34 and Figure 4.35 show the streamline traces across the XZ centre plane, for Re_h=*3584* and Re_h=*40000* for all submergence depths. The streamlines show that the wake region for all cases remains unsteady, consisting of multiple vortices that either merge together or dissipate downstream. The lower Re case shows more vortical structures and a slower redirection of the flow towards the wall in comparison to Re_h=*40000*. Similarly, reduction in SBD results in the wake size for the Re_h=*3584* to grow, while the interaction between the free-surface and vortices increases. However in comparison to Re_h=*40000* the influence of vorticity on the surface is less pronounced this is due to the higher levels of viscous dissipation existing, reducing the strength/effect of the vorticity. For Re_h=*40000* reduced viscous effects results in a stronger vorticity causing stronger surface deformation which is noticeable for *d/h=1.7* at *T+22.5* in Figure 4.35. This increase in wave height in turn causes a reduction in the reattachment distance through increased hydrodynamic pressure.

4.5.3 Vortical Structures

Vortical structures in the flow are identified using the Q-criterion [Hunt *et al* (1988)]. The Q-criterion is based on the assumption that for a vortex to exist the vorticity is required to exceed the strain. This means vortical boundaries can be determined for Q > 0.

$$Q = \frac{\left(\|\Omega\|^2 - \|S\|^2\right)}{2} \tag{4.3}$$

where, Ω and S are the symmetric and anti-symmetric components of the velocity gradient tensor ∇u .

$$\Omega = 0.5\left(\nabla v - (\nabla v)^t\right) \tag{4.4}$$

$$S = 0.5\left(\nabla v + (\nabla v)^t\right) \tag{4.5}$$

4.5.3.1 Junction Vortex

Iso-surfaces of vorticity using the Q criterion are used to identify vortical structures in the near-wall region for a cube in a matrix configuration. Figure 4.36 and Figure 4.37 show the near wall region for z/h<0.3, for $Re_h=3584$ and $Re_h=40000$. Data above this height has been blanked out so as to show clearly how the flow varies within this region. The iso-surfaces are visualised at Q=130, and show the flow in the near wall region is constantly altering regardless of depth and Re. A typical structure expected to be present ahead of any protruding body is the junction/horseshoe vortex, which forms and wraps itself around the body. However, due to the strong variation in flow within the IOR the horseshoe vortex which is usually well defined is constantly being altered as can be noted in both figures. These visualisations confirm the earlier noted effect (section 4.5.2) of strong flow variation past the frontal region of the cube causing the horseshoe vortex (HSV) to exist in a broken and distorted shape. The distorted HSV is clearly observable in Figure 4.36$a_{T+1.2}$ and Figure 4.37$b_{T+0.45}$ for both Re cases. For all the plotted cases vortical structures are observable wrapped around or along the leading face of the cube at various positions and orientations. All of these structures though varying with the local state of the flow, aid in the redistribution of the flow around the frontal facial region of the cube.

For the cube in a matrix configuration the effect of an increased Re shows an overall increase in the level of vortical structures present ahead and behind the cube in the near-wall region. Furthermore, on average the HSV/vortical structures near the wall region are located further ahead of the frontal face of the cube while exhibiting increased vortex stretching. Whilst the reduction in SBD is noted to cause a reduction of vortical structures in the near-wall region.

4.5.3.2 Flow structure

Variations in vortical structures around the multiple cube case are shown in Figure 4.38 and Figure 4.39 at various instances in time, for all SBDs considered. Due to the three-dimensionality and strong concentration of turbulence around the cube, the vortical structures are visualised in two planes. Figure 4.38 shows the iso-surfaces around the body with a view point directly head on with a tilt angle of 10˚, while Figure 4.39 shows the iso-surfaces about the XZ plane in order to show the inclinations and heights of the vortical structures that cannot be clearly seen from Figure 4.38 alone. Both

figures correspond to each other in time and threshold. As with the visualisation of vortical structures in the near-wall region, vortical structures (VS) are visualised for Q=130, such that a sufficient portion of the vortices are captured.

The general trend for VS is to show a higher presence in the IOR and above the cube, while the total level of structures reduces towards the spanwise boundaries. However, though the structures appear reduced on average the size of the structures is larger. The alignment of structures can be observed to be constantly changing about the YZ plane, indicating a strong influence of cross flow on the VS above the cube. Furthermore, regardless of the direction in which the vortices translate, large vortices travelling over the cubic body are broken (if they come into contact with the cube) and experience increased stretching. The effect of depth variation results in an increase in the level of interaction between vortices and the free-surface for reducing SBD. This increased level of interaction is directly related with the reduction in depth, no increase in rise time of vorticity for this configuration was observed. Furthermore, the reduction in SBD results in the overall change in the directional alignment of vorticity at/near the free-surface boundary, from mostly a surface normal interaction at the largest submergence ratio to vortical structures being mostly aligned parallel to the surface at the smallest SBD. While from Figure 4.39 the inclination of vortices on average appears reduced.

Figure 4.40 and Figure 4.41 show the VS around the cube for $Re_h=40000$. Again as noted in the preceding subsection the effect of an increased Re shows an overall increase in the level of vortical structures present above and around the cube. Furthermore, both the *d/h=2.53* and *d/h=2.0* show a reduced interaction with the free-surface, while *d/h=1.73* shows an increased level of interaction between the free-surface and surface parallel alignment of vortices.

Figure 4.42 and Figure 4.43 show the VS around a single cube placed in a uniform flow, at various instants in time, for $Re_h=3584$ for all SBDs considered. Again VS are visualised in a similar manner to that of the previously discussed case. Iso-surface visualisations of VS are performed for Q=1. The HSV is well captured in all plotted cases, and remains wrapped around the cube with the legs extending around the body. However the legs of the HSV extending into the wake region (as shown in the streamline visualisation - Figure 4.31) are not captured for Q=1, indicating the vorticity/circulation is reduced within this region. Vortices for all cases are

consecutively shed from the top and lateral sides of the cube, showing increased levels of interaction and deformation with the wake further downstream. Vortices shed from the lateral extents of the cube show a faster decay rate and breakdown than vortices shed from the upper region of the cube, mainly due to the von kármán instability that reduces along the height of the cube. Vortices are also observed to show a change in orientation and inclination angle downstream of the average reattachment point.

The effects of reduction in SBD can be seen to cause an increase in the rise time of vortices (Figure 4.43), through increased wave effects. Similarly, the reduction in SBD results in VS persisting longer downstream in comparison with higher SBDs. Increasing Re (Figure 4.44 and Figure 4.45) also results in an increase in the rise time of vortices; whilst with reducing depth, vortices show a stronger tendency to align themselves parallel to the free-surface downstream of the immediate wake. In both cases, vortices that connect/interact with the free-surface which are shed from the immediate wake vicinity of the cube do so in the forms of hockey-stick and hairpin vortices. The head portion of these vortices is seen to dissipate, with the legs connecting normal to the free-surface; a behaviour observed by other researchers including Shen *et al* (1999) and Tsai (1998).

4.5.3.3 Vortex alignment and persistence

Figure 4.46, shows the vortex data for Q>0 in the wake region of a cube in a matrix configuration along the XZ centre plane and near the cube edge, at streamwise positions PT_{mc1} (*2.54x/h* – with respect to the leading boundary face) and PT_{mc2} (*3.44x/h*) for Re_h*=3584* and Re_h*=40000* for all SBD. Data plots for both PT_{mc1} and PT_{mc2} extend across the total channel depth (*d*). The data presented are the average value of Q for instances that VS are known to be present (Q>0), while the remaining plots provide insight into the persistence, alignment and orientation of vortical structures over the total monitored time. The results show that on average the VS have the greatest level of vorticity within the IOR and above the cube, with the level of vorticity reducing as the free-surface is approached. Furthermore, the average readings of Q are normalised by Q=130, readings greater than 1 in the near upper region of the cube and across the cubes height close to the edge indicate a strong circulation is associated with vortical structures in the IOR. Comparing PT_{mc1} to PT_{mc2} shows a reduction in the level of vorticity and a stabilisation in the level of vorticity along the height of the cube at

PT_{mc2}. The persistence of the vorticity along PT_{mc1} and PT_{mc2} is found to be as high as 65% of the total monitored time making VS within this vicinity a well defined feature of the flow. Variation between the monitored positions yields little change in the level of persistence. In all cases the level of vorticity exhibits a drop within the near surface region, which increases sharply with the reduction in SBD. Little influence in terms of Re on the persistence of structures is found. The remaining plots in Figure 4.46 are used to examine the average alignment of VS along PT_{mc1} and PT_{mc2}. The plotted results are the total alignment for Q to individual vorticity components and no contribution from vorticity components. The results show that vortex alignment for both points occurs mostly in the vertical direction along the cubes height, while a reduction in the vertical alignment occurs towards the wall where an increase in alignment in the streamwise direction is observed. It should be noted that all components show a certain percentage of complete vortex alignment along the height of the cube, with the highest being along the vertical axis. This shows that the flow is strongly varying and unsteady. Similarly, the percentage of times the vorticity has no contribution from a given component are also plotted. The results show that over the monitored period vortical structures showed the lowest alignment in the spanwise direction in the IOR and near the free-surface, with the VS alignment further reducing with reducing SBD. The opposite is true for the vertical and streamwise components.

Figure 4.47 shows the vortex data for Q>0 in the wake region of a single cube placed in a uniform flow along the XZ centre plane and near the cubes edge. Data presented are extracted at positions PTsc1 (*5.56x/h* – with respect to the leading boundary face), PTsc2 (7.54*x/h*) and PTsc3 (9.41*x/h*) in the streamwise direction across the total channel depth (*d*). Note, the data for *d/h=2.0* for Re_h*=3584* is omitted from Figure 4.47 due to an error in acquiring data (data set did not conform). The time averaged values for Q show that the strongest level of circulation/VS exists in the wake region, while in the near wake the maximum level is found along the shear layer region. For *z/h>1.0* the strength of VS shows a reduction towards the surface, similarly, VS also exhibit a reduction in strength further downstream of the wake. The effect of increased Re is an increased strength of VS, while the effects of variation in position (centre and edge of cube) on the strength of VS is less clear. Persistence of VS shows that vortical structures are well established within the wake region with results showing the presence of vorticity up to 50% of the total monitored time. Furthermore, an increase in the level of persistence is notable near the free-surface boundary, though on average the circulation

in quite weak. The effect is seen to increase with SBD, while increased Re results in a reduced persistence downstream. The vortex alignment plots show that in general vortices show a relatively low level of alignment with any given direction indicating that VS passing these points are tilted to some degree. The strongest non-alignment is recorded along PT_{sc2}. Similarly, the plots of zero contribution of vortical components are also found to be the highest at this position. The reduction in alignment and increased tilting of VS in this region is attributed due to flow reattachment occurring near/across this region. In general it can be concluded to some degree that the vortex structures in the wake of a single cube are tilted and are constantly being stretched.

4.6 Forces and Shedding Frequencies

This section examines the effects that both Re and SBD have on the forces, variation in forces and shedding frequencies acting about a cube for the two examined configurations. The calculated forces and shedding frequencies for both cases are not non-dimensionalised, for the sole reason of the uncertainty in the use of a reference for multiple cube case, especially for $Re_h=40000$.

4.6.1 Effects of Re and SBD on Forces

Figure 4.48 shows the time history of the measured forces around a matrix of cubes and a single cube in a uniform flow after the initial start cycles. The forces measured are lift, pressure drag in the streamwise direction, the pressure loading occurring around the body, friction and the total drag force, for both cases the forces are calculated about the cubic body. Both Figure 4.48a and Figure 4.48b show that the sufficient time was provided for both cases for the simulations to stabilise, given that in both cases the lift force centres about zero.

Table 4.10 lists the time averaged forces and variation in forces for the flow around a matrix of cubes for both $Re_h=3584$ and $Re_h=40000$. The force values are recorded and processed after the total statistical run time had completed, in all cases the time averaged forces and force variations are dimensionless (note: this is due to the code and that the values are not coefficients). The listed forces are the resultant lift, total drag and pressure force acting on the cubic body. The average lift force appears to be unsteady

due to the nature of the flow, but is effectively small (zero if non-dimensionalised) in comparison to the pressure difference around the body in the streamwise direction. Although the lift variation is effectively small, the variation in the lift force is comparable to the level of variation experienced in the total drag, with the largest variation occurring for the total pressure force. For $Re_h=3584$ the effect of reducing SBD on the total drag and pressure force is a reduction in their averaged values. Similarly the variation in both the total drag and pressure force are also found to reduce for reducing SBD. For $Re_h=40000$ a similarly trend for the average forces is found for the variation in depth, however the force variations show an opposite behaviour where the reduction in depth causes an increase in the level of force variation. This increase can only be explained through an increase in gradients and velocity variations caused by reduced viscous (molecular) effects, and attributed as a direct effect of increased Re.

	Forces and variation					
	Re_h = 3584			Re_h=40000		
d/h	*2.53*	*2.0*	*1.73*	*2.53*	*2.0*	*1.73*
Lift	0.740	0.040	0.161	0.548	0.196	0.860
	±8.871	±7.562	±6.252	±11.173	±10.025	±8.646
Total	30.737	26.789	16.351	41.141	39.485	29.527
Drag	±6.889	±5.333	±4.807	±11.361	±12.036	±15.001
Pressure	35.956	31.045	19.922	42.507	40.491	31.102
Loading	±12.066	±10.034	±8.355	±15.943	±16.300	±18.708

Table 4.10: Average force and force variation around a cube in a matrix configuration for all cases considered.

Similarly, Table 4.11 lists the time averaged forces and force variations around a single cube placed in a uniform flow for both $Re_h=3584$ and $Re_h=40000$. The listed forces are again the resultant lift, total drag, and pressure force acting on the body. As with the previously discussed cases the average force is found to be small in comparison with the total drag and pressure force acting on the cube. However, the variation in forces are found to show a greater level of force variation for the lift in comparison to that found for the total drag, while the largest variation occurs for the pressure loading acting on the cube. In all cases a reduction in SBD causes a reduction in the average total drag and pressure loading acting on the cubic body, regardless of Re. Another notable behaviour is an increase in the level of force variation at $h/d=1.73$ for both the moderate and low

Re cases. This change in force variation is attributed to increased wave influence and local vortex interactions with the free-surface. Thesis is well indicated in Figure 4.34 and Figure 4.35.

	Forces and variation					
	Re_h = 3584			*Re_h=40000*		
d/h	*2.53*	*2.0*	*1.73*	*2.53*	*2.0*	*1.73*
Lift	0.014	0.012	0.013	0.012	0.011	0.013
	±0.028	±0.025	±0.017	±0.067	±0.063	±0.065
Total	0.585	0.467	0.361	0.505	0.432	0.289
Drag	±0.012	±0.012	±0.026	±0.053	±0.021	±0.032
Pressure	0.615	0.495	0.390	0.520	0.446	0.305
Loading	±0.032	±0.027	±0.030	±0.086	±0.064	±0.074

Table 4.11: Average force and force variation around a single cube for all cases considered.

Comparison between the two cases examined in this section shows that both cases exhibit a similar trend for increased Re and reducing SBD. In both cases the average forces are noted to show the same trend. Although the trends show a similar behaviour the way in which both come about is quite different. For the single cube, the reduction in the time averaged forces is due to free-surface deformation influencing the pressure field around the cube body; whilst for the multiple cube case the reduction in the time averaged forces is due to a reduced momentum with reducing depth i.e. less re-energisation of the flow around the cube from the free-stream region.

4.6.2 Effects of Re and SBD on shedding frequency

Table 4.12 lists the determined shedding frequencies around a cube in a matrix configuration. Shedding frequencies are obtained using two different methods: i) calculated based on the lift force variation, ii) determined from point-wise monitoring of the velocity variation. The use of two approaches is due to the unsteadiness of the flow as well as to show how the averaged shedding frequency varies when compared to point-wise frequencies. The point-wise shedding frequency is determined at four different locations along the height of the cube. The positions are *z/h=0.25*, *z/h=0.5*, *z/h=0.75* and *z/h=0.95* which are recorded at PT_{mc1} (*2.54x/h*) at distance of *0.1h* in from the cubes edge. The shedding frequencies based on the lift force variation show that

with reducing SBD the average shedding frequency is increased, regardless of Re. From the point-based shedding frequencies it can be seen that no singular distinct frequency exists, instead multiple or small bands within which dominate frequencies exist can be identified. The frequencies contained within brackets correspond to the maxima. The fact that a consistent shedding frequency is not identifiable for the monitored points shows that the IOR region is highly unsteady and intermittent. Frequency plots for various tabulated readings in Table 4.12 are shown in Figure 4.49.

	Shedding frequency					
	Re_h = 3584			*Re_h=40000*		
d/h	*2.53*	*2.0*	*1.73*	*2.53*	*2.0*	*1.73*
Lift	1.171	1.220	1.250	1.346	1.541	1.606
Pt1	0.98-1.52	1.31-2.01	1.05-2.04	0.98-1.52	1.2-3.2	1.34-2.87
Pt2	1.57-2.58	1.42-2.27	1-1.54	0.75-1.62	1.82	2.06-3.25
Pt3	(1.175)	(1.43)	(2.05)	(1.75)	(2.51)	(2.78)
	1.0 - 3.74	0.18-4.83	1.08-2.4	0.8-1.75	0.38-5.4	1.83-8
Pt4	(2.58)				(4.7)	
	1.7 - 7.47	1.85-4.1	2.33	4.87-6.48	3.36-8.8	2.67

Table 4.12: List of dominate frequencies found based on the lift variation and time history of PT_{mc1} in the wake of the cube, for a cube in a matrix configuration for all cases considered.

Similarly, Table 4.13 lists the determined shedding frequencies around a single cube using both the lift force variation and point-wise velocity variation. The point-wise shedding frequency is again determined at four locations along the height of the cube. The positions are consistent with those used for the multiple cube case, which are *z/h=0.25*, *z/h=0.5*, *z/h=0.75* and *z/h=0.95*. The streamwise position about which the data is monitored is PT_{sc1} (*5.56x/h*) at distance of *0.1h* in from the cubes edge. The data for *d/h=2.0* (*Re_h=3584*) is omitted in Table 4.13 due to the dataset not conforming to that of the group. Unlike the multiple cube case, distinct frequencies are found across the major portion of the depth, with multiple/small banded frequencies noted near the top edge of the cube. Frequencies based on the lift variation indicate that for reducing the depth the shedding frequency initially increases before stabilising, with the effect of increasing Re being an overall shedding rate. From the comparison of the point-wise shedding frequencies along the height of the cube it can be concluded that the shedding frequency is altered in both the near wall and near upper separation region due to

increased three-dimensional effects. However, along the mid region the shedding rate remains constant. Effects of increased Re on the point-wise frequencies is to exhibit an increase in the shedding rate. While the effects of SBD show an increase for positions Pt_2 and above, while Pt_1 exhibits a reduction for reducing depth.

	Shedding frequency					
	Re_h = 3584			*Re_h=40000*		
d/h	*2.53*	*2.0*	*1.73*	*2.53*	*2.0*	*1.73*
Lift	0.109	0.117	0.115	0.121	0.127	0.126
Pt1	0.09	-	0.036	0.09	0.09	0.04
Pt2	0.112	-	0.114	0.124	0.125	0.132
Pt3	0.11	-	0.118	0.124	0.124	0.134
Pt4	0.047-0.124	-	0.118	0.024-0.124	0.024-0.124	0.138

Table 4.13: List of dominate frequencies found based on the lift variation and time history of PT_{sc1} in the wake of the cube, for single cube.

Comparison of both cases studied in this section show that the shedding rate between the two cases is quite different. The point-wise frequency shedding rates show that the multiple cube case experiences strong variation and increased intermittency within the wake, showing that the wake is more broken/complex than that around a single cube. Whilst the shedding frequencies based on the lift have shown that the multiple cube cases experience a continual increase in shedding frequency for reducing SBD, while for a single cube a stabilisation in the shedding rate was observed for reducing SBD. However, as neither case is non-dimensionalised, no direct conclusion can be drawn on the average shedding rates.

4.7 Effects of submergence on energy distribution

Transfer of energy in physical flows can occur through various ways, such as through heat, sound and for fluids through the interaction of vortical structures. As the Navier-stokes equations (NSE) describe the motion of a fluid, they can also be used to describe and show how the kinetic energy in the flow is produced, maintained, redistributed and dissipated. For fluids that are governed by the NS equations the process by which

energy is redistributed can be determined through the manipulation of the NSE themselves. This is simply done by multiplying the NSE by u_i yielding:

$$u_i \frac{\partial u_i}{\partial t} + u_i u_j \frac{\partial u_i}{\partial x_j} = -\frac{u_i}{\rho}\frac{\partial p_i}{\partial x_i} + \upsilon u_i \frac{\partial^2 u_i}{\partial x_j{}^2} \tag{4.6}$$

Using Reynolds decomposition, equation 4.6 can be rewritten as follows:

$$\begin{aligned}&(\overline{u}_i + u_i')\frac{\partial(\overline{u}_i + u_i')}{\partial t} + (\overline{u}_i + u_i')(\overline{u}_j + u_j')\frac{\partial(\overline{u}_i + u_i')}{\partial x_j} = \\ &-\frac{(\overline{u}_i + u_i')}{\rho}\frac{\partial(\overline{p} + p')}{\partial x_i} + \upsilon(\overline{u}_i + u_i')\frac{\partial^2(\overline{u}_i + u_i')}{\partial x_j{}^2}\end{aligned} \tag{4.7}$$

Equation 4.7 gives the expansion of the convective term

$$\begin{aligned}&(\overline{u}_i + u_i')(\overline{u}_j + u_j')\frac{\partial(\overline{u}_i + u_i')}{\partial x_j} = \\ &\overline{u}_j \frac{\partial \overline{u}_i{}^2}{2\partial x_j} + \overline{u}_i\overline{u}_j \frac{\partial u_i'}{\partial x_j} + u_i'\overline{u}_j \frac{\partial \overline{u}_i{}^2}{2\partial x_j} + \overline{u}_j \frac{\partial u_i'^2}{2\partial x_j} + \overline{u}_i u_j' \frac{\partial \overline{u}_i}{\partial x_j} + \overline{u}_i u_j' \frac{\partial u_i'}{\partial x_j} + u_i' u_j' \frac{\partial \overline{u}_i}{\partial x_j} + \frac{\partial u_i' u_i' u_j'}{2\partial x_j}\end{aligned} \tag{4.8}$$

Finally, subtracting the mean turbulent energy terms and time averaging such that the fluctuation u_i' tends to 0, yields equation 4.9, where <·> implies the time averaged value.

$$\frac{Du_i'u_i'}{Dt} = -\langle u_i'u_j'\rangle\frac{\partial\langle\overline{u}_i\rangle}{\partial x_j} - \frac{\partial\langle u_j'u_i'u_i'\rangle_i}{2\partial x_j} - u_i'\frac{\partial\langle p'\rangle}{\partial x_i} + (\upsilon + \upsilon_s)u_i'\frac{\partial^2\langle u_i'\rangle}{\partial x_j{}^2} \tag{4.9}$$

Substituting 4.10- 4.12 in 4.9 gives the final form of the turbulent energy budget used to examine the contributions that the various terms play on the point-wise energy transfer (equation 4.13). The relevance of terms on the right hand side of equation 4.13 and their abbreviated forms are also shown.

$$k_{ii} = \frac{\langle u_i'u_i'\rangle}{2} \tag{4.10}$$

$$(\upsilon+\upsilon_s)u_i'\frac{\partial^2 u_i'}{\partial x_j^{\,2}}=\frac{\upsilon+\upsilon_s}{2}\frac{\partial^2 k_{ii}}{\partial x_j^{\,2}}-(\upsilon+\upsilon_s)\frac{\partial\langle u_i'\rangle}{\partial x_j}\frac{\partial\langle u_i'\rangle}{\partial x_j} \tag{4.11}$$

$$u_i'\frac{\partial\langle p'\rangle}{\partial x_i}=\frac{\partial\langle u_i'p'\rangle}{\partial x_i}-\langle p'\rangle\frac{\partial\langle u_i'\rangle}{\partial x_i} \tag{4.12}$$

$$\frac{Dk_{ii}}{Dt}=\underbrace{-\langle u_i'u_j'\rangle\frac{\partial\langle\overline{u}_i\rangle}{\partial x_j}}_{\substack{\text{Turbulent}\\\text{production}\\\text{<GPR>}}}\underbrace{-\frac{\partial\langle u_j'k_{ii}\rangle_i}{2\partial x_j}}_{\substack{\text{Turbulent}\\\text{diffusion}\\\text{<TDR>}}}\underbrace{-\frac{\partial\langle u_i'p'\rangle}{\partial x_i}}_{\substack{\text{Pressure}\\\text{diffusion}\\\text{<PDF>}}}\underbrace{+\langle p'\rangle\frac{\partial\langle u_i'\rangle}{\partial x_i}}_{\substack{\text{Pressure}\\\text{strain}\\\text{<PST>}}}\underbrace{+\frac{\upsilon+\upsilon_s}{2}\frac{\partial^2 k_{ii}}{\partial x_j^{\,2}}}_{\substack{\text{Viscous}\\\text{diffusion}\\\text{<VDF>}}}\underbrace{-(\upsilon+\upsilon_s)\frac{\partial\langle u_i'\rangle}{\partial x_j}\frac{\partial\langle u_i'\rangle}{\partial x_j}}_{\substack{\text{Dissipation}\\\text{<}\varepsilon\text{>}}} \tag{4.13}$$

The left hand side of equation 4.13 represents the total change in turbulent kinetic energy, and is accounted for in its partial form equation 4.14. The terms on the right hand side are the time variation (unsteadiness) of TKE [<*DKT*>] and the convection of TKE [<*CV*>].

$$\frac{Dk_{ii}}{Dt}=\frac{\partial k_{ii}}{\partial t}+\langle\overline{u}_j\rangle\frac{\partial k_{ii}}{\partial x_j} \tag{4.14}$$

Figure 4.50 shows the time averaged terms of the turbulent kinetic energy budget (TKEB) and their contributions to the associated processes of creating, enhancing, redistributing and dissipating TKE, along the centred XZ plane. Results are extracted across the total depth for 0.7*x/h*, 1.3*x/h*, 2.7*x/h* and 3.3*x/h* positions in the streamwise direction for the multiple cube cases. Due to the large amount of data, the contributions of each term in equations 4.13 and 4.14 are plotted individually. Note that the scaling of components in Figure 4.50 are not the same and that the appropriate scaling is indicated on all the variable plots. This is done to better interpret the effects that each term has on the TKEB.

From Figure 4.50 it can be observed that the greatest variation and change occurs along and above the cube and concentrates along the separated shear layer. <DKT> shows that on average the flow is enhanced along the shear layer and over the upper surface of the cube. <GPR> is most active over the cube and along the separated shear layer. While in the IOR, <GPR> is substantially reduced with the highest production concentrated near the intercellular region. Negative <GPR> is detected in the near-wall region for the forward flowing cell (horseshoe cell). <CV> and <TDR> are noted to show a similar

trend of enhancement of TKE along the upper portion of the shear layer (SHRL) region above the cube and IOR, while showing a strong redistribution of TKE in the separation region above the cube. Furthermore, <TDR> exhibits an increased region of redistribution of TKE ahead and behind the cube (upper edge), whilst across the mid-portion of the IOR experience an increase in the enhancement and redistribution of TKE along the SHRL. The <PST> term in general is found to contribute to the redistribution of TKE in the near-wall region and around the separated SHRL. <PDF> tends to show an opposite behaviour in the near-wall regions, while along the separated SHRL <PDF> also aids in the redistribution of TKE. Both <PST> and <PDF> exhibit strong variations within the IOR obscuring direct analysis of what effect both terms have on the TKE in this region. However, it can be concluded that both <PST> and <PDF> are strongly influenced by the intermittency of the flow in the IOR. In terms of the viscous effects on the TKE distribution, both <VDF> and <ε> show the strongest influence in the near-wall region. Loss of TKE is seen to occur in regions of high shear including the separated SHRL. Comparison of <GPR> and <ε> show that production is higher above the cube and along the separated SHRL. For all the terms that contributed to the TKEB, <VDF> is found to have the smallest influence across the mid XZ plane.

Figure 4.51 shows the TKEB about the XY plane for a *z/h=0.4*, it can be seen that the strongest variation in the TKEB terms occur around the lateral faces of the cube and along the shear layer defining the rear recirculation cell. Whilst across the wake the effect of the TKEB terms all show a relatively smaller influence. <GPR> shows an increase in production of TKE at the lateral faces of the cube and along the edges of the IOR. The effects of depth variation on the <GPR> show that the maxima in <GPR> across the height of the cube is achieved at mid-height, while <GPR> is also noted to increase within the IOR with increasing height, expect in the near wake (recirculation region) where <GPR> remains constant. Again, <TDR> and <CV> show similar trends around the lateral faces of the cube as noted about the XZ plane. In the near region of the IOR (recirculation cell), <CV> exhibits a strong gradient across the shear layer in enhancing and in the redistribution of TKE, while the effects of <CV> on TKE are less obscure in the forward flow cell due to increased spanwise influence. A similar behaviour is also noticed for <TDR> near the cellular interface region (*2.7x/h*), whilst ahead of the cube and along a major portion of the IOR edge <TDR> is found to aid in the redistribution of TKE. The effect of both <TDR> and <CV> along the cube height are that both to exhibit their maximum variation around the lateral faces at mid-height

of the cube, while in the wake both terms exhibit an increase in the redistribution of TKE. <CV> shows the larger influence across most of the IOR, while <TDR> shows the largest influence on redistribution ahead of the cube. <PDF> is found to aid in the redistribution of TKE along the edges of the IOR region ahead of the cube and near the intercellular region, as well as around the lateral faces. The influence of <PDF> in or across either cell is less pronounced. Variation along the cubes height shows that <PDF> enhances the TKE in the IOR near-wall region ahead of the cube, while <PDF> is found reducing with increasing height. Near the upper edge <PDF> is found to aid in the redistribution of TKE. Other notable effects of variation along the cube height include the reduced influence on the redistribution of TKE along the lateral faces and increased unsteadiness in the near wake. Similarly, <PST> shows its strongest contribution along the lateral faces, showing that it contributes to enhancing TKE in the near-wall region and near the SHRL, while redistributing TKE in the lateral separation region. The <PST> is noted to further contribute to the enhancement of TKE in the near-wall region with increasing height along the cube, while other mentioned effects along the lateral faces reduce. <PST> is found to be strongly influenced by the flow variation in the IOR for all cube heights examined. <VDF> contributions to the TKEB are again found to be small, while <ε> shows to peak in regions of high shear. The effect of <ε> along the cubes height is to increase the dissipation of TKE along the lateral faces of the cube and in the near wake region. A comparison of <GPR> and <ε> shows that production is higher around the cube and IOR edges.

The effects of varying Re are noticeable around the cubic body, while along the separated SHRL and near wake region the effects of Re are less pronounced. The effects of Re are noticeable on the <ε> and <VDF>, showing a reduction for increasing Re. An expected behaviour due to the reduced influence of molecular viscosity with increased Re. The effects of varied submergence show that with reducing depth the TKEB is reduced, while the influence of the free-surface and TKEB terms close the surface boundary exhibit notable changes. The effects of depth variation can be observed on <GPR>, <VDF>, <PDF>, <CV> and <DKT>.

Figure 4.52 shows the TKEB about the XZ centre plane for a single cube placed in a uniform flow. The strongest variations (unsteadiness) in TKE concentrate along the upper shear layer formed by the separation of flow over the cube and the encapsulated wake region. <DKT> shows that on average TKE is enhanced along the shear layer,

while downstream of reattachment diffusion/dissipation of TKE shows an increased influence. <GPR> shows an increase in production along the SHRL and near the reattachment region. <TDR> shows a strong change from enhancing to redistributing TKE across the SHRL in the near wake region that reducing further downstream. The influence of <TDR> also increases near the reattachment region of the wake, where <TDR> shows a greater contribution to the redistribution of TKE. The <CV> is found to contribute to the redistribution of TKE along the SHRL and near the rear face of the cube, while in the lower wake region <CV> aids in enhancing the TKE. The effect of enhancement of TKE due to <CV> is observed aft of the reattachment region. <PDF> is found to aid in the redistribution of TKE along the SHRL, while in the wake it is too unsteady to draw any definitive effects. A similar behaviour in the wake region is also observed for <PST>, along the separated SHRL the <PST> aids in the enhancement of TKE. <VDF> shows its strongest influence on the rear wall and near wall region, where <VDF> contributes to increasing the local TKE. Similarly, <ε> shows increased levels of dissipation in regions of high shearing, these again include the separated SHRL, near-wall region and the rear face region. <ε> is noted to increase aft of the reattachment point.

Figure 4.53 shows the variation in the TKEB about the XY plane at *z/h=0.4*, the strongest variation in TKEB terms occurs along the wake SHRL. The behaviour of the terms contributing to the TKEB are found to show the same behaviour along the XY plane at *z/h=0.4*, as was found for along the XZ centre plane. The general effect of variation in position along the cubes height on the terms that contribute to the TKEB, is to exhibit a change in behaviour or reduction in strength/contribution. Furthermore, unsteadiness in the wake is noted for <TDR>, <PDF> and <PST> which reduces along the cubes height and aft of flow reattachment. A comparison of <GPR> and <ε> shows that production is higher around the cube, along the wake SHRL layer and near reattachment region, while <ε> shows a stronger influence near the rear face.

The effects of varying Re and SBD on the TKEB are notable around the cube, with the effects of SBD are more apparent in the XZ plane than in the XY plane. Increase in Re results in the increase in the level of TKE variation along the separated SHRL, wake region and near wall regions, while the reduction in molecular viscosity result in lower <ε> found in the surrounding reattachment region and upper SHRL. The effects of reducing SBD results in the SHRL being recorded lower, while the level of variation in

the TKEB terms is seen to increase across the SHRL. Effects of redistribution of TKE in the near surface region are noted to increase with a decreasing SBD. Interaction of the wake with the free-surface is notable at the lowest SBD considered, which in turn shows the strongest influence on the TKEB terms near the free-surface boundary.

From analysing both cases the greatest variation in the TKEB occurs in regions that experience the greatest shear stress. In both cases the regions of greatest variation (shear stress) are found to be the near-wall, wake and separated along the SHRL, whilst else where the contributions/variations are comparably small. Reduction in molecular viscosity with increasing Re shows that the dissipation in the wake region and along the natural SHRL in both cases is reduced, while in the near-wall region dissipation is enhanced. The effects of SBD on TKEB shows an increased influence for reducing SBD, in addition to an increased influence near the free-surface boundary region which is noted in both cases. The type of influence that reduction in SBD has on the single and multiple cube cases is different. For the multiple cube case reduction in SBD results in a drop in the level of velocity variations i.e. the level of velocity fluctuations is reduced, resulting in the TKEB terms becoming smaller. Whilst for the single cube case the lateral SHRL over the cube and TKEB terms along the SHRL show the most notable variation for a decreasing SBD.

4.8 Free-Surface Signatures

Magnifications of the free-surface viewed about the XY plane are plotted in Figure 4.54 and Figure 4.55, for $Re_h=3560$ and $Re_h=40000$ for all considered SBDs. The images are consistent with the earlier VS presented in section 4.5.3.2 and displayed in the same manner. Analysis of the surface structures is performed solely in a qualitative manner. Figure 4.54 shows that the free-surface is constantly changing due to the variation in flow behaviour regardless of SBD, with the presence and influence of VS increasing with reducing SBD. For $d/h=2.533$ ($Fr=0.3$) the dominant surface signature is seen to be upwellings on the free-surface created due to vortices attaching normal to the free-surface, however the presence of vortices parallel to the free-surface is also noticeable. Reducing the depth (increasing Fr) results in the level of distortions occurring on the free-surface to increase; this is due to the presence of stronger surface parallel vorticity. The distortions are varied and directionally independent due to the highly unstable and three-dimensional flow generated around the matrix of cubes. A similar trend is

observable in Figure 4.55 for $Re_h=40000$, namely, that as the depth is reduced the level of surface distortion arising from surface parallel vortices is increased. However, at the larger SBDs (lower Fr) the effect of increased Re appears to exhibit a reduction in the level of surface distortions due to VS, whereas, at the lowest SBD an increase in VS influence on the free-surface is clearly noted. Furthermore, for $d/h=1.7$ ($Fr=0.37$) the free-surface distortions are more confined over the cubic body for $Re_h=40000$ in comparison to the lower Re case. The reduction in free-surface deformation at larger depths is the result of a reduced level of direct interaction occurring over the plotted images (Figure 4.41). However, it was also noted earlier that the total level of vortical structures are increased, for increased Re. Hence the reduced imprints of vortical structures can be due to the overall increase in surface turbulence/variation. Unfortunately this can only be hypothesised, as no quantitative analysis has been performed for/on the free-surface.

Similarly, Figure 4.56 and Figure 4.57 show the free-surface magnifications about the XY plane for $Re_h=3560$ and $Re_h=40000$. The images are kept consistent with the earlier extracted VS presented in section 4.5.3.2 and displayed in the manner. All results show the initial surface depression occurring over the cube, with the presence of surface signatures and surface distortions increasing with the reduction in depth. All surface signatures are confined within the wake. Furthermore, no surface waves or wave envelopes are detected showing that for $Fr \leq 0.37$ gravity acts as a strong resorting force. In all cases distortions in the free-surface initially register due to the interaction of the head-portion of VS that tends to be dissipated as the vortex flows downstream. Vortices that interact or distort the free-surface further downstream either connect in this similar manner or align parallel to the free-surface boundary. The notable effect of an increased Re on surface deformation is an increased presence and level of unsteadiness (variation) in the attachment and distribution of vortical structures. In all cases free-surface distortions due to vortical structures persist beyond the outflow boundary.

4.9 Summary

In summary, free-surface flow past a wall mounted cubic body has been examined for two very different configurations at various SBDs and Reynolds numbers. Results have shown that on average for both cases the free-surface registers lower for increased Re,

whilst time averaged wake lengths show the opposite behaviour. When reducing depth the multiple cube case was found to show a slight growth in the length of the rear recirculation cell, whilst for the single cube, the increased free-surface influence resulted in the average wake length to reduce. For both a single cube and a cube in a matrix configuration the well-defining features of the flow are well captured, these include a vortex ahead of the cubic body, an separation region on the upper surface of the cube and wake region. For the multiple cube case, 2D instantaneous results show that the IOR is unsteady and constantly altering with time, with the rear recirculation region having a strong influence on the horse-shoe vortex. Similarly, 3D streamlines show that the lower region is strongly influenced by the spanwise velocity and is dependent on the shedding rate, whilst the upper portion of the flow shows an increased influence from the VS and flow over and around the separated shear-layer region. Constant variation of the flow in the IOR region is found to result in the horse-shoe vortex being distorted, broken and unsteady in its position. For the single cube case, the horseshoe vortex is found to be steady around the body, with the horse-shoe vortex legs downstream of the wake showing an influence resulting from the shedding of structures. The unsteadiness of the flow is confined to the separated flow and wake regions generated about the cube.

The presence of VS and free-surface signatures were also examined for both cases. In both cases vortices were found to be confined around the cubic body and in the wake region, with both showing an increase in the level of interaction with a decreasing SBD. For the multiple cube case it was found that with reducing depth the dominant surface signature was altered, at the largest SBD the dominate surface signature was seen to be upwellings created due to vortices attaching normal to the free-surface. Whilst at the lowest SBD surface parallel vortices were found to become common. For a single cube, reduction in depth was noted to cause a faster rise in VS, with vortices connecting in a surface normal fashion. Structures were found to connect in the form of hockey/horseshoes, while downstream surface parallel vortices were found to become common with reducing SBD. In both cases, at fixed monitoring positions vortices were found to be present for up and over 50% of the total monitored time showing that they are a well established feature of the flow. For the multiple cube case a reduction in persistence noted close to the free-surface boundary which increases for reducing SBD.

For both cases, turbulent intensities, Reynolds stresses and the TKEB were found to be the greatest in regions of high shear. Increasing Re was found to increase the turbulence in the flow, resulting in higher levels being recorded for the turbulent intensities, Reynolds stresses and TKEB. The damping of vertical flow variation and redistribution was found to increase with reducing depth and based on the single cube results is noted to occur only if turbulence or turbulent structures are present near the free-surface boundary.

In terms of the forces generated around the cubic body for both the studied configurations the averaged forces were found to reduce with reducing SBD. While the variation in forces shows an increase. In terms of shedding frequency, the multiple cube was found to show an increase with a reducing depth, while for the single cube a stabilisation in the shedding rate was observed.

4.10 Figures

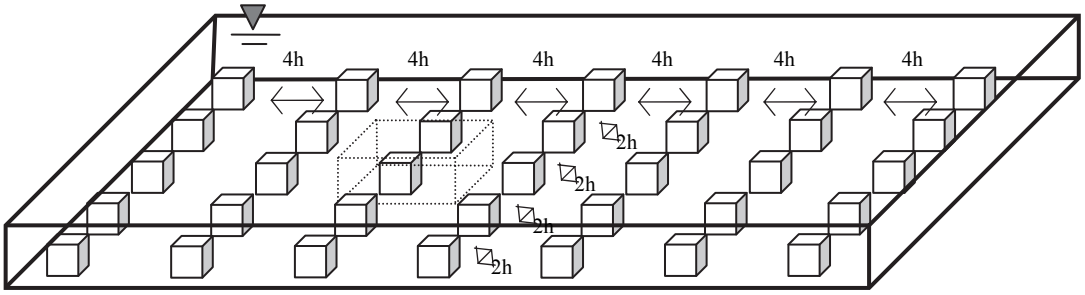

Figure 4.1: Layout of cubes in the matrix formation that is considered in this work and arranged as that considered by Meinders & Hanjalic (1999).

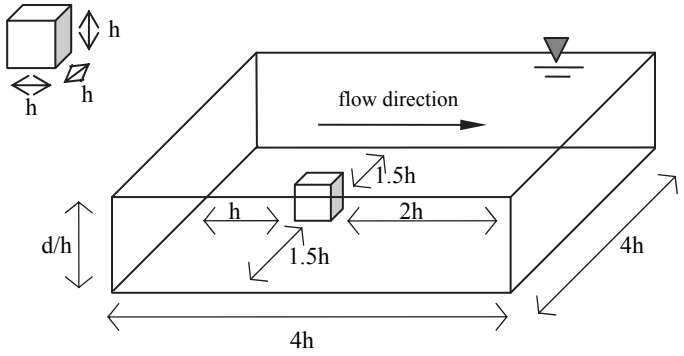

Figure 4.2: Simplified representation of the matrix formation due to the use of periodic boundary conditions in the streamwise and spanwise directions.

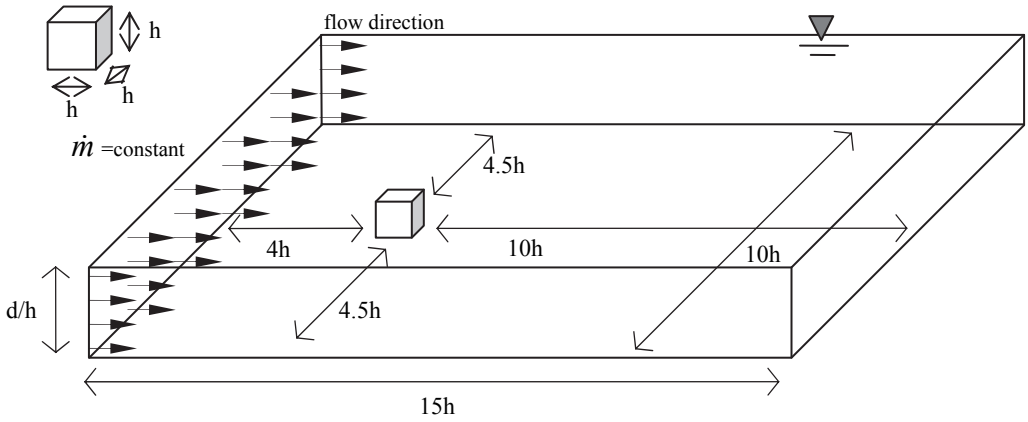

Figure 4.3: Schematic layout for the modelling of a single wall-mounted cube.

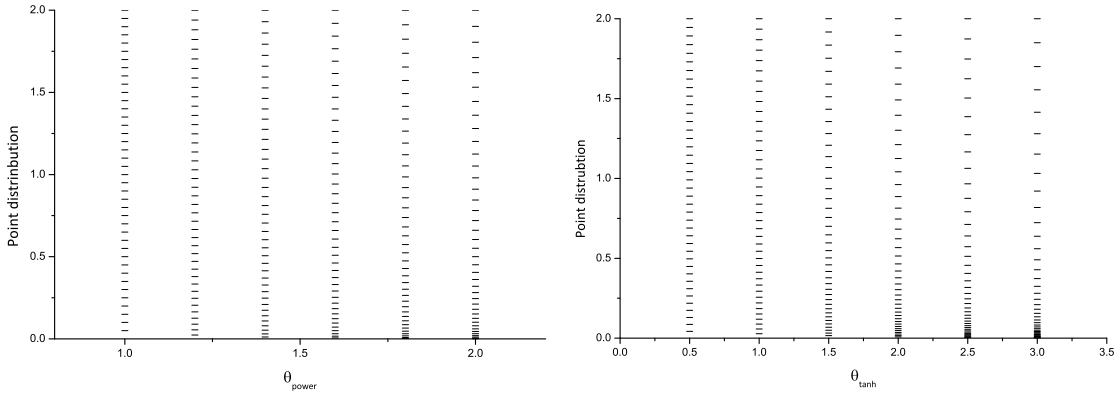

Figure 4.4: Distribution of cells for power (left) and hyperbolic (right) stretching functions for various values.

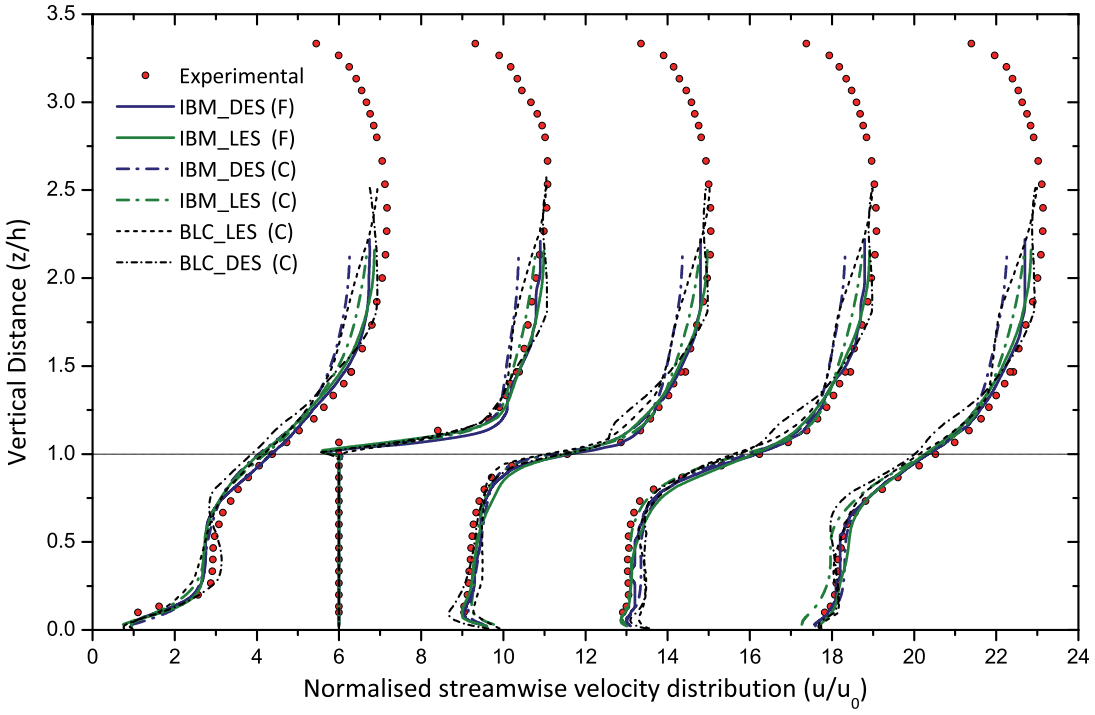

Figure 4.5: Normalised streamwise velocity comparison for LES and DES against experimental measurements of Meinders & Hanjalic (1999), for both fine (F) and coarse (C) simulated using the GC modelling approach (IBM) and block cell modelling (BLC) approach.

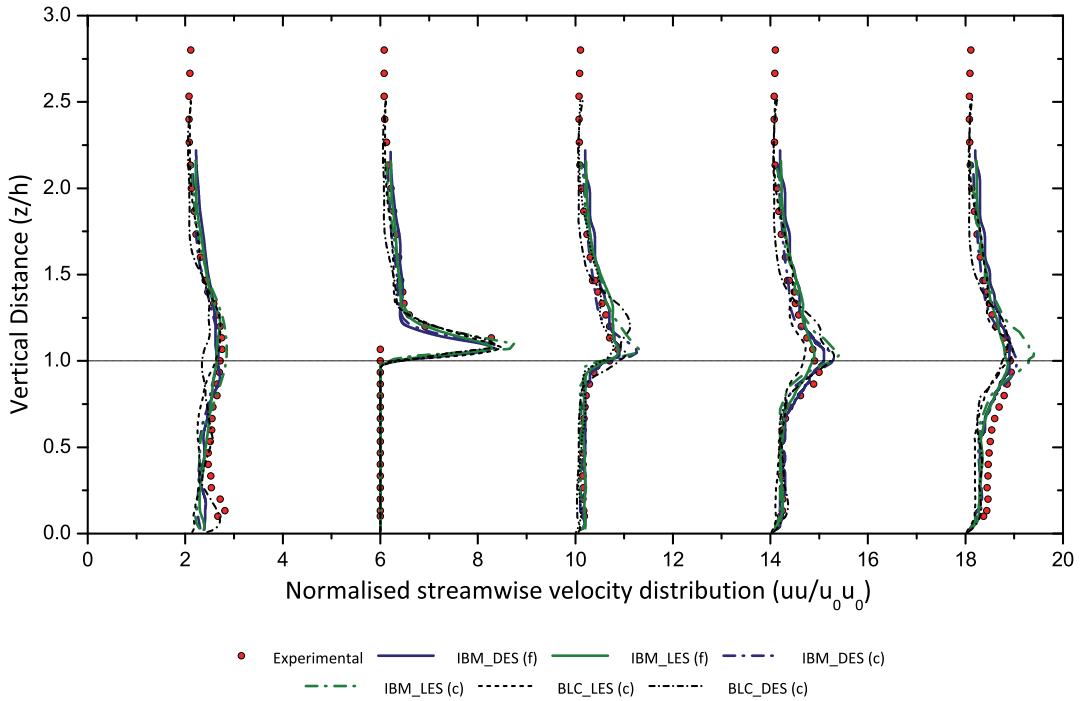

Figure 4.6: Comparison of normalised Reynolds stresses <u'u'>/u_0^2 for LES and DES against experimental measurements of Meinders & Hanjalic (1999), for both fine (F) and coarse (C) simulated using the GC modelling approach (IBM) and block cell modelling (BLC) approach.

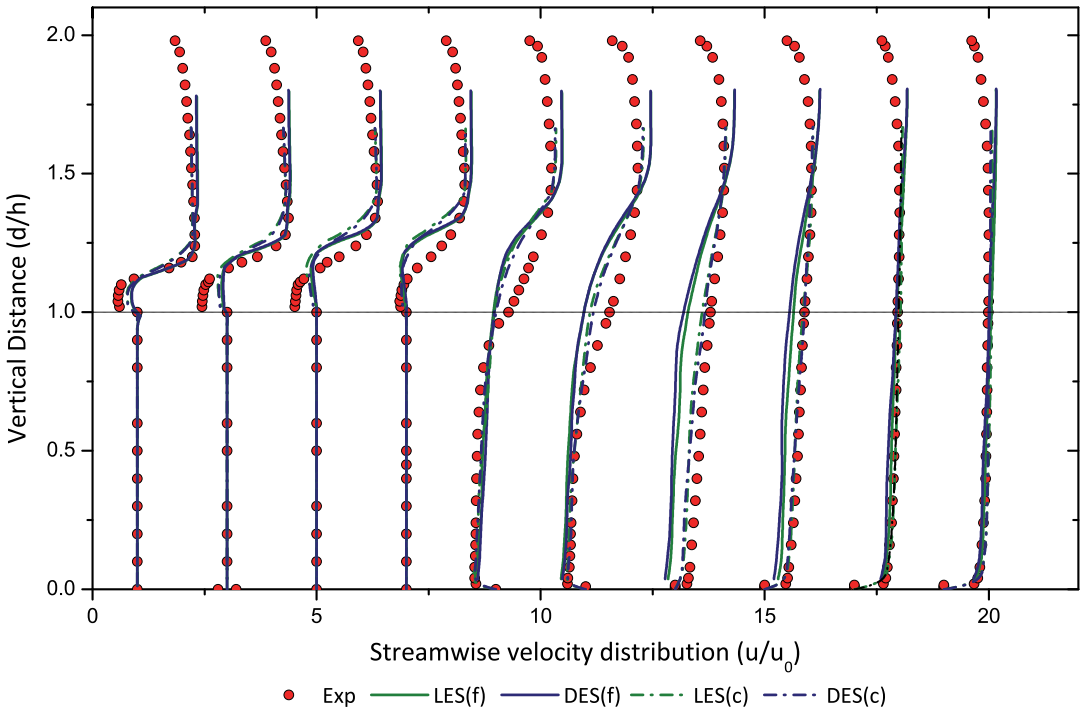

Figure 4.7: Normalised streamwise velocity comparison for LES and DES against experimental measurements of Hussein & Martinuzzi (1996), for both fine (f) and coarse (c) simulated results using the GC modelling approach. Results from coarse block cell modelling are also included.

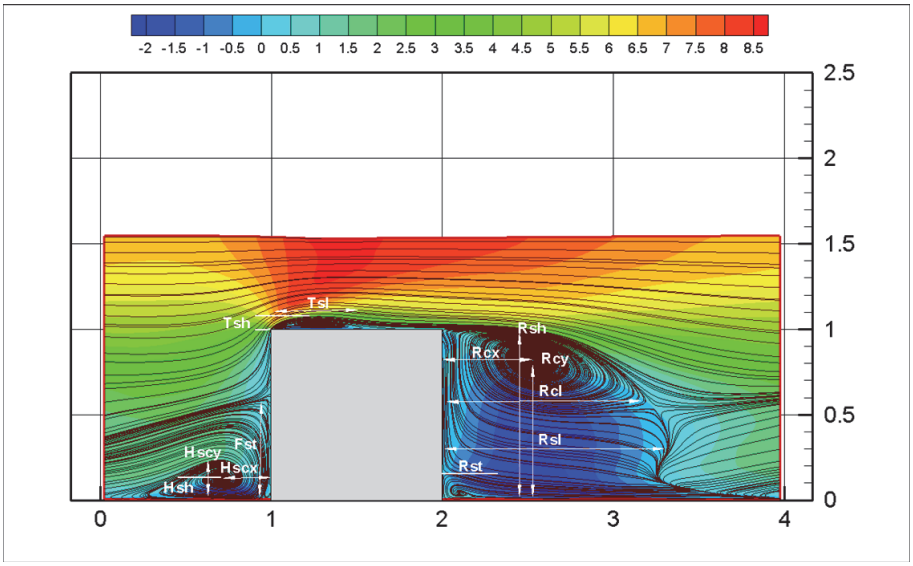

Figure 4.8: Streamline illustration and notations of recorded measurements for the time flow in terms of averaged separation regions and structure positions about the symmetric plane.

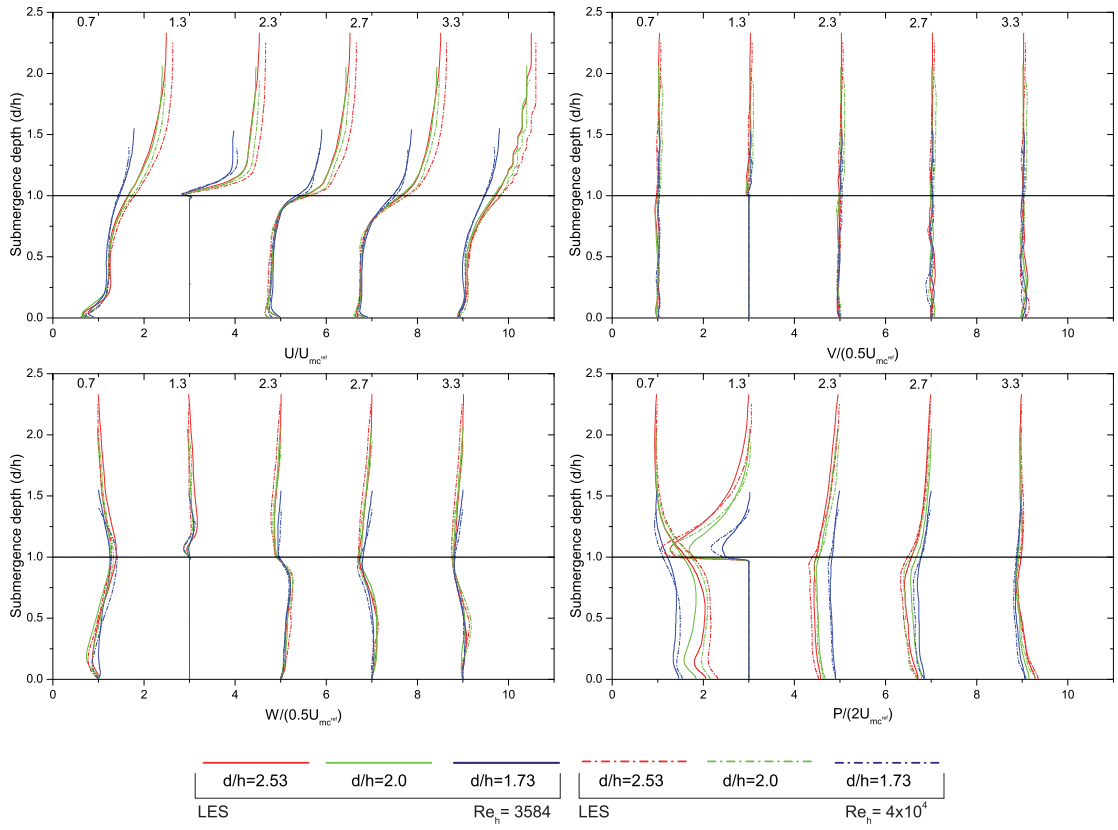

Figure 4.9: Time averaged mean velocity (components) and mean pressure distributions around a cube in a matrix configuration, for all Reynolds number and submergence depths considered.

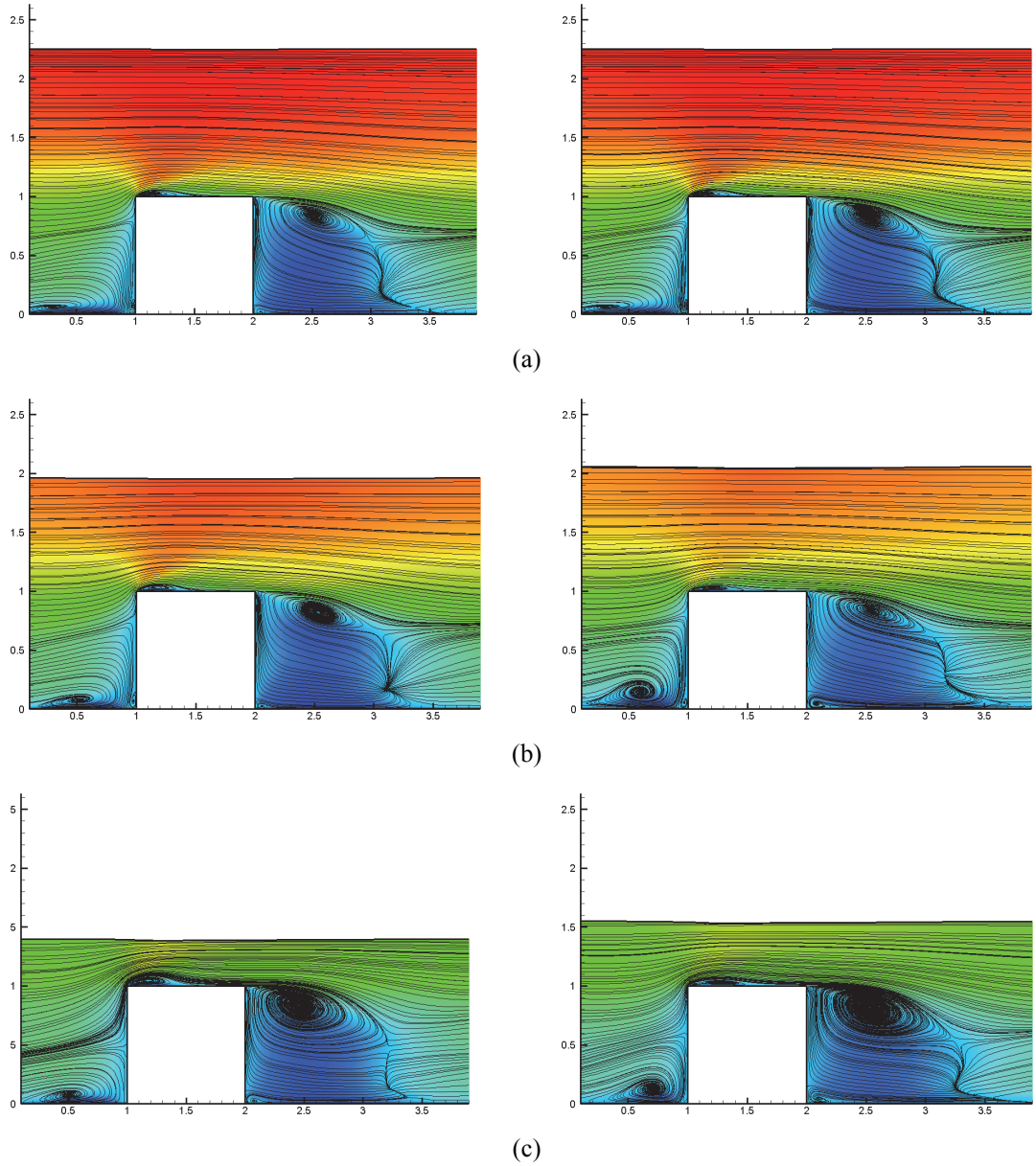

Figure 4.10: Time averaged streamline traces for flow around a cube in a matrix configuration taken about the XZ plane for Re_h=40,000(left) and Re_h=3,584 (right) for (a) d/h=2.53, (b) d/h=2.2, (c) d/h=1.73.

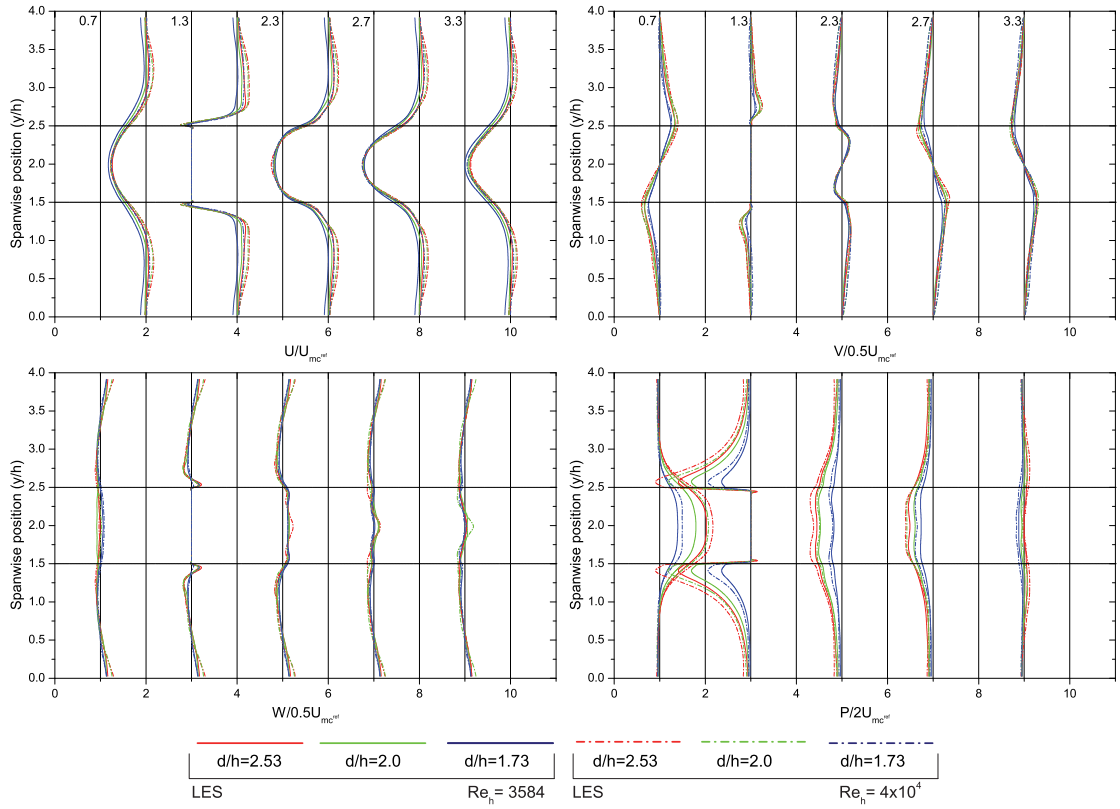

Figure 4.11: Time averaged mean velocity (components) and mean pressure distributions around a cube in a matrix configuration about the XY plane for z/h=0.4.

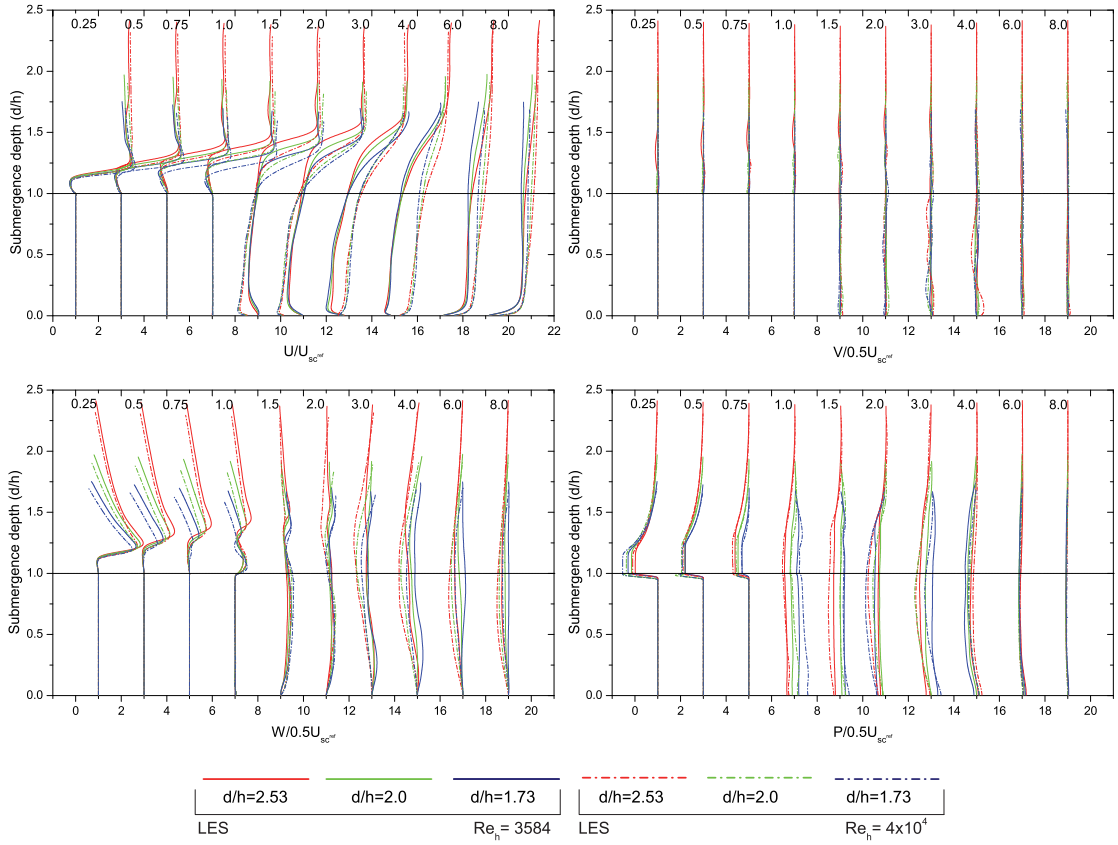

Figure 4.12: Time averaged mean velocity (components) and mean pressure distributions around a single cube, for all Reynolds number and submergence depths considered.

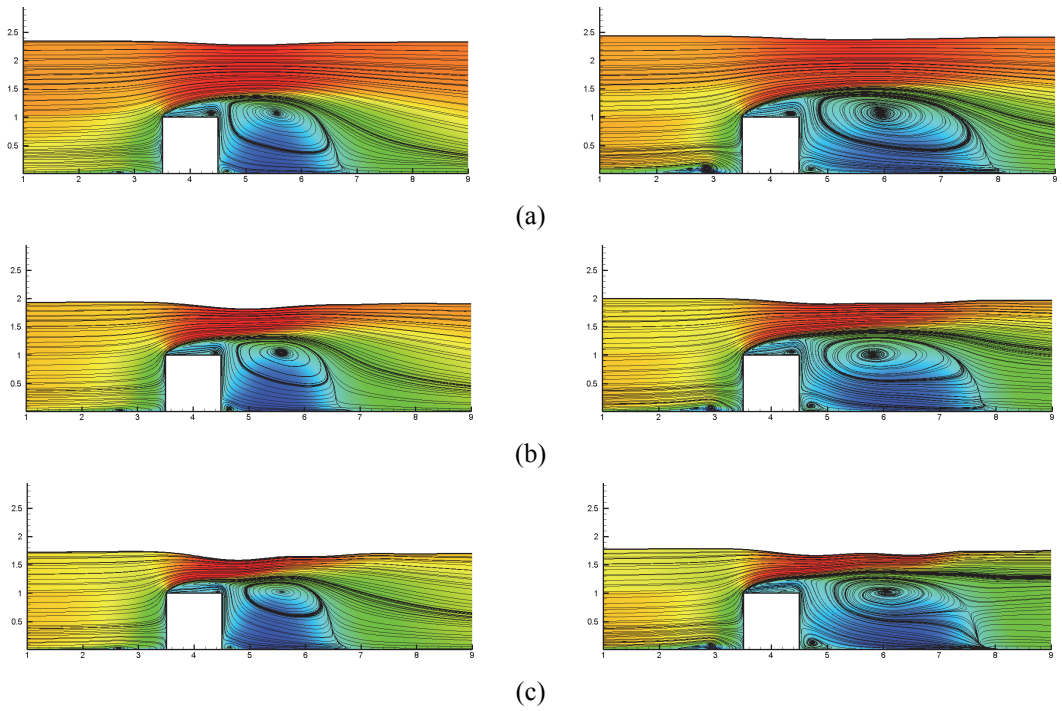

Figure 4.13: Time averaged streamline traces for flow around a single cube taken about the XZ plane for Re_h=40000(left) and Re_h=3584 (right) for (a) d/h=2.53, (b) d/h=2.2, (c) d/h=1.73.

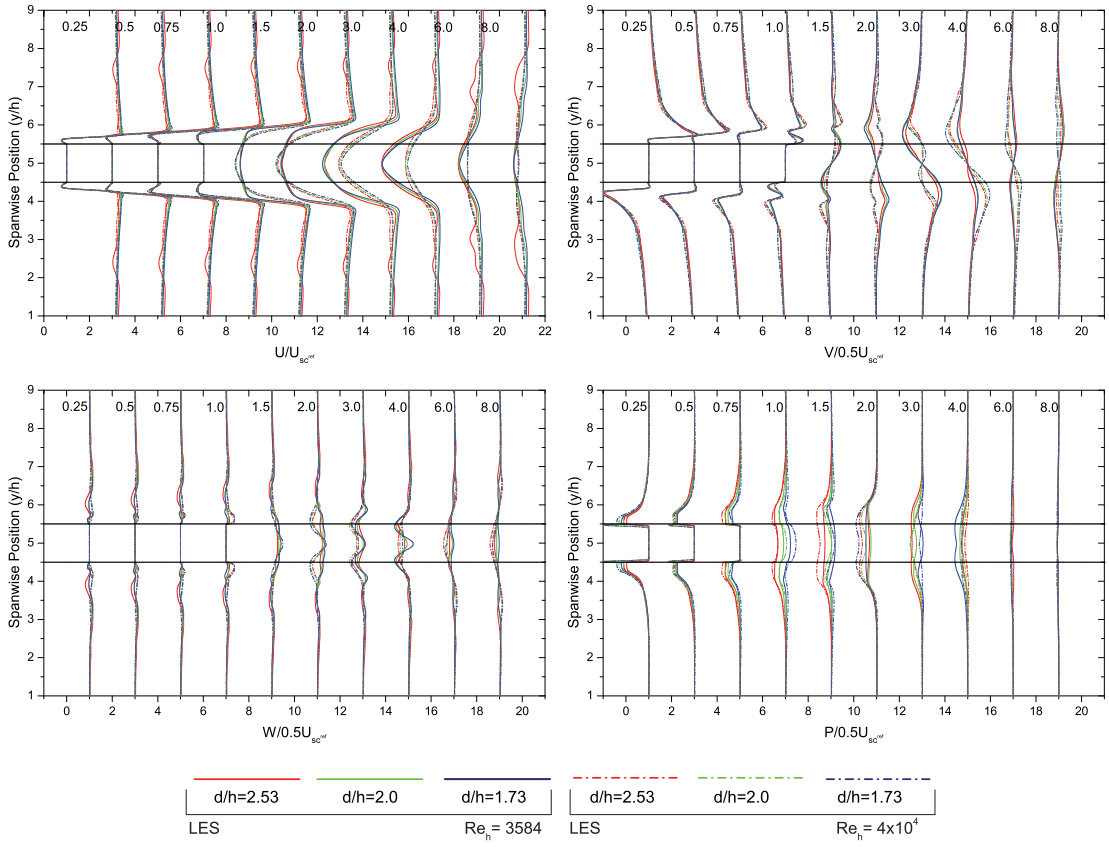

Figure 4.14: Time averaged mean velocity (components) and mean pressure distributions around a single cube about the XY plane for z/h=0.4.

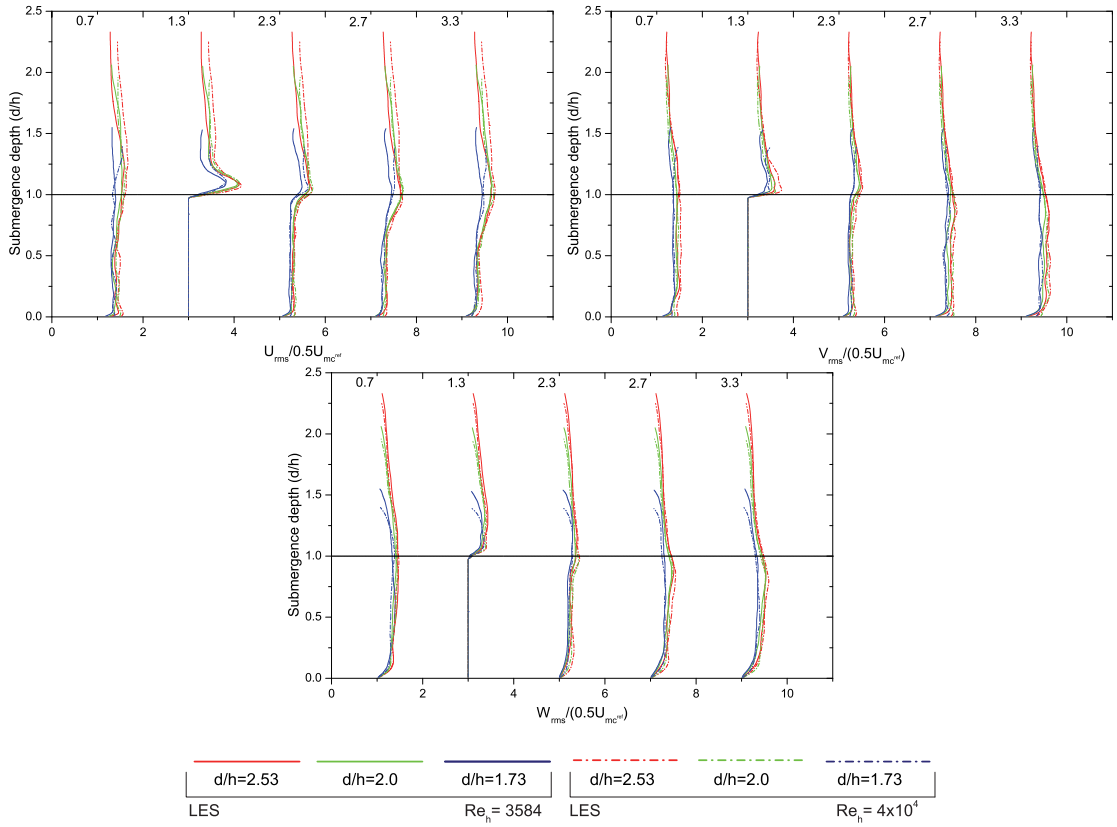

Figure 4.15: Time averaged turbulent intensity distributions around a cube in a matrix configuration.

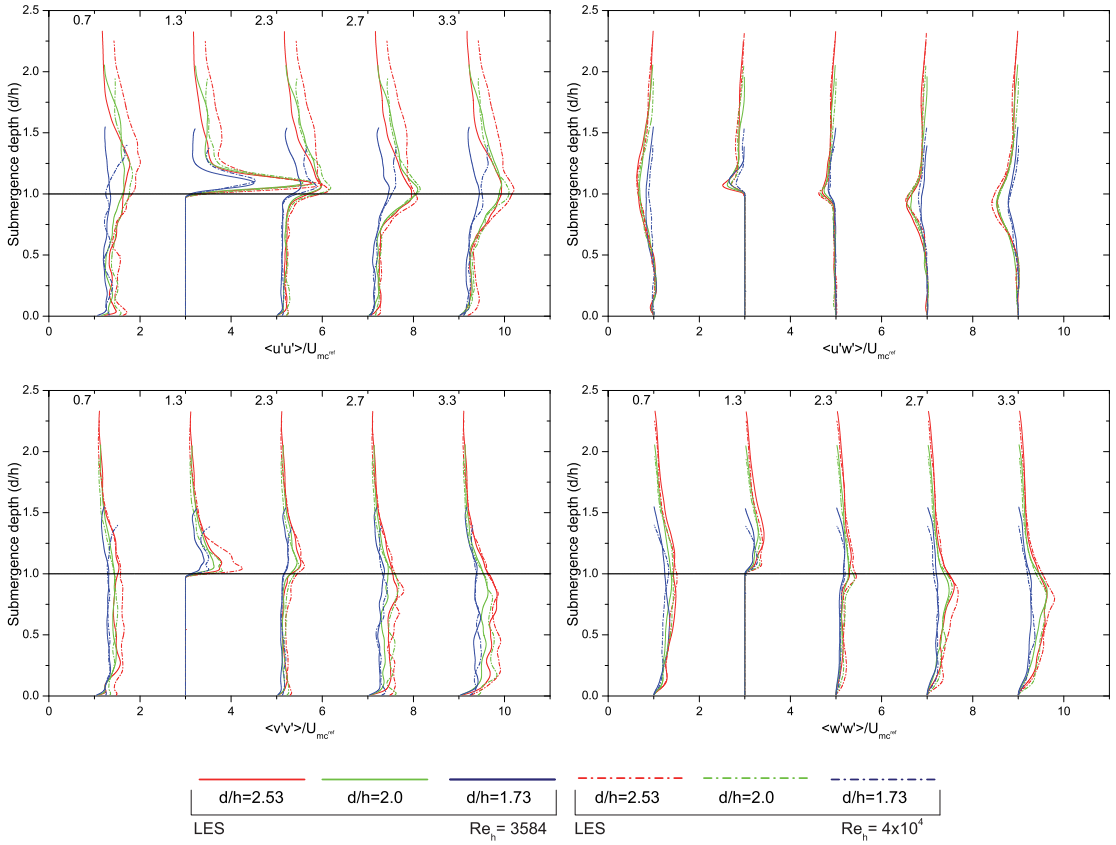

Figure 4.16: Distribution of the time averaged Reynolds stress terms about the symmetric plane, for a cube in a matrix configuration.

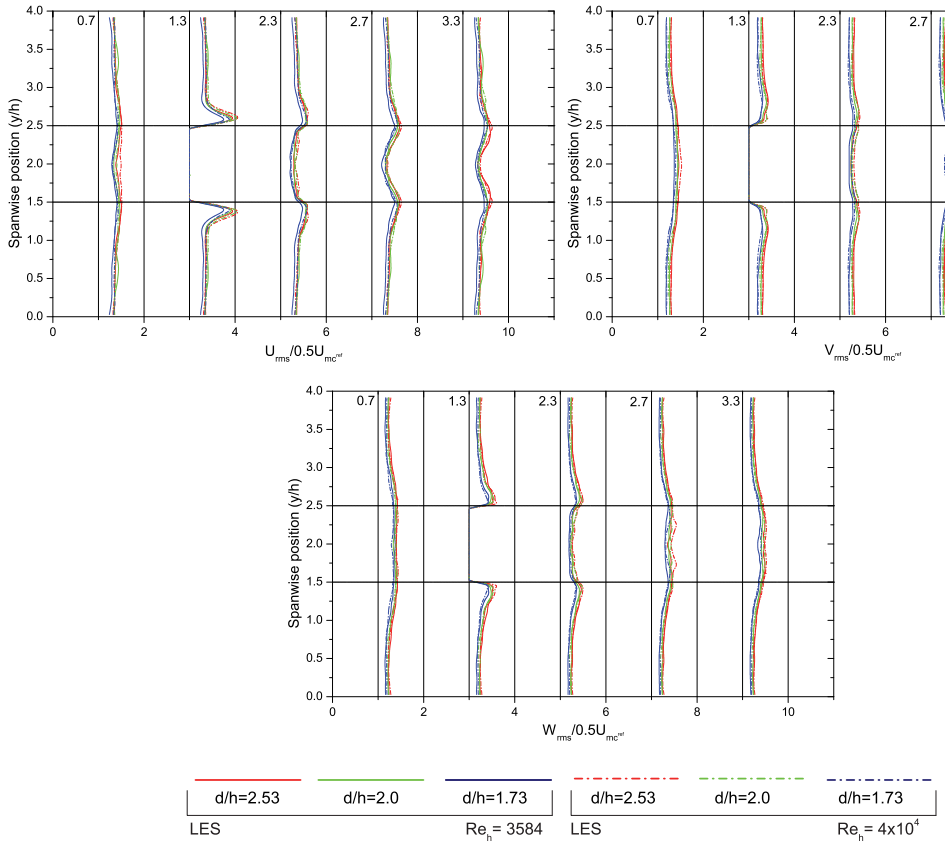

Figure 4.17: Time averaged turbulent intensity distributions around a cube in a matrix configuration at z/h=0.4.

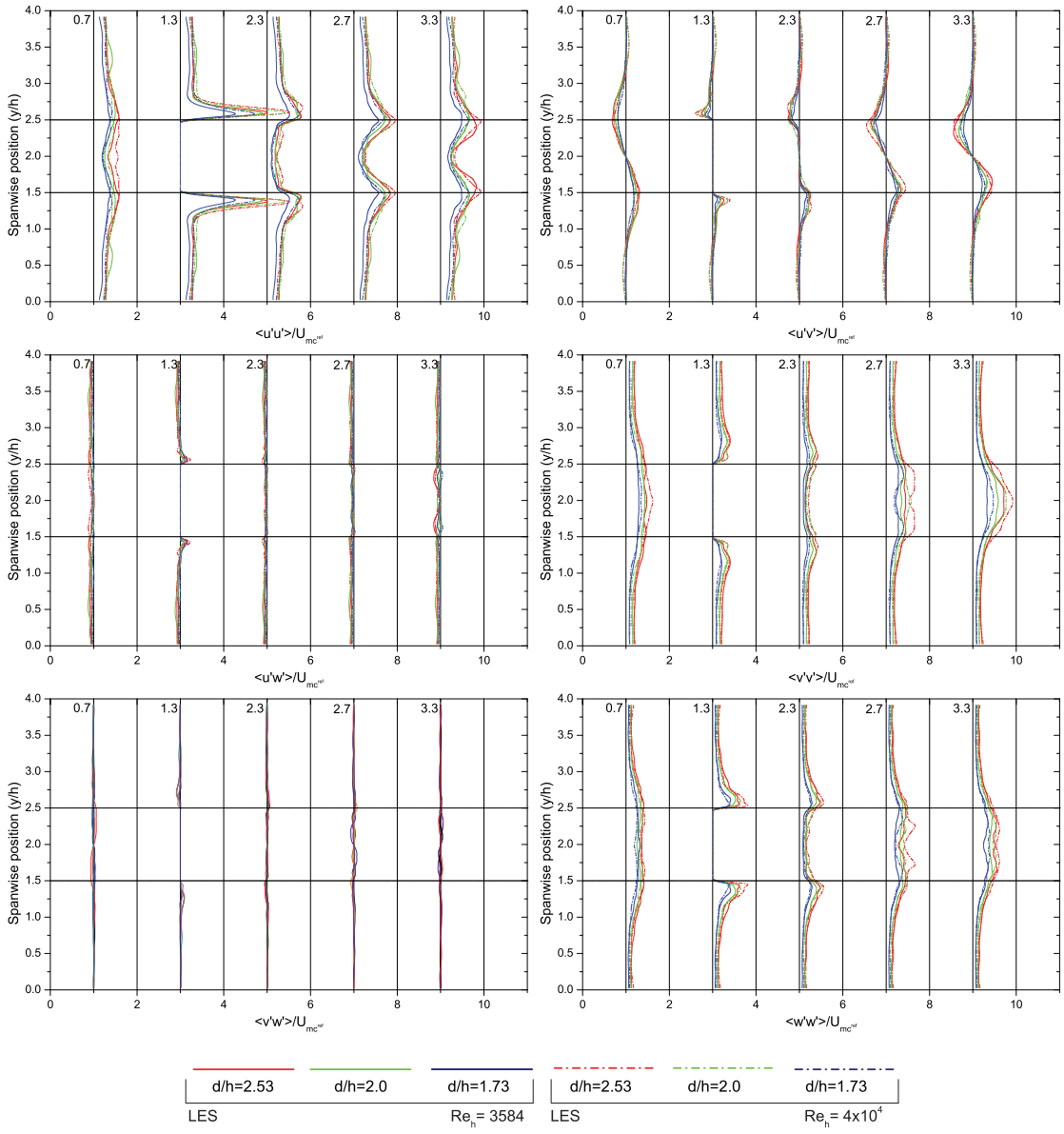

Figure 4.18: Distribution of time averaged Reynolds stresses around a cube in a matrix configuration about the XY plane for z/h=0.4.

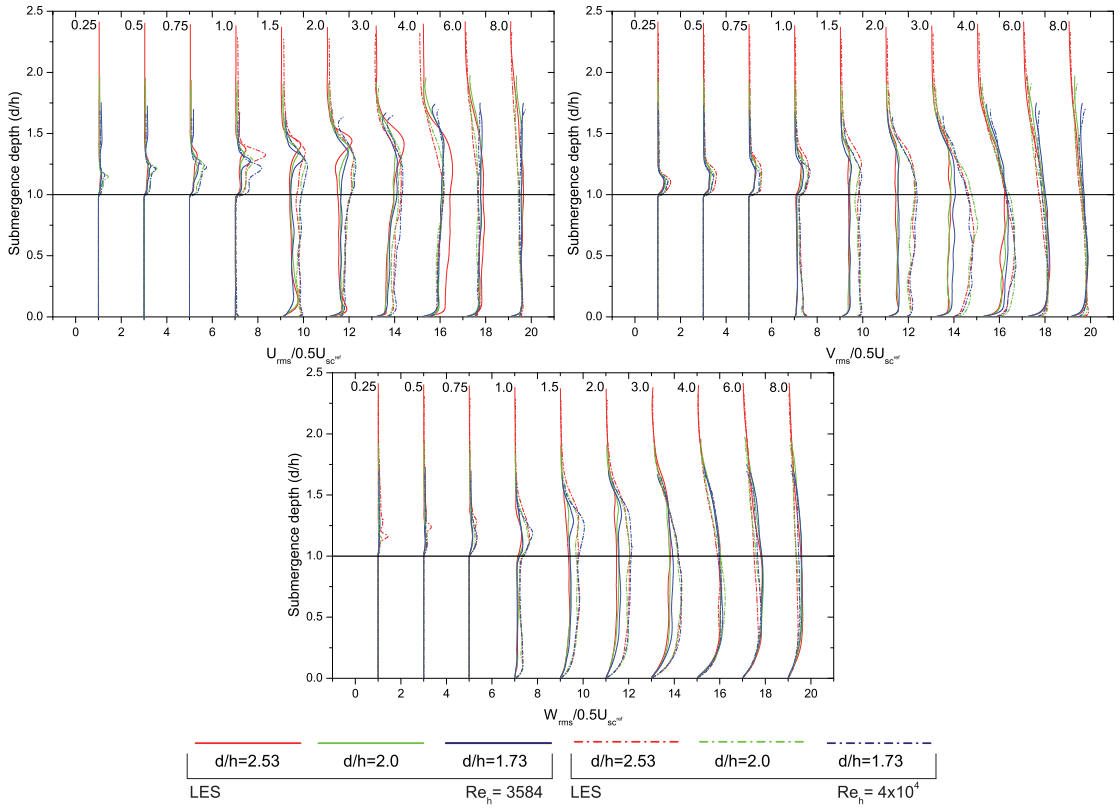

Figure 4.19: Time averaged turbulent intensity distributions around a single cube.

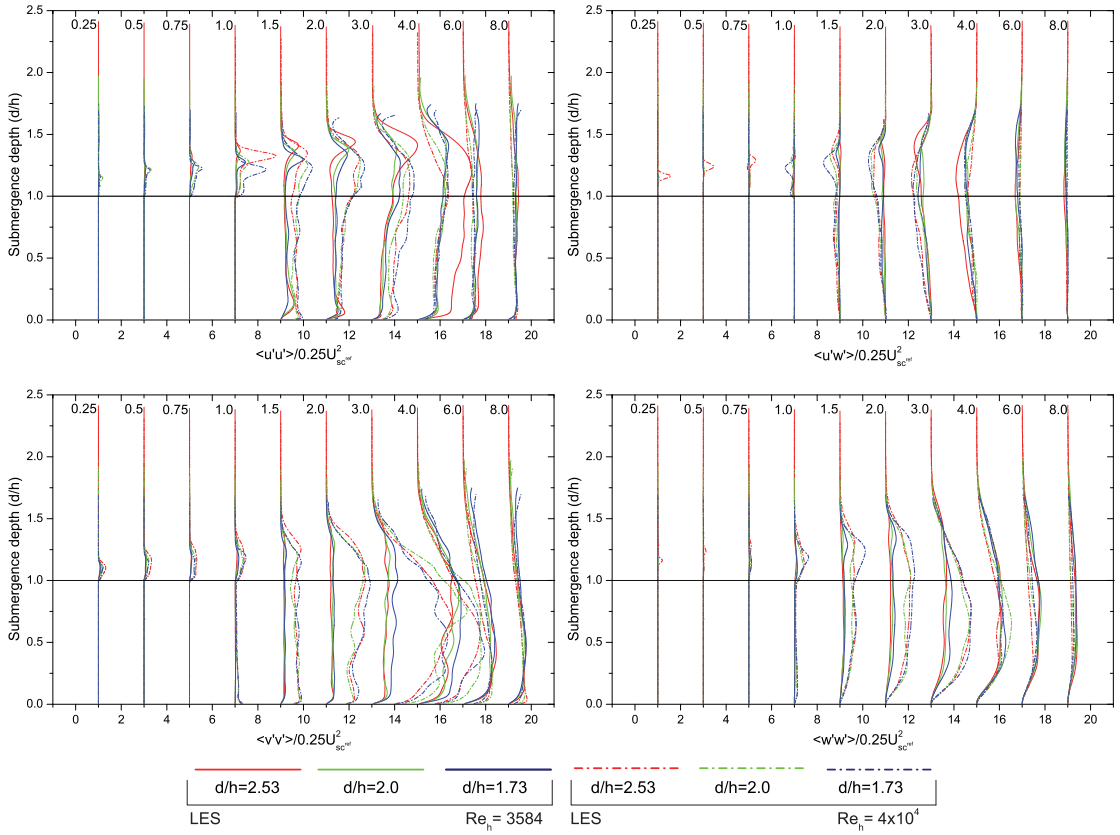

Figure 4.20: Distribution of the time averaged Reynolds stress terms about the symmetric plane, for a single cube placed in a uniform free-surface flow.

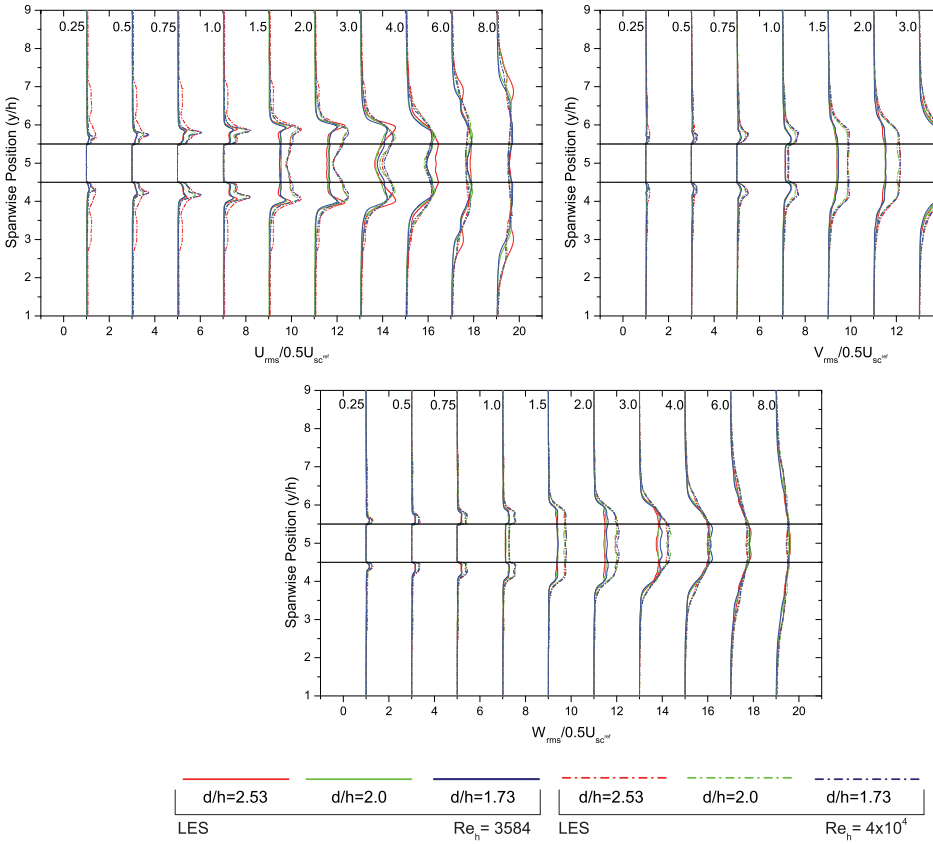

Figure 4.21: Time averaged turbulent intensity distributions around a single cube placed in a uniform flow at z/h=0.4.

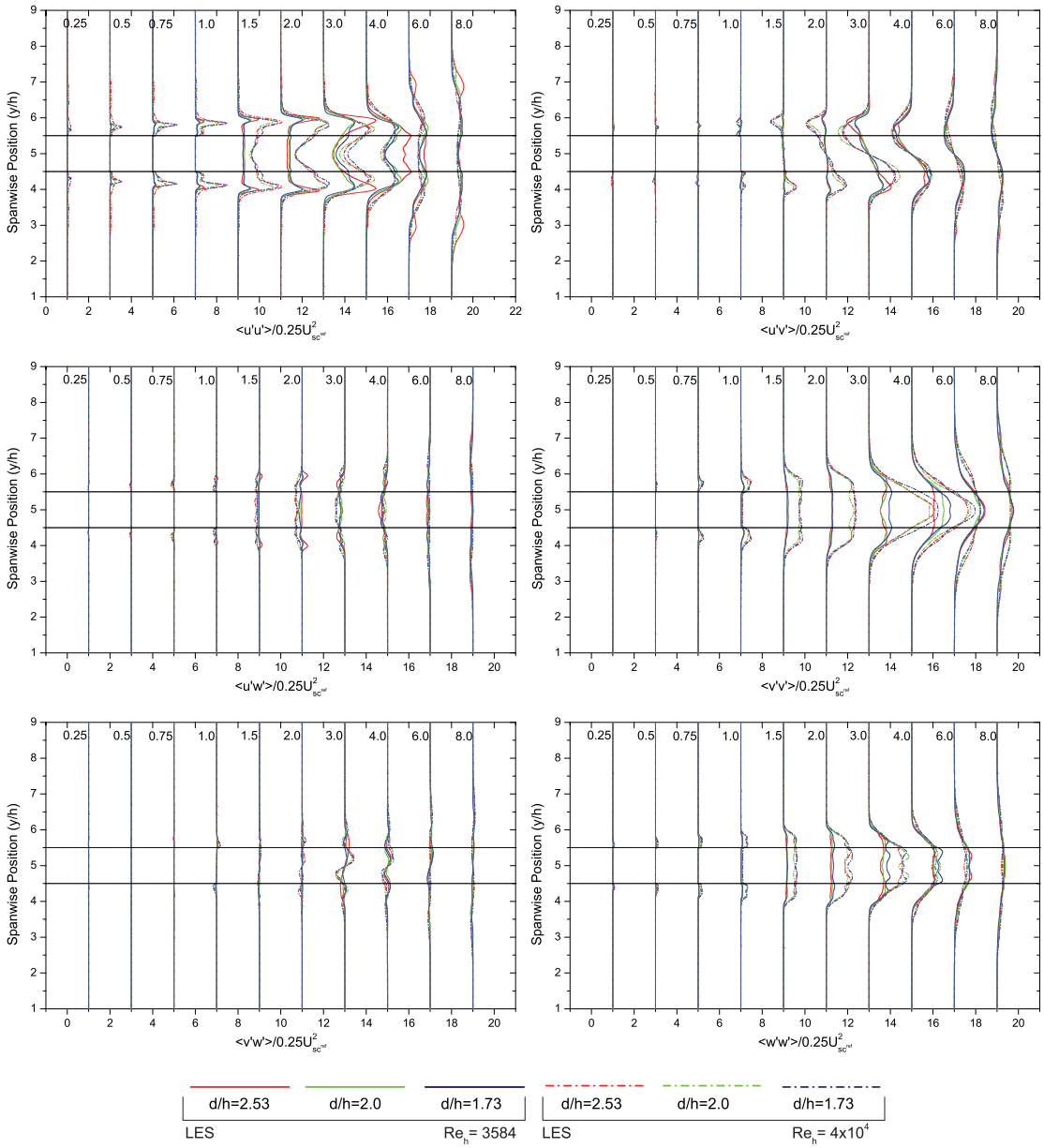

Figure 4.22: Distribution of time averaged Reynolds stresses around a single cube placed in a uniform flow about the XY plane for z/h=0.4.

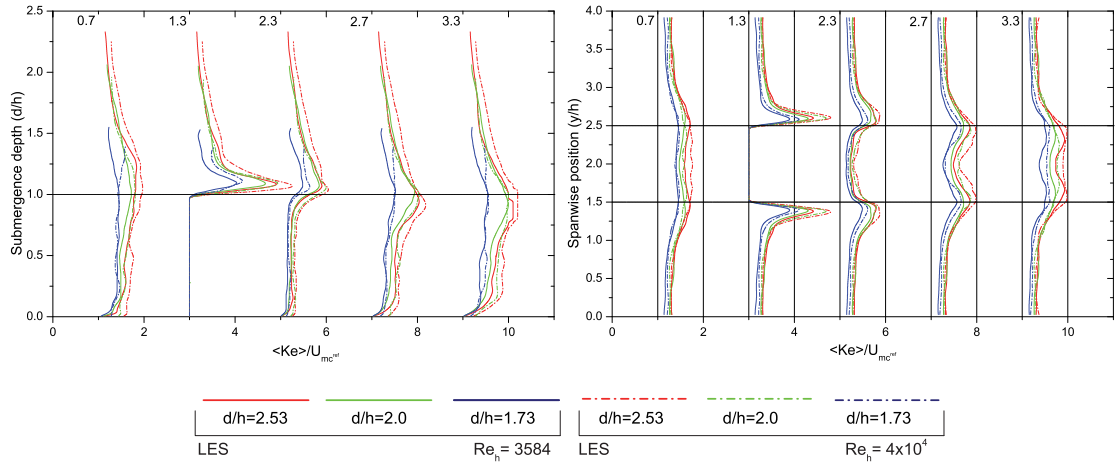

Figure 4.23: Time averaged distribution of turbulent kinetic energy about the symmetric plane (left) and XY plane for z/h=0.4 (right) around a cube in a matrix configuration.

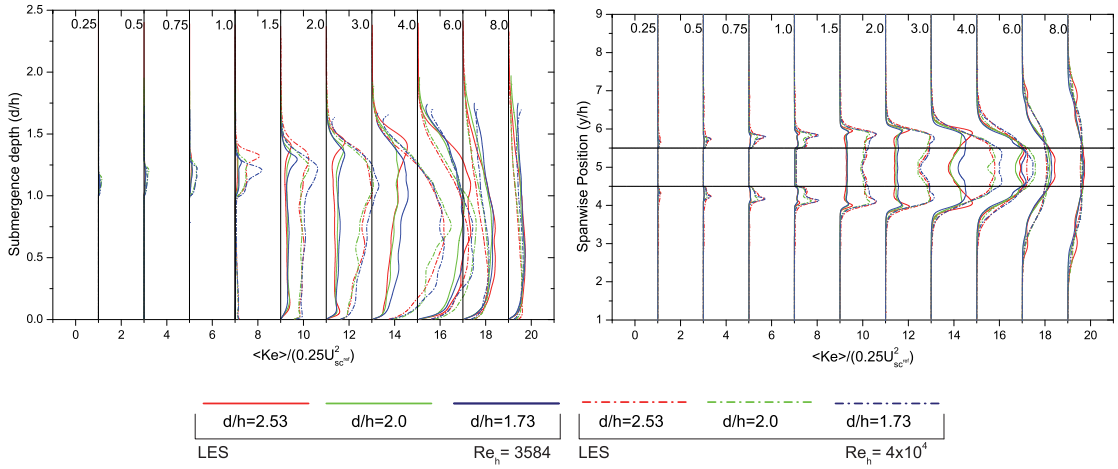

Figure 4.24: Time averaged distribution of turbulent kinetic energy about the symmetric plane (left) and XY plane for z/h=0.4 (right) around a single cube in a uniform flow.

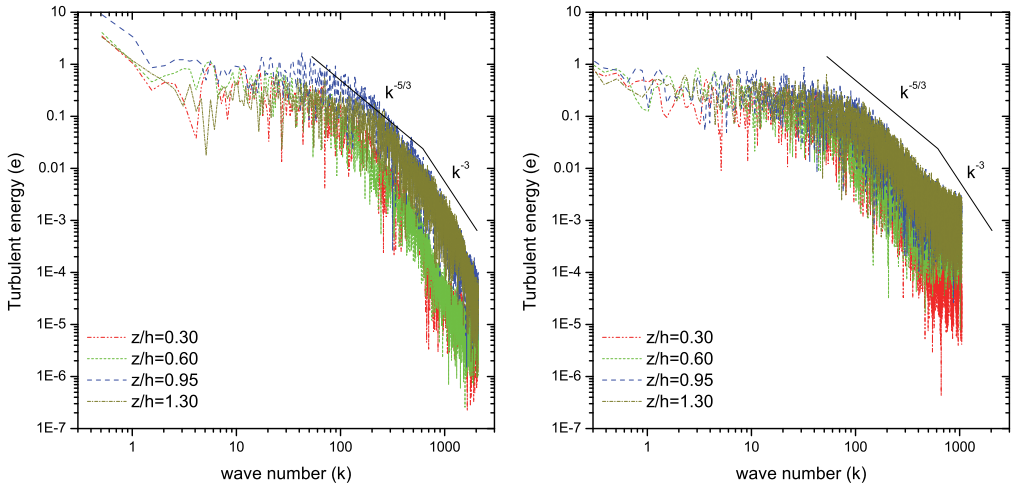

(a) d/h=2.533

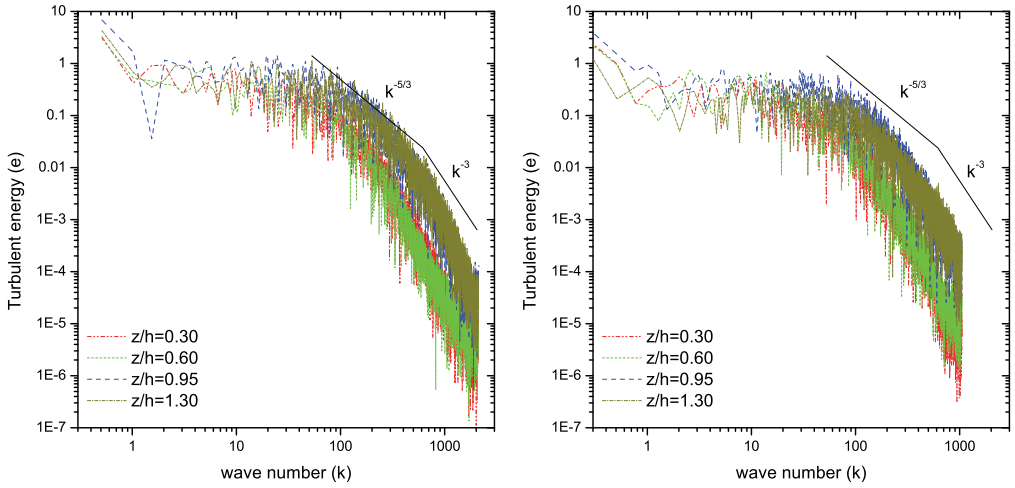

(b) d/h=2.0

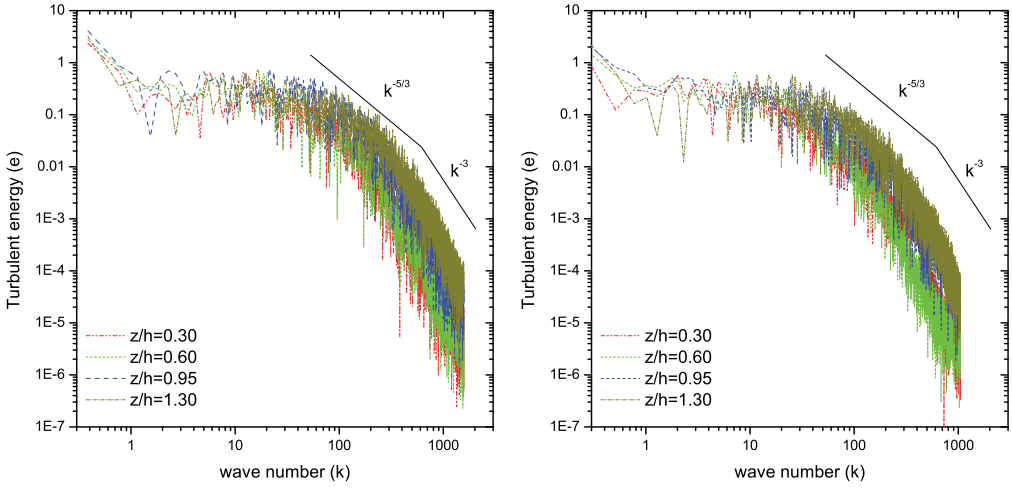

(c) d/h=1.7

Figure 4.25: Energy spectrums for Re_h=40000 (left) and Re_h=3584 (right), for a cube in a matrix configuration, plotted at PT_{mc1} along the central XZ plane.

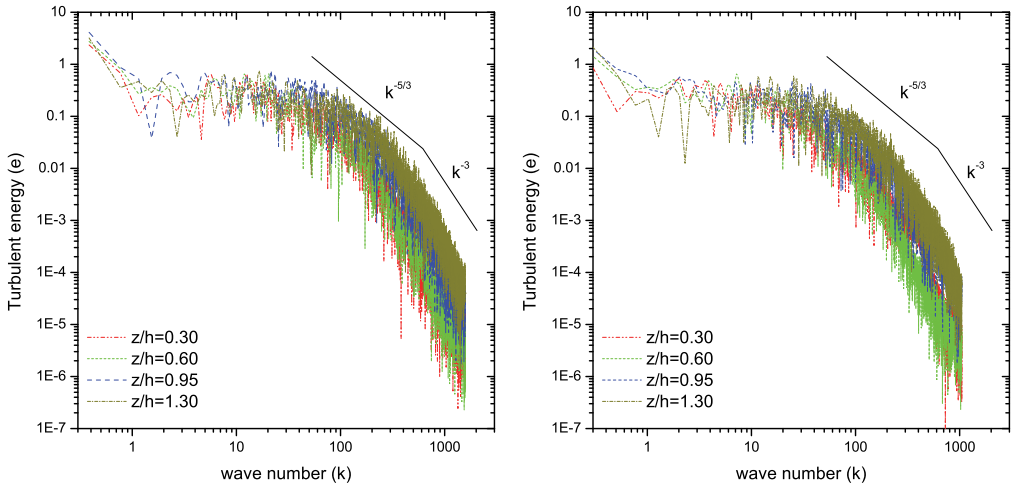

(a) PT_{mc1}

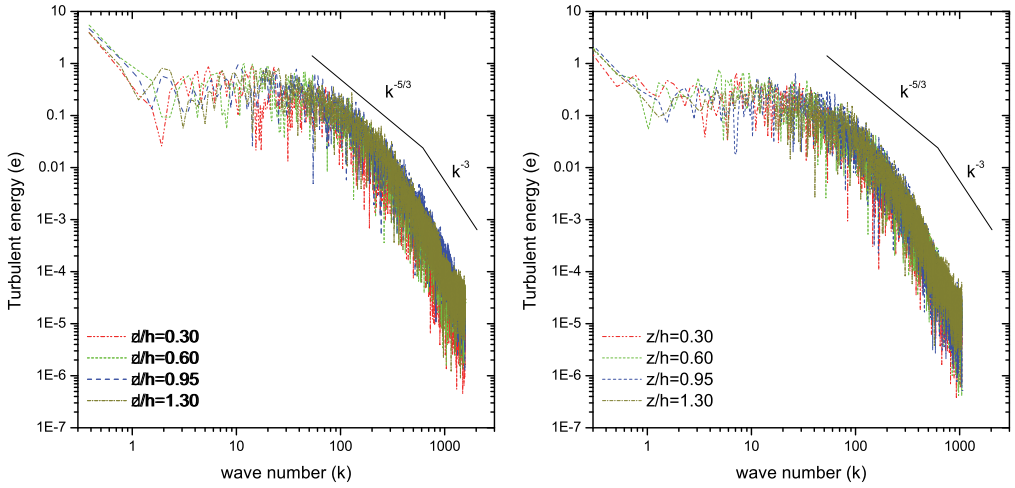

(b) PT_{mc2}

Figure 4.26: Energy spectrums for Re_h=40000 (left) and Re_h=3584 (right), for a cube in a matrix configuration, plotted at various locations in the wake along the central XZ plane for d/h=1.7.

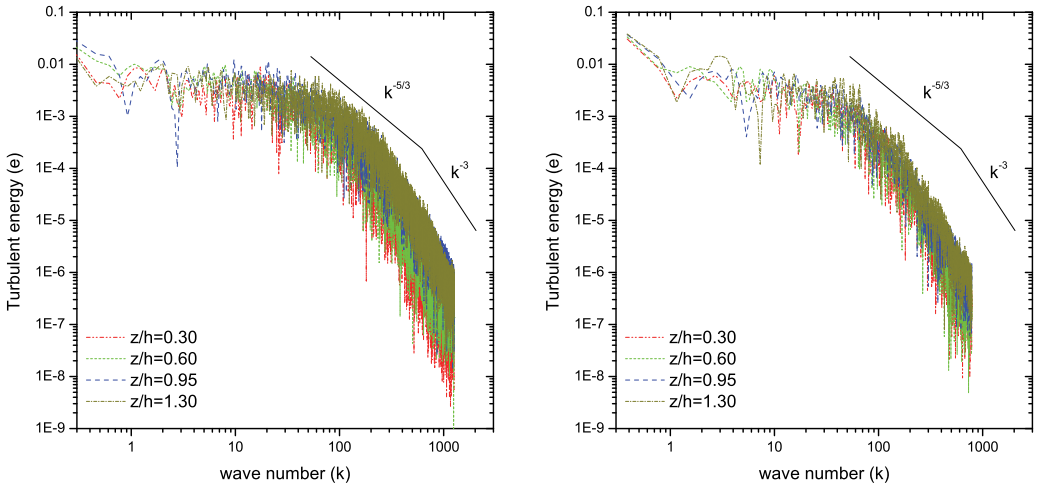

(a) d/h=2.533

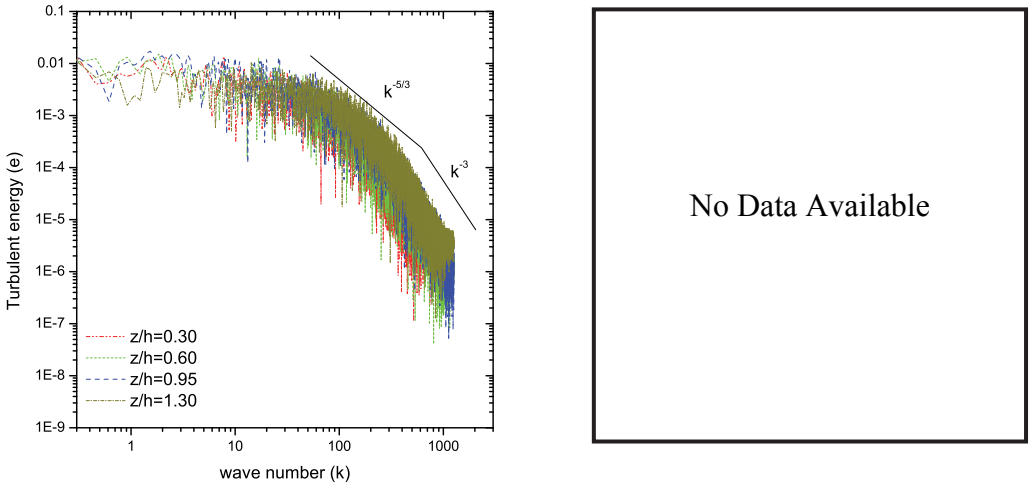

(b) d/h=2.0

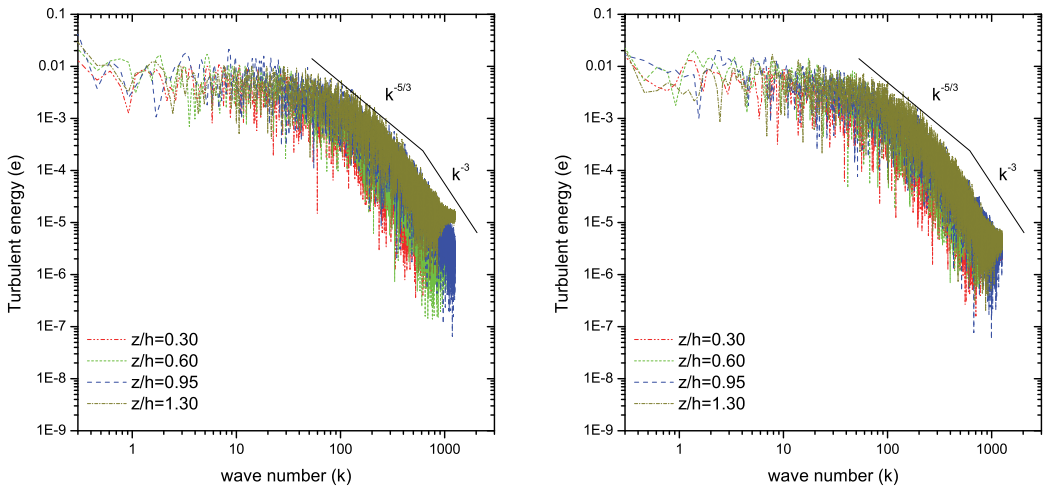

(c) d/h=1.7

Figure 4.27: Energy spectrums for Re_h=40000 (left) and Re_h=3584 (right), for a single cube in a uniform flow, plotted at PT_{sc1} along the central XZ plane.

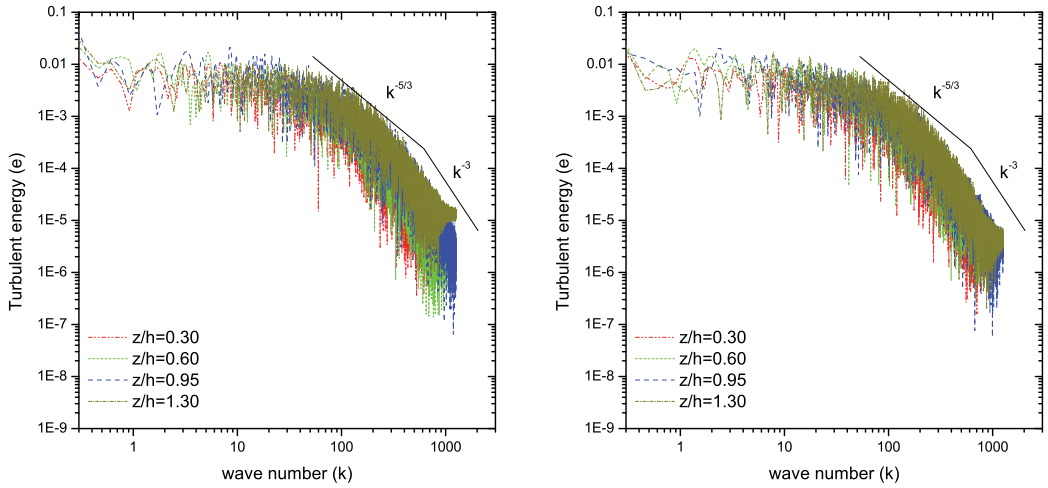

(a) PT_{sc1}

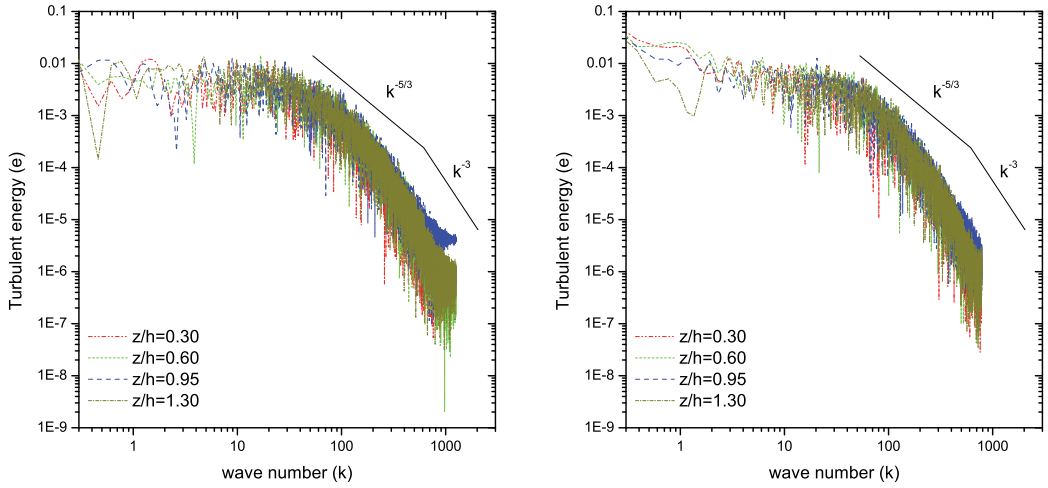

(b) PT_{sc2}

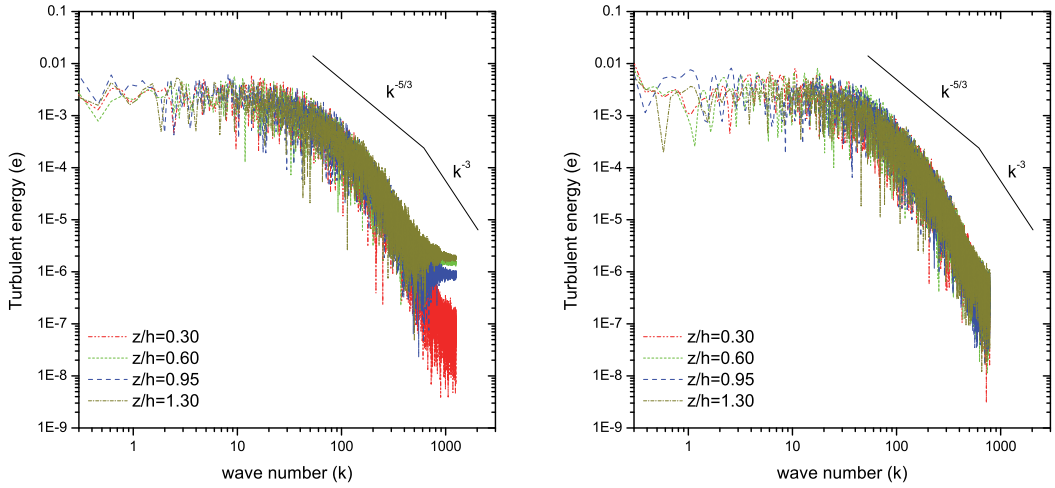

(c) PT_{sc3}

Figure 4.28: Energy spectrums for Re_h=40000 (left) and Re_h=3584 (right), for a single cube in a uniform flow, plotted at various locations in the wake along the central XZ plane for d/h=1.7.

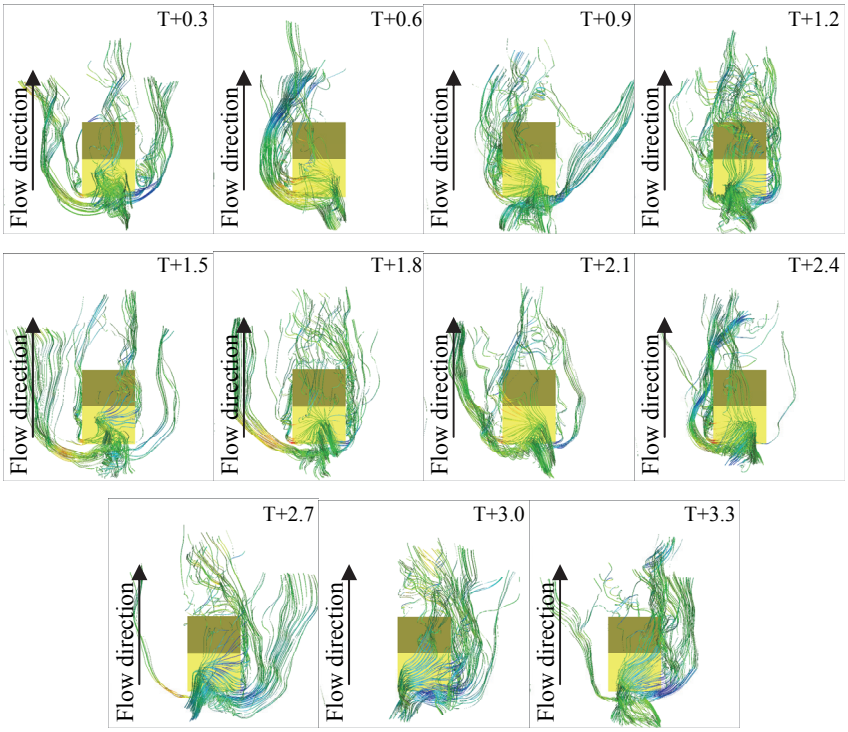

(a) d/h=2.0, Re_h=3584

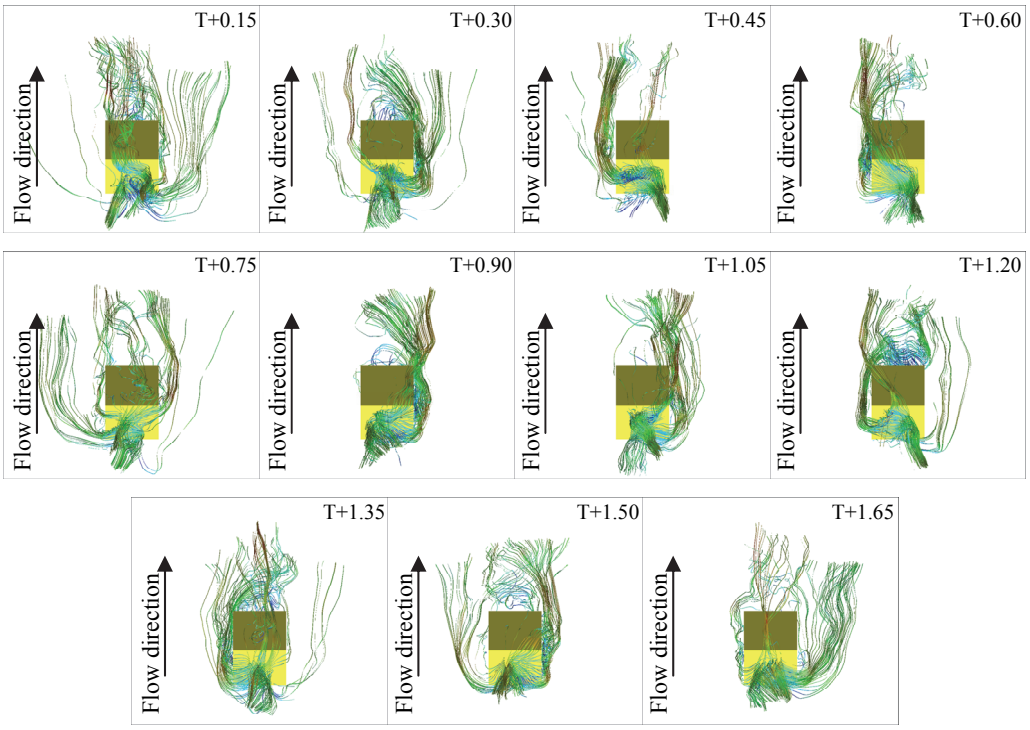

(b) d/h=2.0, Re_h=40000

Figure 4.29: Instantaneous streamline traces along the frontal face (60% of the face) of a cube in a matrix configuration at various times.

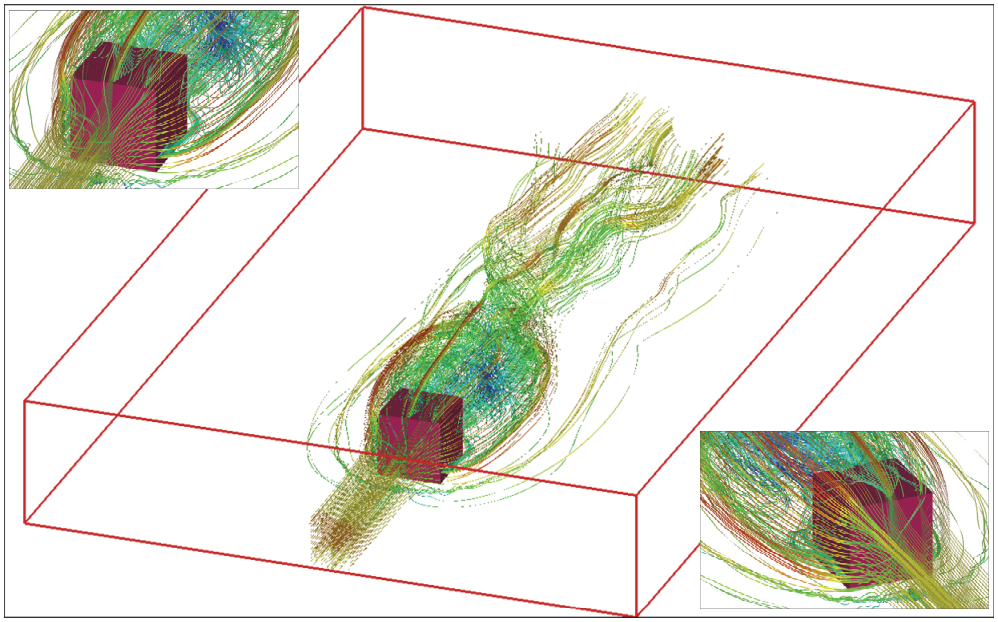

(a) d/h=2.0, Re_h=3584

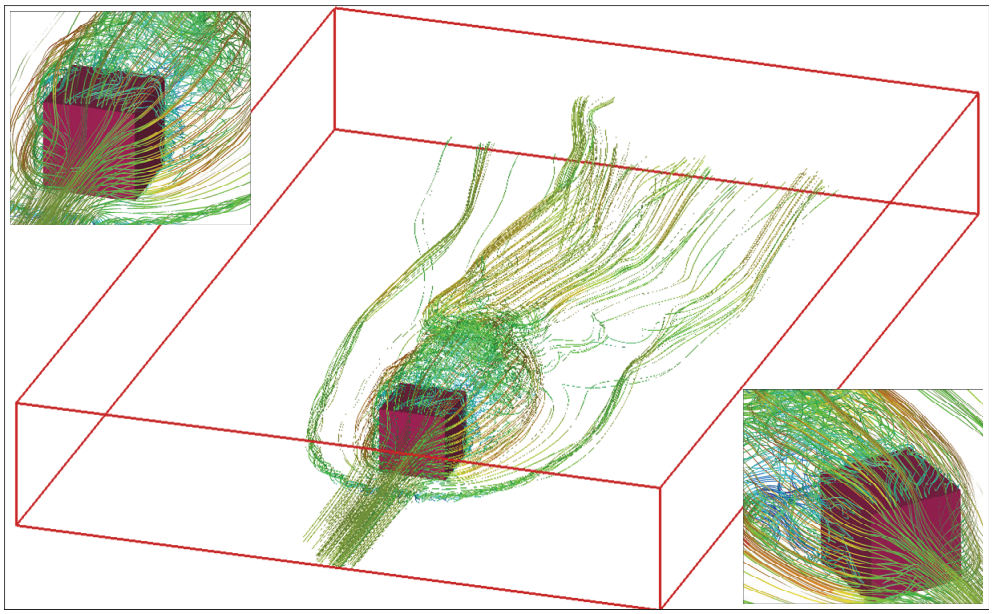

(b) d/h=2.0, Re_h=40000

Figure 4.30: Instantaneous streamline traces along the frontal face of a cube placed in a uniform flow.

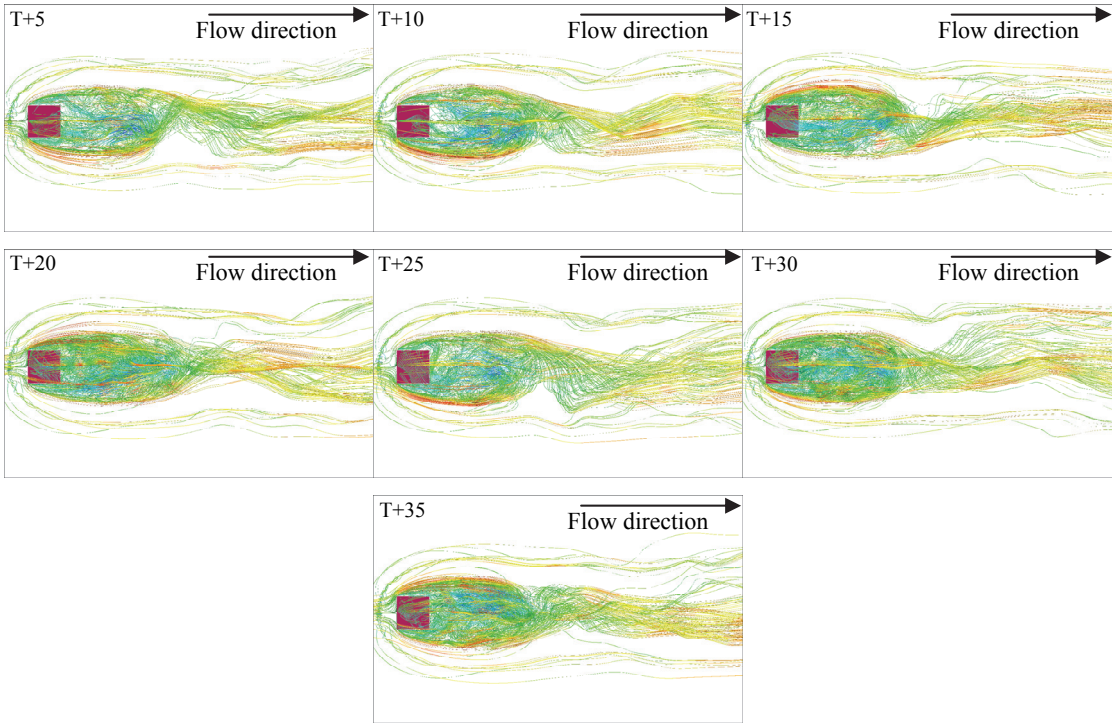

(a) d/h=2.0, Re_h=3584

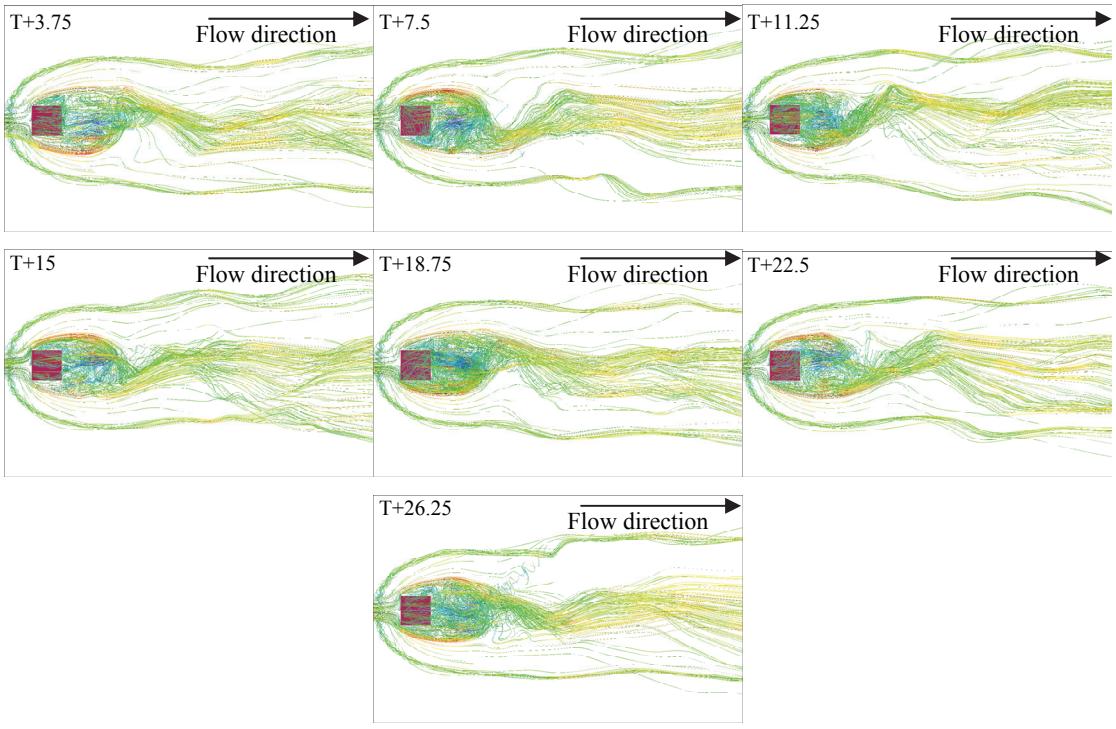

(b) d/h=2.0, Re_h=40000

Figure 4.31: Instantaneous streamline traces along the frontal face of a cube placed in a uniform flow, viewed at various instants in time about the XY plane.

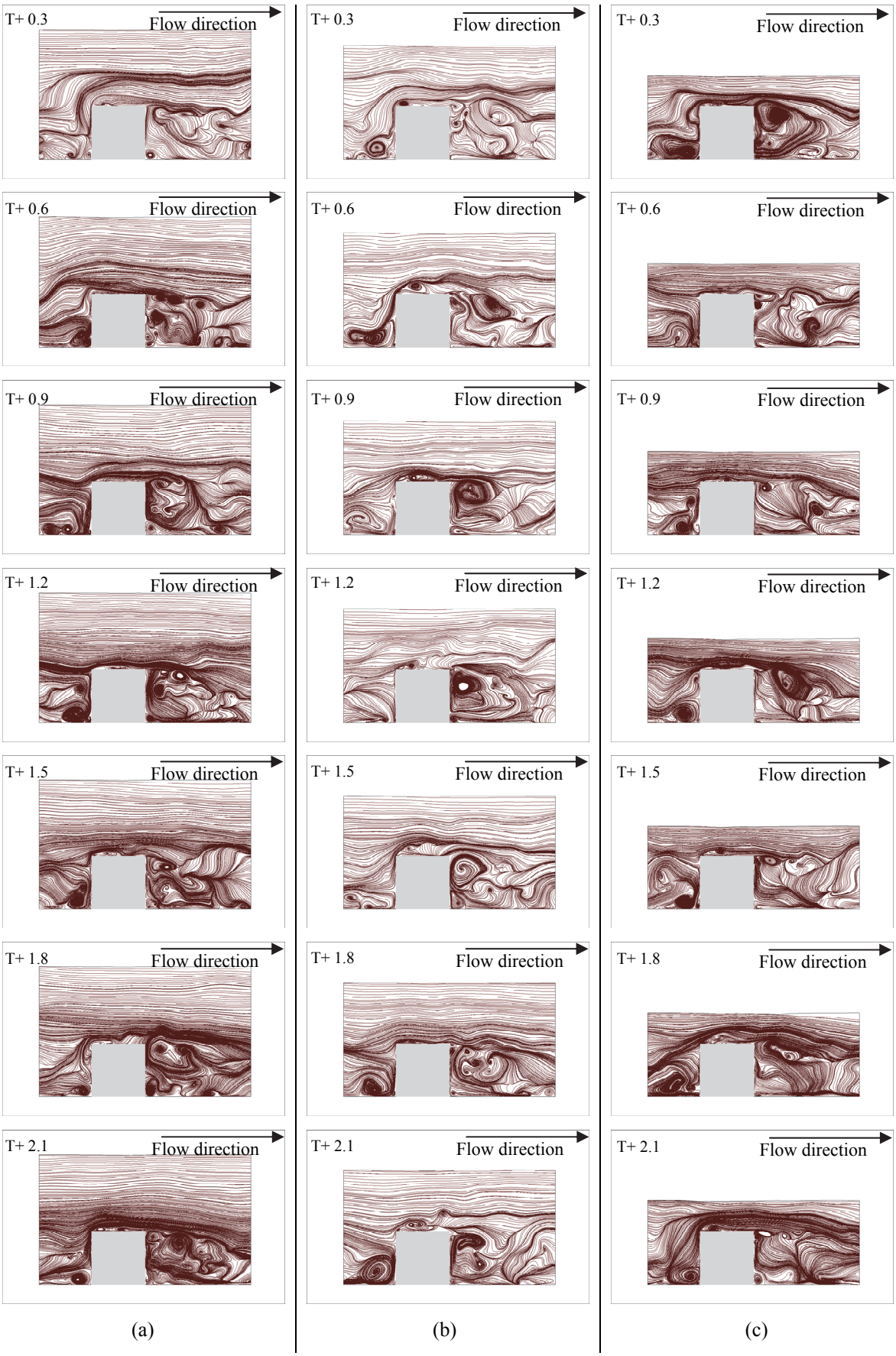

Figure 4.32: Instantaneous streamlines about the XZ mid-plane for a matrix of cubes at Re_h=3584 for submergence ratios (a) d/h=2.533, (b) d/h=2.0 and (c) d/h=1.73.

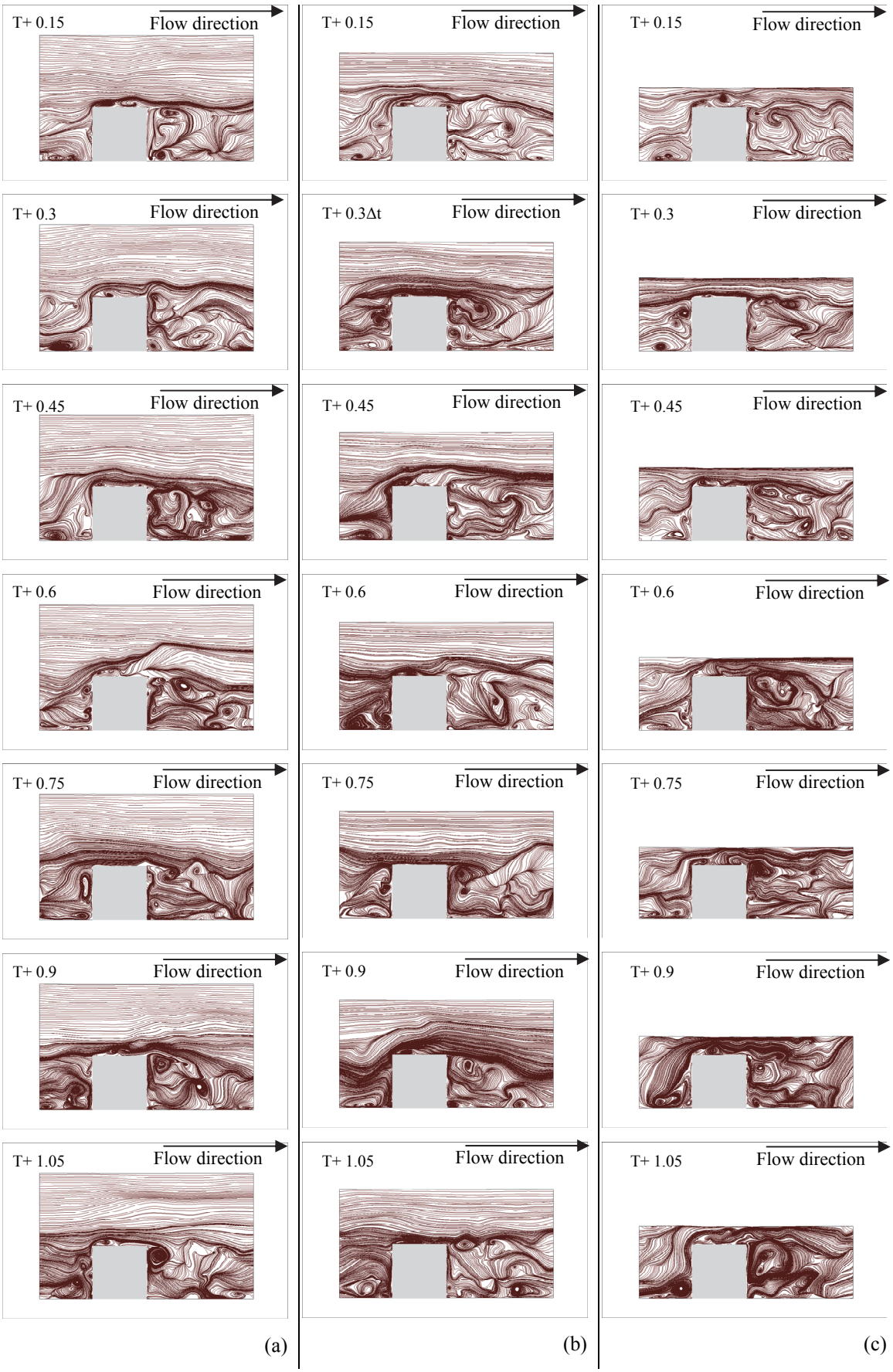

Figure 4.33: Instantaneous streamlines traces about the XZ mid-plane for a matrix of cubes at Re_h=40000 for submergence ratios (a) d/h=2.533, (b) d/h=2.0 and (c) d/h=1.73.

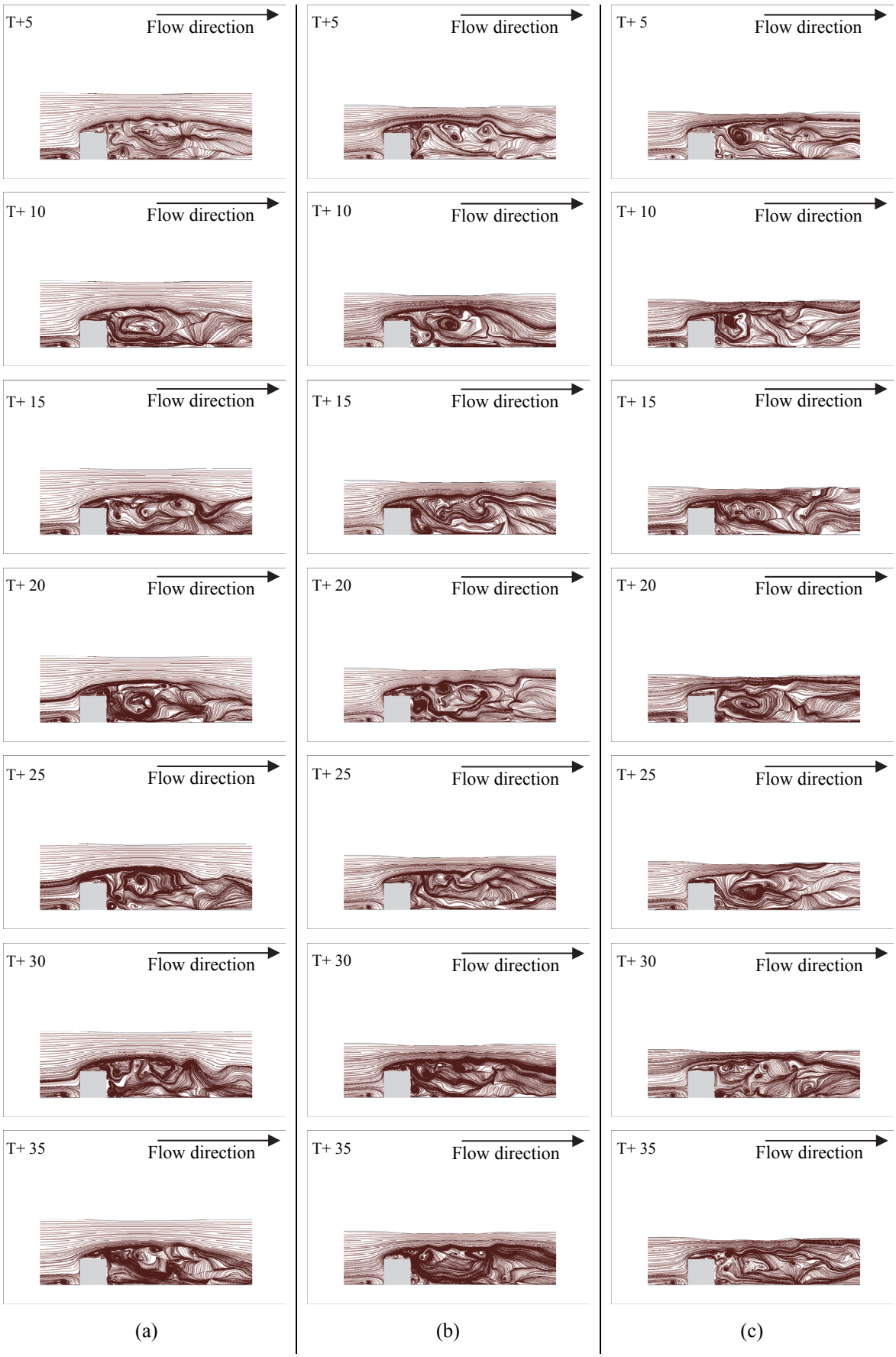

Figure 4.34: Instantaneous streamlines traces about the XZ mid-plane for a single cube at Re_h=3584 for submergence ratios (a) d/h=2.533, (b) d/h=2.0 and (c) d/h=1.73.

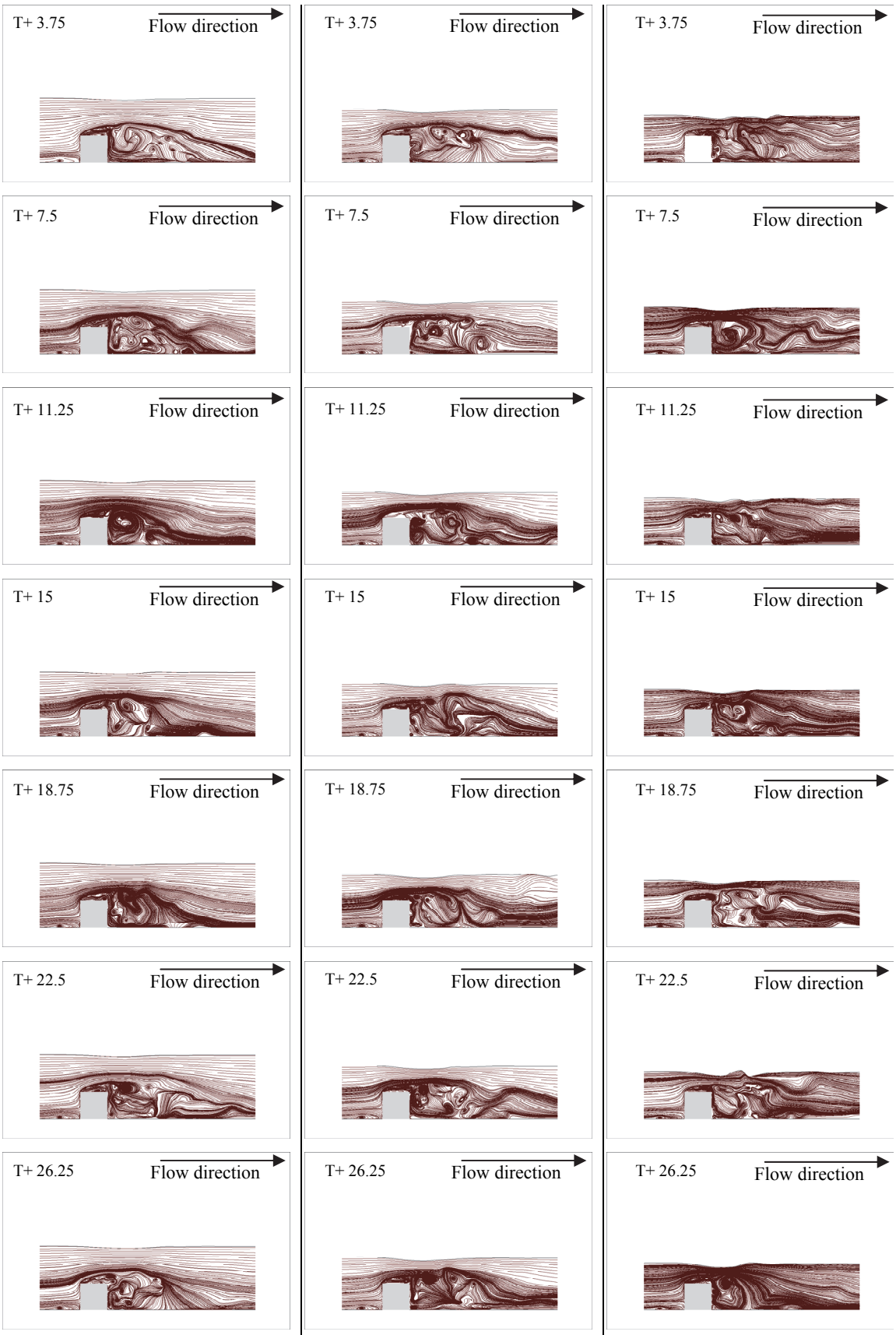

Figure 4.35: Instantaneous streamlines traces about the XZ mid-plane for a single cube at Re_h=40000 for submergence ratios (a) d/h=2.533, (b) d/h=2.0 and (c) d/h=1.73.

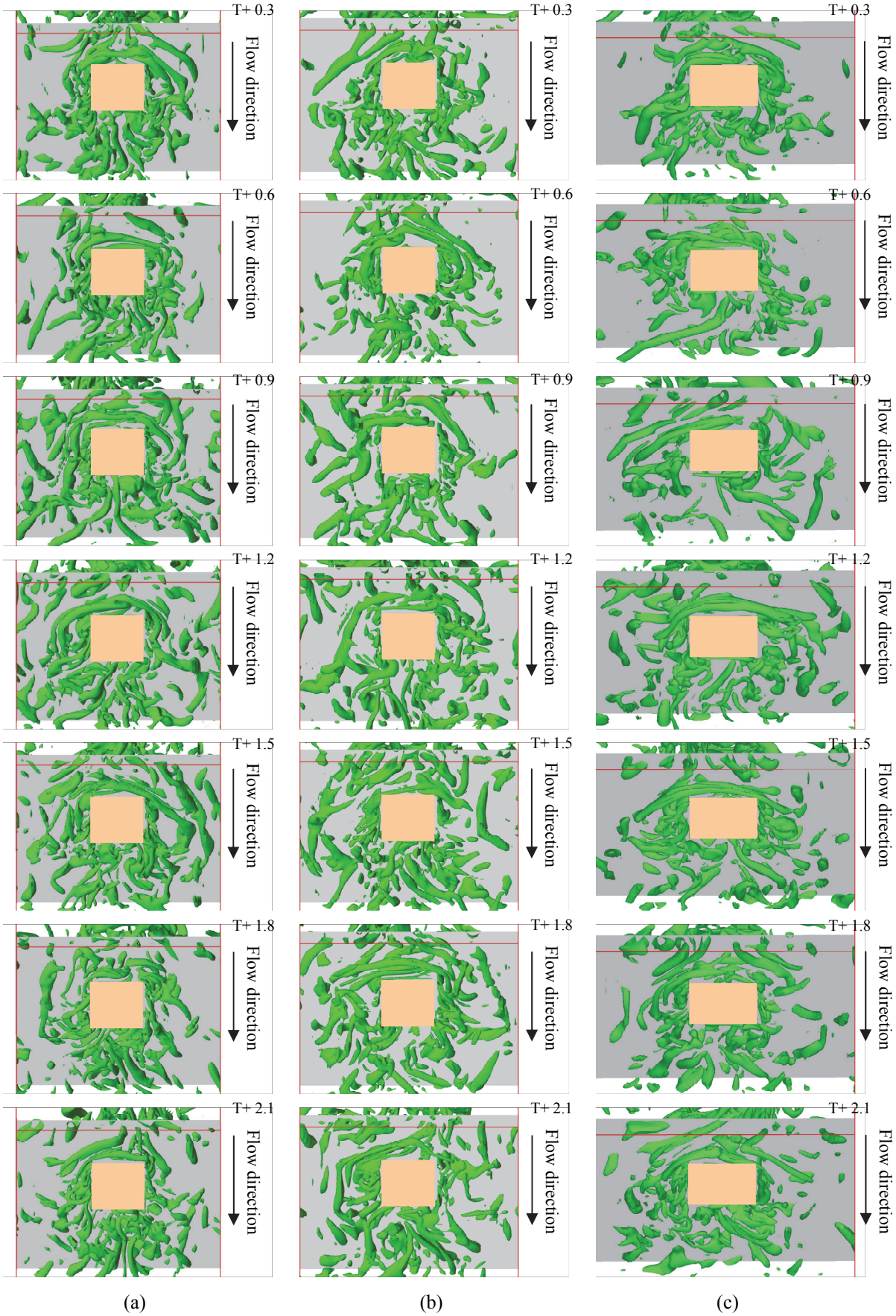

Figure 4.36: Instantaneous vortical structures for Q=130 in the near wall region (z/h<0.3) at Re_h=3584 for submergence ratios: (a) 2.533, (b) 2.0 and (c) 1.73.

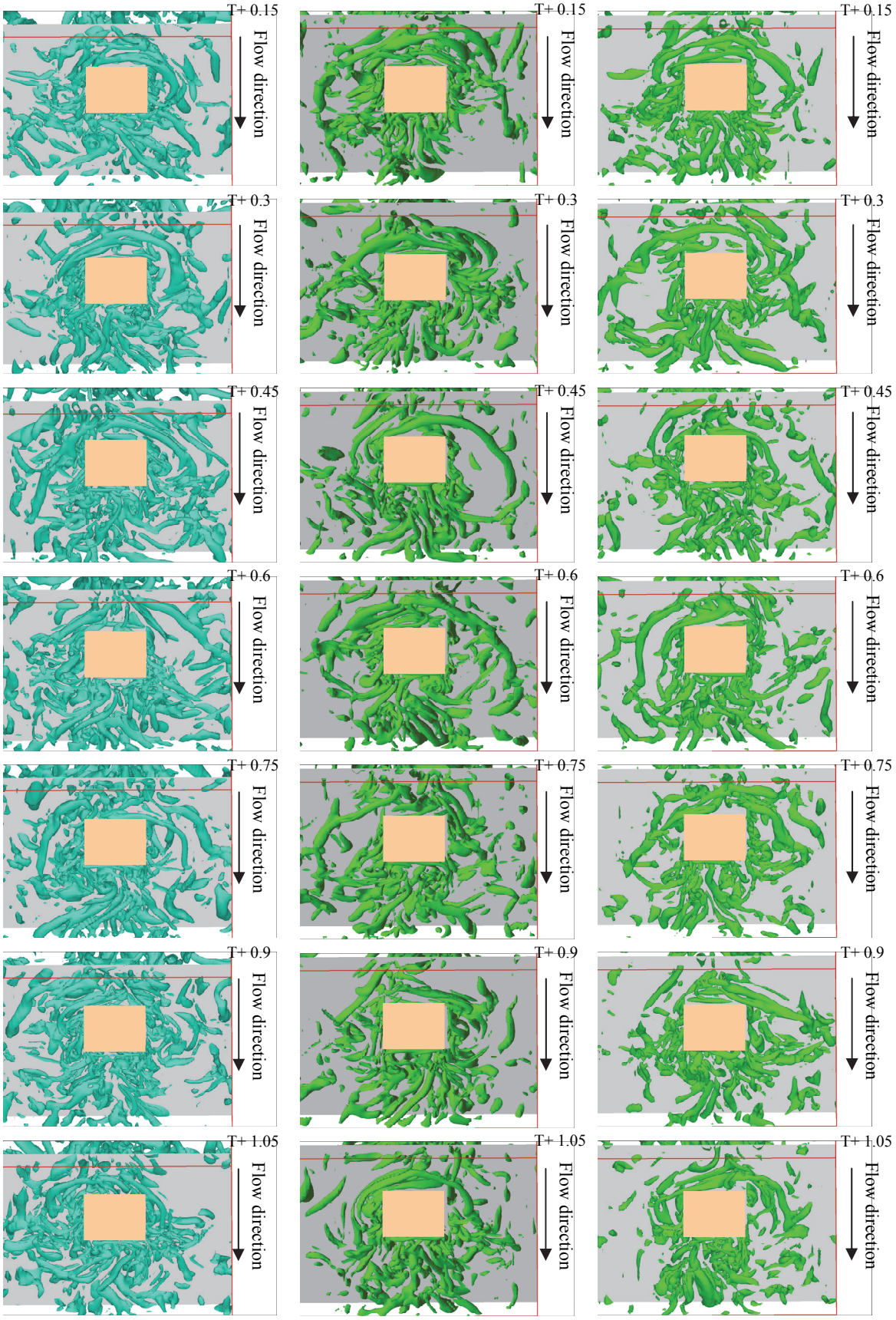

Figure 4.37: Instantaneous vortical structures for Q=130 in the near wall region (z/h<0.3) at Re_h=40000 for submergence ratios: (a) 2.533, (b) 2.0 and (c) 1.73.

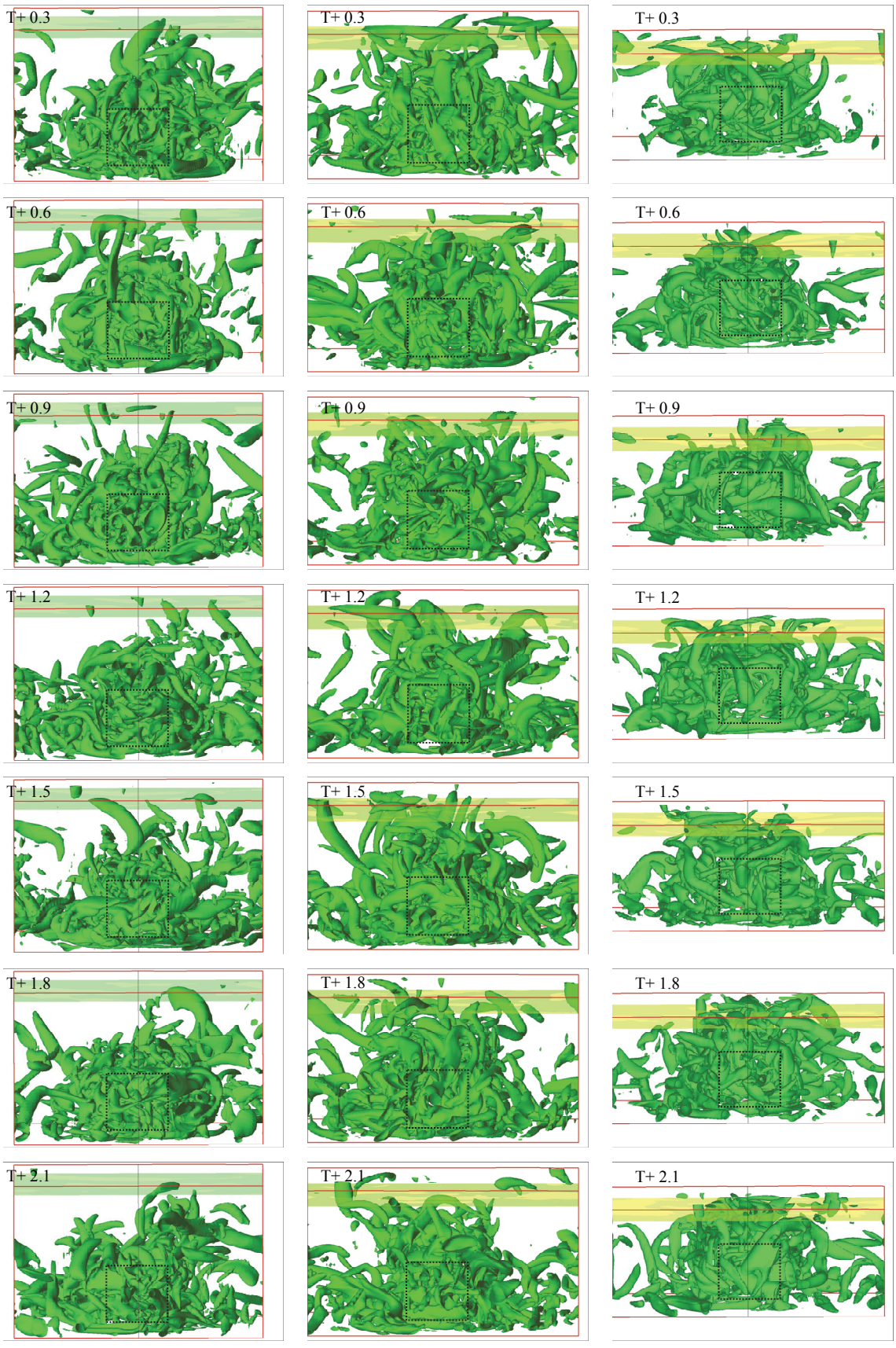

Figure 4.38: Instantaneous vortical structures for Q=130 viewed head-on with a surface plane active at ((d/h)-0.1) at Re_h=3584 for submergence ratios: (a) 2.533, (b) 2.0 and (c) 1.73.

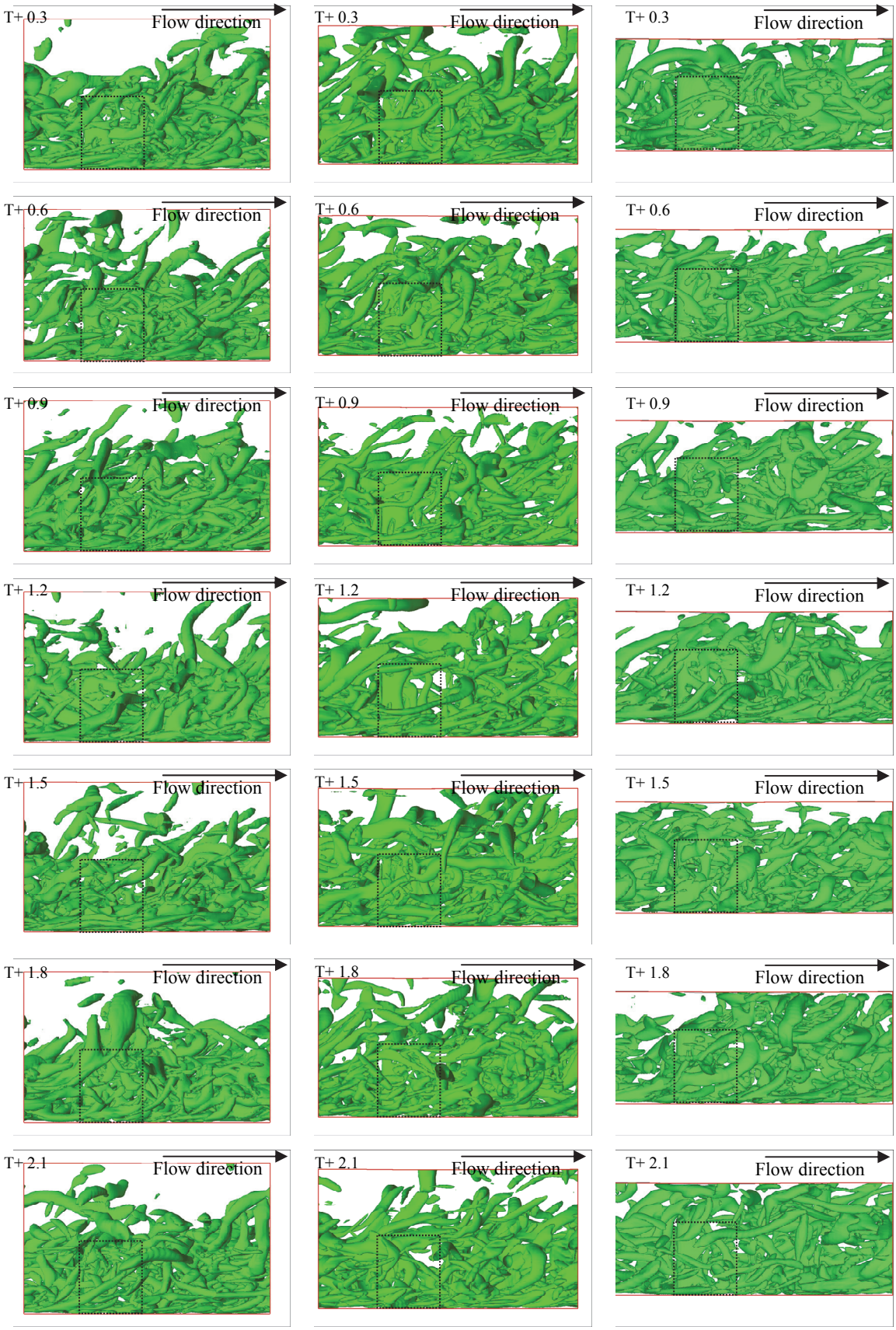

Figure 4.39: Instantaneous vortical structures for Q=130 viewed about the XZ plane for Re_h=3584 and submergence ratios (a) 2.533, (b) 2.0, (c) 1.73.

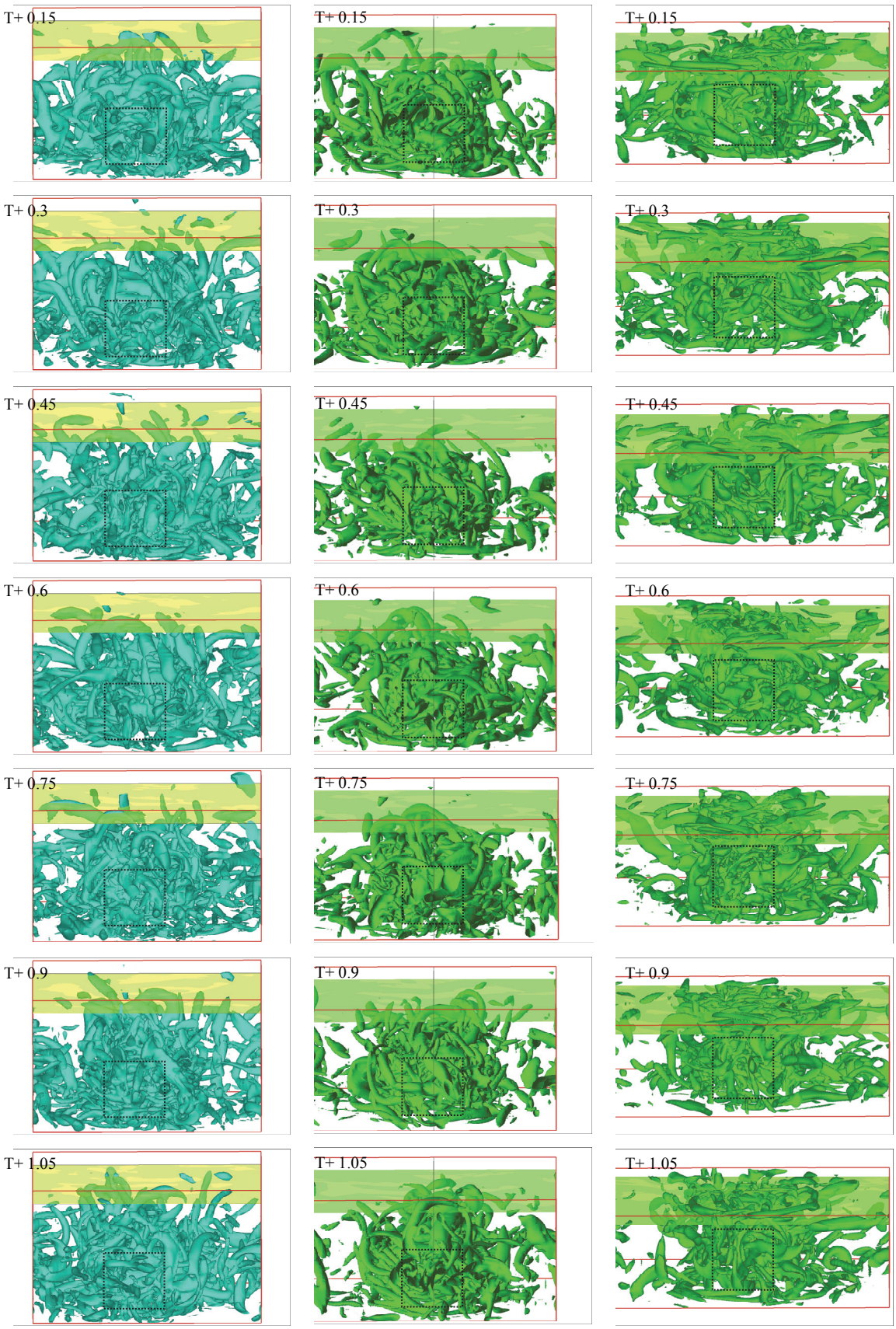

Figure 4.40: Instantaneous vortical structures for Q=130 viewed head-on with a surface plane active at ((d/h)-0.1) at Re_h=40000 for submergence ratios: (a) 2.533, (b) 2.0 and (c) 1.73.

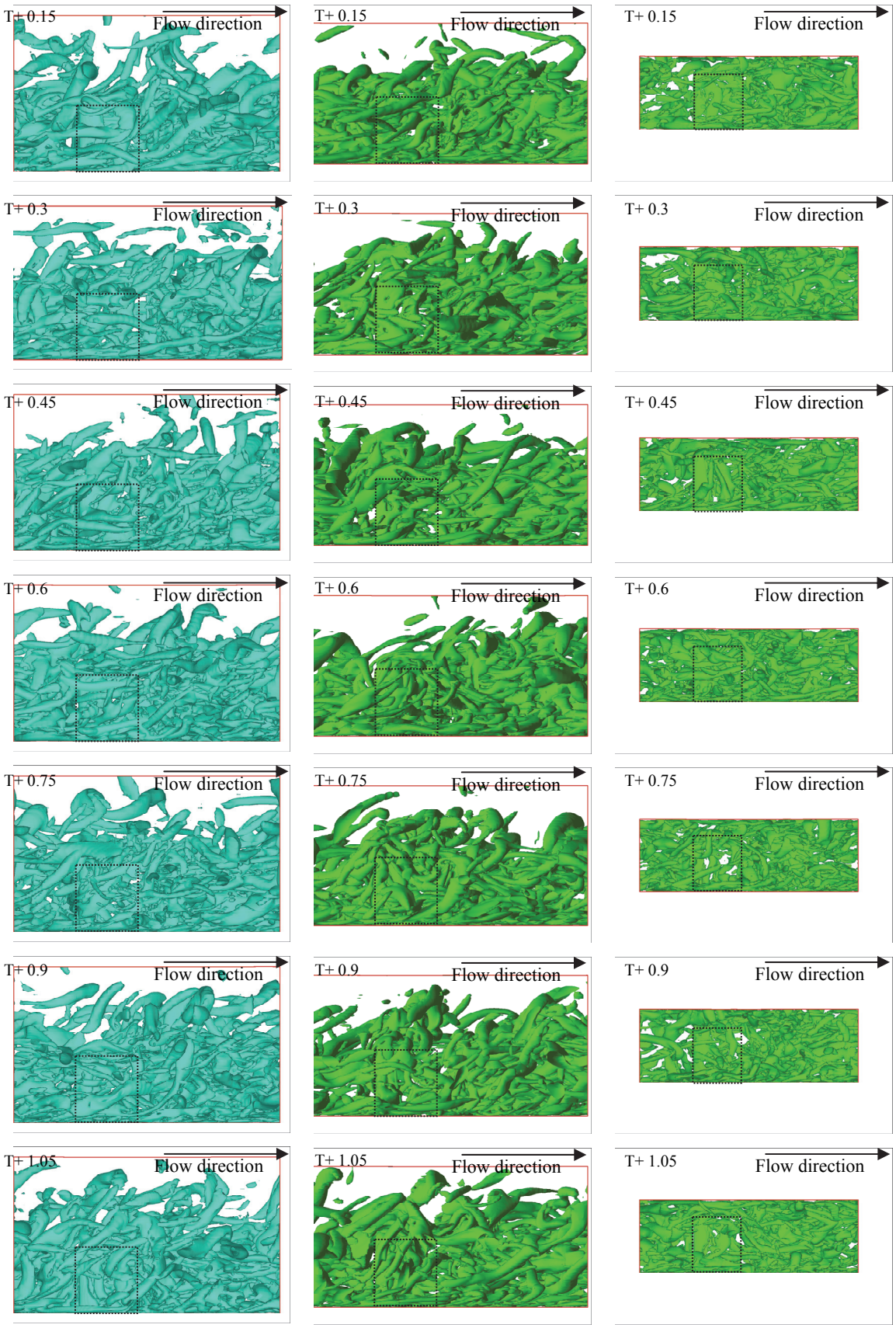

Figure 4.41: Instantaneous vortical structures for Q=130 viewed about the XZ plane for Re_h=40000 and submergence ratios (a) 2.533, (b) 2.0, (c) 1.73.

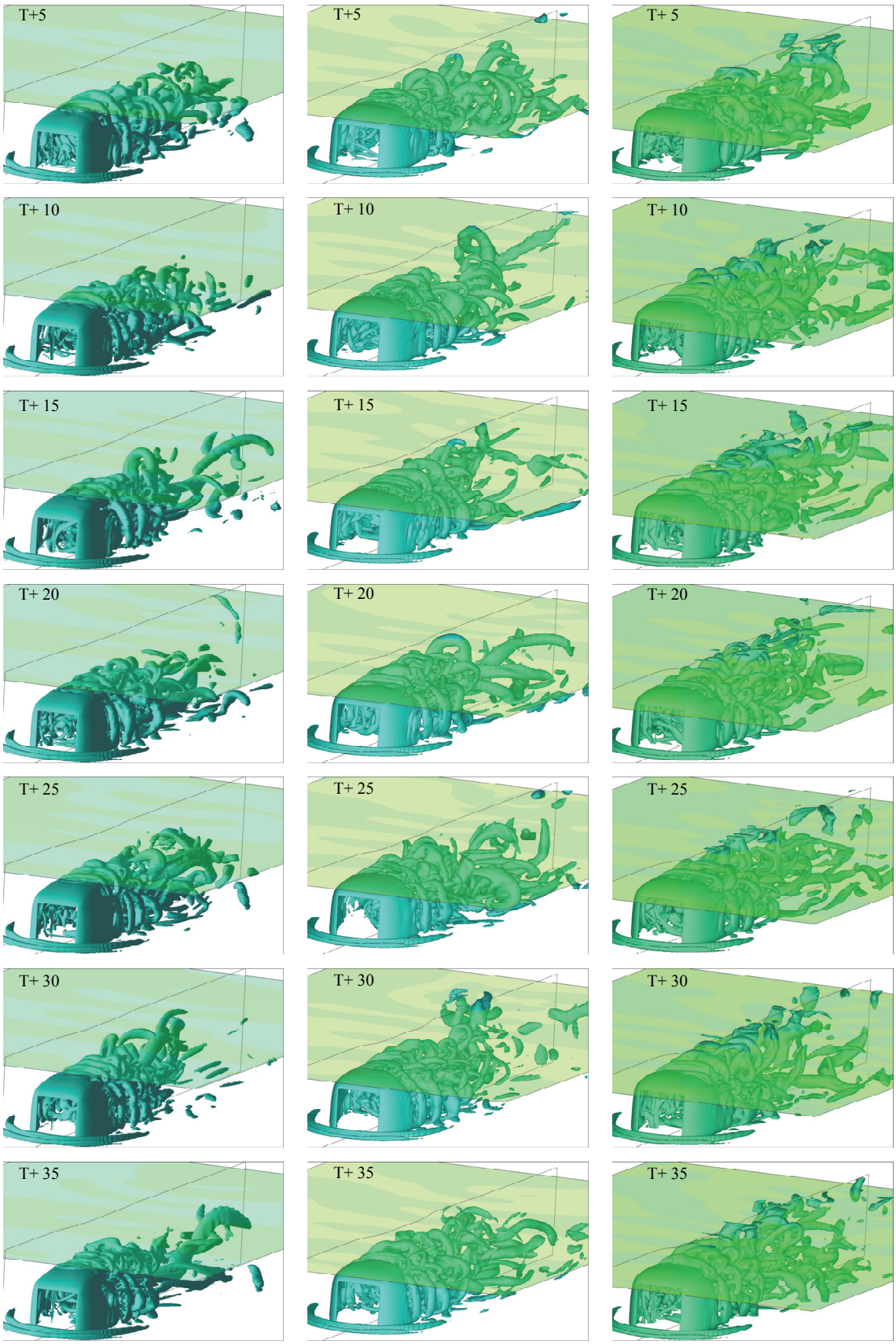

Figure 4.42: Instantaneous vortical structures for Q=1 viewed head-on with a surface plane active at ((d/h)-0.1) at Re_h=3584 for submergence ratios: (a) 2.533, (b) 2.0 and (c) 1.73.

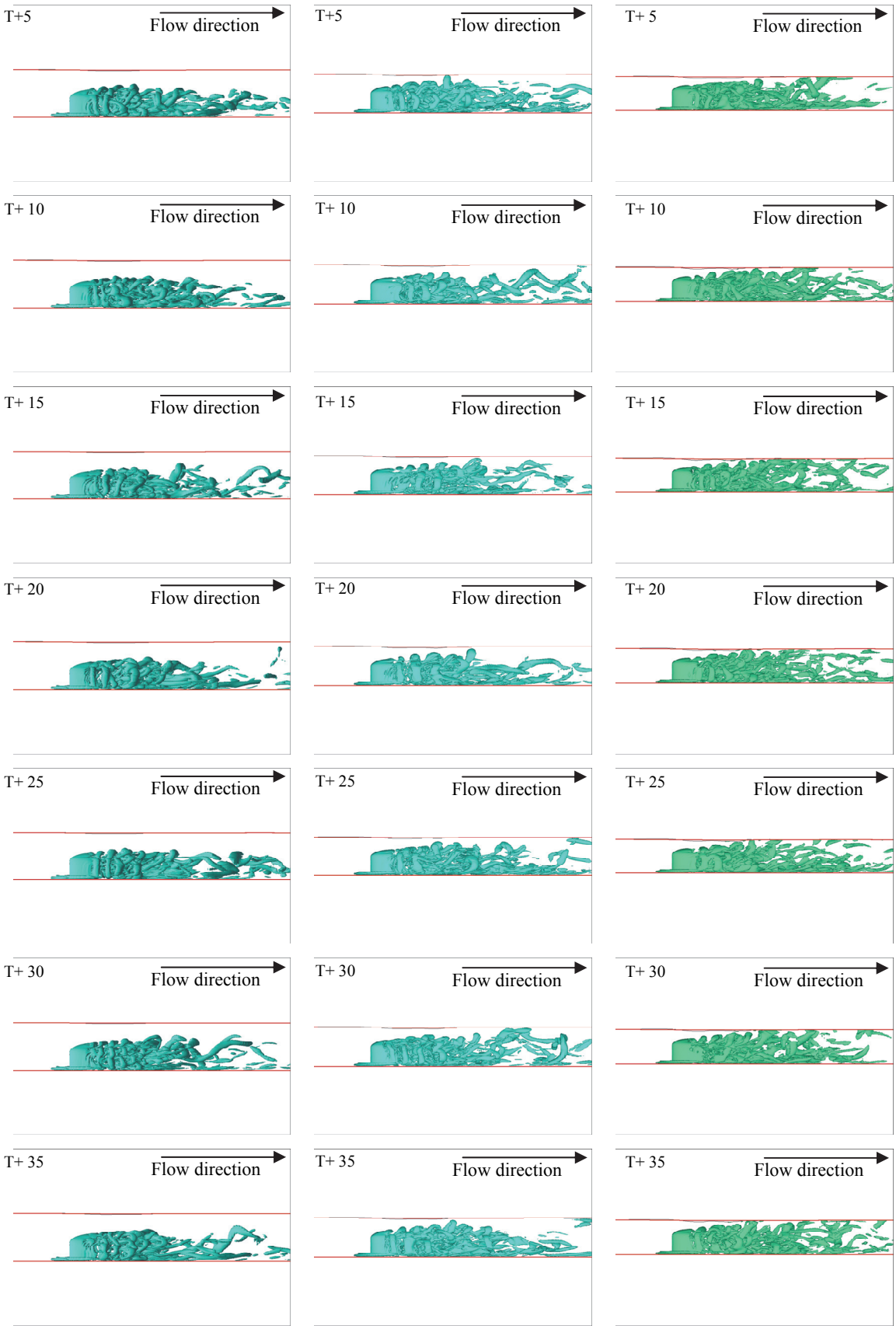

Figure 4.43: Instantaneous vortical structures for Q=1 viewed about the XZ plane for Re_h=40000 and submergence ratios (a) 2.533, (b) 2.0, (c) 1.73.

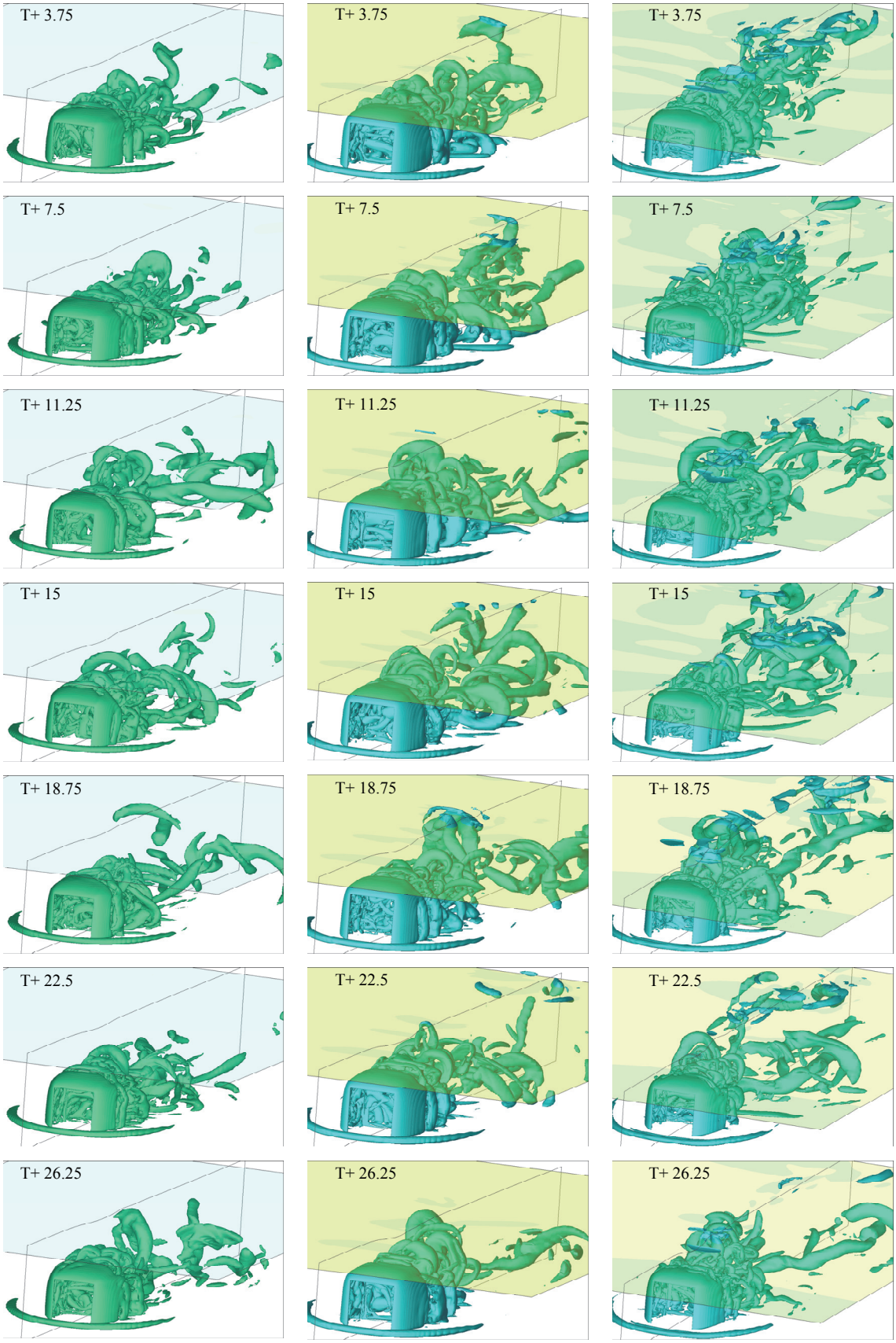

Figure 4.44: Instantaneous vortical structures for Q=1 viewed head-on with a surface plane active at ((d/h)-0.1) at Re_h=40000 for submergence ratios: (a) 2.533, (b) 2.0 and (c) 1.73.

Figure 4.45: Instantaneous vortical structures for Q=1 viewed about the XZ plane for Re_h=40000 and submergence ratios (a) 2.533, (b) 2.0, (c) 1.73.

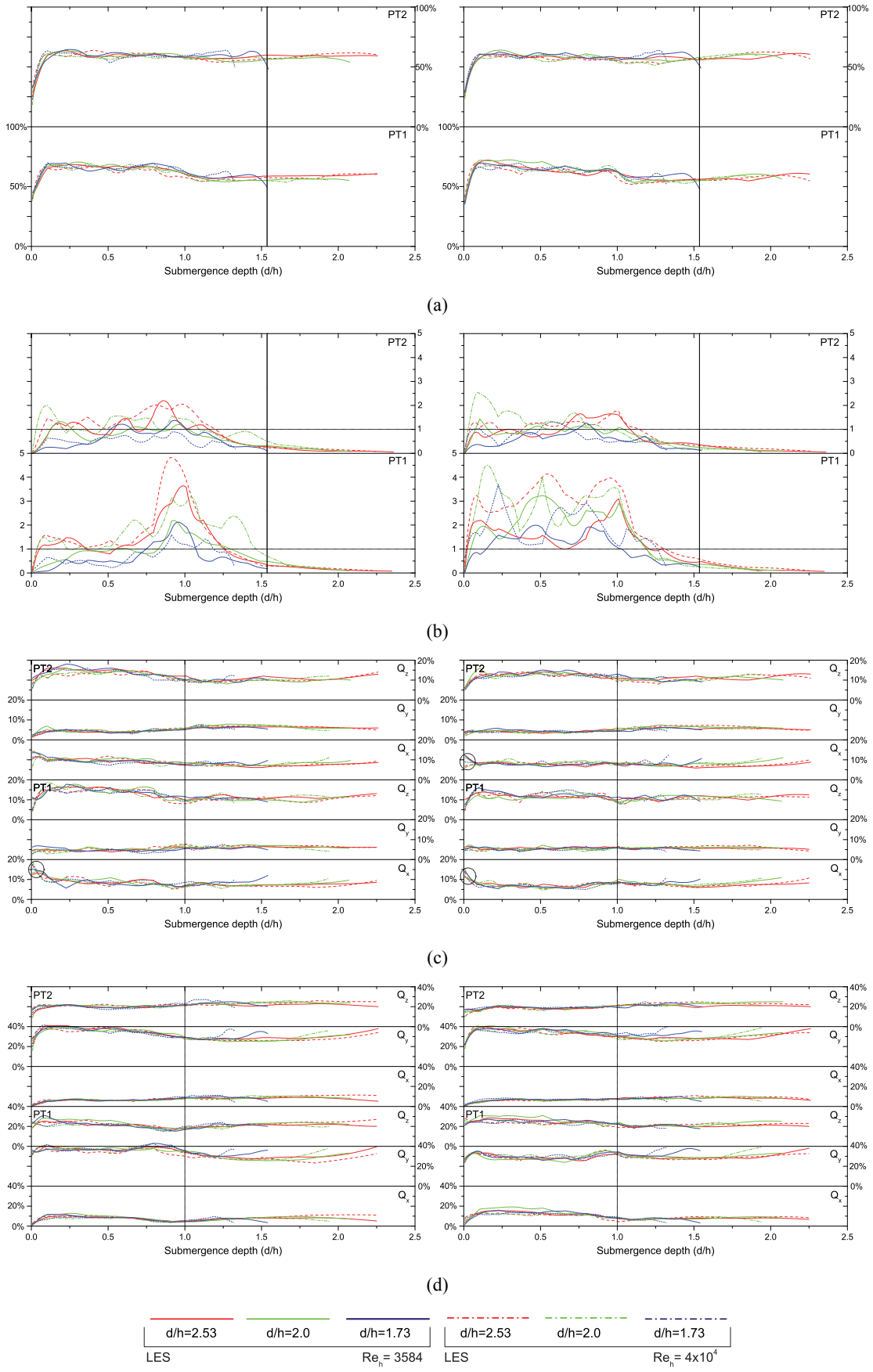

Figure 4.46: Vortex statistical data for (a) persistence, (b) time averaged normalised Q, (c) complete vortex alignment to an axis, (d) zero alignment to an axis, for a cube in a matrix configuration, plotted about the XZ mid-plane (right) and along the cube edge (left).

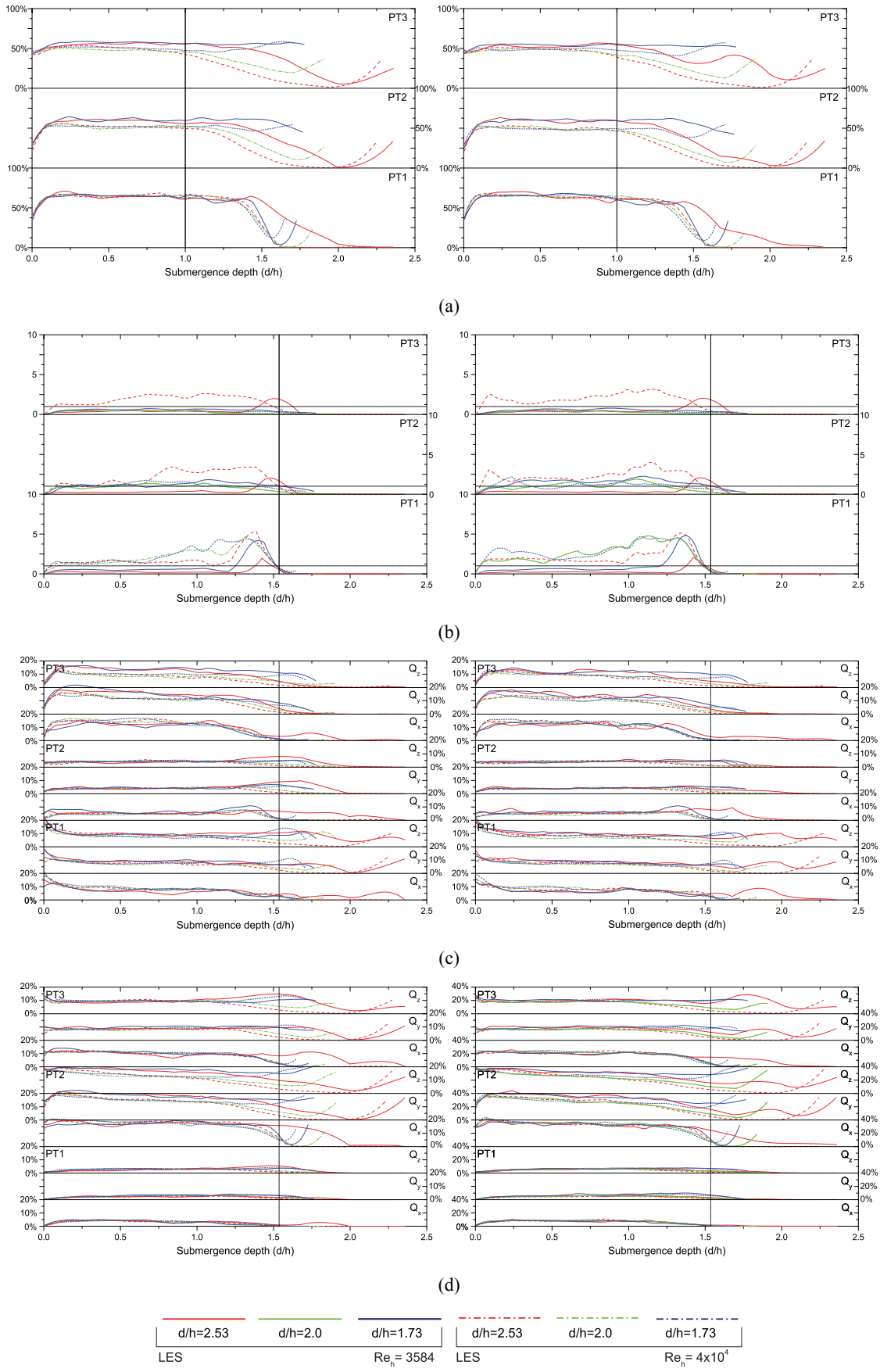

Figure 4.47: Vortex statistical data for (a) persistence, (b) time averaged normalised Q, (c) complete vortex alignment to an axis, (d) zero alignment to an axis. For a single cube placed in a uniform flow plotted about the XZ mid-plane (right) and along the cube edge (left).

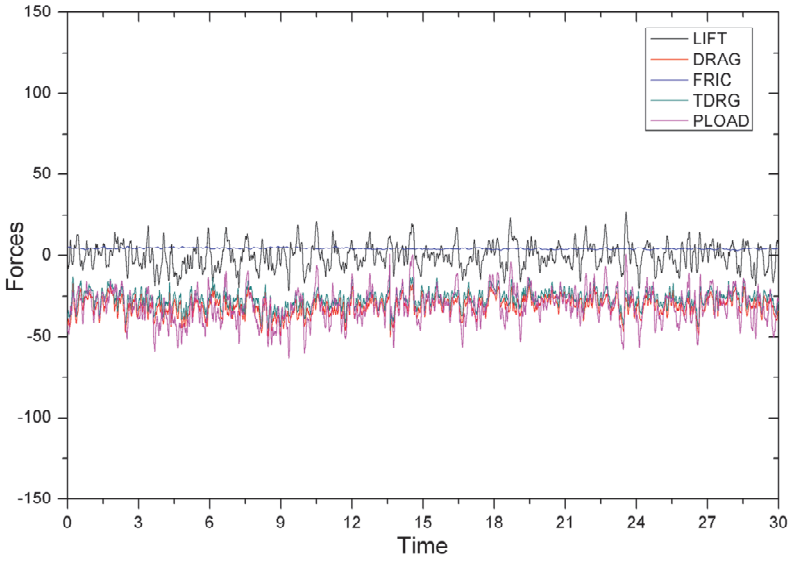

(a) d/h=1.7, Re_h=3584

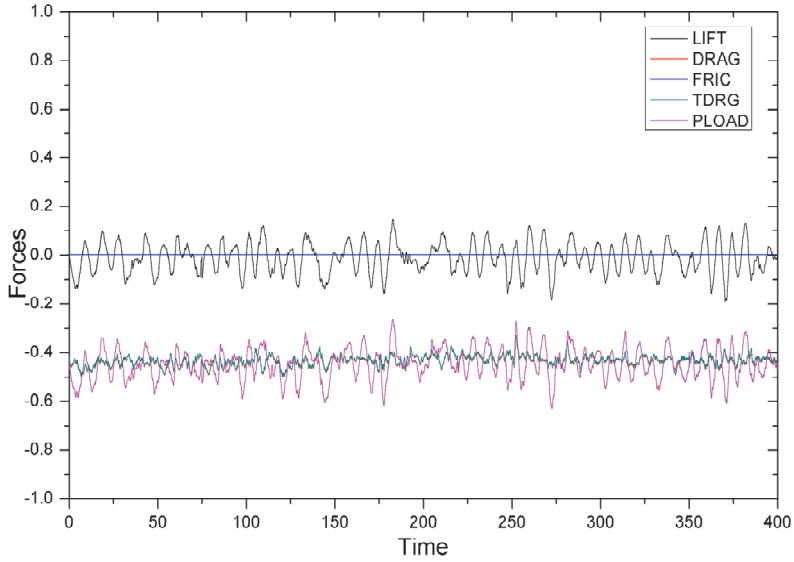

(b) d/h=2.0, Re_h=40000

Figure 4.48: Force time history around a single cube (top) and a cube in a matrix configuration (bottom).

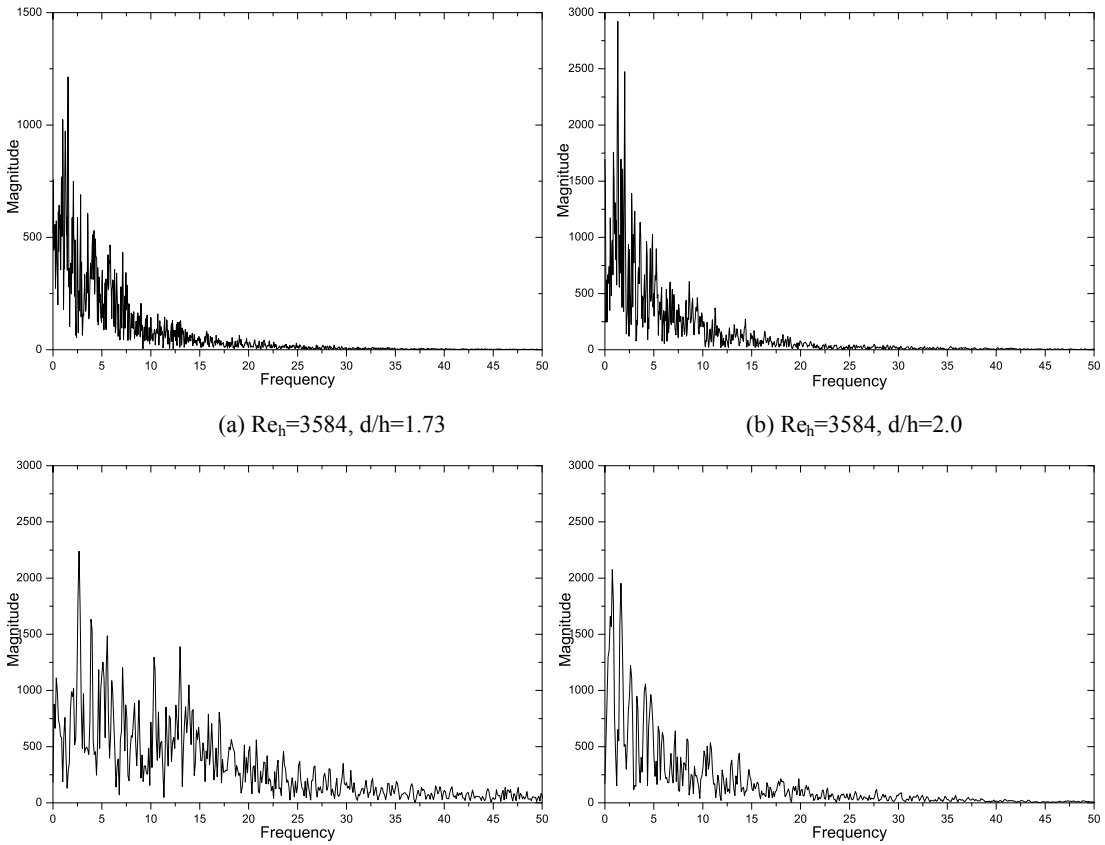

(a) Re_h=3584, d/h=1.73

(b) Re_h=3584, d/h=2.0

(c) Re_h=40000, d/h=1.73

(d) Re_h=40000, d/h=2.53

Figure 4.49: Frequencies plots for various positions along cubes height (matrix configuration). The relevant Reynolds numbers and submergence depth is indicated for all figures, the monitored positions along the cube height are: (a) z/h=0.5, (b) z/h=0.25, (c) z/h=0.95 and (d) z/h=0.5.

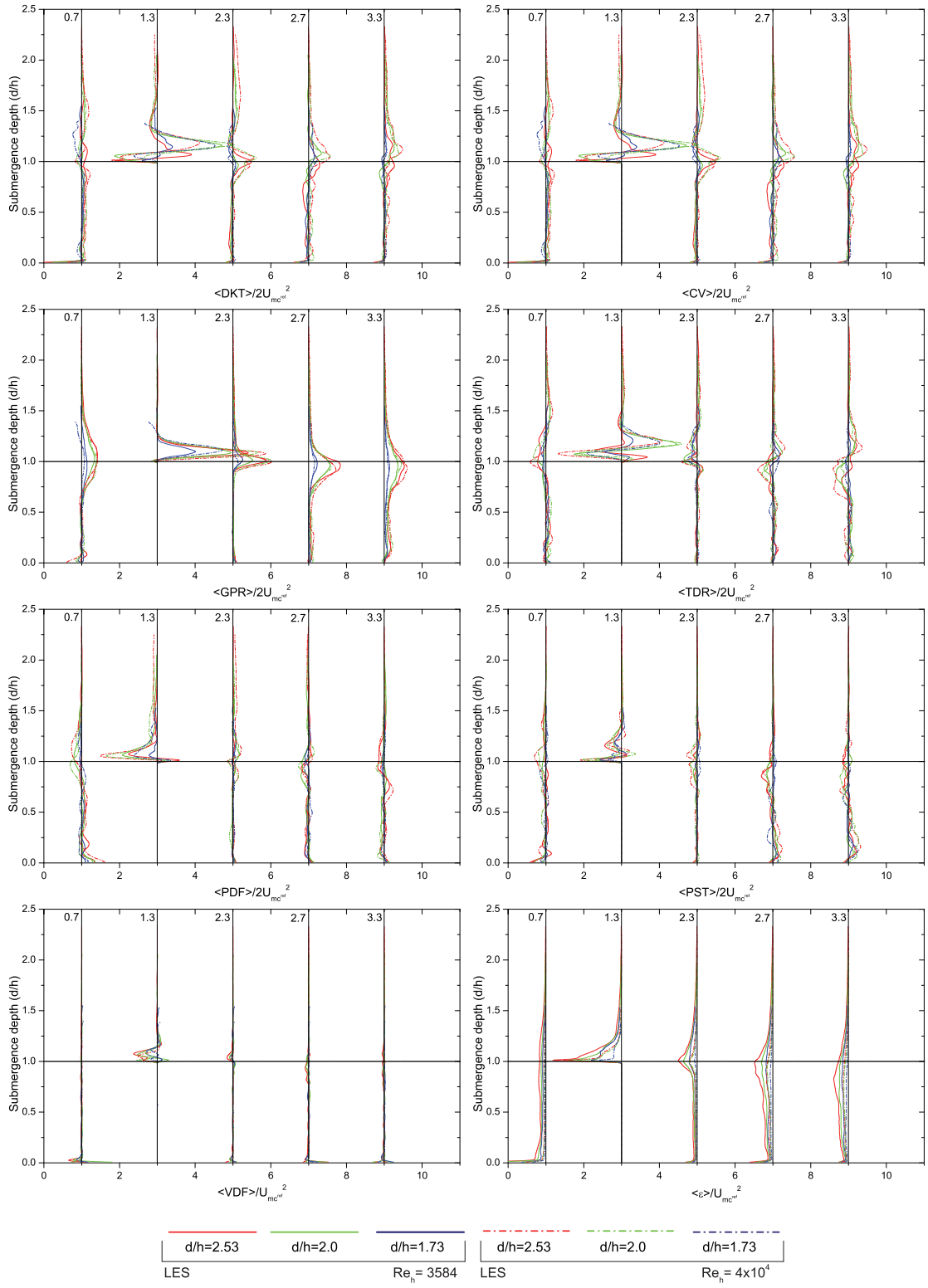

Figure 4.50: Turbulent kinetic energy budget terms at various positions in the XZ plane around a cube with a matrix formation plotted along the central XZ plane.

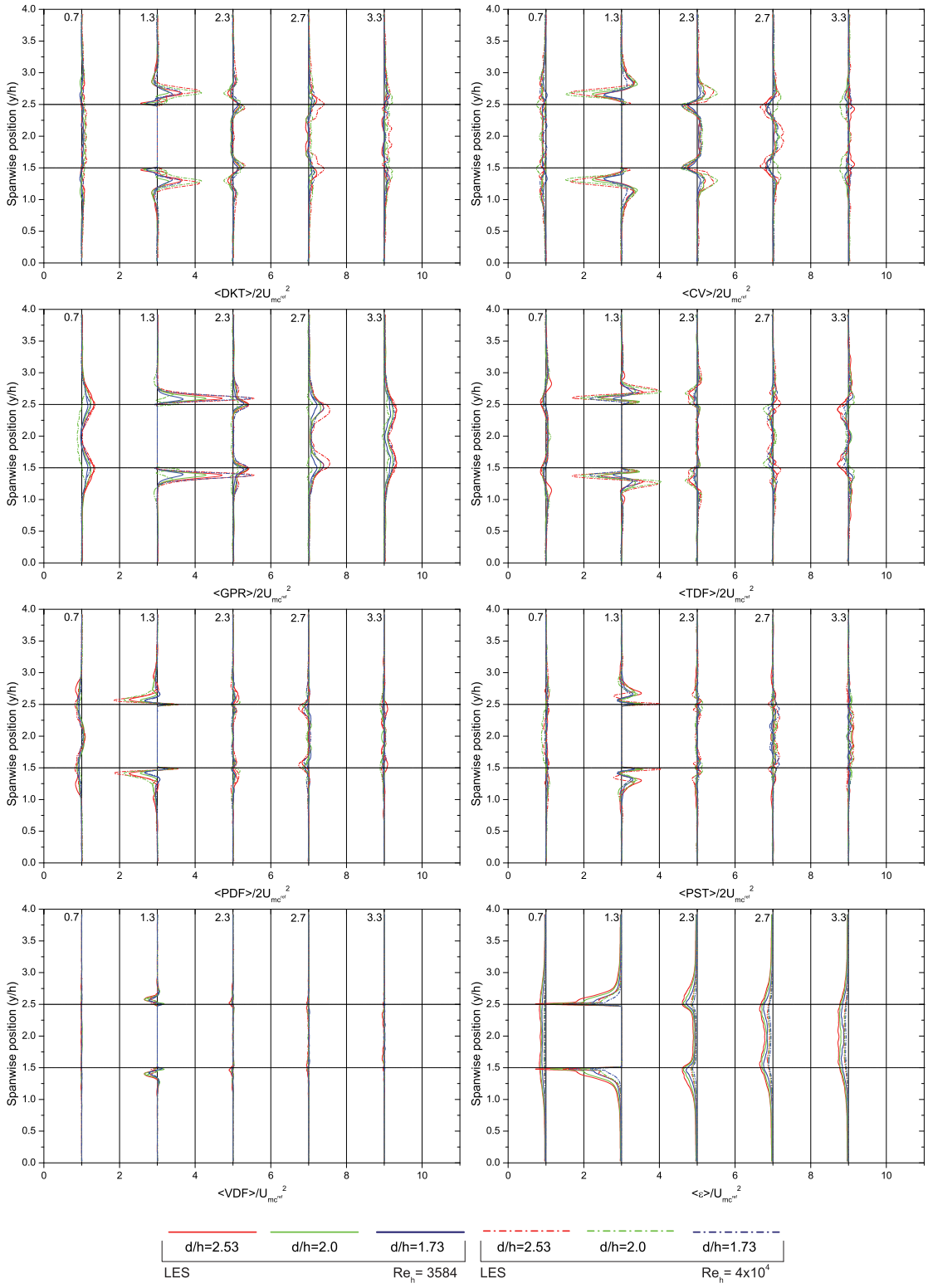

Figure 4.51: Turbulent kinetic energy budget terms at various positions in the XY plane around a cube with a matrix formation plotted at z/h=0.4.

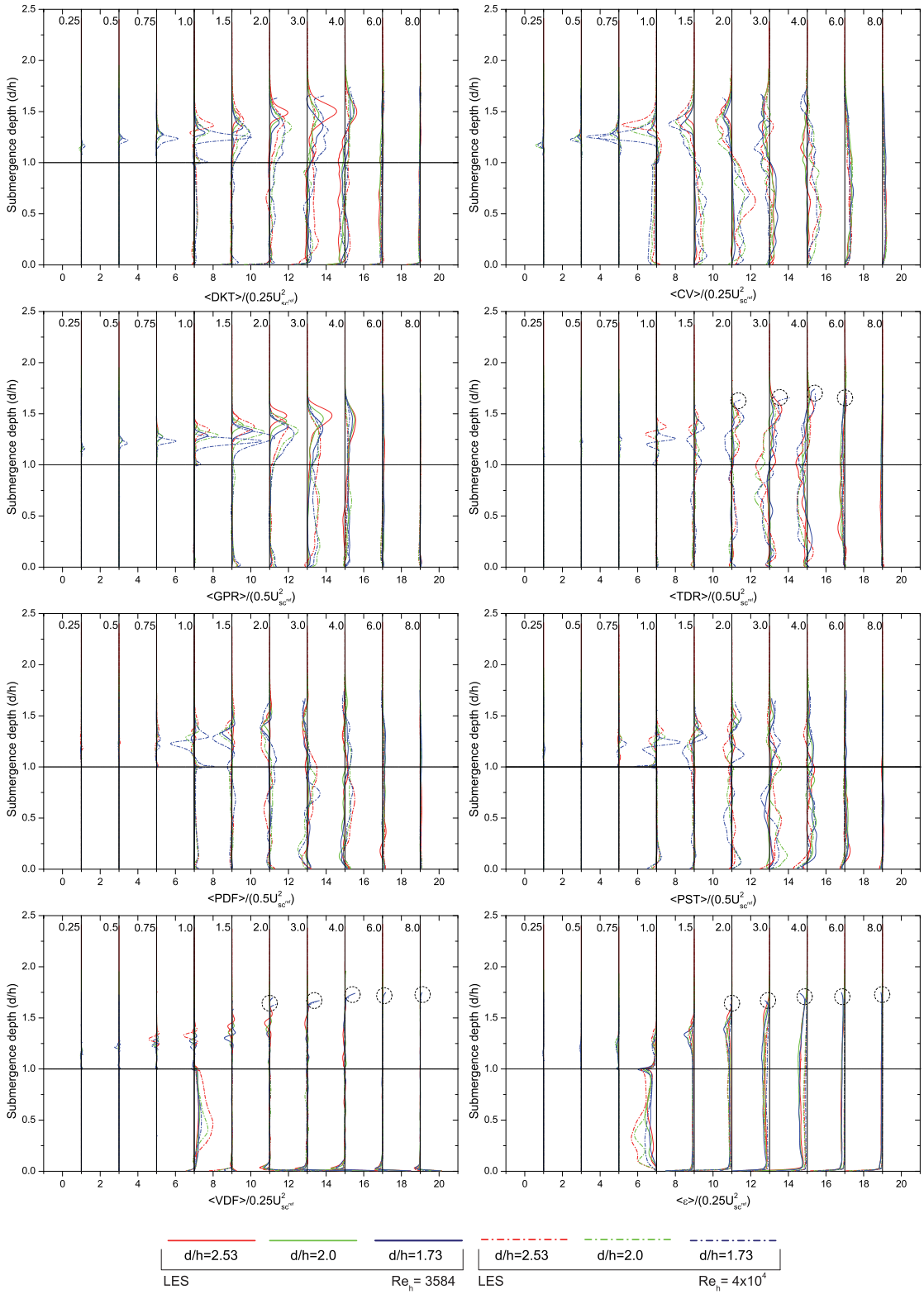

Figure 4.52: Turbulent kinetic energy budget terms at various positions in the XZ plane around a single cube plotted along the central XZ plane.

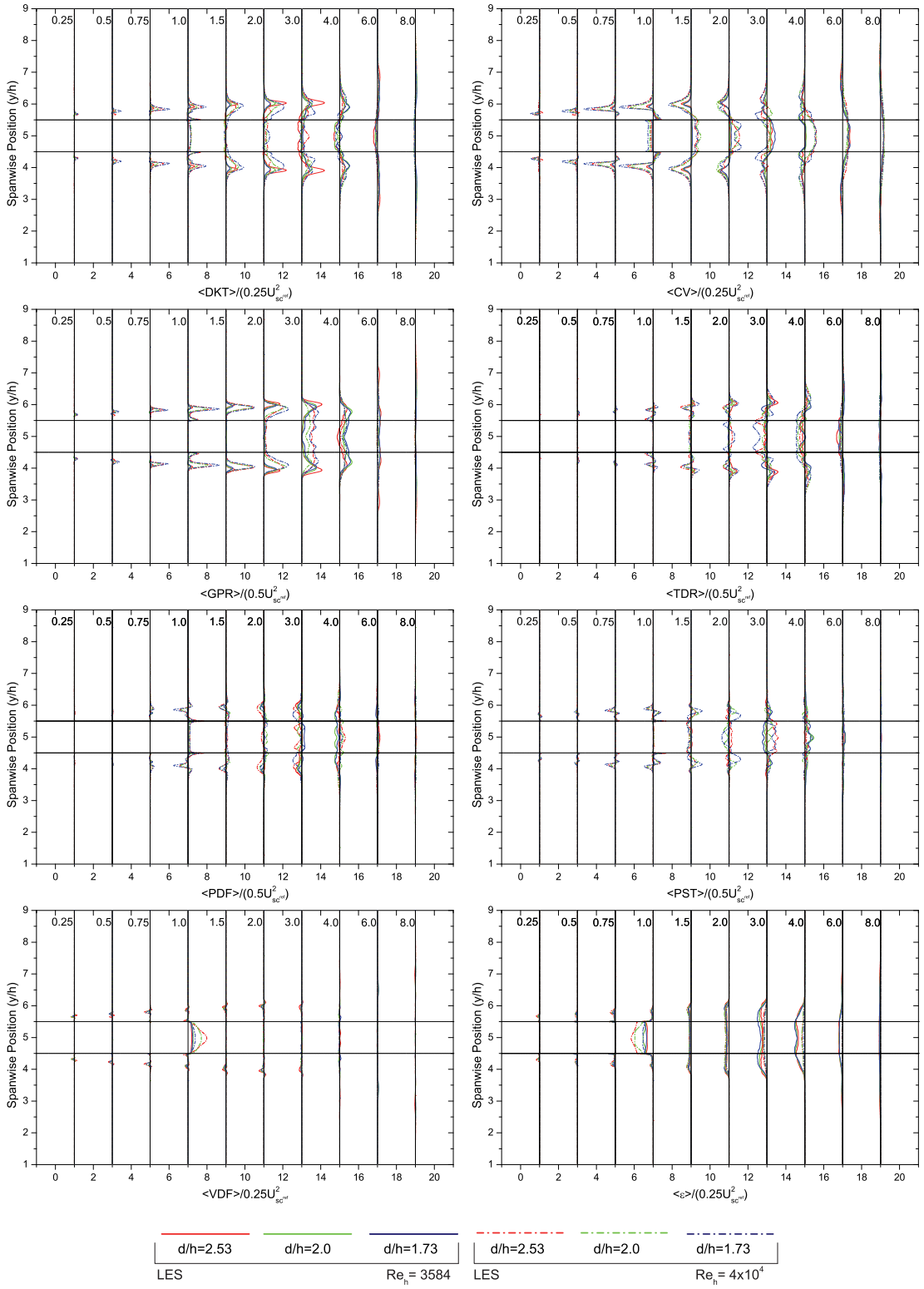

Figure 4.53: Turbulent kinetic energy budget terms at various positions in the XY plane around a single cube plotted at z/h=0.4.

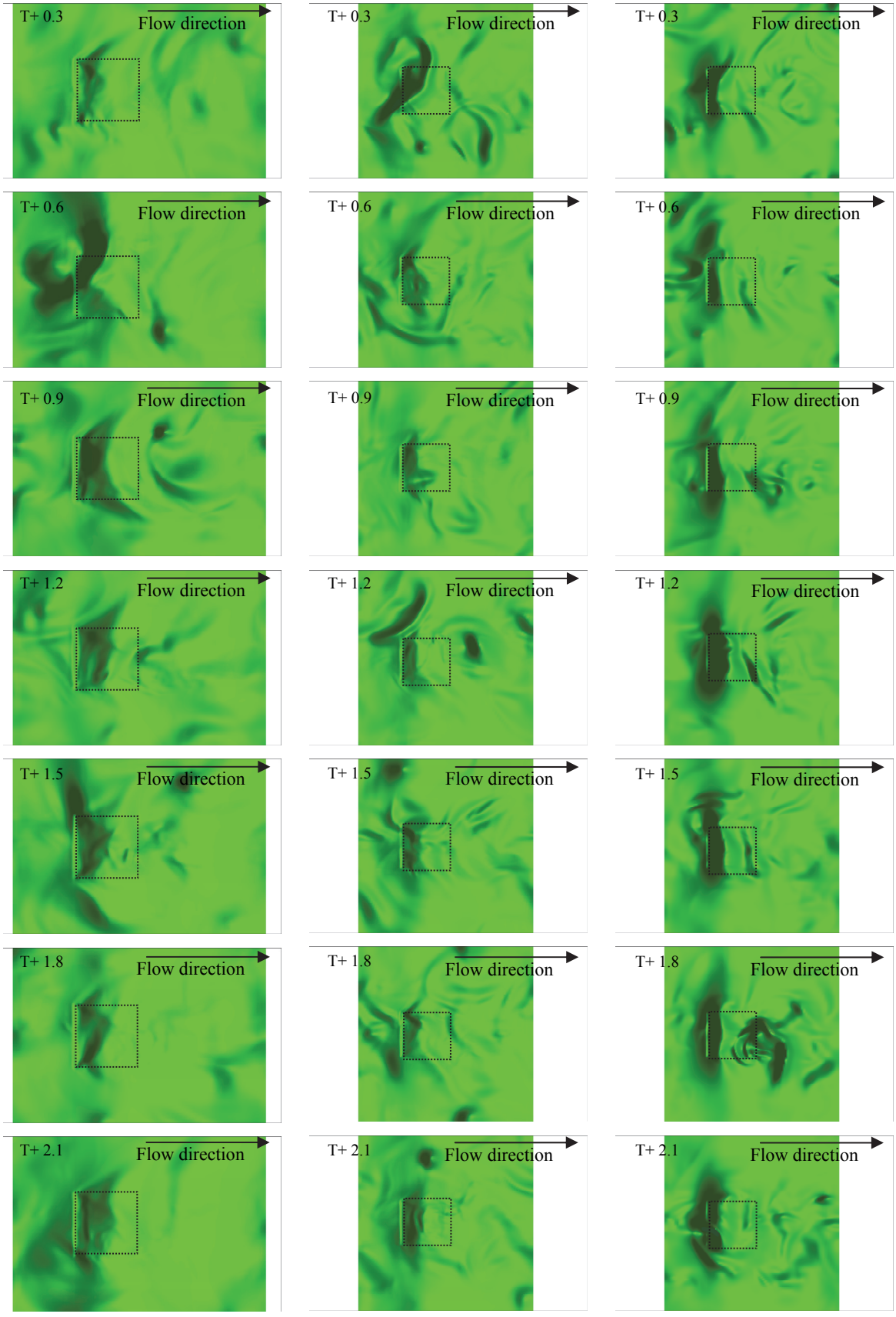

Figure 4.54: Instantaneous surface plots (100 Magnification) showing the evolution of surface structures, for Re_h=3584 and submergence ratios of (a) 2.533, (b) 2.0 and (c) 1.73.

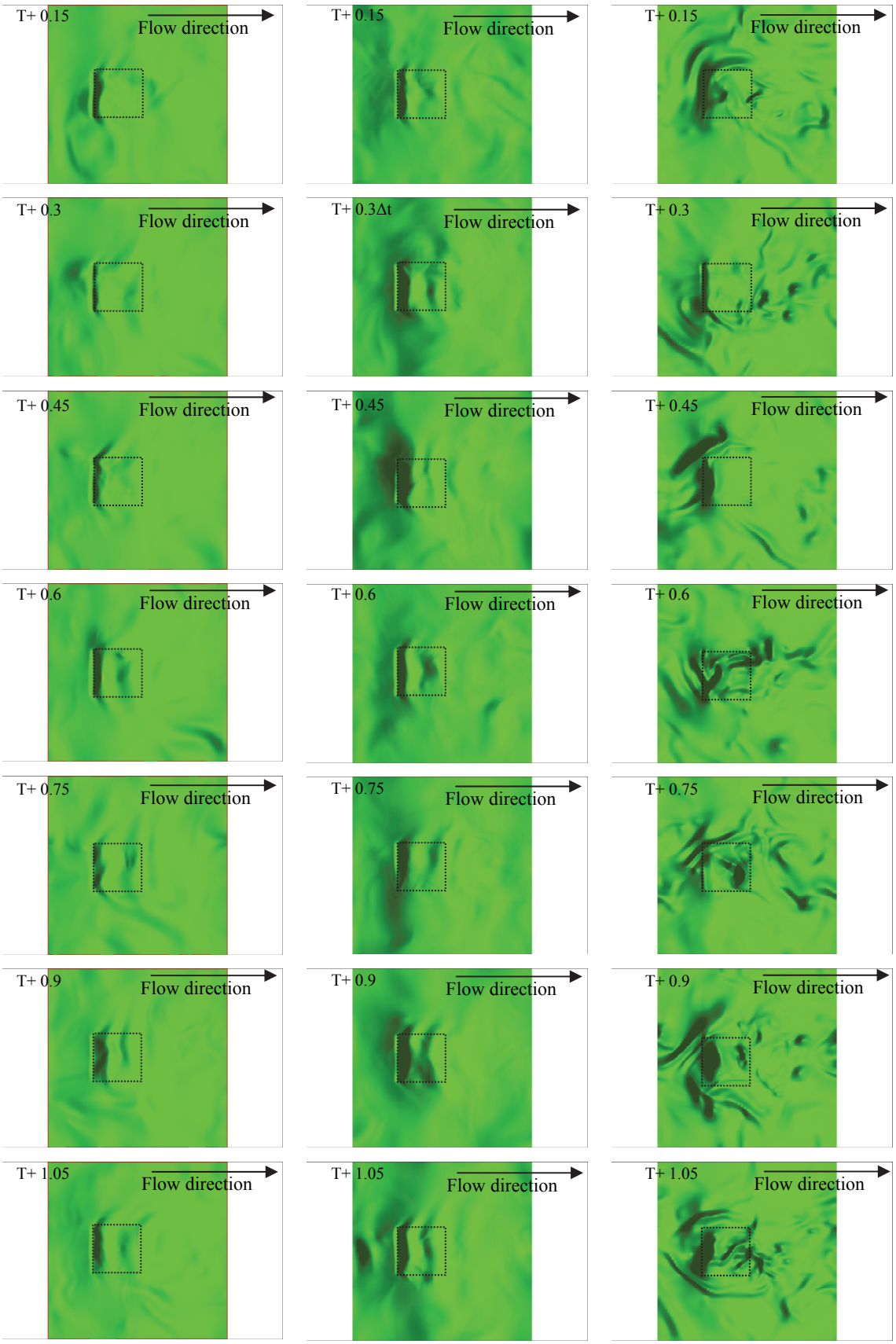

Figure 4.55: Instantaneous surface plots (100 Magnification) showing the evolution of surface structures, for Re_h=40000 and submergence ratios of (a) 2.533, (b) 2.0 and (c) 1.73.

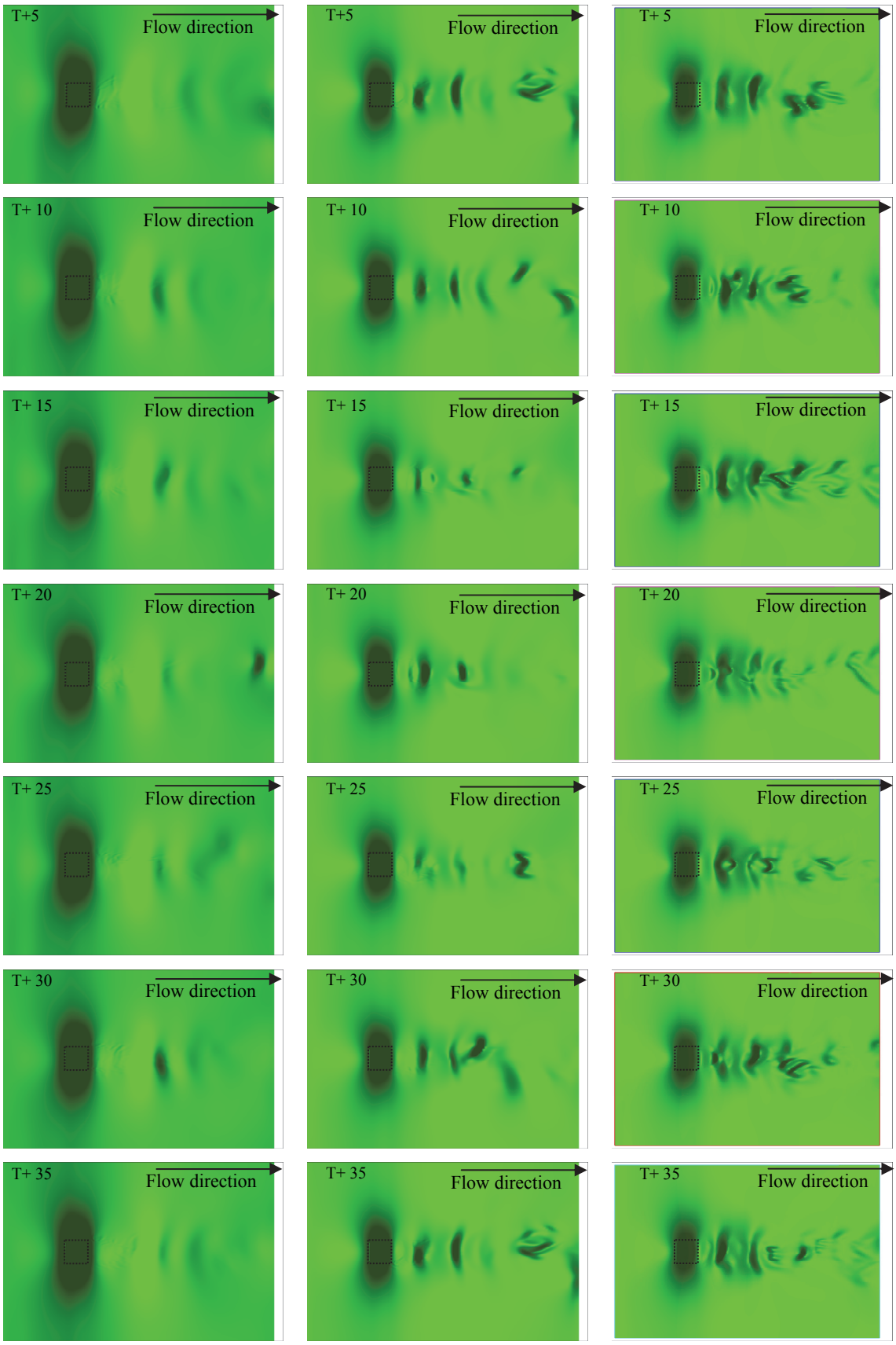

Figure 4.56: Instantaneous surface plots (50 Magnification) showing the evolution of surface structures, for Re_h=3584 and submergence ratios of (a) 2.533, (b) 2.0 and (c) 1.73.

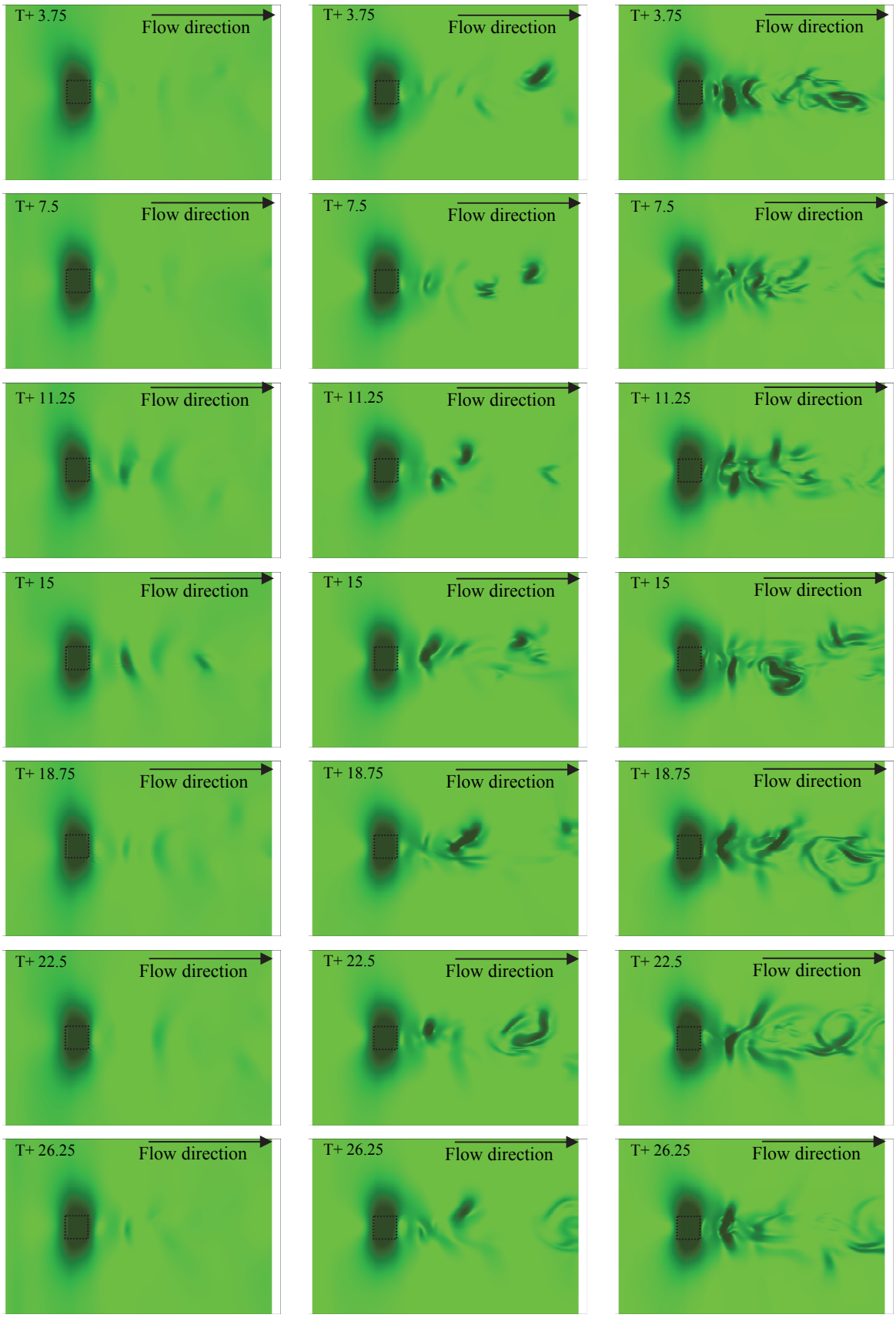

Figure 4.57: Instantaneous surface plots (50 Magnification) showing the evolution of surface structures, for Re_h=40000 and submergence ratios of (a) 2.533, (b) 2.0 and (c) 1.73.

Chapter 5 Effects of Submergence Depth on a Streamlined Body

This chapter examines the effect which depth variation has on the flow behaviour around a streamlined body for high Reynolds numbers. Initially, the computational capability of using the GCIBM on streamlined bodies for high Re flows is validated. Whilst the later study of the effects of a free-surface on a fully submerged fairwater is conducted at a relatively high Re and at operating conditions. LES and DES methods are used for the initial cases of validation and for the relatively high Re number case, while at operating conditions only DES is used.

5.1 Introduction

As reviewed in chapter 1, the last decade has been marked by vast improvements in computational resources. This increase in computer capability is reflected throughout many fields through the modelling of complex problems, which at one stage was not possible. Moreover, only recently researchers have begun performing full scale simulations of entire vehicles such as submarines with both the LES and DES approaches. One of the main reasons numerical simulations have seen a rapid growth, aside from the fact that results obtained using such techniques in general are comparable to those obtained experimentally, is the fact that on the whole, numerical simulations are far more detailed than what would otherwise be obtained by experimental means. In addition to being far less costly than experimental means, computational approaches are simpler in modelling the required conditions without the need for scaling. As a result, many industries as well as researchers have started to use such tools to understand

complex flow configurations of engineering interest. For example, from a naval point of view computational simulations have been used to examine the flow behaviour around and in the wake of a fully surfaced submarine for low Froude numbers [Zhang *et al* (2005)] as well as how the variation in flow condition around a submarine influence its stability during manoeuvres [Bettle *et al* (2009)].

To date, the study of flow around underwater vessels continues to present a computational challenge. This is due to generally having to deal with complex bodies at high Reynolds numbers. Whilst the interaction between the vessels wake and the free surface adds further complexity but also further interest. Such interaction can alter the behaviour of the wake, affect the flow loading (as seen in the previous chapter for a bluff body) on the vessel and can be used for detection purposes, especially in the case of submerged vehicles like submarines. The rapid development of computational resources and improvements in computational tools means that simulations with some sort of modelling of the turbulence are feasible for full-scale bodies. However, these simulations still require a significant use of computational power that is not widely available. Full body/geometry simulations are useful in showing how the flow tends to behave and the type of interaction and forces that arise. If such solutions are to be truly understood, it is necessary to understand the effect of all major parts separately or as simplified cases. In terms of submarines, simplified cases that have been examined to date include the effects on the flow on a bare hull [Yang & Lohner (2003)], flow separation and the stern [Svennberg & Fureby (2003)] and flow around surface piercing obstacles [Xing *et al* (2007)]. However no work has been performed on simplified cases in the presence of a free-surface boundary (non-surface piercing).

This chapter examines the effect that the free-surface boundary has on the structure and statistical behaviour of the flow around a fully submerged fairwater with no appendages for various submergence depths. Both LES and DES simulations are initially conducted in order to assess the accuracy of results predicted by both models; while later the DES method is used to study the effect of submergence on the fairwater without appendages at its operating condition.

5.2 Numerical outline

This section outlines the basic set-up for the numerical simulations for both the two-dimensional and three-dimensional streamlined geometries considered. Initially, the capabilities of the GCIBM in modelling streamlined bodies is validated by performing simulations around two, two-dimensional streamlined profiles, namely, the NACA 0012 and SUBOFF fairwater. The later study of flow past a fully submerged streamline body (fairwater) is performed at two different Reynolds numbers of $Re_{lc}=8\times10^4$ and $Re_{lc}=11\times10^6$, where l_c is the maximum chord length.

5.2.1 Two-dimensional

Both the NACA 0012 and SUBOFF fairwater geometries are modelled in a domain of $9l_c \times 4l_c \times 0.6l_c$ (streamwise, spanwise and vertical directions respectively), with the body being located at a position of $3l_c$ from the inflow boundary and centred about the spanwise domain extents. The domain extents in the streamwise and spanwise direction are kept consistent to those used for the fully submerged case. They are considered large enough such that neither boundary exerts any influence on the solution around the fairwater body. The NACA 0012 and SUBOFF fairwater profiles are incorporated into the grid-file using the same program that is used to generate the grid for the fully submerged fairwater. The NACA 0012 and SUBOFF fairwater profiles are obtained from Abbott & Doenhoff (1959) and Groves *et al* (1989) respectively, and given by equation 5.1 and 5.2 to 5.4. The profiles are also plotted in Figure 5.3.

$$y = \frac{t}{0.2}c\left[0.2969\sqrt{\frac{x}{c}} - 0.1260\left(\frac{x}{c}\right) - 0.3516\left(\frac{x}{c}\right)^2 + 0.2843\left(\frac{x}{c}\right)^3 - 0.1015\left(\frac{x}{c}\right)^4\right] \tag{5.1}$$

Fore-body x/l_c = 0.000000 to 0.269397

$$y = y_{\max}\left[1.73359\left(2A(A-1)^4\right) + 0.17146\left(\frac{A^2(A-1)^3}{3}\right) + \left(1-(A-1)^4(4A+1)\right)\right]^{0.5} \qquad A = 0.03229x \tag{5.2}$$

Mid-body x/l_c = 0.269397 to 0.435345

$$y = y_{\max} = \tag{5.3}$$

Aft-body x/l_c = 0.435345 to 1.000000

$$y = 0.09052\left[1.85244\left(B(B-1)^4\right)+2.5709\left(B^2(B-1)^3\right)+\left(1-(B-1)^4(4B-1)\right)\right] \qquad B=\frac{1-x}{0.82444} \tag{5.4}$$

As with the bluff body grids, stretching of grid cells is utilized to provide an increased resolution in the near vicinity of the body. Grid stretching is applied in both the streamwise and spanwise directions, while grid points in the vertical direction are distributed uniformly. Table 5.1 provides the basic grid information for both the NACA 0012 and SUBOFF fairwater geometries. The free-surface is neglected for both cases, instead the upper and lower boundaries are both set as non-slip walls. This is done to avoid any issues with the flow in the near vicinity of either body which would arise from using a free-surface (moving) boundary. The streamwise boundary conditions are set to inflow and outflow while a periodic boundary condition is applied on the spanwise domain extents. In both cases a uniform inflow is prescribed at the inlet while the outflow is set to be continuative.

			NACA 0012		**SUBOFF**	
Direction	**Domain Length**	**Cell No**	**Min Length**	**Max Length**	**Min Length**	**Max Length**
X	9	550	0.00569	0.03384	0.00569	0.03384
Y	4	260	0.00400	0.03037	0.00255	0.04129
Z	0.6	30	0.02000	0.02000	0.02000	0.02000

Table 5.1: Basic grid information for both NACA 0012 and SUBOFF fairwater.

As the purpose of these simulations is to validate the GCIBM application to a streamlined body, the solutions are allowed to run till shedding is achieved. This enables the pre-shedding pressure distribution around both cases to be obtained. The Re numbers for both the NACA 0012 and SUBOFF fairwater geometries are 9×10^6 and 1.012×10^6, respectively.

5.2.2 Three-dimensional

The fully submerged fairwater is modelled in a domain of size $9l_c \times 4l_c \times d\ l_c$, with the fairwater body being located at a position of $3l_c$ from the inflow boundary and centred about the spanwise domain extents, as illustrated in Figure 5.1. The geometry profile

and dimensions were provided by DSTL and is not a standardised/known body profile. The basic dimensions for the fairwater are $1l_c \times 0.22l_c \times 0.61l_c$ which correspond to the maximum length, thickness and height of the fairwater, respectively. Inflow and outflow boundary conditions are imposed in the streamwise extents while a periodic boundary condition is applied in the spanwise direction. The domain extents are considered large enough such that neither the streamwise and spanwise boundaries affect the solution around the fairwater body. The size of the domain was chosen based on numerous runs of various domain sizes, from which the current domain was found to be the most effective in balancing grid resolution, stretching and domain extent. Also no disturbances from the fairwater and surface waves were found to reach the spanwise boundaries. As noted earlier the inflow is prescribed as a constant flux boundary condition, set initially based on a uniform flow of unity in the streamwise direction. The use of the uniform inflow rather than a developed or prescribed distribution is due to the fact that at operating conditions of a submarine the flow ahead the body is not fully known. For the current case the depths of interest are when a submarine is close to periscope depth, though the flow in this region can be unsteady, it can be viewed as fluctuating about a mean or uniform distribution. Furthermore as the flow is free-developing ahead of a submarine the flow would not have a developed profile. Therefore a perturbated inflow would be the most ideal method for setting the inflow if the turbulent intensity ahead of a submarine was known. In this work, fluctuations are not added to the inflow for three main reasons:

1) The level and distribution is unknown.
2) Uncertainty in prescribing the fluctuation.
3) The need to increase the distance of the inflow boundary in order to allow for the fluctuations to stabilise.

The third factor also entails the need to increase the total grid resolution, this is currently unfeasible with the use of OMP parallelisation in both time and resource requirements.

As with the meshing of the two-dimensional cases, sufficient resolution around the fairwater is achieved through the utilisation of a stretched grid. The mesh size is reduced as the fairwater body is approached, with the smallest cells concentrating around and in the fairwater body. Stretching of the grid cells is applied in all directions, in both streamwise and spanwise directions the mesh reduces near the fairwater. While in the vertical direction the stretching of the cells is performed between the bed and the

upper extent of the fairwater. Figure 5.2 shows the typical mesh and distribution used. Stretching is again performed via the use of a hyperbolic function (4.1). Table 5.2 provides the basic domain information for the submerged fairwater. The flow around the fairwater is simulated at two very different Re numbers. Initially a simulation is conducted at $Re_{lc}=8\times10^4$ based on the inflow velocity and length of the fairwater, respectively. This is done such that the results of both LES and DES can be compared, while the later simulation is performed using the DES for $Re_{lc}= 11\times10^6$. The grid size is kept the same for both Re numbers considered.

Direction	Domain Length	Cell No	Min Length	Max Length
X	9.0	550	0.00569	0.03384
Y	4.1	260	0.00371	0.03613
	1.02133		0.00623	0.01901
Z	0.96237	80	0.00601	0.01768
	0.90474		0.00563	0.01707

Table 5.2: Grid information for fully submerged fairwater.

The Froude ranges between 0.4-0.44 for the three different submergence depths examined. All the simulations are started from a uniform inflow velocity distribution. The time given for the flow to stabilise is 2.5 domain wash through lengths, this corresponds to a non-dimensional time of 22.5. In terms of shedding frequency this corresponds to ~15 shedding cycles. The stabilisation cycles are to ensure that the wake is fully developed. Statistics are then taken over ~15 shedding cycles. Furthermore, all the simulations are initially started as LES, this is done to avoid the need to prescribe an initial value for the transport variable for the DES model.

5.3 Validation of IBM for streamlined bodies

In order to further validate the current code and the application of the GCIBM to streamlined bodies, the pressure distributions around two different streamlined bodies are considered at zero incidence to the flow and are compared with available data. The studied cases are for a NACA 0012 at $Re_{lc}=9\times10^6$ and the SUBOFF fairwater at $Re_{lc}=1.3\times10^6$. Figure 5.3 shows the cross-section profiles for the NACA 0012,

SUBOFF fairwater and also the cross-sectional profile for the studied fairwater. It can be seen that the SUBOFF fairwater is a good comparison to the studied case, while the NACA 0012 shows to be far slender than both fairwater profiles. The need for both cases arises due to the Re of the fully submerged fairwater. Although the SUBOFF fairwater profile provides a good comparison in terms of size and shape, the Re is too low for the operating condition of the later studied fairwater that has a Re of 11×10^6. It is for this reason that the NACA 0012 profile is considered. Furthermore both cases can show the predictive capabilities of the code around both bluff and slender streamlined bodies.

Figure 5.4 shows the pressure distribution around the NACA 0012 and the SUBOFF fairwater. The pressure distributions are extracted at the mid-plane in the vertical direction to minimize any possible wall effects on the solution. Both LES and DES modelling approaches are utilized and compared. The plotted pressure distributions for both the NACA 0012 and for the SUBOFF fairwater cross-sectional profiles are obtained prior to shedding, this is to avoid the need of averaging over the shedding cycles. Comparative results for the SUBOFF fairwater are obtained from Liu & Huang (1998), while the NACA 0012 is compared against those predicted by XFOILS. In both cases the Reynolds numbers are high, with the NACA 0012 case at a comparable Reynolds number to that of the fully submerged fairwater at operating conditions. Both predicted pressure distributions show good agreement when compared to the benchmarked distributions. However, regions of abnormal pressure variations are noted near the maximum thickness of both foils. This is partly attributed due to the reduction in the surface angle and possible negative coefficients arising from the stencil used [Tseng & Ferziger (2003)]. Such fluctuations can be removed with the use of higher grid resolution. Overall, the agreement is good especially for the higher Reynolds numbers of this study.

5.4 Effects of submergence on flow statistics

5.4.1 Time averaged data

Time averaged velocity and pressure distributions of the flow around a fully submerged fairwater are provided in Figure 5.5. The results are plotted along the XZ central plane.

The plotted results are extracted at positions $0.4x/l_c$, $0.7x/l_c$, $1.0x/l_c$, $1.5x/l_c$, $2.0x/l_c$ and $4.0x/l_c$ from the leading edge of the fairwater. The positions equate to $3.4x/l_c$, $3.7x/l_c$, $4.0x/l_c$, $4.5x/l_c$, $5.0x/l_c$ *and* $7.0x/l_c$ from the leading boundary, respectively. The positions of the plotted data are identified based on the leading edge of the fairwater (prior numbering convention). In all cases, the scaling of components is varied for clarity with the appropriate scaling shown in all figures. From Figure 5.5 it can be noted that from the time averaged streamwise velocity distribution, the average separation region located directly behind the fairwater is small, this is due to the fact that flow reversal is recorded in the near wake region. Although the separation region is found to be small on average it is also clear that the recovery of the flow profile in the wake region is slow. The flow profile is found to have not fully recovered at $3l_c$ downstream of the trailing edge ($4l_c$ from the leading edge). Furthermore, the flow in the streamwise direction shows a reduction in the near tip region, with the deficit being present across the plotted range (though reducing further downstream). The time averaged spanwise velocity <v> also shows the greatest unsteadiness in the near trailing edge region of the foil with the unsteadiness extending downstream on the wake. Spanwise velocity variations are present across the total measured range, with the strongest level of persistence being noted along the inter-mediatory section of the fairwater height.

The time averaged vertical velocity component <w> along the centre XZ plane shows the expected trend of up-washing ahead of the upper portion of the fairwater, while the acceleration of the fluid over the fairwater (streamwise) results in the reduction of the surface height. In the wake region <w> is also found to be present at all recorded positions downstream, on the fairwater. On average in the fairwater wake the flow experiences a down-wash effect in the vertical direction across the total fairwater height, excluding the near wall region. Furthermore, near the free-surface vertical velocity variations are increased with a reduced depth in the vicinity of the fairwater, this is due to the generation of surface waves by the flow over/around the fairwater. In all cases, all velocity components show unsteadiness across the plotted wake range, while dissipation and diffusive effects increase further downstream. The time averaged pressure <p> distributions show a build up of pressure ahead of the fairwater, while the greatest reduction in <p> occurs in the upper leading edge region of the fairwater due to flow acceleration and separation occurring. An increase in the pressure is also noted along the upper fairwater surface, this is partly attributed due to the reattachment for the flow and deformable behaviour of the free-surface. Like the velocity components, the

pressure variation is found to be the greatest in the near tip region of the trailing edge, while the level of variation in the pressure decreases downstream.

The difference between LES and DES solutions on the time average distributions ahead of the fairwater is most notable for the pressure near the lower wall. While in the wake, the DES solution shows a slightly higher distribution of pressure along the trailing edge. This is also notable on the distribution of <u> and <w> along the trailing edge. Both models show good agreement away from the near wall regions. The effects of depth variation are most notable on <p>, where reducing SBD causes an increase in the change of pressure in the wake of the fairwater attributable to the generation of larger waves. The effects of reduction in SBD on the time averaged velocity components are negligible.

Similarly, Figure 5.6 shows the time averaged velocity and pressure distributions around the fairwater in the XY plane ($0.2h/l_c$) for $Re_{lc}=8\times10^4$. As in the preceding chapter time averaged velocity and pressure profiles are also compared at various locations along the fairwater height. The plotted data are taken and compared about fixed locations of $0.2h/l_c$, $0.5h/l_c$, $0.75h/l_c$ and $0.85h/l_c$ of the fairwater height. The distribution of <u> shows that on average the flow near the trailing edge is separated, while the deficit in the wake diffuses downstream resulting in the reduction of the streamwise deficit and increase the region influenced by the wake. Both the velocity deficit in the wake region and separation regions are found to reduce along the height of the fairwater. Similarly, <v>, <w> and <p> also show strong variations around the fairwater body while diffusing downstream in the wake. The effects on <v>, <w> and <p> distributions along the height of the fairwater are found to be the same as that of <u>. Namely that the flow around the leading edge region remains unaltered, while in the near trailing edge and wake region <v>, <w> and <p> exhibit a reduction along the fairwater height and increased diffusive effects in the wake region. In addition, <w> is found on average to induce a down-washing effect across the wake region for all planes plotted. Again the difference between both the LES and DES solutions is most notable in the near wake region, while results show good agreement in the wake region.

Figure 5.7 compares the time averaged velocity and pressure distributions around the fairwater in the XZ centre plane for both $Re_{lc}=8\times10^4$ and $Re_{lc}=11\times10^6$. The results for $Re_{lc}=11\times10^6$ show little difference in comparison to the lower Re case. The largest

variations occur near the trailing edge where the unsteadiness is the highest. The general trend in the wake is found to be the same, while the effects of increasing Re is notable on the flow in the near wall profiles of the wake region, especially for the streamwise velocity component. Similarly, when comparing the time averaged velocity and pressure distributions about the XY plane (Figure 5.8), the results show no discernable difference, except near the trailing edge and in the near wake region where increasing Re leads to the velocity deficit being reduced. A similar behaviour for the time averaged distributions is also noted along the height of the fairwater.

5.4.2 Turbulent intensity and Reynolds stresses

Figure 5.9 and Figure 5.10 show the turbulent intensity and Reynolds stress distributions about the XZ plane for $Re_{lc}=8\times10^4$. The turbulent intensity plots show that the velocity perturbations are confined to the wake and near body regions. Although the presence of a junction vortex cannot be clearly seen from the time averaged data, it can be observed ahead of the fairwater where its influence is notable on all three components of the turbulent intensities and Reynolds stresses. Furthermore, the presence of both streamwise and spanwise turbulent intensities along the upper surface of the fairwater indicates that unsteadiness and mixing exists. This is partly due to the separation bubble near the leading upper edge and the flow interaction between the fairwater sides and the upper surface. The streamwise turbulence and Re stresses are found to be the highest along the upper surface and along the trailing edge. While across the wake region the streamwise intensities and Re stresses are most persistent over the lower portion of the fairwater height; showing that the flow in the near-wall region of the wake does not recover within the monitored extent ($4x/l_c$). Similarly the spanwise intensities and Re stresses are show a somewhat evenly distributed near the trailing edge, with the greatest variation occurring in the wake at $x/l_c=1.5$ in the near wall region. As with the streamwise intensities and Re stress, the influence of the spanwise velocity variation persists over the lower portion of the fairwater height for the plotted extent of the domain. The vertical intensities and Re stresses also exhibit this behaviour in the wake, while near the trailing edge the vertical velocity variation peak towards the upper portion of the fairwater. Both the streamwise and vertical velocity variations show a slight peaking near the upper extent of the fairwater downstream of wake indicating the presence of a tip vortex. It is also in this region that the cross Reynolds stress component $<u'w'>$ is most active, the Re cross component stresses $<u'v'>$ and

$\langle v'w' \rangle$ are very close to zero along the XZ centre plane for reasons of symmetry ($\langle v \rangle \rightarrow 0$). Similarly Figure 5.11 and Figure 5.12 show the turbulent intensity and Reynolds stress distributions about the XY plane for $0.2h/l_c$. The streamwise stresses and intensities are found to be the greatest around the fairwater body, while the remaining normal and cross components are generated only after flow separation/mixing occurs. In addition, both the streamwise stress and intensity exhibit the greatest variation along the separated shear layer region. This increase in the velocity variation is directly attributed due to the shedding of vortices. Whilst in the wake region both Re stresses and turbulent intensities are found to be the greatest at $1.5x/l_c$. This is also the case for both the vertical and spanwise components, implying that the major generation of turbulent energy is limited to the near wake region. Furthermore, all the normal components aft of $1.5x/l_c$ display a diffusive behaviour, with the level of fluctuations reducing while the influenced area increases. An additional peaking can also be noted in the wake for both the normal Re stresses and turbulent intensities occurring at $x/l_c \geq 2.0$. This in part is attributed to the increased influence and interaction between the wake and junction vortex and/or vortex stretching along the edge of the wake region. It can also be seen that the normal stresses contribute more to the generation and redistribution of turbulent energy than the cross Reynolds stresses. From Figure 5.12 it is found that $\langle u'v' \rangle$ has the highest magnitude from the Reynolds cross stresses at the trailing edge and in the near wake region. Variation along the height of the fairwater results in the influence of $\langle u'v' \rangle$ in the wake to reduce, while at the trailing edge the influence of $\langle u'v' \rangle$ is increased for increasing height along the fairwater. A similar trend for both $\langle u'w' \rangle$ and $\langle v'w' \rangle$ is also observed, namely that with increasing positions along the fairwater height the cross-stresses decrease in the near wake, while increasing at the trailing edge. Furthermore $\langle u'v' \rangle$ is found to produce positive Reynolds stresses along the monitored height of the fairwater, implying that on average u' and v' have a similar relation along the trailing edge and in near wake region. Similarly $\langle u'w' \rangle$ and $\langle v'w' \rangle$ are found on average to have a negative relation near the rear tip of the fairwater. Based on the average Reynolds cross stresses, it can be concluded that on average the cross stresses aid in the redistribution and redirection of TKE around the trailing edge, with their contributions being the greatest between the upper surface and fairwater sides. The fact that all the intensities and Reynolds stresses are much lower in the near wake region located near to the upper trailing edge of the fairwater ($x/l_c \geq 1.5$), shows that the turbulence in this region is relatively low and/or dissipates quickly. In contrast at the trailing edge, the turbulent intensities and Reynolds

stresses are found to be higher along the upper region of the trailing edge, indicating that flow over the trailing edge is constantly changing. This is due to the mixing of the flow occurring between the lateral and upper surface of the fairwater.

The difference between the LES and DES modelling approaches is again notable in the near wall region, where the DES model in general shows higher Reynolds stresses. Though this behaviour is expected from the SA model, the possibility exists that the SMG coefficient requires adjusting for such a case. Nonetheless the models show good agreement away from the wall regions.

Figure 5.13 and Figure 5.14 compare the turbulent intensity and Re stress distributions about the XZ plane for both $Re_{lc}=8\times10^4$ and operating Re numbers. The results show that in both cases a similar trend in the distributions of stresses and turbulent intensities is obtained about the centre plane. The lower Re cases are found to predict higher shear stresses over the fairwater and in the near wake region, however in the near wake region the data for $Re_{lc}=11\times10^6$ shows a stronger spanwise variation. Similarly, Figure 5.15 and Figure 5.16 compare the distribution of turbulent intensities and Reynolds stress distributions about the XY plane for both $Re_{lc}=8\times10^4$ and $Re_{lc}=11\times10^6$. Again, the general trend is found to be in good agreement when compared with the high Re results, the results show that increasing Re results in the increase in Re stresses near the fairwater. Furthermore the effect of depth variation results in the increase in both turbulent intensity and Re stresses in the streamwise direction, while the effect on the other components is less clear.

5.4.3 Turbulent kinetic energy distribution and spectra

Figure 5.17 shows the turbulent kinetic energy distribution about the XZ and XY planes for $Re_{lc}=8\times10^4$. In both planes the turbulent energy is seen to be the highest around the fairwater body and in the near wake region, this was also found to be the case for the Re stresses and turbulent intensities. The turbulent kinetic energy exhibits a strong increase in the near wake region for the lower portion of the fairwater height, before gradually reducing downstream. Variation in height along the fairwater results in the total level of TKE to change. In the wake region TKE is found to decrease with increasing height, while at the trailing edge TKE exhibits an increase. Again both LES and DES models show a variation in the distribution of TKE in the near wall regions and along the wake

extent for $0.2h/l_c$. This is expected as this trend was noted for both the normal Re stresses and turbulent intensity. Similarly, Figure 5.18 compares the TKE distribution about the XZ and XY planes for both $Re_{lc}=8\times10^4$and $Re_{lc}=11\times10^6$. The results show that in the XZ plane TKE *is* higher *for* $Re_{lc}=8\times10^4$ in the near wake, while in the XY plane $Re_{lc}=11\times10^6$ shows higher levels of TKE. The difference in the distribution of TKE in both planes can be attributed due to the coarse grid resolution in the vertical direction for $Re_{lc}=11\times10^6$. Variation in TKE along the height of the fairwater for $Re_{lc}=11\times10^6$ shows the same trend as previously found for $Re_{lc}=8\times10^4$, namely; TKE is found to reduce in the wake region while TKE at the trailing edge increases for increasing height along the fairwater. The effect of variation in SBD is not clearly evident, it is possible that the current statistical time is insufficient and a larger statistical time is required.

TKE spectra for both variations in Re and SBD are plotted in Figure 5.19 for the near wake region at PT_{fn2} ($2.0x/l_c$) along the XZ centre plane, and off-centred position of $(2\pm0.095)y/lc$. The off centred position is located at approximately ~85% of half the maximum thickness from the central XZ plane. Results are extracted at fixed heights of $0.1h/l_c$, $0.4h/l_c$, $0.7h/l_c$ and $0.9h/l_c$ in order to examine how energy transfer is affected in the wake. Only the results for $d/l_c=1.02113$ and $d/l_c=0.90474$ are considered. Results show that for all depths and Re the plotted energy spectra's exhibit the $-5/3$ energy cascade (inertial range), indicating fully developed turbulence in the wake; with the general trend in the energy cascade following a $-5/3$ and -3 behaviour. Both LES and DES results show good agreement along the monitored centre plane position. Increase along the fairwater height results in a net reduction in the TKE across all wave numbers and an increase in the dissipation of energy at the smaller wavelengths. Furthermore, the $-5/3$ energy cascade exists for all monitored points indicating that the wake along the total fairwater height is fully developed. Similarly for the offset position of $(2\pm0.095)y/l_c$ the energy spectrums also show a similar trend, while for the largest SBD a reduction in turbulent energy and increased dissipation is noted for both LES and DES models. A similar trend is also noted for the coarse DES simulation at $Re_{lc}=11\times10^6$, a build up of energy does occur in the smaller length scales. According to Shi *et al* (2000) the build up of energy is due to insufficient resolution, hence increased grid resolution is needed in the wake to reduce the build-up of TKE at the smaller length scales.

Figure 5.20 and Figure 5.21 compare how the transfer of TKE varies for various positions in the wake, results are extracted along the XZ centre plane ($2.0y/l_c$) and an offset plane [$(2\pm0.095)y/l_c$]. The vertical positions considered are for $0.4h/l_c$ and $0.7h/l_c$. The data is monitored at various positions in the wake and are termed $PT_{fn1,}$ PT_{fn2}, and PT_{fn3}, respectively. These points constitute to the following positions in the wake; $PT_{fn1}=0.1x/l_{c,}$ $PT_{fn2}=1.0x/l_c$ and $PT_{fn3}=2.0x/l_c$ and are given about the trailing edge of the fairwater. Comparing the LES and DES, the turbulent kinetic energy spectra plots the results show that in the near wake region (PT_{fn1}) the DES model exhibits a higher level of TKE across the entire spectrum of wave numbers, for the lower Re case ($Re_{lc}=8\times10^4$) for all SBDs. Furthermore, the DES energy spectra exhibit lower energy dissipation for higher wave numbers in comparison with the LES results. Comparing the spectra for PT_{fn1}, PT_{fn2} and PT_{fn3} shows that the TKE is continually dissipated downstream in the wake; in addition the wake flow is found to be fully developed for all considered positions. For $0.7h/l_c$ the TKE spectrums show an increased dissipation in the near wake region, this is indicated by an increased reduction of TKE for wake positions PT_{fn2} and PT_{fn3} when compared with the spectra plots for $0.4h/l_c$. In all cases reduction in SBD results in the increase in TKE across the spectra. This can be observed in both the DES results for $Re_{lc}=8\times10^4$ and $Re_{lc}=11\times10^6$ at the larger wave numbers. Furthermore the effect of reduction in SBD also results in the energy to increase at higher wave lengths. Again the same trends in the TKE spectra are noted to occur for the coarser DES simulation at fairwater operating condition of $Re_{lc}=11\times10^6$, with the notable build up of TKE at the smaller length scales.

5.5 Effect of submergence on flow structure

This section examines the instantaneous data of the flow around the submerged fairwater through the use of streamlines and vortical structures (VS). The VS are identified using the Q criterion, while the streamline traces are used to examine the near wall flow.

5.5.1 3D streamline traces

Figure 5.22 shows the instantaneous streamline plots around the fairwater for the three cases considered. Streamlines are traced trough points $y/l_c=1.95$, 1.98, 2.0, 2.02 and

2.05, along the leading face of the fairwater to ensure that the flow variation around the fairwater is well captured. The images are shown at two different time intervals for a SBD ratio of $d/l_c=0.96237$. The images show that the HSV in all cases forms and is wrapped around the fairwater with the legs extending downstream. The images show the HSV remains steady around the fairwater, while downstream of the fairwater the wake shows influence on the HSV legs. Comparing the streamline traces around the fairwater for both LES and DES ($Re_{lc}=8\times10^4$) shows that both models successfully capture the junction vortex around the fairwater and shedding in the wake. The notable difference between the two is in the junction vortex ahead of the fairwater, where the DES shows it to be closer than that of the LES results. The streamline traces also show that increasing Re results in the HSV being closer to the body.

5.5.2 Vortical Structures

Figure 5.23 to Figure 5.25 show VS generated about the fairwater body for all cases and SBDs considered. Vortices are identified for a value of Q=1. As with the Streamline traces the solutions are shown at two different time intervals. In all cases the general features of the flow are captured and are; the presence of a junction vortex in the form of a HSV, the generation of a tip vortex from the trailing tip of the fin and the wake region generated by the flow around the body. The HSV shows good agreement with the streamline traces, showing that the HSV is steady around the fairwater and with increased Re moves closer to the fairwater body. The tip vortex in all cases is found to be most clearly defined for the largest SBD and can be noted to persist for a large distance downstream. Reducing SBD results in the tip vortex shedding being influenced by the wake and occurs in a more broken state, meaning that the length and type of structure shed from the near tip region is altered. This is owed in part due to the shedding of VS at the trailing edge being unsteady, hence the size of the shedding structures at the trailing edge is constantly being altered, which increases with reducing SBD. It is for this reason that the wake structures are shown to occupy a larger portion of the fairwater height. Another possible explanation for the changing in the behaviour of the tip vortex is the reduction in vorticity in the near tip region; again this would be attributed due to the increased unsteadiness near the tip region.

The vortices shed from the lateral extents of the fairwater are found to be quite complex. The shedding structures are interlinked with streamwise vortices and constantly altering

due to the effects of the wall and free-stream flow, in addition to pressure variations due to waves generated by the deformation of the free-surface boundary. The wake structures are noted to persist beyond the outflow boundary; this implies that the flow does not fully recover after $5l_c$ downstream. Vortices are also observed to show a change in orientation and inclination angle further downstream of the wake. Similarly, the same behaviour is noted in the tip vortex for variation in SBD for $Re_{lc}=11\times10^6$. Furthermore the structure of the flow in terms of vortex arrangement is in good agreement with both LES and DES results for $Re_{lc}=8\times10^4$. In all cases neither the tip vortex nor any other VS exhibits any significant rise towards the surface.

5.5.2.1 Vortex alignment and persistence

Figure 5.26 shows the vortex data for Q>0 in the wake region of the fairwater for $Re_{lc}=8\times10^4$. The plotted data is extracted and complied along the centre XZ plane and a offset distance of 85% of half the maximum thickness of the foil [$(2\pm0.095)y/l_c$]. The data is extracted at the following positions in the wake of the fairwater PT_{fn1} ($1.1x/l_c$ – with respect to the leading boundary face), PT_{fn2} ($2x/l_c$) and PT_{fn3} ($3x/l_c$) in the streamwise direction across the total channel depth (d). As in the previous chapter the average value of Q is determined for times that Q is greater than zero. The time averaged value for Q shows that the strongest level of circulation/VS exists in the near wake region of the fairwater for $d/l_c<0.3$, while on average the strength of VS shows a reduction towards the upper surface of the fairwater. Above the fairwater the average value for Q is found to be very low all the way to the surface boundary. Similarly, the VS show a reduction in strength further downstream of the wake. The persistence of VS shows that VS are well established within the wake region. Results show that vorticity is present for up to and over 50% of the total monitored time across the total fairwater height and monitored positions. Furthermore, an increase in the level of persistence is notable near the free-surface boundary, though on average the circulation is found to be very weak. The effect is seen to increase when reducing SBD. The detected circulation is attributed due to the generation of surface waves as no VS are found near the free-surface. The vortex alignment plots show that in general vortices show a relatively low level of alignment with any given direction indicating that VS passing these points are tilted to some degree. However at PT_{fn3} vortices show a notable increase in alignment in the streamwise direction. The strongest non-alignment is recorded along PT_{fn2}. The increase in non-alignment in this region is attributed due to the increased intermittency

(mixing) occurring near/across the region. Similar observations can be drawn based on the vortex data for the offset plane; however it is in the near wake region that both planes show the greatest difference. Both LES and DES predictions of the statistical description of the VS in the wake and the associated alignments are found to be in good agreement, with the greatest variation occurring over the upper portion of the near wake region behind the fairwater. Finally, Figure 5.27 compares the vortex data for Q>0 in the wake region of the fairwater for $Re_{lc}=8\times10^4$ to $Re_{lc}=11\times10^6$. Results show that the general trend between the two flows remains unaltered, the effects of increased Re shows higher values of Q in the near wake region for the centre plane, while the alignment and persistence show little change. In general, it can be concluded to a certain degree that the vortex structures in the wake of fairwater are constantly being altered and stretched, and are a regular feature of the flow.

5.6 Forces and Shedding Frequencies

This section examines the effects that both Re and SBD have on the average forces, the variation in forces and shedding frequencies about the fairwater body. The calculated forces and shedding frequencies are presented in non-dimensional forms.

5.6.1 Effects of Re and SBD on Forces

Table 5.3 lists the time averaged forces and variation in forces for both LES and DES simulations at $Re_{lc}=8\times10^4$. The listed forces are the coefficient of lift (the resulting lift from spanwise and vertical pressure components), coefficient of the total drag which is comprised of both friction and pressure drag and also the coefficient of pressure (the total pressure difference acting around the fairwater). On average it is found that the reduction in SBD results in both an increase in the coefficient of pressure and the coefficient of the total drag force acting on the fairwater, whilst the variation in lift is found to exhibit an unsteady behaviour. The lift can be concluded to be unsteady for the simple reason that for a symmetrical body as in the case of the fairwater the average lift should be zero, if averaged over a shedding cycle. Furthermore, comparison of the variation in forces for both the lift and drag components shows that lift exhibits a larger variation. The effect of reducing the SBD causes the level of force variation to increase for all the listed coefficients. From comparing all the listed coefficients and variations

the largest changes are noted to occur for the pressure loading (coefficient of pressure) acting on the fairwater. Comparison between the LES and DES predicated coefficients and variation in coefficients, shows that both models exhibit the same trend.

	Forces and variation					
$Re_{lc}=8\times10^4$	*LES*			*DES*		
d/l_c	*1.02113*	*0.96237*	*0.90474*	*1.02113*	*0.96237*	*0.90474*
Lift	0.00418 ±0.00584	0.00396 ±0.0643	0.00260 ±0.00710	0.00490 ±0.00554	0.00342 ±0.00638	0.00123 ±0.00780
Total Drag	0.00194 ±0.00135	0.00271 ±0.00151	0.00594 ±0.00250	0.00209 ±0.00182	0.00380 ±0.00236	0.00466 ±0.005379
Pressure Loading	0.00594 ±0.00732	0.00586 ±0.00690	0.00656 ±0.00772	0.00482 ±0.0072	0.00486 ±0.00712	0.00572 ±0.00820

Table 5.3: Average force and force variation around a submerged fairwater LES and DES results.

Similarly, Table 5.4 compares the time averaged force coefficients and variation in forces for both the high and Reynolds number cases. On average it is found that the reduction is submergence depth results in the increase of the total drag coefficient acting on the fairwater. Variation in the force coefficients shows a good agreement between both Re cases, with the trend still showing an increase in force variation for reducing depth. The increased variation is attributed due to the alteration of VS in the near wake region for reducing depth; created due to an increased alteration in the pressure distribution due to the formation of large surface waves.

	Forces and variation					
Des	$Re_{lc}=11\times10^6$			$Re_{lc}=8\times10^4$		
d/l_c	*1.02113*	*0.96237*	*0.90474*	*1.02113*	*0.96237*	*0.90474*
Lift	0.00650 ±0.01018	0.00139 ±0.01062	0.00234 ±0.01204	0.00490 ±0.00554	0.00342 ±0.00638	0.00123 ±0.00780
Total Drag	0.00178 ±0.00074	0.00244 ±0.00149	0.00385 ±0.00334	0.00209 ±0.00182	0.00380 ±0.00236	0.00466 ±0.005379
Pressure Loading	0.00733 ±0.01036	0.00307 ±0.01090	0.00260 ±0.01344	0.00482 ±0.0072	0.00486 ±0.00712	0.00572 ±0.00820

Table 5.4: Comparison of average force and force variation around a submerged fairwater for $Re_{lc}=8\times10^4$ and $Re_{lc}=11\times10^6$.

5.6.2 Effects of Re and SBD on shedding frequency

Table 5.5 lists the determined shedding frequencies in the form of Strouhal numbers around the submerged fairwater for all considered depths. The listed data is that for both the LES and DES simulations conducted for $Re_{lc}=8\times10^4$. The shedding frequencies are obtained in a similar manner to that used in the previous chapter, namely, the shedding frequencies are determined based on the lift force variation and compared to the shedding frequency at various positions along the fairwater height at a fixed position in the wake. The use of two approaches is due to the unsteadiness of the flow, as well as to show how the averaged shedding frequency varies compared to point-wise frequencies. The point-wise shedding frequency is determined at three different locations along the height of the fairwater. The heights considered are $h/l_c=0.1$, $h/l_c=0.4$ and $h/l_c=0.7$, while the data is monitored along the central XZ plane at position PT_{fn2} (*2.0x/h*). The characteristic length used to compute the Strouhal number is that of the maximum thickness of the fairwater cross-section. The Strouhal number based on the lift force variation shows that with reducing SBD the average Strouhal numbers are reduced, regardless of which modelling approach is used the LES and DES trend remains the same. This means that the unsteadiness in the wake is increased with reducing submergence depth. Furthermore, LES is found to predict a slightly higher Strouhal number in comparison to the DES results. From the point-based Strouhal numbers it is found that the shedding frequency in most of the cases is altered along the height of the fairwater, which indicates that the wake is highly intermittent and constantly altering.

The point frequencies like the lift force all show that the unsteadiness in the wake is increased with reducing SBD. This behaviour is independent of the fairwater height.

	Shedding frequency					
$Re_{lc}=8\times10^4$	*LES*			*DES*		
d/l_c	*1.02113*	*0.96237*	*0.90474*	*1.02113*	*0.96237*	*0.90474*
Lift	0.3463	0.3282	0.3152	0.3344	0.3276	0.3090
Pt1	0.3605	0.3512	0.3143	0.3248	0.3213	0.3114
Pt2	0.3565	0.3512	0.3143	0.3441	0.3251	0.3150
Pt3	0.3565	0.3143	0.3143	0.3539	0.3438	0.3214
Pt_{avg}	0.3578	0.3389	0.3143	0.3409	0.3301	0.3159

Table 5.5: List of dominate frequencies found based on the lift variation and time history of PT_{fn2} in the wake of the fairwater for LES and DES data.

Similarly, Table 5.6 compares determined shedding frequencies in the form of Strouhal numbers for both $Re_{lc}=8\times10^4$ and $Re_{lc}=11\times10^6$. The shedding frequencies are obtained and listed in the same manner as previously used. Results show that regardless of Re the Strouhal numbers show little change, while the effects of reducing SBD are found to cause a reduction in the Strouhal number. From the point-based Strouhal numbers it is again found that the shedding frequency is altered along the height of the fairwater, which shows that the shedding behaviour/unsteadiness is independent of Re.

	Shedding frequency					
DES	$Re_{lc}=11\times10^6$			$Re_{lc}=8\times10^4$		
d/l_c	*1.02113*	*0.96237*	*0.90474*	*1.02113*	*0.96237*	*0.90474*
Lift	0.3336	0.3268	0.3120	0.3344	0.3276	0.3090
Pt1	0.3452	0.3234	0.3210	0.3248	0.3213	0.3114
Pt2	0.3388	0.3312	0.3219	0.3441	0.3251	0.3150
Pt3	0.333	0.3234	0.3173	0.3539	0.3438	0.3214
Pt_{avg}	0.3390	0.3260	0.3201	0.3409	0.3301	0.3159

Table 5.6: List of dominate frequencies found based on the lift variation and time history of PT_{fn2} in the wake of the fairwater for $Re_{lc}=8\times10^4$ and $Re_{lc}=11\times10^6$.

5.7 Effects of submergence on turbulent energy budget

Figure 5.28 shows the time averaged terms of the turbulent kinetic energy budget (TKEB) and their contributions to the associated processes of creating, enhancing, redistributing and dissipation of TKE, along the centred XZ plane. Again results are extracted from positions $0.4x/l_c$, $0.7x/l_c$, $1.0x/l_c$, $1.5x/l_c$, $2.0x/l_c$ and $4.0x/l_c$ (based on leading edge of fairwater) along the streamwise direction for all SBDs. As is the preceding chapter each term of the TKEB are plotted individually, again the scaling of components varies and the appropriate scaling is indicated on all the variable plots.

Figure 5.28 shows the TKEB about the XZ mid-plane for the submerged fairwater body. The significant variations in all the terms of the TKEB are found to concentrate around the fairwater and in the near wake region at $1.5x/l_c$, while further downstream in the wake the TKEB terms are found to be significantly lower and only show a notable contribution close to the wall. <DKT> shows that on average TKE is enhanced along the upper surface of the fairwater and along the upper shear layer at the tip of the trailing edge. Whilst along the region connecting the upper surface and fairwater sides, <DKT> is found to show an increase in dissipation/diffusion. TKE is also found to be enhanced along the trailing edge of the fairwater profile, while in the wake the level of variation in TKE reduces rapidly. The DES results are noted to show larger variations in <DKT> in contrast with the plotted LES results. <CV> shows the greatest influence in enhancement of TKE along the trailing edge over the range $0.2h/l_c$ to $0.5h/l_c$, whilst in the near wall region at the trailing edge the influence of <CV> reduces rapidly in comparison to the mid-upper portion. <CV> in the near wake is also found to enhance the TKE in the near wall region. <GPR> shows that the generation of turbulent energy is concentrated around the fairwater and reduces rapidly in the wake. The time averaged turbulent diffusion <TDR> shows the greatest influence on the redistribution of TKE in the near wake region, while enhancing the flow over the trailing edge tip. The <PDF> term is found to be responsible for the enhancement of the TKE along the lower region near the trailing edge of the fairwater; in addition the time averaged pressure diffusion is also responsible for the redistribution of turbulent kinetic energy over the upper surface near/at the separation region. The influence of <PST> is found to be relatively low to the aforementioned terms with the general trend being the redistribution of TKE in the near wake. Similarly, the time averaged viscous diffusion <VDF> and dissipation <ε> also show relatively low contributions to the TKEB away from the near wall regions.

Over the upper surface of the fairwater and along the trailing edge, <VDF> and <ε> both show strong diffusive and dissipative effects on the TKE. Both LES and DES models are found to show similar trend on the distribution and influence on the turbulent kinetic energy arising from the TKEB terms. However, due to the strong unsteadiness of the flow in the near wake region, a longer averaging time period is required in order to better examine the effect of SBD on the TKEB distributions in this region. Figure 5.30 compares the TKEB for DES results for $Re_{lc}=8\times10^4$ and $Re_{lc}=11\times10^6$, results show that the behaviour of the TKEB terms show little change with increasing Re. The clear notable differences are the greater influence of <ε> and <VDF> on TKE in the near wall regions.

Figure 5.29 shows the TKEB about the XY plane for $0.2h/l_c$ along submerged fairwater body. The significant variations occurring in the terms of the TKEB are once again found to concentrate around the fairwater and in the near wake region, while further downstream of the wake the TKEB terms show a significantly lower contribution. <DKT> shows that on average the TKE is enhanced in the wake along the separated shear layer generated near the trailing edge, whilst in the wake <DKT> is found to show an increase in the diffusion/dissipation of TKE along the central plane at $y/l_c=2.0$. For an increasing height <DKT> is found to display a similar behaviour in the near tip region, however the spanwise effected region reduces due to the size of the separation region reducing with increasing height. Similarly, <GPR> and <TDR> also show a similar behaviour in the near tip region and along the height of the fairwater. <CV> is found to show the opposite behaviour along the separated shear layer, hence <CV> is mainly responsible for the redistribution of TKE along the separated shear and near the trailing edge. <CV> also shows a strong influence in the near wake region. Along the height of the fairwater <CV> exhibits a similar behaviour as the aforementioned terms, namely, <CV> exhibits an reduction in the near wake region and reduced spanwise influence near the trailing edge. The <PDF> and <PST> show the same behaviour along the separation shear layer near the tip and near wake region, both <PDF> and <PST> aid in the redistribution of energy around the outer shear layer region, while assisting in enhancing the TKE along the inner shear layer region. A similar behaviour is noted for both <PDF> and <PST> in the near wake region. However, near the trailing edge tip <PST> is found to aid in the redistribution of TKE, whilst <PDF> aids in the local enhancement of TKE. Again the effects of <VDF> and <ε> are found to be small and concentrated along the body and in the near wake region.

All terms are found to have a reduced area of influence along the near wake and trailing edge region for increasing fairwater height, whilst the level of contribution of all terms to the TKEB initially show an increase with increasing height along the fairwater before reducing. Near the upper surface of the fairwater nearly all TKEB terms show an increase, this increase is directly related to the presence of the tip vortex. No discernable effects of reduction in SBD are found for the TKEB and between the DES and LES simulations. Both LES and DES results show the same trend, whilst discrepancies in some terms are due to unsteadiness, showing that certain terms may require a longer period to stabilize and that the current statistical time may be insufficient.

Figure 5.31 compares the TKEB results for both high and operating Reynolds numbers. It is found that the behaviour of the TKEB terms show little change with an increasing Re and with notable increases occurring in <GPR>, <DKT> and <CV>. Furthermore, both <ε> and <VDF> also show little change away from the near wall regions, implying that the eddy viscosity controls the level of dissipation around the fairwater and near wake region. Again, no significant effect of reduction in SBD can be noted on TKEB terms for $Re_{lc}=11\times10^{6}$.

5.8 Free-Surface Signatures

Figure 5.32 through to Figure 5.34 show the free-surface wave profiles generated by the submerged fairwater body for all of the SBDs considered. Figure 5.32 shows the surface wave profiles generated using the LES modelling approach ($Re_{lc}=8\times10^{4}$) whilst Figure 5.33 and Figure 5.34 show the surface wave profiles for the DES results for $Re_{lc}=8\times10^{4}$ and $Re_{lc}=11\times10^{6}$, respectively. In all cases the surface waves are shown about the XY plane and magnified in the lateral direction to show the waves at the surface boundary. The images are kept consistent with the earlier extracted vortical structures (VS) presented in section 5.5.2 . In all cases no surface distortion due to turbulent structures or interaction with turbulent structures is found. This is due to the fact that VS behind the fairwater (in the wake region) exhibits no significant rise towards the surface. Hence in all cases the surfaces waves and distortions are generated solely due to the fairwater body. In all cases the effect of reducing SBD results in an increase to the amplitude of the propagating surface waves and the number of trailing waves. The increase in the number of trailing waves is due to the fact that the generated waves require a larger

period to dissipate. In all cases the surface restoring force is that manly of gravity. Similarly, the wave dispersive angle for all cases are found to be the same, this is expected as the only waves are due to the fairwater body. The enclosing wave angle is indicated on all the wave plots, and a enlarged wave is shown in Figure 5.35 which corresponds to LES for $(d-h)/l_c=0.32847$. Two wave angles are indicated in Figure 5.35 as well as all other surface wave images, the inner wave angle is based on the starting location of the fairwater, while the outer angle is based on the intersection of the wave angle and the symmetry line. The measured wave angles for all cases are found to be between 38°- 40° showing that the surface waves are that of a Kelvin kind. This behaviour was also observed by Chang *et al* (2006) and Yu *et al* (2008). The length of the domain is considered acceptable though some waves are found to extend past the lateral boundaries, this is because the wave intersects only near the outflow boundary hence not influencing the solution.

5.9 Summary

In summary, this chapter has examined the effects that depth variation, Re and turbulence models have on the statistical behaviour of the flow around a fully submerged fairwater body. The time averaged data, Re stresses and TKE distributions have shown that the major part of the turbulent energy and flow variation is confined to the near wake region of the fairwater. The wake is found to grow behind the fairwater whilst the level of turbulence reduces and continues to do so further downstream. Within the measured wake range the flow is found to have not fully recovered even though on average the wake/separation region is found to be small. In all cases for all monitored positions the TKE spectrums have shown that the wake is fully developed and that with reducing depth the level of TKE in the wake is increased. Similarly, the effects of reducing SBD is noted to result in the increase in TKE along all wave numbers, whilst the effects are less pronounced on the time averaged velocity components. The pressure, streamwise intensity and Re stresses are found to be influenced by reducing SBD.

No vortices generated around the fairwater are found to rise near to or interact with the free-surface boundary. The general VS captured around the fairwater are the junction vortex in the form of a HSV, the tip vortex originating from the trailing tip of the fairwater and the wake region generated by the flow around the body. The HSV remains

steady around the fairwater, whilst downstream of the fairwater the wake shows influence on the HSV legs. Reducing SBD results in the tip vortex shedding being influenced by the wake and occurs in a more broken state. This behaviour is observed in all cases and partly attributed to the increase in unsteadiness in the shedding of structures along the height of the fairwater. Both of the LES and DES results show good agreement for the behaviour in VS, with the notable difference being the location of the head portion of the HSV, while increasing Re results in the HSV being closer to the body. Furthermore, vortex persistence is found to be well established within the wake region with results showing that vorticity is present for up to and over 50% of the total monitored time across the total fairwater height and monitored positions, with the average strength reducing downstream. The strongest non-alignment of VS is found at PT_{fn2}, with the increase in non-alignment in this region attributed due to the increased intermittency.

The time averaged forces and variation in forces have shown that the reduction in the submergence depth results in the increase in the coefficients of both the pressure and total drag coefficients determined about the fairwater, whilst the variation in the lift coefficient is found to be unsteady. Comparison of the variation in forces for both the lift and drag components shows that lift exhibits a larger variation. The effect of reducing the SBD causes the level of force variation to increase for all the listed coefficients. Both LES and DES are found to show the same behaviour, similarly increasing Re also exhibits the same trend. Furthermore, increasing Re is also found to show an increase in the variation of the lift and pressure forces.

In terms of shedding frequencies (Strouhal numbers), both point based and lift force based indicate that for reducing SBD the Strouhal number reduce. Again both LES and DES modelling approaches show the same trend. Increasing Re is found to show the same discernable influence on the Strouhal number for the examined depths. In all cases the Strouhal number ranges between 0.3-0.36.

The TKEB terms are found to show the greatest variation in the near tip and near wake region, while further downstream the contribution of the TKEB terms is found to reduce substantially. For both $Re_{lc}=8\times10^4$ and $Re_{lc}=11\times10^6$ <DKT>, <CV> and <GPR> are found to show the strongest variation. Furthermore increasing Re shows little change in the <ε> and <VDF> implying that the eddy viscosity exceeds the molecular viscosity

and controls the level of dissipation around the fairwater and in the near wake region. In all cases <GPR> is found to exceed <ε> around the fairwater. Furthermore, the TKEB terms for all cases show a reduction in influence in the wake region and along the height of the fairwater.

Finally, in all cases the surface waves are generated solely due to the fairwater body, whilst the effects of reducing SBD results in increasing the amplitude of the propagating surface waves and the number of trailing waves. In all cases the surface resorting force is that of gravity. In all cases [LES ($Re_{lc}=8\times10^4$), DES ($Re_{lc}=8\times10^4$) and DES ($Re_{lc}=11\times10^6$)] the wave behaviour is found to remain the same. The enclosing wave angle is measured to be between 38°- 40° for all cases showing that the surface waves are that of a Kelvin kind, controlled by gravity and local inertial effects.

5.10 Figures

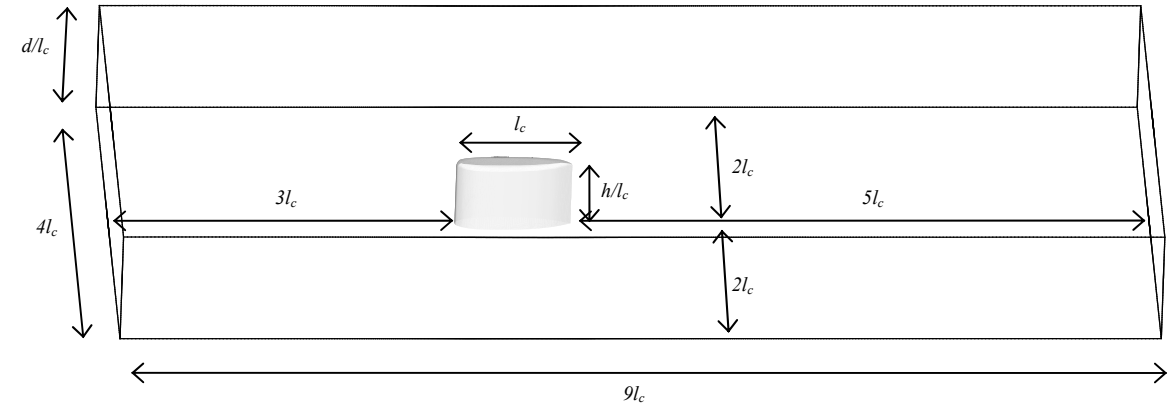

Figure 5.1: Domain size and standard configuration for submerged fairwater.

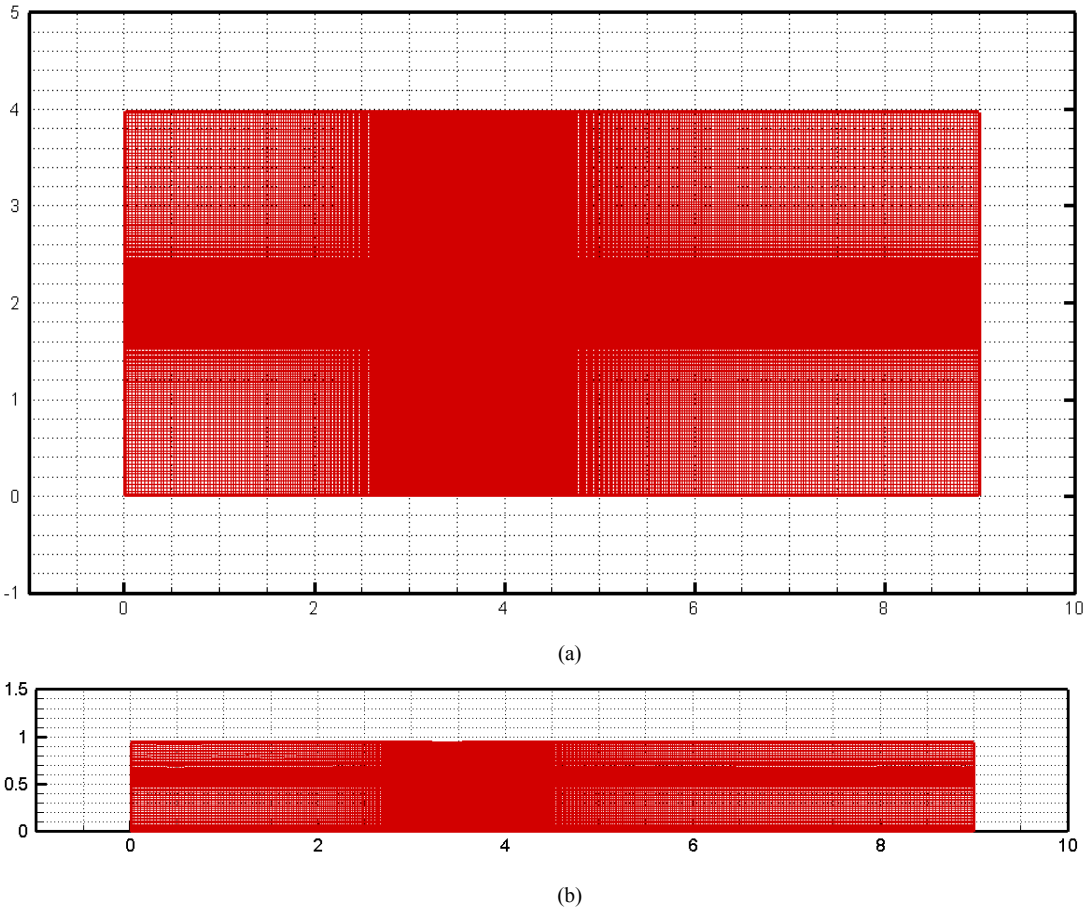

Figure 5.2: Domain mesh distribution for the modelling the submerged fairwater.

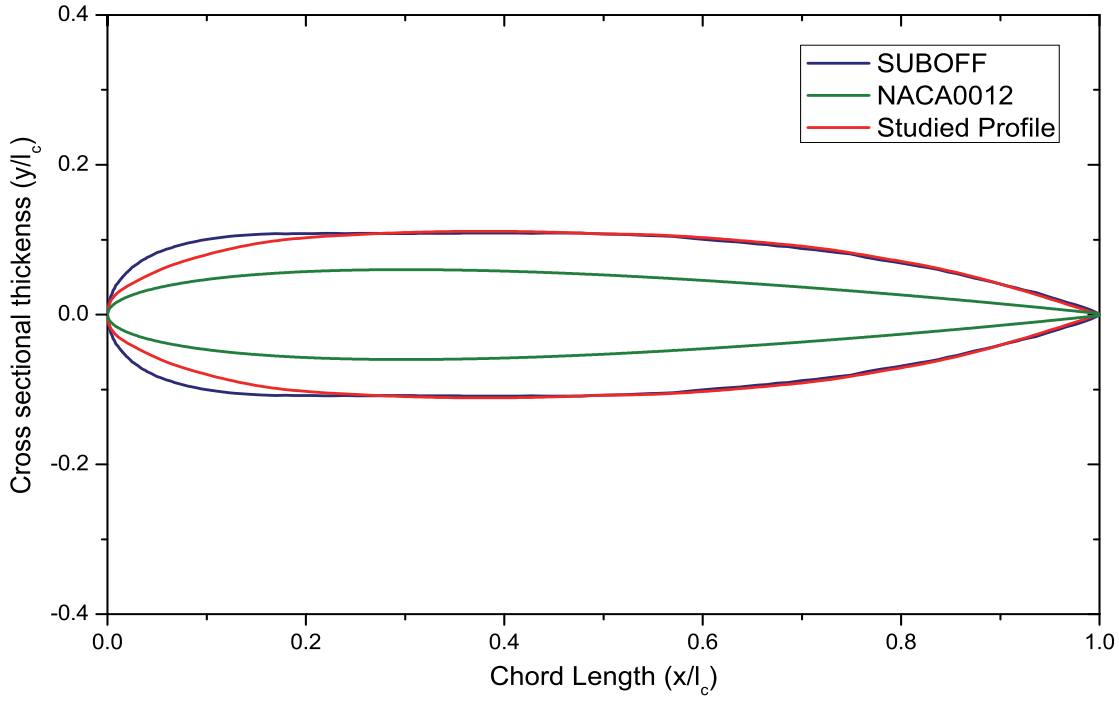

Figure 5.3: Cross sectional profile for NACA 0012, SUBOFF and studied fairwater.

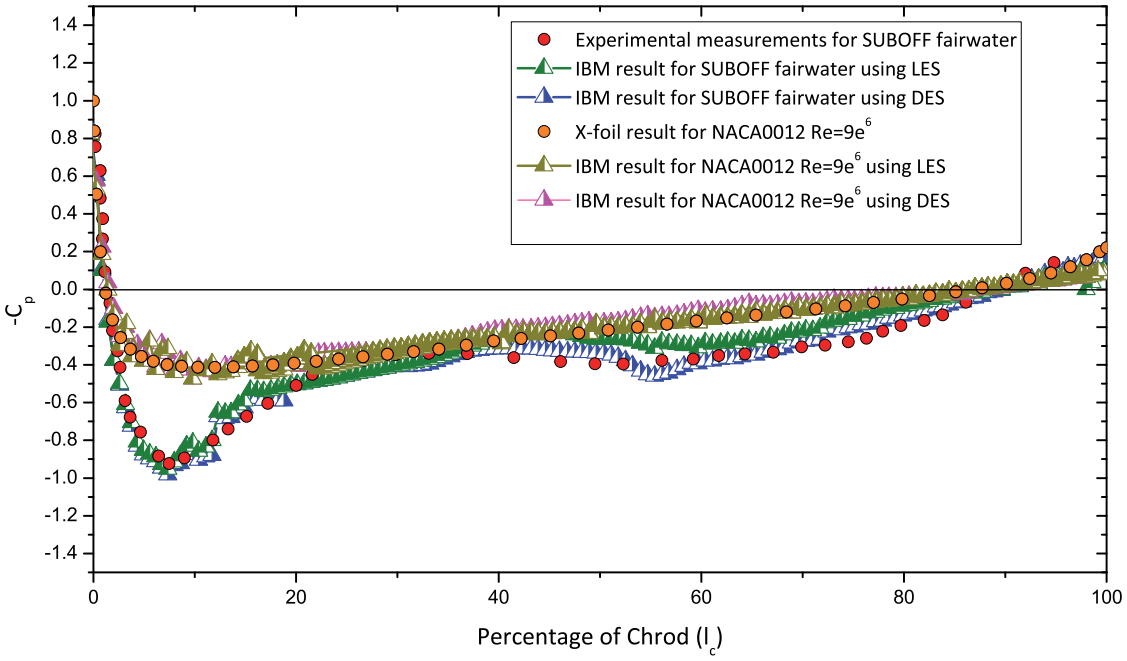

Figure 5.4: Pressure distribution around NACA 0012 and SUBOFF fairwater.

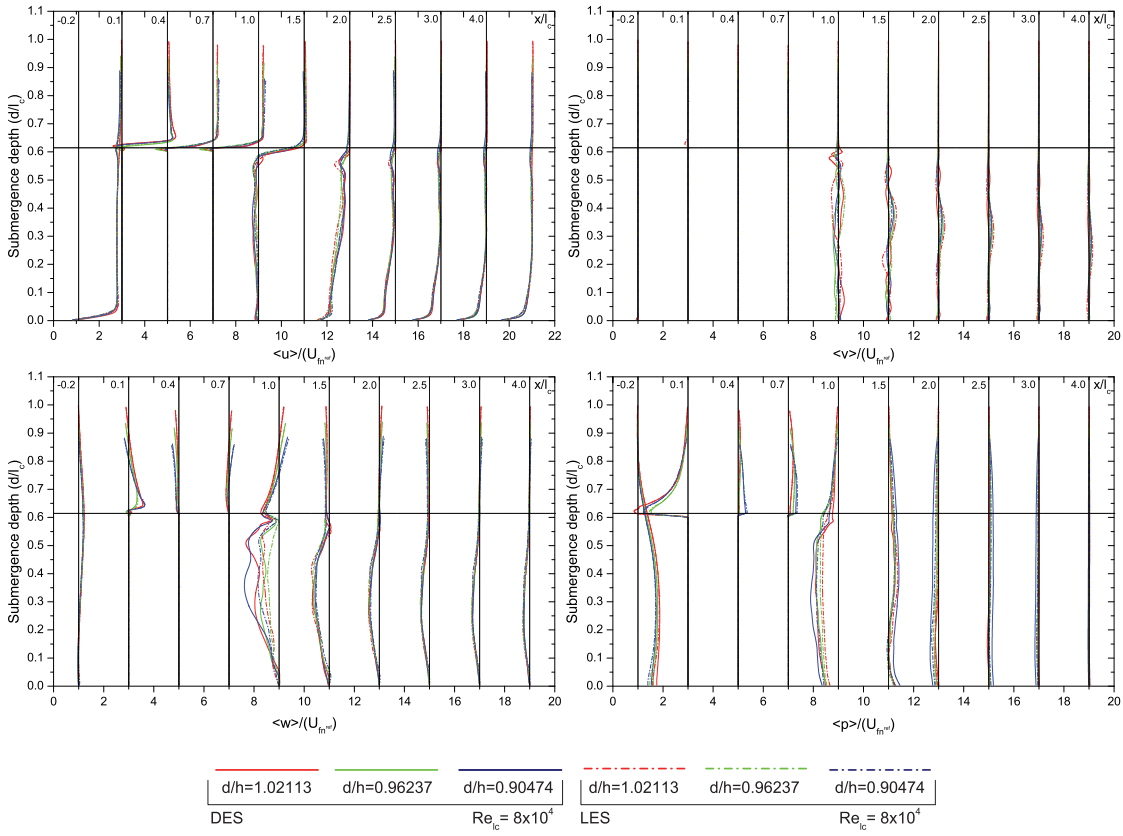

Figure 5.5: Time averaged mean velocity (components) and mean pressure distributions about the centre XZ plane for $Re=8\times10^4$.

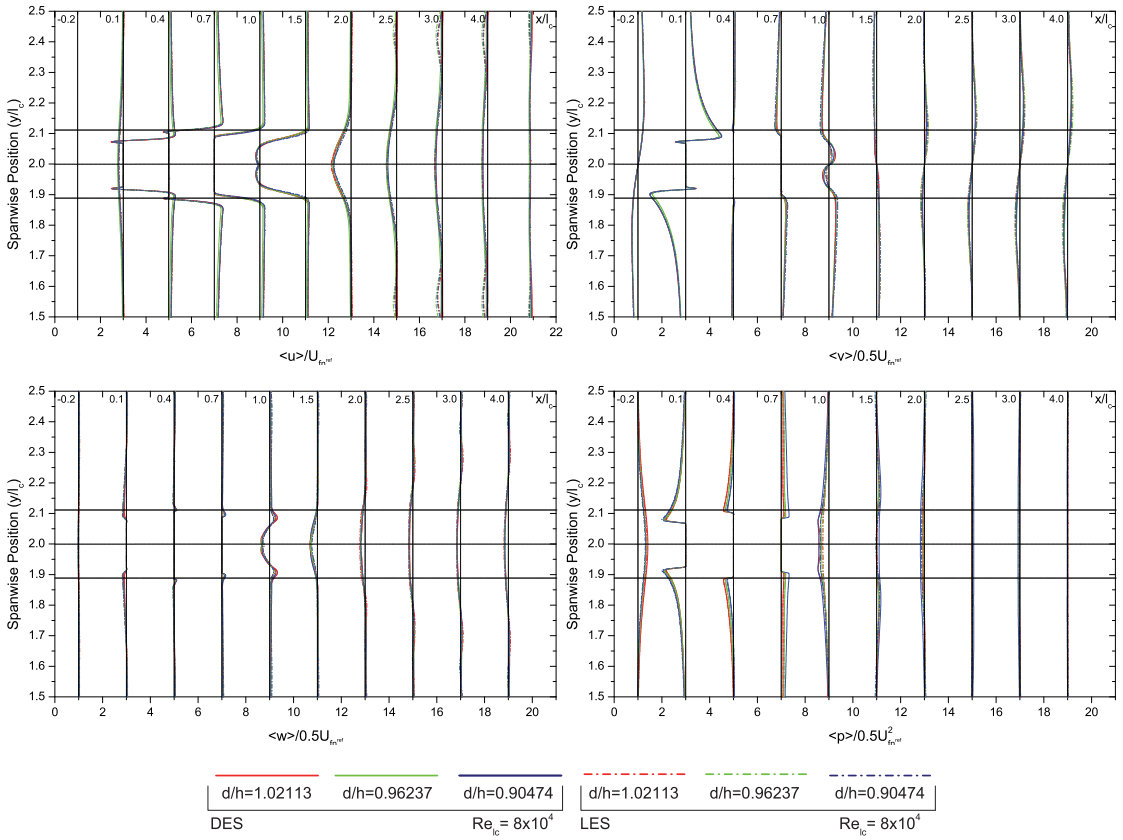

Figure 5.6: Time averaged mean velocity (components) and mean pressure distributions about the XY plane($0.2h/l_c$) for $Re=8\times10^4$

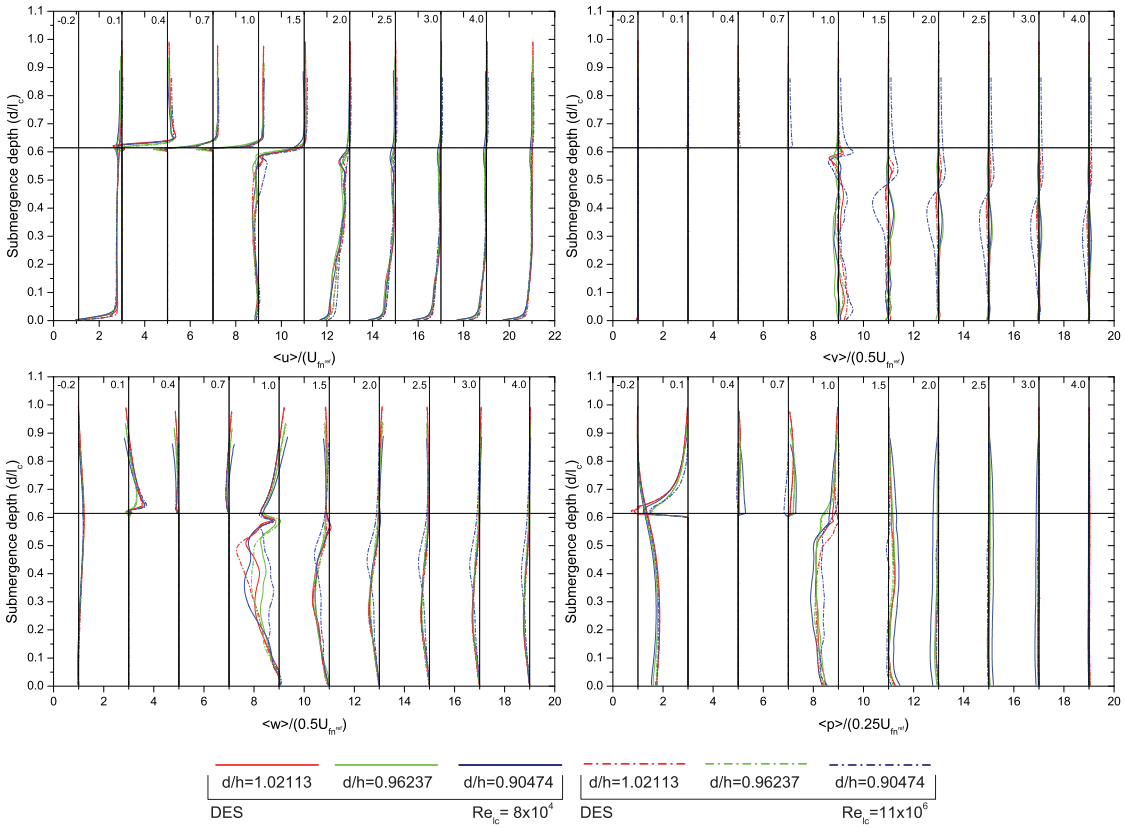

Figure 5.7: Comparison of time averaged mean velocity (components) and mean pressure distributions about the centre XZ plane for high and operating Re numbers.

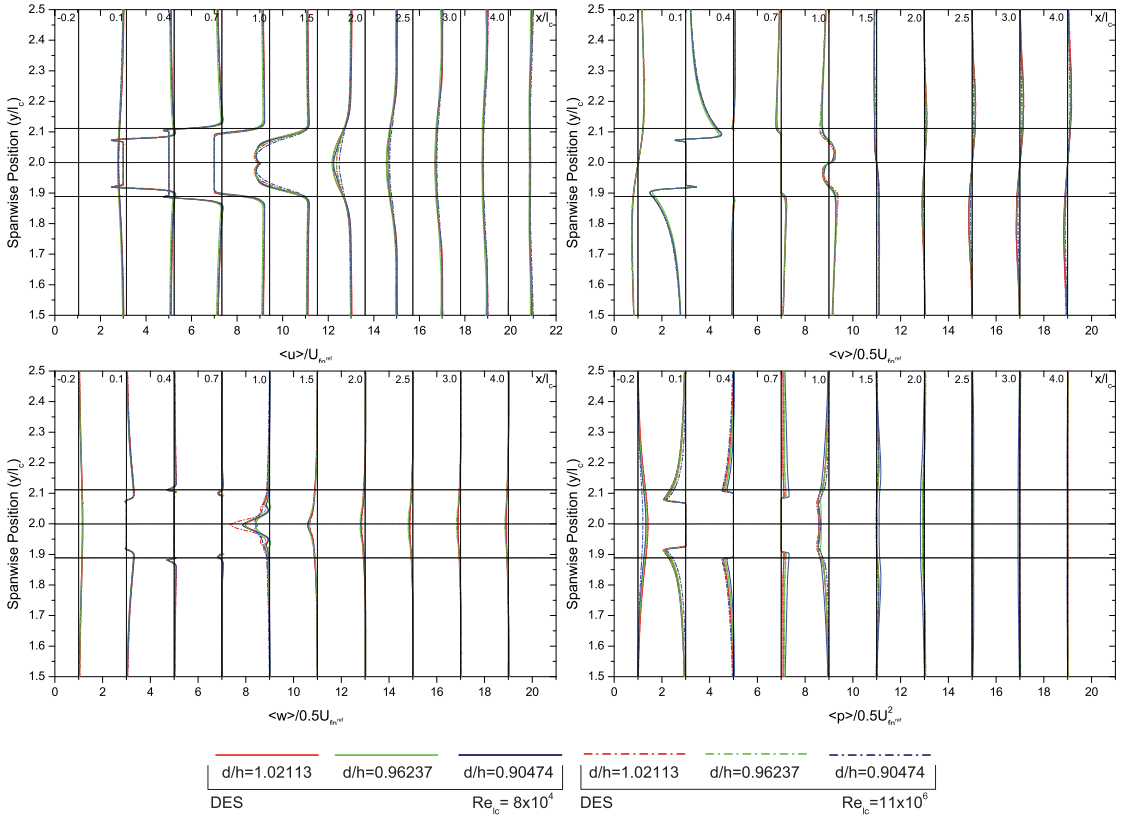

Figure 5.8: Comparison of time averaged mean velocity (components) and mean pressure distributions about the centre XY plane for high and operating Re numbers.

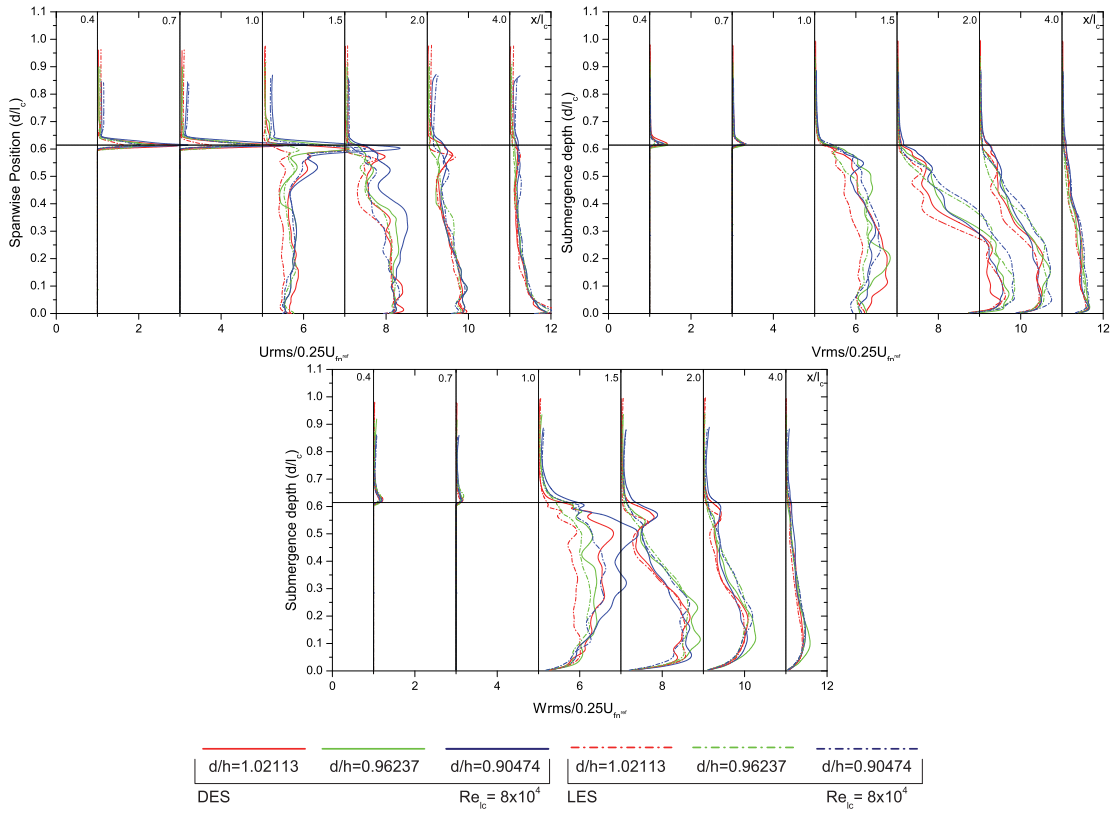

Figure 5.9: Time averaged turbulent intensity distributions about the centre XZ plane for $Re=8\times10^4$.

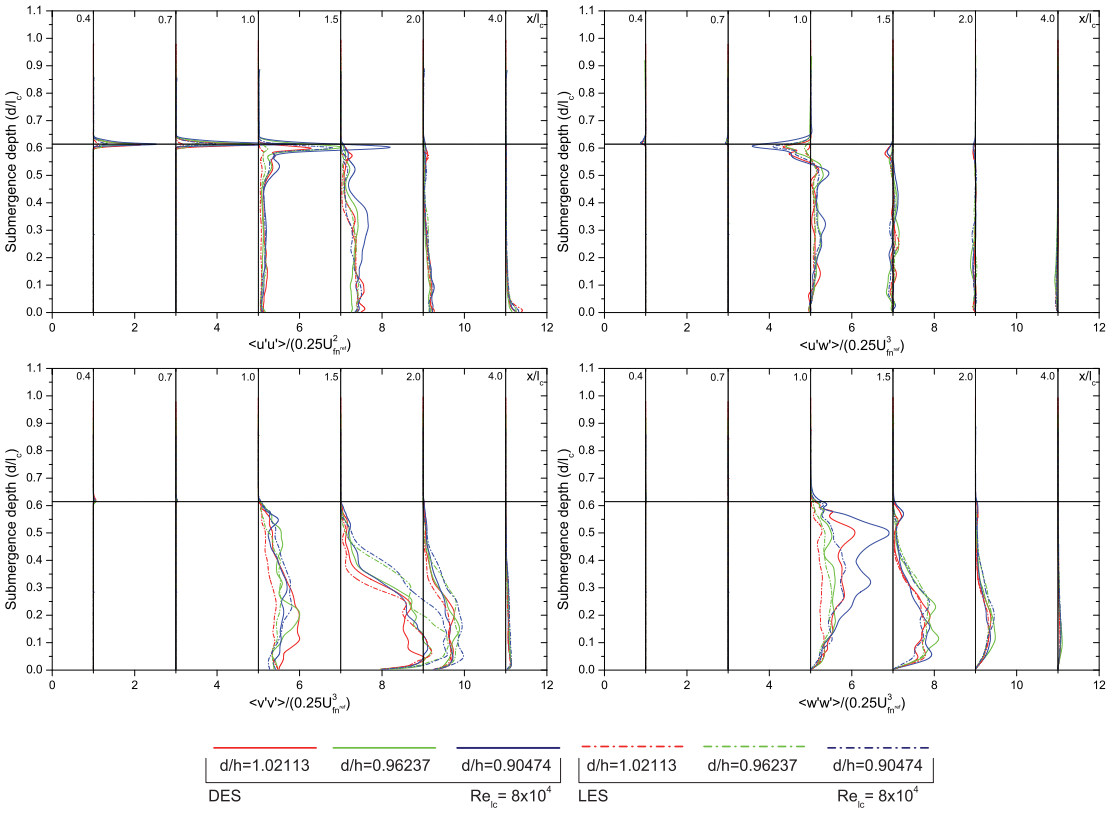

Figure 5.10: Time averaged Reynolds stresses about the centre XZ plane for $Re=8\times10^4$.

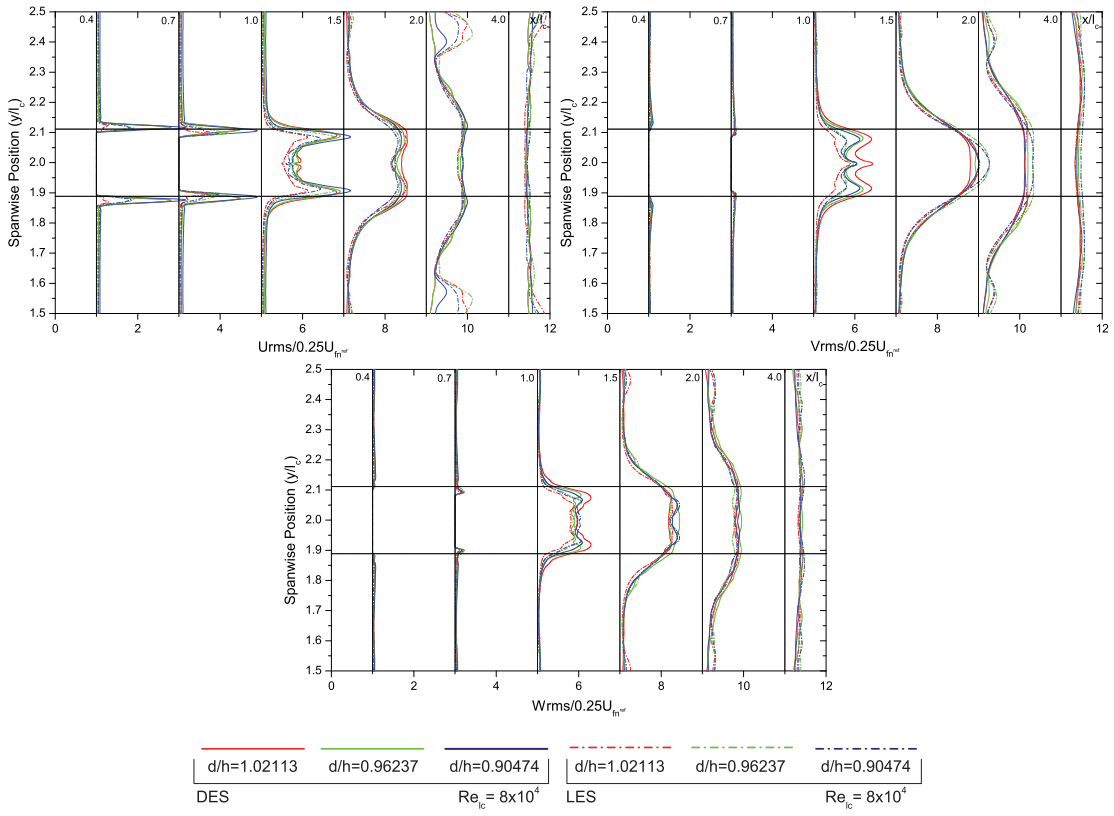

Figure 5.11: Time averaged turbulent intensity distributions about the centre XY ($0.2h/l_c$) plane for $Re=8\times10^4$.

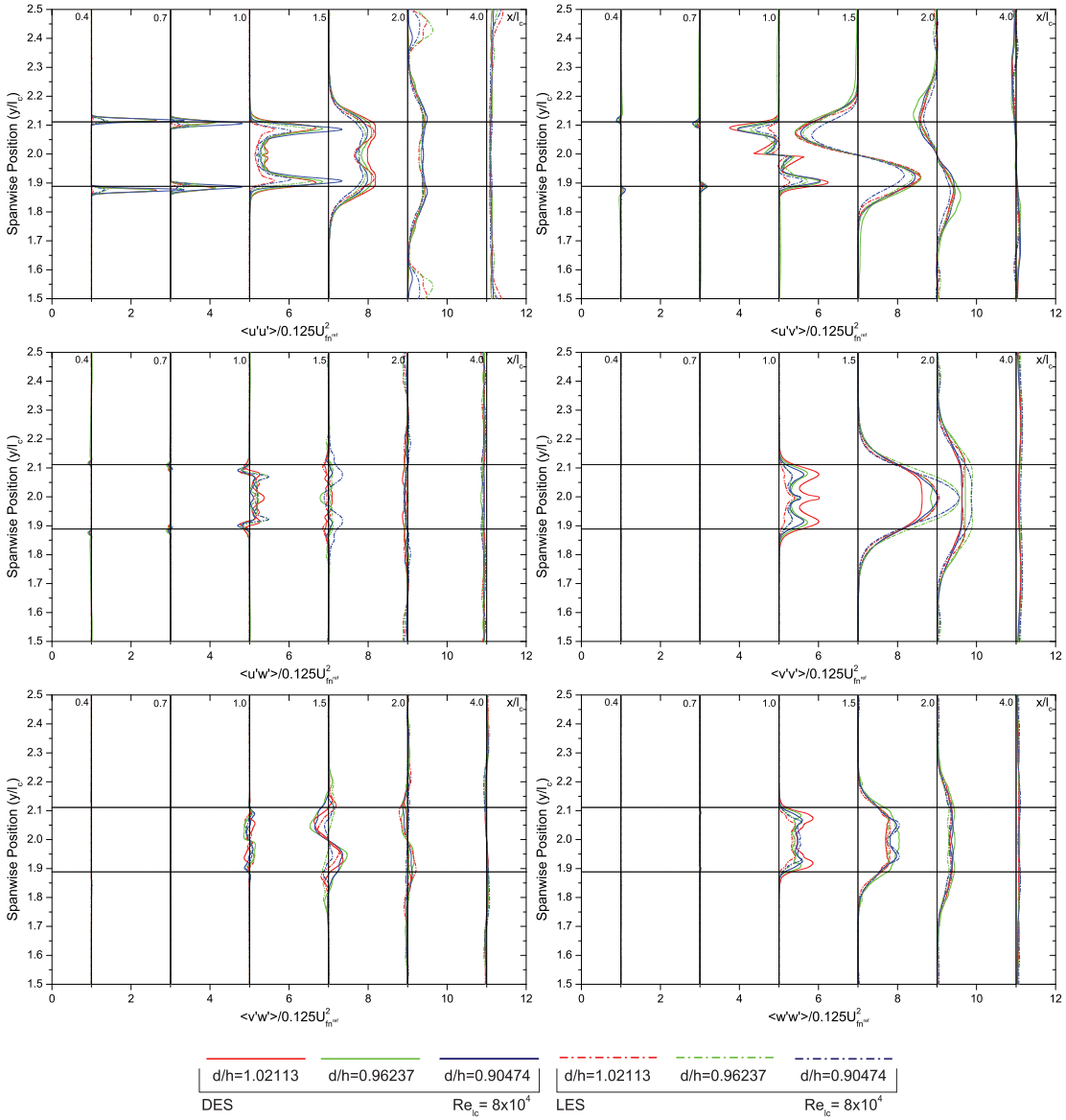

Figure 5.12: Time averaged Reynolds stresses about the centre XY plane ($0.2h/l_c$) for $Re=8\times10^4$.

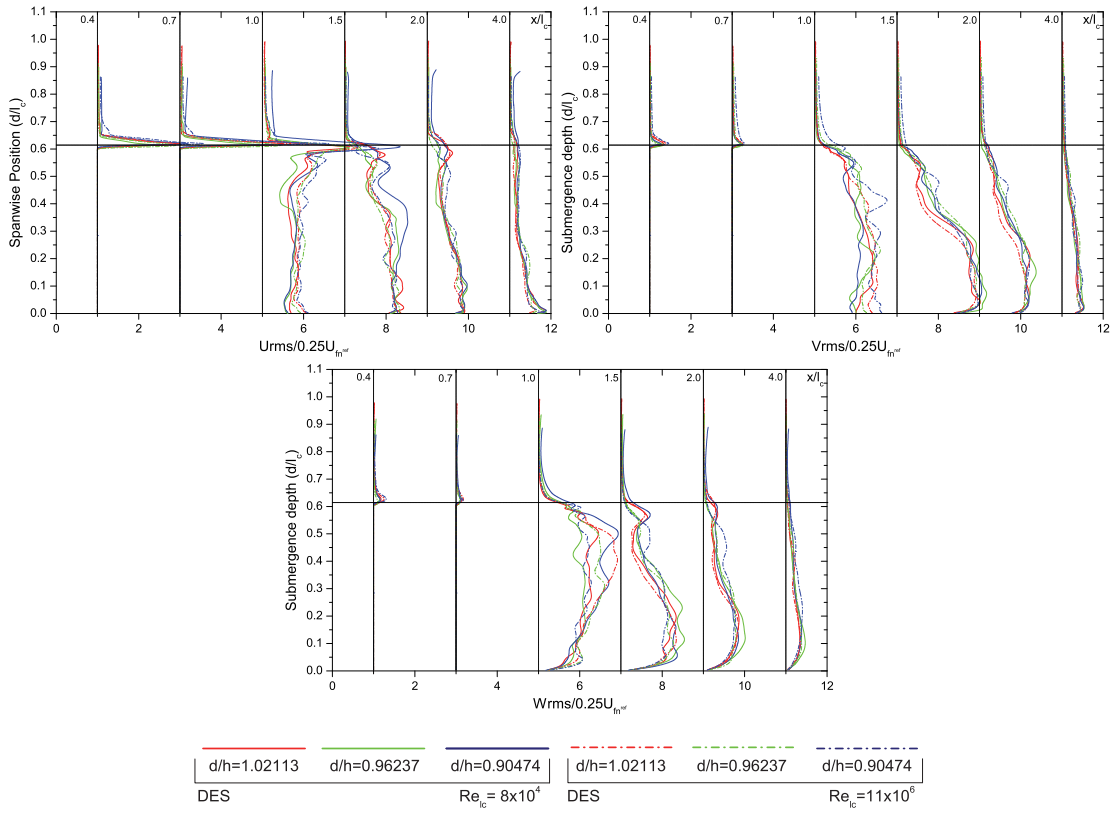

Figure 5.13: Comparison of time averaged turbulent intensity distributions about the centre XZ plane for high and operating Re numbers.

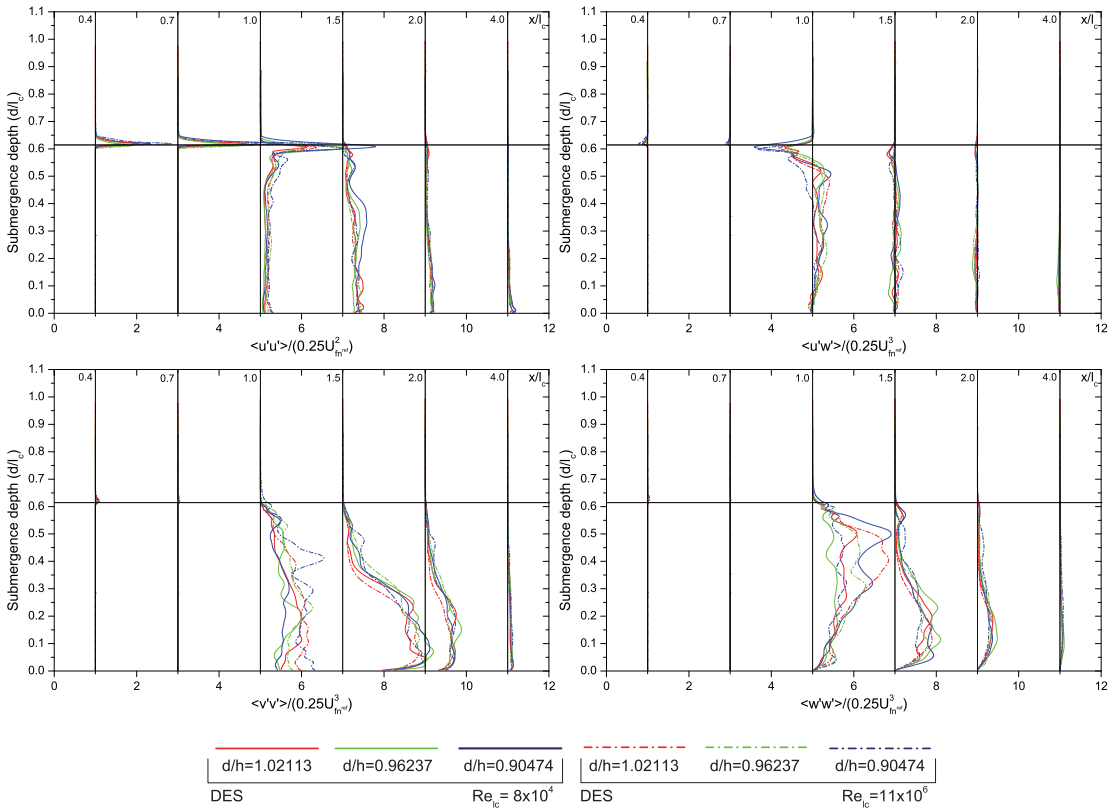

Figure 5.14: Comparison of time averaged Reynolds stresses about the centre XZ plane for high and operating Re numbers.

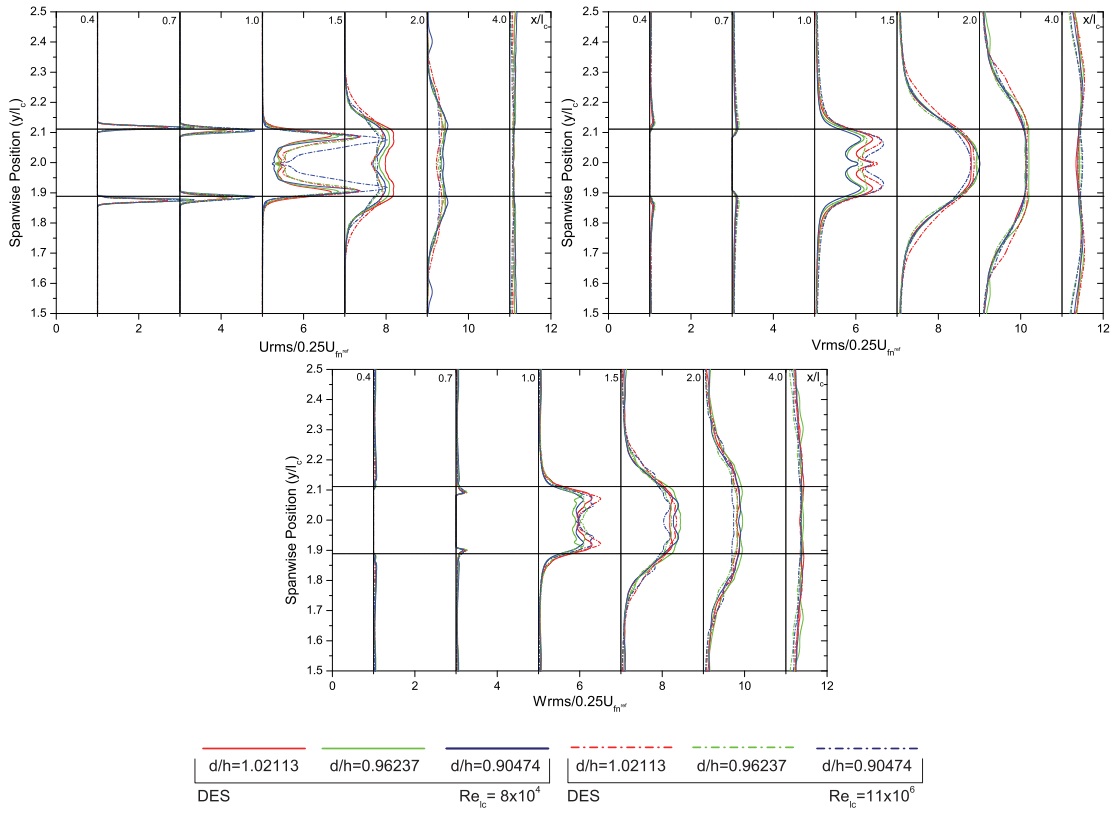

Figure 5.15: Comparison of time averaged turbulent intensity distributions about the centre XY ($0.2h/l_c$) plane for high and operating Re numbers.

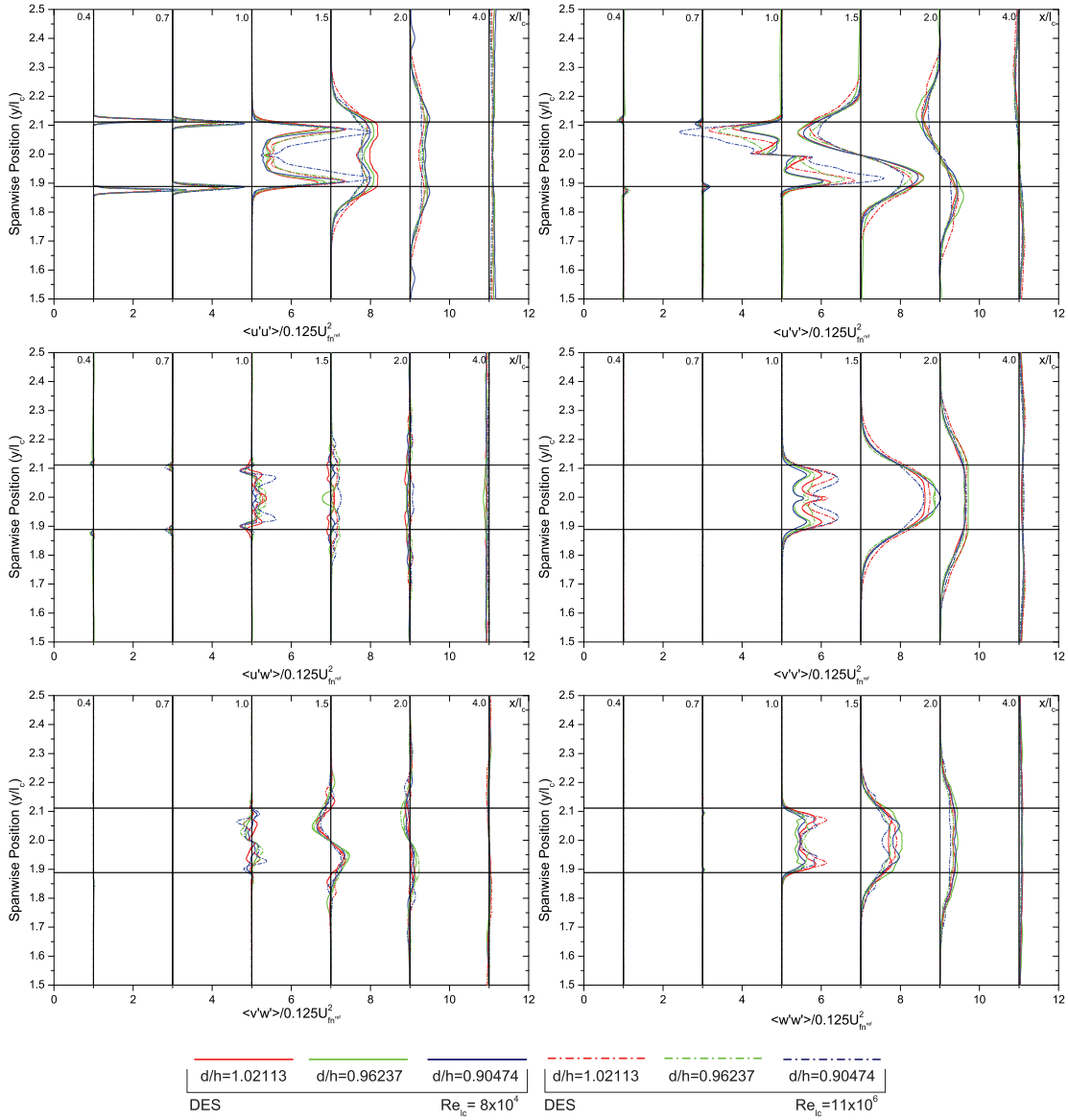

Figure 5.16: Comparison of time averaged Reynolds stresses about the centre XY plane for high and operating Re numbers.

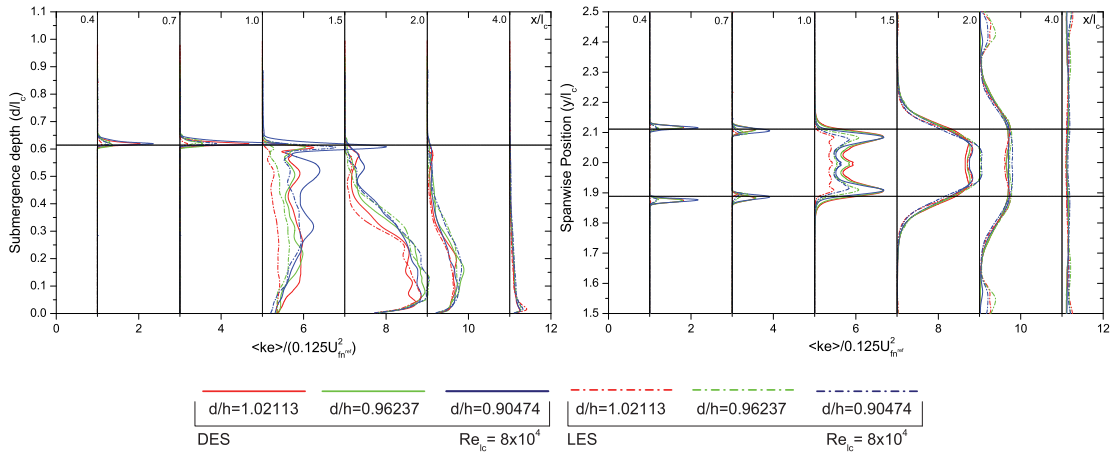

Figure 5.17: Time averaged turbulent kinetic energy distributions about the centre XZ (left) and XY (right) planes for $Re=8\times10^4$.

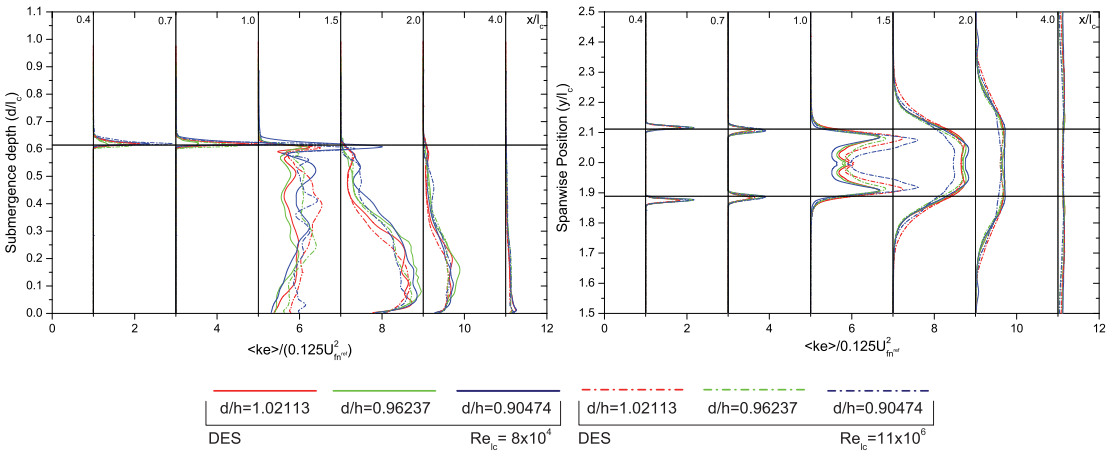

Figure 5.18: Comparison of time averaged turbulent kinetic energy distributions about the centre XZ (left) and XY (right) planes for high and operating Re.

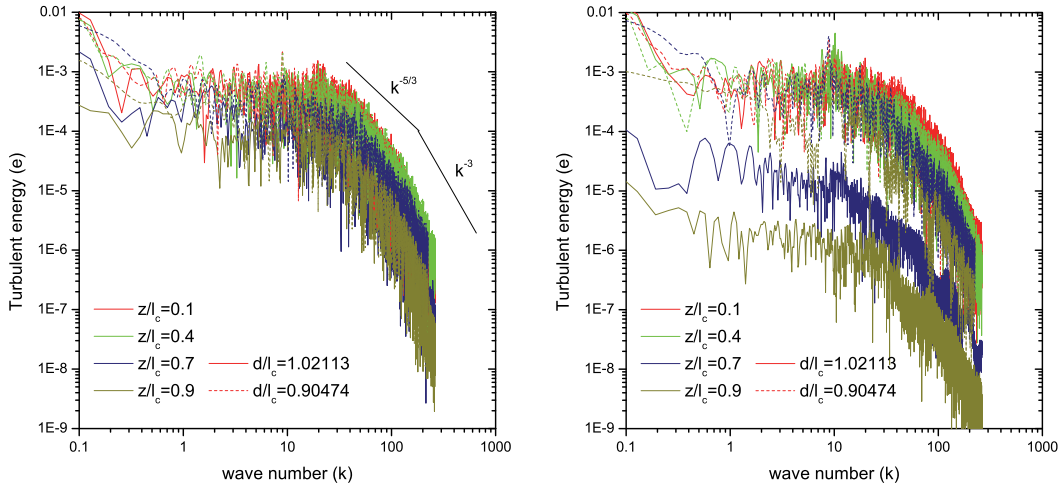

(a) LES Re=8×10^4

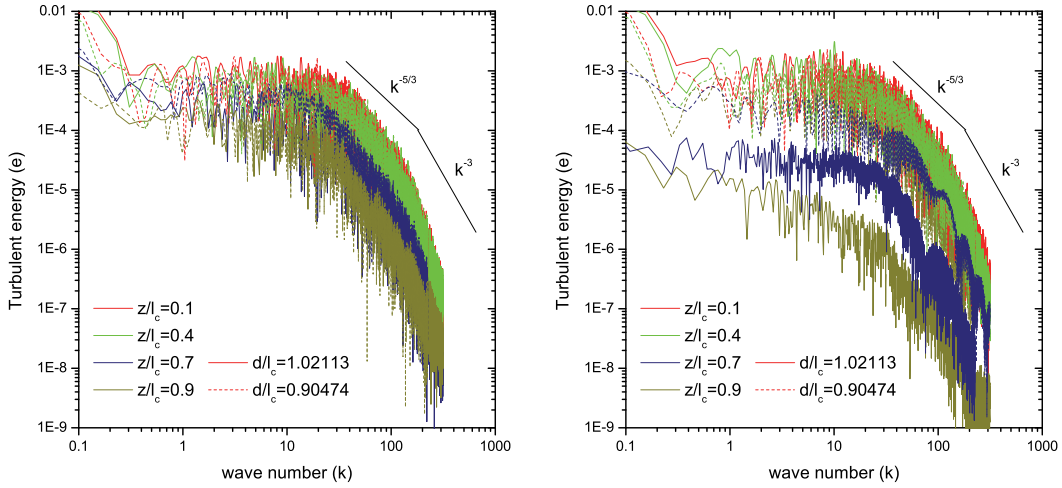

(b) DES Re=8×10^4

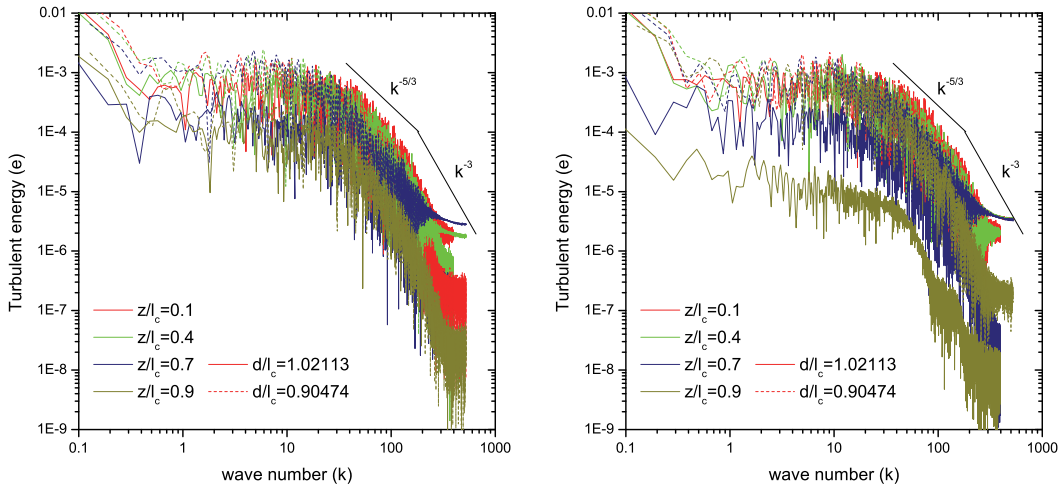

(c) DES Re=11×10^6

Figure 5.19: TKE spectra at PT_{fn2} in the fairwater wake at various positions along the fairwater height.

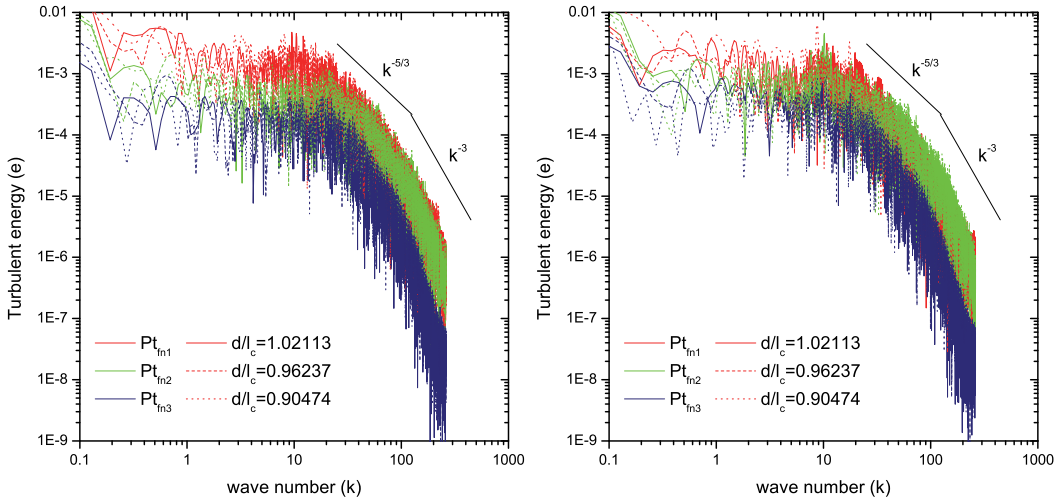

(a) LES Re=8×10^4

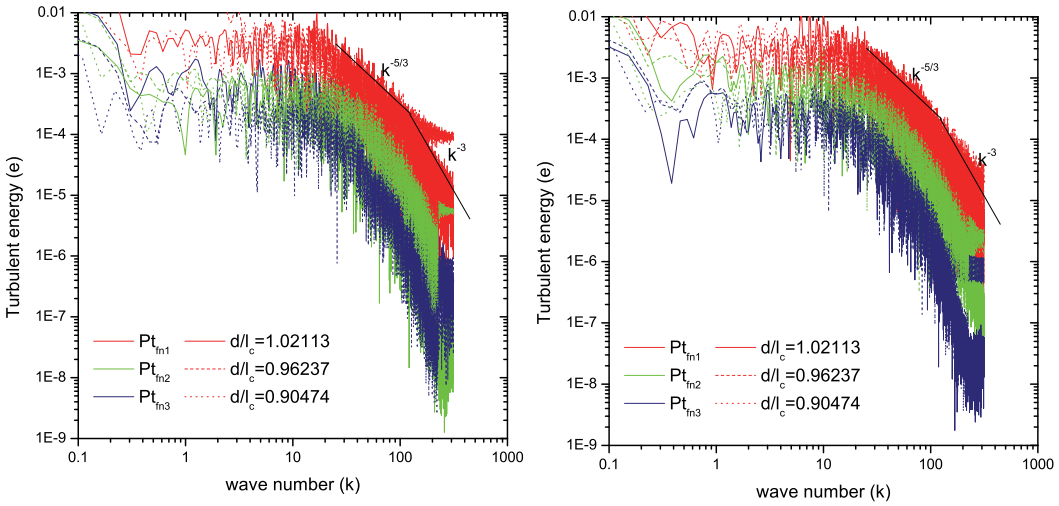

(b) DES Re=8×10^4

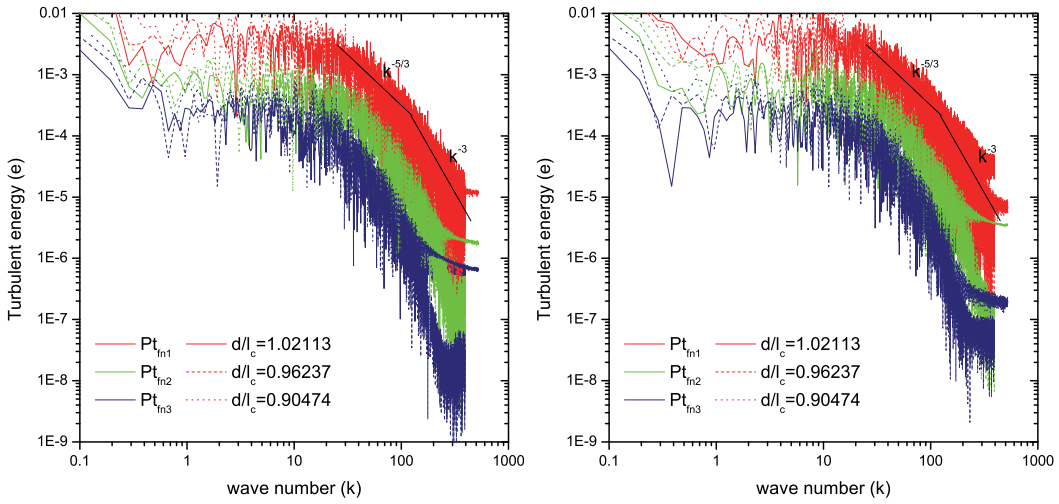

(c) DES Re=11×10^6

Figure 5.20: TKE spectra at various positions along the fairwater wake at $0.4h/l_c$.

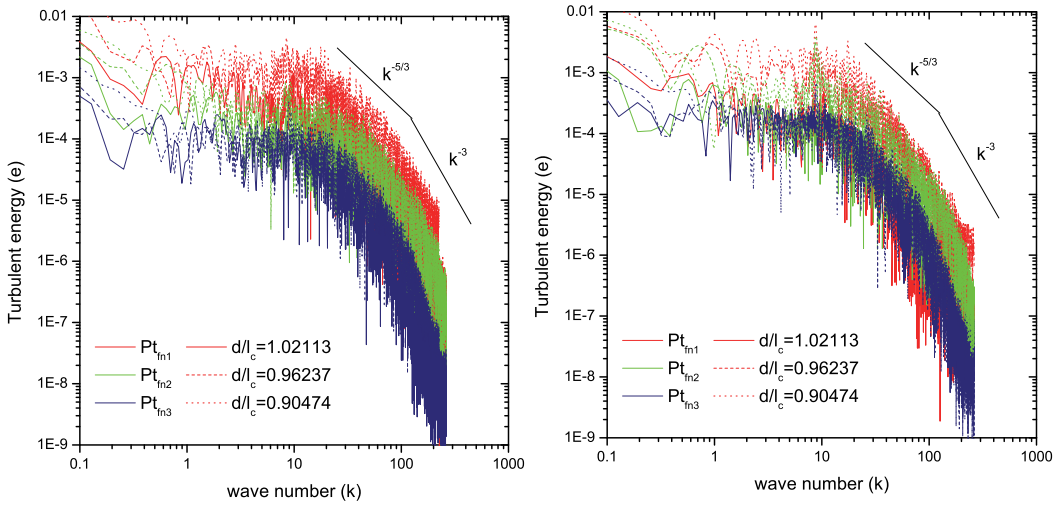

(a) LES Re=8×10^4

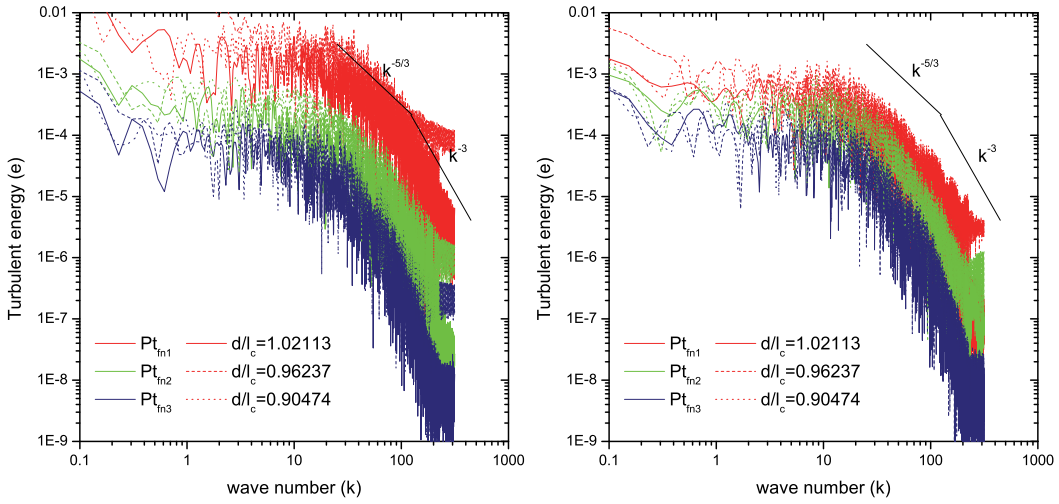

(b) DES Re=8×10^4

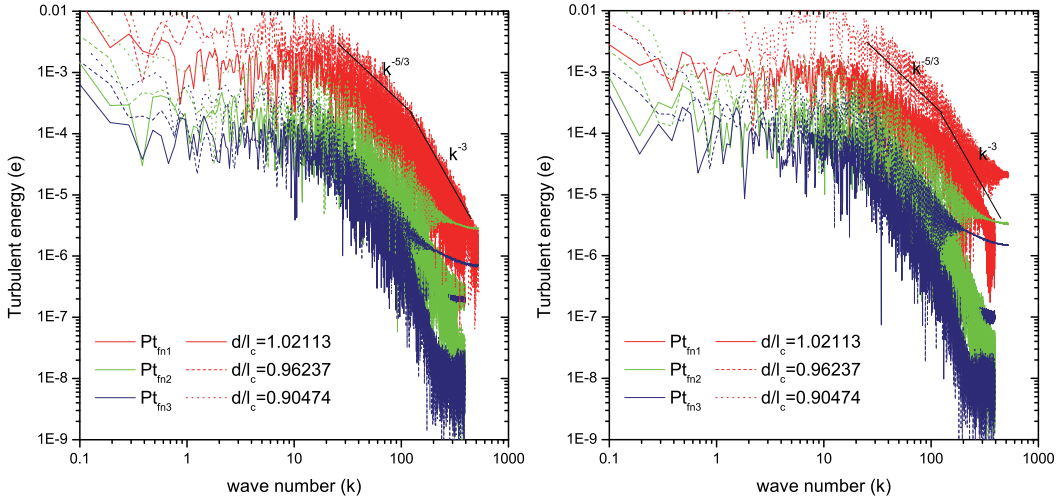

(c) DES Re=11×10^6

Figure 5.21: TKE spectra at various positions along the fairwater wake at 0.74h/lc.

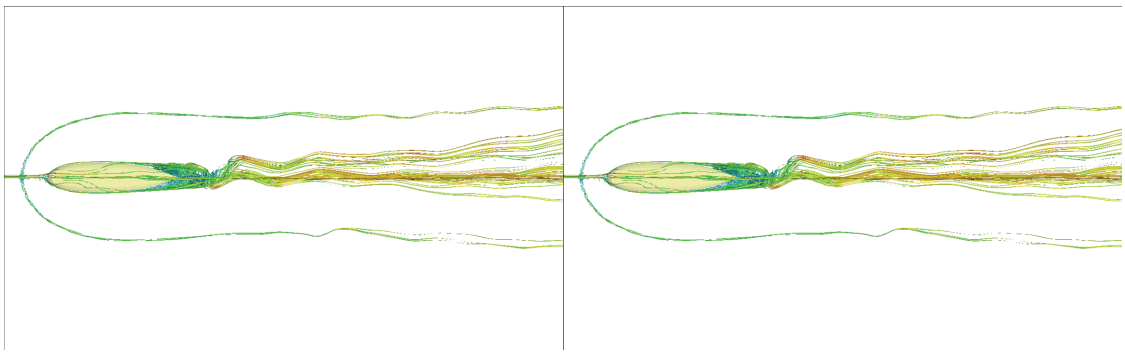

(a) Re=8×10^4, d/l_c=0.96237 (LES)

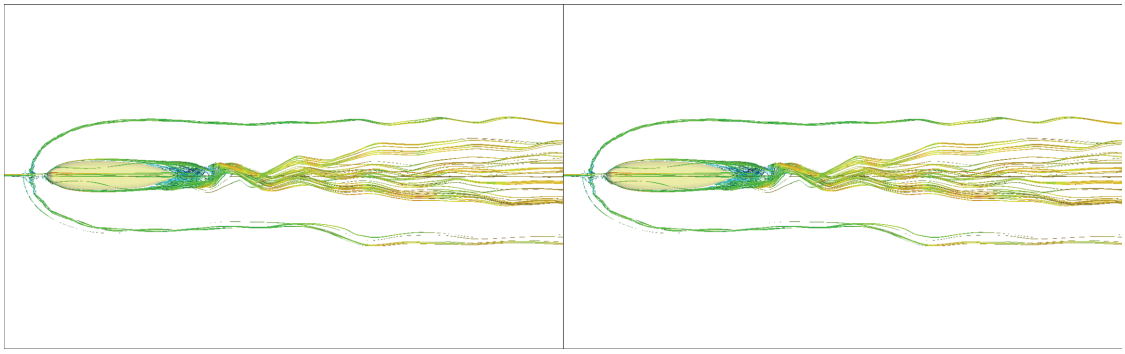

(b) Re=8×10^4, d/l_c=0.96237 (DES)

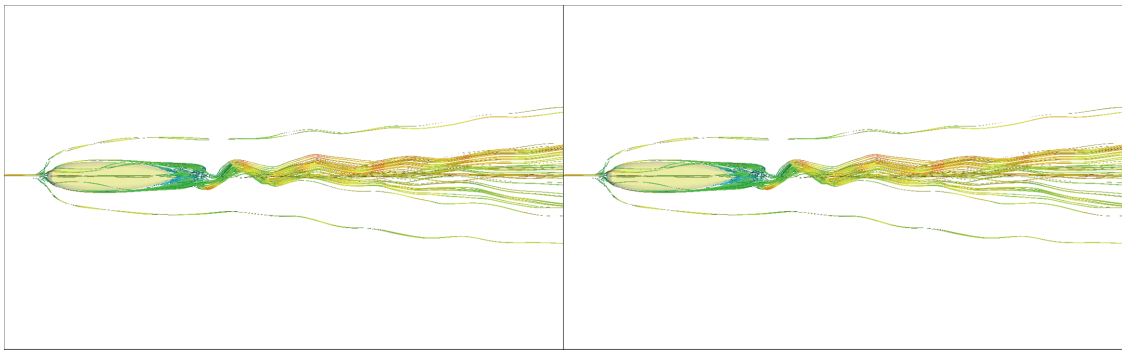

(a) Re=11×10^6, d/l_c=0.96237 (DES)

Figure 5.22: Streamline traces around the fairwater body about the XY plane, for both high and operating Re cases.

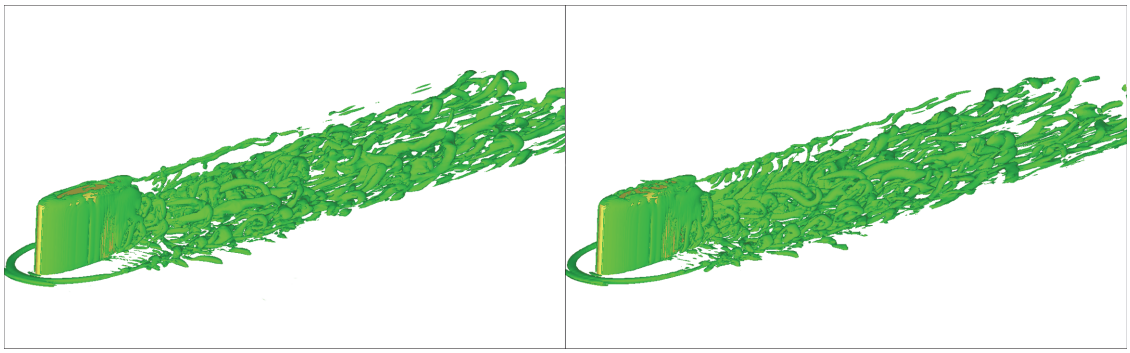

(a) $Re=8\times10^4$, $d/l_c=1.02113$ (LES)

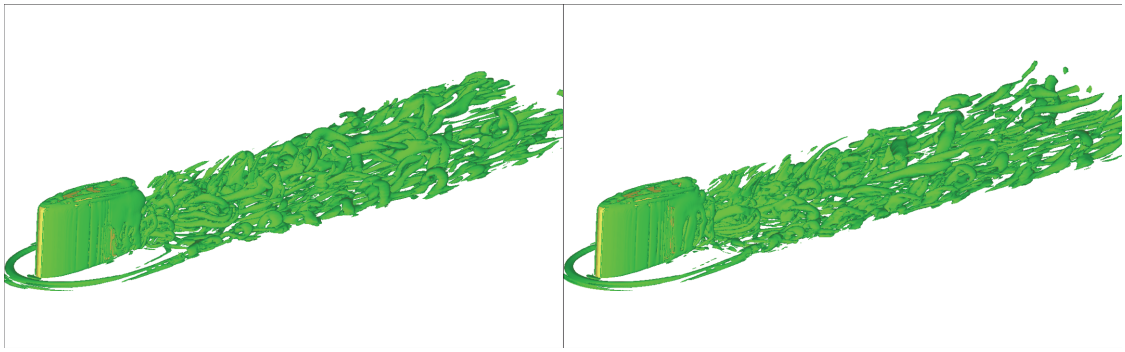

(b) $Re=8\times10^4$, $d/l_c=0.96237$ (LES)

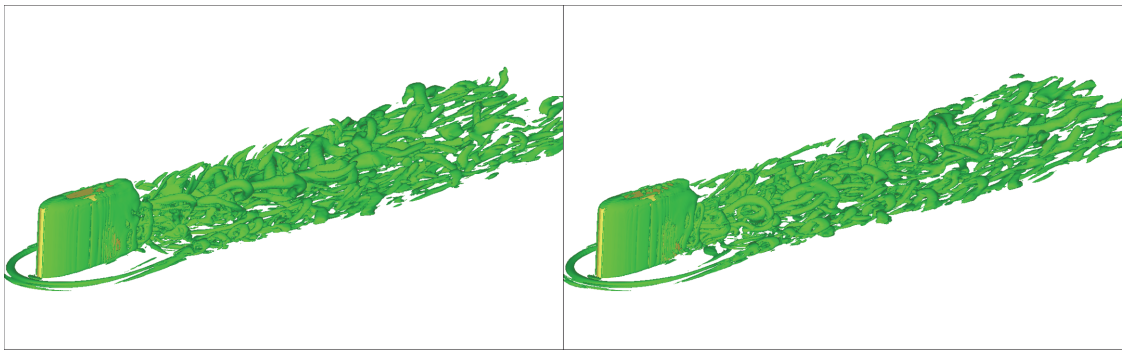

(c) $Re=8\times10^4$, $d/l_c=0.90474$ (LES)

Figure 5.23: Instantaneous VS for Q=1 for $Re=8\times10^4$ for all depths using LES.

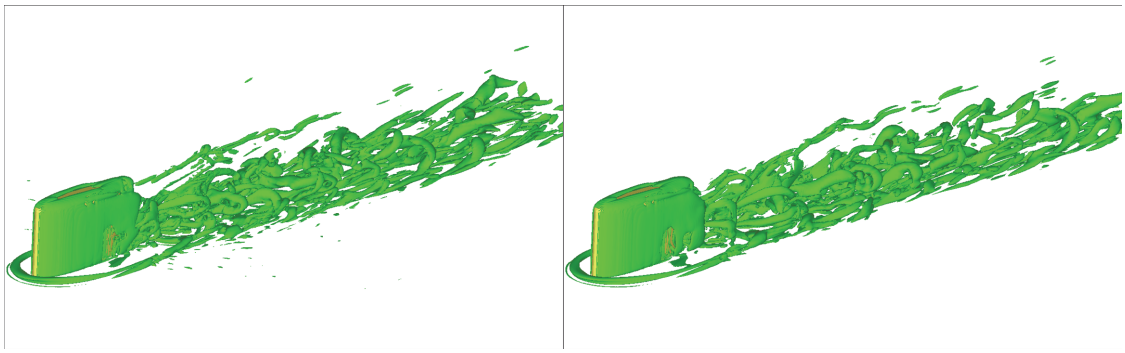

(a) $Re=8\times10^4$, $d/l_c=1.02113$ (DES)

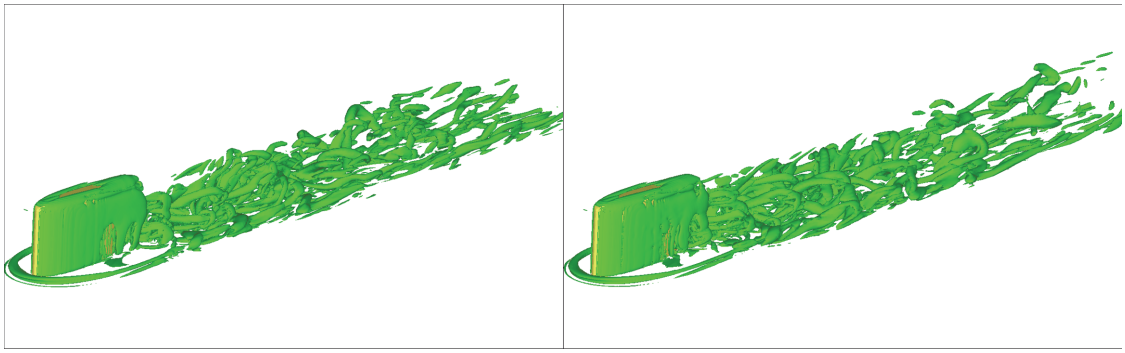

(b) $Re=8\times10^4$, $d/l_c=0.96237$ (DES)

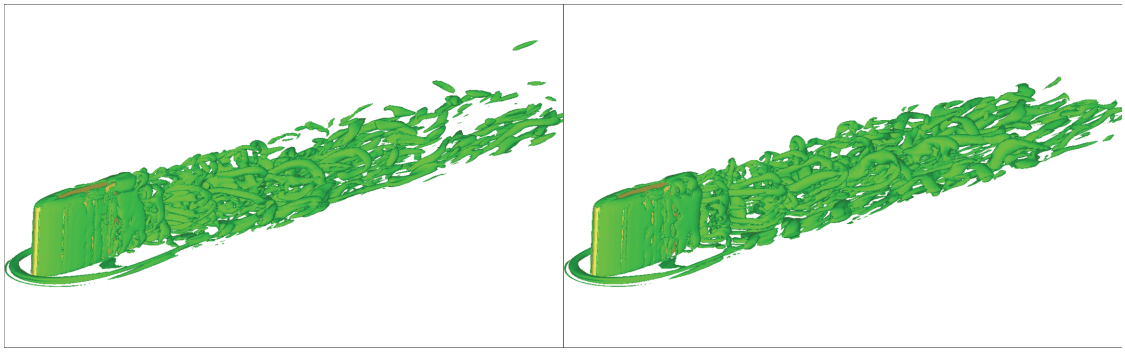

(c) $Re=8\times10^4$, $d/l_c=0.90474$ (DES)

Figure 5.24: Instantaneous VS for Q=1 for $Re=8\times10^4$ for all depths using DES.

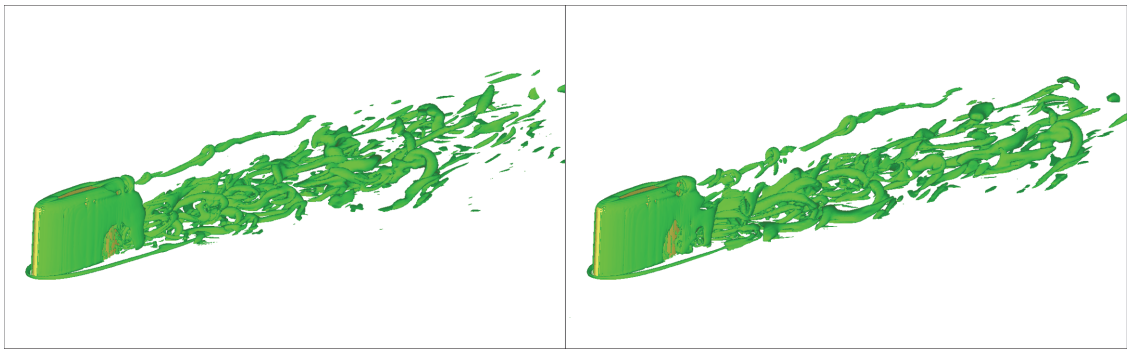

(a) $Re=11\times10^6$, $d/l_c=1.02113$ (DES)

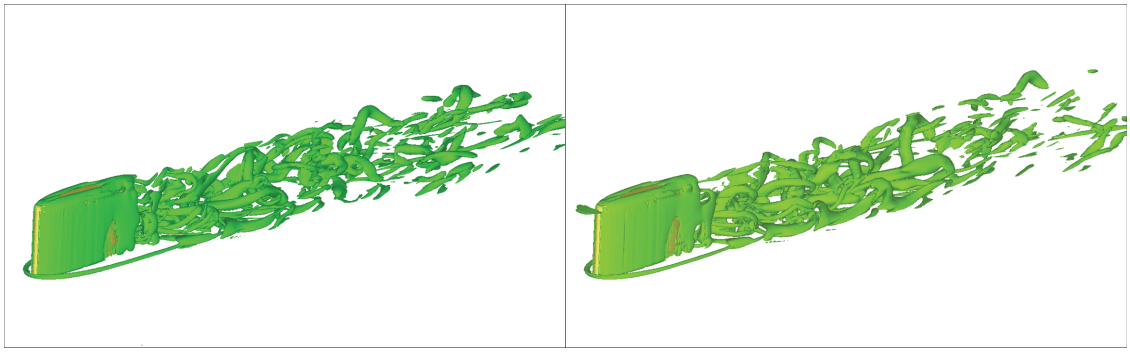

(b) $Re=11\times10^6$, $d/l_c=0.96237$ (DES)

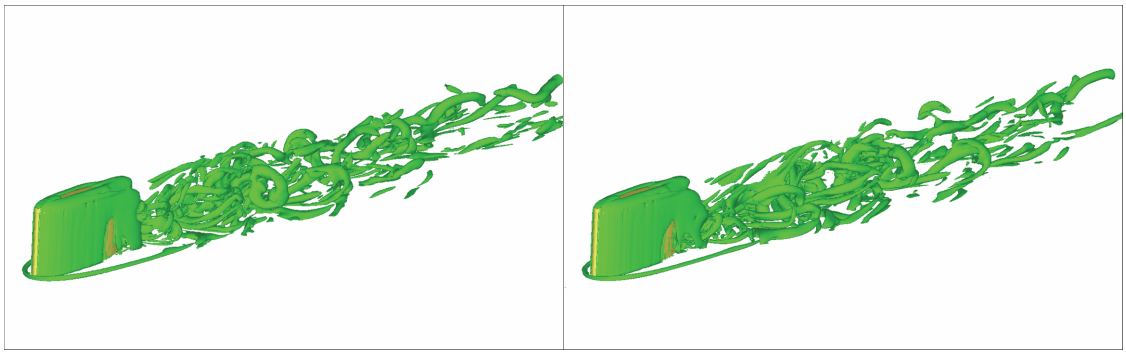

(c) $Re=11\times10^6$, $d/l_c=0.90474$ (DES)

Figure 5.25: Instantaneous VS for Q=1 for $Re=11\times10^6$ for all depths using DES.

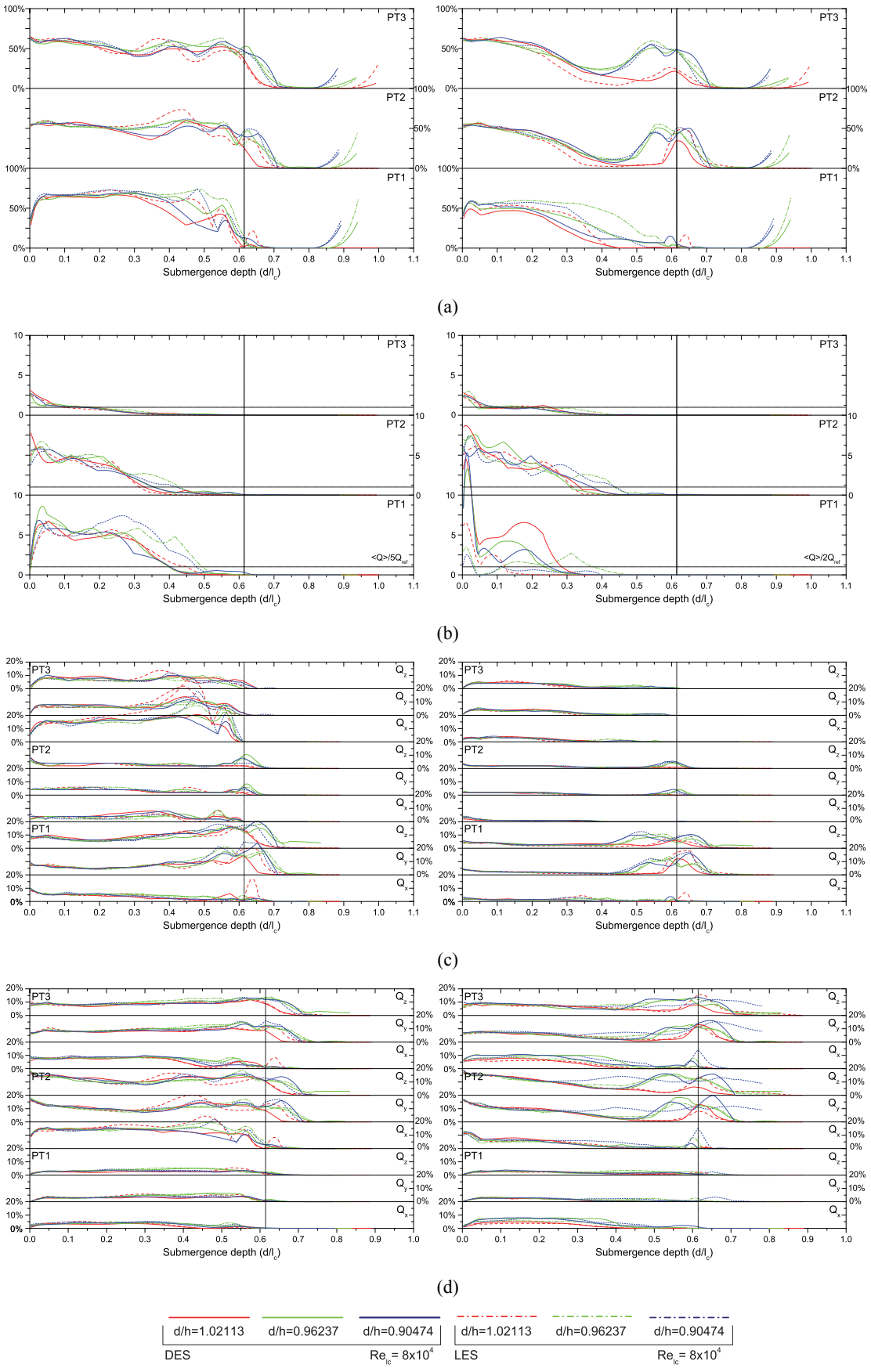

Figure 5.26: Vortex statistical data for (a) persistence, (b) time averaged normalised Q, (c) complete vortex alignment to an axis, (d) zero alignment to an axis. Data is recorded for Q>0 in the wake region about the centre (left) and off-centre (right) XZ plane, for Re=8×10⁴.

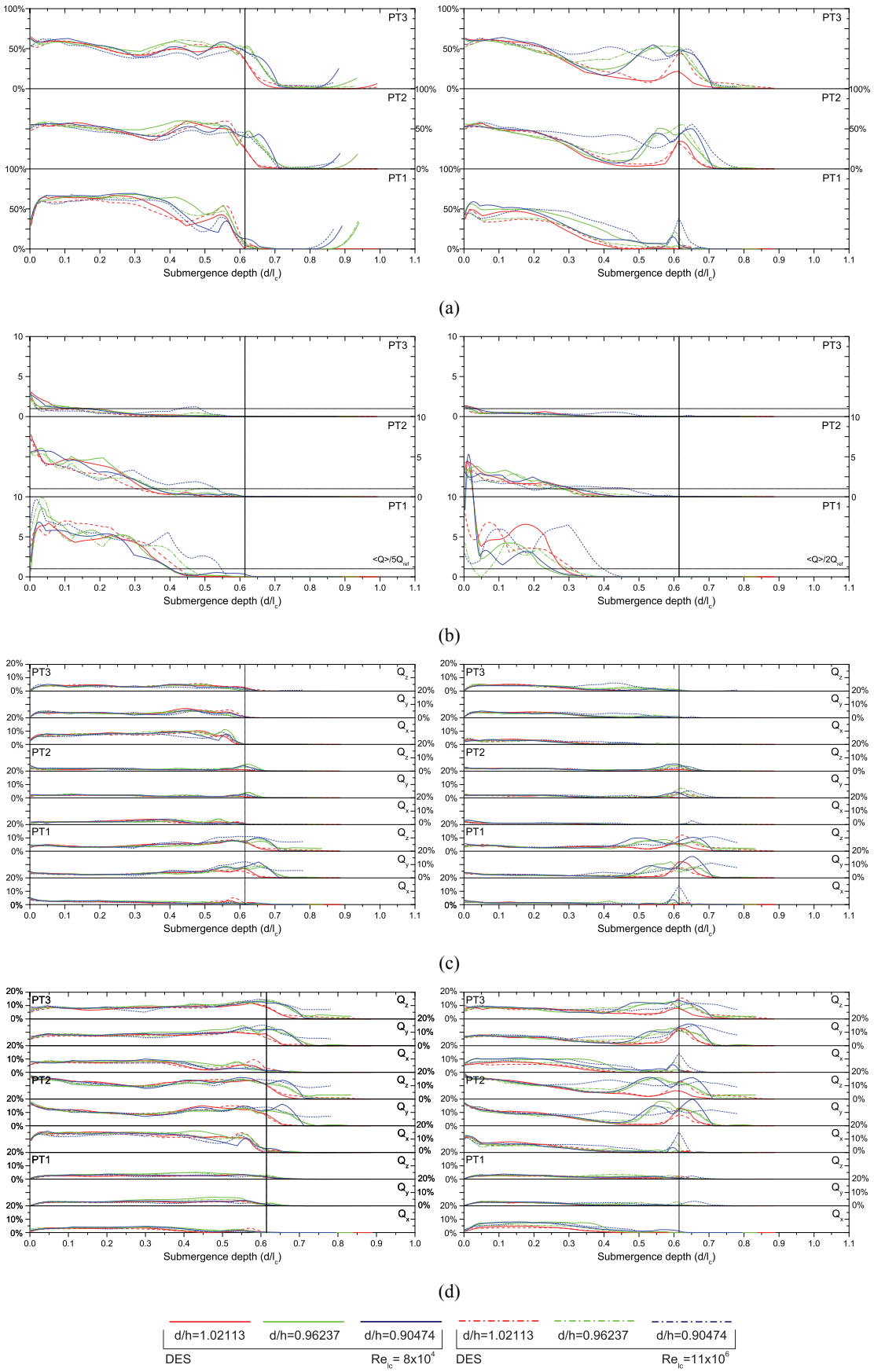

Figure 5.27: Vortex statistical data for (a) persistence, (b) time averaged normalised Q, (c) complete vortex alignment to an axis, (d) zero alignment to an axis. Data is recorded for Q>0 in the wake region about the centre (left) and off-centre (right) XZ plane.

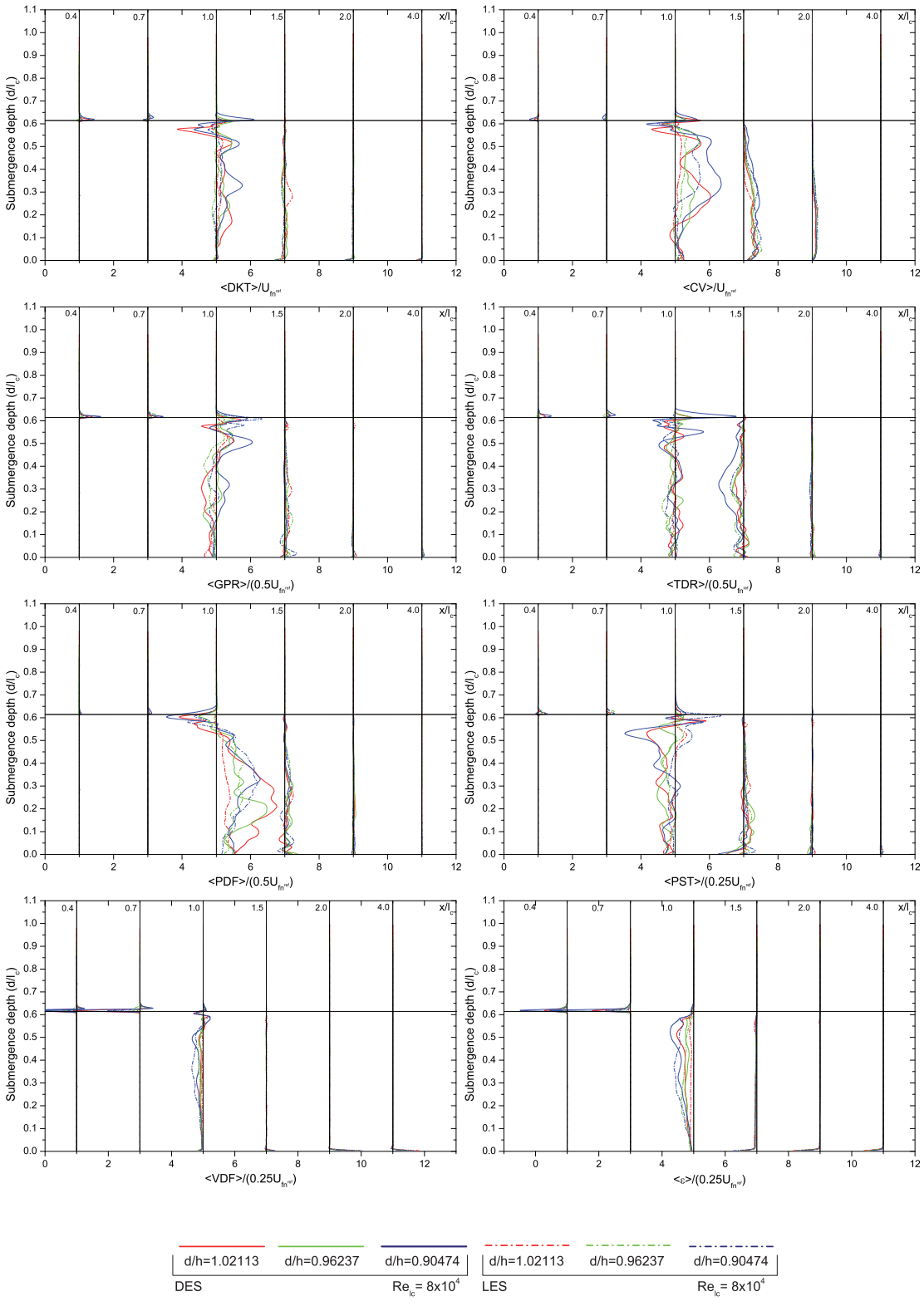

Figure 5.28: Time averaged turbulent energy budget terms about the centre XZ plane, $Re=8\times10^4$

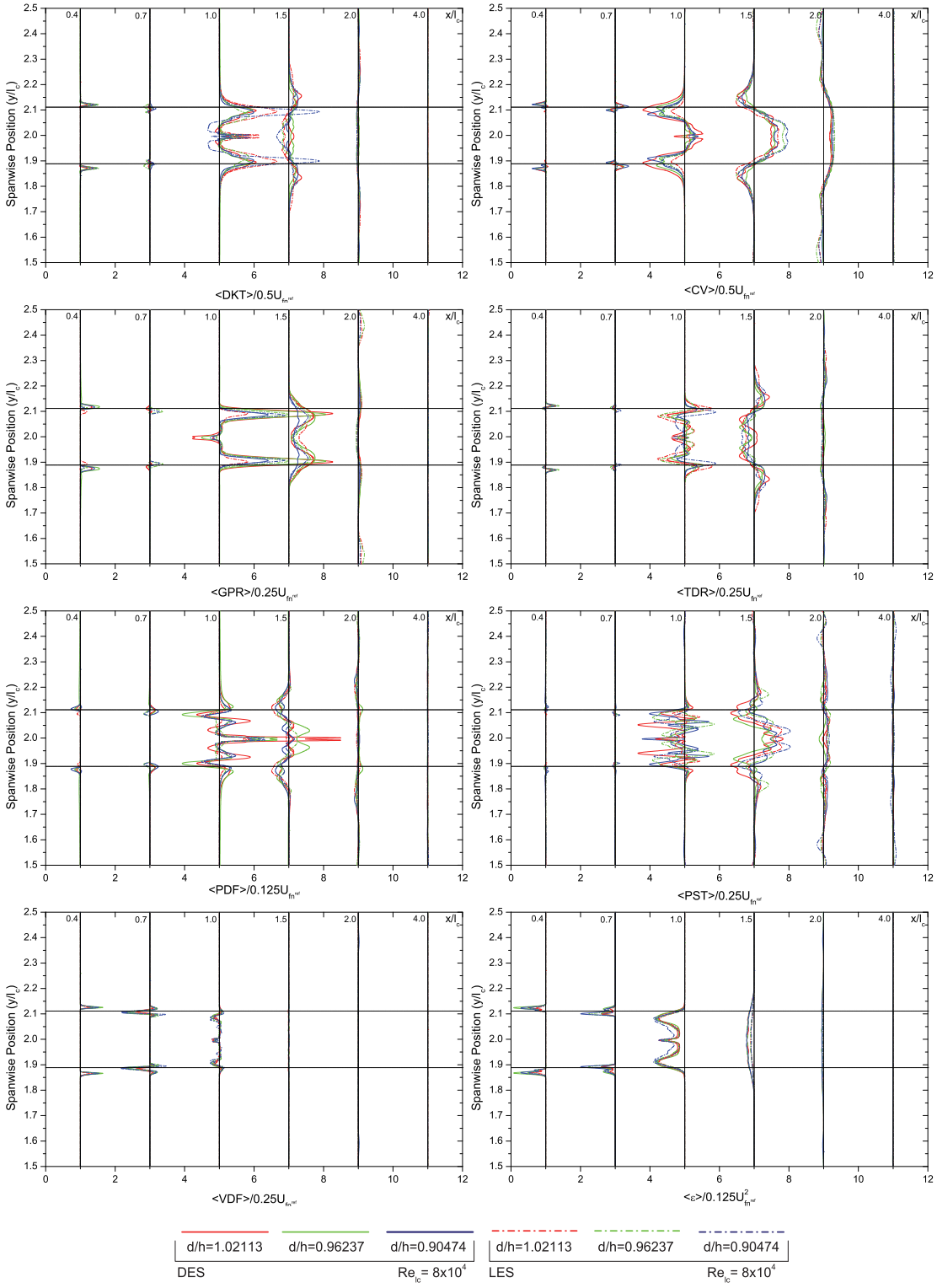

Figure 5.29: Time averaged turbulent energy budget terms about the centre XY plane, $Re=8\times10^4$.

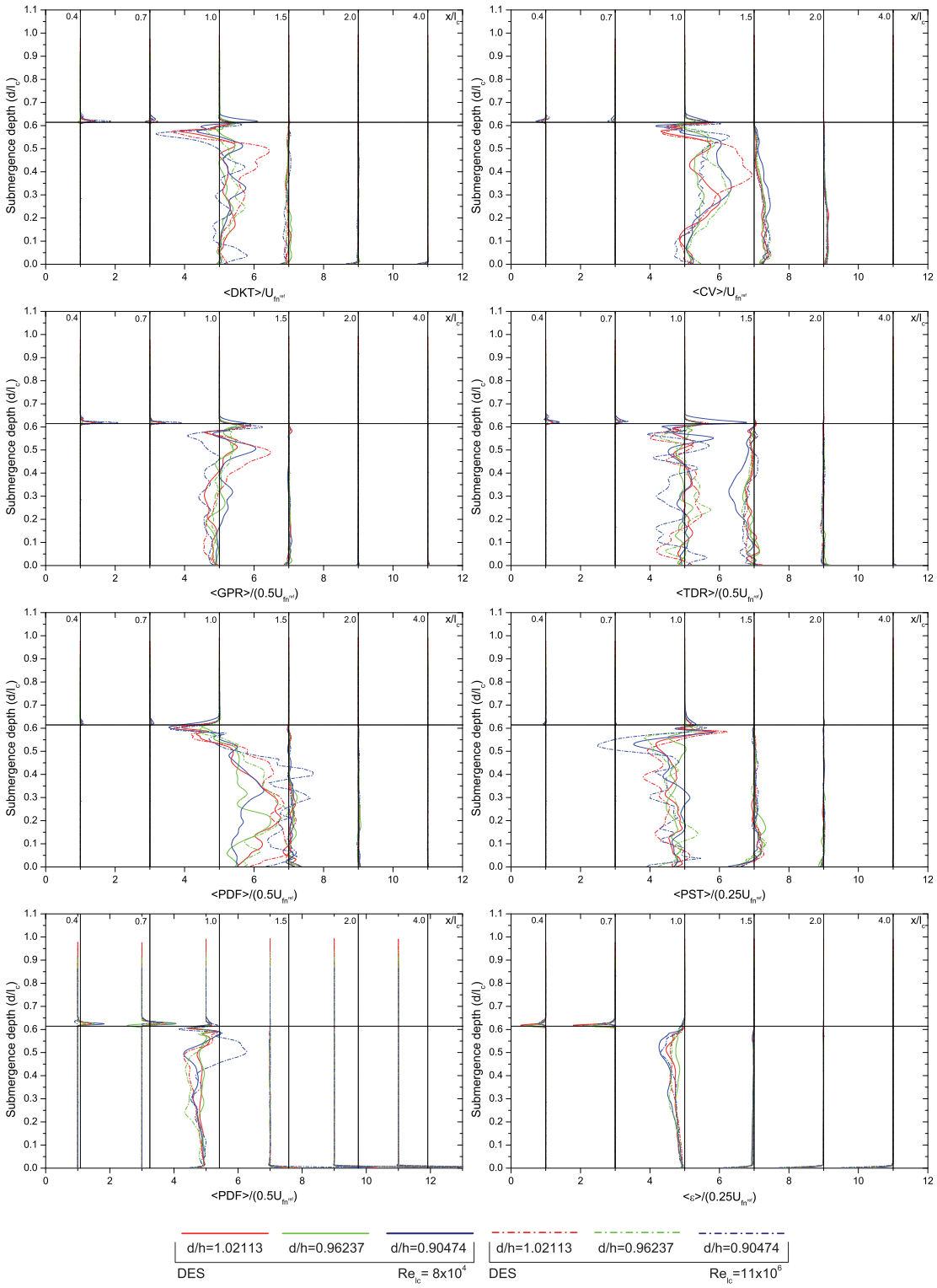

Figure 5.30: Comparison of time averaged turbulent energy budget terms about the centre XZ plane, for high and operating Reynolds numbers.

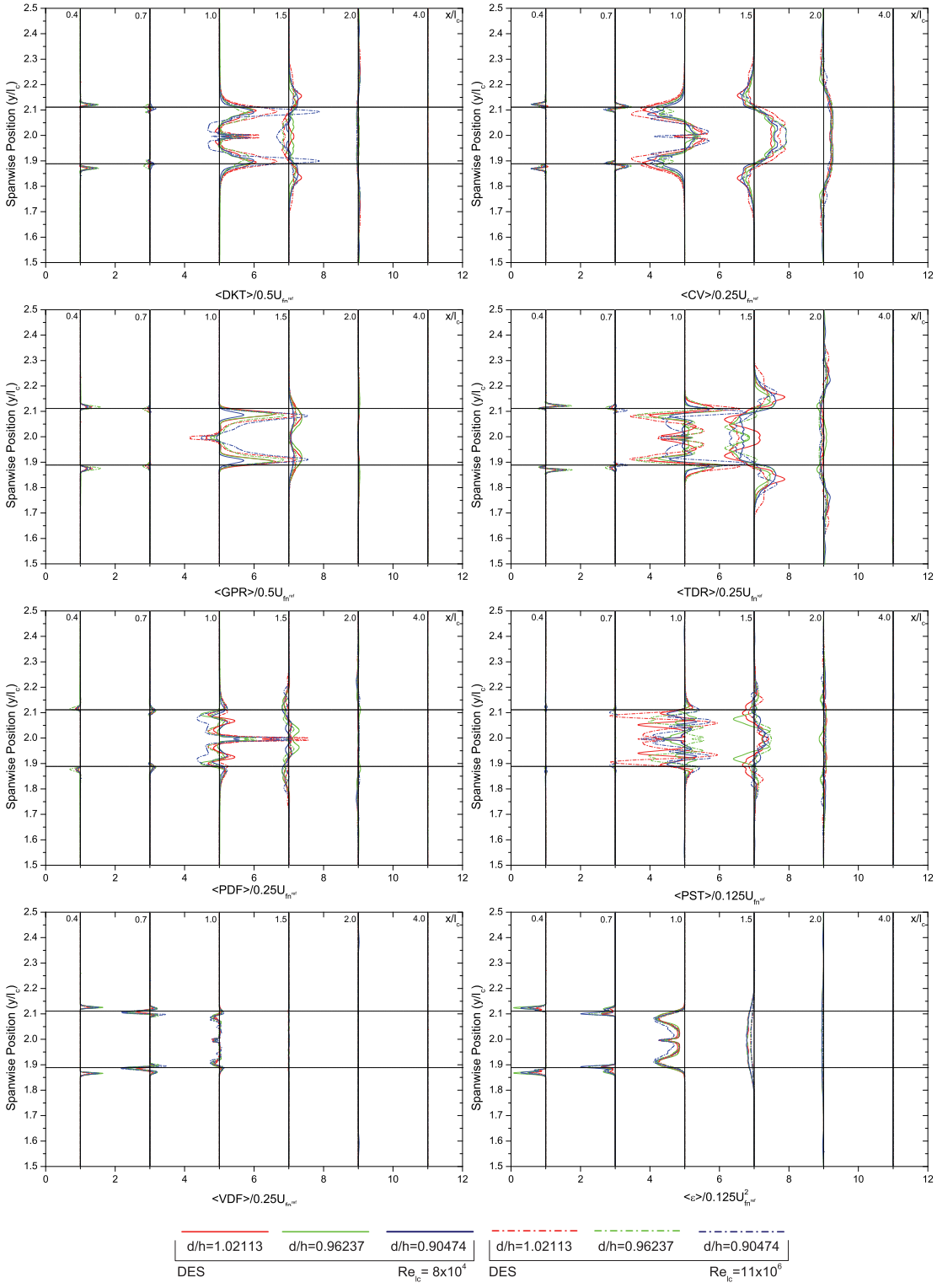

Figure 5.31: Comparison of time averaged turbulent energy budget terms about the centre XY plane, for high and operating Reynolds numbers.

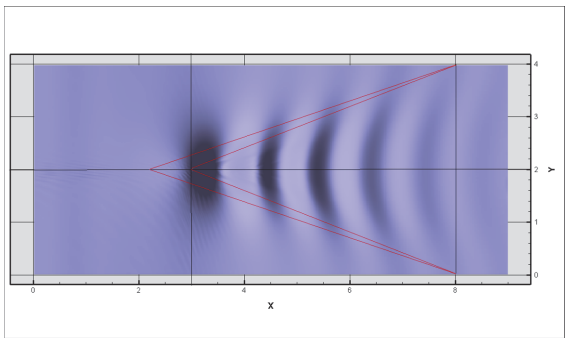

(a) d/lc=1.02113

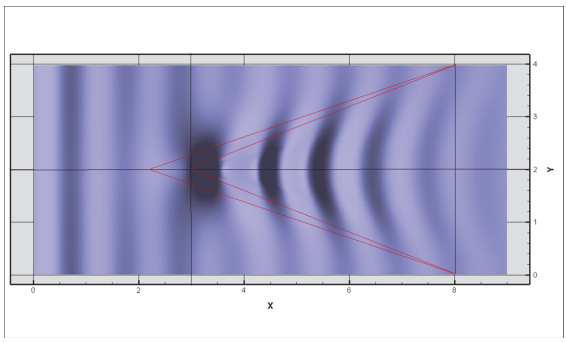

(b) d/lc=0.96237

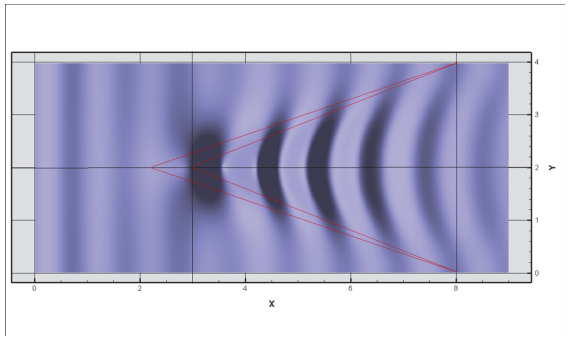

(c) d/lc=0.90474

Figure 5.32: Surface wave profiles and enclosed angles for all studies depths for Re=8×10^4 (LES).

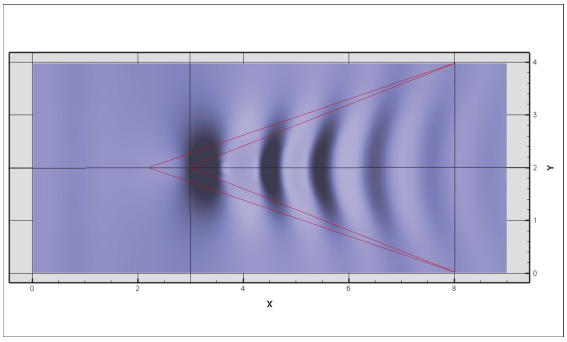

(a) d/lc=1.02113

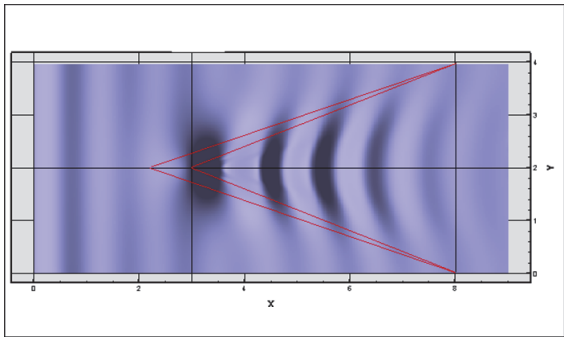

(b) d/lc=0.96237

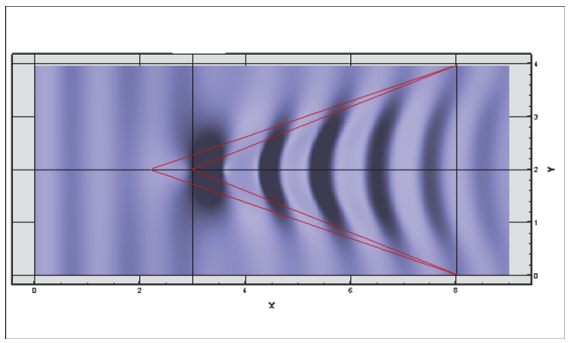

(c) d/lc=0.90474

Figure 5.33: Surface wave profiles and enclosed angles for all studies depths for Re=8×10^4 (DES)

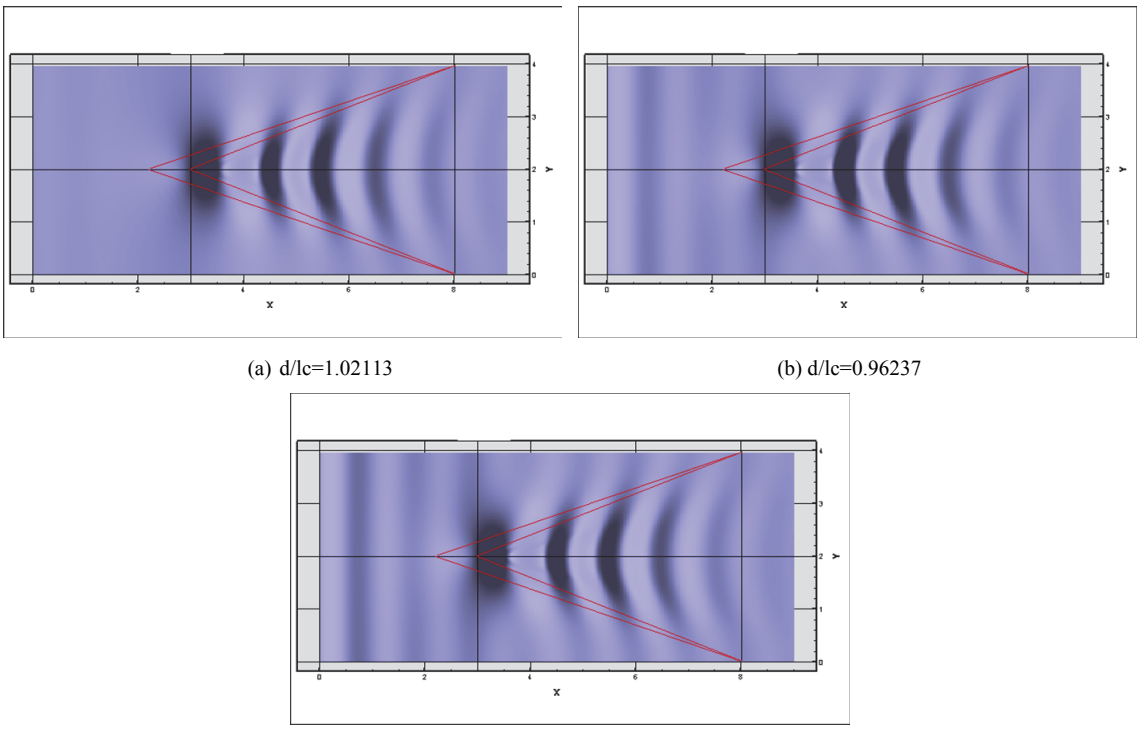

(a) d/lc=1.02113 (b) d/lc=0.96237

(c) d/lc=0.90474

Figure 5.34: Surface wave profiles and enclosed angles for all studies depths for Re=11×10^6 (DES)

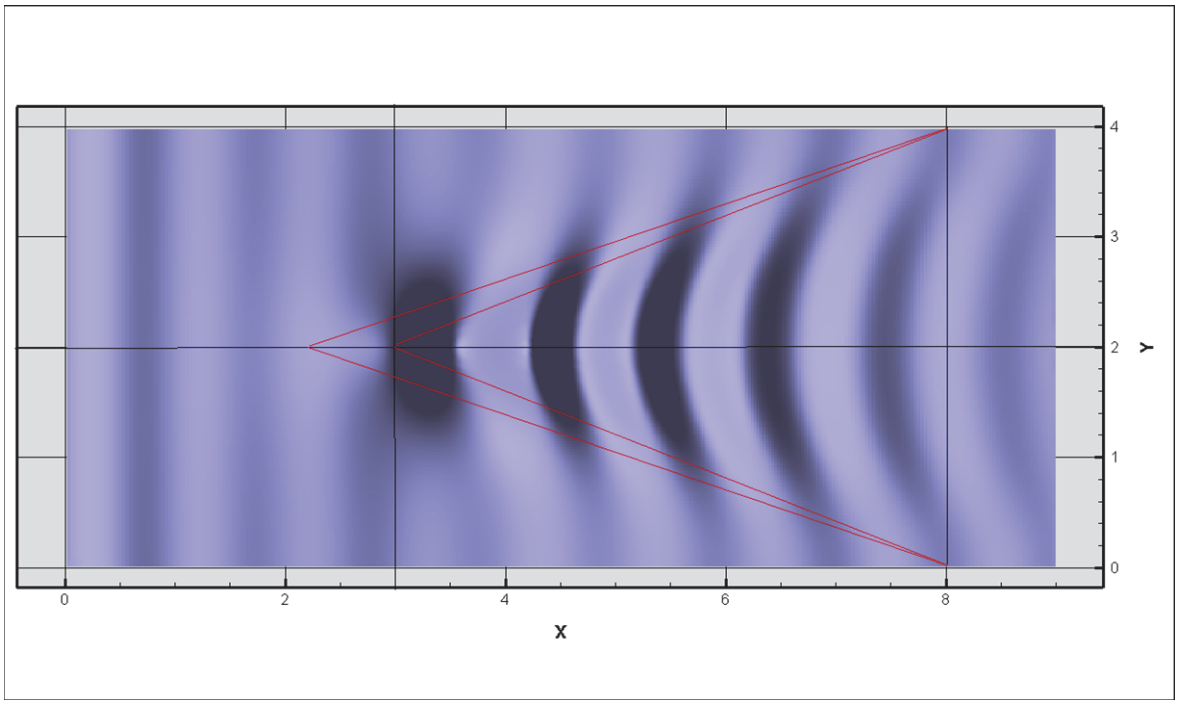

Figure 5.35: Enlarged Image of enclosing wave angle for surface waves generated by flow past the submerged fairwater.

Chapter 6 Conclusions & Further Work

This chapter concludes this thesis by reviewing the presented work. In addition, areas in which further research is recommended and ways in which the current work can be expanded are discussed.

6.1 Conclusions

Free-surface flow past both bluff and streamlined bodies has been numerically studied using LES and DES modelling approaches for a range of Froude and Reynolds numbers. In both cases the bodies of interest were enforced on the domain using the GCIBM concept rather than the conventional mapping of the grid around the body. The free-surface is accounted for by the use of a moving mesh. In order to prevent the need to re-evaluate the GCIMB representation at every time step, only the part of the mesh above the modelled geometries is allowed to deform.

Initially wave analysis was conducted to examine how the code behaved in the modelling of surface waves. The considered wave types were that of low amplitude standing waves, viscous low amplitude waves, reflection of non-linear waves and the behaviour of non-linear waves when encountering a submerged obstacle. Results from that study showed that the code was capable of accurately modelling both freely evolving and obstructed wave behaviours. From varying both the time step and spatial resolutions it was found that, both temporal and spatial resolution had an equal influence on the dissipation of wave energy if either was significantly large.

Further validation in terms of flow statistics and behaviour was also performed over a range of Re ranging from 3854 to 9×10^{6}. In all cases the bodies were generated using

the GCIBM approach and both LES and DES modelling techniques were tested. In all cases both LES and DES results showed good agreement with each other and against the comparative data and reported behaviours.

The studied bluff body was that of a cube with two different configurations. The first configuration was that of a matrix of equally spaced cubes, whilst the second configuration was that of a single cube placed in a uniform flow. The Reynolds numbers considered where that of $Re_{mc/sc}=3854$ and $Re_{mc/sc}=4\times10^{4}$. It was found that on average the free-surface boundary registered lower for increased Reynolds number for both cases. For both the single cube and a cube in a matrix configuration the well-defining features of a vortex ahead of the cubic body, an upper separation region above the cube and a wake region are captured in the numerical simulations. For the matrix cube configuration, 2D instantaneous streamline traces showed that the IOR is unsteady and constantly altering with time, with the rear recirculation region having a strong influence on the horse-shoe vortex. Similarly, instantaneous 3D streamlines around the multiple cube case revealed that the lower region was strongly influenced by the spanwise velocity, while the upper portion of the flow showed an increased influence from VS and the separated shear-layer region. The HSV was found to exist in an unsteady, distorted and broken state. For the single cube case, the horseshoe vortex was found to be steady around the body. While the unsteadiness in the horseshoe vortex was found to be confined to the separated flow region, with the HSV legs downstream of the wake showing an influence resulting from the shedding of structures. In both the single and multiple cube cases the reduction in SBD resulted in an increase in the vortical structures and interaction with the free-surface.

For the multiple cube case it was found that reducing submergence depth affected the dominant surface signature of the vortices. For the studied matrix configuration the vortex-free-surface interaction was found to change from an upwellings type of interaction to vortices aligning parallel to the free-surface. For a single cube reduction in SBD was found to cause a faster rise in VS, with VS in the near wake region interacting with the free-surface in the form of hockey/horseshoes; whilst downstream of the reattachment point surface signatures result from surface parallel vortices. For both the single and multiple cube cases vortices were a well established feature of the flow with vortices present for around 60% of the total monitored time. Increasing Re is found to increase the number of vortices and unsteadiness of vortical structures, giving rise to

higher Re stresses for both bluff body cases. While for the single cube increasing Re had influence on the horseshoe vortex ahead of the cube and on the length of the separation region behind the cube. The effect of increased Re on the HSV was the disappearance of multiple vortical structures ahead of the cube, whilst for the separation length increased Re resulted in the reduction of the average wake extent.

In terms of the turbulent intensities, Reynolds stresses and TKEB distributions both the single and matrix cube configurations were found to experience the greatest variation in regions where the shearing of the flow was the greatest. Increasing Re was found to increase the level of shearing and turbulence in the flow, resulting in an increase in the turbulent intensities, Re stresses and the TKEB. Furthermore, from comparing the single cube and matrix cube configurations it was found that damping of the vertical flow variation and redistribution only occurred if turbulence or turbulent structures were present near the free-surface boundary.

The average forces acting on the cube for both the single and matrix configurations were found to reduce for a decreasing SBD, whilst the variation in forces increased. In terms of shedding frequency the matrix cube configuration is found to show an increase for reducing depth (based on lift), similarly the single cube was also found to show the same trend (averaged point frequency).

For the fully submerged fairwater, simulations were performed at $Re_{lc}=8\times10^{4}$ and $Re_{lc}=11\times10^{6}$. The time averaged data, Re stresses and TKE distribution, revealed that the major part of the turbulent energy and flow variation was confined to the near wake region of the fairwater. While the TKE spectrums have shown that the wake was fully developed and that with reducing submergence depth the level of TKE in the wake was increased for all length scales. The effects of depth variation on the time averaged quantities are most notable on <p>, where reducing SBD was found to increase the variation of pressure in the wake due to the presence of larger waves. Furthermore the reduction in depth was found increase in turbulent intensity and Re stresses in the streamwise direction, while the effect on other time averaged components were to be less clear. For fairwater cases, both the LES and DES show the same behaviour for reducing SBD on the statistical and time averaged data.

The most notable vortical structures identified with the aid of streamline traces and Q iso-surfaces were the junction vortex which appeared in the form of a HSV, the tip vortex originating from the trailing tip of the fairwater and the wake region generated by the flow around the fairwater. Reducing SBD caused the tip vortex to occur in a more broken state due to increased influence of the wake. This behaviour was observed in all simulated cases and is partly attributed due to the unsteadiness in the shedding of structures along the height of the trailing edge which increased with the reduction in SBD. In all cases, vortex persistence was found to be well established within the wake region with results showing that vorticity was present for up to ~60-70% of the total monitored time, with the strongest mixing occurring at PT_{fn2}.

In terms of the average forces and force variation acting on the fairwater it was found that a reduction in the SBD resulted in an increase in both the forces and force variation. This was found to be the cases for both Re cases considered. The same trend was also found for the shedding frequency. The TKEB terms showed the greatest variation in the near tip and near wake region, while further downstream the contribution of the TKEB terms decreased substantially. For all cases the TKEB terms show a reduced area of influence in the near wake region for increasing fairwater height, whilst the level of contribution of all terms to the TKEB initially show an increase with increasing height along the fairwater before reducing. Near the upper surface of the fairwater nearly all TKEB terms show an increase, this increase is directly related to the presence/creation of the tip vortex. Furthermore, the effect of varying the Re was found to exhibit in little change in the <ε> and <VDF> implying that the eddy viscosity exceeded the molecular viscosity and controlled the level of dissipation in near wake region.

The surface waves were found to be enclosed within a wave angle between 38˚- 40˚ for all considered fairwater SBDs, hence the surface waves were of the Kelvin wave type. The waves are generated solely due to the fairwater body, while the effect of reducing SBD resulted in an increase in the amplitude of the propagating surface waves and the number of trailing waves. No direct vortex-free-surface interaction was found.

Comparatively, even though both the bluff body and streamline body are very different, not just in shape but in the general flow behaviour, there are similarities to the effects of depth variation in both cases. In both cases the reduction in SBD resulted in the variation in forces and shedding frequencies to increase. While in the wake the vortical

structures and TKE were enhanced. However it can not be clearly concluded that these are the generalised effects of depth variation for a submerged object due to the difference in the Froude number and a lack of variants in the studied geometries.

6.2 Further Work

In this thesis only coarse simulations of a submerged fairwater have been possible due to limitations in time and computational resources. It is possible to perform higher resolution simulations using the current parallelisation method of OMP. However, in order to obtain a better speed-up for increased grid resolution, implementation of MPI parallelisation is needed. This would make better use of the computational resources available to better study a fully submerged fairwater.

The current study has examined the affects of SBD on a fairwater in isolation; the geometry can be expanded by the inclusion of the appendages that are located on the fairwater. Such appendages that are usually located on the fairwater include the fairwater planes and a extendable periscope. Studying such cases (i.e. fairwater with planes and extended periscope) will better allow for the combined interactions and the effect of the free-surface to be understood.

For the multiple cube case variation in cube spacing could be examined, only a fixed spacing of 4 cube lengths was studied in this work. Therefore studying cubes at further distances apart or for different aspect ratios will better aid in the understanding of how free-surface flow influences the flow pattern and structure for such configurations. In addition, the transport of material can be also included for such cases which will be useful for coastal and civil considerations.

In terms of further work that can be done on the IBEXVOLES code, better results can be obtained by the inclusion of a better sub-grid scale model like the dynamic Smagorinsky model, to better account for the unresolved scales. Also the BCGSTAB pressure solver can be modified to run with the ghost-cell immersed boundary method, to allow faster are higher accuracy in the convergence criteria for the pressure solution.

The code written to generate all the geometries used in this thesis can also be improved. This can be done by modifying the code to accept a geometry created by a commercial meshing software. This will allow for the generation of more complex bodies.

Appendix 1 Grid Construction

There are numerous approaches for accounting for the presence of an geometry in a given domain. Typically, numerical grids in the past have been constructed from one of the following approaches:

1. Normal Cartesian
2. Curvilinear
3. Body fitted
4. Chimera
5. Unstructured

The most versatile of the grids mentioned is the unstructured. Unfortunately unstructured grids suffer from the problem of the mesh locally degenerating if uncontrolled, which can adversely affect the accuracy. In addition, the overall time for the pressure solver is generally longer than its counterparts based on structured approaches. Similarly, the use of a body fitted grid has the advantage of being able providing a structured grid with the ease of concentrating the mesh around the geometry. The disadvantage for the body fitted grid is similar to that of the unstructured grid in the sense the equations need to be transformed, hence increased solving time. Furthermore, if the body lies far from the domain boundaries, body fitted grids have a tendency of becoming very coarse towards the boundaries.

The chimera grid (also referred to as overlapping grids) tries to combine the effectiveness of body fitted grids in resolving the near boundary flow, around a given geometry. While using a normal Cartesian grid elsewhere to reduce the computational effort and solve time. Though the approach appears attractive its drawback lays in the coupling and maintaining conservation between the two grids.

The simplest grid generation methods involve using Cartesian and curvilinear grids. Until recently codes designed to handle curvilinear grids have been the most effective in their ease and applicability to various geometries, especially in two-dimensional domains. The use of a Cartesian grid in the actual representation of the geometry is limited due to the cells being simple cube. Complex geometries have been modelled on simple Cartesian grid (staircase approximation), however they have always invoked local grid refinement to improve the geometric representation.

Recent, work into advancing the immersed boundary method to handle rigid complex geometries seems to provide the most versatile approach. This is as the immersed boundary technique allows for the mapping of the geometry in to both structured and unstructured domains, with relatively simpler meshes. As aforementioned this approach is used to model/represent the desired geometries. This appendix provides the basic strategy for the imposition of an geometry into a grid, as well as, the extraction of information necessary to impose an immersed boundary technique successfully within a numerical code.

A1.1 Basic Grid

As previous indicated the generation of the grid is relatively simple, as since the grid is generated without any real regard for the body. However, factors that do need to be considered during the initial stage of grid construction include the position(s) and necessary grid refinement around the forced body/bodies.

Although grid generation is somewhat trivial the extraction of necessary body information required to impose the body is not. This is an additional necessary step needed once both the grid and body have been explicitly defined. The body can be either defined as by a set of points, a mesh, an equation or mathematical model. In this thesis, geometries generated have either used points, mesh or an equation, in the mapping and defining of the body.

A1.2 Mapping of Body

Once both the body and grid have been defined, it is necessary to subdivide the body into the corresponding cells within the grid. This can be done via the use of linear/bilinear or higher order interpolation stencils. Since faces are imposed as linear

segments the order of the stencil is not important as long as sufficient resolution is used in defining the body. It is important to identify all intersections that occur within the cell to better predict the correct approximation for the modelled face. Figure A1.1 shows how two-dimensional and three dimensional faces are imposed. For the three dimensional case more then one combination exits and all types of intersections do need to be considered, some examples of possible facial intersections are provided in Figure A1.2. The centre for the imposed face is then taken as an average of all the identified points.

The facial area and the face normal vector can then be determined as follows. Firstly the cell centre is selected and used as a fixed point of reference for this procedure. Two additional points are then also used that intersections within the cell, such that a total of three points are selected to form a plane, upon which the facial area and face normal are determined from A1.1-A1.8.

$$n_x x + n_y y + n_z z + d = 0 \tag{A1.1}$$

$$n_x = \begin{vmatrix} 1 & P_{1y} & P_{1z} \\ 1 & P_{2y} & P_{2z} \\ 1 & P_{3y} & P_{3z} \end{vmatrix} \tag{A1.2}$$

$$n_y = \begin{vmatrix} P_{1x} & 1 & P_{1z} \\ P_{2x} & 1 & P_{2z} \\ P_{3x} & 1 & P_{3z} \end{vmatrix} \tag{A1.3}$$

$$n_z = \begin{vmatrix} P_{1x} & P_{1y} & 1 \\ P_{2x} & P_{2y} & 1 \\ P_{3x} & P_{3y} & 1 \end{vmatrix} \tag{A1.4}$$

$$A_x = \left(P_{2y} - P_{1y}\right)\cdot\left(P_{3z} - P_{1z}\right) - \left(P_{2z} - P_{1z}\right)\cdot\left(P_{3y} - P_{1y}\right) \tag{A1.5}$$

$$A_y = \left(P_{2x} - P_{1x}\right)\cdot\left(P_{3z} - P_{1z}\right) - \left(P_{2z} - P_{1z}\right)\cdot\left(P_{3x} - P_{1x}\right) \tag{A1.6}$$

$$A_z = \left(P_{2x} - P_{1x}\right)\cdot\left(P_{3y} - P_{1y}\right) - \left(P_{2y} - P_{1y}\right)\cdot\left(P_{3x} - P_{1x}\right) \tag{A1.7}$$

$$A = \frac{\sqrt{A_x^{\,2} + A_y^{\,2} + A_z^{\,2}}}{2} \tag{A1.8}$$

The aforementioned procedure is repeated in either a clockwise or anti-clockwise direction till all facial areas and normal vectors have been determined. This is illustrated in Figure A1.3. The resulting normal is then taken as a weighted average based upon the calculated surface area for each section. The need for determining the face normal is crucial such that the necessary ghost-cells can determined, to aid in the identification of cells need for the interpolation stencil and is essential for determine that matrix inverse for the pressure. The importance of knowing the area is also crucial for similar reasons. Furthermore, both are helpful in post-grid generation stages such for analysis and post-processing.

A1.3 Identification of cell types

The use of the GCIMB implies that the fluid and solid cells need to be identified. Although the above mentioned procedures is capable of marking the body into the grid at this stage it is not known if these cells are ghost-cells and which cells are fluid or wall cells. A simple method to aid in identifying the face relation with respect to the grid, body and flow is to use a set or a single reference point(s) which exist inside the body or in the fluid part of the domain. The location of this point(s) must be known in prior. Hence, from constructing two vectors using the facial centre and a point based upon the normal as a guide, one can identify whether the normal faces into or out of the body. This is illustrated in Figure A1.4; note that if the surface normal is found to face into the body it needs to be corrected such that a consistent procedure is used, or vice versa (normals in this work are chosen to face into the flow).

To verify whether the cell in which the face is constructed is indeed a ghost cell, a commonly used approach in computer gaming, of comparing the angle between two vectors via the dot product can be used. By the use of this approach one can tell with respect to the imposed face whether the cell centre falls within the body or not. This is achieved via computing equation A1.9, if the solution is positive both vectors face in the same directions whilst negative would indicate the opposite is true.

$$\cos\phi = \frac{\left(V_1 \bullet V_2\right)}{\left|V_1\right|\left|V_2\right|} \tag{A1.9}$$

To ease calculation time requited per computational step whilst running the simulation a 'identity' matrix is also constructed to identify fluid, body, interface and ghost cells. This is such that wall cells are conveniently skipped and corrections are applied as ghost-cells with relative ease.

A1.4 Setting up interpolation for forcing function

Cells required for the interpolation and imposition of the ghost cell value are chosen based upon the surface normal vector. It should be noted that at this stage as illustrated in Figure A1.5, for all cells marked as ghost-cells there is a high probability that these cells will have multiple faces exposed to the flow. Two different approaches can be used deal with this problem. Firstly, the ghost-cell procedure can be applied to all exposed faces (multi-directional), whilst the alternative is to further simplify the facial expression so that a single stencil is needed per ghost-cell. The drawback of the first approach is the need for a larger portion of memory[6]. Whilst the drawback of the second approach is to that part of the sharpness ob the body is lost. The latter approach is used within this work, Figure A1.6 shows that the use of this method does not produce a loss in the modelling of a shape edge.

In general the points for the stencil coincide with data points, in the case of a collocated grid these are the cell centres. However, if the grid upon which the body is imposed is stretched, the use of such positions can prove to be problem-some, a result owed due to the compressing of cells. Furthermore, if the face point of the imposed face lies close to any of the points chosen, large negative weighted coefficients can be encountered that can also prove problem-some. A few procedures to overcome the issue of large negative weighted are addressed in Tseng & Ferziger (2003). Though these approaches are capable of fixing the latter problem, a different approach is used to overcome both of the aforementioned issues. The approach used is; to expand the stencil such that data is evaluated at the faces of the cells rather then at cell centres. Moving the points to the faces is found to produce a stable quadratic stencil from which the velocities can be determined, however expanding the stencil does mean that part of the sharpness of the flow close to the wall is lost. To minimize this one can find a stable position for the

[6] The use of a matrix approach for quadratic stencil is far higher then the use of a linear stencil. It would prove very costly if the forcing value was computed separately for all three directions via three matrices.

inner points. Once the points have been computed the inverse can be calculated (section 2.4.1).

A1.5 Determining wall normal distance

In many applications especially high Reynolds number flow situations the use of a wall, subgrid, or shear stress model would require for the wall normal distance to be determined. In this case the distance for cells that are either touching or a cell away from an identified ghost cell may require their normal point to the boundary to be determined. A noval approach to do this is to find where a line (based on the normal projection) crosses a given plane. This done by solving equations A1.10 through to A1.12,where points P, P1, P2 and P3 are; the point of intersection on the plane, the point of interest, a projected point based on the surface normal behind the face of interest and arbitrary point on the face respectively.

$$\mathrm{N} \bullet \left(P_1 + f_x\left(P_2 - P_1\right)\right) = \mathrm{N} \bullet P_3 \tag{A1.10}$$

$$f_x = \frac{\mathrm{N} \bullet \left(P_3 - P_1\right)}{\mathrm{N} \bullet \left(P_2 - P_1\right)} \tag{A1.11}$$

$$P = P_1 + f_x\left(P_2 - P_1\right) \tag{A1.12}$$

If the intersection point P is found to lie outside of the given facial area limit the surface area and normal should then be weighted with neighbouring cells to find the approximate point of intersection P. For cells further then a cell away for a known ghost-cell the application of such a procedure becomes very tedious. This is owed due to the body being defined through some procedure listed in section A1.2, regardless of any procedure used the method of trying to projection of a point on to a body to find its normal would prove too tricky if not impossible. In this work an approximate distance can be taken instead, by determining the resultant distance from the point of interest to an interface cell for which the distance to the wall is already known.

A1.6 Figures

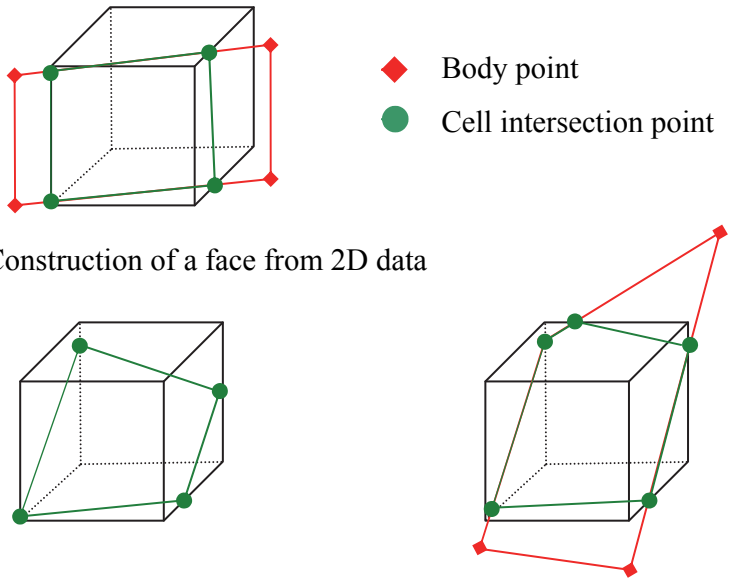

(a) Construction of a face from 2D data

(b) Construction of face for 3D data for points contained (right) and not contained (left) within the cell

Figure A1.1: Face Mapping for a two-dimensional and three-dimensional body points in to a grid cell

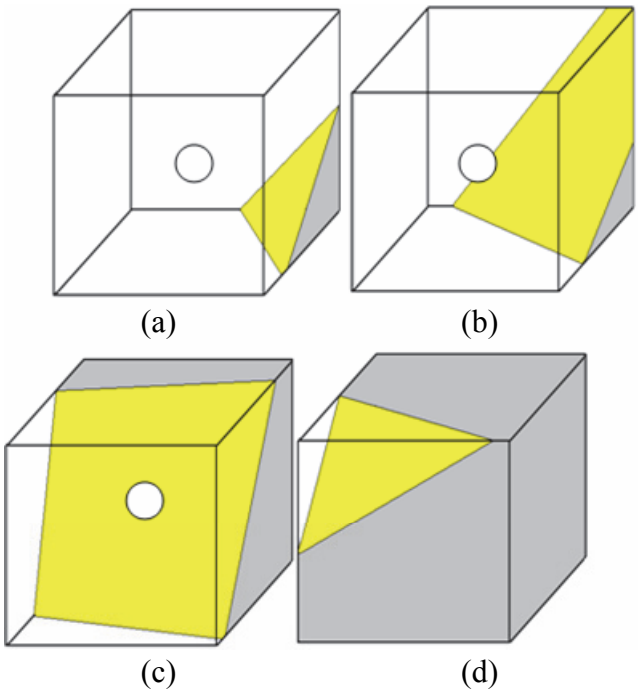

Figure A1.2: Possible intersection of an immersed boundary face within a cell volume

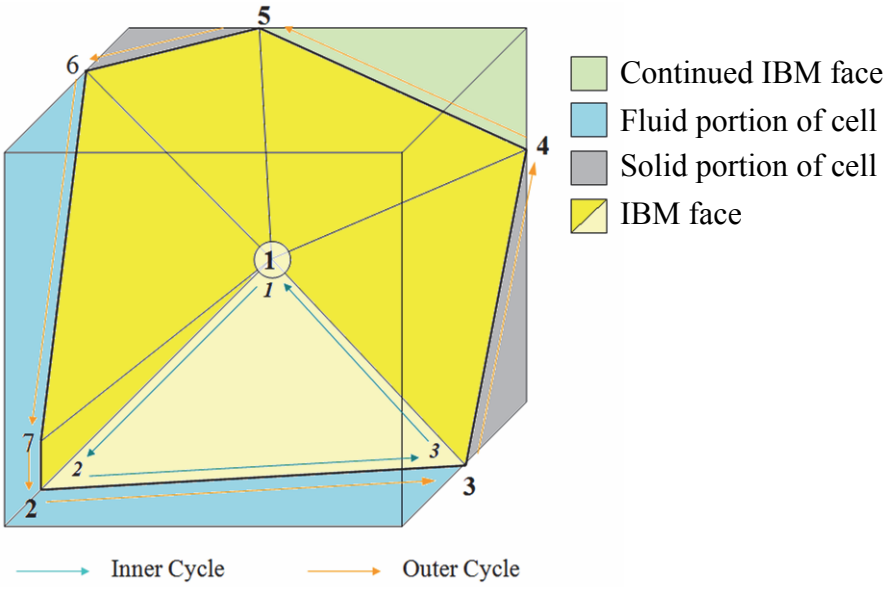

Figure A1.3: Calculating facial normal for immersed boundary face through an area weighted averaging of all sectional faces defined within a cell

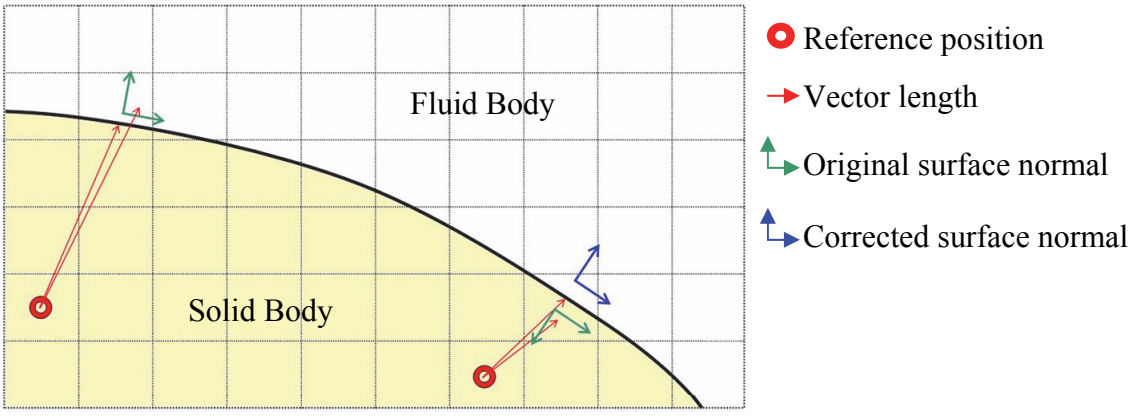

Figure A1.4: Determination and correcting the direction of immersed boundary facial norms based upon known reference(s) position

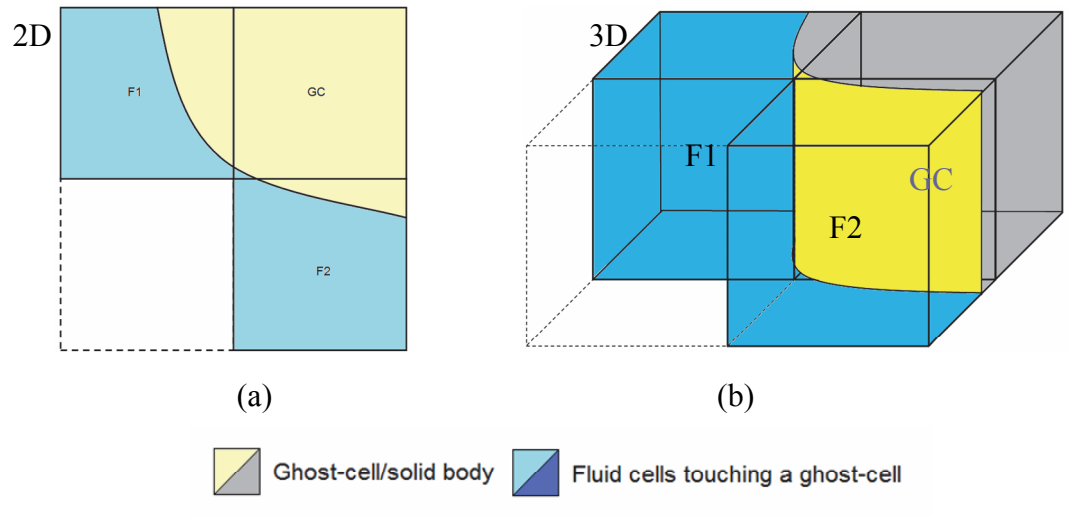

Figure A1.5: Interaction of a ghost-cell with multiple fluid faces in two-dimensional and three-dimensional cases

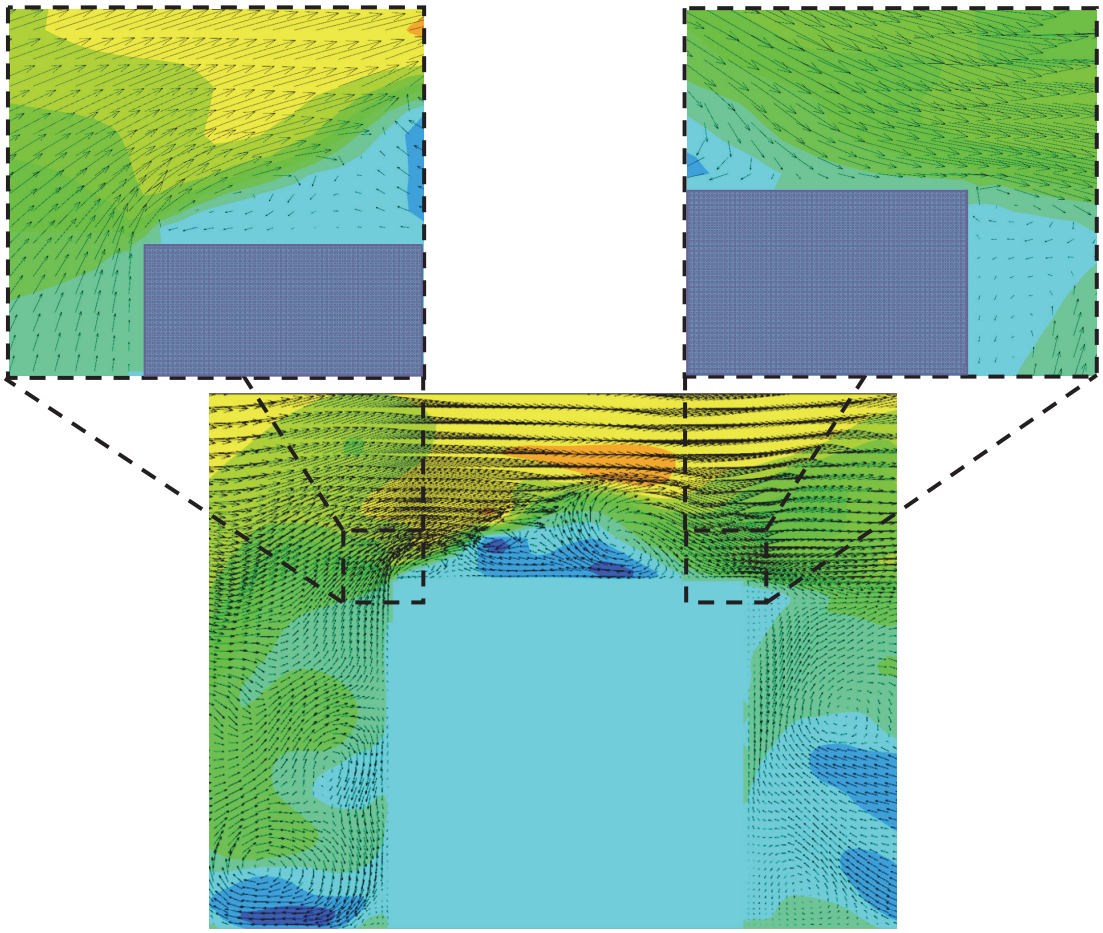

Figure A1.6: Immersed boundary solution around a cube showing the sharpness of vectors near the edge of a cube, where the ghost-cell enforces an average value in order to consider all sides exposed to the flow

Appendix 2 Additional XY Plane Plots for Flow around Multiple and Single cube(s)

List of Figures for multiple cube

Figure Legend

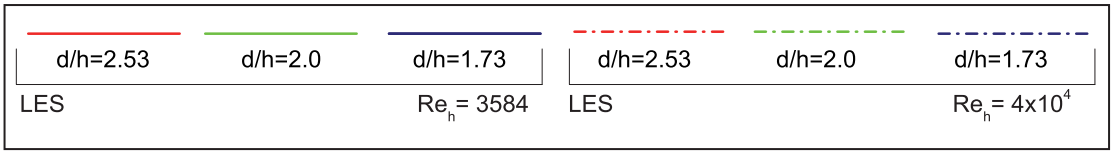

List of figures for Single cube

Figure Legend

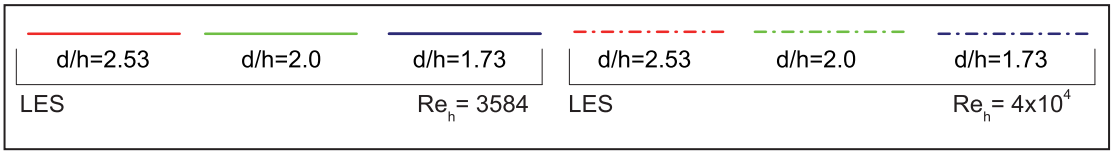

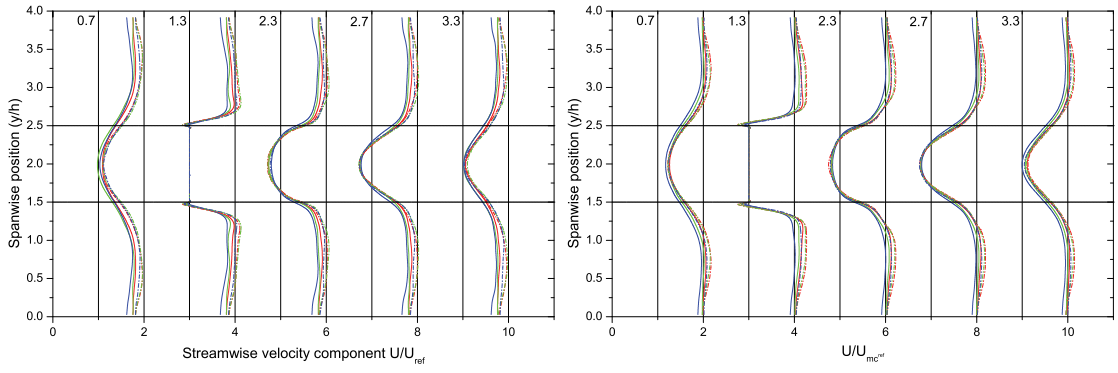

(a) *z/d=0.1*

(b) *z/d=0.4*

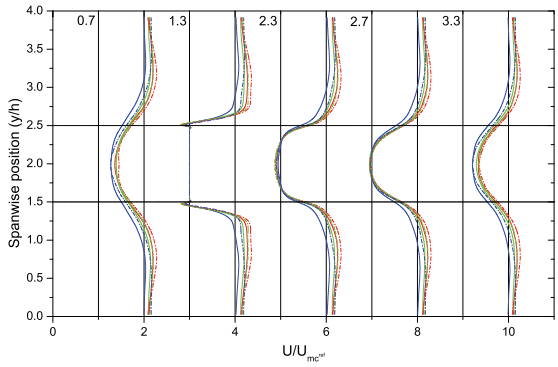

(c) *z/d=0.7*

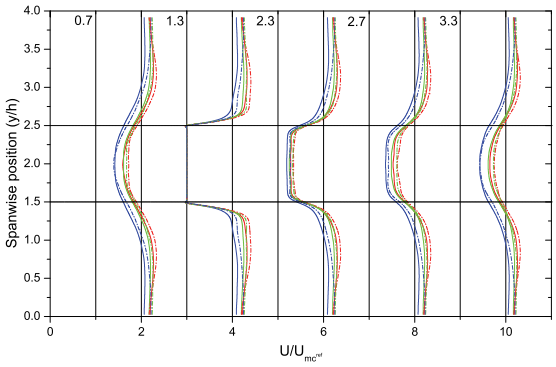

(d) *z/d=0.95*

Figure A2.1: Mean streamwise velocity distribution around a cube in a matrix configuration in the XY plane.

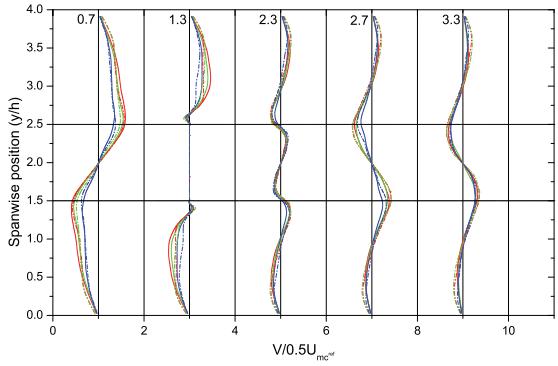

(a) *z/d=0.1*

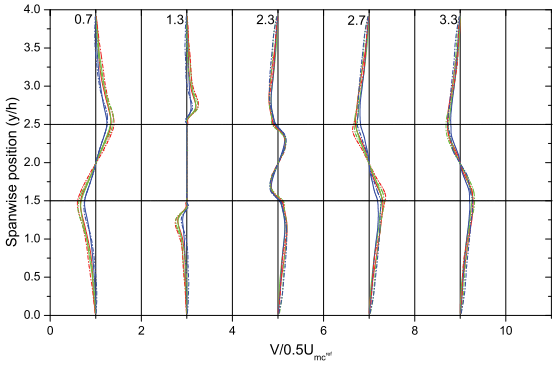

(b) *z/d=0.4*

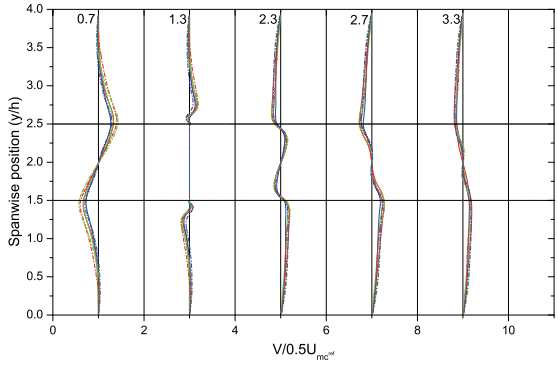

(c) *z/d=0.7*

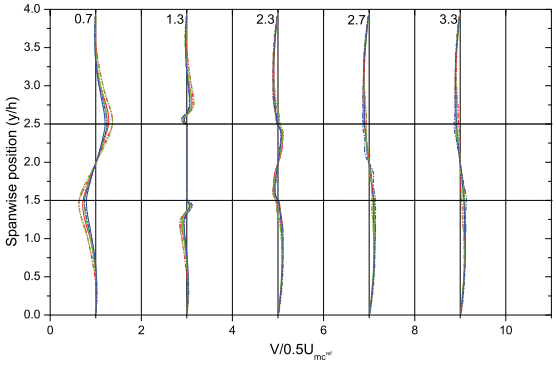

(d) *z/d=0.95*

Figure A2.2: Mean spanwise velocity distribution around a cube in a matrix configuration in the XY plane.

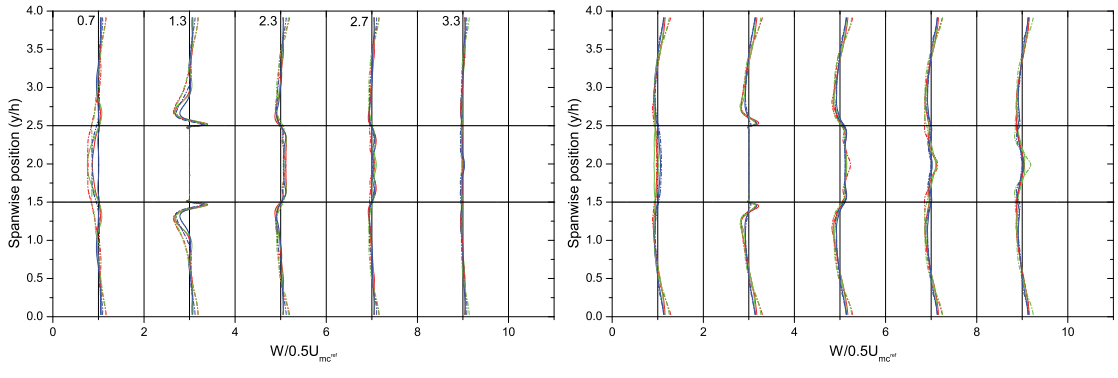

(a) *z/d=0.1* (b) *z/d=0.4*

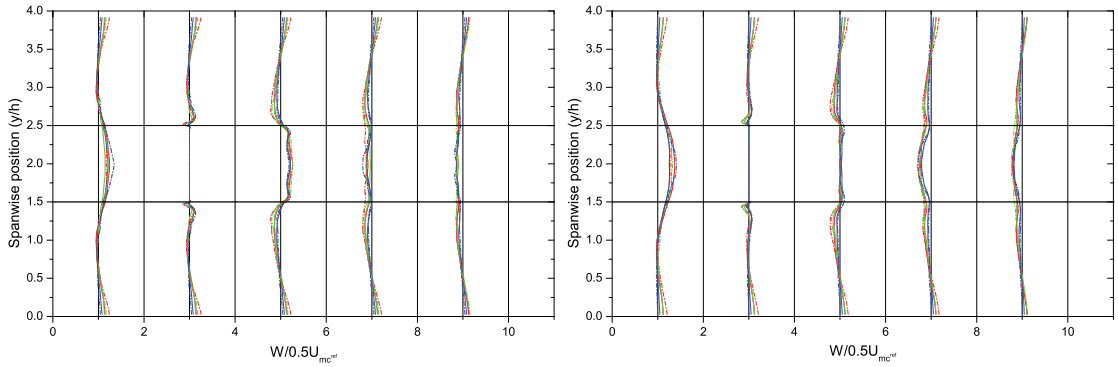

(c) *z/d=0.7* (d) *z/d=0.95*

Figure A2.3: Mean vertical velocity variation around a cube in a matrix configuration in the XY plane.

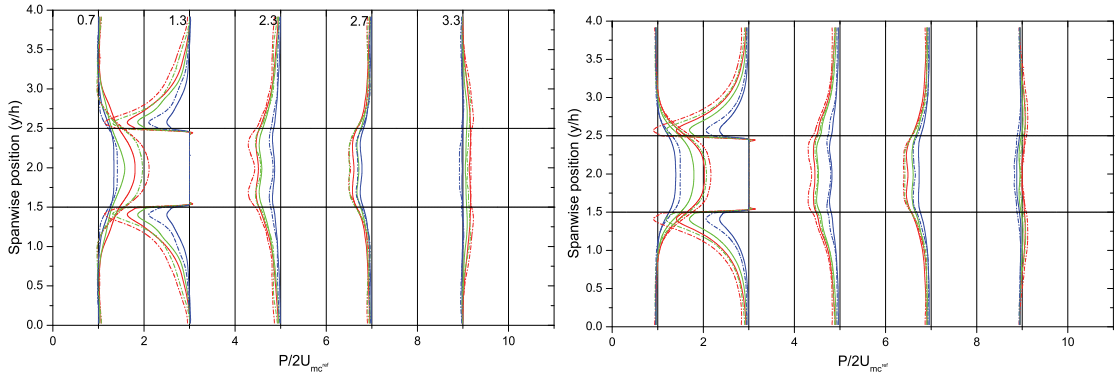

(a) *z/d=0.1* (b) *z/d=0.4*

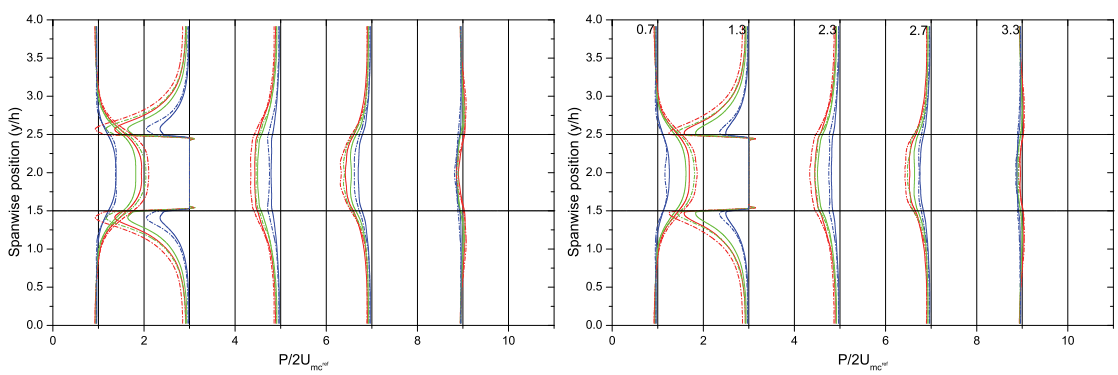

(c) *z/d=0.7* (d) *z/d=0.95*

Figure A2.4: Mean pressure distribution around a cube in a matrix configuration in the XY plane.

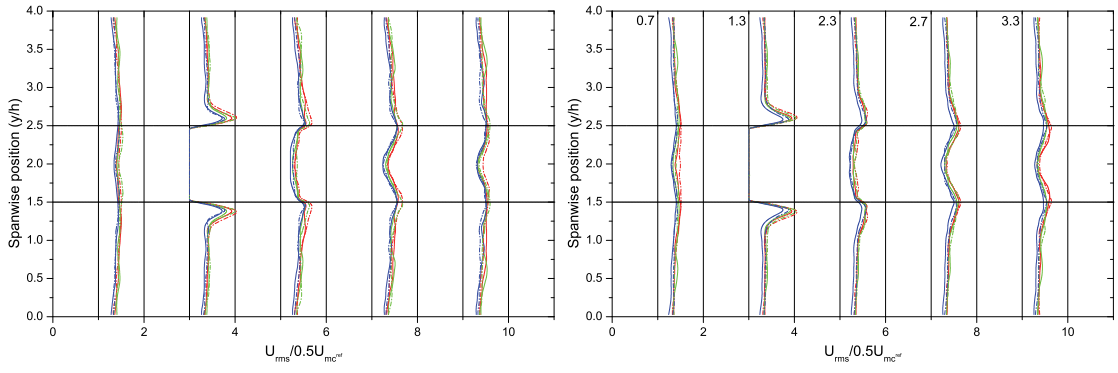

(a) *z/d=0.1* (b) *z/d=0.4*

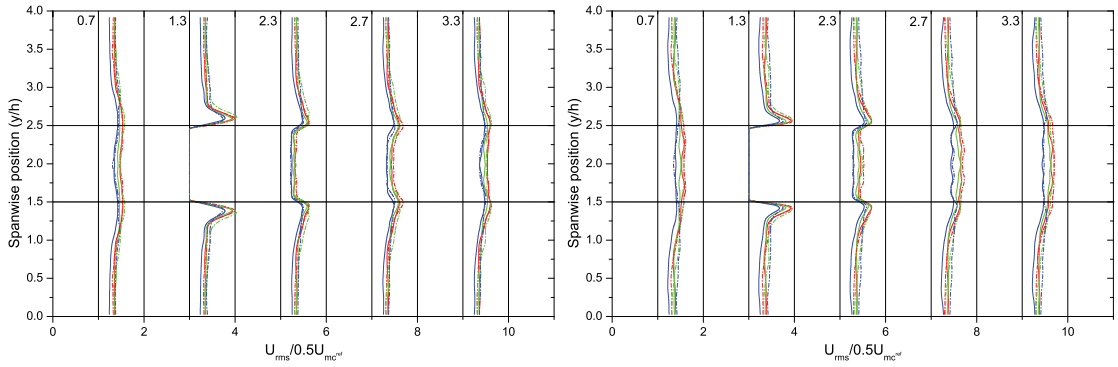

(c) *z/d=0.7* (d) *z/d=0.95*

Figure A2.5: Streamwise turbulent intensity distribution around a cube in a matrix configuration in the XY plane.

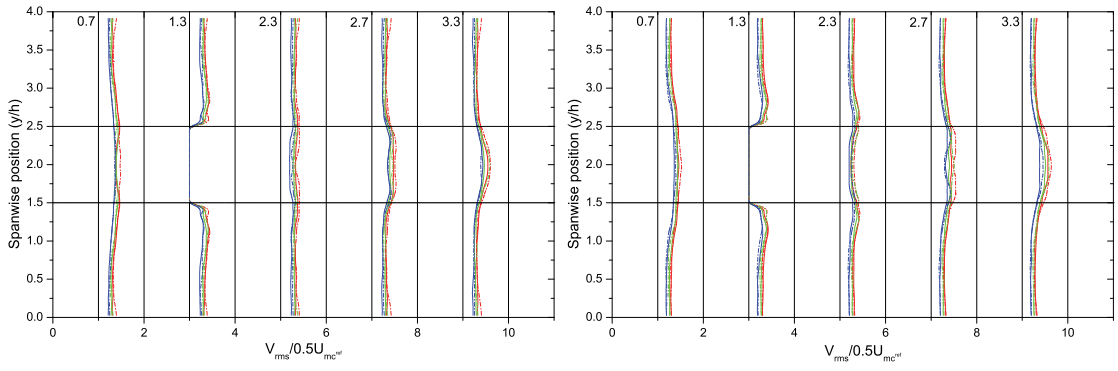

(a) *z/d=0.1* (b) *z/d=0.4*

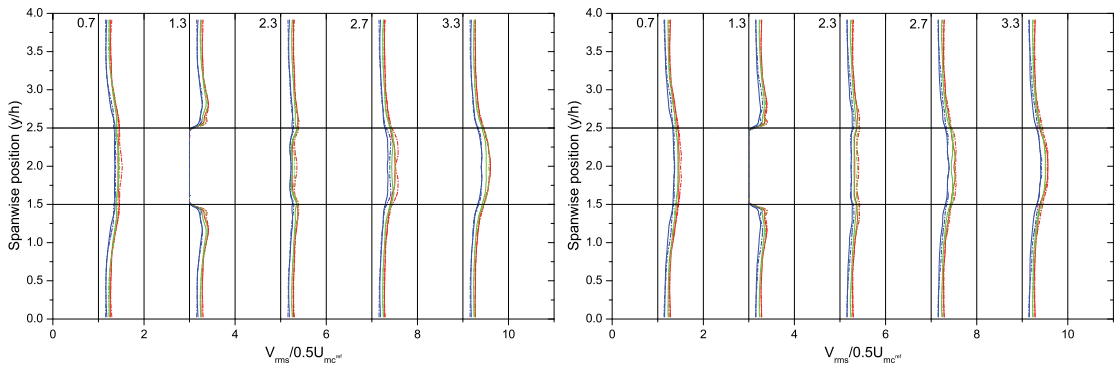

(c) *z/d=0.7* (d) *z/d=0.95*

Figure A2.6: Spanwise turbulent intensity distribution around a cube in a matrix configuration in the XY plane.

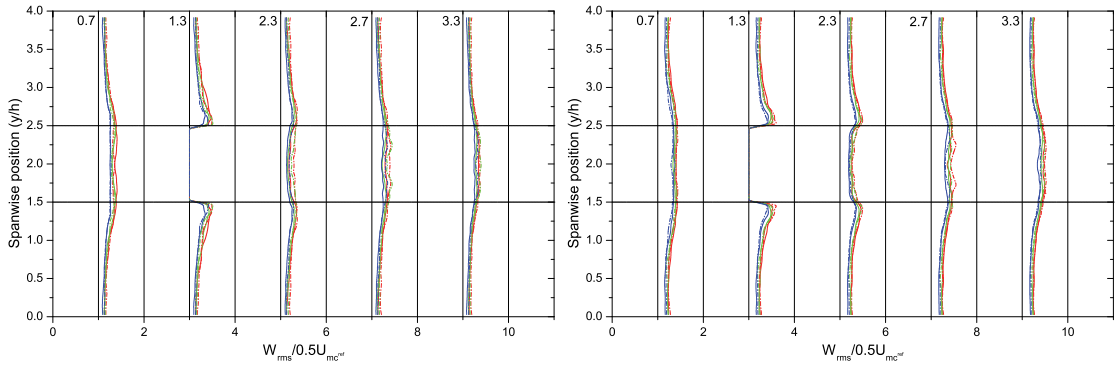

(a) *z/d=0.1* (b) *z/d=0.4*

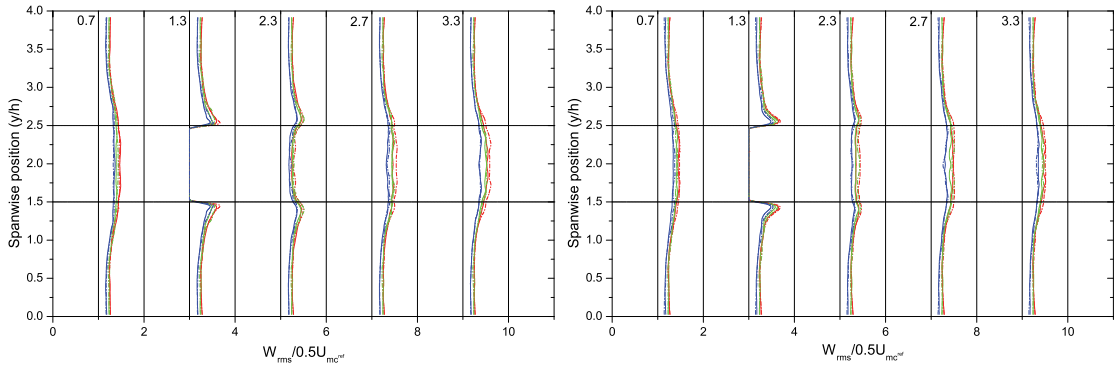

(c) *z/d=0.7* (d) *z/d=0.95*

Figure A2.7: Vertical turbulent intensity distribution around a cube in a matrix configuration in the XY plane.

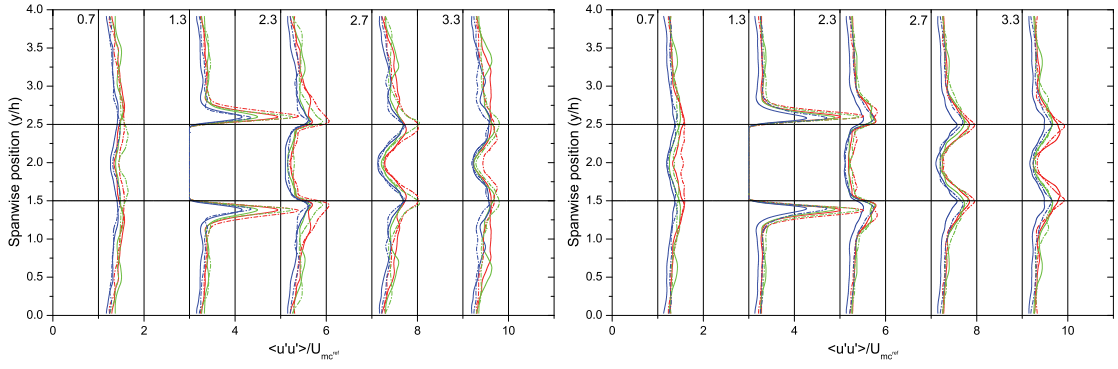

(a) *z/d=0.1* (b) *z/d=0.4*

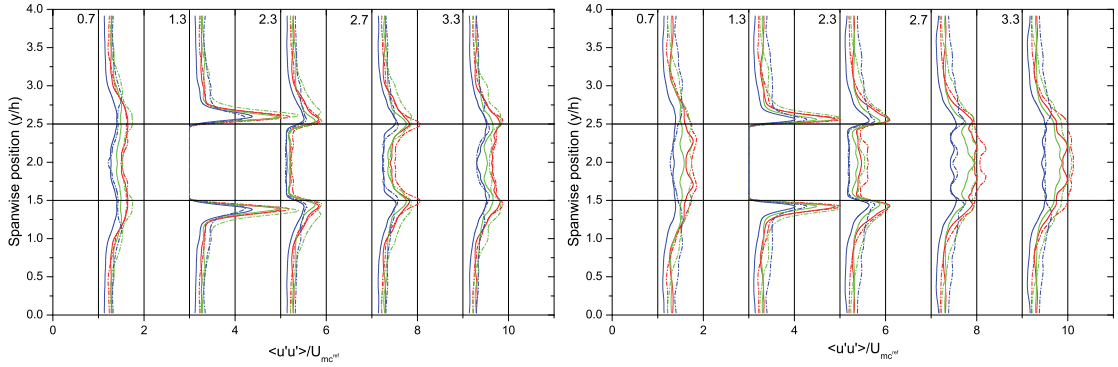

(c) *z/d=0.7* (d) *z/d=0.95*

Figure A2.8: Time averaged u'u' normal Reynolds stress distribution around a cube in a matrix configuration in the XY plane.

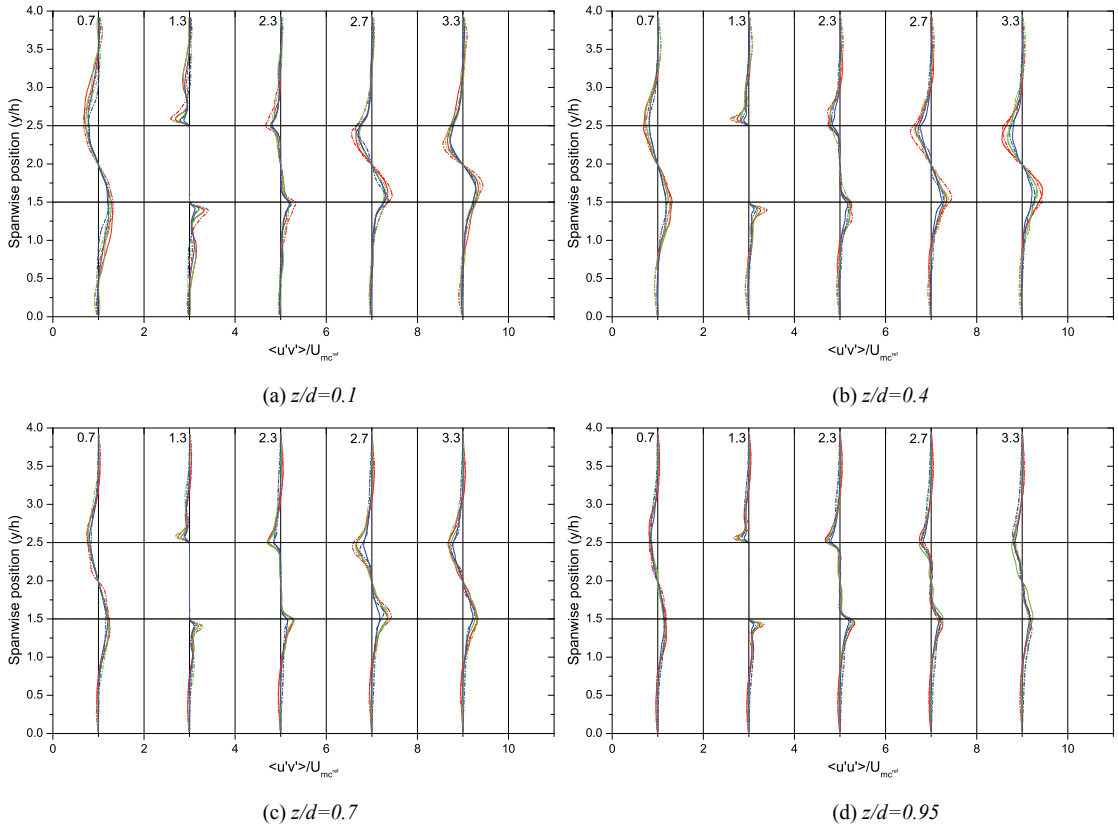

(a) *z/d=0.1* (b) *z/d=0.4*

(c) *z/d=0.7* (d) *z/d=0.95*

Figure A2.9: Time averaged u'v' cross Reynolds stress distribution around a cube in a matrix configuration in the XY plane.

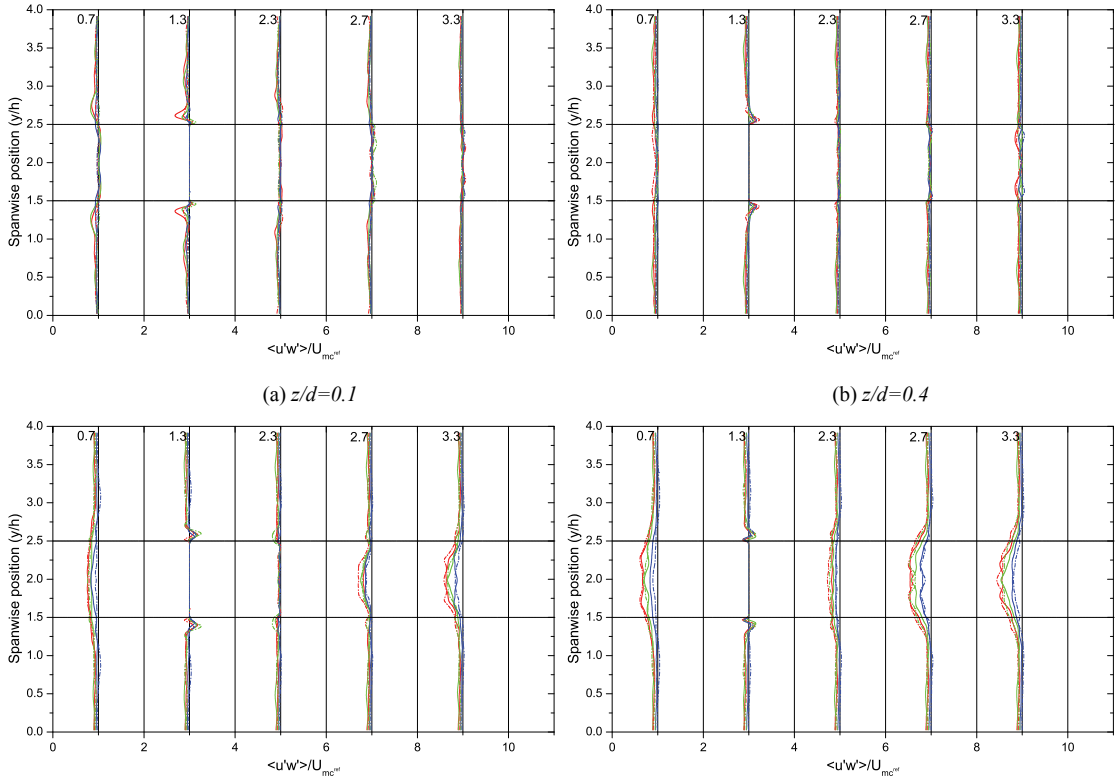

(a) *z/d=0.1* (b) *z/d=0.4*

(c) *z/d=0.7* (d) *z/d=0.95*

Figure A2.10 Time averaged u'w' cross Reynolds stress distribution around a cube in a matrix configuration in the XY plane.

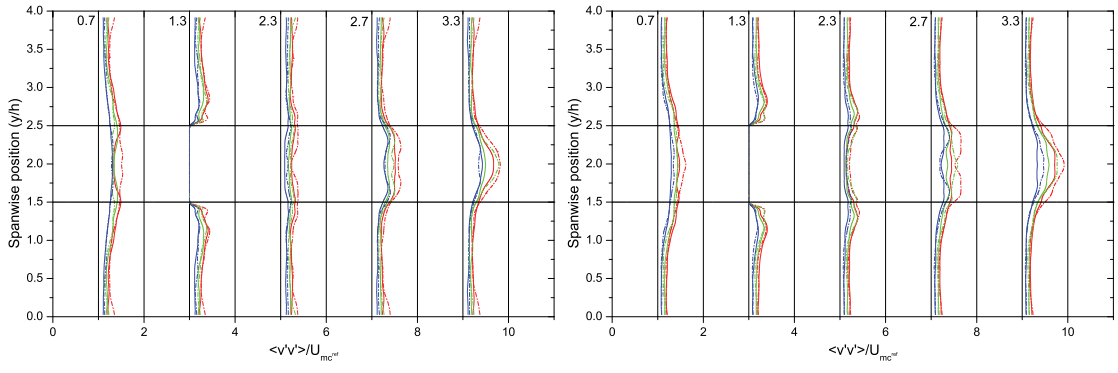

(a) *z/d=0.1* (b) *z/d=0.4*

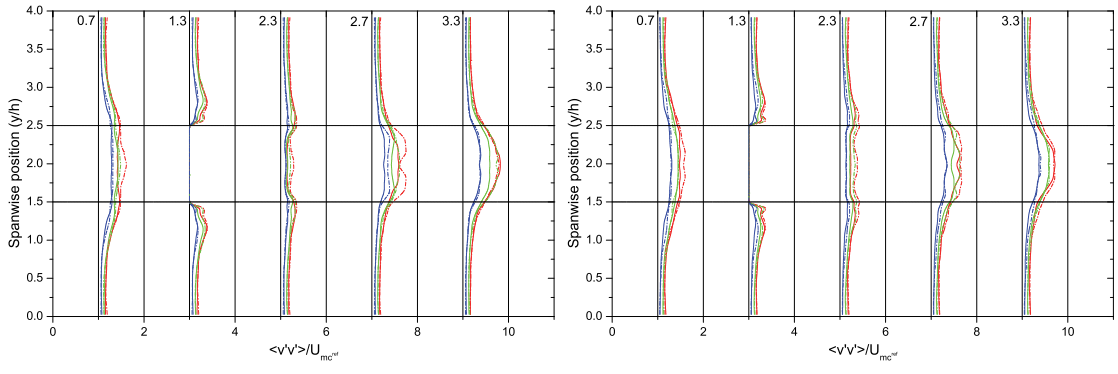

(c) *z/d=0.7* (d) *z/d=0.95*

Figure A2.11: Time averaged v'v' normal Reynolds stress distribution around a cube in a matrix configuration in the XY plane.

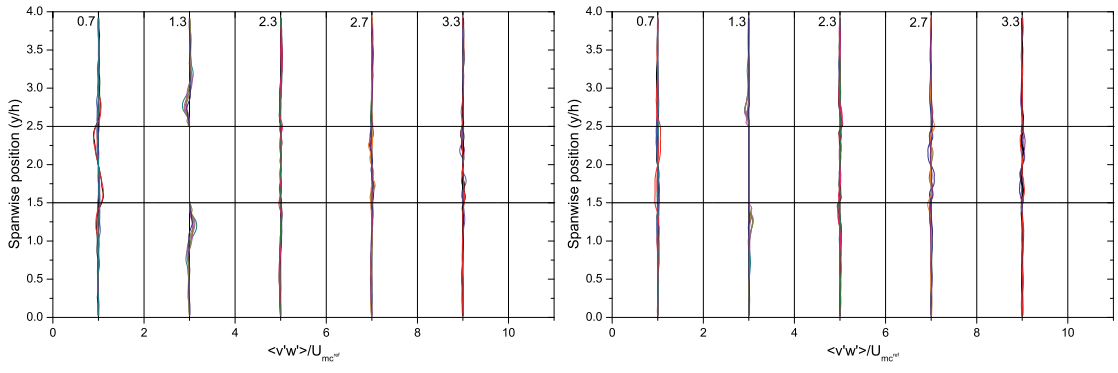

(a) *z/d=0.1* (b) *z/d=0.4*

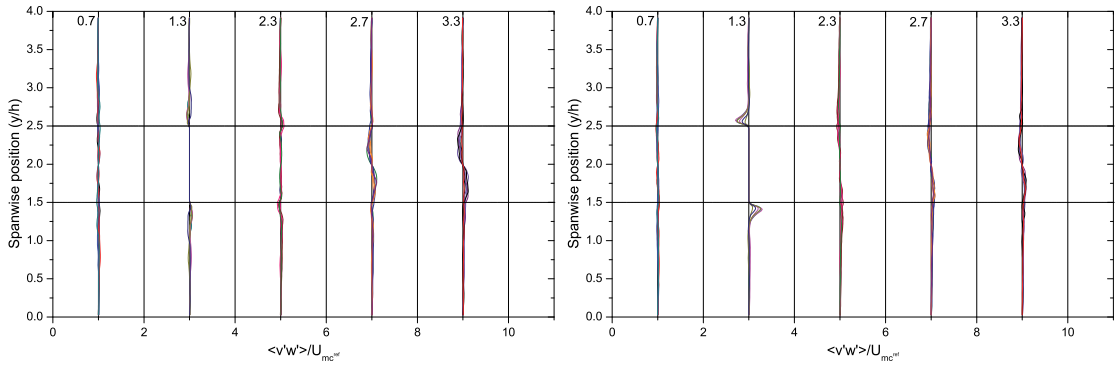

(c) *z/d=0.7* (d) *z/d=0.95*

Figure A2.12: Time averaged v'w' cross Reynolds stress distribution around a cube in a matrix configuration in the XY plane.

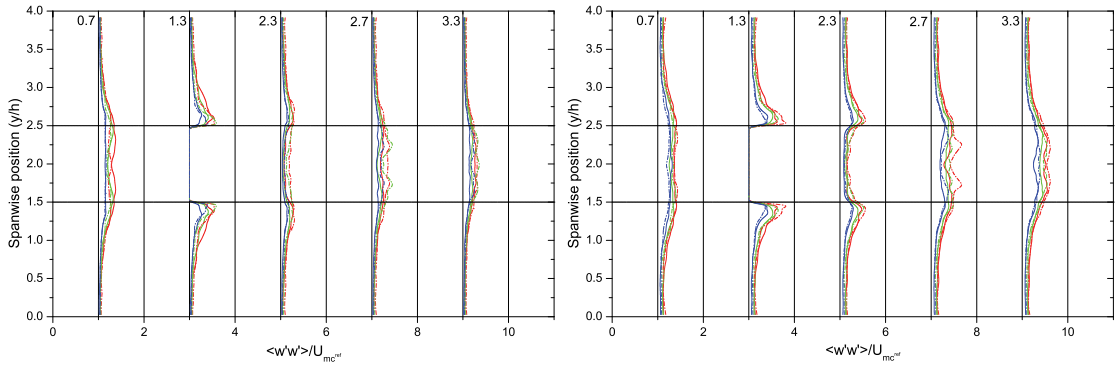

(a) *z/d=0.1* (b) *z/d=0.4*

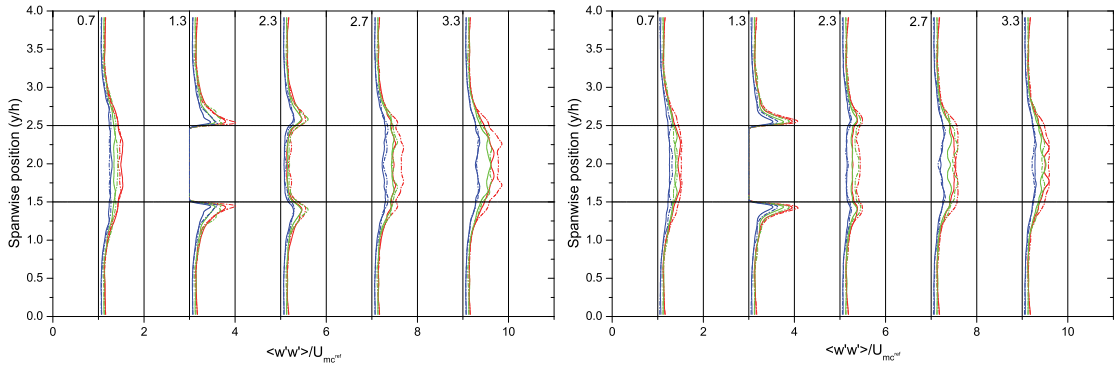

(c) *z/d=0.7* (d) *z/d=0.95*

Figure A2.13: Time averaged w'w' normal Reynolds stress distribution around a cube in a matrix configuration in the XY plane.

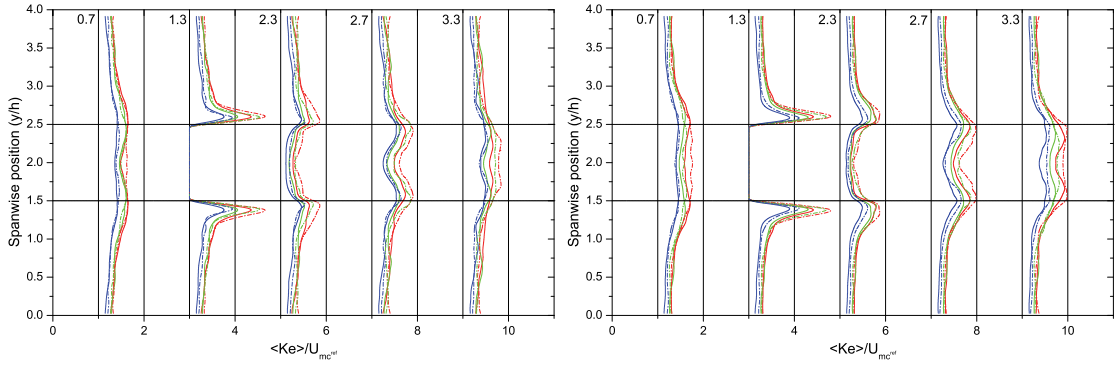

(a) *z/d=0.1* (b) *z/d=0.4*

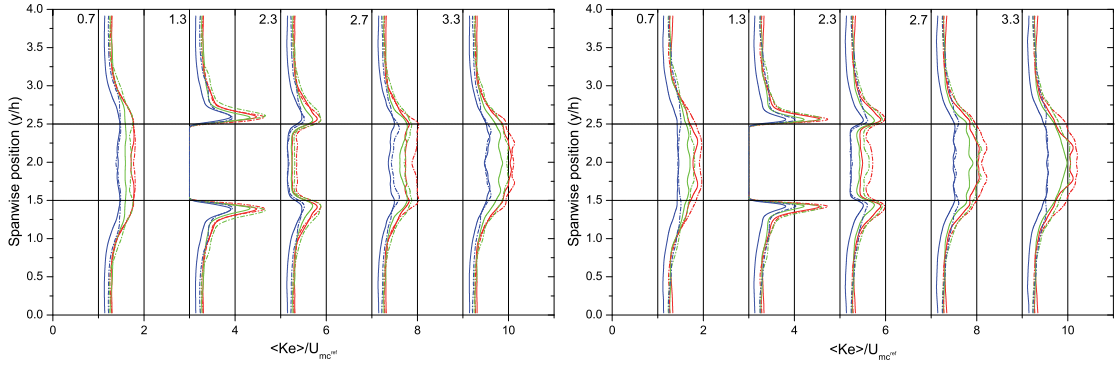

(c) *z/d=0.7* (d) *z/d=0.95*

Figure A2.14: turbulent kinetic energy distribution around a cube in a matrix configuration in the XY plane.

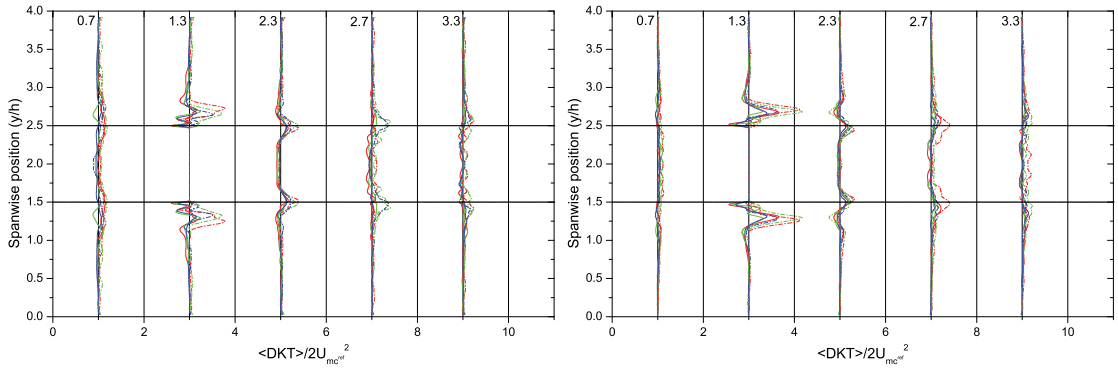

(a) *z/d=0.1* (b) *z/d=0.4*

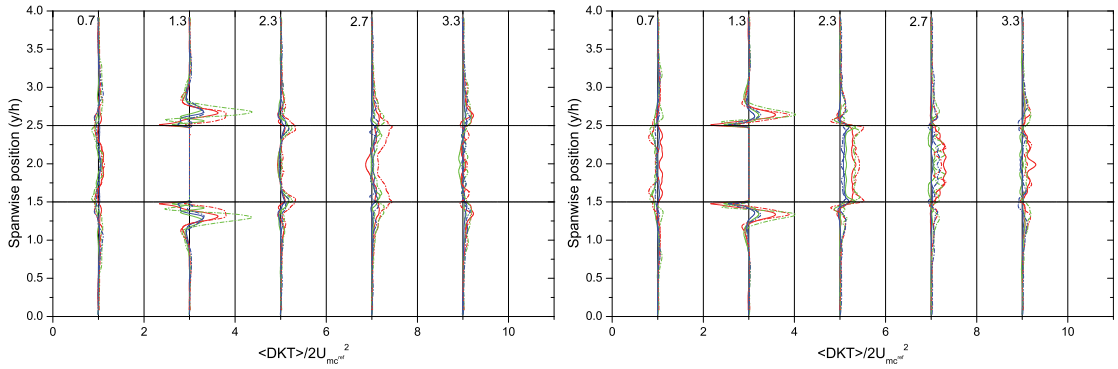

(c) *z/d=0.7* (d) *z/d=0.95*

Figure A2.15: Time averaged DKT distribution around a cube in a matrix configuration in the XY plane.

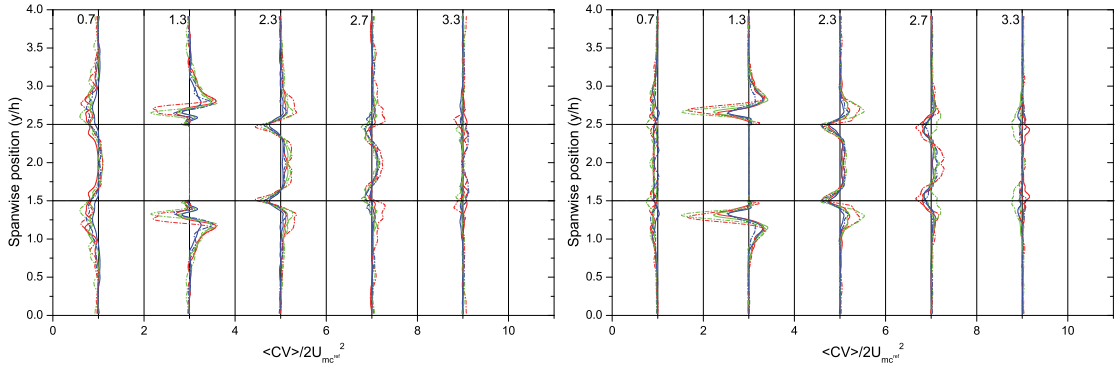

(a) *z/d=0.1* (b) *z/d=0.4*

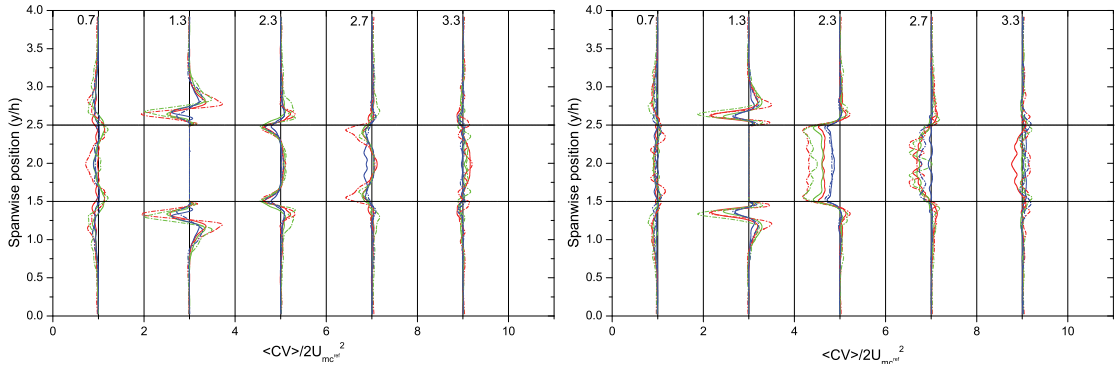

(c) *z/d=0.7* (d) *z/d=0.95*

Figure A2.16: Time averaged CV distribution around a cube in a matrix configuration in the XY plane.

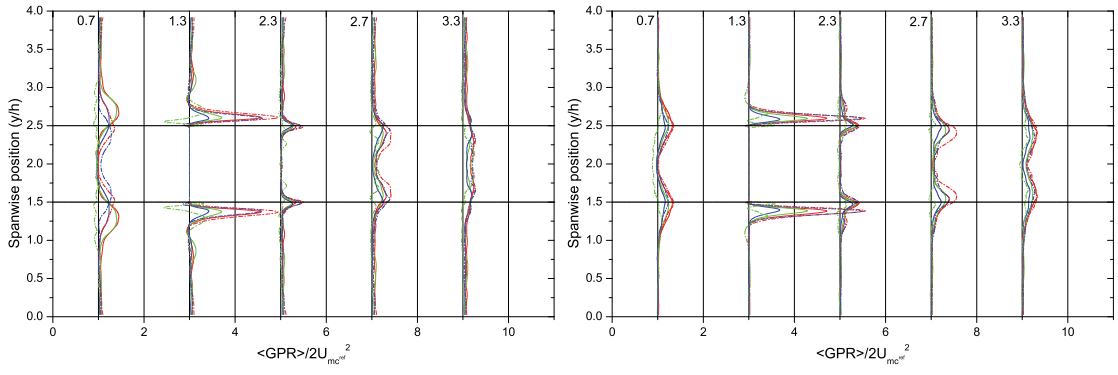

(a) *z/d=0.1* (b) *z/d=0.4*

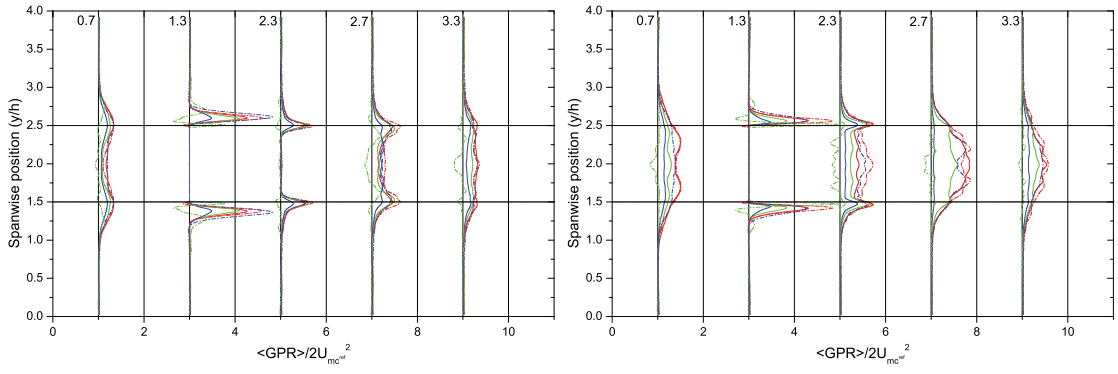

(c) *z/d=0.7* (d) *z/d=0.95*

Figure A2.17: Time averaged GPR distribution around a cube in a matrix configuration in the XY plane.

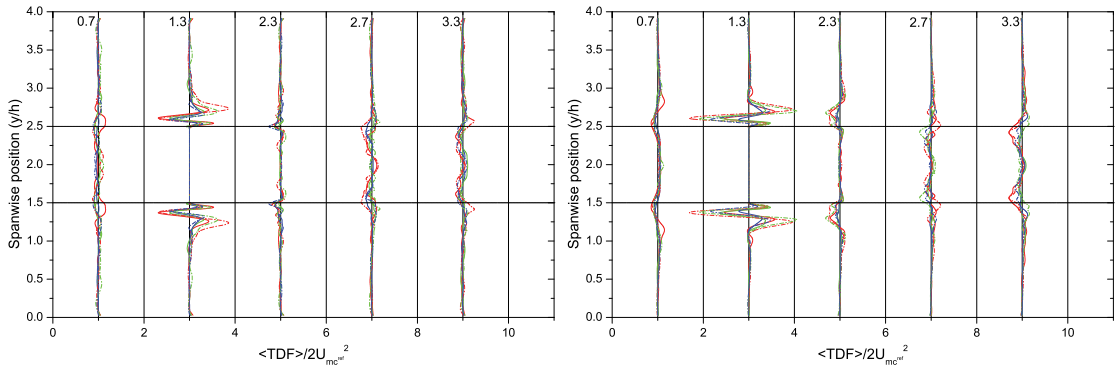

(a) *z/d=0.1* (b) *z/d=0.4*

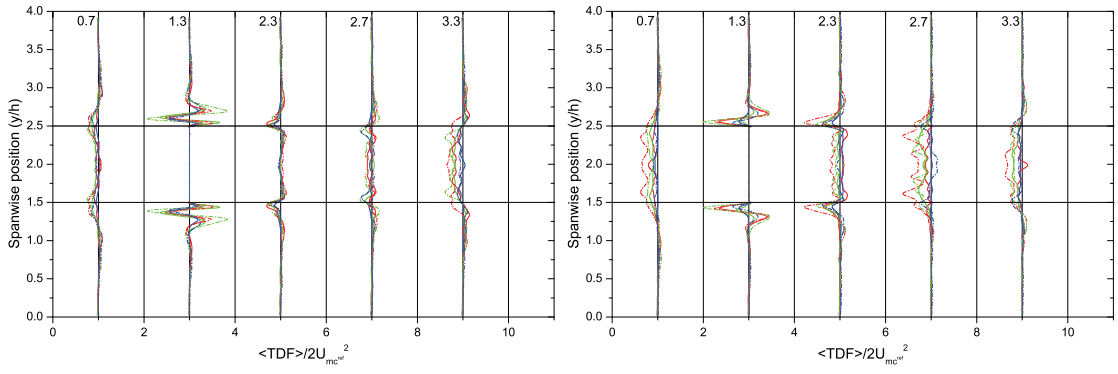

(c) *z/d=0.7* (d) *z/d=0.95*

Figure A2.18: Time averaged TDR distribution around a cube in a matrix configuration in the XY plane.

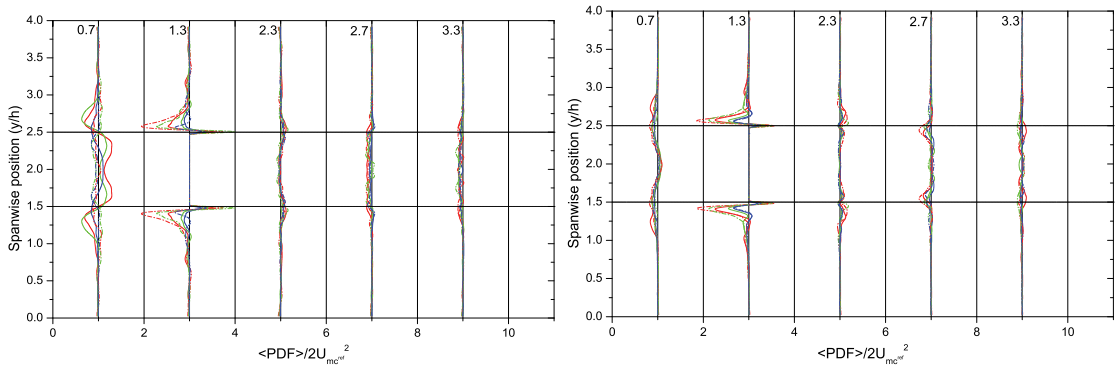

(a) *z/d=0.1* (b) *z/d=0.4*

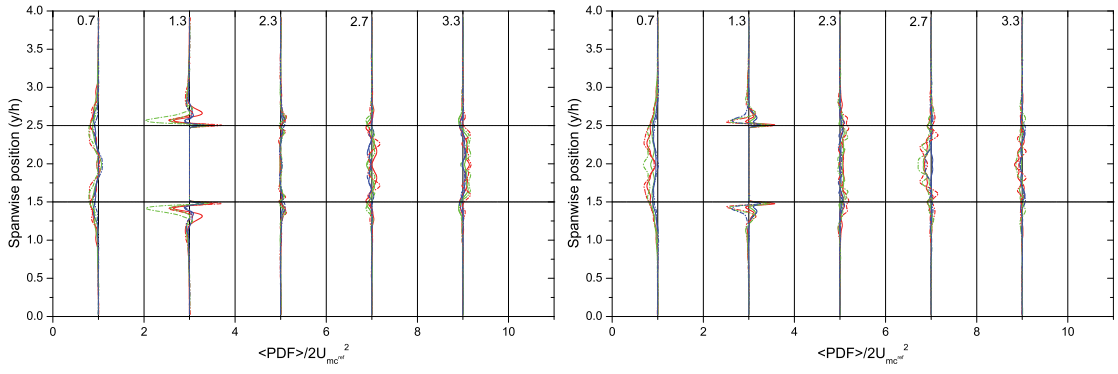

(c) *z/d=0.7* (d) *z/d=0.95*

Figure A2.19: Time averaged PDF distribution around a cube in a matrix configuration in the XY plane.

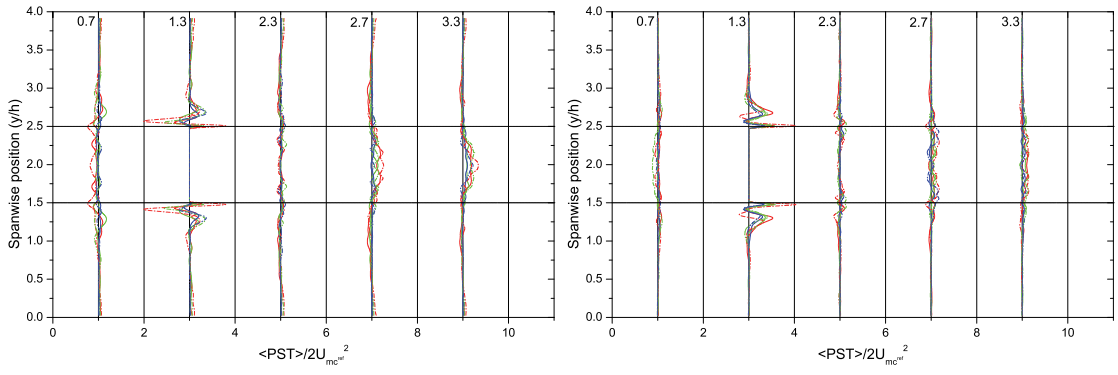

(a) *z/d=0.1* (b) *z/d=0.4*

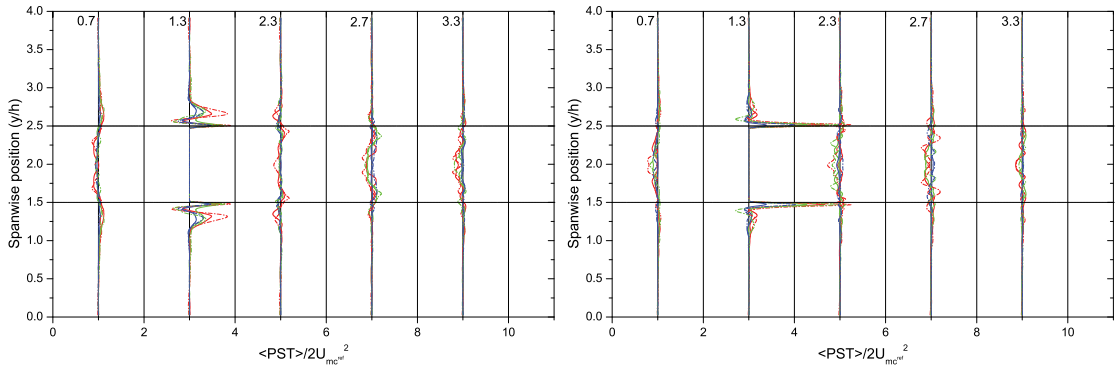

(c) *z/d=0.7* (d) *z/d=0.95*

Figure A2.20: Time averaged PST distribution around a cube in a matrix configuration in the XY plane.

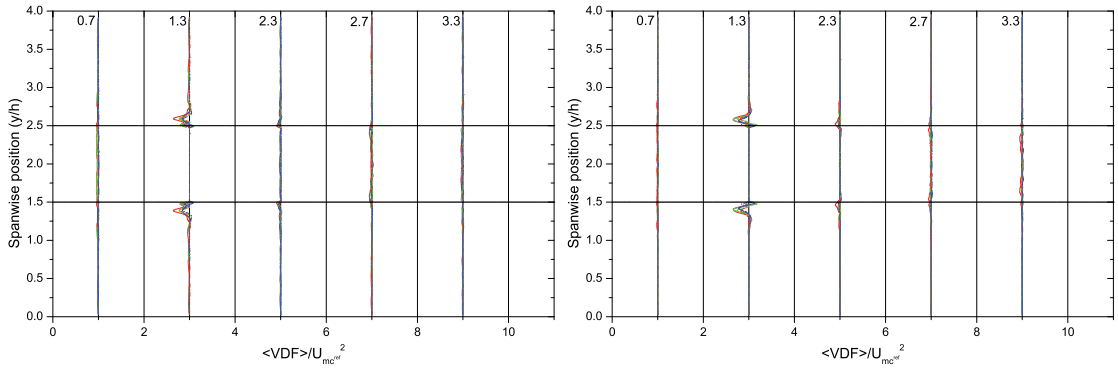

(a) *z/d=0.1* (b) *z/d=0.4*

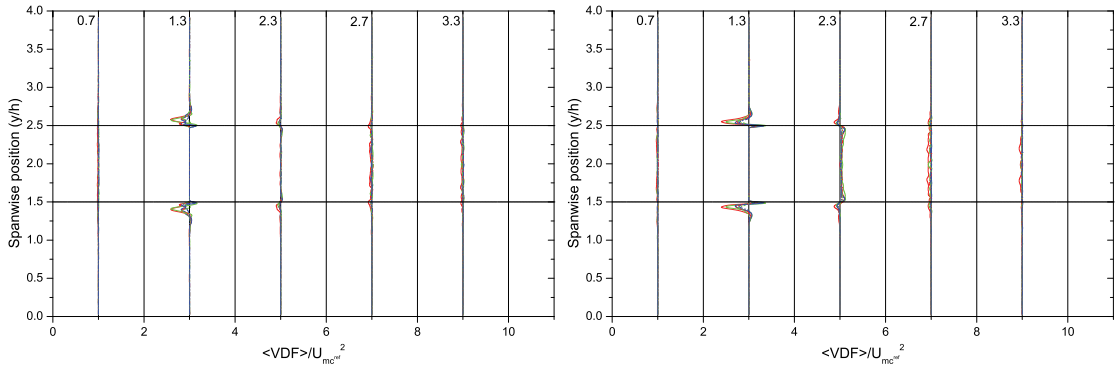

(c) *z/d=0.7* (d) *z/d=0.95*

Figure A2.21: Time averaged VDF distribution around a cube in a matrix configuration in the XY plane.

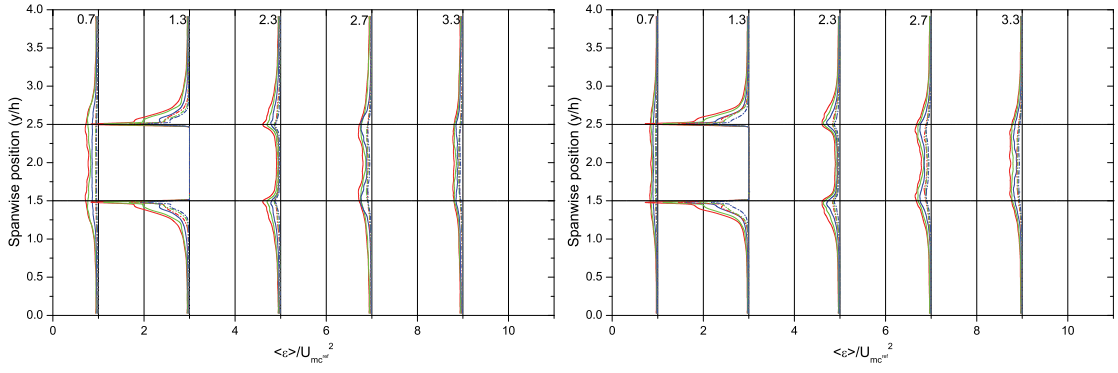

(a) *z/d=0.1* (b) *z/d=0.4*

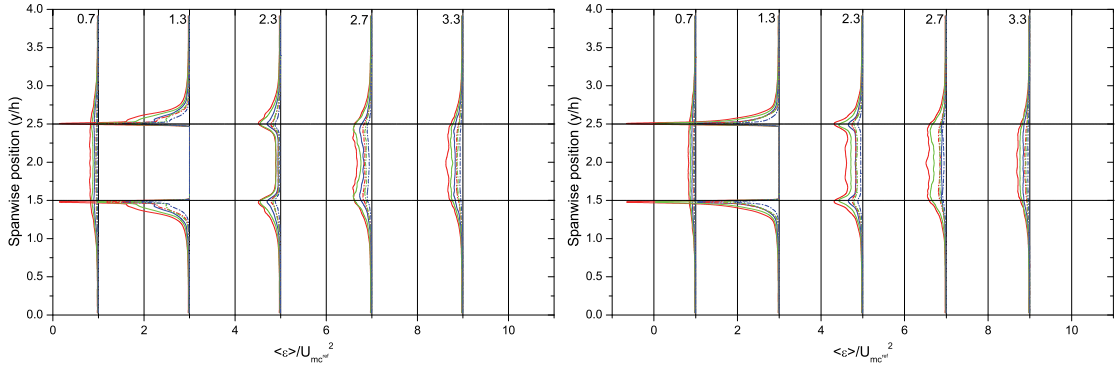

(c) *z/d=0.7* (d) *z/d=0.95*

Figure A2.22: Time averaged ε distribution around a cube in a matrix configuration in the XY plane.

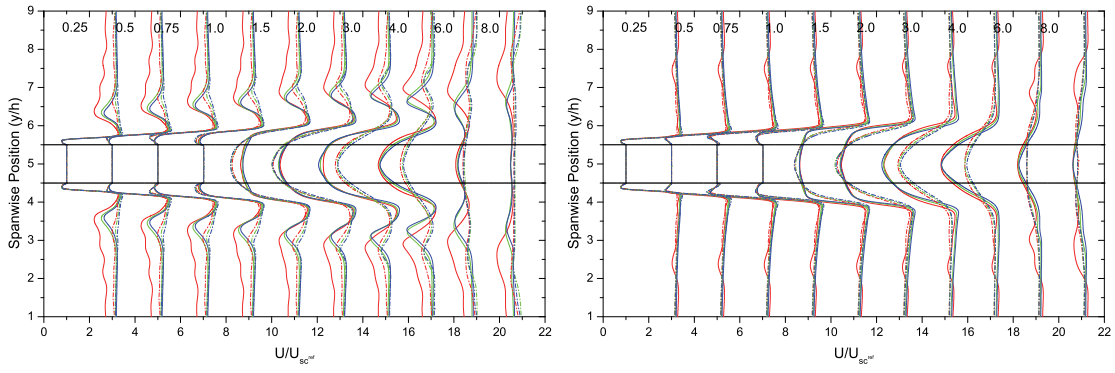

(a) *z/d=0.1* (b) *z/d=0.4*

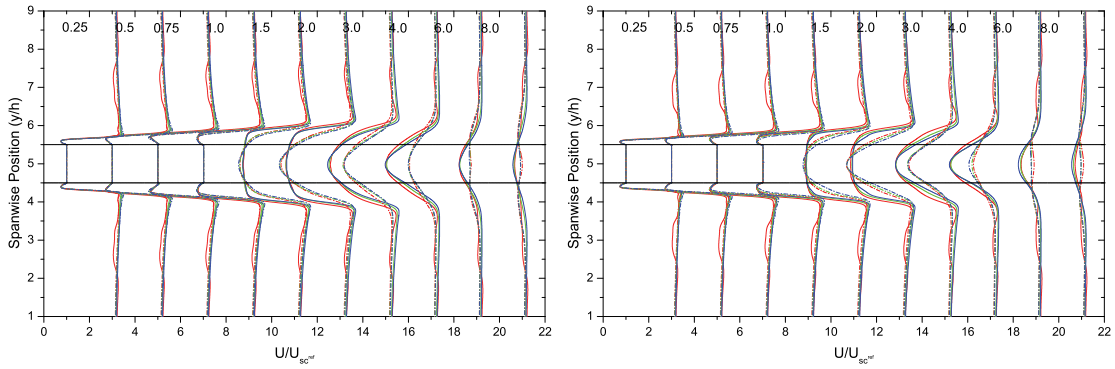

(c) *z/d=0.7* (d) *z/d=0.95*

Figure A2.23: Mean streamwise velocity distribution around a single cube in a uniform flow about the XY plane.

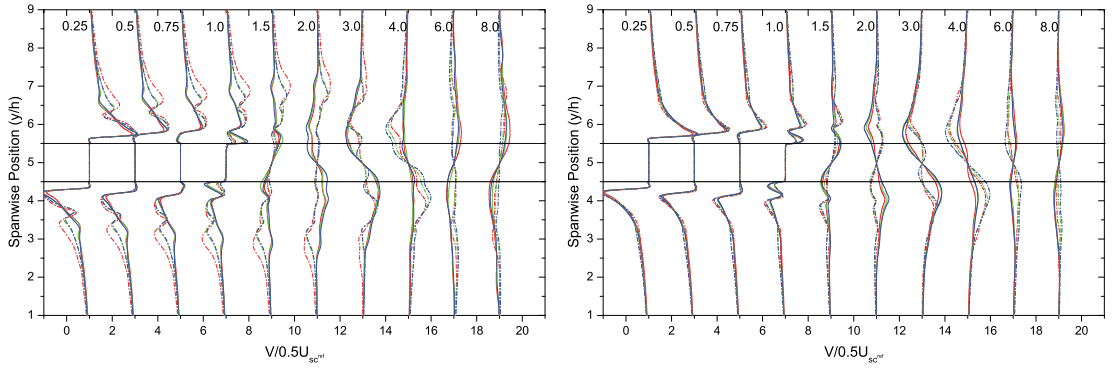

(a) *z/d=0.1* (b) *z/d=0.4*

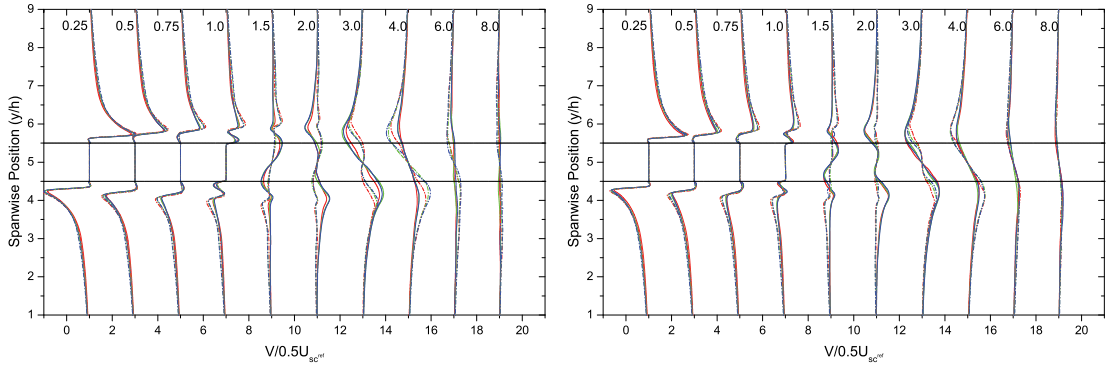

(c) *z/d=0.7* (d) *z/d=0.95*

Figure A2.24: Mean spanwise velocity distribution around a single cube in a uniform flow about the XY plane.

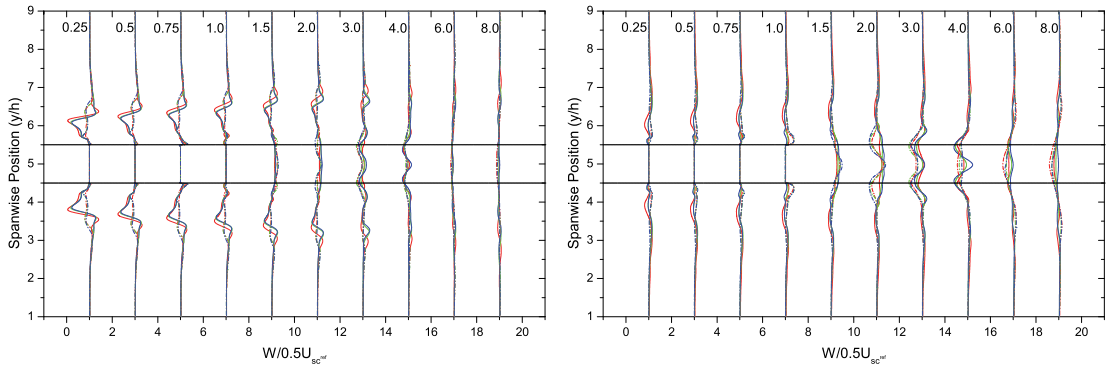

(a) *z/d=0.1* (b) *z/d=0.4*

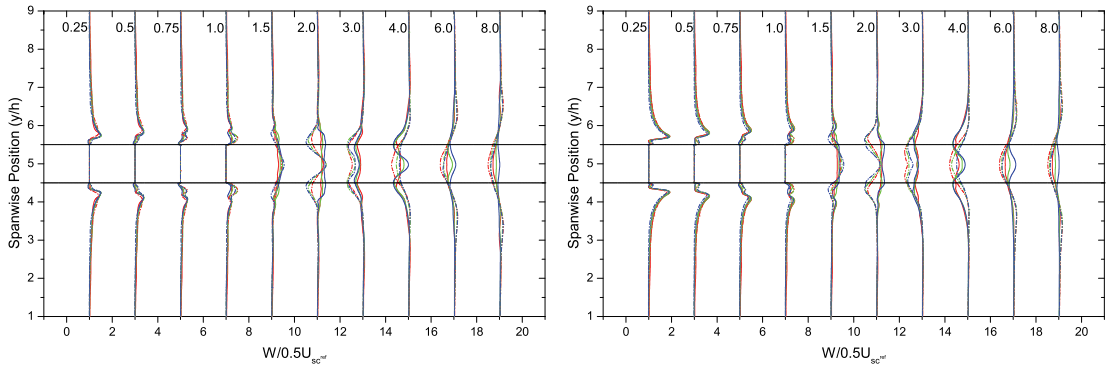

(c) *z/d=0.7* (d) *z/d=0.95*

Figure A2.25: Mean vertical velocity distribution around a single cube in a uniform flow about the XY plane.

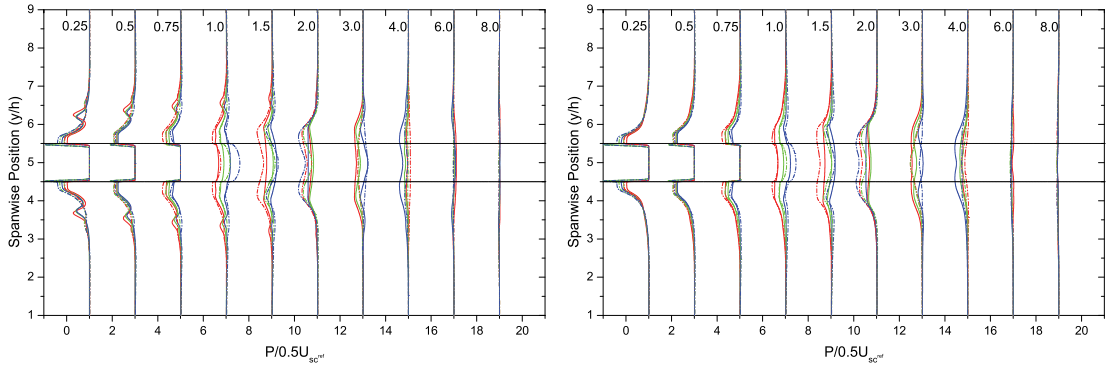

(a) *z/d=0.1* (b) *z/d=0.4*

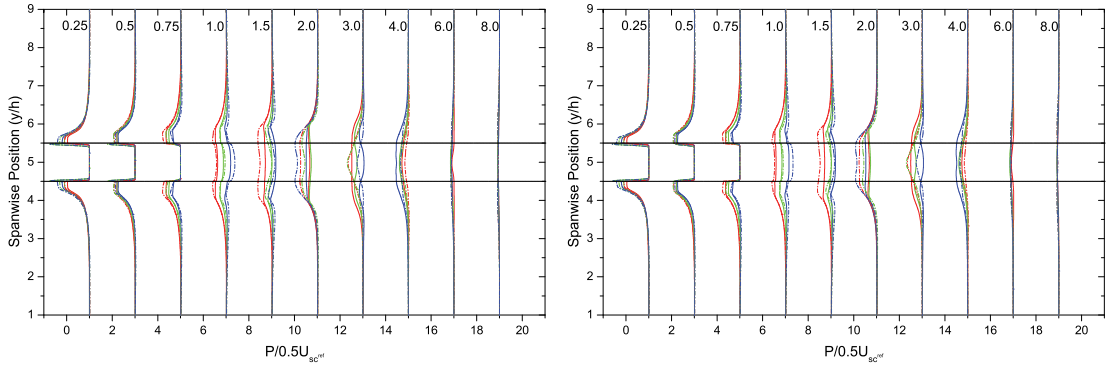

(c) *z/d=0.7* (d) *z/d=0.95*

Figure A2.26: Mean pressure distribution around a single cube in a uniform flow about the XY plane.

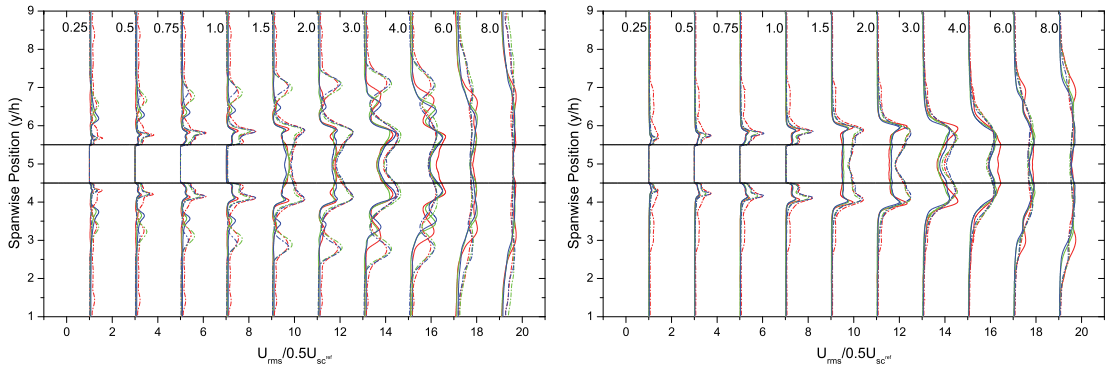

(a) *z/d=0.1* (b) *z/d=0.4*

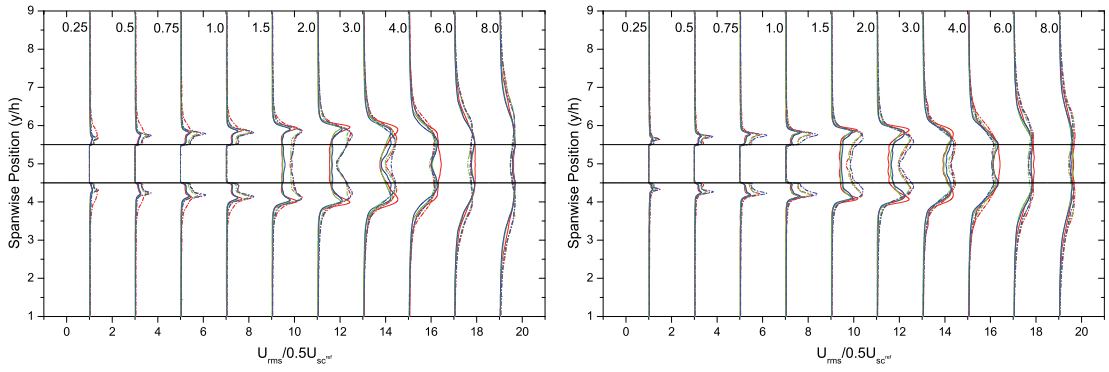

(c) *z/d=0.7* (d) *z/d=0.95*

Figure A2.27: Streamwise turbulent intensity distribution around a cube in a uniform flow about the XY plane.

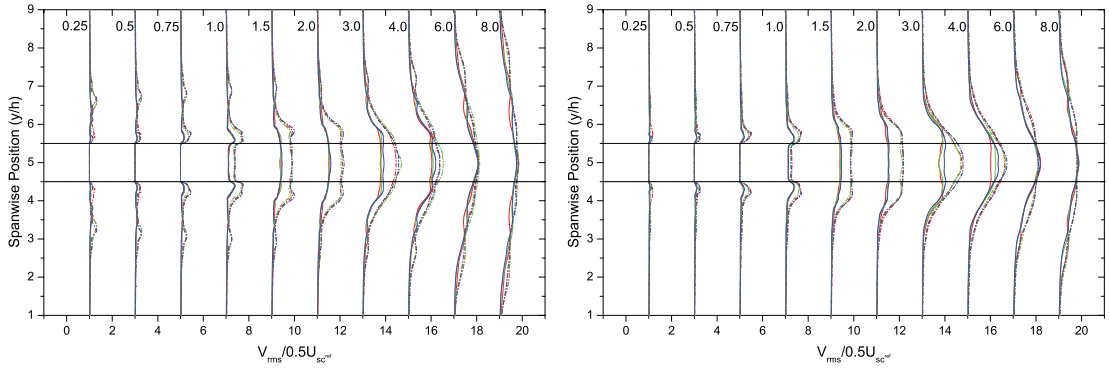

(a) *z/d=0.1* (b) *z/d=0.4*

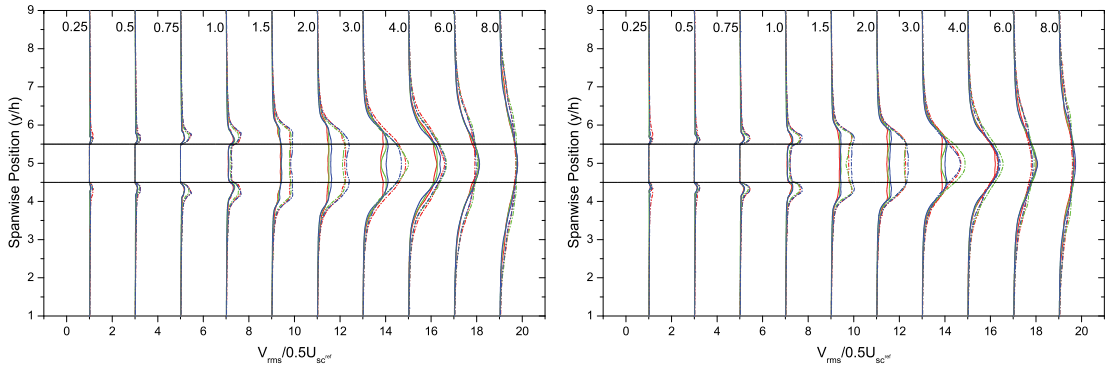

(c) *z/d=0.7* (d) *z/d=0.95*

Figure A2.28: Spanwise turbulent intensity distribution around a cube in a uniform flow about the XY plane.

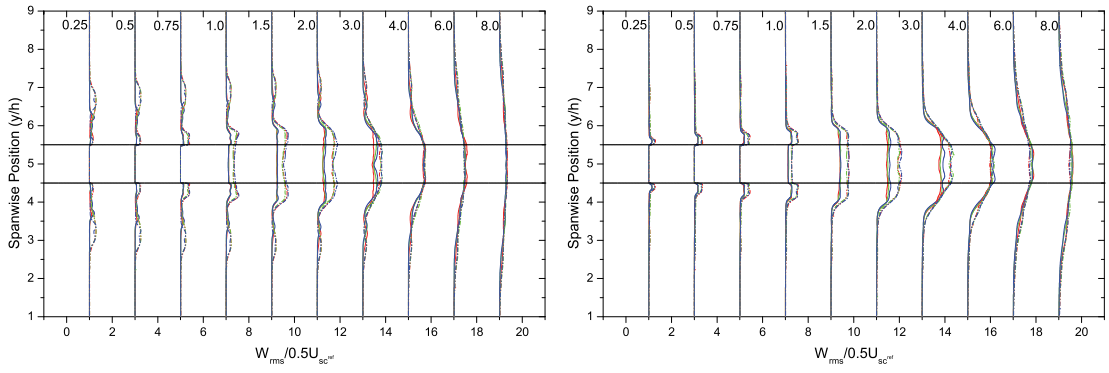

(a) *z/d=0.1* (b) *z/d=0.4*

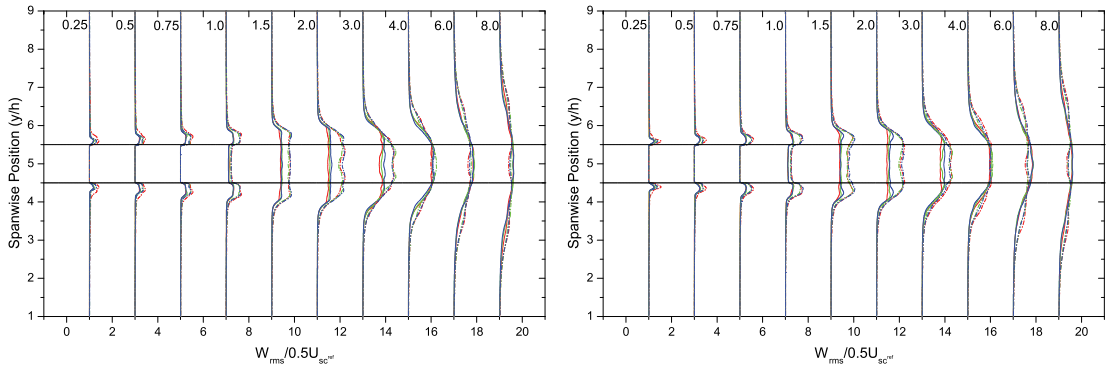

(c) *z/d=0.7* (d) *z/d=0.95*

Figure A2.29: Vertical turbulent intensity distribution around a cube in a uniform flow about the XY plane.

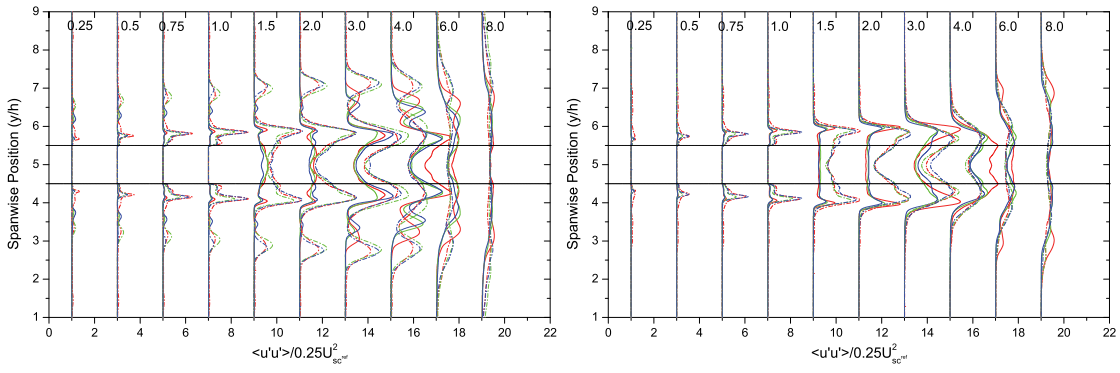

(a) *z/d=0.1* (b) *z/d=0.4*

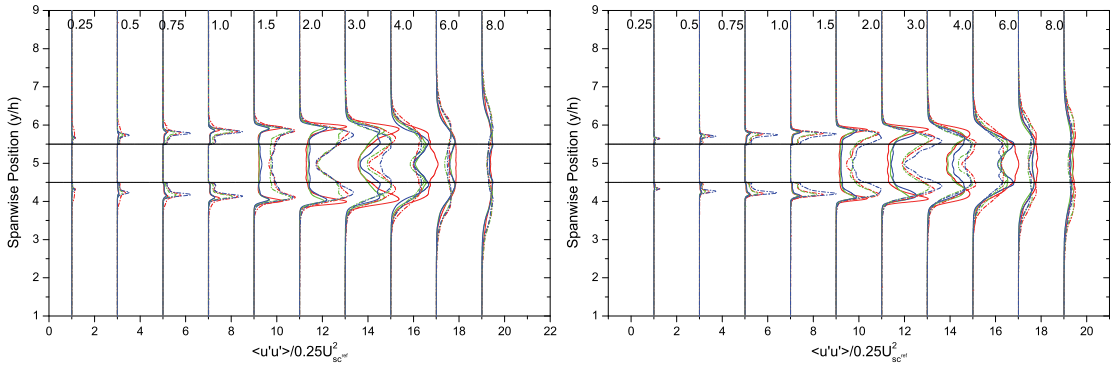

(c) *z/d=0.7* (d) *z/d=0.95*

Figure A2.30: Time averaged u'u' normal Reynolds stress distribution around a single cube in a uniform flow about the XY plane.

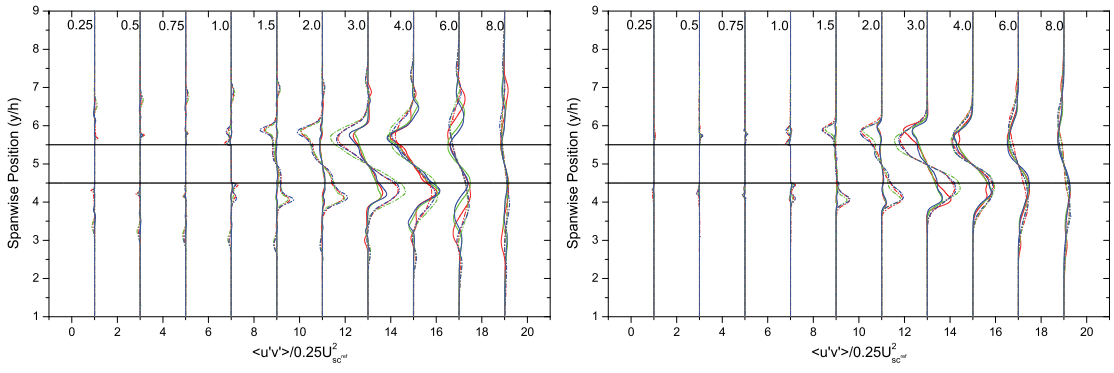

(a) *z/d=0.1* (b) *z/d=0.4*

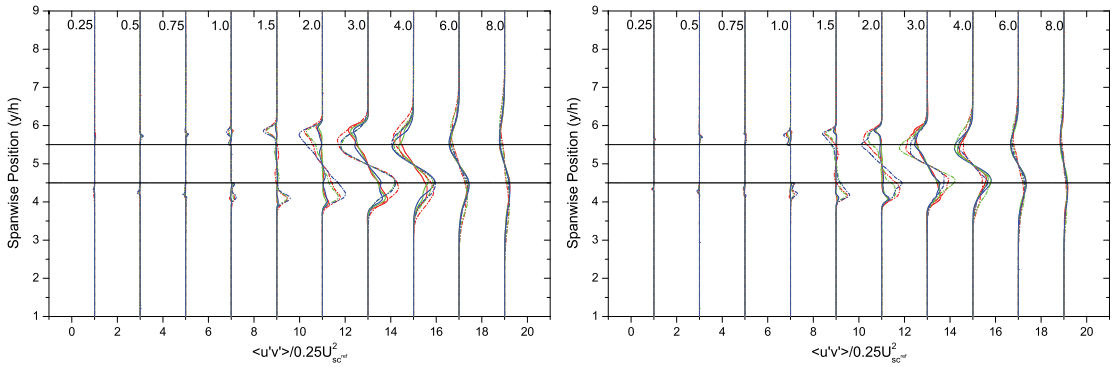

(c) *z/d=0.7* (d) *z/d=0.95*

Figure A2.31: Time averaged u'v' cross Reynolds stress distribution around a single cube in a uniform flow about the XY plane.

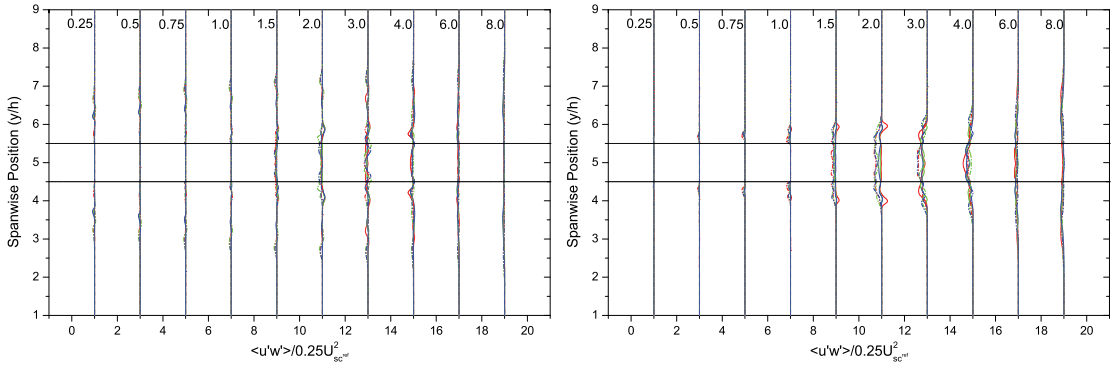

(a) *z/d=0.1* (b) *z/d=0.4*

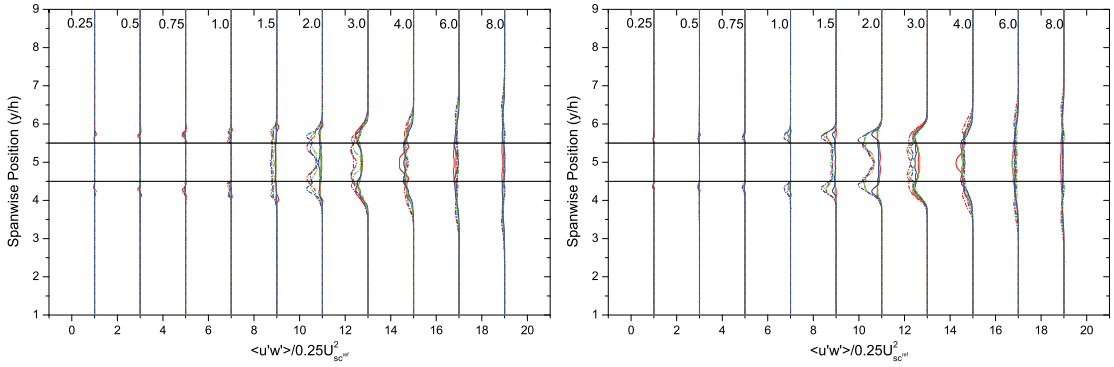

(c) *z/d=0.7* (d) *z/d=0.95*

Figure A2.32: Time averaged u'w' cross Reynolds stress distribution around a single cube in a uniform flow about the XY plane.

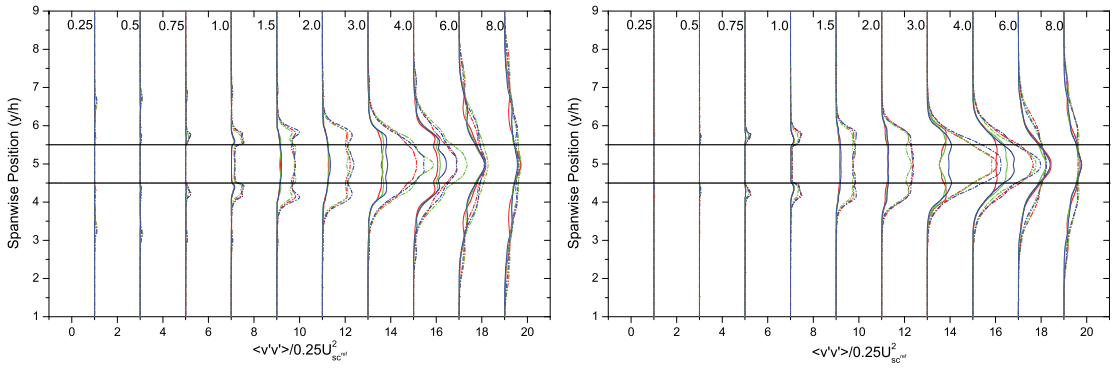

(a) *z/d=0.1* (b) *z/d=0.4*

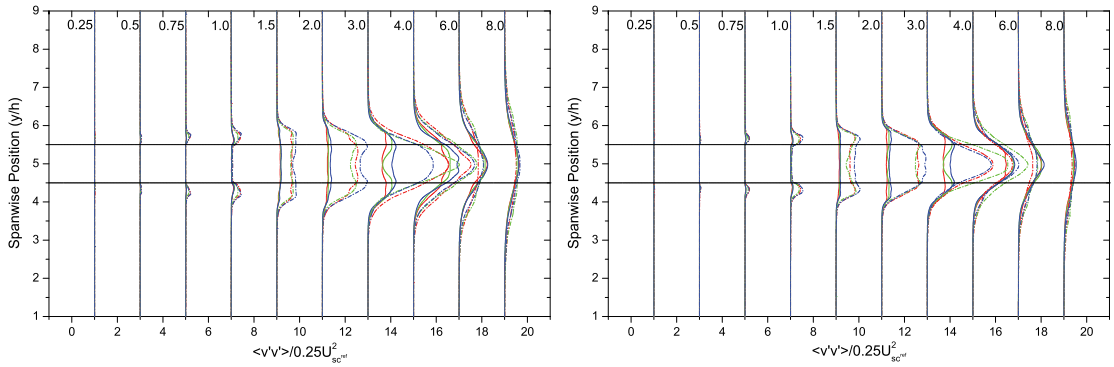

(c) *z/d=0.7* (d) *z/d=0.95*

Figure A2.33: Time averaged v'v' normal Reynolds stress distribution around a single cube in a uniform flow about the XY plane.

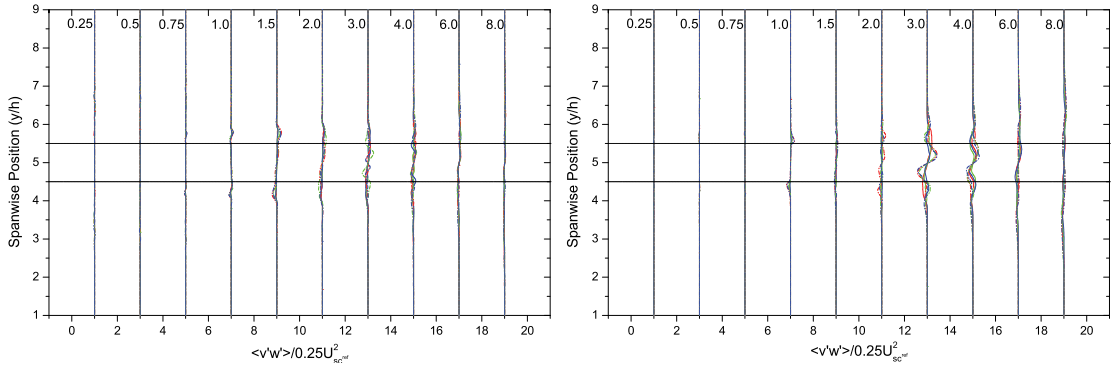

(a) *z/d=0.1* (b) *z/d=0.4*

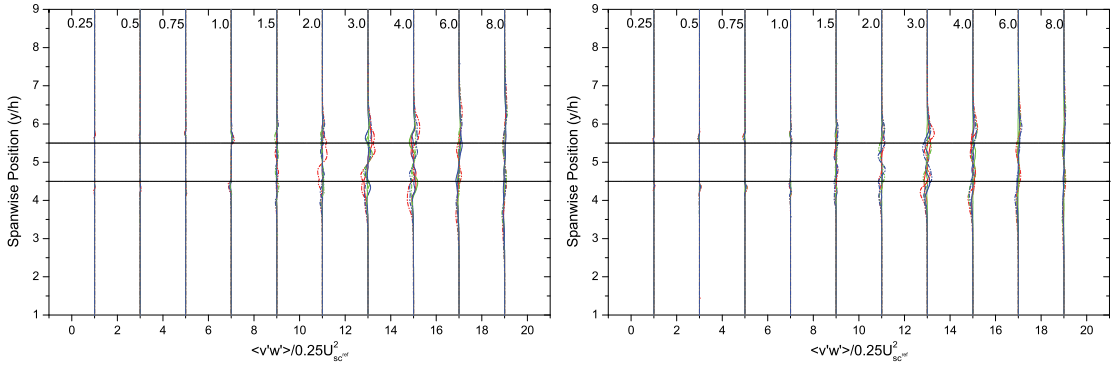

(c) *z/d=0.7* (d) *z/d=0.95*

Figure A2.34: Time averaged v'w' cross Reynolds stress distribution around a single cube in a uniform flow about the XY plane.

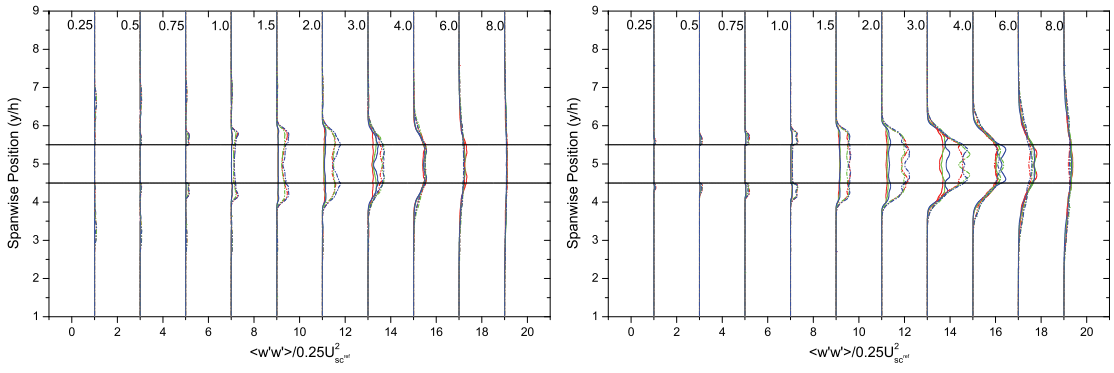

(a) *z/d=0.1* (b) *z/d=0.4*

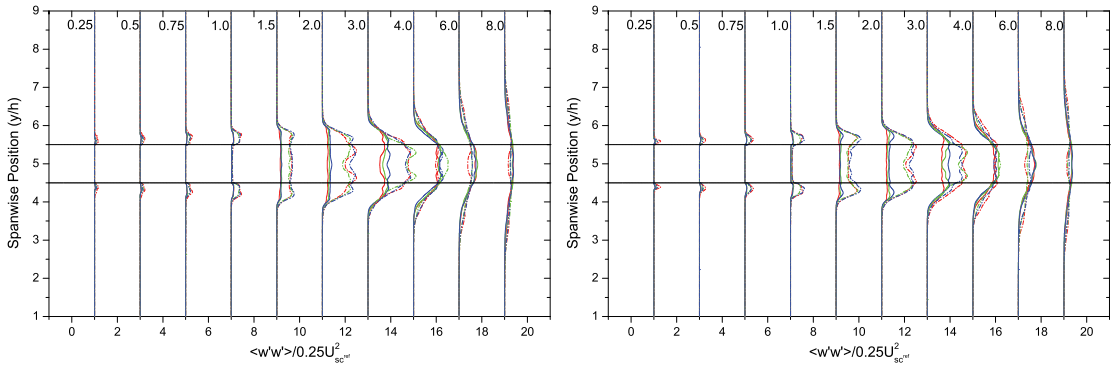

(c) *z/d=0.7* (d) *z/d=0.95*

Figure A2.35: Time averaged w'w' normal Reynolds stress distribution around a single cube in a uniform flow about the XY plane.

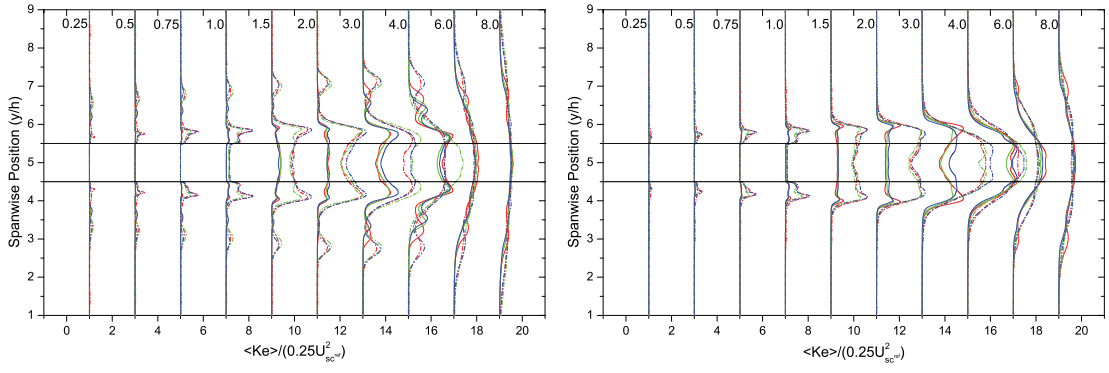

(a) *z/d=0.1* (b) *z/d=0.44*

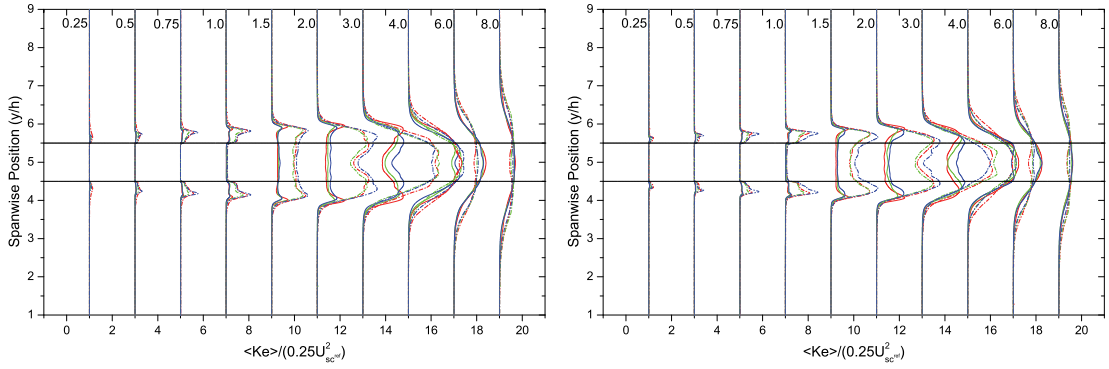

(c) *z/d=0.7* (d) *z/d=0.95*

Figure A2.36: Turbulent kinetic energy distribution around a single cube in a uniform flow about the XY plane.

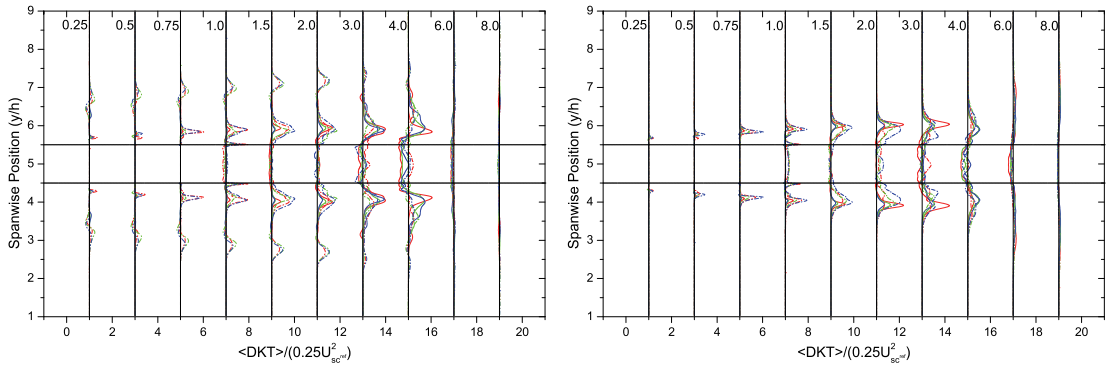

(a) *z/d=0.1* (b) *z/d=0.44*

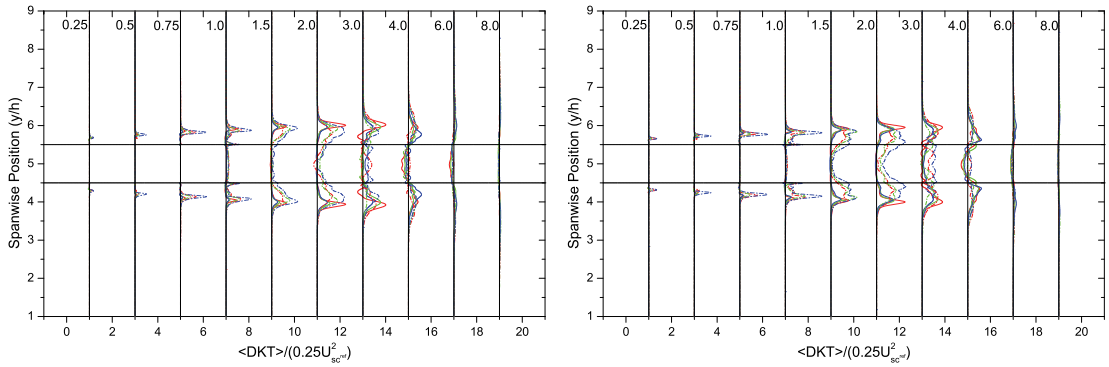

(c) *z/d=0.7* (d) *z/d=0.95*

Figure A2.37: Time averaged DKT distribution around a single cube in a uniform flow about the XY plane.

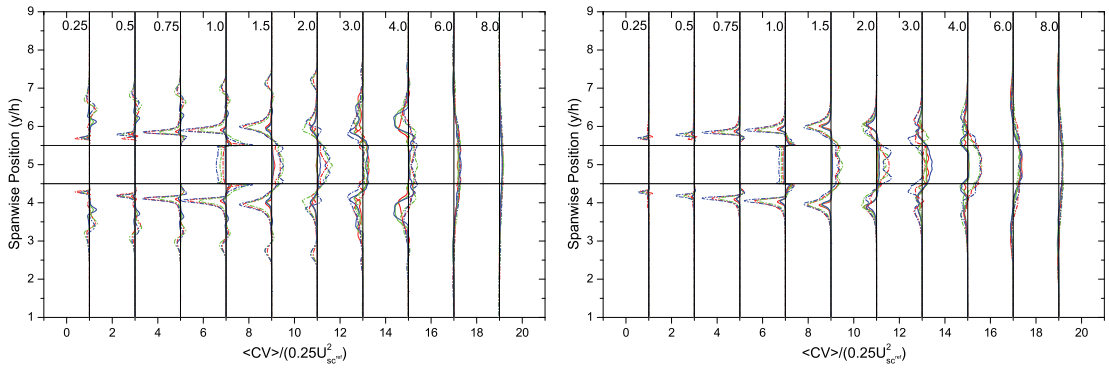

(a) *z/d=0.1* (b) *z/d=0.44*

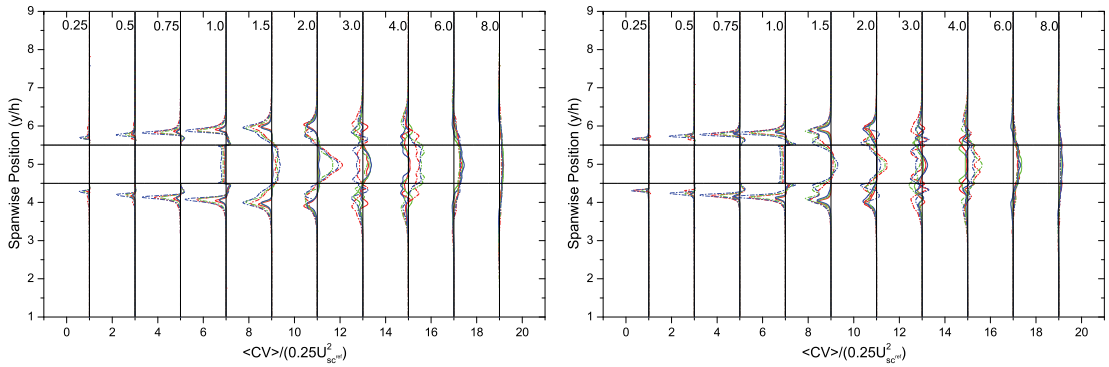

(c) *z/d=0.7* (d) *z/d=0.95*

Figure A2.38: Time averaged CV distribution around a cube in a uniform flow about the XY plane.

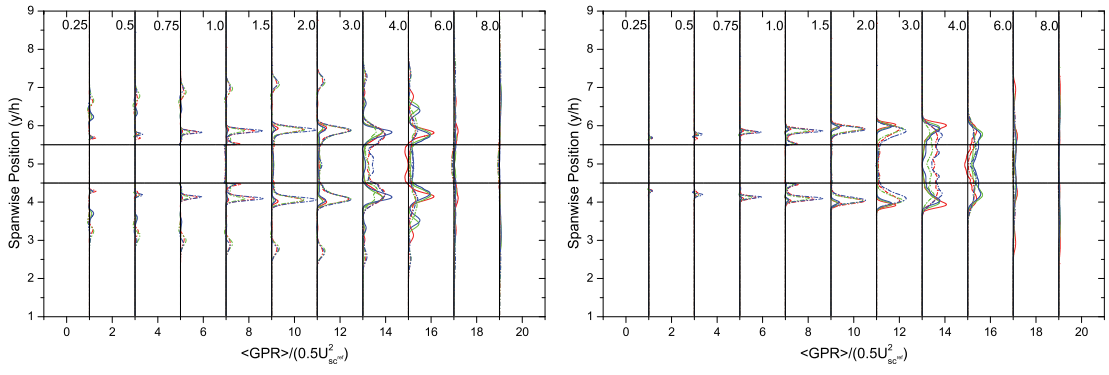

(a) *z/d=0.1* (b) *z/d=0.44*

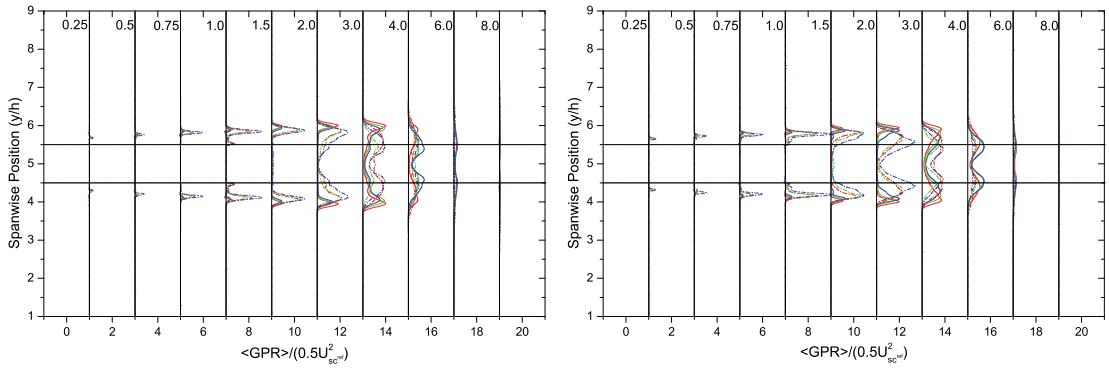

(c) *z/d=0.7* (d) *z/d=0.95*

Figure A2.39: Time averaged GPR distribution around a cube in a uniform flow about the XY plane.

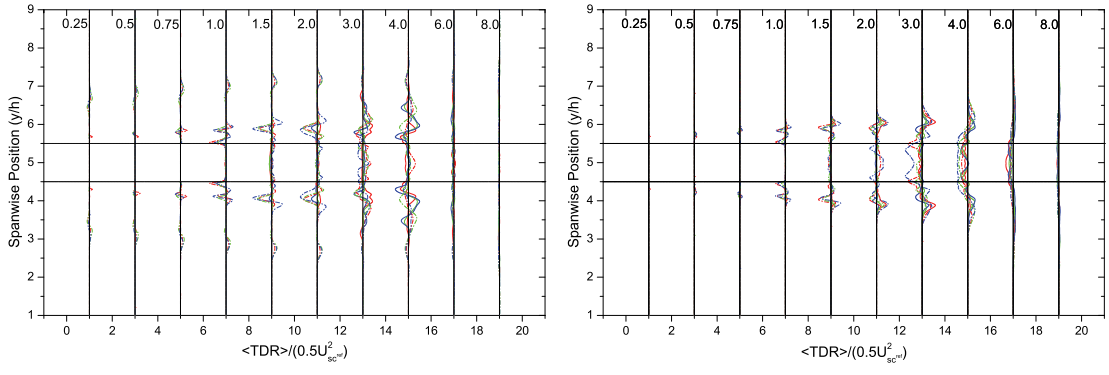

(a) *z/d=0.1* (b) *z/d=0.44*

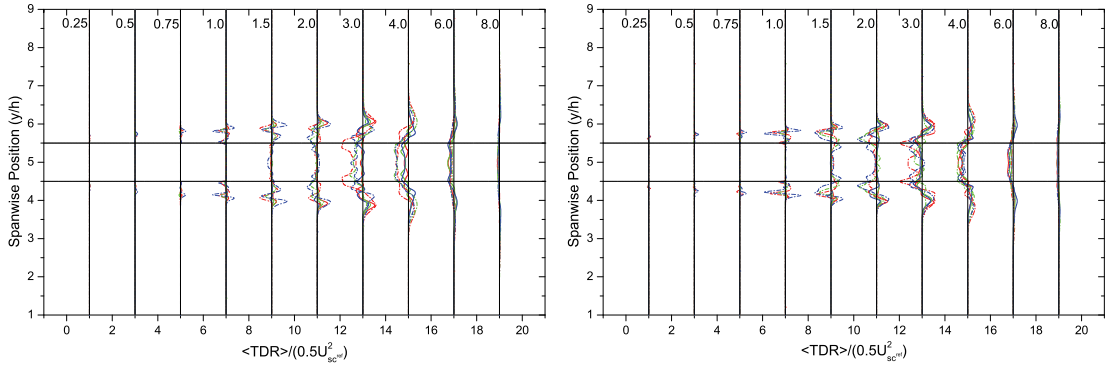

(c) *z/d=0.7* (d) *z/d=0.95*

Figure A2.40: Time averaged TDR distribution around a single cube in a uniform flow about the XY plane.

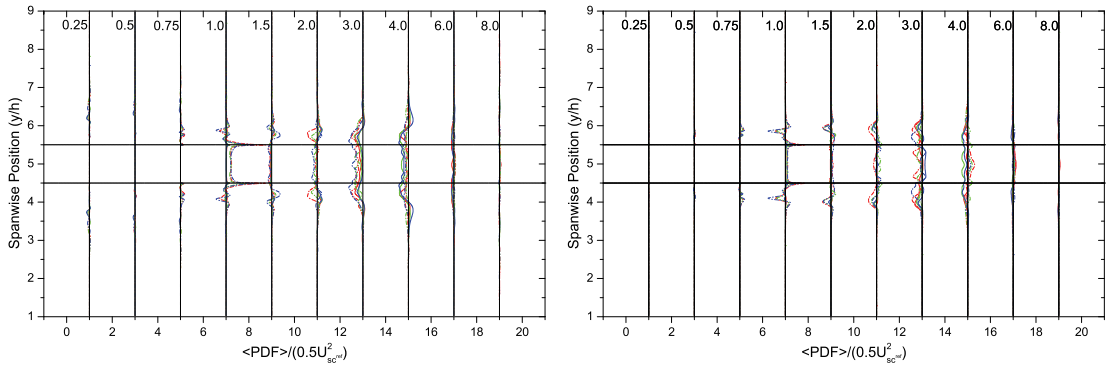

(a) *z/d=0.1* (b) *z/d=0.44*

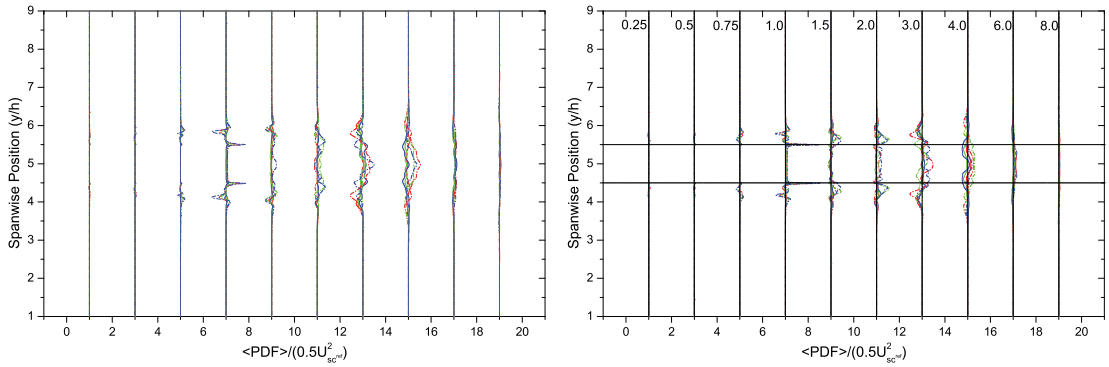

(c) *z/d=0.7* (d) *z/d=0.95*

Figure A2.41: Time averaged PDF distribution around a single cube in a uniform flow about the XY plane.

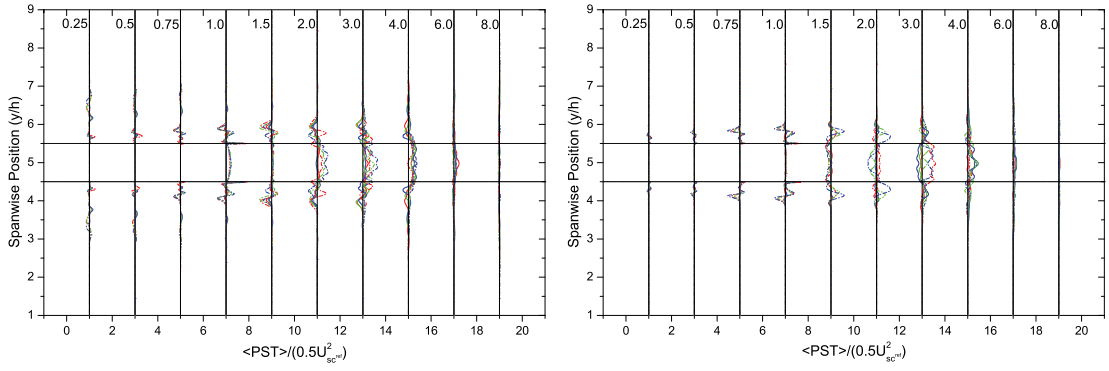

(a) *z/d=0.1* (b) *z/d=0.44*

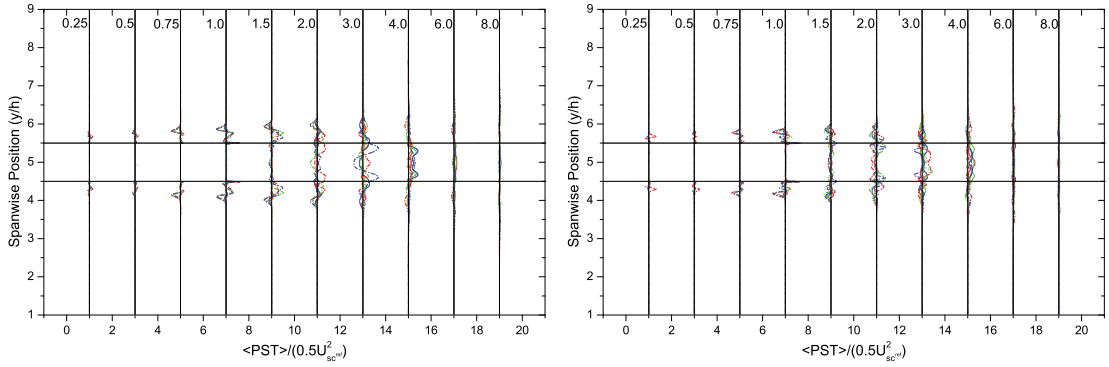

(c) *z/d=0.7* (d) *z/d=0.95*

Figure A2.42: Time averaged PST distribution around a cube in a uniform flow about the XY plane.

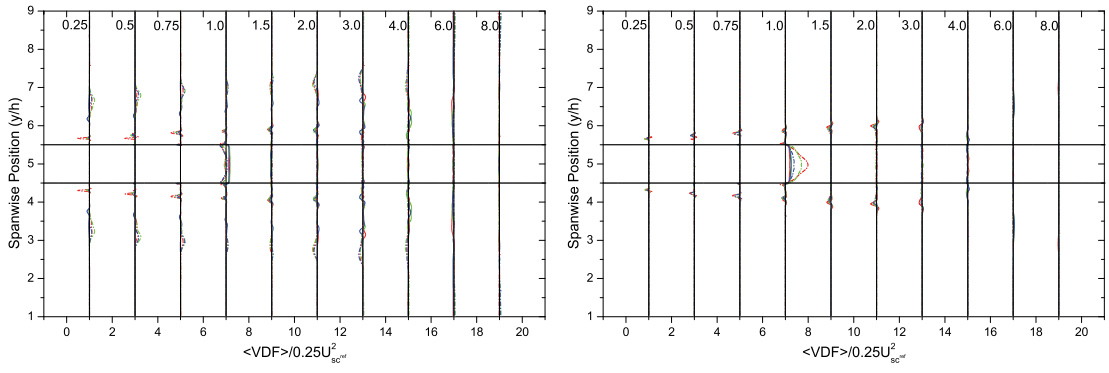

(a) *z/d=0.1* (b) *z/d=0.44*

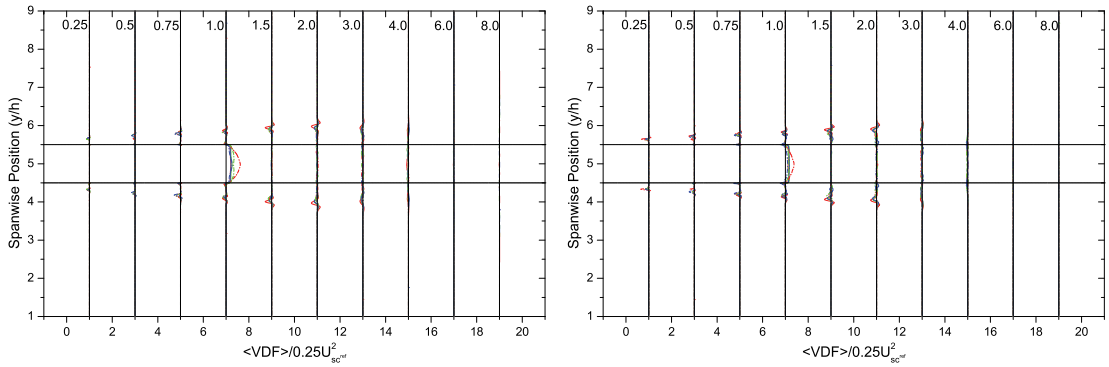

(c) *z/d=0.7* (d) *z/d=0.95*

Figure A2.43: Time averaged VDF distribution around a cube in a uniform flow about the XY plane.

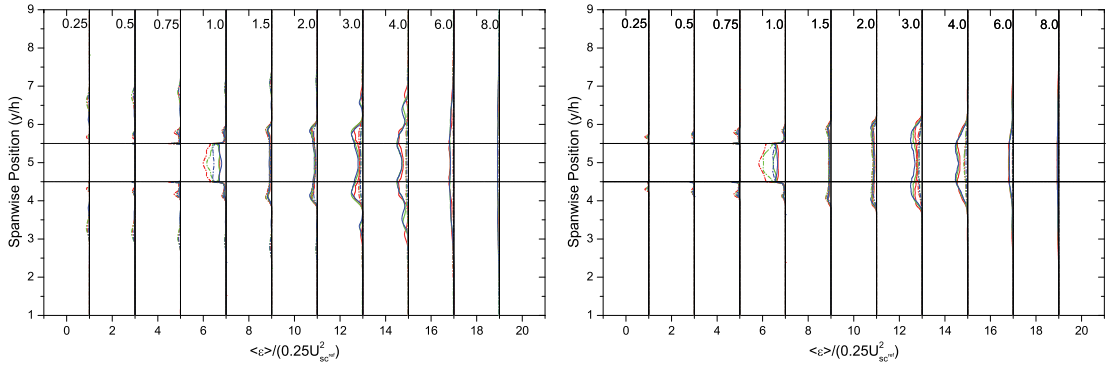

(a) *z/d=0.1* (b) *z/d=0.44*

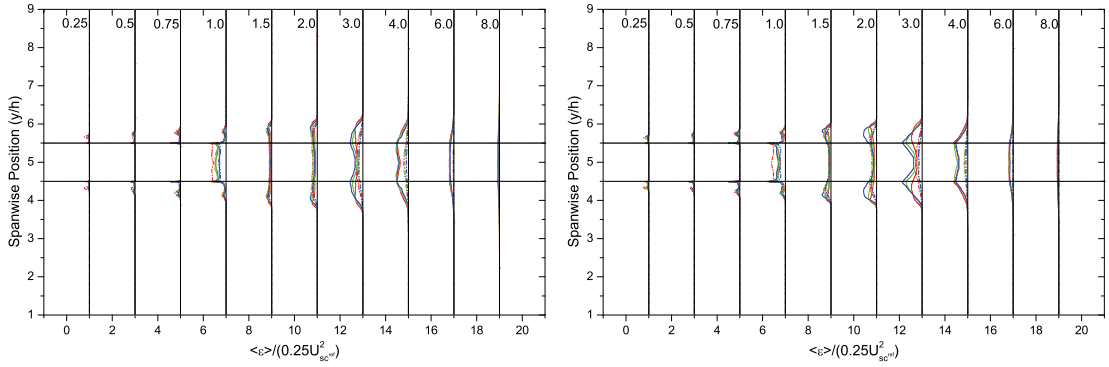

(c) *z/d=0.7* (d) *z/d=0.95*

Figure A2.44: Time averaged ε distribution around a cube in a uniform flow about the XY plane.

Appendix 3 Comparison of LES and DES for a Fully-Submerged Fairwater

List of Figures

Figure Legend

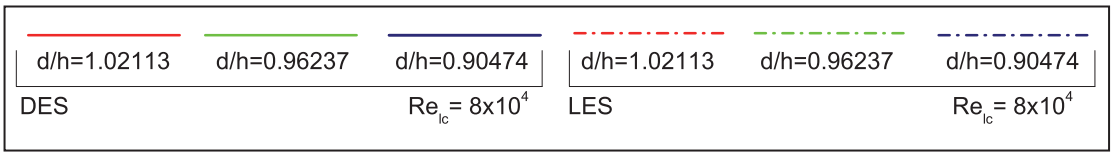

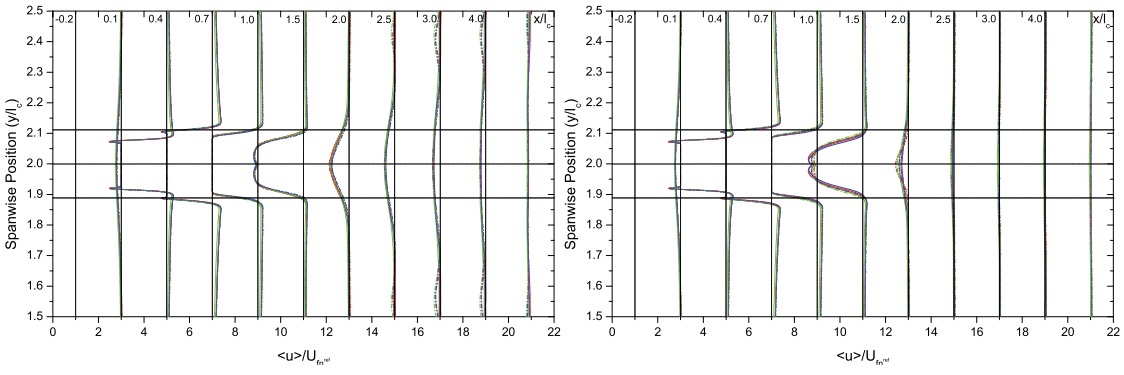

(a) *0.2h/l$_c$* (b) *0.5h/l$_c$*

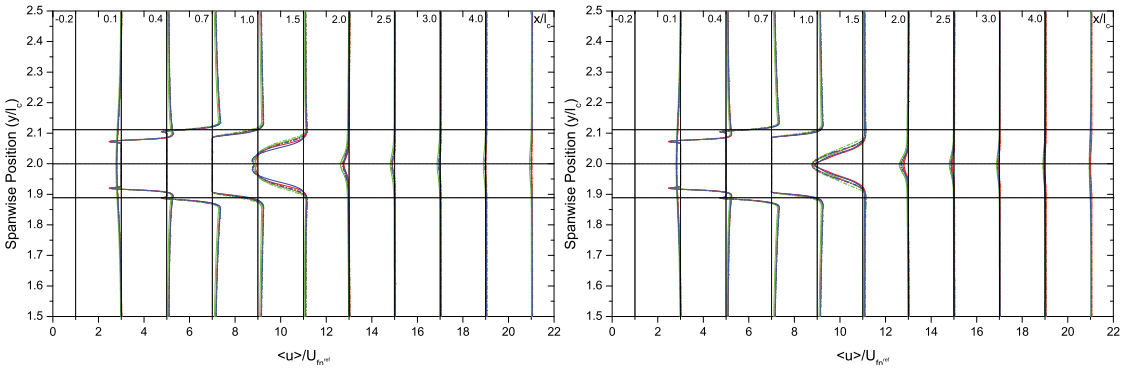

(c) *0.7h/l$_c$* (d) *0.9h/l$_c$*

Figure A3.1: Comparison of LES and DES around a submerged fairwater at different positions long the fairwater height for the mean streamwise velocity in the XY plane.

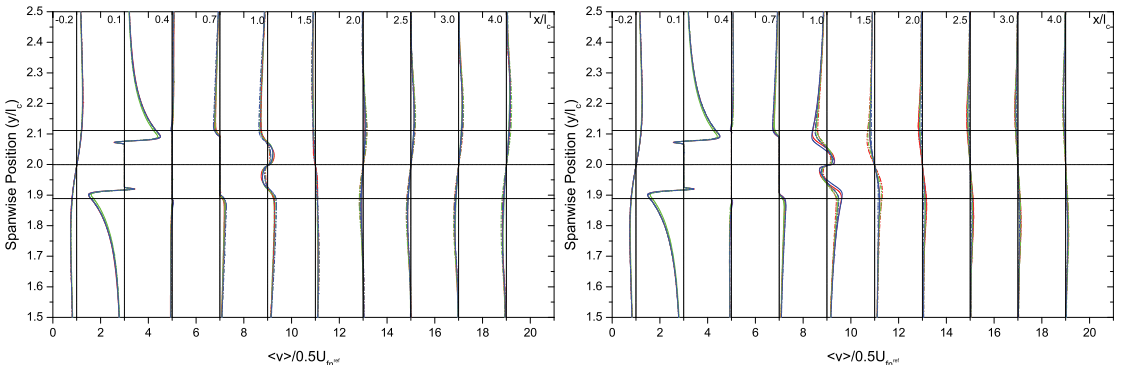

(a) 0.2h/lc (b) 0.5h/lc

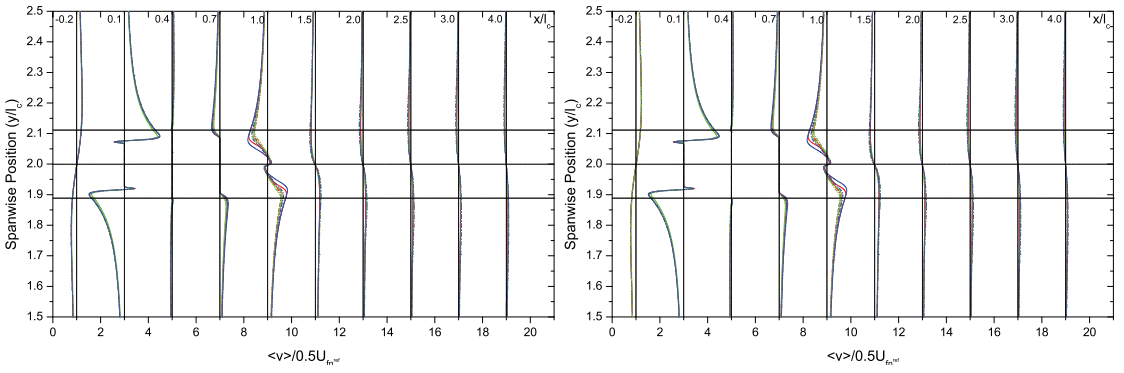

(c) 0.7h/lc (d) 0.9h/lc

Figure A3.2: Comparison of LES and DES around a submerged fairwater at different positions long the fairwater height for the mean spanwise velocity distribution in the XY plane.

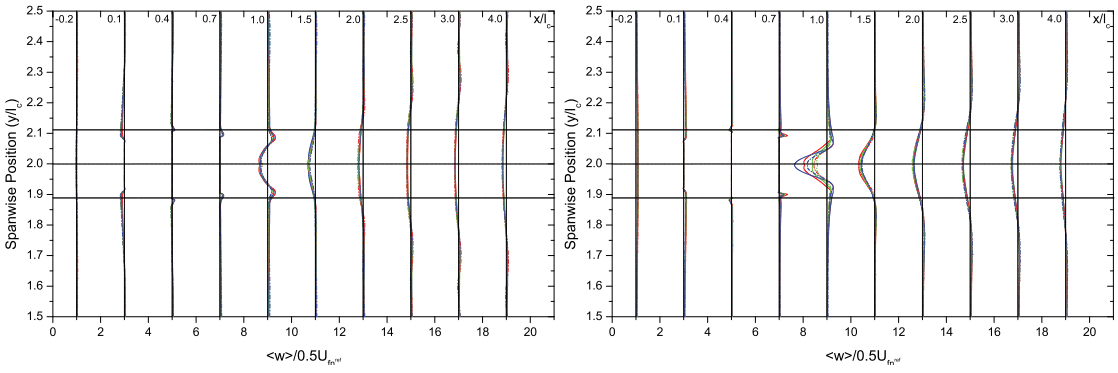

(a) 0.2h/lc (b) 0.5h/lc

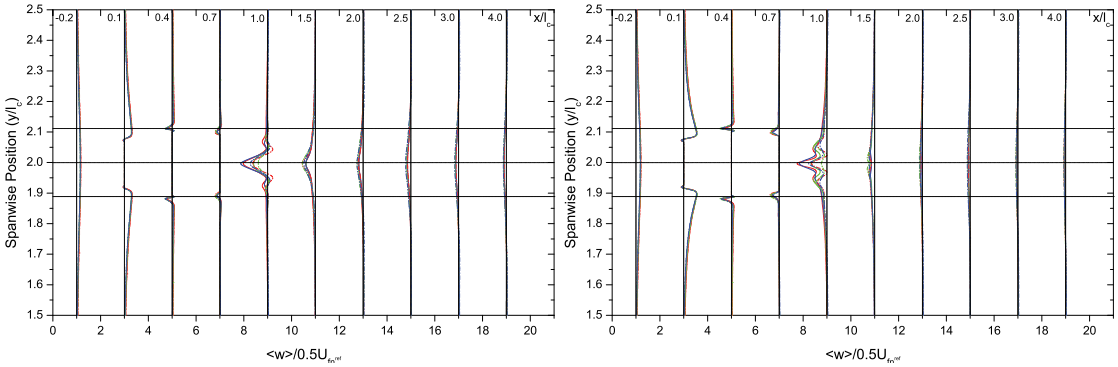

(c) 0.7h/lc (d) 0.9h/lc

Figure A3.3: Comparison of LES and DES around a submerged fairwater at different positions long the fairwater height for the mean vertical velocity variation in the XY plane.

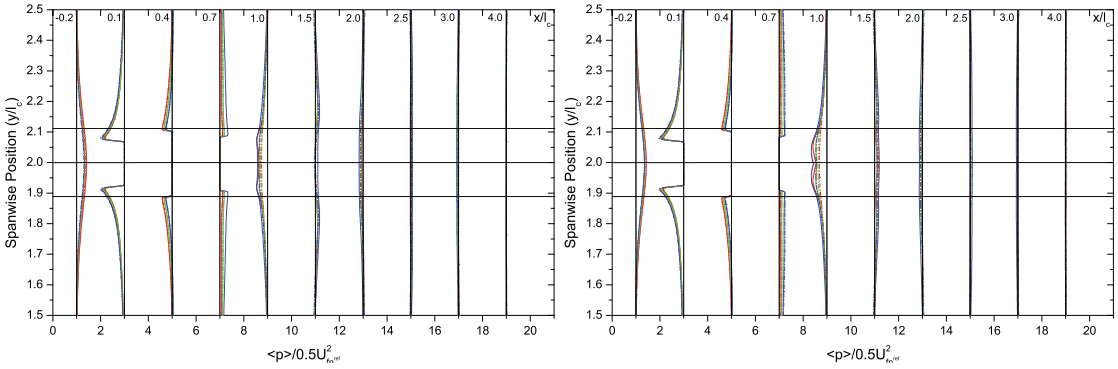

(a) 0.2h/lc (b) 0.5h/lc

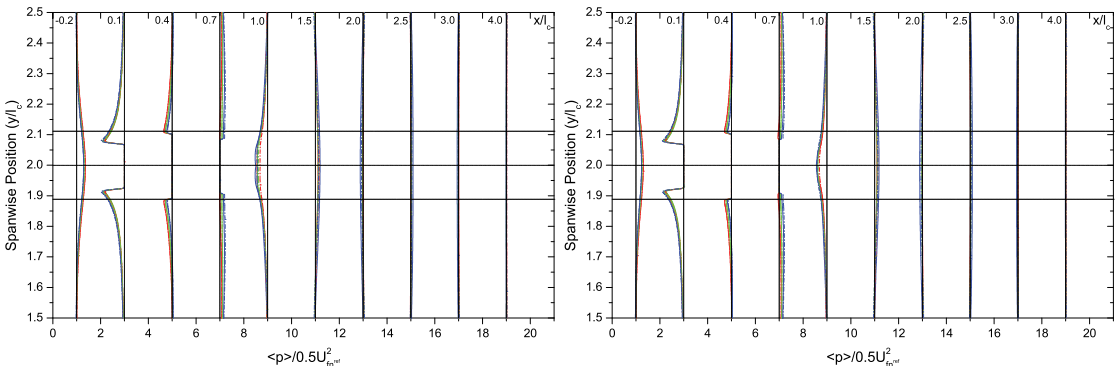

(c) 0.7h/lc (d) 0.9h/lc

Figure A3.4: Comparison of LES and DES around a submerged fairwater at different positions long the fairwater height for the mean pressure distribution in the XY plane.

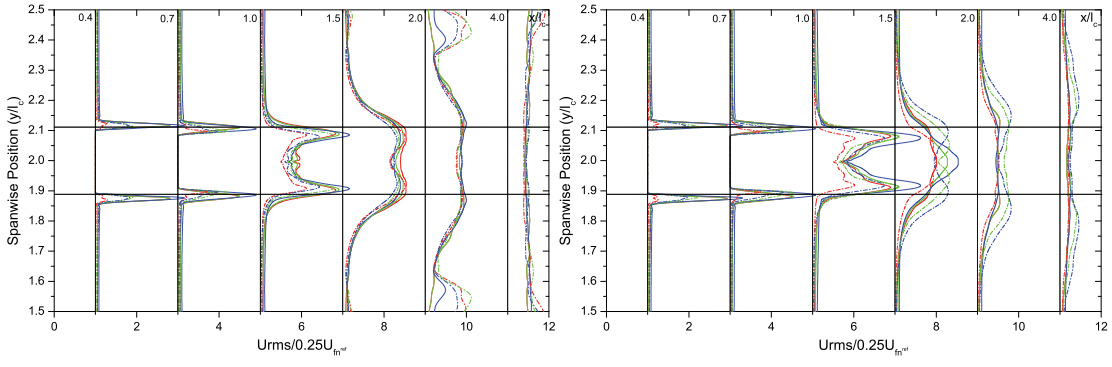

(a) 0.2h/lc (b) 0.5h/lc

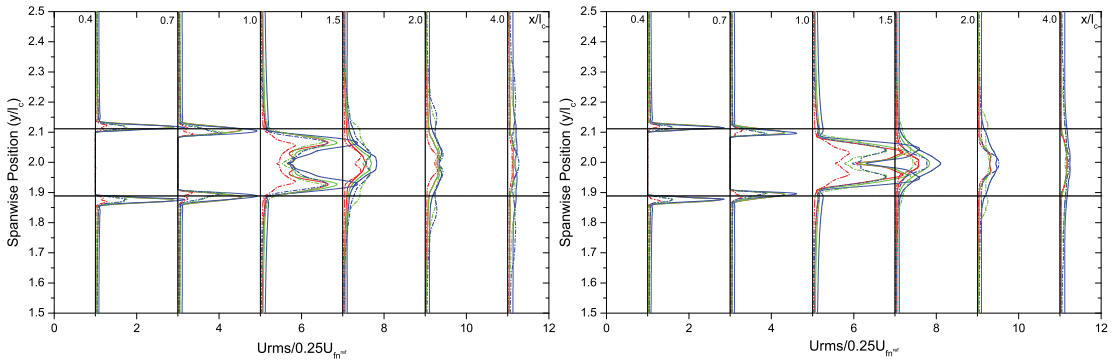

(c) 0.7h/lc (d) 0.9h/lc

Figure A3.5: Comparison of LES and DES around a submerged fairwater at different positions long the fairwater height for the streamwise turbulent intensity distribution in the XY plane.

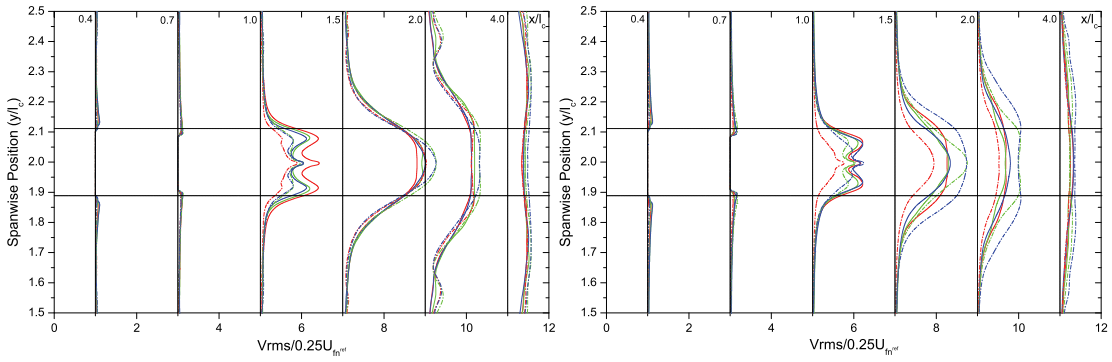

(a) 0.2h/lc (b) 0.5h/lc

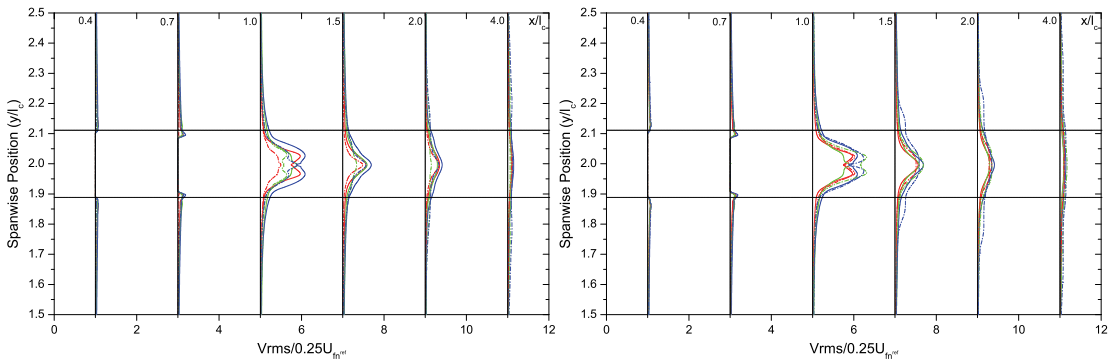

(c) 0.7h/lc (d) 0.9h/lc

Figure A3.6: Comparison of LES and DES around a submerged fairwater at different positions long the fairwater height for the spanwise turbulent intensity distribution in the XY plane.

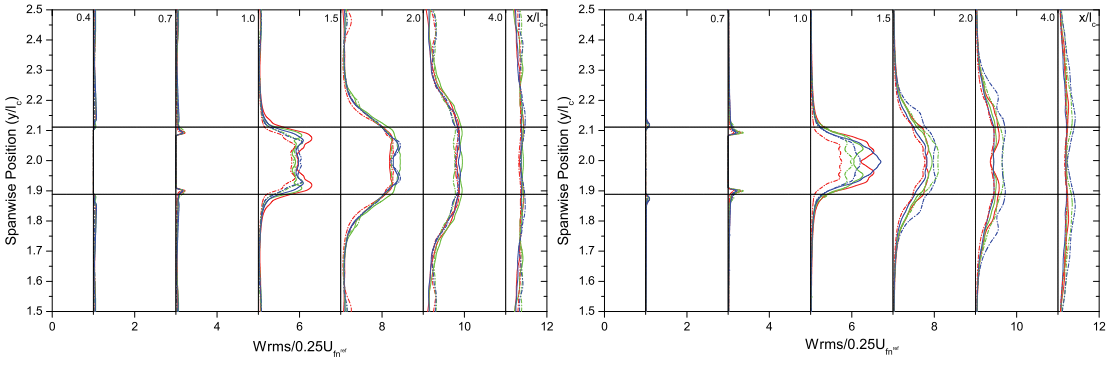

(a) 0.2h/lc (b) 0.5h/lc

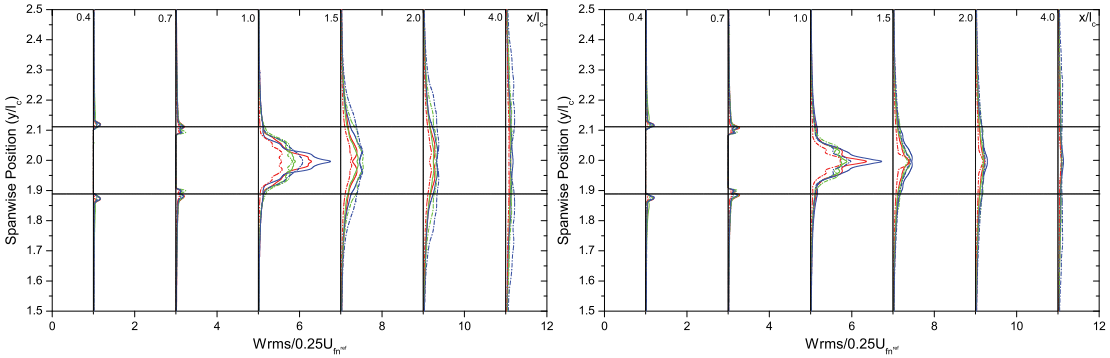

(c) 0.7h/lc (d) 0.9h/lc

Figure A3.7: Comparison of LES and DES around a submerged fairwater at different positions long the fairwater height for the vertical turbulent intensity distribution in the XY plane.

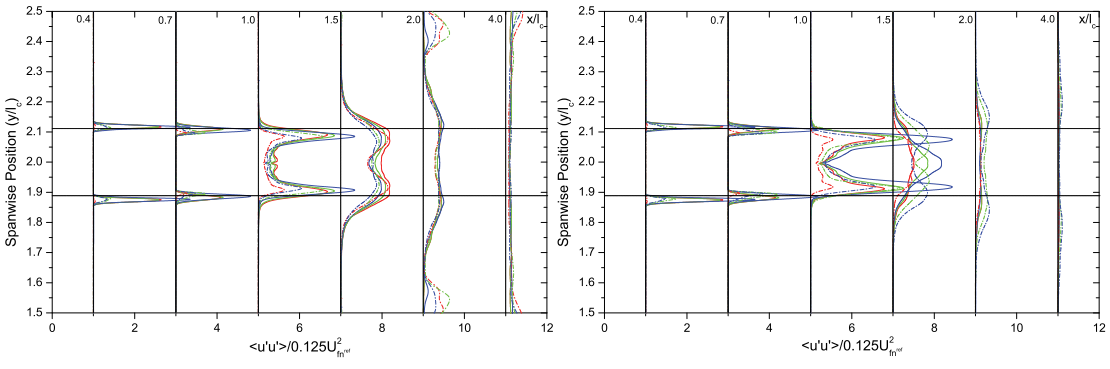

(a) 0.2h/lc (b) 0.5h/lc

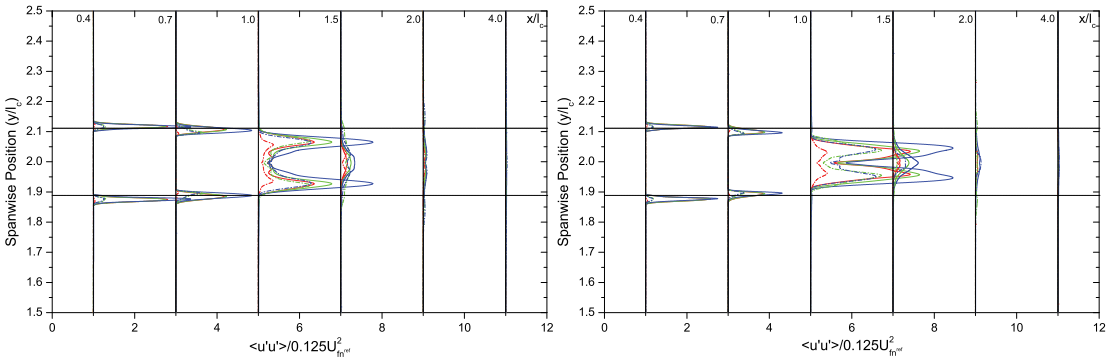

(c) 0.7h/lc (d) 0.9h/lc

Figure A3.8: Comparison of LES and DES around a submerged fairwater at different positions long the fairwater height for the time averaged u'u' normal Reynolds stress distribution.

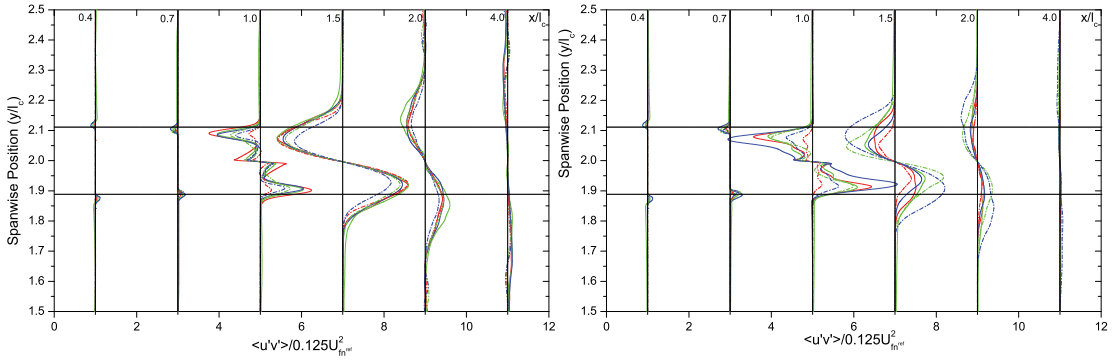

(a) 0.2h/lc (b) 0.5h/lc

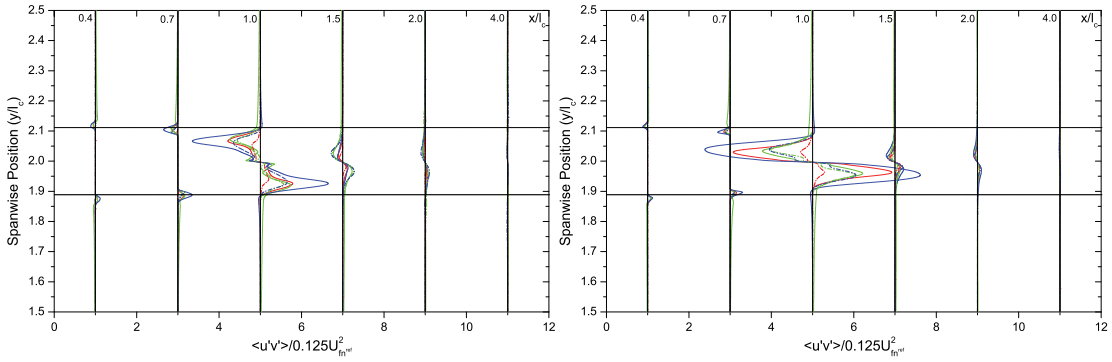

(c) 0.7h/lc (d) 0.9h/lc

Figure A3.9: Comparison of LES and DES around a submerged fairwater at different positions long the fairwater height for the time averaged u'v' cross Reynolds stress.

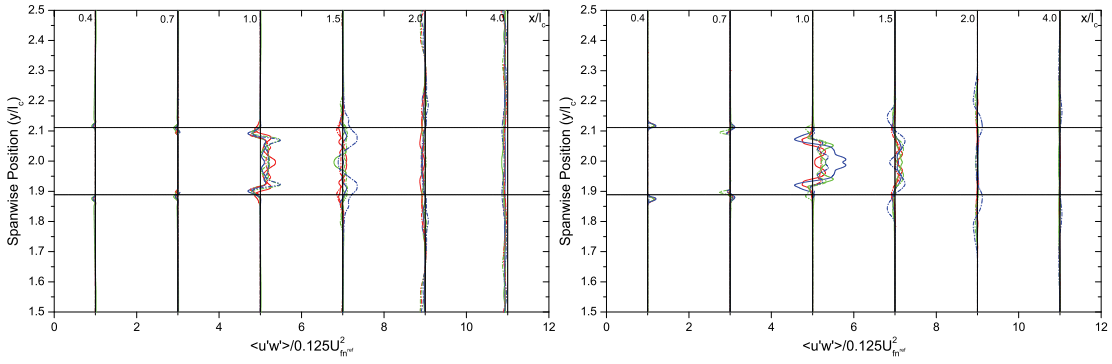

(a) 0.2h/lc (b) 0.5h/lc

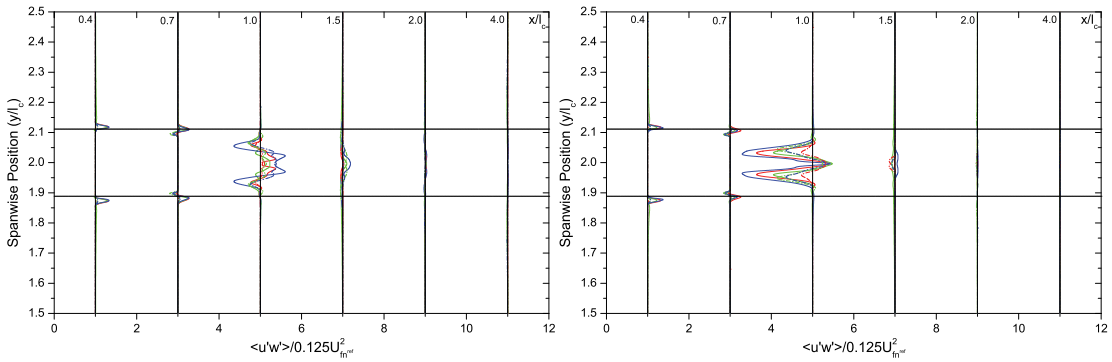

(c) 0.7h/lc (d) 0.9h/lc

Figure A3.10: Comparison of LES and DES around a submerged fairwater at different positions long the fairwater height for the time averaged u'w' cross Reynolds stress distribution.

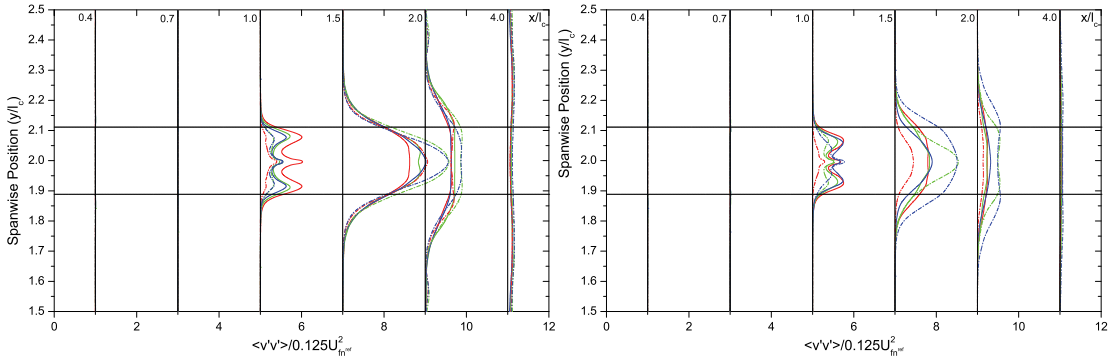

(a) 0.2h/lc (b) 0.5h/lc

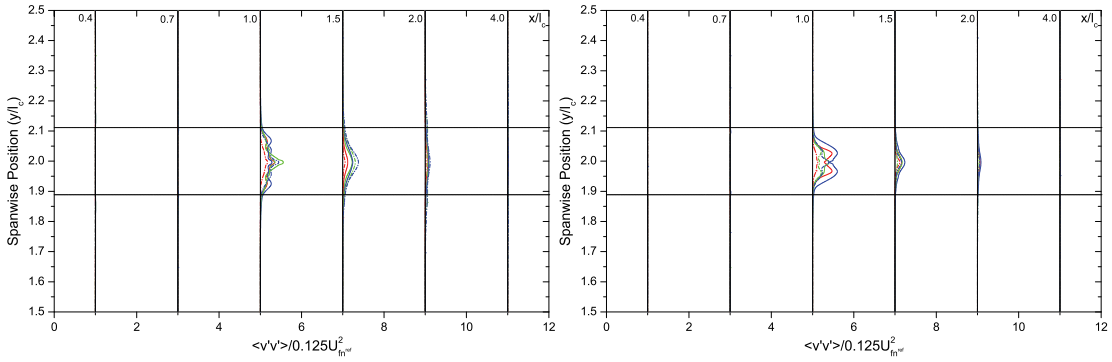

(c) 0.7h/lc (d) 0.9h/lc

Figure A3.11: Comparison of LES and DES around a submerged fairwater at different positions long the fairwater height for the time averaged v'v' normal Reynolds stress.

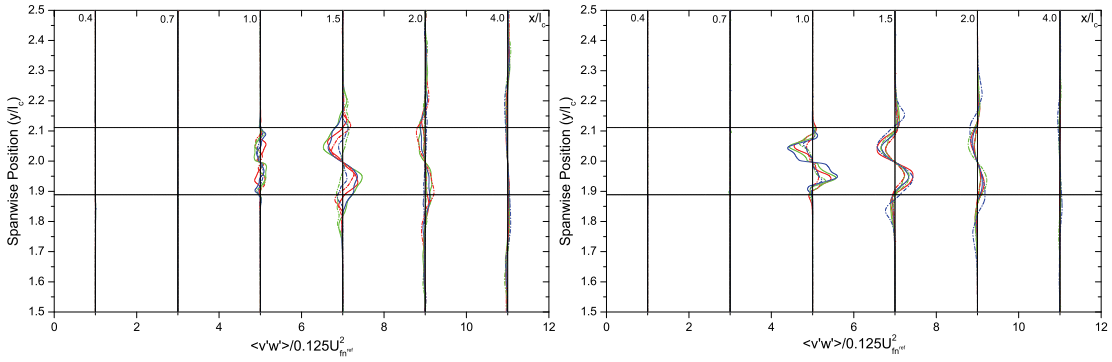

(a) 0.2h/lc (b) 0.5h/lc

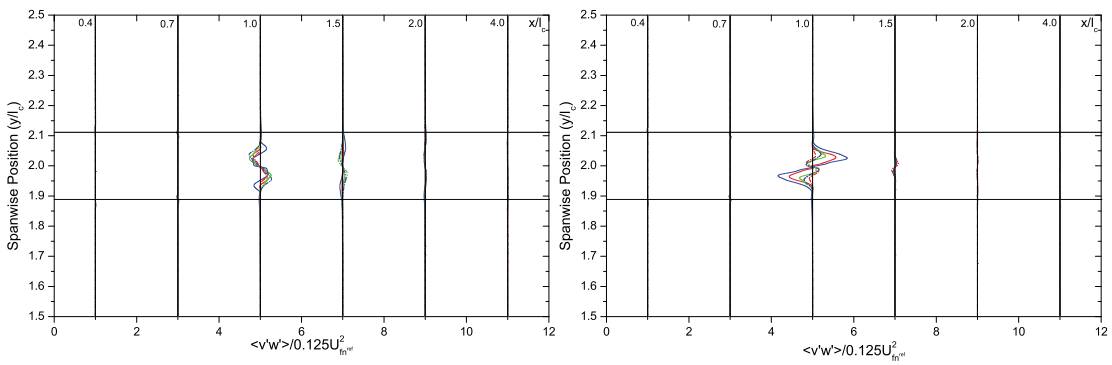

(c) 0.7h/lc (d) 0.9h/lc

Figure A3.12: Comparison of LES and DES around a submerged fairwater at different positions long the fairwater height for time averaged v'w' cross Reynolds stress distribution.

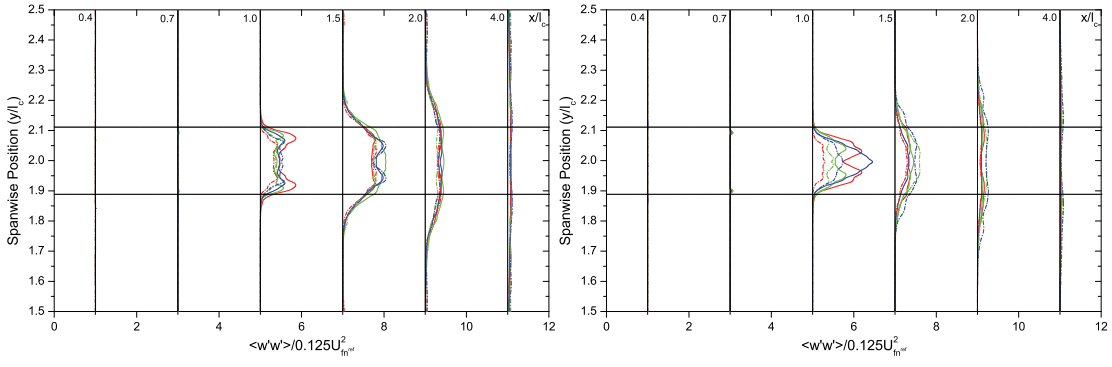

(a) 0.2h/lc (b) 0.5h/lc

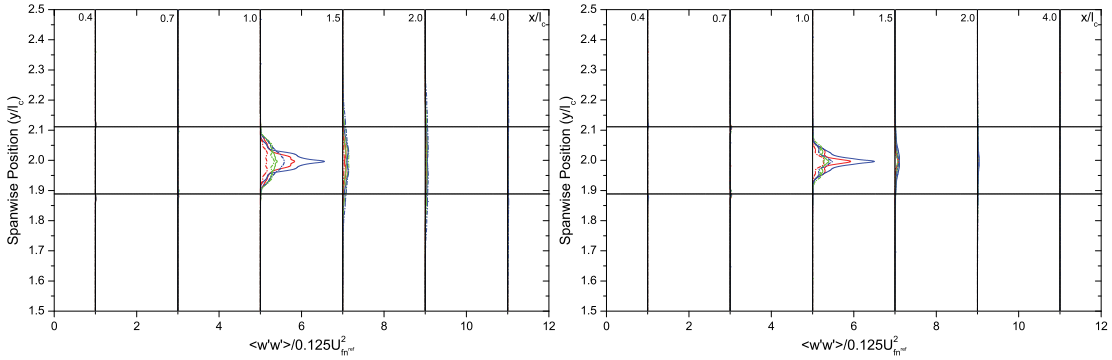

(c) 0.7h/lc (d) 0.9h/lc

Figure A3.13: Comparison of LES and DES around a submerged fairwater at different positions long the fairwater height for the time averaged w'w' normal Reynolds stress.

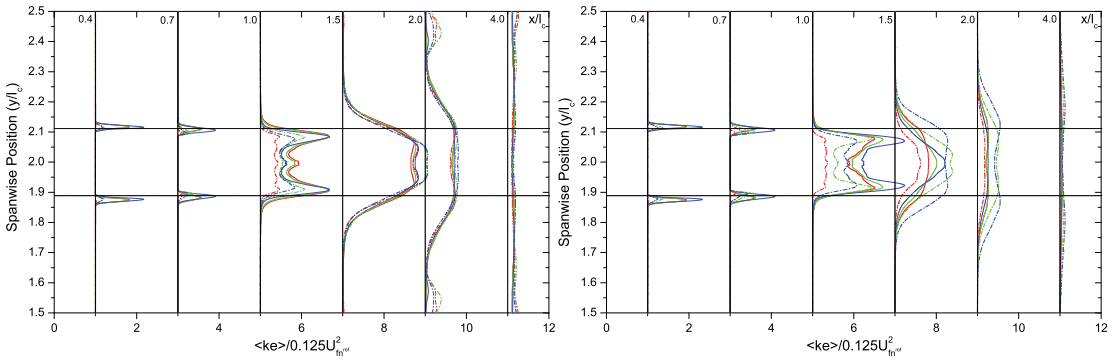

(a) 0.2h/lc (b) 0.5h/lc

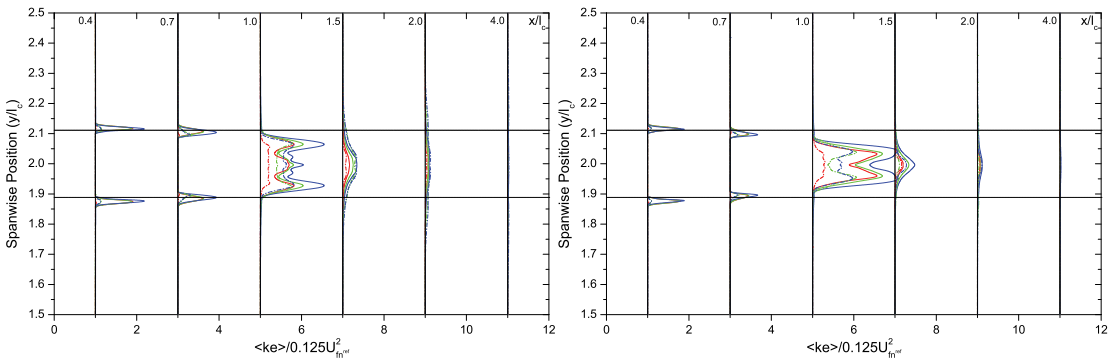

(c) 0.7h/lc (d) 0.9h/lc

Figure A3.14: Comparison of LES and DES around a submerged fairwater at different positions long the fairwater height for c in the XY plane.

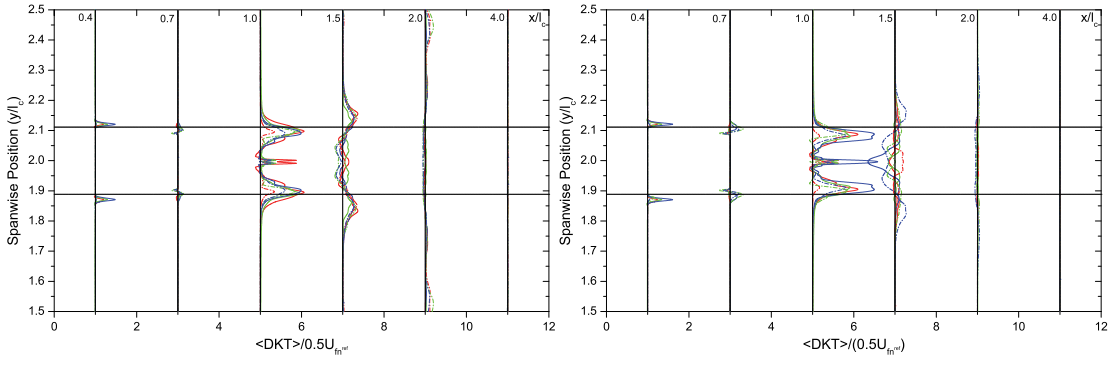

(a) 0.2h/lc (b) 0.5h/lc

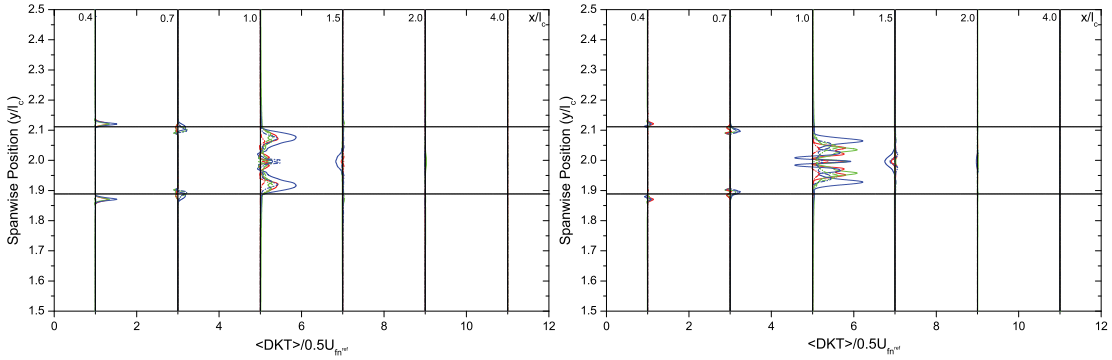

(c) 0.7h/lc (d) 0.9h/lc

Figure A3.15: Comparison of LES and DES around a submerged fairwater at different positions long the fairwater height for the time averaged DKT distribution in the XY plane.

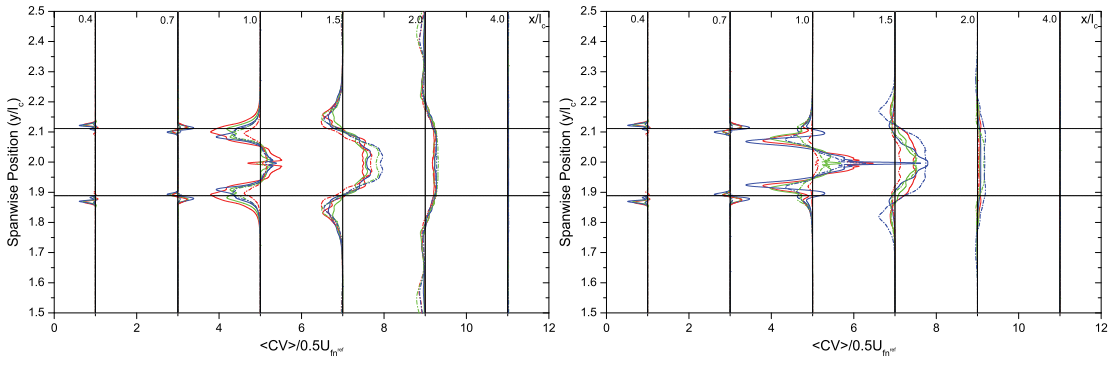

(a) 0.2h/lc (b) 0.5h/lc

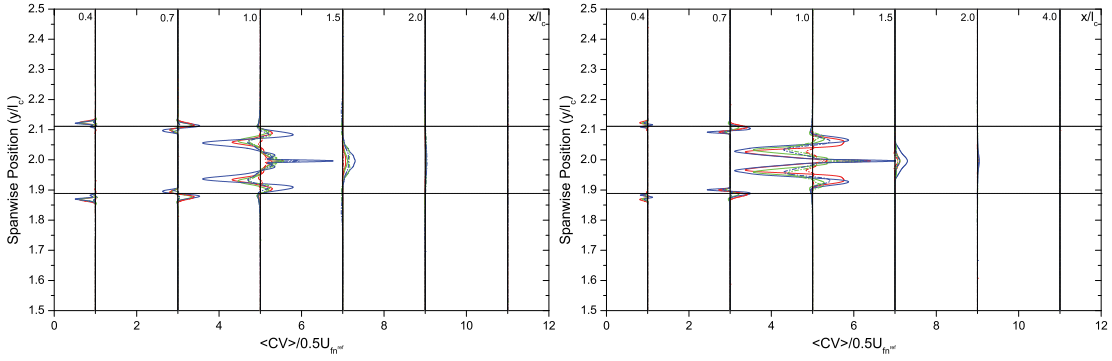

(c) 0.7h/lc (d) 0.9h/lc

Figure A3.16: Comparison of LES and DES around a submerged fairwater at different positions long the fairwater height for the time averaged CV distribution in the XY plane.

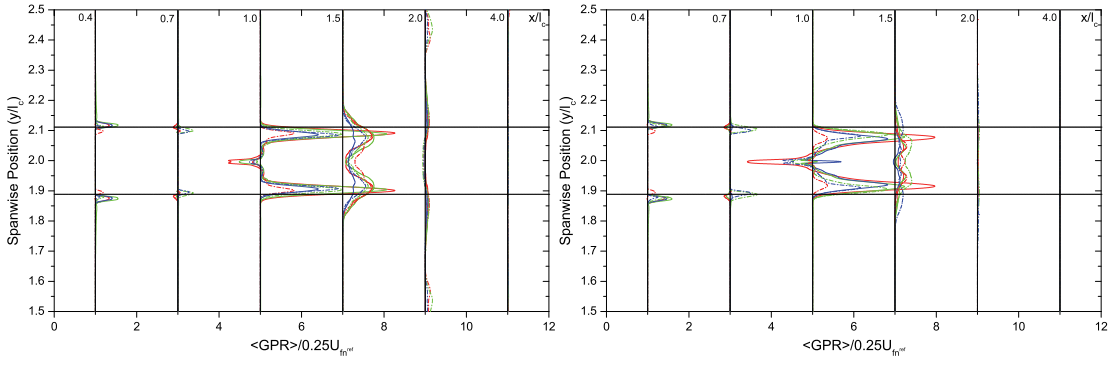

(a) 0.2h/lc (b) 0.5h/lc

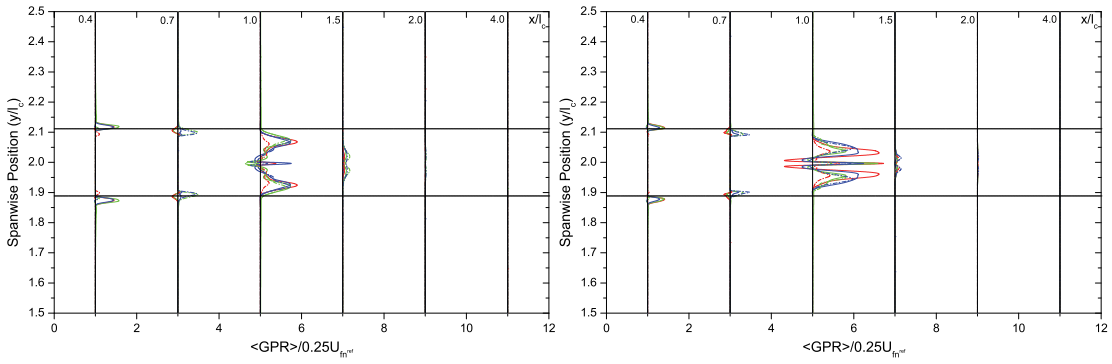

(c) 0.7h/lc (d) 0.9h/lc

Figure A3.17: Comparison of LES and DES around a submerged fairwater at different positions long the fairwater height for the time averaged GPR distribution in the XY plane.

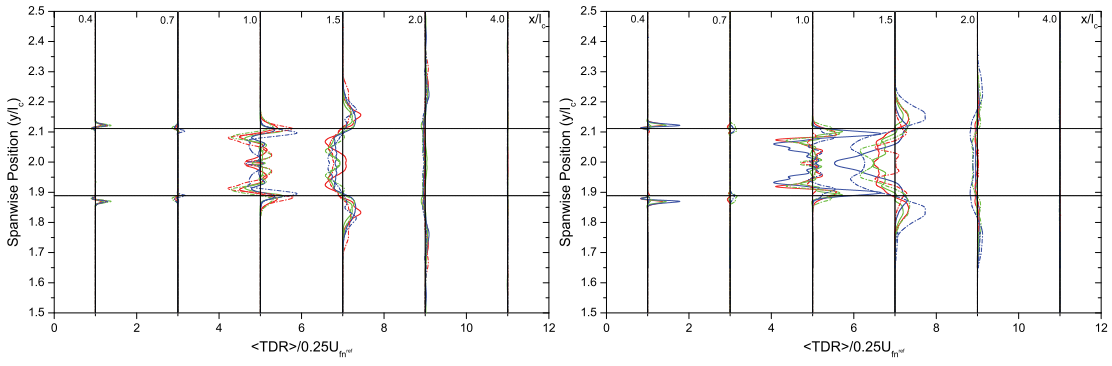

(a) 0.2h/lc (b) 0.5h/lc

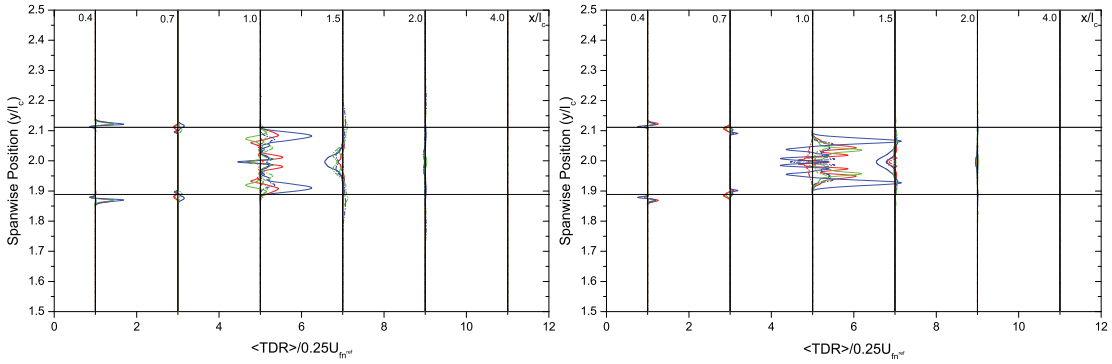

(c) 0.7h/lc (d) 0.9h/lc

Figure A3.18: Comparison of LES and DES around a submerged fairwater at different positions long the fairwater height for the time averaged TDR distribution in the XY plane.

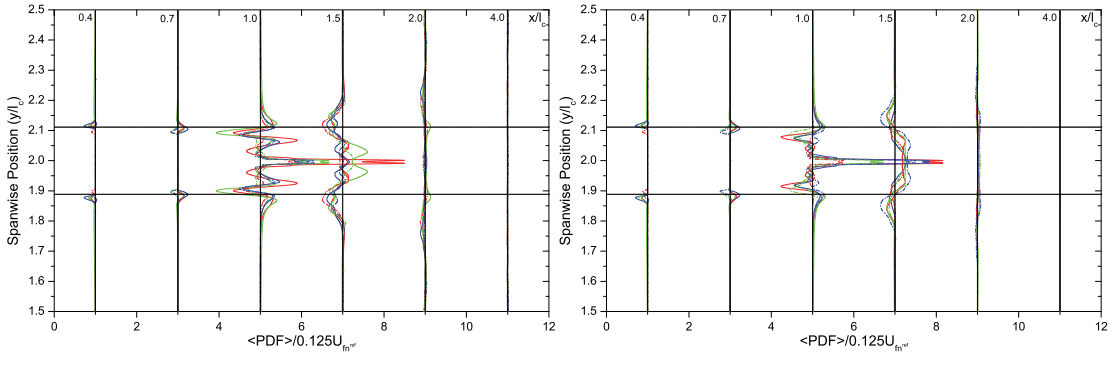

(a) 0.2h/lc (b) 0.5h/lc

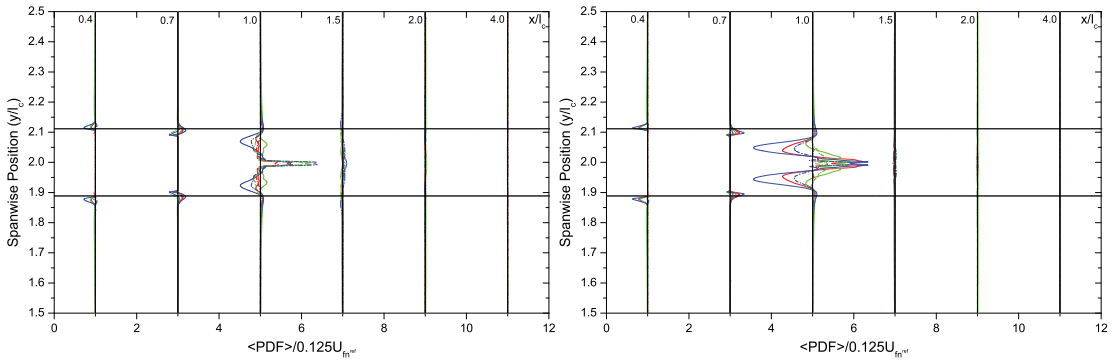

(c) 0.7h/lc (d) 0.9h/lc

Figure A3.19: Comparison of LES and DES around a submerged fairwater at different positions long the fairwater height for the time averaged PDF distribution in the XY plane.

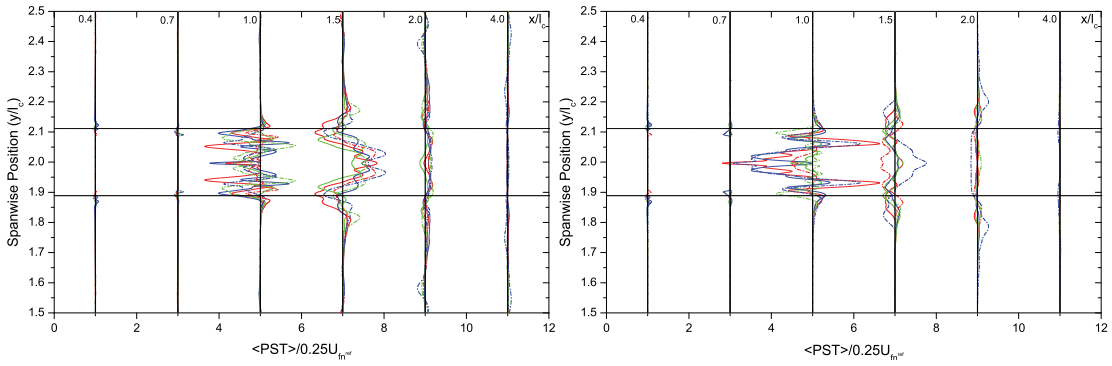

(a) 0.2h/lc (b) 0.5h/lc

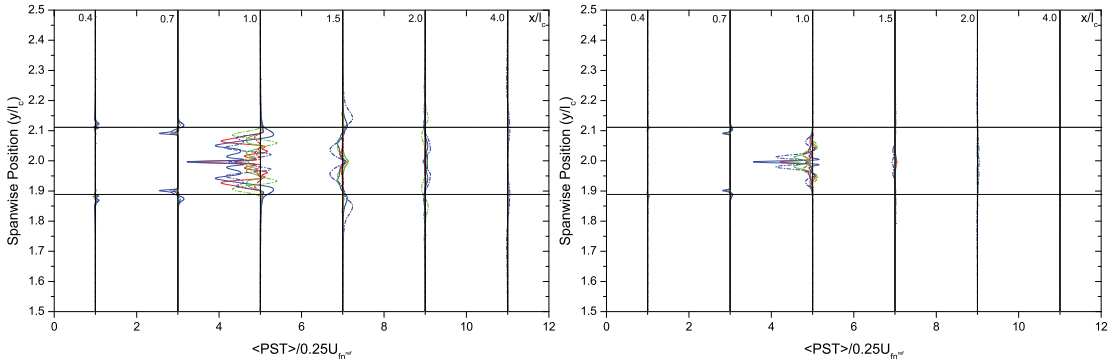

(c) 0.7h/lc (d) 0.9h/lc

Figure A3.20: Comparison of LES and DES around a submerged fairwater at different positions long the fairwater height for the time averaged PST distribution in the XY plane.

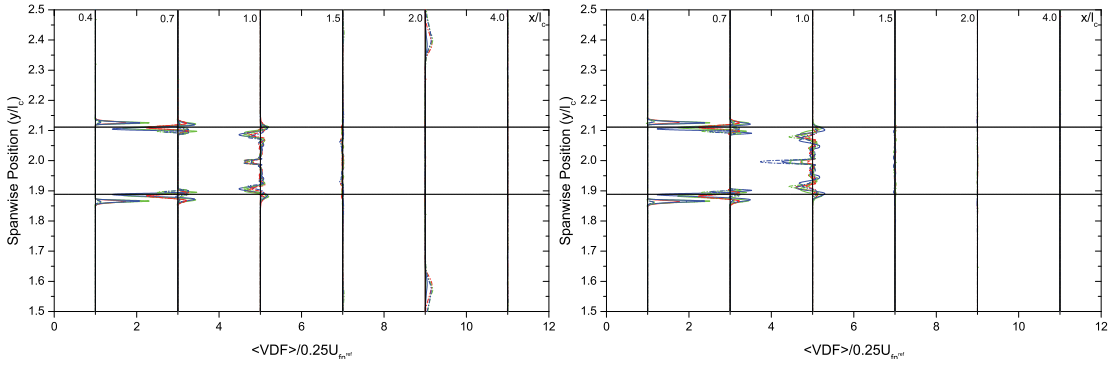

(a) 0.2h/lc (b) 0.5h/lc

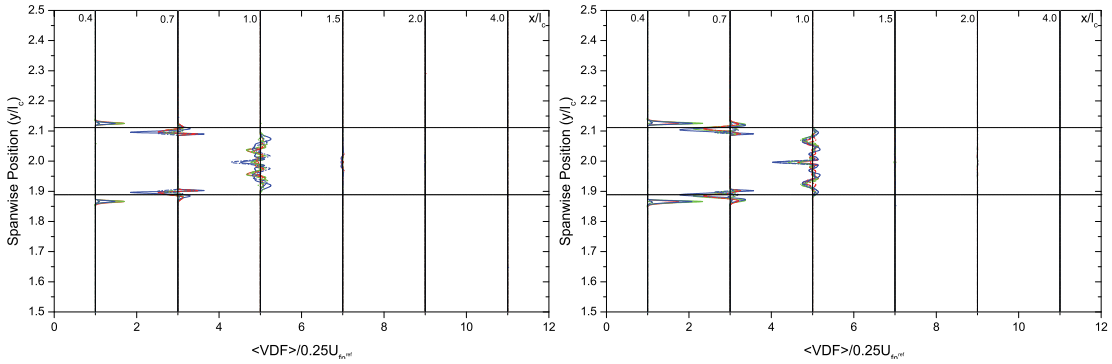

(c) 0.7h/lc (d) 0.9h/lc

Figure A3.21: Comparison of LES and DES around a submerged fairwater at different positions long the fairwater height for the time averaged VDF distribution in the XY plane.

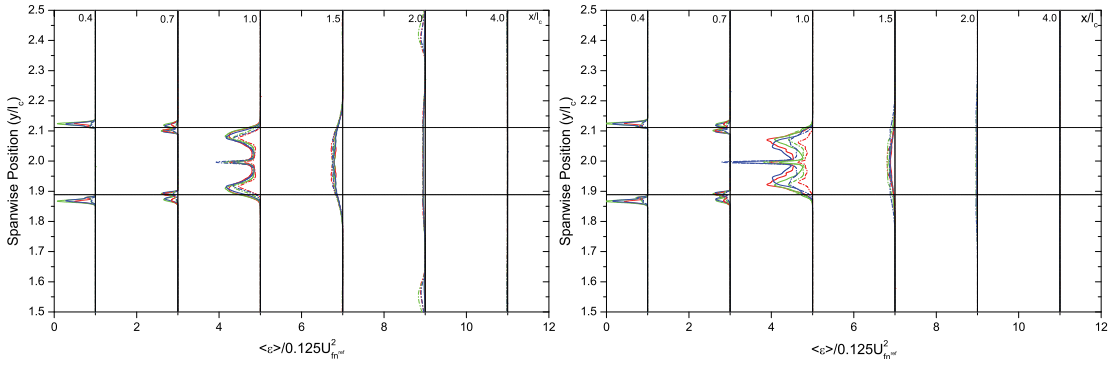

(a) 0.2h/lc (b) 0.5h/lc

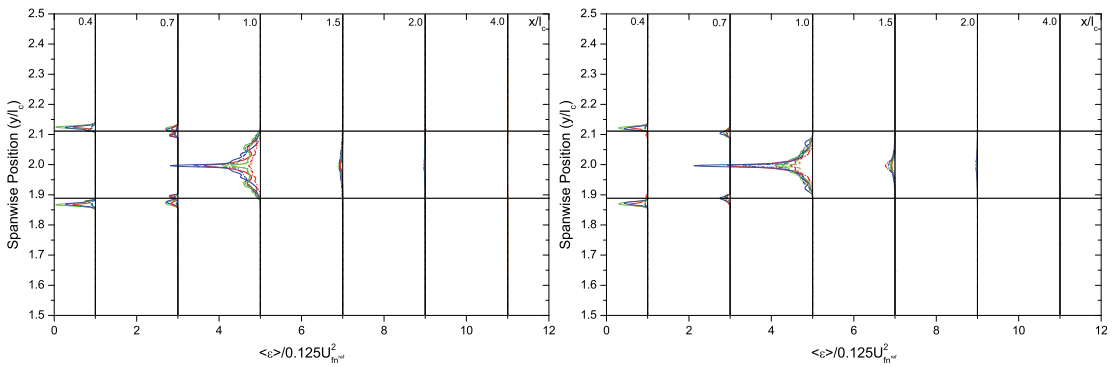

(c) 0.7h/lc (d) 0.9h/lc

Figure A3.22: Comparison of LES and DES around a submerged fairwater at different positions long the fairwater height for the time averaged ε distribution in the XY plane.

Appendix 4 Comparison of Re effect along the height of a Fully-Submerged Fairwater

List of Figures

Figure Legend

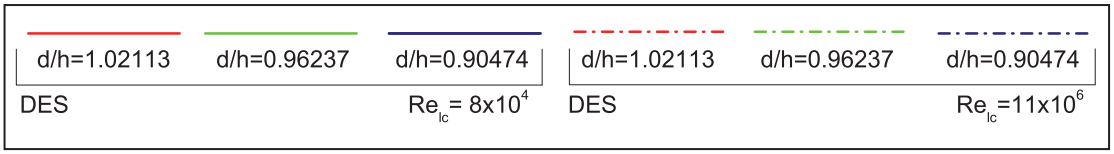

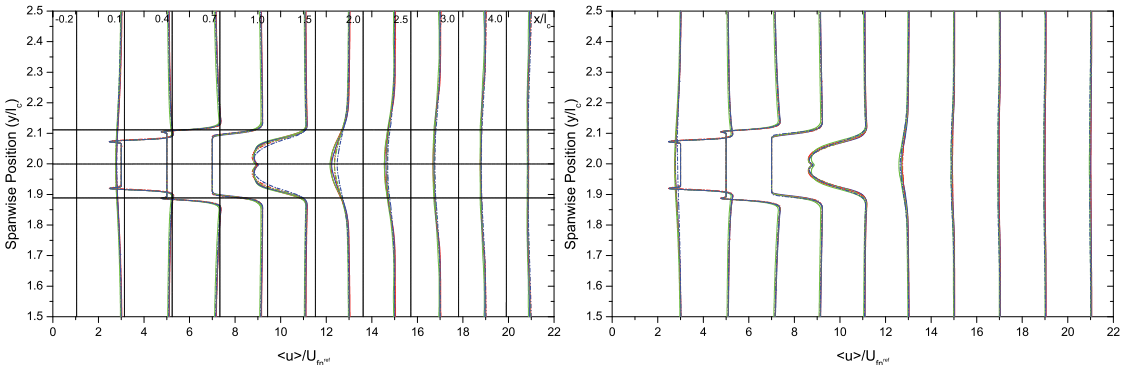

(a) $0.2h/l_c$ (b) $0.5h/l_c$

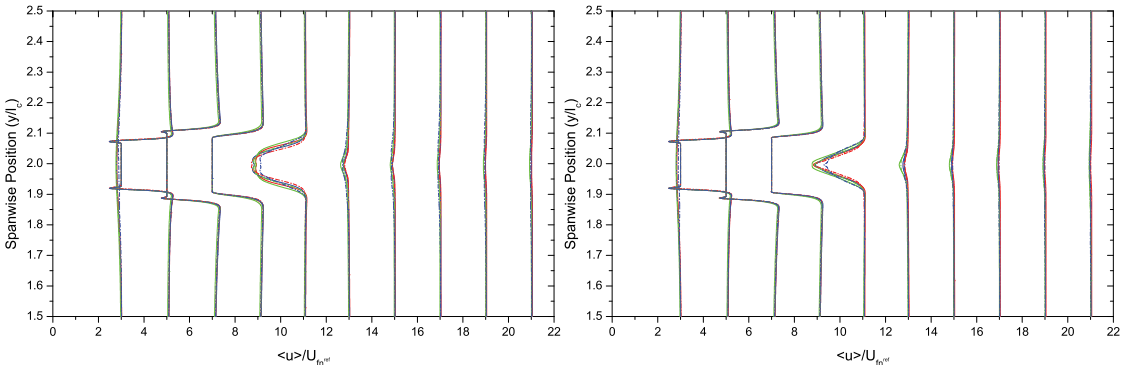

(c) $0.7h/l_c$ (d) $0.9h/l_c$

Figure A4.1: Comparison of the mean streamwise velocity distribution around the fairwater at different heights for $Re_{lc}=8\times10^4$ and $Re_{lc}=11\times10^6$.

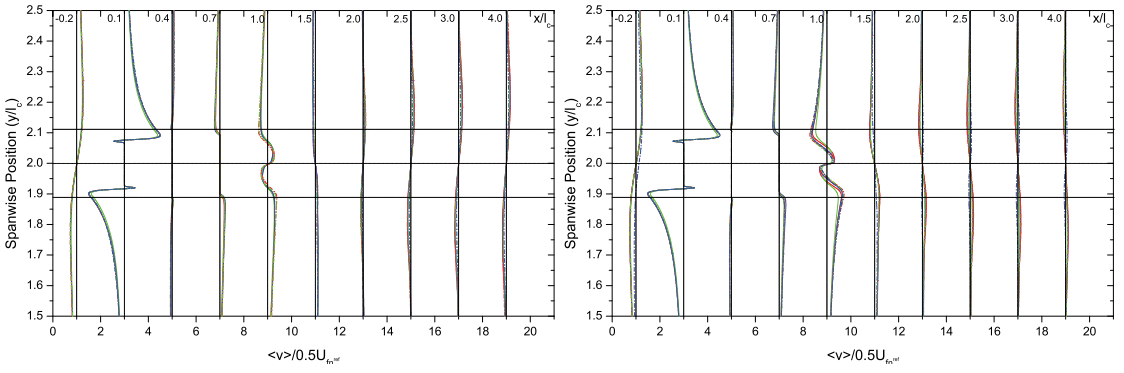

(a) $0.2h/l_c$ (b) $0.5h/l_c$

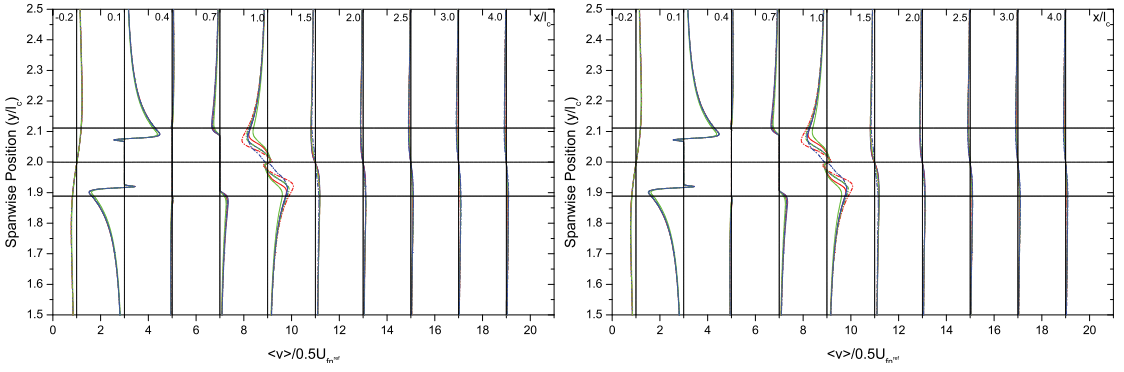

(c) $0.7h/l_c$ (d) $0.9h/l_c$

Figure A4.2: Comparison of the mean spanwise velocity distribution around the fairwater at different heights for $Re_{lc}=8\times10^4$ and $Re_{lc}=11\times10^6$.

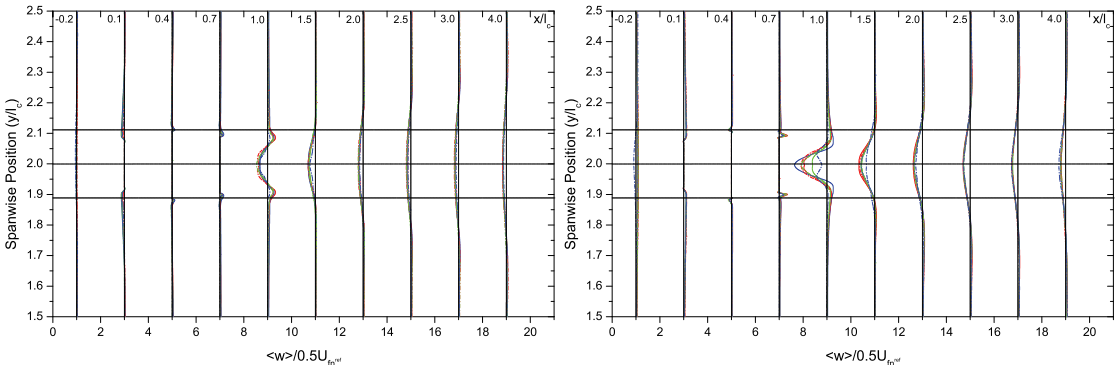

(a) $0.2h/l_c$ (b) $0.5h/l_c$

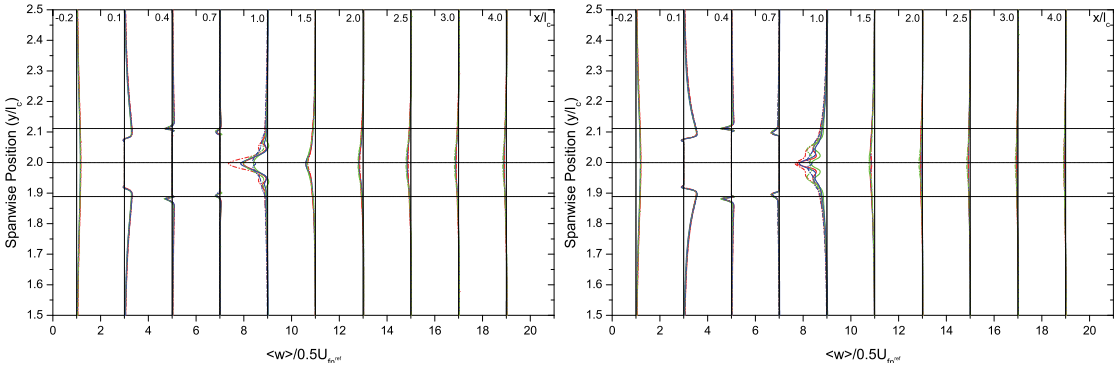

(c) $0.7h/l_c$ (d) $0.9h/l_c$

Figure A4.3: Comparison of the mean vertical velocity distribution around the fairwater at different heights for $Re_{lc}=8\times10^4$ and $Re_{lc}=11\times10^6$.

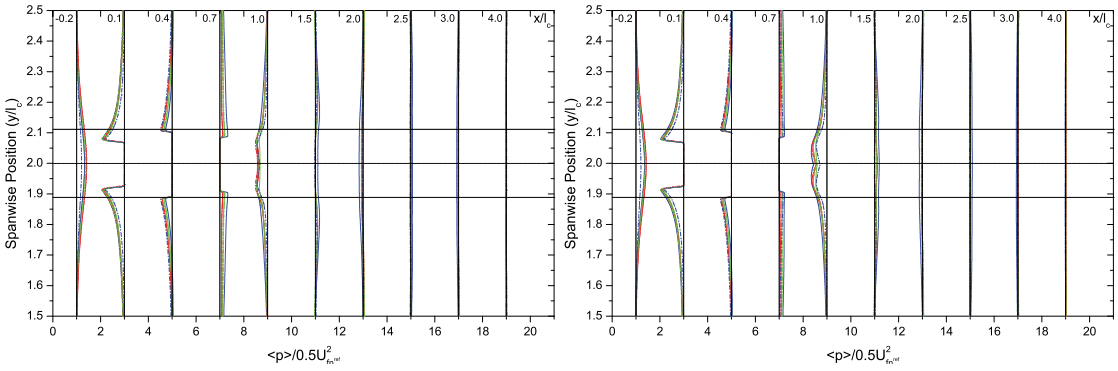

(a) $0.2h/l_c$ (b) $0.5h/l_c$

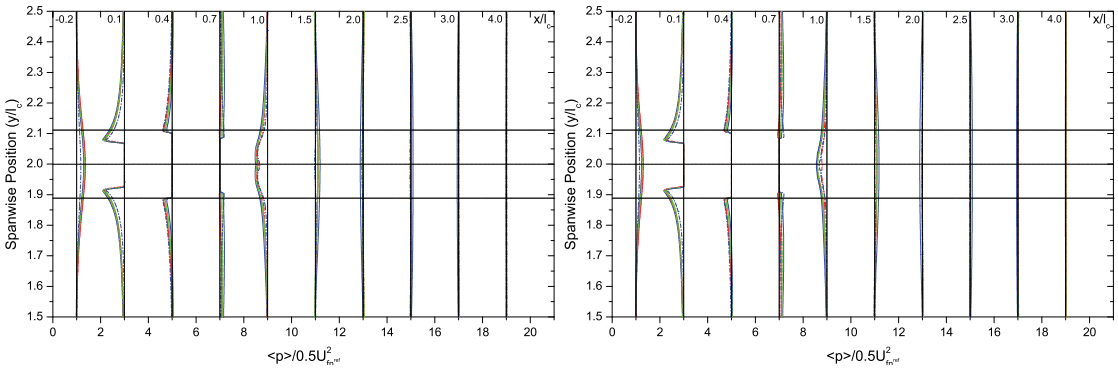

(c) $0.7h/l_c$ (d) $0.9h/l_c$

Figure A4.4: Comparison of the mean pressure distribution around the fairwater at different heights for $Re_{lc}=8\times10^4$ and $Re_{lc}=11\times10^6$.

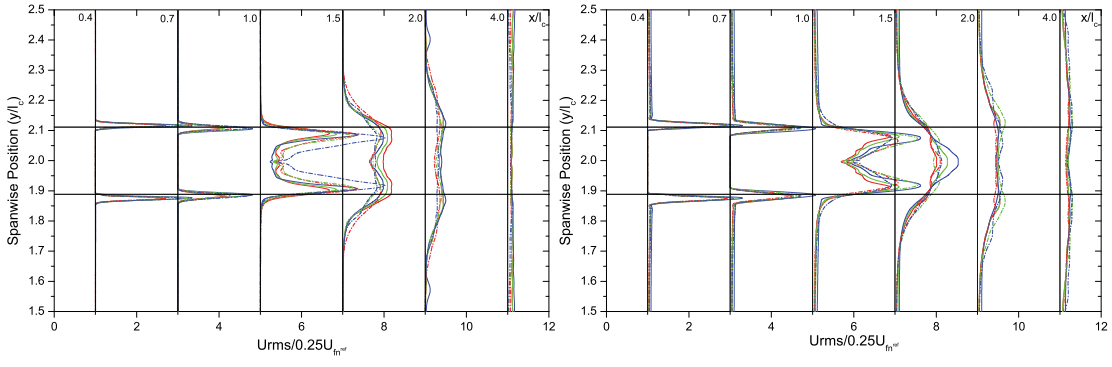

(a) $0.2h/l_c$ (b) $0.5h/l_c$

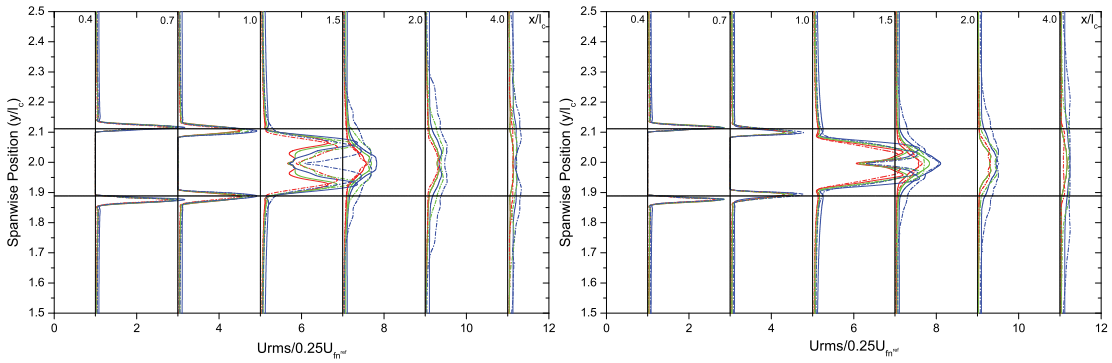

(c) $0.7h/l_c$ (d) $0.9h/l_c$

Figure A4.5: Comparison of the streamwise turbulent intensity distribution around the fairwater at different heights for $Re_{lc}=8\times10^4$ and $Re_{lc}=11\times10^6$.

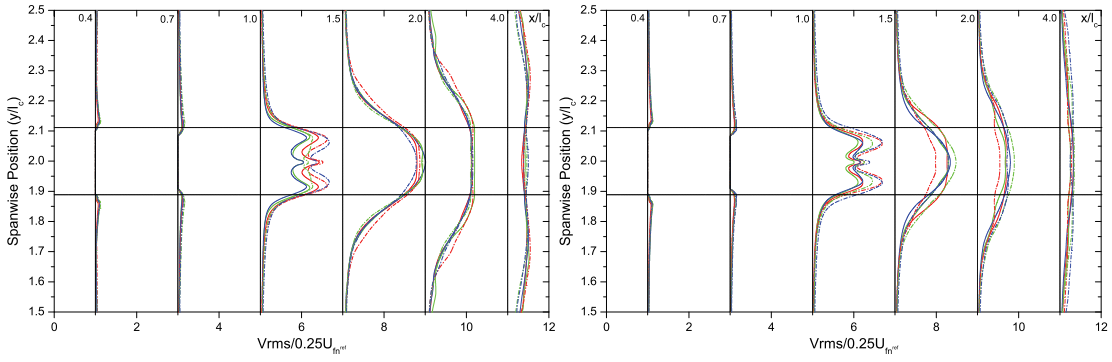

(a) $0.2h/l_c$ (b) $0.5h/l_c$

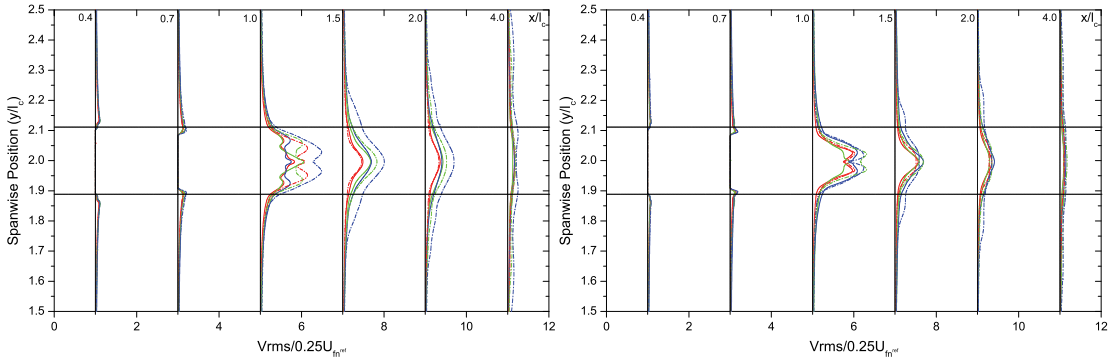

(c) $0.7h/l_c$ (d) $0.9h/l_c$

Figure A4.6: Comparison the spanwise turbulent intensity distribution around the fairwater at different heights for $Re_{lc}=8\times10^4$ and $Re_{lc}=11\times10^6$.

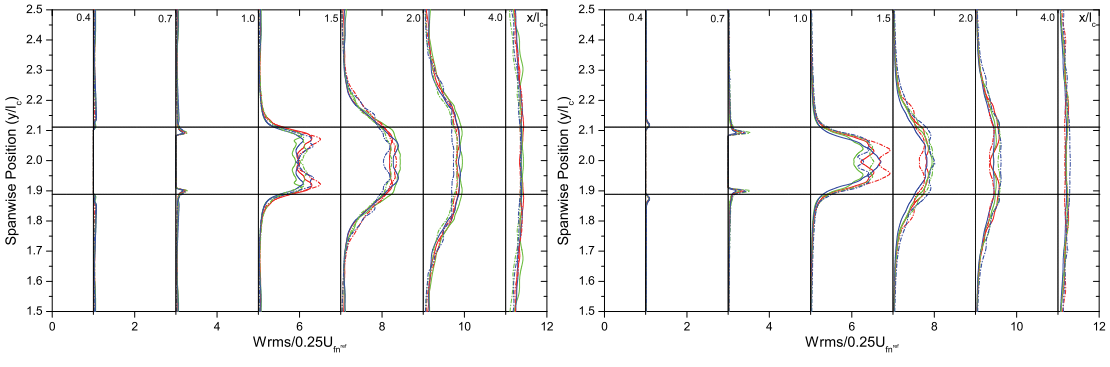

(a) $0.2h/l_c$ (b) $0.5h/l_c$

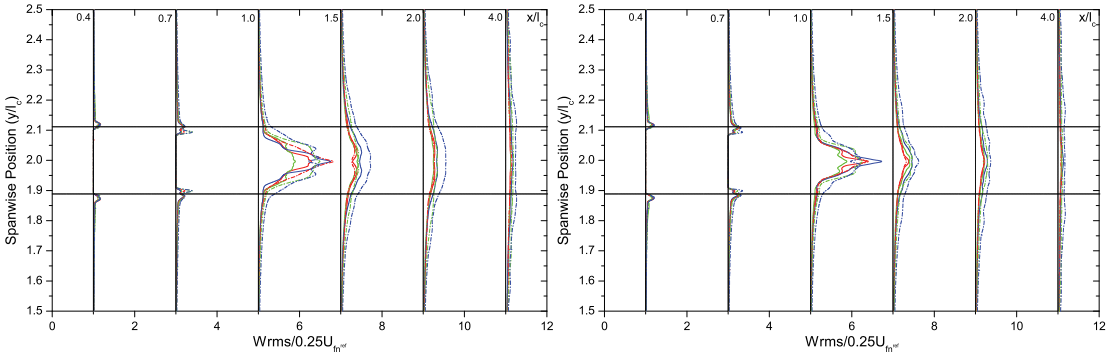

(c) $0.7h/l_c$ (d) $0.9h/l_c$

Figure A4.7: Comparison of the vertical turbulent intensity distribution around the fairwater at different heights for $Re_{lc}=8\times10^4$ and $Re_{lc}=11\times10^6$.

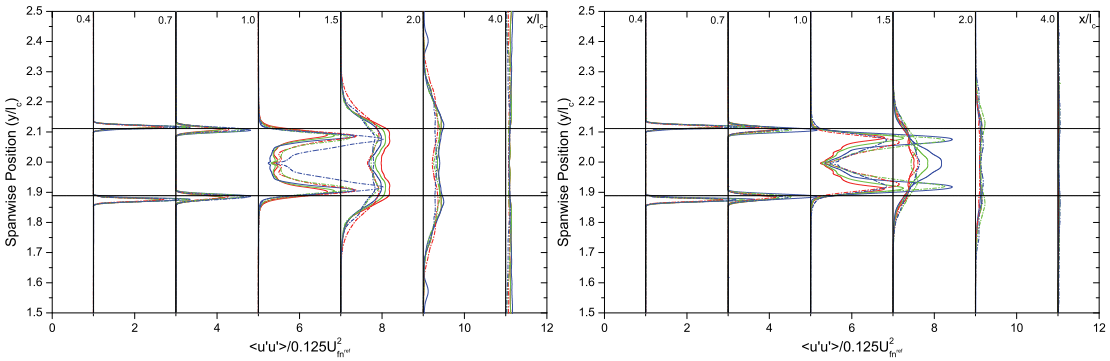

(a) $0.2h/l_c$ (b) $0.5h/l_c$

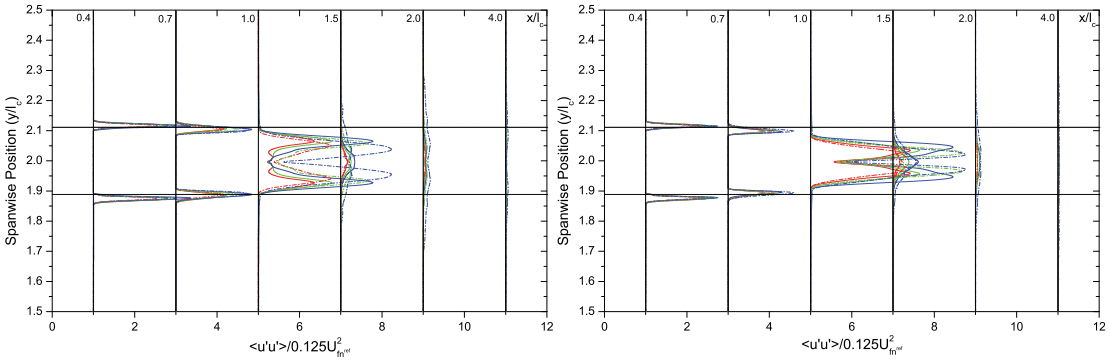

(c) $0.7h/l_c$ (d) $0.9h/l_c$

Figure A4.8: Comparison of the time averaged u'u' normal Reynolds stress distribution around the fairwater at different heights for $Re_{lc}=8\times10^4$ and $Re_{lc}=11\times10^6$.

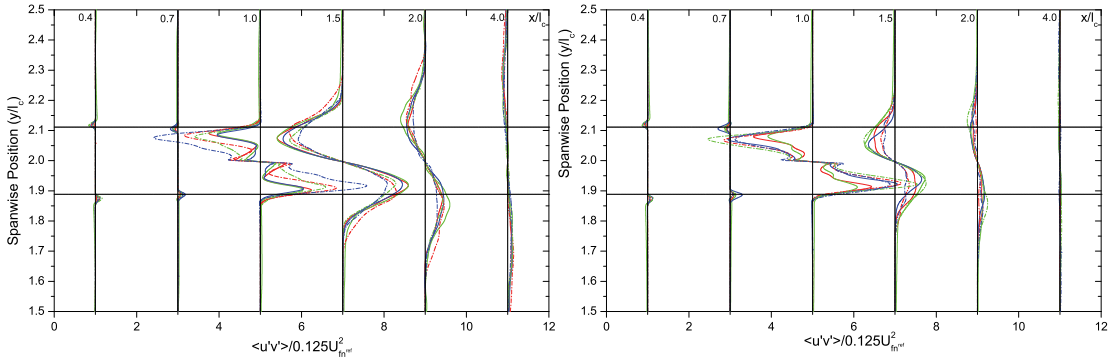

(a) $0.2h/l_c$ (b) $0.5h/l_c$

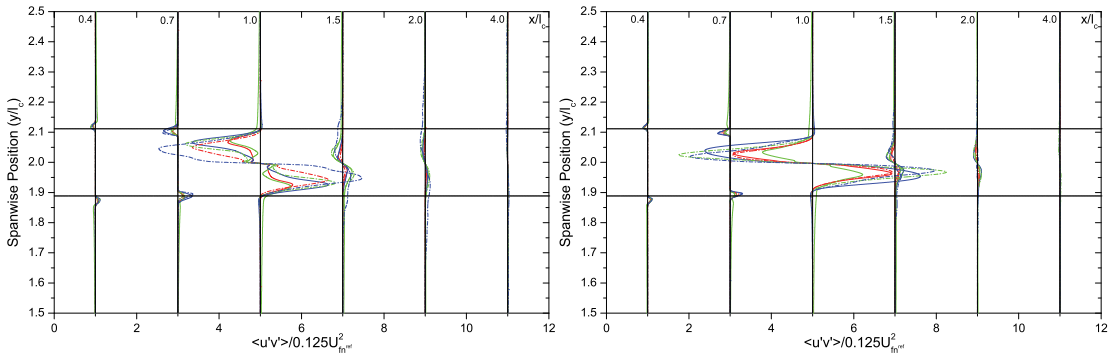

(c) $0.7h/l_c$ (d) $0.9h/l_c$

Figure A4.9: Comparison of for the time averaged u'v' cross Reynolds stress distribution around the fairwater at different heights for $Re_{lc}=8\times10^4$ and $Re_{lc}=11\times10^6$.

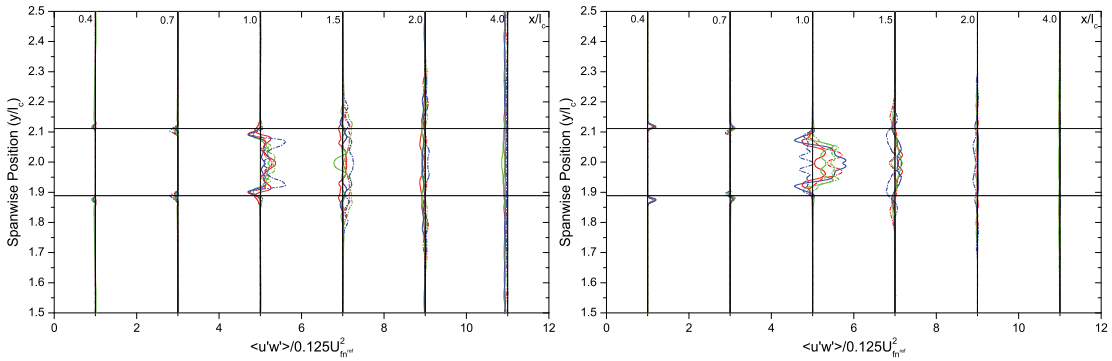

(a) $0.2h/l_c$ (b) $0.5h/l_c$

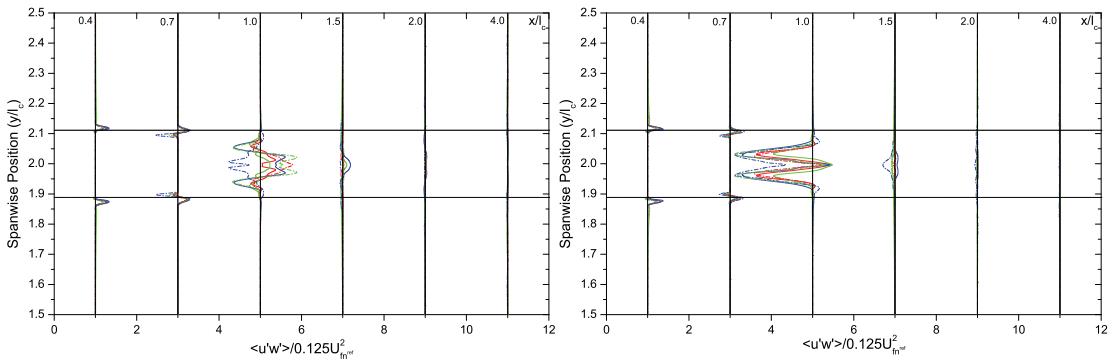

(c) $0.7h/l_c$ (d) $0.9h/l_c$

Figure A4.10: Comparison of for the time averaged u'w' cross Reynolds stress distribution around the fairwater at different heights for $Re_{lc}=8\times10^4$ and $Re_{lc}=11\times10^6$.

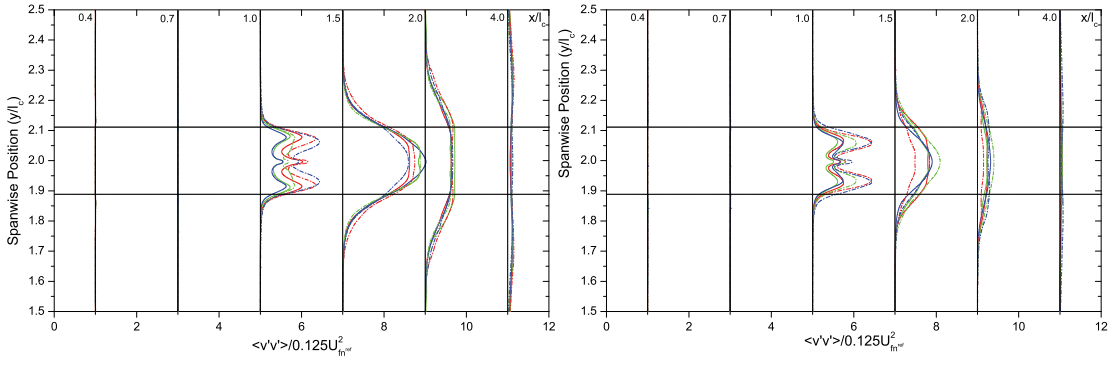

(c) $0.7h/l_c$ (d) $0.9h/l_c$

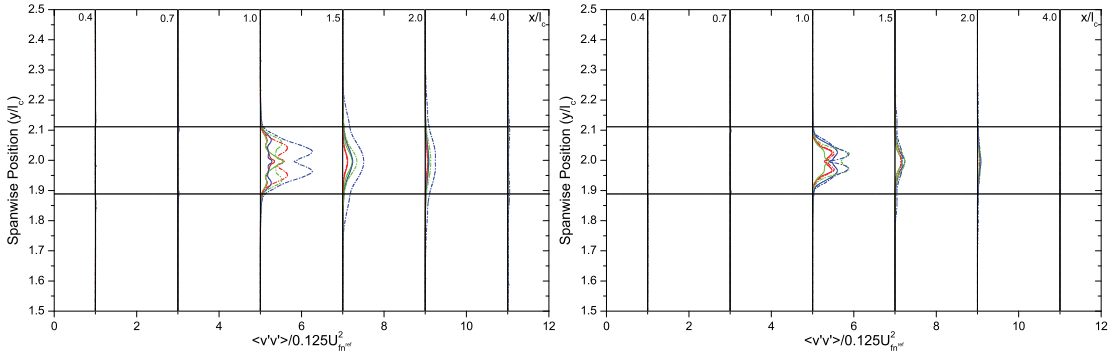

(c) $0.7h/l_c$ (d) $0.9h/l_c$

Figure A4.11: Comparison the time averaged v'v' normal Reynolds stress distribution around the fairwater for $Re_{lc}=8\times10^4$ and $Re_{lc}=11\times10^6$.

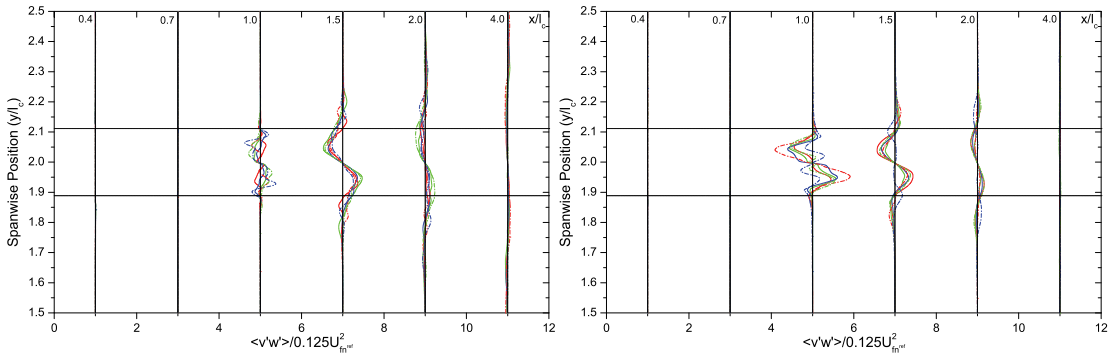

(a) $0.2h/l_c$ (b) $0.5h/l_c$

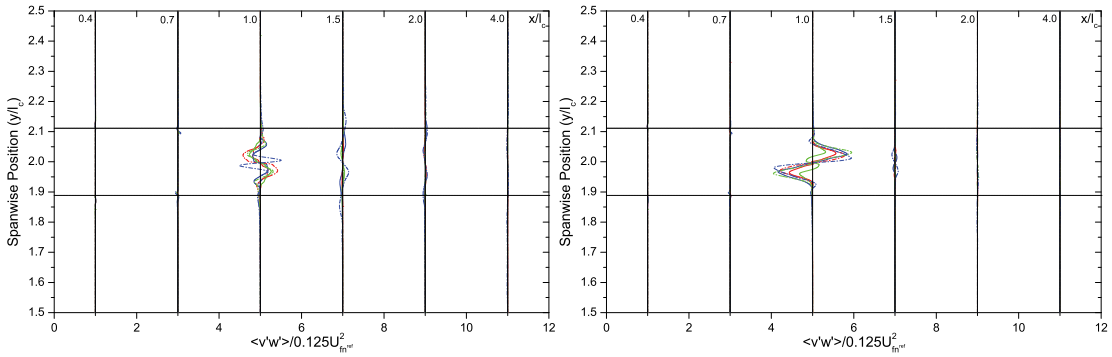

(c) $0.7h/l_c$ (d) $0.9h/l_c$

Figure A4.12: Comparison of the time averaged v'w' cross Reynolds stress distribution around the fairwater for $Re_{lc}=8\times10^4$ and $Re_{lc}=11\times10^6$.

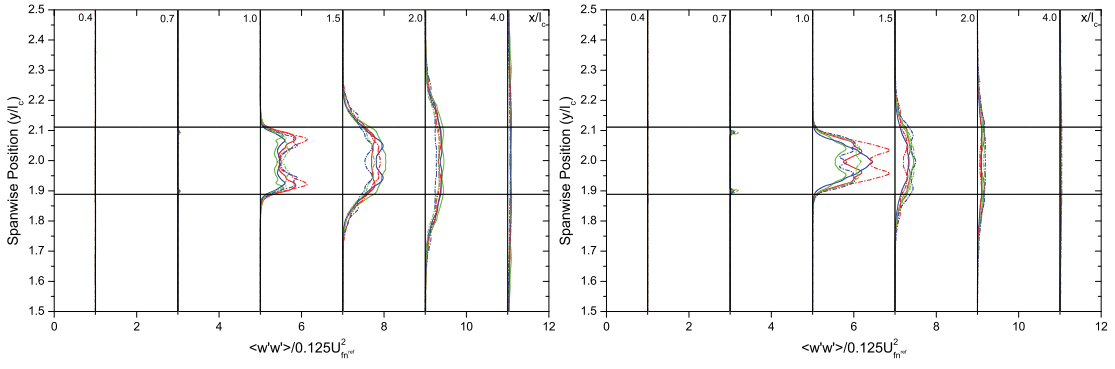

(a) $0.2h/l_c$ (b) $0.5h/l_c$

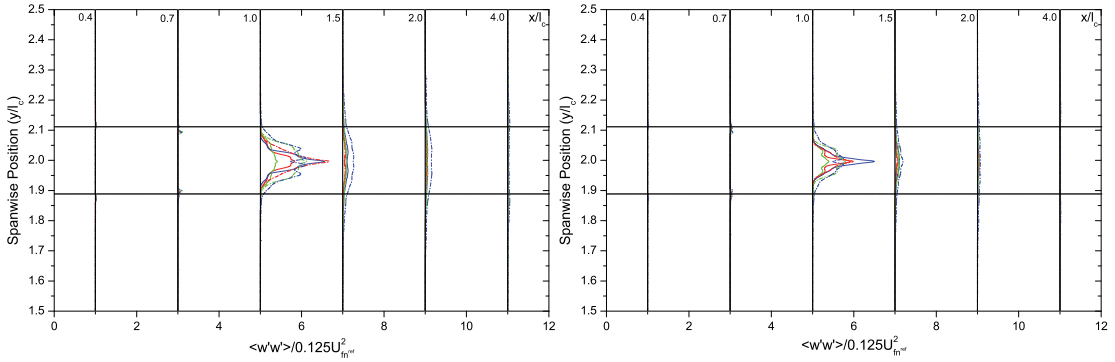

(c) $0.7h/l_c$ (d) $0.9h/l_c$

Figure A4.13: Comparison of the time averaged w'w' normal Reynolds stress distribution around the fairwater at different heights for $Re_{lc}=8\times10^4$ and $Re_{lc}=11\times10^6$.

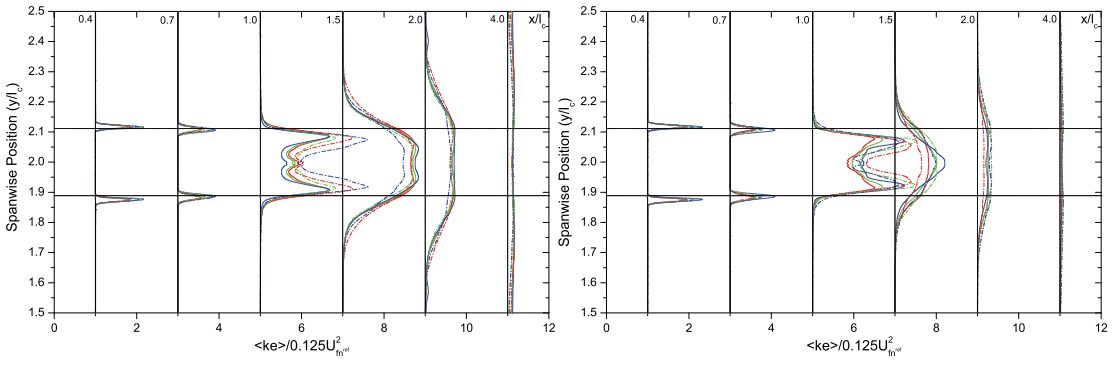

(a) $0.2h/l_c$ (b) $0.5h/l_c$

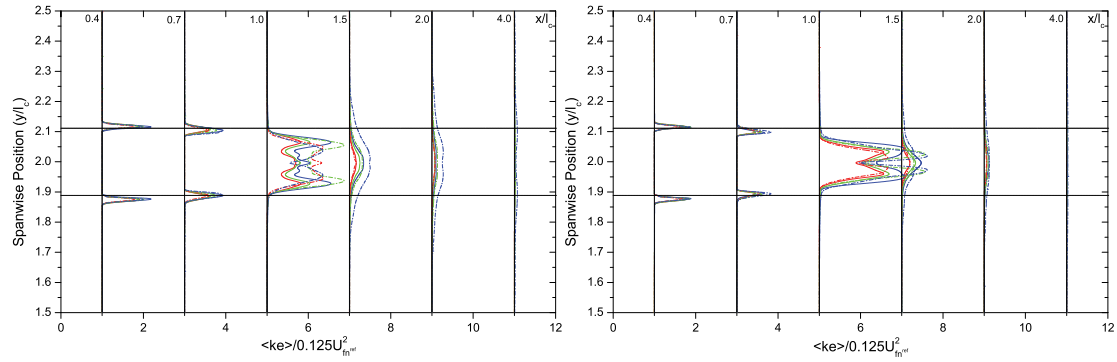

(c) $0.7h/l_c$ (d) $0.9h/l_c$

Figure A4.14: Comparison of the time averaged w'w' normal Reynolds stress distribution around the fairwater at different heights for $Re_{lc}=8\times10^4$ and $Re_{lc}=11\times10^6$.

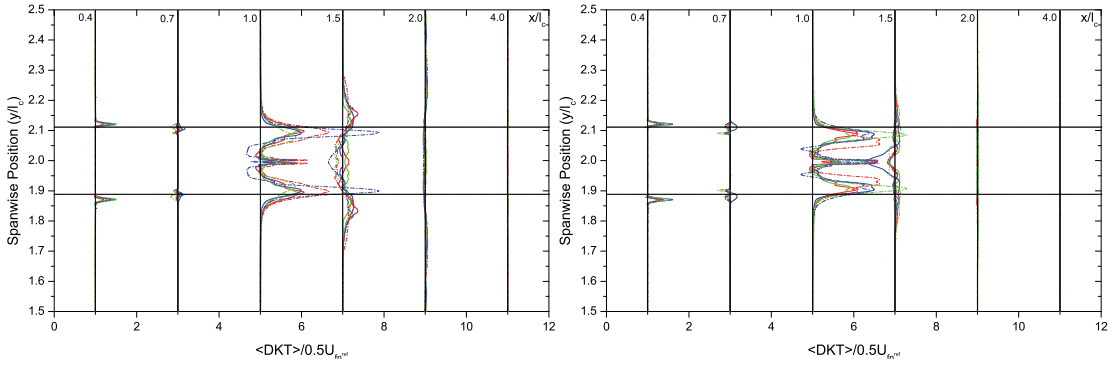

(a) *0.2h/l_c* (b) *0.5h/l_c*

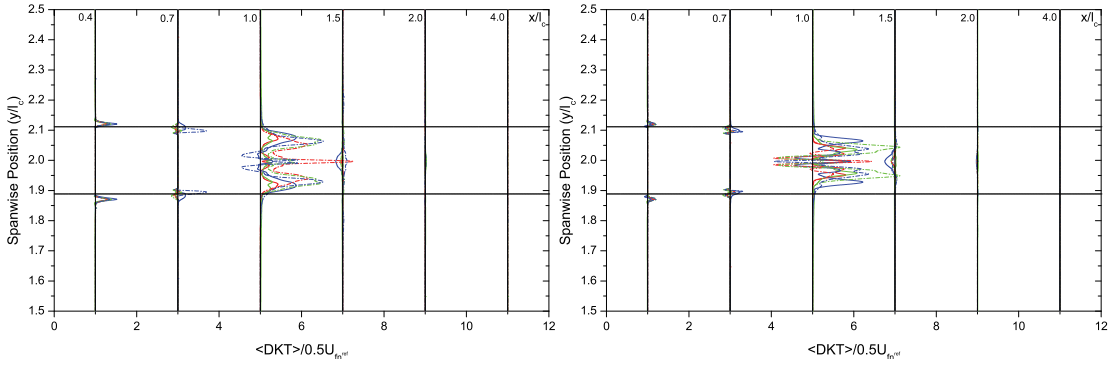

(c) *0.7h/l_c* (d) *0.9h/l_c*

Figure A4.15: Comparison of the time averaged DKT distribution around the fairwater at different heights for $Re_{lc}=8\times10^4$ and $Re_{lc}=11\times10^6$ about the XY plane.

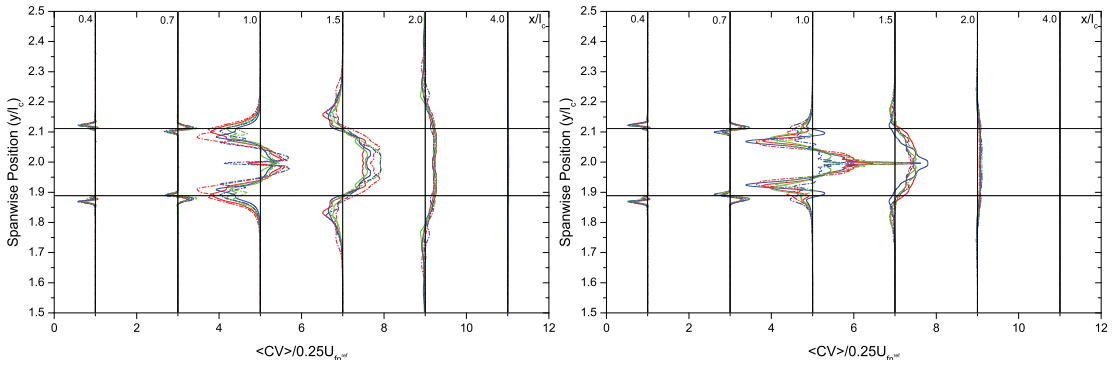

(a) *0.2h/l_c* (b) *0.5h/l_c*

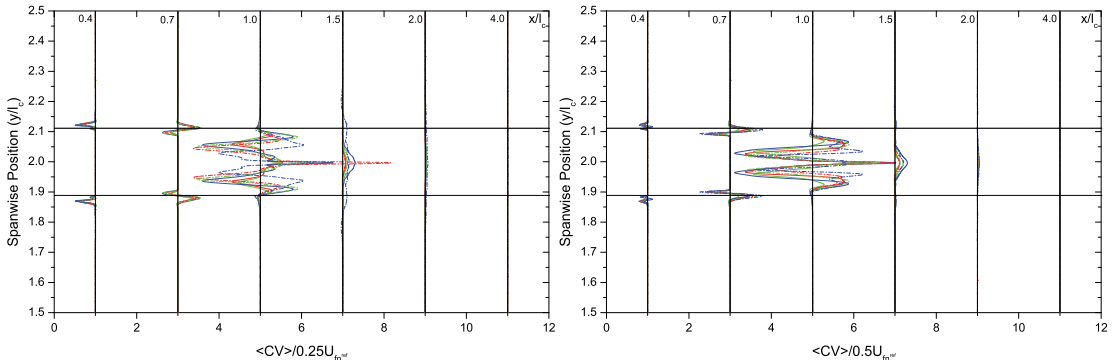

(c) *0.7h/l_c* (d) *0.9h/l_c*

Figure A4.16: Comparison of the time averaged CV distribution around the fairwater at different heights for $Re_{lc}=8\times10^4$ and $Re_{lc}=11\times10^6$ about the XY plane.

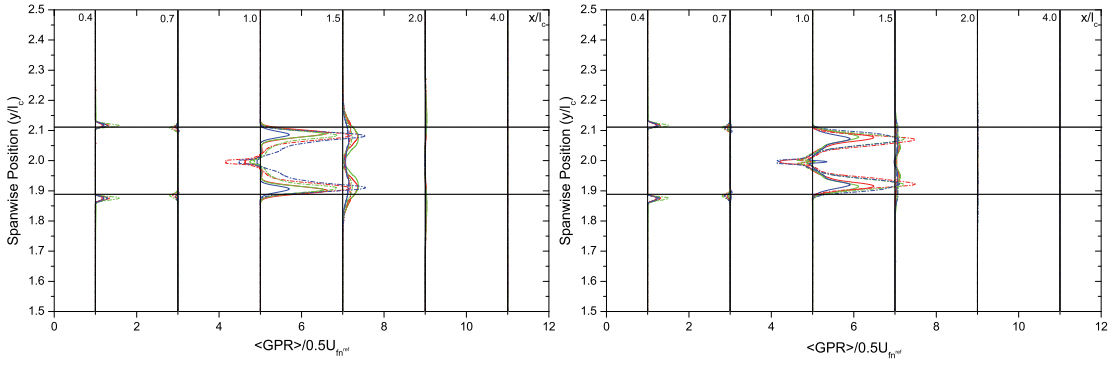

(a) $0.2h/l_c$ (b) $0.5h/l_c$

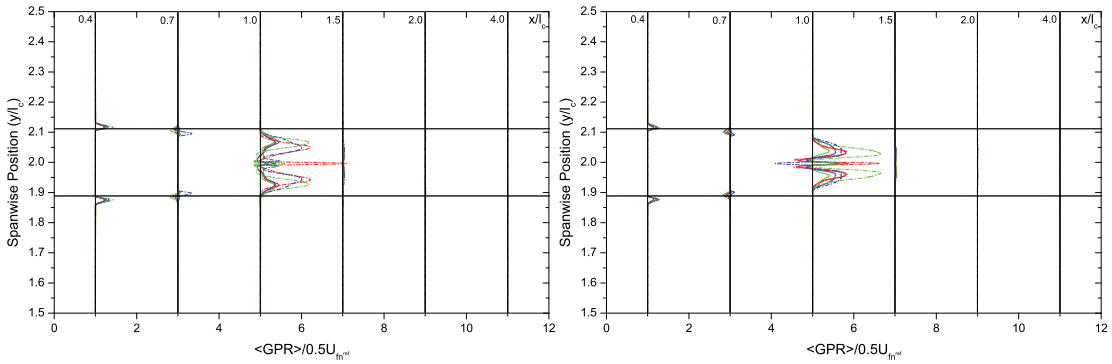

(c) $0.7h/l_c$ (d) $0.9h/l_c$

Figure A4.17: Comparison of the time averaged GPR distribution around the fairwater at different heights for $Re_{lc}=8\times10^4$ and $Re_{lc}=11\times10^6$ about the XY plane.

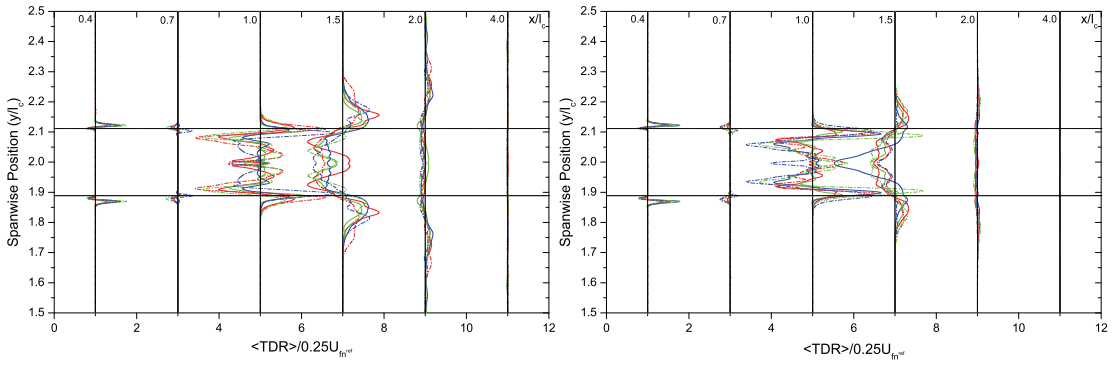

(a) $0.2h/l_c$ (b) $0.5h/l_c$

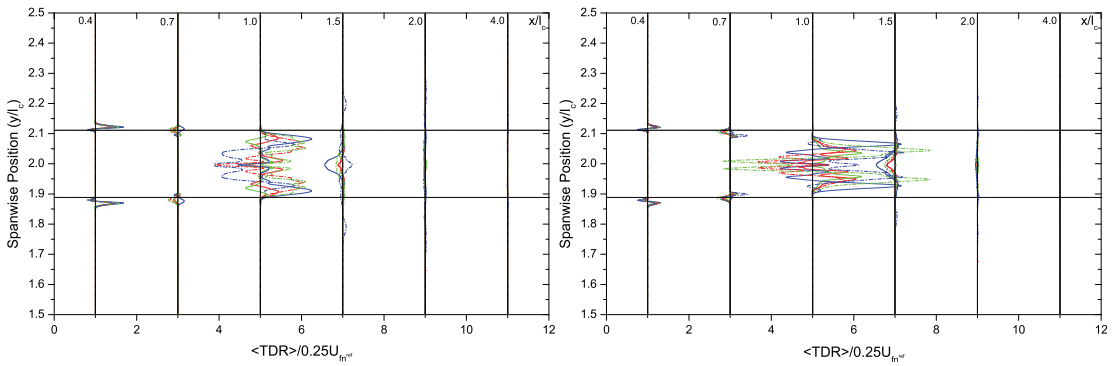

(c) $0.7h/l_c$ (d) $0.9h/l_c$

Figure A4.18: Comparison of the time averaged TDR distribution around the fairwater at different heights for $Re_{lc}=8\times10^4$ and $Re_{lc}=11\times10^6$ about the XY plane.

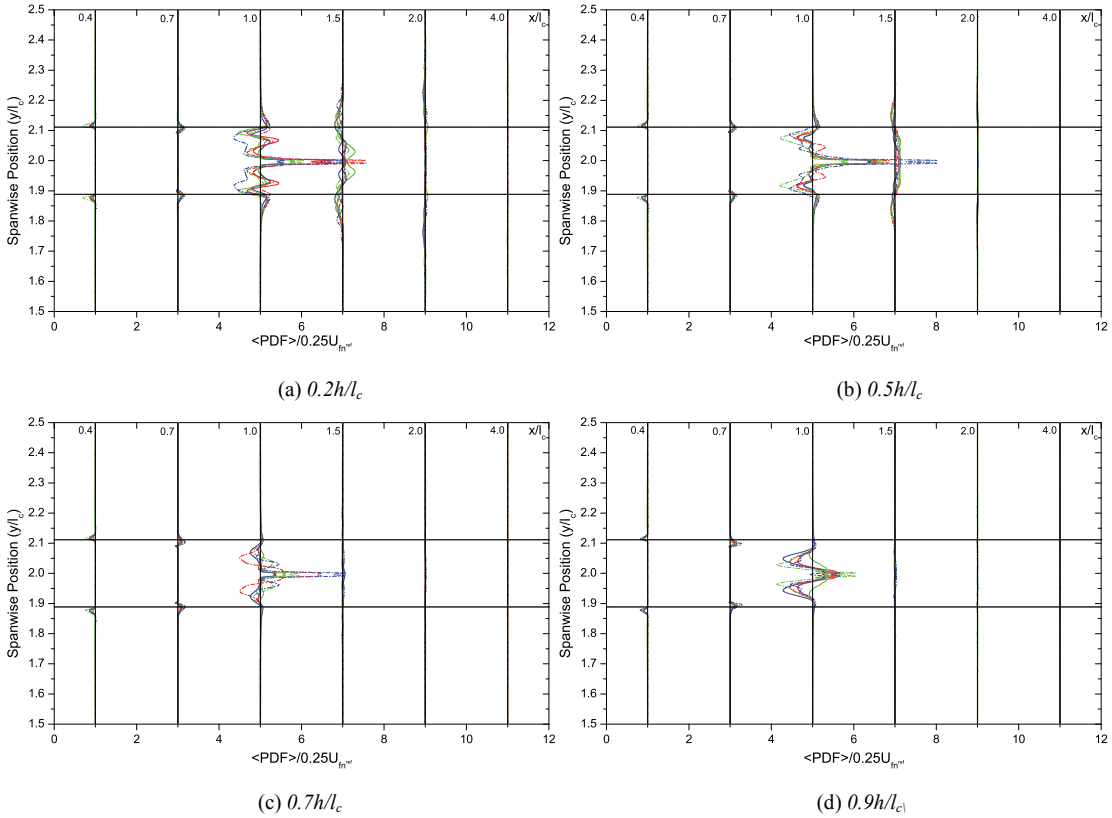

(a) $0.2h/l_c$ (b) $0.5h/l_c$

(c) $0.7h/l_c$ (d) $0.9h/l_c$

Figure A4.19: Comparison of the time averaged PDF distribution around the fairwater at different heights for $Re_{lc}=8\times10^4$ and $Re_{lc}=11\times10^6$ about the XY plane.

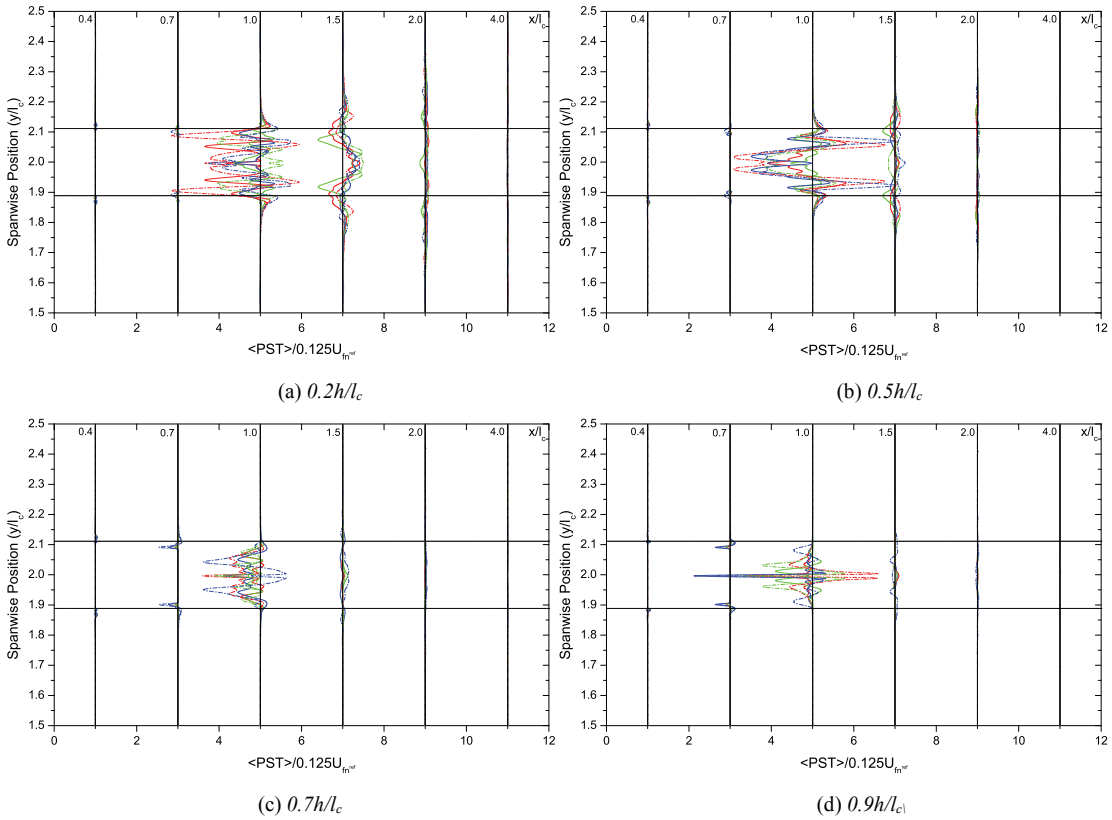

(a) $0.2h/l_c$ (b) $0.5h/l_c$

(c) $0.7h/l_c$ (d) $0.9h/l_c$

Figure A4.20: Comparison of the time averaged PST distribution around the fairwater at different heights for $Re_{lc}=8\times10^4$ and $Re_{lc}=11\times10^6$ about the XY plane.

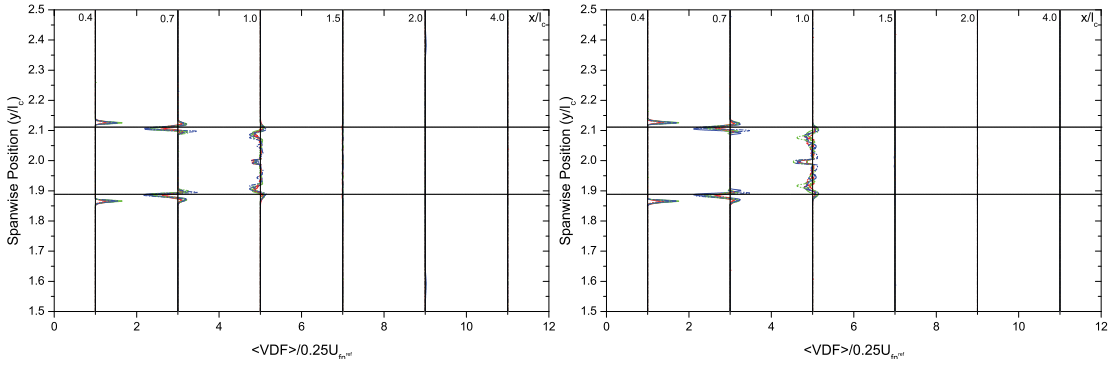

(a) $0.2h/l_c$ (b) $0.5h/l_c$

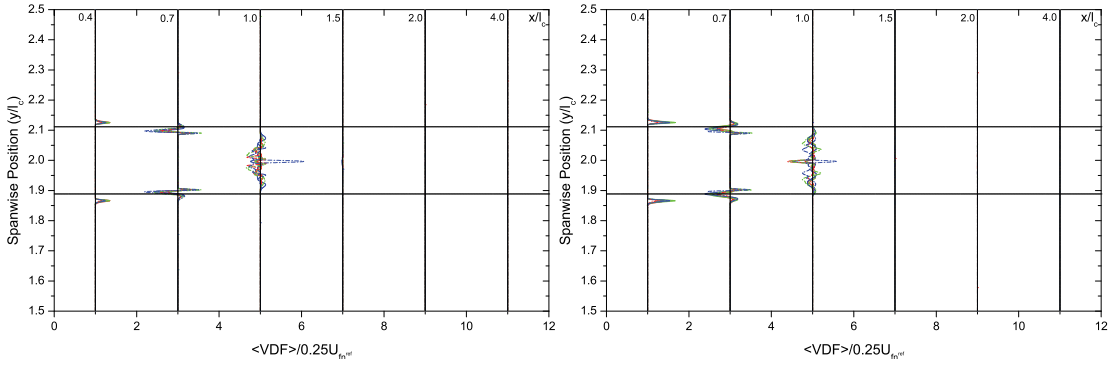

(c) $0.7h/l_c$ (d) $0.9h/l_c$

Figure A4.21: Comparison of the time averaged VDF distribution around the fairwater at different heights for $Re_{lc}=8\times10^4$ and $Re_{lc}=11\times10^6$ about the XY plane.

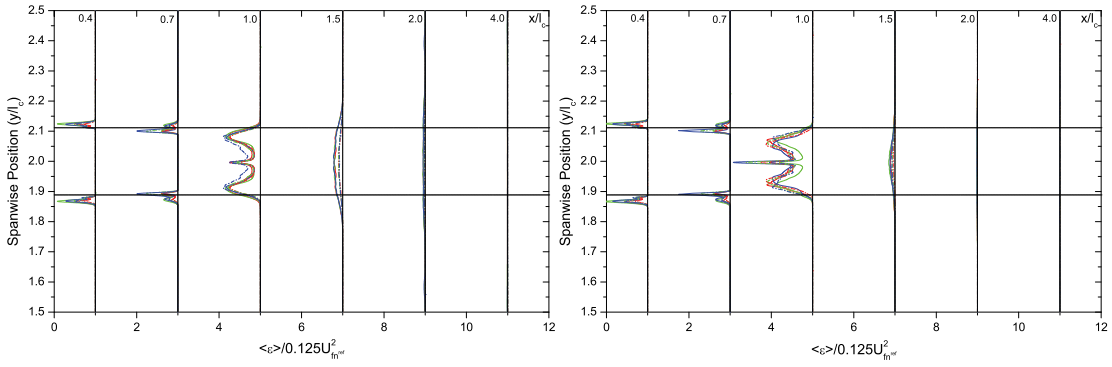

(a) $0.2h/l_c$ (b) $0.5h/l_c$

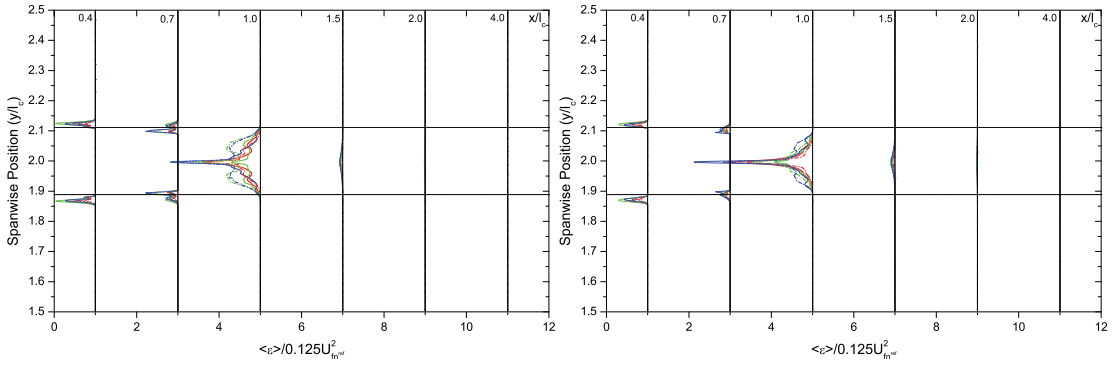

(c) $0.7h/l_c$ (d) $0.9h/l_c$

Figure A4.22: Comparison of the time averaged ε distribution around the fairwater at different heights for $Re_{lc}=8\times10^4$ and $Re_{lc}=11\times10^6$ about the XY plane.

References

Abbott IH, Doenhoff AE. 1959. *Theory of wing sections : including a summary of airfoil data*. New York: Dover.

Alfonsi G, Restanto C, Primavera L. 2003. Coherent structures of the flow around a surface-mounted cubic obstacle in turbulent channel flow. *Journal of Wind Engineering and Industrial Aerodynamics* 91: 495-511

Alin N, Fureby C, Svennberg SU, Wikstrom N, Sandberg WC, Ramamurti R, Bensow RE, Persson T. *2005*. 3D unsteady computations for submarine-like bodies. *Reno, NV, United states*: 353-69. American Institute of Aeronautics and Astronautics Inc.

Apsley D, Hu W. 2003. CFD simulation of two- and three-dimensional free-surface flow. *International Journal for Numerical Methods in Fluids* 42: 465-91

Bensow RE, Persson T, Fureby C, Svennberg U, Alin N. *2004*. Large eddy simulation of the viscous flow around submarine hulls. *25th Symposium on Navel Hydrodynamics, St. John's, Newfoundland and Labrador, Canada*: 1-16.

Bettle MC, Gerber AG, Watt GD. 2009. Unsteady analysis of the six DOF motion of a buoyantly rising submarine. *Computers & Fluids* 38: 1833-49

Camfield FE, Street RL. 1969. Shoaling of solitary waves on small slopes. *ASCE J. Waterw. Harbours. Div.* 94 (WW1): 1-22

Castro IP, Robins AG. 1977. The flow around a surface-mounted cube in uniform and turbulent streams. *Journal of Fluid Mechanics* 79: 307-35

Chan RK-C, Street RL, . 1970. A Computer Study of Finite-Amplitude Water Waves. *Journal of Computational Physics* 6: 68

Chandra R, Dagum L, Hohr D, McDonald J, Menon R. 2001. *Parallel programming in OpenMP*. San Deigo CA: Academic press.

Chang Y, Zhao F, Zhang J, Hong F-W, Li P, Yun J. 2006. Numerical simulation of internal waves excited by a submarine moving in the two-layer stratified fluid. *Journal of Hydrodynamics* 18: 330-6

Chen T, Chwang AT. 2002. Trailing vortices in a free-surface flow. *Physics of Fluids* 14: 827-38

Choi JI, Oberoi RC, Edwards JR, Rosati JA. 2007. An immersed boundary method for complex incompressible flows. *Journal of Computational Physics* 224: 757-84

Choi SK, Nam HY, Cho M. 1995. A comparison of higher-order bounded convection schemes. *Computer Methods in Applied Mechanics and Engineering* 121: 281-301

Crapper GD. 1984. *Introduction to water waves*. pp. 1-53. Ellis Horword Ltd.

Dacles-Mariani J, Zilliac GG, Chow JS, Bradshaw P. 1995. Numerical/experimental study of a wingtip vortex in the near field. *AIAA* 33: 1561-8

Duncan JH. 1983. Breaking and non-breaking wave resistance of a two-dimensional hydrofoil. *Journal of Fluid Mechanics* 126: 507-20

Eckelmann H. 1974. Structure of the viscous sublayer and the adjacent wall region in a turbulent channel flow. *Journal of Fluid Mechanics* 65: 439-59

Fadlun EA, Verzicco R, Orlandi P, Mohd-Yusuf J. 2000. Combined immersed-boundary finite-difference methods for three-dimensional complex flow simulations. *Journal of Computational Physics* 161: 35-60

Farhadi M, Rahnama M. 2006. Large eddy simulation of separated flow over a wall-mounted cube. *Scientia Iranica* 13: 124-33

Farhadi M, Sedighi K. 2008. Flow over two tandem wall-mounted cubes using large eddy simulation. *Proceedings of the Institution of Mechanical Engineers, Part C: Journal of Mechanical Engineering Science* 222: 1465-75

Ferziger JH, Peric M. 2002. *Computational methods for fluid dynamics*. Heidelberg, Germany: Springer-Verlag.

Forsythe JR, Squires KD, Wurtzler KE, Spalart PR. 2004. Detached-eddy simulation of the F-15E at High Alpha. *Journal of Aircraft* 41: 193-200

Franke R. 1982. Scattered data interpolation: tests of some methods. *Math. Comput.* 38: 181-200

Ghias R, Mittal R, Dong H, Lund TS. 2005. *Study of tip-vortex formation using large-eddy simulation.* Presented at American Institue of Aeronautics and Astronautics, Reno NV

Gilmanov A, Sotiropoulos F. 2005. A hybrid Cartesian/immersed boundary method for simulating flows with 3D, geometrically complex, moving bodies. *Journal of Computational Physics* 207: 457-92

Glowinski R, Pan TW, Helsa TI, Joseph DD. 1999. A distributed Lagrange multiplier/fictitious domain method for particulate flows. *International Journal of Multiphase Flow* 25: 755-94

Goldstein D, Handler R, Sirovich L. 1993. Modeling a No-Slip Flow Boundary with an External Force-Field. *Journal of Computational Physics* 105: 354-66

Groves N, Huang TT, Chang MS. 1989. Geometric Characteristics of DARPA SUBOFF Models*DTRC/SHD-1298-01*

Hama FR, Nutant J. 1963. Presented at Proceeding of the Heat Transfer and Fluid Mechanics Insitute, Standford, U.P, Sanford, California

Handler RA, Swean TF, Leighton RI, Swearingen JD. 1993. Length scales and the energy balance for turbulence near a free surface. *AIAA Journal* 31: 1998-2007

Hedges LS, Travin AK, Spalart PR. 2002. Detached-eddy simulation over a simplified landing gear. *J. Fluids Eng.* 124: 413-23

Heun K. 1889. Zur Theorie der Riemann'schen Functionen zweiter Ordnung mit vier Verzweigungspunkten. *Mathematische Annalen* 33

Hinze JO. 1975. *Turbulence*. McGraw-Hill.

Hsu MH, Chen CH, Teng WH. 2001. An arbitrary Lagrangian-Eulerian finite difference method for computations of free surface flows. *Journal of Hydraulic Research/De Recherches Hydrauliques* 39: 481-91

Huang CJ, Dong CM. *1998.* Numerical simulation of nonlinear water waves propagating over a submerged dike. *Montreal, Can,* 3: 313-19. ISOPE, Golden, CO, USA.

Huang CJ, Dong CM. 2001. On the interaction of a solitary wave and a submerged dike. *Coastal Engineering* 43: 265-86

Huang J, Carrica PM, Stern F. 2008. Semi-coupled air/water immersed boundary approach for curvilinear dynamic overset grids with application to ship hydrodynamics. *International Journal for Numerical Methods in Fluids* 58: 591-624

Huang TT, Liu HL, Groves NC, Forlini TJ, Blanton JN, Gowing S. 1992. *Measurements of Flows over an Axisymmetric Body with Various Appendages (DARPA SUBOFF Experiments).* Presented at Proceedings of the 19th Symposium on Naval Hydrodynamics, Seoul, Korea

Hunt JCR, Abell CJ, Peterka JA, Woo H. 1978. Kinematical studies of flows around free or surface-mounted obstacles - applying topology to flow visualization. *Journal of Fluid Mechanics* 86: 179-&

Hunt JCR, Wray AA, Moin P. 1988. *Eddies, streams, and convergence zones in turbulent flows.* Presented at Centre of turbulence research, CTR-S88

Hussain A. 1983. Coherent structures - reality and myth. *Physics of Fluids* 26: 2816-50

Hussein HJ, Martinuzzi RJ. 1996. Energy balance for turbulent flow around a surface mounted cube placed in a channel. *Physics of Fluids* 8: 764-64

Iaccarino G, Durbin P. *2000.* Unsteady 3D RANS simulations using the v^2-f model. *Center for Turbulence Research Annual Research Briefs*: 7.

Iaccarino G, Ham F. 2005. *Automatic mesh generation for LES in complex geometries.* Presented at Centre of turbulence research,

Iaccarino G, Verzicco R. 2003. Immersed boundary technique for turbulent flow simulations. *Applied Mechanics Reviews* 56: 331-47

Ippen AT, Raichlen F. 1957. Turbulence in civil engineering; measurements in free surface streams. *J. Hydraulics Div.,ASCE* 83: 1-27

Isaev SA, Lysenko DA. 2009. Calculation of unsteady flow past a cube on the wall of a narrow channel using URANS and the Spalart-Allmaras turbulence model. *Journal of Engineering Physics and Thermophysics* 82: 488-95

Iseya F, Ikeda H. *1986.* Effect of dune development on sediment suspension under unsteady flow conditions. *Proc. 30th Japanese Conference on Hydrualics, JSCE*: 505-10.

Jackson RG. 1976. Sedimentological and fluid-dynamic implications of the turbulent bursting phenomenon in geophysical flows. *Journal of Fluid Mechanics* 77: 531-60

Jasak H, Weller HG, Gosman AD. 1999. High resolution NVD differencing scheme for arbitrarily unstructured meshes. *International Journal for Numerical Methods in Fluids* 31: 431-49

Johnson W, Trickey C, Forsythe J, Albertson J, Leigh E. 2002. Experimental and computational investigation of the flow behind a C-130 with tailgate down. *AIAA*

Kalitzin G, Iaccarino G, Khalighi B. 2003. Towards an immersed boundary solver for RANS simulations. *AIAA*

Kanda M, R. M, Kasamatsu F. 2004. Large-eddy simulation of turbulent organized structures with and above explicitly resolved cube arrays. *Boundary-Layer Meteorology* 113

Kim J, Moin P, Moser R. 1987. Turbulence statistics in fully-developed channel flow at low Reynolds number. *Journal of Fluid Mechanics* 177: 133-66

Kim J, Park IR, Van SH. 2005. RANS computations of hydrodynamic forces and moments acting on a submarine. *Hydrodynamics VI - Theory and Applications*: 83

Kline SJ, Reynolds WC, Schraub FA, Rundstadler PW. 1967. The structure of turbulent boundary layers. *Journal of Fluid Mechanics* 30: 741

Komori S. 1989. Relationship between surface-renewal and bursting motions in an open-channel flow. *Journal of Fluid Mechanics* 203: 103-23

Komori S, Nagaosa R, Murakami Y, Chiba S, Ishii K, Kuwahara K. 1993. Direct numerical simulation of three-dimensional open-channel flow with zero-shear gas-liquid interface. *Physics of Fluids a-Fluid Dynamics* 5: 115-25

Krajnovic S, Davidson L. 2002. Large-eddy simulation of the flow around a bluff body. *AIAA Journal* 40: 927-36

Kumar S, Gupta R, Banerjee S. 1998. An experimental investigation of the characteristics of free-surface turbulence in channel flow. *Physics of Fluids* 10: 437-56

Lai MC, Peskin CS. 2000. An immersed boundary method with formal second-order accuracy and reduced numerical viscosity. *Journal of Computational Physics* 160: 705-19

Laitone EV. 1960. The second order approximation to cnoidal and solitary waves. *Journal of Fluid Mechanics* 9: 430-44

Lam K, Banerjee S. 1992. On the condition of streak formation in a bounded turbulent flow. *Physics of Fluids A (Fluid Dynamics)* 4: 306

Lamb H. 1975. *Hydrodynamics*. Cambridge University Press. 604 pp.

Laufer J. 1951. Investigation of turbulence in fully developed channel flow, NACA

Le H, Moin P. 1991. An improvement of fractional step methods for the incompressible Navier-Stokes equations. *Journal of Computational Physics* 92: 369-79

Leonard A. 1974. Energy cascade in large-eddy simulations of turbulent fluid flows. *Advances in geophysics* A 18: 237-48

Leonard BP. 1990. A stable and accurate convective modelling procedure based on quadratic upstream interpolation. *Comput. Methods Appl. Mech. Eng.*: 59-98

Leonard BP. 1991. The ULTIMATE conservative difference scheme applied to unsteady one-dimensional advection. *Comput. Methods Appl. Mech. Eng.* 88: 17-74

Leupi C, Altinakar MS. 2005 *3D finite element modeling of free-surface flows with efficient κ-ε turbulence model and non-hydrostatic pressure*. Atlanta, GA, United States: Springer Verlag, Heidelberg, D-69121, Germany. 33-40 pp.

Li CW, Wang JH. 2000. Large eddy simulation of free surface shallow-water flow. *International Journal for Numerical Methods in Fluids* 34: 31-46

Liu HL, Huang TT. 1998. Summary of DARPA Suboff Experimental Program Data*CRDKNSWC/HD-1298-11*

Liu WK, Liu Y, Farrell D, Zhang L, Bajaj C, Lee J, Hong J, Chen X, Hsu H. 2006. Immersed finite element method and its applications to biological systems. *Computer Methods in Applied Mechanics and Engineering* 195: 1722-49

Lohner R, Cebral JR, Camelli FE, Appanaboyina S, Baum JD, Mestreau EL, Soto OA. 2008. Adaptive embedded and immersed unstructured grid techniques. *Computer Methods in Applied Mechanics and Engineering* 197: 2173-97

Lombardi P, De Angelis V, Banerjee S. 1996. Direct numerical simulation of near-interface turbulence in coupled gas-liquid flow. *Physics of Fluids* 8: 1643

Lugt HJ. 1979. *The dilemma of defining a vortex.* Presented at Recent developments in theoretical and experimental fluid mechanics: Compressible and incompressible flows., Berlin

Majumdar S, Iaccarino G, Durbin P. *2001.* RANS solvers with adaptive structured boundary non-conforming grids. *Annual Research Briefs Stanford, CA*: 353-66.

Martinuzzi R, Tropea C. 1993. Flow around surface-mounted, prismatic obstacles placed in a fully developed channel flow. *Journal of Fluids Engineering, Transactions of the ASME* 115: 85-92

Martinuzzi RJ, Havel B. 2004. Vortex shedding from two surface-mounted cubes in tandem. *International Journal of Heat and Fluid Flow* 25: 364-72

Mathey F, Frohlich J, Rodi W. 1999. *Flow in a matrix of surface mounted cubes – Test case 6.2.* Presented at Proceedings, 8th ERCOFTAC/IAHR/COST Workshop on Refined Turbulence Modelling, Helsinki University of Technology, Helsinki, Finland

McQuivey RS, Richardson EV. 1969. Some turbulence measurements in open-channel flow. *J. Hydraulics Div.,ASCE* 95: 209-23

Meinders ER. 1998. *Experimental study of heat transfer in turbulent flows over wall-mounted cubes.* Delft University of Technology, Delft

Meinders ER, Hanjalic K. 1999. Vortex structure and heat transfer in turbulent flow over a wall-mounted matrix of cubes. *International Journal of Heat and Fluid Flow* 20: 255-67

Mendonca F, Allen R, de Charentenay J, Lewis M. *2002.* Towards understanding LES and DES for industrial aeroacoustic predictions. *Int.Workshop LES Acoust., Gottingen*.

Menter FR, Kuntz M. 2002. Adaptation of eddy viscosity turbulence models to unsteady seperated flow behind vechicles In *In The aerodynamics of heavy vehicles: trucks, buses and trains*, ed. R McCallen, F Browand, JC Ross. New York: Springer

Meselhe EA, Sotiropoulos F, Patel VC. *1995.* Three-dimensional numerical model for open-channels. *San Francisco, CA, USA,* 3: 2315-24. ASCE, New York, NY, USA.

Metcalf B, Longo J, Ghosh S, Stern F. 2006. Unsteady free-surface wave-induced boundary-layer separation for a surface-piercing NACA 0024 foil: Towing tank experiments. *Journal of Fluids and Structures* 22: 77-98

Metcalfe RW, Hussain AKMF, Menon S. *1985.* Coherent structures in a turbulent mixing layer: a comparison between direct numerical simulations and experiments. *Ithaca, NY, USA*: 4. 13-4. 19.

Mittal R, Iaccarino G. 2005. Immersed boundary methods. *Annual Review of Fluid Mechanics* 37: 239-61

Modh-Yosuf J. 1997. Combined immersed boundary/B-slpine methods for simulations of flows in complex geometries, in Annual Research Briefs. pp. 317-27: NASA Ames Research Centre/Standford University Centre for Turbulence Research, Stanford

Morton SA, Forsythe J, Squires KD, Cumming RM. 2003. *Detached-eddy simulations of fully aircraft experiencing Massively separated flows.* Presented at The 5th Asian Computational Fluid Dynamics Conference Busan, Korea

Muller A, Gyr A. 1986. On the vortex formation in the mixing layer behind dues. *J. Hydraulic Research, IAHR* 24: 359-75

Murayama M, Ito Y, Nakahashi K, Matsushima K, Iwamiya T. 2006. Viscous flow computations of aircraft with changing control surface deflection using

unstructured dynamic meshes. *International Journal for Numerical Methods in Fluids* 52: 925-40

Naheer E. 1978. Damping of solitary waves. *Journal of Hydraulic Research* 16: 235-49

Nakagawa H, Nezu I. 1979. Structure of instantaneous Reynolds stress over a permeable open-channel with suction or injection. *Memoirs of the Faculty of Engineering, Kyoto University* 41: 240-67

Nakagawa H, Nezu I. 1981. Structure of space-time correlations of bursting phenomena in an open-channel flow. *Journal of Fluid Mechanics* 104: 1-43

Nakagawa H, Nezu I, Ueda H. 1975. Turbulence of open-channel flow over smooth and rough beds. *Doboku Gakkai Rombun-Hokokushu/Proceedings of the Japan Society of Civil Engineers*: 155-68

Nezu I, Nakagawa H. 1989. Turbulent structure of backward facing step flow and coherent vortex shedding from reattachemnt in open channel flows. *Turbulent Shear flows* 6: 313-37

Nezu I, Nakagawa H. 1993. *Turbulence in open-channel flows*. Rotterdam: A.A.Balkema.

Nezu I, Rodi W. 1986. Open-channel flow measurements with a laser doppler anemometer. *Journal of Hydraulic Engineering* 112: 335-55

Niceno B, Dronkers ADT, Hanjalic K. 2002. Turbulent heat transfer from a multi-layered wall-mounted cube matrix: A large eddy simulation. *International Journal of Heat and Fluid Flow* 23: 173-85

Nikuradse J. 1929. Untersuchungen über die Strömungen des Wasser in Konvergenten und divergenten Kanälen *Forsh. Geb. Ing., Heft*: 289

Okamoto S, Tsunoda K, Katsumata T, Abe N, Kijima M. 1996. Turbulent near-wakes of periodic array of square blocks on a plate. *International Journal of Heat and Fluid Flow* 17: 211-18

Paik J, Sotiropoulos F, Porte-Agel F. 2009. Detached eddy simulation of flow around two wall-mounted cubes in tandem. *International Journal of Heat and Fluid Flow* 30: 286-305

Pan D. 2006. An immersed boundary method on unstructured Cartesian meshes for incompressible flows with heat transfer. *Numerical Heat Transfer Part B-Fundamentals* 49: 277-97

Pan Y, Banerjee S. 1995. A numerical study of free-surface turbulence in channel flow. *Physics of Fluids* 7: 1649-64

Pascarelli A, Iaccarino G, Fatica M. *2002.* Toward the LES of flow past a submerged hydrofoil. *Center for Turbulence Research*.

Peskin CS. 1972. Flow patterns around heart valves - Numerical method. *Journal of Computational Physics* 10: 252-&

Peskin CS. 1977. Numerical-Analysis of Blood-Flow in Heart. *Journal of Computational Physics* 25: 220-52

Peskin CS, McQueen DM. 1989. A 3-Dimensional Computational Method for Blood-Flow in the Heart .1. Immersed Elastic Fibers in a Viscous Incompressible Fluid. *Journal of Computational Physics* 81: 372-405

Piomelli U, Balaras E. 2002. Wall-layer models for large-eddy simulations. *Annual Review of Fluid Mechanics* 34: 349-74

Piomelli U, Zang TA. 1991. Large-eddy simulation of transitional channel flow. *Computer Physics Communications* 65: 224-30

Piomelli U, Zang TA, Speziale CG, Hussaini MY. 1990. On the large-eddy simulation of transitional wall-bounded flows. *Physics of Fluids A (Fluid Dynamics)* 2: 257-65

Rashidi M. 1997. Burst-interface interactions in free surface turbulent flows. *Physics of Fluids* 9: 3485-501

Rashidi M, Banerjee S. 1990. The effect of boundary conditions and shear rate on streak formation and breakdown in turbulent channel flows. *Physics of Fluids A: Fluid Dynamics* 2: 1827-38

Reichardt H. 1938. Messungen turbulenter Schwankungen. *Naturwissenschaften* Jahrg. 26: 404

Robinson SK. 1990. *Kinematics of turbulent boundary layer structure*. Stanford university, California

Robinson SK. 1991. Coherent motions in the turbulent boundary-layer. *Annual Review of Fluid Mechanics* 23: 601-39

Rodi W. 1997. Comparison of LES and RANS calculations of the flow around bluff bodies. *Journal of Wind Engineering and Industrial Aerodynamics* 69-71: 55-75

Roe PL. 1983. *Some contributions to the modelling of discontinuous flows*. La Jolla, CA, USA.

Sagaut P. 2002. *Large eddy simulation for incompressible flows*. Verlag Berlin Heidelburg: Springer.

Saha AK. 2006. Three-dimensional numerical study of flow and heat transfer from a cube placed in a uniform flow. *International Journal of Heat and Fluid Flow* 27: 80-94

Sakamoto S, Murakami S, Mochida A. 1993. Numerical study on flow past 2D square cylinder by large eddy simulation: comparison between 2D and 3D computations. *Journal of Wind Engineering and Industrial Aerodynamics* 50: 61-68

Sarpkaya T. 1971. Stationary and travelling vortex breakdowns. *Journal of Fluid Mechanics* 45: 545-&

Sarpkaya T. 1983. Trailing vortices in homogeneous and desity-stratified media. *Journal of Fluid Mechanics* 136: 85-109

Sarpkaya T. 1996. Vorticity, free surface and surfactants. *Annual Review of Fluid Mechanics* 28

Sarpkaya T, Elnitsky J, Leeker RE. *1988.* Wake of a vortex pair on the free surface *Proceedings of the 17th Sympsium on Naval Hydrodynamics, Washington DC*: 53-60.

Sarpkaya T, Merrill C, Carroll J. *1994.* Coherent structures in vortex/free-surface interaction *AIAA, Aerospace Sciences Meeting and Exhibit, 32nd, Reno*. AIAA.

Sarpkaya T, Neubert DE. 1994. Interaction of a streamwise vortex with a free-surface. *Aiaa Journal* 32: 594-600

Sarpkaya T, Suthon P. 1991. Interaction of a vortex couple with a free surface. *Experiments in Fluids* 11: 205-17

Schmidt S, Thiele F. 2002. Comparison of numerical methods applied to the flow over wall-mounted cubes. *International Journal of Heat and Fluid Flow* 23: 330-39

Sedighi K, Farhadi M. 2006. Three-dimensional study of vortical structure around a cubic bluff body in a channel. *FACTA UNIVERSITATIS series: Mechanical Engineering* 4: 1-16

Senocak I, Iaccarino G. *2005.* Progress towards RANS simulation of free surface flow around modern ships. *Centre of turbuence research Annual briefs*

Serrano M, Leigh E, Johnson W, Forsythe J, Morton SA, Squires KD. 2003. *Compitational aerodynamics of the C-130 in drop configurations.* Presented at 41st AIAA Aerospace Science Meeting and Exhibit, Reno, NV

Shah KB, Ferziger JH. 1997. A fluid mechanicians view of wind engineering: large eddy simulation of flow past a cubic obstacle. *Journal of Wind Engineering and Industrial Aerodynamics* 67-68: 211-24

Shekarriz A, Katz J, Liu HL, Huang TT, Fu TC. 1992. Study of junction and tip vortices using particle displacement velocimetry. *AIAA* 30: 145-52

Shen L, Zhang X, Yue DKP, Triantafyllou GS. 1999. The surface layer for free-surface turbulent flows. *Journal of Fluid Mechanics* 386: 167-212

Sheridan J, Lin JC, Rockwell D. 1995. Metastable states of a cylinder wake adjacent to a free surface. *Physics of Fluids* 7: 2099

Sheridan J, Lin JC, Rockwell D. 1997. Flow past a cylinder close to a free surface. *Journal of Engineering and Applied Science* 330: 1-30

Shi J, Thomas TG, Williams JJR. 2000. Free-Surface Effects in Open Channel Flow at Moderate Froude and Reynold's Numbers. *Journal of Hydraulic Research* 38

Simpson RL. 1996. Aspects of turbulent boundary layer separation. *Progress in Aerospace Sciences* 32: 457-521

Simpson RL. 2001. Junction flows. *Annual Review of Fluid Mechanics* 33: 415-43

Smutek R. 1969. Discussion of "Measurement of Turbulence in Water," by EV Richardson and RS McQuivey. *J. Hydraulics Div., ASCE*: 519-23

Song S, Eaton JK. 2004. Reynolds number effects on a turbulent boundary layer with separation, reattachment, and recovery. *Experiments in Fluids* 36: 246-58

Spalart PR. 2009. Detached-Eddy Simulation. *Annual Review of Fluid Mechanics* 41: 181-202

Spalart PR, Deck S, Shur ML, Squires KD, Strelets MK, Travin A. 2006. A new version of detached-eddy simulation, resistant to ambiguous grid densities. *Theoretical and Computational Fluid Dynamics* 20: 181-95

Spalart PR, Jou WH, Strelets M, Allmaras SR. *1997.* Comments on the feasibility of LES for wings, and on a hybrid RANS/LES approach. *1st AFOSR Int. Conf. on DNS/LES, Ruston, LA*. Greyden Press.

Squires KD. *2003.* Detached-eddy simulation: Current status and perspectives *5th International ERCOFTAC Workshop on Direct and Large-Eddy Simulation, Munich GERMANY* 9: 465-80.

Stoesser T, Mathey F, Frohlich J, Rodi W. 2003. *LES of flow over multiple cubes.* Presented at ERCOFTAC Bulletin,

Sue YC, Chern MJ, Hwang RR. 2005. Interaction of nonlinear progressive viscous waves with a submerged obstacle. *Ocean Engineering* 32: 893-923

Sung C-H, Jiang M-H, Rehee B, Percival S, Atsavaprance P, Hoh I-Y. 2002. *Validation of flow around a turing submarine.* Presented at 24th Symposium on Naval Hydrodynamics, Fukuoka, Japan

Svennberg SU, Fureby C. *2003.* LES computation of the flow over a smoothly contoured ramp. *41st AIAA Aerospace Sciences Meeting & Exhibit Reno, NV*.

Tennekes H, Lumley JL. 1972. *A first course in turbulence*. The M.I.T Press.

Thomas TG, Leslie DC, Williams JJR. 1994. Free-surface simulations using a conservative 3D code. *Journal of computational physics* 161: 52-68

Thomas TG, Williams JJR. 1995. Turbulent simulation of open channel flow at low Reynolds number. *International Journal of Heat and Mass Transfer* 38: 259-66

Thomas TG, Williams JJR. 1999. Simulation of skewed turbulent flow past a surface mounted cube. *Journal of Wind Engineering and Industrial Aerodynamics* 81: 347-60

Tsai W-T. 1998. A numerical study of the evolution and structure of a turbulent shear layer under a free surface. *Journal of Fluid Mechanics* 354: 239-76

Tseng Y-H, Meneveau C, Parlange MB. 2006. Modeling flow around bluff bodies and predicting urban dispersion using large eddy simulation. *Environmental Science and Technology* 40: 2653-62

Tseng YH, Ferziger JH. 2003. A ghost-cell immersed boundary method for flow in complex geometry. *Journal of Computational Physics* 192: 593-623

Tseng YH, Ferziger JH. 2004. Large-eddy simulation of turbulent wavy boundary flow-illustration of vortex dynamics. *Journal of Turbulence* 5

van Albada GD, van Leer B, Roberts JWW. 1982. a comprehensive study of computational methods in cosmic gas dynamics. *Astronomy and Astrophysics* 108: 76-84

van den Vorst HA. 1992. BI-CGSTAB: a fast and smoothly converging variant of BI-CG for the solution of non-symmetric linear systems. *SIAM J.Sci. Stat. Comput.* 13: 631-44

Venayagamoorthy SK, Koseff JR, Ferziger JH, Shih LH. 2003. Testing of RANS turbulence models for stratified flows based on DNS data. *Center for Turbulence Research, Annual Research Briefs*

Versteeg HK, Malalasekera W. 2007. *An introduction to Computational fluid dynamics the finite volume method*. Harlow, England: Pearson Education Limited.

Verzicco R, Orlandi P, Mohd-Yusuf J, Haworth D. *1998.* LES in complex geometries using boundary body forces. *Centre of Turbulence Research*: 171-86.

Wan D, Turek S. 2007. Fictitious boundary and moving mesh methods for the numerical simulation of rigid particulate flows. *Journal of Computational Physics* 222: 25-56

Wang L, Dong YH, Lu XY. 2005. An investigation of turbulent open channel flow with heat transfer by large eddy simulation. *Computers & Fluids* 34: 23-47

Wasistho B, Squires KD. *2001*. Numerical investigation of the separated flow over a smoothly contoured ramp. *2nd Symp. on Turbulence and Shear Flow Phenomena*.

Watt GD, Baker CR, Gerber AG. 2006. ANSYS CFX-10 RANS normal force predictions for the series 58 model 4621 unappended axisymmetric submarine hull in translation. *Defence Research and Developement, Canada*

Werner H, Wengle H. *1991*. Large-Eddy Simulation of turbulent flow over and around a square cube in a plate channel. *8th Symposium on Turbulent Shear Flows*: 155-68.

Widnall SE. 1975. The structure and dynamics of a vortex filaements *Annual Review of Fluid Mechanics* 7: 141-65

Wu BS, Xing F, Kuang XF, Miao QM. 2005. Investigation of hydrodynamic characteristics of a submarine moving close to the sea bottom with CFD methods. *Journal of Ship Mechanics* 9

Xie Z, Castro IP. 2006. LES and RANS for turbulent flow over arrays of wall-mounted obstacles. *Flow, Turbulence and Combustion* 76: 291-312

Xing T, Kandasamy M, Stern F. 2007. Unsteady free-surface wave-induced separation: analysis of turbulent structures using detached eddy simulation and single-phase level set. *Journal of Turbulence* 8: 1-35

Yakhot A, Liu H, Nikitin N. 2006. Turbulent flow around a wall-mounted cube: A direct numerical simulation. *International Journal of Heat and Fluid Flow* 27: 994-1009

Yang C, Lohner R. 2003. *Prediction of Flows over an Axisymmetric Body with Appendages.* Presented at *The 8th International Conference on Numerical Ship Hydrodynamics*, Busan, Korea

Yeung RW, Nguyen TC. 1999. waves generated by a moving source in a two-layer ocean of finite depth. *Journal of Engineering Mathematics* 35: 85-107

Young DMJ. 1971. *Iterative Solution of Large Linear Systems*. Academic Press.

Yu G, Avital EJ, Williams JJR. 2008. Large Eddy Simulation of Flow Past Free Surface Piercing Circular Cylinders. *J. Fluids Eng.* 130: 101304-1 - 04-9

Yue W, Lin C-L, Patel VC. 2005. Large eddy simulation of turbulent open-channel flow with free surface simulated by level set method. *Physics of Fluids* 17: 025108

Zhang N, Ying L, Yao H, Shen H, Gao Q. 2005. Numerical simulation of free surface viscous flow around submarine. *Journal of Ship Mechanics* 9: 29-39

Zhang N, Zheng ZC. 2007. An improved direct-forcing immersed-boundary method for finite difference applications. *Journal of Computational Physics* 221: 250-68

Zhu J. 1992. ON THE HIGHER-ORDER BOUNDED DISCRETIZATION SCHEMES FOR FINITE VOLUME COMPUTATIONS OF INCOMPRESSIBLE FLOWS. *Computer Methods in Applied Mechanics and Engineering* 98: 345-60

Zhu Q, Liu YL, Yue DKP. 2006. Dynamics of a three-dimensional oscillating foil near the free surface. *AIAA* 44: 2997-3009